THE UNIVERSITY *of* EDINBURGH

Triggering the Cambrian Explosion: Carbon Cycle reorganisation and the rise of Metazoans

Frederick T. Bowyer

A dissertation submitted to the University of Edinburgh in accordance with the requirements for award of the degree of Doctor of Philosophy in the Faculty of Science

School of Geosciences

Date of submission: 05/06/2018

Author Declaration

I, Frederick Bowyer, confirm that the work submitted is my own, except where work which has formed part of jointly-authored publications has been included. My contribution and those of the other authors to this work have been explicitly indicated throughout the thesis. I confirm that appropriate credit has been given within this thesis where reference has been made to the work of others. This thesis is submitted to the University of Edinburgh in accordance with the requirements for award of the degree of Doctor of Philosophy in the Faculty of Science. The work presented herein has not been submitted for any other degree or professional qualification.

Frederick Bowyer (04/09/2018)

Abstract

Numerous detailed geochemical studies of Ediacaran (~635 – 541 Ma) marine successions provide snapshots into the palaeoenvironmental redox conditions which accompanied examples of the earliest metazoans in the fossil record. Spatial heterogeneity with respect to palaeomarine redox is evident from reconstructions of geographically-widespread Ediacaran environments. This project provides new data of local-scale redox within a paleogeographic and sequence stratigraphic framework in order to explore the mechanisms which controlled water column redox variations and the potential impact on early macro-benthic ecosystems.

Lower than present atmospheric and oceanic oxygen concentrations enabled some shallow marine settings to remain poised at iron reduction until well into the Cambrian and likely influenced regional-scale ecosystem structure and stability. Many basins had a shallow and highly dynamic chemocline above anoxic (ferruginous or euxinic) or low oxygen (manganous) waters. Regional differences in palaeoredox were likely controlled primarily by local detrital nutrient provision and organic matter remineralisation and the redox state of the global deep ocean was most likely similarly heterogeneous (but this remains uncertain). It is suggested that cratonic positioning and migration throughout the Ediacaran Period, in combination with gradually increasing dissolved oxygen loading, may have provided a long-term control on redox evolution through regulating circulation mechanisms in the Mirovian Ocean. Some unrestricted lower slope environments from mid-high latitudes benefited from sustained oxygenation via downwelling, whilst cratonic isolation or transit towards more equatorial positions stifled pervasive ventilation either through ineffective surface ocean mixing, Ekman-induced upwelling, elevated surface ocean productivity, or a combination of these processes.

Co-preservation of largely-enigmatic fossil forms within sedimentary rocks of the late Ediacaran Nama Group of southern Namibia have allowed the four-dimensional reconstruction of local redox dynamics and associated biotic establishment. This has been made possible through collation of previously published fossil occurrence and geochemical information alongside new palaeoredox and palaeoproductivity estimates based on iron speciation, major element and carbonate-bound iodine data. This is further supplemented by the first detailed assessment of the paragenetic sequence and diagenetic relationships of carbonates which precipitated within the earliest metazoan reef framework.

Skeletal invertebrate taxa in the Zaris Sub-Basin of the lower Nama Group (~550-547 Ma), grew above wave base where micritic carbonate sediment often shows evidence for early dolomitisation. Mid-ramp *Cloudina* reefs composed of open, highly porous structures formed multiple, successive assemblages. Thin layers of dolomitised sediment and dolomite cement terminate each assemblage. Reef cements show a paragenetic sequence from synsedimentary, early marine cement through to final burial,

each of which were precipitated under dynamic redox conditions. These cements likely record a general shallow to deeper water transect, from oxic shallow waters to low oxygen manganous waters and finally to oxic, shallow burial conditions. Transient incursions of upwelled, anoxic, ferruginous and dolomitising waters may have occurred during short-term, transgressive cycles, although the timing for this is poorly constrained. Such incursions may have terminated Ediacaran benthic communities that grew close to the chemocline.

Viewed in its entirety, the palaeoredox record of the Nama Group reveals evidence for a pronounced shift in the depth of the ferruginous redoxcline from shallow to deeper levels in the water column through time, which was accompanied by a reduced frequency of anoxic incursions onto the shallow shelf. This transition approximately coincided with the first appearance and subsequent diversification of novel sediment bioturbators in the Lower Urusis Formation (~547-542 Ma). It is proposed that the observed coevolution of palaeoredox and ichnofossil diversity may directly relate to the impact of bioturbation on phosphorus retention. In this way, the diversification of burrowing forms effectively oxygenated the sediment column, prevented efficient P recycling to the water column and limited the detrimental impact of productivity-induced anoxia in the local environment. However, this hypothesis remains to be tested and would benefit from a focused study of palaeoproductivity employing targeted analyses of total organic carbon and sedimentary phosphorus speciation. It is further proposed that the persistent spatial separation of anoxic deep waters from habitable ecospace, implied by the fossil distribution of phylogenetically-enigmatic soft-bodied forms, qualitatively supports the inference that at least intermittently oxic conditions (at or above E_H typical of ferrous iron oxidation) were a metabolic requirement of these organisms.

Finally, four new sections of the late Ediacaran, deposited approximately time-equivalent to aforementioned sediments of the Nama Group, are described and preliminary geochemical data reported. These include two shallow marine carbonate-dominated sections of the southeast Siberian Craton which correspond to the Yudoma Formation and two sections of the Dengying and lower Zhujiaqing (and correlative) Formations deposited on the Yangtze Block, South China. Integrated proxy methods are able to distinguish palaeoredox heterogeneity between and within early animal ecosystems and test the influence of anoxia on ecosystem structure. The first and last appearances of *Treptichnus pedum* and *Cloudina* respectively, which globally bracket the boundary between the Ediacaran and Cambrian Periods, show no identifiable range overlap in any sections analysed in this study. This suggests that the first appearance of the organism responsible for characteristic *T. pedum* may have lived approximately contemporaneous in oxic habitable refuges of all regions in this study, regardless of the dominance of reducing conditions that persisted in coeval deeper environments in many areas.

Lay Summary

Candidate fossils of the earliest animals are found in rocks which date to between 635 and 571 million years ago (Ma). However, it is not until the latest Ediacaran period (< 550 Ma) that some body fossils and trace fossils are confidently thought to represent mobile and active animals. These organisms inhabited marine environments and are found globally in rocks which represent shallow platform to slope settings. Over the past ~30 years, numerous studies have aimed to chemically characterise these sedimentary rocks and better understand the integrated history of early animal ecosystem evolution within an environmental context. In order to correctly identify primary water column chemistry from sedimentary rocks, it is necessary to develop and utilise proxy methods which are based on elemental concentrations, elemental compounds, species, and isotopic ratios. Crucially, this proxy toolkit must successfully discriminate between primary depositional, and diagenetically altered elemental compositions. Diagenesis is the post-depositional physical and/or chemical alteration of rock during shallow and deeper burial. A primary focus of Ediacaran palaeoenvironmental research has concerned changes to the oxygen concentration of the water column, which is thought to directly relate to the evolution of animals and energetic lifestyles. This is due to the requirement of oxygen in providing high energy yields associated with aerobic respiration in mitochondria.

This study focuses on reconstructing chemical environments in the final ten million years of the Ediacaran in three globally-distributed, fossiliferous sedimentary successions of southeast Siberia, south China and southern Namibia. Particular attention is given to the characterisation and interpretation of primary water column redox conditions.

We find that it is possible to associate relative sea level with changes in original water column redox conditions where patterns of regional sedimentation are best characterised. The earliest animals to form shells or skeletons inhabited well-oxygenated shallow waters where the influence of anoxia was minimal. Finally, the evolution of burrowing occurred in shallow, well oxygenated environments irrespective of dominant redox conditions in coeval deeper waters and this ecological habit likely resulted in profound feedbacks on local nutrient cycling.

Acknowledgements

Being given the opportunity to study something in which I am fascinated for four years has been a tremendous privilege and I am very thankful to many people for making it possible. There is a wealth of dedicated research by many scientists that have together shone a torch into this mysterious period of Earth's history and I have found their combined works extremely inspiring. I hope that this thesis may contribute, in some small way, to the understanding of our peculiar ancestors and their world.

I would firstly like to thank my supervisors: Rachel Wood, Alex Thomas and Simon Poulton. I could never have asked for a more inspirational and entertaining crew to work with and, should I be fortunate enough to continue research in this field, I hope I have the chance to collaborate with you throughout. Rachel, you have been a fantastic mentor ever since my undergraduate years and I am enormously grateful for your guidance and encouragement in all aspects of academic life. Your positivity and enthusiasm have kept me afloat throughout my PhD and countless enlightening discussions over coffee and, perhaps occasionally, wine have always steered me in the right direction. Being part of your research team on fieldwork expeditions include some of my happiest memories. Simon, for the record, you have exceptional taste in music and a talent for karaoke. Thank you for sharing the best Leeds has to offer and for making me feel like part of the family in the Cohen Labs alongside the great Jenny Thompson, Kathy Doyle and Mark Xiong. Your work has been particularly inspiring to me and without your generosity and openness, iron speciation in Edinburgh would have remained merely a dream. Alex, you have been great fun to work with in the lab and without your direction, much of the data in this thesis would not exist! Thank you for being patient with my stupid questions and helping refine my craggy geologist brain to the technicalities of applied chemistry and critical thinking.

All of this started with the tireless help of Romain Guilbaud during my Masters year. Romain, without your meticulous skill in the lab, I would have no doubt stumbled blindly into a hole. Your careful tutelage and supervision taught me a great deal and nurtured my interest in the methodologies employed in this thesis. You are also a great singer, don't doubt it.

Amelia Penny, exploring in the field and working in the lab with you has been terrific fun. Thank you so much for your expert driving skills, fantastic music taste and for braving the Newfoundland clifftops! Thanks most of all for your encouragement and help. I am certain your Helsinki postdoc is just the beginning of a spectacular academic career.

Throughout my PhD years, I have had the good fortune to be surrounded by great drivers. Rosalie Tostevin, thank you for saving all of our lives when you avoided that gas canister. Working with you in the field and the laboratory is extreme fun. Thank you for all the technical discussions and for soothing

Amelia and I with that terrible Christmas film in the tent. I'm very much looking forward to reading your future publications of which I'm sure there will be many greats!

Everyone in the Nama team: Andrew Curtis, Shona Curtis-Walcott, Cecilie Iipinge, Amelia Penny, Rosalie Tostevin, Andrey Zhuravlev and of course, Rachel Wood, thank you all so much for two of the most exciting and scientifically stimulating expeditions I have been a party to. The long days in the vast palaeontologist's playground of Namibia and late night wine-infused fireside conversations under the Milky Way seem like a beautiful dream. Special thanks particularly go to Andrew Curtis, without whose generosity I would have been left living in a hedge for the five months prior to final thesis hand-in!

Much of the work presented in this thesis would not have been possible without the skilled technical assistance provided by Ian Butler, Chris Hayward, John Craven, Clare Peters, Elaine McDougall, Nic Odling, Andy Connelly, Stephen Reid, Mike Hall and the Grant Institute workshop. You are all legends and I am hopelessly in your debt.

Many thanks also to the 'Friends of the Ediacaran' group: Phil Wilby, Charlotte Kenchington, Alex Liu, Emily Mitchell, Frances Dunn and Jennifer Hoyal Cuthill for stimulating conversations and pro insight into the details of Ediacaran stratigraphy and palaeontology. I would further like to thank Sasha Turchyn and Harold Bradbury for providing novel calcium isotope data for the Nuuchchalakh section of Siberia in addition to Dalton Hardisty and Tim Lyons for providing data of carbonate-bound iodine for carbonates of the Nama and Yudoma Groups. The collection of these preliminary data are no small feat and provide the opportunity for exciting future research collaborations.

I have been incredibly fortunate during my PhD to have benefited from expert advice provided by people outwith my immediate research group. I would particularly like to thank Gerard Germs for kindly sharing his enthusiasm for the Nama Group and providing specific unpublished information which has greatly influenced fieldwork sampling strategies and aided greater understanding of the Nama Group as a whole. Thanks also go to Charlie Hoffmann for clarifying details of stratigraphy of the Naukluft Nappe complex and Gobabis area and for providing large quantities of sample material for zircon U-Pb dating. In the latter regard, I would also like to sincerely thank Dan Condon, Adrian Wood and Joshua Bright for encouraging ongoing efforts to infill the gaps in the Nama Group geochronological record. This constitutes an ongoing research project in collaboration with the NERC Isotope Geoscience Facility at the BGS in Keyworth.

Louis Kinnear, without your delicious vegan cuisine I would likely have shrivelled to the size of a shrimp and without the rantings of your great philosophical mind, I might have slipped into the dangerous

position of becoming a massive bore. The six months of our co-habitation will forever stand out in my memory!

I am greatly indebted to my family. To my parents, you have both been there for me throughout all hardship and you have both taught me the importance of perseverance, which is undoubtedly one of the key skills required in the completion of a PhD. To my siblings, each one of you have inspired me in your own wonderfully unique way and, as the youngest member of the knobbly knees club, I owe you all a debt of gratitude. To the family Villevielle for welcoming me into your astonishingly relaxing home with open arms and always treating me like one of your own when I stole away on your family vacations. Lastly, to Mélissa, the final and possibly the greatest singer in this list, thank you for being by my side through everything and putting up with my gradual introversion in the final months of thesis writing. I couldn't have made it without the splashes of your artistic colour.

I dedicate this thesis to my grandfather, whose keen scientific and artistic imagination unsuspectingly cultivated a path along similar interests and to my family, who have been there for me throughout.

Glossary of Common Abbreviations

AAS ..... Atomic Absorption Spectrometry

BSR ..... Bacterial sulfate reduction

CA-ID-TIMS ..... Chemical Abrasion Isotope Dilution Thermal Ionisation Mass Spectrometry

Ce/Ce* ..... Cerium anomaly

$\delta^{13}C_{carb}$ ..... Carbon isotope composition of carbonate

$\delta^{13}C_{org}$ ..... Carbon isotope composition of organic carbon

$\delta^{18}O_{carb}$ ..... Oxygen isotope composition of carbonate

$\delta^{98/95}Mo$ ..... Molybdenum isotope composition

$\delta^{34}S_{CAS}$ ..... Sulfur isotope composition of Carbonate Associated Sulfate

$\delta^{34}S_{py}$ ..... Sulfur isotope composition of pyrite

E_H ..... Reduction potential

EPMA ..... Electron Probe Micro-analysis

Fe_{HR} ..... Highly reactive iron

Fe_{PR} ..... Poorly reactive iron

Fe_{py} ..... Pyrite bound iron

Fe_T ..... Total iron (wt%)

Ga ..... Giga-annum ($x10^9$ years ago/billion years ago)

HST ..... Highstand Systems Tract

ICP-OES ..... Inductively Coupled Plasma Optical Emission Spectrometry

K1 ..... First transgressive sequence of Witputs Subbasin (Kanies and Mara Members) (after Saylor et al., 1995)

K2 ..... Second transgressive sequence of Wiputs Subbasin (Kliphoek and Mooifontein Members) (after Saylor et al., 1995)

Ma ..... Mega-annum (x10^6 years ago/million years ago)

MFS ..... Maximum Flooding Surface

Myrs ..... Millions of years

NOE ..... Neoproterozoic oxygenation event

OMZ ..... Oxygen minimum zone

OS1 ..... Lower Omkyk Member

OS2 ..... Upper Omkyk Member

PAL ..... Present atmospheric levels

REE ..... Rare Earth Elements

REE(+Y) ..... Rare Earth Elements (+Yttrium)

RSE ..... Redox Sensitive Elements

S1 – S5 ..... Sequence stratigraphic subdivision of the Schwarzrand Subgroup in the Witputs Subbasin (after Saylor et al., 1995)

SB ..... Sequence Boundary

SHRIMP ..... Sensitive High Resolution Ion Microprobe

SIMS ..... Secondary Ionisation Mass Spectrometry

TST ..... Transgressive Systems Tract

$\delta^{238/235}U$ ..... Uranium isotope composition

XRD ..... X-ray Diffraction

Table of Contents

Author's declaration 1

Abstract 3

Lay Summary 5

Acknowledgements 7

Glossary of common abbreviations 13

Table of contents 15

List of Figures 21

List of Tables 25

1 Introduction: Animal evolution and the role of oxygen

Title page and author contributions 27

1.1 The record of Ediacaran Macrobiota and Metazoa 28

1.2 Oxygen and metabolism 36

1.3 Redox and metazoan ecology in the modern 37

1.4 Controls on redox zonation in the modern

1.4.1 Productivity and the Biological Pump 40

1.4.2 Upwelling and Downwelling 41

1.4.3 Restricted Environments 42

1.4.4 Unrestricted continental shelf 43

1.5 Rationale of palaeoredox proxies 44

1.6 Global ocean proxies

1.6.1 Redox sensitive elements 46

1.6.2 Redox sensitive isotopic fractionation 46

1.6.3 Sulfur isotope compositions of sulfate and pyrite ($\delta^{34}S_{CAS}$ and $\delta^{34}S_{py}$) 48

1.7 Determining basin restriction 50

1.8 Local/regional proxies
1.8.1 The iron shuttle and iron speciation 50
1.8.2 Rare Earth Elements and Cerium anomalies 54
1.8.3 Iodine/Calcium 54
1.8.4 Trace fossils 55
1.9 Proxy limitations 55
1.10 Methodologies employed in this thesis
1.10.1 Fieldwork and sample preparation 56
1.10.2 Iron speciation and major element analysis 56
1.10.3 Cathodoluminescence microscopy 59
1.10.4 Electron Microprobe and X-Ray Diffraction analyses 59
1.10.5 Iodine/(Calcium + Magnesium) 59
1.10.6 Calcium isotope 60
1.11 Thesis Aims and Hypotheses 60
1.12 Thesis outline 62
1.13 Thesis contributions 63

2 The record of Ediacaran marine redox

Title page, abstract and author contributions 65
2.1 Introduction: The Ediacaran global ocean 66
2.2 Records of local/regional redox in Ediacaran palaeoenvironments 67
2.2.1 Yangtze Block 68
2.2.2 Laurentia 79
2.2.3 Avalonia 83
2.2.4 East European Platform 84
2.2.5 Río de la Plata Craton 86
2.2.6 Kalahari Craton 87
2.3 Discussion
2.3.1 Palaeogeographic context 98
2.3.2 Complex multicellular eukaryotes 102
2.3.3 Benthic sulfide stress of the Yangtze Block 103
2.3.4 Skeletal metazoans 104
2.3.5 Earliest metazoan reefs 105
2.4 Conclusions 106

3 Enhancing the palaeoredox record of the Nama Group, Namibia

Title page, abstract and author contributions **109**

3.1 Introduction **110**

3.2 The Nama Group: Geological and palaeontological overview **112**

3.3 Samples and Methods **115**

3.4 Section Details

3.4.1 Farm Omkyk: Omkyk Member **118**

3.4.2 Farm Driedoornvlakte: Omkyk Member **119**

3.4.3 Farm Kliphoek: Nudaus Formation **119**

3.4.4 Zaris Subbasin; Schwarzrand Subgroup **120**

3.5 Results and Interpretations

3.5.1 I/(Ca+Mg) of the Omkyk Member **121**

3.5.2 Slope sediments at Driedoornvlakte **123**

3.5.3 Nudaus Formation, Farm Kliphoek **126**

3.5.4 The Schwarzrand Subgroup, Zaris Subbasin **128**

3.6 Sedimentation rate and basal Nama age estimate updated **133**

3.7 A preliminary assessment of palaeoproductivity

3.7.1 Phosphorus **135**

3.7.2 Excess barium **137**

3.8 Note on elemental characteristics of sampled sediments

3.8.1 Titanium, Aluminium and Chromium **139**

3.8.2 The Chemical Index of Alteration **140**

3.9 Discussion

3.9.1 Redox evolution and fossil occurrence **142**

3.9.2 Oxygen requirerments and Nama organisms **146**

3.10 Conclusions **152**

4 The paragenetic sequence of carbonate cements at Driedoornvlakte: inferring water column palaeoredox

Title page, abstract and author contributions **155**

4.1 Introduction **157**

4.1.2 The dolomite dilemma **157**

4.1.3 Petrographic and paragenetic evidence for penecontemporaneous marine

dolomite cements in the Precambrian 159
4.2 Redox and ecology during deposition of the Omkyk Member 162
4.2.2 Architecture of the Driedoornvlakte reef complex 163
4.3 Reconstructing cement stratigraphy of *Cloudina* reef carbonates
4.3.1 Methods 167
4.3.2 Results 168
4.4 Discussion
4.4.1 Interpreting combined visual microscopy and electronprobe data 179
4.4.2 Origin of dolomite cements 181
4.4.3 Regional dolomitisation in the Nama basin 186
4.5 Conclusions 187

5 Precambrian – Cambrian sections of the southeast Siberian craton and Yangtze Block
Title page, abstract and author contributions 189
5.1 Introduction: The Basal Cambrian Conundrum 190
5.2 Methods 192
5.3 Introduction to the Siberian Platform Ediacaran-Cambrian boundary problem 194
5.3.1 The Yudoma-Maya Depression 198
5.3.2 Yudoma-Maya Confluence 200
5.3.3 Nuuchchalakh 200
5.3.3.2 Nuuchchalakh geochemistry 201
5.3.4 Kyra-Ytyga 204
5.3.4.2 Kyra-Ytytga geochemistry 205
5.3.5 Southeast Siberia synthesis 205
5.4 The Dengying and Zhujiaqing Formations of the Yangtze Block 208
5.4.1 Yinchangpo, Yunnan 209
5.4.1.2 Yinchangpo geochemistry 210
5.4.2 Wuhe, Hubei 215
5.4.2.2 Wuhe geochemistry 218
5.4.3 Yangtze Block synthesis 221
5.5 Discussion: Shallow habitable space, fossil affinities and oxygen requirements 223
5.5.1 Southeast Siberia 223
5.5.2 Yangtze Block 225
5.6 Conclusions 226

6 Discussion and conclusions

Title page **229**

6.1 A biotic response to redox in the Ediacaran **230**

6.2 Redox evolution and biodiversity of the Nama Group **233**

6.3 Through the veil of diagenesis **234**

6.4 How distinct were the Ediacaran and Cambrian **237**

6.5 Future work **238**

References **241**

Appendices

A. Figure and sample site information **293**

B. Compiled elemental data **359**

C. EPMA cement stratigraphy raw data **409**

D. Fossil diagram key and occurrence catalogue **441**

E. Contribution to Scientific Publications **467**

List of Figures

1.1 Schematic representation of major changes in marine redox, secular variation in the carbonate carbon isotope record, major evolutionary innovations and stratigraphic correlation of major deposits across the terminal Cryogenian to terminal Cambrian Periods **29**

1.2 Fossil examples of the Avalon assemblage **31**

1.3 Fossil examples of the White Sea assemblage **33**

1.4 Fossil examples of the Nama assemblage **33**

1.5 Skeletal invertebrates of the terminal Ediacaran Period **35**

1.6 Schematic diagram of the mitochondrial electron transport chain **36**

1.7 Schematic representation of redox zonation in productive near-shore environments **41**

1.8 Schematic representation of hierarchical electron acceptor zonation **45**

1.9 Schematic representation of low temperature iron cycling in an anoxic basin **51**

2.1 Summary figure of local palaeoredox studies utilising iron speciation for sedimentary deposits of the Ediacaran to early Cambrian Periods and their geographic position **68**

2.2 Correlation and schematic palaeoredox representation of Ediacaran to early Cambrian age sections in South China. Palaeoredox interpretation based on referenced publications **73**

2.3 Correlation and schematic palaeoredox representation of sections from Laurentia (Canada). Palaeoredox data from cited publications based on iron speciation **81**

2.4 Correlation and schematic palaeoredox representation of sections from western Avalonia (Newfoundland), the East European Platform (western Russia) and the Río de la Plata Craton (Uruguay). Palaeoredox data from cited publications based on iron speciation **85**

2.5 Correlation and schematic palaeoredox representation of sections from the Kalahari Craton (Nama Group, Namibia). Iron speciation data from cited publications and new data **89**

2.6 Schematic dioramas illustrating mechanisms controlling local palaeoredox distribution on the Yangtze Block and the Kalahari craton **97**

2.7 A model for partial control on nutrient upwelling and oxygenated surface water downwelling by palaeogeographic position and associated changes in long-term local redox state across the Ediacaran and early Cambrian Periods **99**

3.1 Geological map and schematic subbasin cross section of the Nama Group and major sampling sites discussed in the text **113**

3.2 Stratigraphic log and accompanying published and unpublished chemical data of the Omkyk Member exposed on Farm Omkyk **122**

3.3 (**a**) Geological map and (**b**) stratigraphic log of Driedoornvlakte reef complex and accompanying chemical data **124**

3.4 (**a**) Geological map and (**b**) stratigraphic log of Nudaus Formation deposits on Farm Kliphoek and accompanying chemical data **127**

3.5 (**a**) Geological map of the Schwarzrand Subgroup north of Osis showing relative positions of individual sampling localities, and (**b**) schematic log and accompanying chemical data of samples collected along the D850 road transect **129**

3.6 Schematic log and accompanying geochemical data of samples collected along the D860/C14 road transect **131**

3.7 Schematic stratigraphic log and additional compiled chemical data for samples of the Kuibis and Schwarzrand Subgroups collected on the 2016 field excursion **132**

3.8 Relationships between phosphorus and elemental indicators of detrital input and biogenic enrichment in sediments of the Nama Group **136**

3.9 Ternary diagrams to show the chemical index of alteration for siliciclastic samples of the Kuibis and Schwarzrand Subgroups collected on the 2016 field excursion **140**

3.10 Composite figure of carbonate carbon isotopes, iron speciation and all published fossil occurrence in the Nama Group (not to scale). Breakdown of taxonomic diversity on reverse **143**

3.11 Schematic representation of changing redox profiles in the water column during deposition of the Nama Group **147**

3.12 Schematic plan view representations of fossil distribution and redox throughout deposition of the Nama Group **149**

3.13 Dioramas depicting proposed feedbacks of regional facies changes, ichnotaxa diversity and nutrient cycling on water column redox in the Nama basin..... **150**

4.1 Structure of calcite relative to stoichiometric dolomite (well ordered)..... **158**

4.2 Crystallographic diagrams for rhombic carbonates..... **160**

4.3 Geological map of the Nama Group of southern Namibia with study area indicated and schematic stratigraphic column of sediments on Farm Driedoornvlakte..... **163**

4.4 Geological map of isolated carbonate platform build-up on Farm Driedoornvlakte, highlighting position of sampled Unit..... **164**

4.5 Field photographs of *Cloudina* reef in Unit 3m..... **165**

4.6 Size distribution and *Cloudina* abundance through selected reef layer..... **166**

4.7 Proposed paragenetic sequence of cements in the Driedoornvlakte reef of Unit 3m..... **169**

4.8 Transmitted light photomicrographs of Driedoornvlakte cements (PPL)..... **171**

4.9 Cathodoluminescence photomicrographs of Driedoornvlakte cements..... **172**

4.10 Selected photomicrographs to show the petrographic characteristics of D2 and C1 cement generations at Driedoornvlakte..... **173**

4.11 Additional selected photomicrographs of Driedoornvlakte carbonate cements..... **174**

4.12 Box and whisker plots of basic statistics and ranges in elemental concentration between *Cloudina* and individual cement generations at Driedoornvlakte..... **176**

4.13 $\delta^{13}C_{carb}$ and $\delta^{18}O_{carb}$ cross plot for separated skeletal, calcite and dolomite cements at Driedoornvlakte..... **178**

4.14 Schematic illustration of Omkyk Member during reef growth of Unit 3m at Driedoornvlakte and associated paragenetic sequence..... **184**

4.15 Simplified cross section of water column palaeoredox in the Zaris Sub-basin during deposition of the Omkyk Member..... **185**

5.1 The series of events which bracket the Ediacaran-Cambrian transition..... **191**

5.2 Map of Siberia with major structural units and geological map of southeast Siberia with major sections discussed in the text..... **195**

5.3 Chemostratigraphic relationships between sections along the Aldan, Uchur and Yudoma Rivers of the Uchur-Maya region, southeast Siberia..... **197**

5.4 Stratigraphic relationship of sections along the Maya and Yudoma Rivers..... **199**

5.5 Stratigraphic log with biostratigraphic and geochemical data of Nuuchchalakh section..... **202**

5.6 Stratigraphic log with biostratigraphic and geochemical data of the Kyra-Ytyga section..... **204**

5.7 Ternary diagram showing variability in the chemical index of alteration (CIA) between siliciclastic samples of the Yudoma River..... **207**

5.8 Graphs to show the difficulty involved in assessment of local baseline Ba/Al (and Ba/Ti) for samples of the Yudoma River..... **208**

5.9 (**a**) Stratigraphic log with biostratigraphic and geochemical data of the Yinchangpo section..... **211**

5.9 (**b**) enlarged view of the proposed Ediacaran-Cambrian boundary interval at Yinchangpo..... **212**

5.10 (**a**) Proxies for degree of alteration including covariation of $\delta^{13}C$ and $\delta^{18}O$ and the relationship between depleted $\delta^{18}O$ and FeT enrichment and (**b**) The relationship between Ba and detrital elements at Yinchangpo..... **213**

5.11 Stratigraphic log with biostratigraphic and geochemical data of the Wuhe section..... **216**

5.12 Outcrop and transmitted light photomicrographs of burrow systems in organic carbon-rich sediments of the Shibantan Member at Wuhe section..... **217**

5.13 (**a**) Proxies for degree of alteration including covariation of $\delta^{13}C$ and $\delta^{18}O$ and the relationship between depleted $\delta^{18}O$ and FeT enrichment and (**b**) The relationship between Ba and detrital elements at Wuhe..... **219**

5.14 Dioramas showing the shallow redoxcline which persisted throughout deposition of the (**a**) Aim Formation and distribution of biota along the Yudoma River sections, southeast Siberian Platform and (**b**) The Dengying Formation of the Yangtze Block, South China..... **224**

6.1 Dioramas demonstrating a compendium of local redox conditions and biotic occurrences for individual environments of the Ediacaran and early Cambrian discussed in this thesis..... **232**

6.2 Diagram illustrating temporal ranges of fossil taxa across the Ediacaran – Cambrian boundary including so-called 'transitional' biota..... **236**

List of Tables

1.1 Summary of major paleoredox proxies, the redox potentials at which they record transformation, and lithologies targeted for their application. **52**

2.1 Summary of six paleogeographic provinces considered in this study with inferred paleolatitude, degree of environmental restriction, associated biota and dominant redox conditions during colonization. **69**

4.1 Elemental concentrations of Fe, Mn, and Sr, and Mg/Ca and Mn/Sr for un-dolomitised *Cloudina* and each cement type represented in Omkyk Member Unit 3m at Driedoornvlakte **169**

Chapter 1

Introduction: Animal evolution and the role of oxygen

Author Contributions: This chapter benefitted from helpful discussions with Rachel Wood, Alex Thomas and Simon Poulton. This chapter is adapted and updated from sections 1 and 2 of a review article published in *Geobiology* as Bowyer et al. (2017).

1.1 The record of Ediacaran Macrobiota and Metazoa

The Ediacaran (635 – 541 Ma) represents the concluding period of the Neoproterozoic Era with a stratigraphic base immediately underlying a globally identifiable cap dolostone deposited atop Upper Cryogenian-age glacial diamictites of the final 'Snowball Earth' (Marinoan) glacial (Figure 1.1) (Shields, 2005; Knoll et al., 2006). The Ediacaran – Cambrian boundary witnesses the disappearance of the earliest biomineralising organisms (*Cloudina* and *Namacalathus*) and is defined by the first appearance of the distinctive trace fossil *Treptichnus pedum* in the stratigraphic record (Narbonne et al., 1987; Brasier et al., 1994; Knoll et al., 2006). However, the complex geochemical and palaeontological records which define the transition to the Phanerozoic age of animals remain, to a large extent, mystifying. Fossils of the Ediacaran Period are both intriguing and bewildering, with many morphologies completely dissimilar to anything found in the natural world today. Through the veil of diagenesis, chemical proxies continue to elucidate the palaeoenvironmental conditions which accompanied these earliest complex organisms, and it is the combined records of local palaeoenvironment and fossil occurrence which is investigated herein.

Whilst the earliest complex fossils ascribed (with significant uncertainty) to the Metazoa are found in deposits of the middle Ediacaran Period, molecular clock dating places the earliest crown group metazoans much earlier, somewhere between 850 and 650 million years ago (Ma) within the late Tonian to Cryogenian Periods (Figure 1.1c[1]) (dos Reis et al., 2015; Shields-Zhou et al., 2016). Moreover, recent phylogenomic analyses have suggested a pre-Ediacaran origin for all non-bilaterian phyla and total-group Bilateria (Dohrmann and Worheide, 2017). There is inherent difficulty in estimating molecular divergence times associated with the patchiness of the fossil record and uncertain affinity of these curious early forms, however animal origination within this time interval is in broad agreement with the earliest evidence for basal animals interpreted from fossil demosponge sterols (preserved as steranes, Figure 1.1c[2]) at ~713 Ma (Love et al., 2009). Beyond these sponge biomarkers, the archive of animal life remains relatively barren until the appearance of diverse ecosystems of the Ediacaran Period wherein predominantly enigmatic forms are preserved via a number of taphonomic pathways (Narbonne, 2005; Liu, 2016).

Candidates for the oldest Metazoa are found in successions of the Doushantuo Formation and the equivalent Lantian Formation in South China (635–590 Ma), which host putative phosphatized animal embryos, and possible Cnidaria, respectively (Figure 1.1c[5, 4]) (Xiao et al., 1998; Yuan et al., 2011; Van Iten et al., 2013; Wan et al., 2016). Whilst the metazoan affinity of the Lantian biota remains equivocal, the first appearance of an exceptionally preserved suite of body fossils, including forms with probable diploblastic and sometimes even triploblastic organization –the so-called 'Ediacara biota'– is recorded

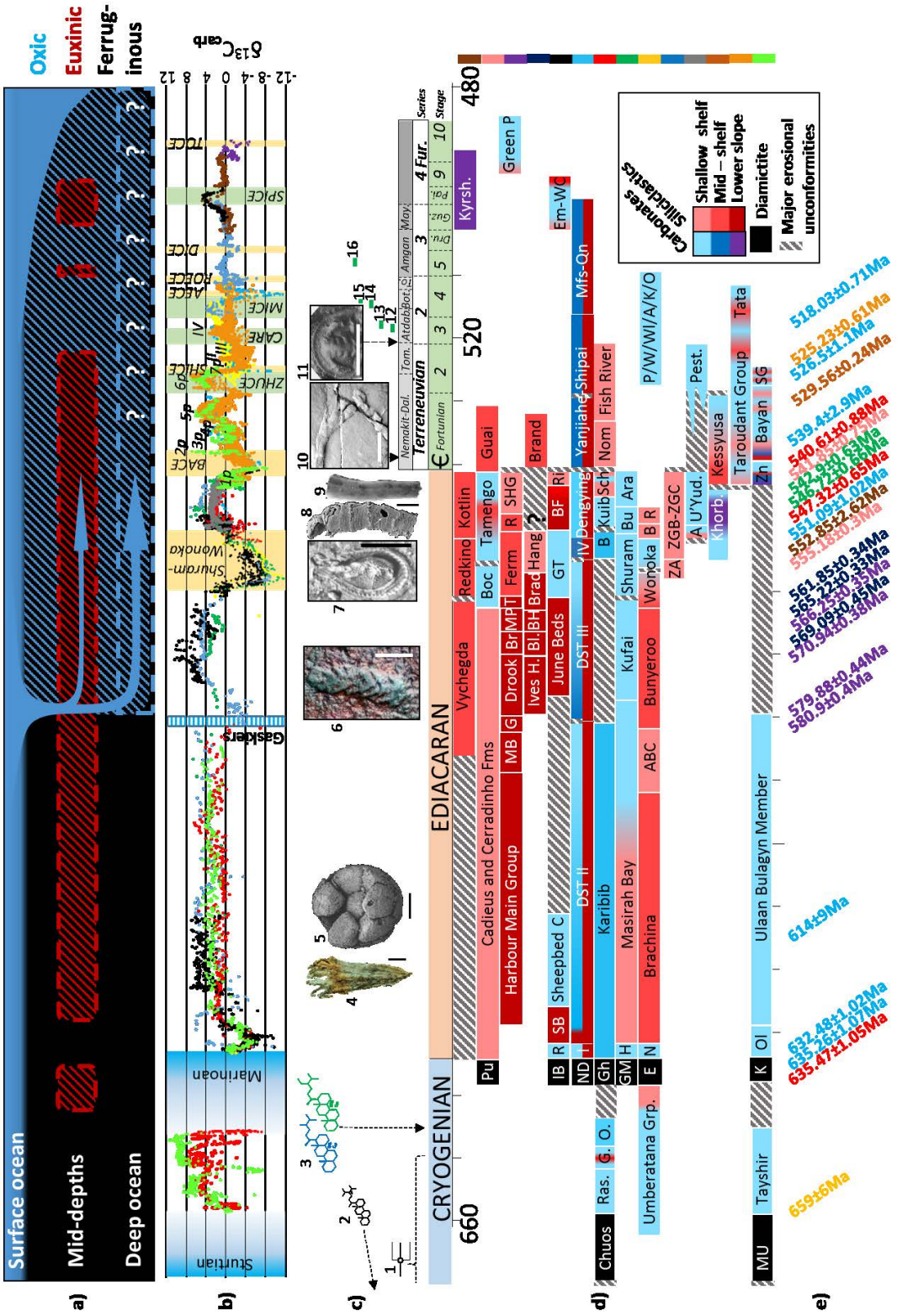

Figure 1.1 Chemical and evolutionary backdrop to the Late Cryogenian to Cambrian Periods (key overleaf)

Figure 1.1 The Cryogenian to Cambrian Periods

a) Schematic redox representation based on compiled iron speciation data in Canfield et al. (2008), Sperling et al. (2015) and Bowyer et al. (2017) and additional information from the Cryogenian (Hood and Wallace, 2015; Johnson et al., 2017) and Cambrian (Gill et al., 2011; Guilbaud et al., 2018), Figure modified after Wood et al. (in prep).

b) Carbonate carbon isotope profile largely adapted after Halverson et al. (2005, 2010), Macdonald et al. (2010, 2013) and Bowyer et al. (2017) with Cambrian data conforming to curve of Zhu et al. (2006) using available raw data. Data colour coded to source area (below).

c) Major evolutionary innovations: [1]Origin of metazoans from molecular clock dating 850–650 Ma (dos Reis et al., 2015; Dohrmann and Worheide, 2017); [2]713 Ma, Maximum age of demosponge biomarkers (24-isopropylcholestane), Huqf Supergoup, Oman (Love et al., 2009); [3]Minimum age for emergence of Archaeplastida 659 – 645 Ma inferred from abundant ergostane and stigmastane biomarkers (Brocks et al., 2017), [4]635–590 Ma, Possible stem-group Cnidaria *Lantianella laevis*, Lantian member II, Anhui, South China, scale bar = 3mm (Yuan et al., 2011), [5]Phosphatised animal embryos of the Doushantuo members II and III, Weng'an section, Guizhou, scale bar = 200µm (Xiao et al., 1998), [6]>570.95 Ma Juvenile *Charnia masoni* (Ford, 1958), Drook Formation (Liu et al., 2012; chronological constraint after Pu et al., 2016), [7]~558–555 Ma, Earliest motile bilaterian body fossil, *Kimberella* (PIN 3993-5604 of Fedonkin et al., 2007b), [8]~550 Ma, Earliest skeletal animals *Cloudina* (Germs, 1972b) and earliest evidence for predation in *Cloudina*, Gaojiashan Member, Shaanxi, South China (image Hua et al., 2003) scale bar = 200µm, [9] < 550 Ma, *Anabarites valkovi*, Ust'-Yudoma Formation (Zhu et al., 2017), scale bar = 100µm for *Anabarites*, [10]First appearance datum of *Treptichnus pedum*, Chapel Island Formation, Fortune Head, Newfoundland (Narbonne et al., 1987; image credit Herringshaw et al., 2017) scale bar = 1 cm, [11]Example of earliest trilobite (Richter, 1932): *Profallotaspis jakutensis* cephalon, lower Atdabanian strata, Pestrotsvet Formation, Lena River, Siberian platform (image credit: Pegel, 2000), scale bar = 1cm. Approximate relative ages of subsequent Cambrian Lagerstätten after Holmes et al. (2018): [12] Chengjiang, [13]Sirius Passet, [14]Emu Bay, [15]Sinsk, [16]Burgess Shale.

d) Stratigraphy coloured according to depositional environment. East European Platform (Baltica), Corumbá Group (Brazil), West Avalonia (eastern Newfoundland), Charnian Supergroup (England), Laurentia (NW Canada), Yangtze Block (South China), combined Congo and Kalahari Cratons (Namibia), Arabian-Nubian Shield (Oman), South Australia, White Sea, Winter Coast (Baltica), Yudoma-Maya Depression (southeast Siberian Platform), Olenek Uplift (northeast Siberian Platform), Anti-Atlas (Morocco), Zavkhan terrane (Mongolia). Radiometric ages colour coded according to provenance. Modified after Bowyer et al. (2017), inspired by Macdonald et al. (2013) and adapted after Wood et al. (in prep). References for C isotopes and radiometric age constraints in appendix A.

from deep marine siliciclastic strata deposited bordering the volcanic island arc of Avalonia (~579–575 Ma) (Liu et al., 2015). The Ediacara biota are subsequently observed in marine sediments on a global scale, until the Precambrian/Cambrian boundary.

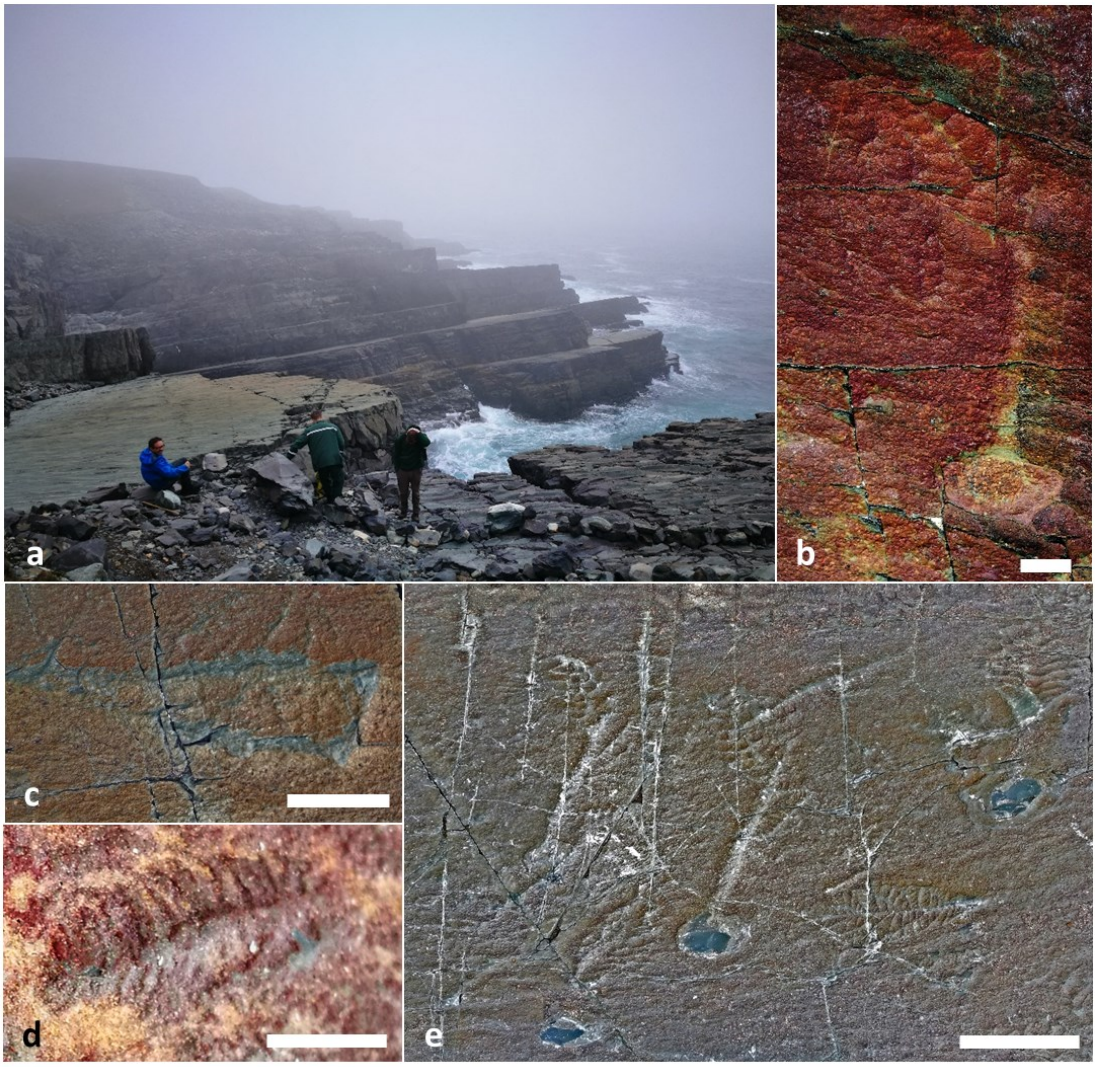

Figure 1.2: Example specimens of the Avalon assemblage exposed on the southern Avalon Peninsula, Newfoundland.

a) The classic Mistaken Point 'D surface' wreathed in sea mist (Professor Graham Budd sits in blue for scale), **b)** *Charniodiscus*, 'E surface', scale bar = 1cm (own image), **c)** *Thectardis*, (possible sponge), Mistaken Point 'E surface', scale bar = 2 cm (own image), **d)** Juvenile frond (possible *Fractofusus*), Drook Formation, Mistaken Point Ecological Reserve, scale bar = 0.25cm (own image), **e**) 'Seilacher's corner' on Mistaken Point 'E surface' with various fronds including stalked *Charniodiscus* and horizontally oriented *Beothukis* (lower right), scale bar = 4cm (own image).

The distinctive fossils in 580–540 Ma strata have classically been grouped into the Avalon, White Sea and Nama taxonomic assemblages, based on biogeographic and biostratigraphic subdivision (Waggoner, 2003). The Avalon assemblage (Figure 1.2) is the oldest, with fossils noted from a number of marine siliciclastic successions, including sections from Newfoundland (Narbonne, 2005; Liu et al., 2015), Charnwood Forest in England (Wilby et al., 2011) and the Mackenzie Mountains, Canada (Narbonne et al., 2014). Examples of Avalon assemblage biota include soft-bodied rangeomorphs and frond-like arboreomorphs with isolated occurrences of sponges and triradialomorphs (Laflamme et al., 2013).

In addition to these forms, the subsequent White Sea assemblage (Figure 1.3) contains the earliest examples of dickinsoniomorphs, erniettamorphs, tetraradialomorphs, pentaradialomorphs, bilateralomorphs, kimberellomorphs and *Eoandromeda* within sections of Siberia (Grazhdankin, 2014), western Russia (Fedonkin et al., 2007), Australia (Gehling and Droser, 2009) and the Yangtze Block, South China (Zhu et al., 2008; Yuan et al., 2011).

Examples of the Nama assemblage (Figure 1.4) are represented in successions of the Nama Group, Namibia (Narbonne et al., 1997), Dengying Formation, China (Chen, Z. et al., 2014), Erga and Chernokamen Formations, Russia, Khatyspyt Formation, Siberia (Grazhdankin, 2014), Miette Group, British Columbia (Hofmann and Mountjoy, 2001) and Wood Canyon, California (Corsetti and Hagadorn, 2000). It has been statistically shown that the Nama assemblage constitutes the assemblage of lowest diversity and contains examples of rangeomorphs, erniettamorphs, arboreomorphs and sponges (Darroch et al., 2015). Recent multivariate statistical analyses support classic assemblage partitioning based on taxonomically distinct groups, however significant proportions of the paleogeographically disparate Avalon and White Sea assemblages are seen to have occupied time-equivalent environments (Boag et al., 2016).

Evidence for the earliest motile bilaterians is eagerly sought and oxygen requirements of such an active, sediment-disruptive lifestyle are confidently considered to have been higher than for the aforementioned benthic and sessile soft-bodied assemblages. Earliest candidate trace fossils have previously been reported from middle Ediacaran (>585 ± 3.3 Ma) strata of the Tacuarí Formation, Uruguay (Pecoits et al., 2012), however the age of the Tacuarí Formation has since been disputed and remains controversial (Gaucher et al., 2013, but see Pecoits et al., 2013). A second candidate for the oldest traces are found in the Mistaken Point Formation (566.25 ± 0.35 Ma, Pu et al., 2016) of the Avalon Peninsula, Newfoundland and represent a simple un-branched morphology with crescentic infill and length of up to 17cm (Liu et al., 2010). Subsequent deposits of the White Sea area (Russia) and Ediacara Member (South Australia) reveal trace fossil evidence for motility alongside co-preservation of

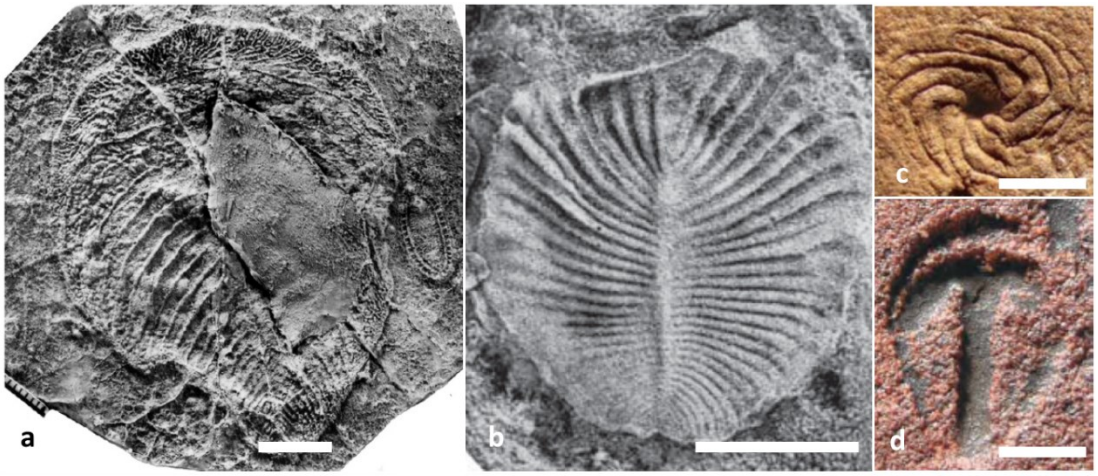

Figure 1.3 Example specimens of the White Sea assemblage**.**
a) *Yorgia* (centre) and *Kimberella* (right). Latex peel of specimens from the Zimnie Gory locality, White Sea area, scale bar = 1cm (Ivantsov, 2011), **b)** *Dickinsonia*. Latex peel of specimen from Zimnie Gory, White Sea region, scale bar = 1cm (Zakrevskaya and Ivantsov, 2017), **c)** *Eoandromeda octobrachiata* (Tang et al., 2008) from the Ediacara Member, Rawnsley Quartzite, South Australia, scale bar = 1cm (image: Zhu et al., 2008), **d)** *Parvancorina* (Glaessner, 1958) from the Ediacara Member, Rawnsley Quartzite, South Australia, scale bar = 3.5mm (image: Lin et al., 2006).

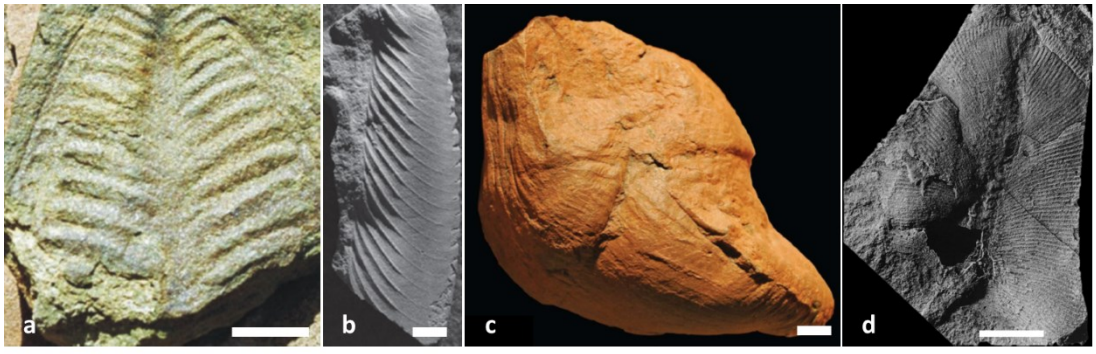

Figure 1.4 Example specimens of the Nama assemblage.
a) *Rangea schneiderhoeni* (Gurich, 1930), Hansburg area, Kuibis Subgroup, Nama Group, Namibia (image: Bouougri et al., 2011) **b)** *Pteridinium simplex*, delta-front sands of the Ediacara Member, Rawnsley Quartzite, Australia, scale bar = 1cm (Gehling and Droser, 2013) **c)** *Ernietta plateuensis*, Aar Member, Farm Aar, Nama Group, Namibia, scale bar = 1cm (Elliot et al., 2016), **d)** *Swartpuntia germsi*, Spitskop Member, Farm Swartpunt, Nama Group, Namibia, scale bar = 5cm (Narbonne et al., 1997).

the culprit molluscan trace maker, *Kimberella quadrata* (Figures 1.1c[7] and 1.3a) (Martin et al., 2000; Fedonkin et al., 2007; Gehling et al., 2014).

The Ediacaran Period also witnessed the advent of biomineralization and whilst the genomic toolkit required for this evolutionary innovation was available to micro-organisms as early as 812–717 Ma (Cohen et al., 2011), the first skeletal metazoans appear in the fossil record at ~550 Ma (Grant, 1990). The early record of biomineralization in multicellular organisms is represented in the fossil record by sessile, benthic forms including *Cloudina* (Figures 1.1c[8] and 1.5a, Germs, 1972b; Grant, 1990), the possible lophophorate *Namacalathus hermanastes* (Figure 1.5b) (Zhuravlev et al., 2015), the probable sponge *Namapoikia* (Figure 1.5c) (Wood et al., 2002; Wood and Penny, 2018) and putative serpulid *Sinotubulites* (Figure 1.5d) (Chen, Z. et al., 2008). Biomineralization marks a step-change in the workings of the global carbon cycle and colonization by calcifying biota is seen to have spread throughout shallow and mid-ramp environments of the terminal Ediacaran, including the Kalahari Craton (Namibia and South Africa), São Francisco Craton (Brazil), (possibly) Río de la Plata Craton (Uruguay), Yangtze Block (South China), Iberian Peninsula (Spain), Laurentia (Southern Canadian Cordillera and Mexico), the Arabian-Nubian shield (Oman), and Siberia (Bengtson and Zhao, 1992; Gaucher and Sprechmann, 1999; Hofmann and Mountjoy, 2001; Hua et al., 2003; Cortijo et al., 2010; Sour-Tovar et al., 2007; Zhuravlev et al., 2012; Warren et al., 2014; Becker-Kerber et al., 2017).

The adoption of biomineralization as a life habit is thought to have required not only the environmental availability of biologically exploitable compounds (e.g. carbonate ions and calcium), but also an external stimulus, with some suggesting the rise of predators as a candidate pressure (Wood, 2011). Earliest evidence for active predation has been documented from organic walled microfossils within facies of the late Tonian (~780–740 Ma) Chuar Group (Porter, 2016; Shields-Zhou et al., 2016). Suggested predatory borings in *Cloudina* have also been reported from the ~550 Ma Dengying Formation, South China (Bengtson and Zhao, 1992), the Kuibis Subgroup of the Nama Group, Namibia (Brain, 2001) and most recently the Tamengo Formation of the Corúmba Group, Brazil (Becker-Kerber et al., 2017).

Of all the organisms represented in the diverse Ediacaran paleontological record, only a few can be assigned to the Metazoa with any degree of confidence. Examples of the earliest animals include aforementioned biomineralizing forms (*Cloudina*, *Namacalathus* and *Corumbella*), putative sponge fossils (e.g. *Thectardis* and *Palaeophragmodictya*), the bilaterian organisms *Kimberella* and *Dickinsonia*, the peculiar, octoradially symmetrical *Eoandromeda*, and bilaterian organisms responsible for the characteristic trace fossils *Streptichnus narbonnei* and *Treptichnus pedum* (Martin et al., 2000; Jensen and Runnegar, 2005; Zhu et al., 2008; Sperling et al., 2011; Wilson et al., 2012; Cunningham et al., 2017a). By contrast, the large

majority of soft-bodied forms represented throughout fossiliferous strata of Ediacaran environments (e.g. rangeomorphs, erniettamorphs, arboreomorphs etc.) are, at present, most accurately described as complex multicellular eukaryotes (Laflamme et al., 2013; Liu et al., 2015).

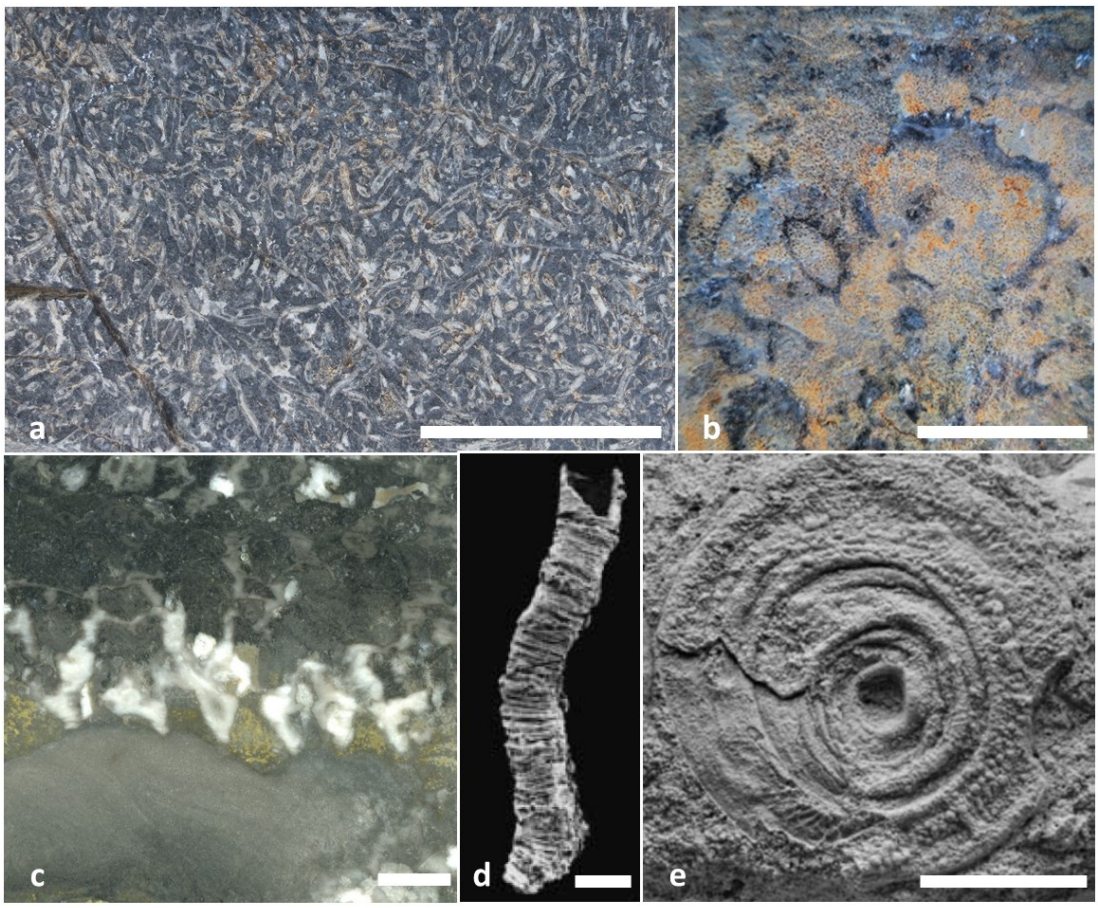

Figure 1.5 Skeletal fossils of the terminal Ediacaran Period**.**
a) *Cloudina hartmannae*, Driedoornvlakte pinnacle reef complex, Omkyk Member, Farm Driedoornvlakte, Nama Group, Namibia, scale bar = 10 cm (image courtesy of Rachel Wood), **b)** Spiny *Namacalathus hermanastes*, Omkyk Member, Zebra River Farm, Nama Group, Namibia, scale bar = 1cm (image courtesy of Rachel Wood), **c)** *Namapoikia rietoogensis*, image shows detail of skeletal attachment to substrate, Driedoornvlakte pinnacle reef complex, Omkyk Member, Farm Driedoornvlakte, Nama Group, Namibia, scale bar = 1cm (image: Wood and Penny, 2018), **d)** *Sinotubulites*, Dengying Formation, Shaanxi Province, South China, scale bar = 1mm (Chen et al., 2008), **e)** *Suvorovella aldanica* (Vologdin and Maslov, 1960), Aim Formation, Yudoma-Maya confluence, southeast Siberian platform, scale bar = 1cm (Wood et al., 2017c).

1.2 Oxygen and metabolism

The hypothesis that an increase in atmospheric oxygen concentration permitted the evolution of animals was first published by Nursall (1959) in an article entitled 'Oxygen as a prerequisite to the origin of the metazoa'. This hypothesis was based on the assumptions that 1) the paucity of metazoan fossils prior to the Cambrian radiation does not reflect a taphonomic artefact and, 2) that metazoan metabolism requires correspondingly high energy yield permissible only by aerobic respiration. This theory has driven longstanding debate on the possibility of an increase in marine dissolved oxygen (beyond a threshold concentration) as a primary factor enabling the rise of animals (Runnegar, 1991; Sperling et al., 2013b, 2015c). However, only now are scientific proxy methods being established which, used

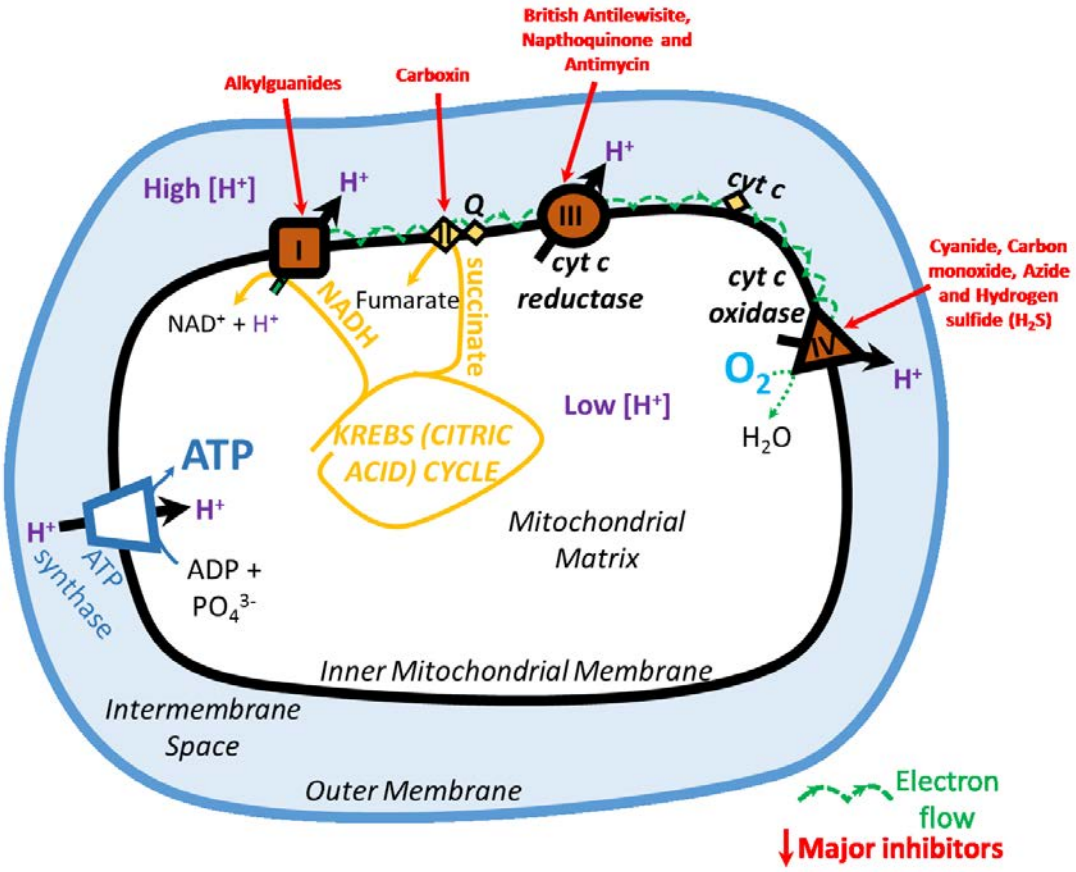

Figure 1.6 Simplified schematic diagram illustrating the process of aerobic respiration. Three main complexes along an electron transport chain allow proton transfer from the mitochondrial matrix to the intermembrane space. The terminal electron acceptor is oxygen, yielding the highest Gibbs free energy change which fuels the production of ATP. Figure redrawn after Berg et al. (2002) and Albert et al., (2002).

correctly, are able to tease apart cause and effect with respect to environmental conditions and ecosystem habitation at the dawn of animal life.

During aerobic respiration, molecular oxygen (O_2) is the most electronegative (molecule with the highest reduction potential) electron acceptor and thus acts as the terminal electron acceptor in an electron transport chain composed of three main enzymatic complexes (I, III, and IV, Figure 1.6) (Berg et al., 2002; Albert et al., 2002). This electron transport chain is fuelled through electron acceptance by oxygen and electrons donated as by-products of the citric acid cycle (e.g. NADH). This is linked in turn to proton transfer across the inner mitochondrial membrane (Figure 1.6) which results in an electrochemical gradient, ultimately driving the production of adenosine triphosphate (ATP) (and waste in the form of CO_2 and water). The use of oxygen as the terminal electron acceptor generates the largest change in Gibbs free energy (amounting to the maximum work done by the thermodynamic system at constant pressure and temperature) and this translates as a higher energy yield (~2,880 $kJmol^{-1}$ glucose). This energy yield is subsequently stored within ATP as highly strained chemical bonds (Berg et al., 2002; Sperling et al., 2015c). In contrast, anaerobic respiration uses elements other than O_2 as the terminal electron acceptor, including nitrate, ferric (Fe(III)) iron, manganese oxides and sulfate (Figure 1.7), resulting in an energy yield which is significantly reduced when compared with aerobic respiration (Albert et al., 2002). This is a gross simplification of the processes of aerobic and anaerobic respiration and electron transport chains are significantly distinct between bacteria, archaea and eukaryotes.

1.3 Redox and metazoan ecology in modern marine environments

Studies on the colonization and structuring of modern marine ecosystems under variable redox potentials have shown that well-oxygenated, nutrient-rich environments permit sustained habitation by larger organisms and predators in addition to the potential for biomineralization (e.g. Sperling et al., 2015c). Contrastingly, benthic metazoan trophic structure in suboxic/anoxic waters is limited to low diversity and usually characterised by small, unmineralized organisms (Levin et al., 2009; Sperling et al., 2015c). Even metazoans that live a dominantly anaerobic lifestyle require oxygen during short periods, with the single known exception of some loriciferans which are able to convert their mitochondria into hydrogenosomes (organelles that produce ATP in the absence of O_2) and consequently live as obligate anaerobes (Hackstein et al., 1999; Danovaro et al., 2010; Sperling et al., 2015c; Mills et al., 2018).

With substantial contention remaining in the phylogenetic affinities of the majority of soft-bodied Ediacara biota, it is unclear what environmental requirements may have facilitated their diversification (Liu et al., 2015). In light of this, hereon the discussion of physiological oxygen

requirements within diverse fossil assemblages of the Ediacaran can only be considered to represent end-member taxa whose presence required elevated levels of dissolved oxygen in the water column, rather than the conditions which dictated establishment of assemblages as a whole.

Recent investigation into one of the most basal modern diploblastic organisms (*Halichondria panicea*) has revealed oxygen concentration requirements between 0.5 – 4 % of present atmospheric levels (PAL) (Mills et al., 2014). This experimental evidence has been taken to suggest that many of the peculiar, inferred-diploblastic organisms represented in the Ediacaran fossil record may similarly have required vanishingly low oxygen concentrations (Mills et al., 2014; Sperling et al., 2015c). Furthermore, there is now experimental evidence to suggest that primitive metazoans such as Cnidaria and Ctenophora lack aspects of a pathway made from a particular set of proteins, known as 'hypoxia-inducible factors' (HIF), which enable the cellular maintenance of steady oxygen concentrations (Mills et al., 2018). This suggests that such basal animals (which likely include the last metazoan common ancestor) were able to maintain an aerobic metabolism even under extremely low oxygen concentrations (Mills et al., 2018). In contrast, the more complex, likely triploblastic and motile organisms such as *Kimberella* are suggested to have required relatively elevated oxygen levels (Sperling et al., 2015c). However, atmospheric oxygen concentrations during the Meso-Neoproterozoic are poorly constrained and widely debated, with the latest estimates from modelling of proxy data ranging from <0.1 to >4% PAL until at least 800 Ma (Chapter 2; Planavsky et al., 2014; Cole et al., 2016; Gilleaudeau et al., 2016; Zhang et al., 2016). By contrast, gas inclusion in ~815 Ma halite from the Officer Basin, South Australia have been interpreted to suggest an atmospheric oxygen concentration of >10% PAL (Blamey et al., 2016).

Whilst the absolute concentration of atmospheric oxygen in the Ediacaran is poorly understood, it is clear that the oceans were characterized by continued redox stratification throughout most of the Neoproterozoic, with well-mixed oxic surface waters being dominantly underlain by anoxic and ferruginous deep waters, and intervals of localised mid-depth euxinia (Figure 1.1a; Chapter 2) (Canfield et al., 2008; Johnston et al., 2010; Li, C., et al., 2012; Sperling et al., 2013a; Hood and Wallace, 2015; Guilbaud et al., 2015). Furthermore, considerable lateral heterogeneity likely produced dynamic redox zonation established through patterns of global ocean circulation, localized nutrient recharge and productivity (Reinhard et al., 2016). Despite such instability, however, marine redox conditions during the Cryogenian Period are thought to have been locally permissive for the evolutionary origin of Metazoa (Sperling et al., 2013a).

The geochemical nature of Ediacaran oceans is characterized by profound and long-lived fluctuations in the marine carbon and sulfur cycles, which provide further insight into the extent of global ocean-atmosphere oxygenation. The largest documented negative carbon isotope ($\delta^{13}C$) excursion in the

geological record, known as the 'Shuram-Wonoka' anomaly (Figure 1.1b), is recorded in bulk carbonate from paleogeographically distinct areas, with a disputed initiation at ~575 Ma marking a rapid decline in $\delta^{13}C_{carb}$ to values as low as -12‰ (Huqf Supergroup, Oman) followed by a slow recovery to positive values by ~553 Ma (Fike et al., 2006). Though the excursion is thought to be globally identifiable, the timing of the onset and recovery to positive $\delta^{13}C_{carb}$ may vary between sections, with a possible duration of between 5 and 50 Myr (Condon et al., 2005; Le Guerroué et al., 2006; Jiang et al., 2007; Bjerrum and Canfield, 2011).Though contention remains as to a possible cause (Burns and Matter, 1993; Kaufman et al., 2007; McFadden et al., 2008; Knauth and Kennedy, 2009; Derry, 2010; Bjerrum and Canfeld, 2011; Grotzinger et al., 2011; Swart and Kennedy, 2012; Och and Shields-Zhou, 2012; Schrag et al., 2013; Cui et al., 2016b), late Ediacaran recovery from the Shuram-Wonoka excursion has been proposed to represent global oxygenation of the deep ocean (Rothman et al., 2003; Fike et al., 2006). This is based on evidence supporting enhanced oxidative sulfur cycling (Fike et al., 2006), which was possibly attributable to the advent of sediment ventilation through bioturbation (Wu et al., 2015). However, recent numerical modelling supports a mechanism whereby partial oxidation of the substantial oceanic dissolved organic carbon (DOC) reservoir proceeded heterogeneously as a consequence of locally controlled DOC and oxidant supply (Li, C. et al., 2017; Shi et al., 2017).

High resolution investigations of local-scale palaeoredox within fossiliferous terminal Ediacaran successions indicates continued dynamism between deposition under anoxic and oxic water column conditions in both deep marine and shallow shelf settings (Chapters 2-5; Och et al., 2015; Sperling et al., 2015b; Wood et al., 2015; Tostevin et al., 2016b). Whilst low atmospheric oxygen concentration in the Neoproterozoic may have been a principal reason for sustained local deep water oxygen deficiency, evidence for substantial and longstanding spatial marine redox heterogeneity within approximately time-equivalent Ediacaran sections demands consideration of more subtle physical mechanisms.

Many researchers now believe that the success of early ecosystems was partly dependent upon stable O_2 above a threshold concentration maintained for ecologically significant periods (Johnston et al., 2012, 2013; Wood et al., 2015). Under this hypothesis, local redox instability may have delayed proliferation of early animal ecosystems and resulted in the paucity of fossil Metazoa until the late Ediacaran. In summary, the advent of animals is thought to represent the culmination of inherent prerequisite genomic development, physical and chemical change in the marine environment and predation, which together helped drive the evolutionary step towards skeletonization.

1.4 Controls on redox zonation in modern marine settings

Global atmospheric oxygen concentration is ultimately controlled by the balance between oxygen supply via photosynthetic primary production and long-term burial of reduced elements (e.g. pyrite iron and organic carbon), and oxygen consumption through oxidative weathering of reduced elements within continental sediments and oxidation of reduced gases delivered in volcanic emissions (Canfield, 2014). The primary mechanisms responsible for subsequent atmospheric oxygen delivery to the global ocean include diffusion and efficient physical ventilation of surface waters due to wave agitation and dispersive mesoscale eddies, oxic riverine influx to coastal waters, and downwelling of oxygenated surficial water masses (Broecker, 1997; Petsch, 2003; Algeo and Lyons, 2006; Kershaw, 2015). Finally, the concentration and spatial distribution of dissolved oxygen in the marine environment may fluctuate depending on local circulation and the rate and extent of primary production and remineralization (Petsch, 2003; Helly and Levin, 2004).

1.4.1 Productivity and the Biological Pump

Marine redox on a local scale is subject to substantial variation resulting from the balance between oxygen supply and biological oxygen consumption through energy-yielding organic matter oxidation (remineralization). The initial concentration of organic matter production is primarily dictated by nutrient availability in the surface ocean (Li et al., 2015a). Organic matter remineralization follows a predictable electron acceptor utilization pathway dictated by the associated energy yield per mole of organic carbon derived from each oxidation reaction, with the highest energy yield achieved through oxidation of free O_2 during aerobic respiration (see Section 1.2) (Berner, 1980). As dissolved O_2 concentration decreases with organic matter sinking, the preferred electron acceptor first becomes nitrate within the nitrogenous zone followed by a manganous-ferruginous layer with reduction of continentally derived iron and manganese oxides (Figures 1.7 and 1.8) (Canfield and Thamdrup, 2009; Li et al., 2015a; Cheng et al., 2016). The underlying euxinic zone is defined by sulfate reduction and build-up of aqueous hydrogen sulfide (H_2S_{aq}). The presence or absence of euxinia in an anoxic ocean is partly controlled by the relative fluxes of highly reactive Fe minerals and sulfate (Poulton and Canfield, 2011), in addition to the efficiency of organic carbon delivery from productive surface waters. Furthermore, it has been suggested that longstanding euxinia demands nitrate depletion as a consequence of the higher free energy yield associated with denitrification over dissimilatory sulfate reduction, and new production must accordingly be sustained via nitrate provision in addition to anoxic N_2-fixation (Canfield, 2006; Boyle et al., 2013). In this way, excess bioavailable nitrogen is able to support organic

matter production required for oxidation during sulfate reduction, after quantitative denitrification. This concept has been built upon further by experiments focusing on a modern ferruginous basin (Kabuno Bay in East Africa) which indicate that a large proportion of nitrate reduction results in retention of N as ammonium and that ferruginous conditions are likely phosphorus rather than nitrogen limited (Michiels et al., 2017).

Recent model investigations of the biological pump suggest that enhanced efficiency of surface water organic matter oxidation through reduced rates of sinking and/or enhanced rates of respiration is able to effectively lift the oxycline to shallower depths (Meyer et al., 2016). This supports previous studies invoking oxycline deepening resulting from faster sinking of organic matter due to the consequent increase in remineralization depth (Butterfield, 2009; Lenton et al., 2014).

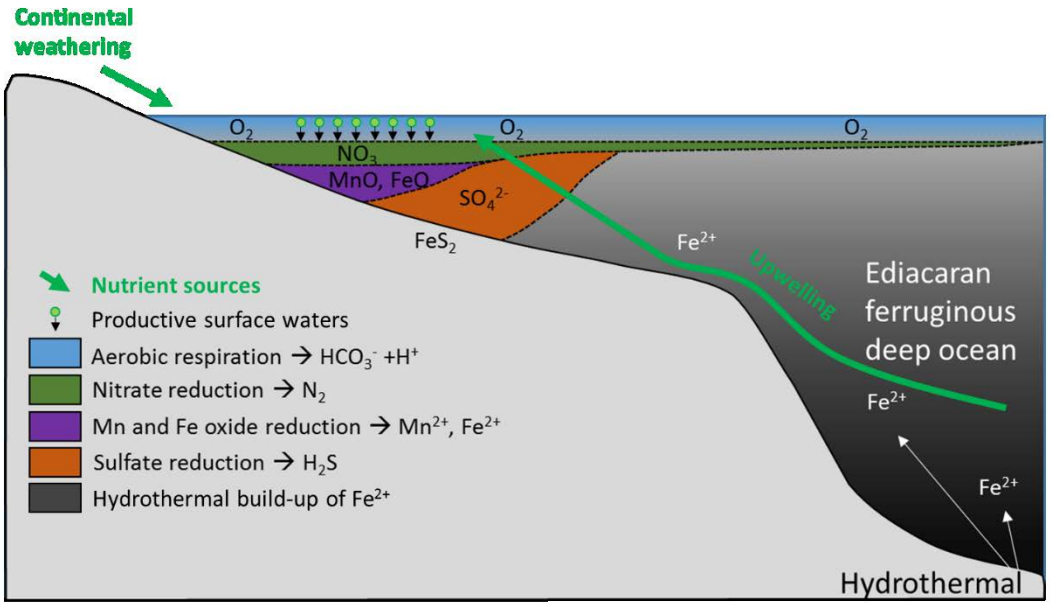

Figure 1.7 Simplified schematic representation of redox zonation in productive near-shore environments of the Precambrian (modified after Li, C. et al., 2015a). Note that the extent to which the Ediacaran deep ocean was ferruginous remains contentious.

1.4.2 Upwelling and Downwelling

Superimposed upon biochemical processes which locally act to consume oxygen are environmental factors which influence dissolved oxygen and nutrient distribution. These include changes in salinity and water temperature, alongside hydrodynamic mechanisms that are subject to local variation as a

function of intrinsic factors such as paleobathymetry and local water column circulation patterns (Petsch, 2003).

Effective downwelling occurs in areas subject to elevated surface density resulting from high salinity and low temperature. In such areas the dissolved oxygen concentration of surface waters is elevated due to the effect of higher oxygen saturation solubility at lower seawater temperatures (Petsch et al., 2003). Downwelling in the modern ocean is therefore principally controlled by paleolatitude, with lower temperature at higher latitudes promoting the formation of oxygenated deep water (Broecker, 1997; Tomczak and Godfrey, 2001). However, regions prone to fresh water dilution as a consequence of low surface evaporation, such as the modern north Pacific, suffer from less efficient downwelling (Bruce, 1983).

By contrast, persistent upwelling systems ordinarily form in mid-latitudes as a consequence of equatorial current activity related to displacement of surficial water masses via Ekman transport and equatorial divergence (Fuenzalida et al., 2009). Upwelling may develop seasonally or inter-annually as an effect of differential wind stress and climatic conditions respectively (Helly and Levin, 2004; Paulmier and Ruiz-Pino, 2009). Nutrient-rich upwelling waters lead to stimulated surface ocean productivity driving oxygen depletion of subsurface waters through organic matter oxidation and often result in shoaling of the oxycline (Fuenzalida et al., 2009).

1.4.3 Restricted Environments

Modern marine environments which lack influence from extensive physical mixing by open ocean current activity include the Black Sea, and the Cariaco Basin on the Venezuelan continental shelf (Ho et al., 2004). In these settings well mixed oxic surface waters transition to anoxic, commonly euxinic, deeper layers due to strong salinity-induced density gradients and the absence of efficient physical ventilation mechanisms at depth (Algeo and Lyons, 2006). The maintenance of euxinia in restricted environments is a consequence of high sulfate supply from oxidative continental weathering of reduced sulfur species (e.g. pyrite) alongside hydrogen sulfide production via bacterial sulfate reduction (BSR) in the oxygen-depleted subsurface water column (Algeo and Lyons, 2006). Under these conditions, available water column ferrous iron delivered to the deep anoxic layer through reductive dissolution of ferric oxides is sulfidized and deposited as pyrite.

Drainage basin area of the enclosing landmass and regional precipitation rates influence the concentration of oxic riverine discharge to the restricted basin which may episodically be of sufficient volume to overcome salinity-induced stratification and result in short-term lowering of the oxycline at basin margins (Kershaw, 2015). Furthermore, the relative stability of chemical stratification in restricted basins is a function of the rate of deep water renewal related to the degree of basin connectivity with the open ocean as indicated by variations in chemocline depth and depth of the basin margin sill relative to total basin depth (Konovalov et al., 2006; Algeo and Lyons, 2006). More effective restriction and reduced mixing of deep basin waters is implied by lower chemocline and sill depth ratios respectively (Algeo and Lyons, 2006).

Mechanisms for deep water oxygenation include extensive cooling above the oxycline and convective overturn of the stratified basin due to density inversion, in addition to submarine mass wasting brought on by slope instability (Anderson and Devol, 1973; Kershaw, 2015). Additionally, enhanced basin connectivity through eustatic sea level rise may result in overflow and breach of well mixed, higher density oxygenated waters into the underlying anoxic zone (Konovalov et al., 2006). However, this hyperpycnal incursion may be accompanied by nutrient replenishment and contrastingly result in consumption of oxygen through short term elevated organic carbon production and remineralization (Li, X. et al., 2012). The efficiency of these mechanisms towards effective oxygenation of the subsurface is dependent upon their frequency and magnitude with respect to basin volume (Algeo and Lyons, 2006).

1.4.4 Unrestricted continental shelf

Open ocean shelf settings lack bathymetric restriction from the well mixed ocean and as a result may be locally subject to vertical and lateral mixing through ocean current activity at mid-depths, Ekman transport and baroclinic transport of surface waters (Fuenzalida et al., 2009). Some shelf and continental slope areas experience oxygen depletion through local enhancement of the biological pump stimulated by upwelling of nutrient-rich bottom water (Helly and Levin, 2004; Fuenzalida et al., 2009). This differs from restriction-induced maintenance of subsurface anoxia in that oxygen minimum zones (OMZs) on the open shelf exhibit variation in the vertical and lateral positioning of upper and lower boundaries, which are generally maintained through relatively sluggish local circulation (Helly and Levin, 2004; Fuenzalida et al., 2009). Volumetric changes in oxygen minima along continental margins of the modern ocean occur on glacial-interglacial timescales and are thus identifiable via paleoredox proxy methods.

Four major OMZ settings in the modern ocean, with dissolved oxygen concentrations <20 $\mu molkg^{-1}$, include the eastern south Pacific, the eastern tropical and sub-tropical north Pacific, the Arabian Sea, and the Bay of Bengal in the northern Indian ocean (Helly and Levin, 2004; Paulmier and Ruiz-Pino, 2009). A further, weaker OMZ (≥20 $\mu molkg^{-1}$ dissolved O_2) is related to upwelling of the Benguela current and occurs off the coast of Walvis Bay, Namibia, in the eastern tropical south Atlantic (Helly and Levin, 2004).

Differential thickness and spatial extent of the OMZ off the coast of Peru in the south-eastern tropical Pacific correlates well with nutrient input via Ekman-induced upwelling, whilst the positional offset of the OMZ is an effect of the disconnect between the physical process of upwelling and regional migration of biological activity (Fuenzalida et al., 2009). Transient adjustment of the mixed layer depth along continental margins such as the Namibian shelf and Arabian Sea are induced through strong seasonal differences in wind stress and sea surface temperature, resulting in shoaling of oxygen depleted water from depth, in addition to convective mixing (Kumar and Narvekar, 2005; Algeo and Lyons, 2006). Variations in areal extent, thickness and intensity of an OMZ may occur on inter-annual timescales associated with cyclic changes in sea surface temperature and circulation. An example of this in the modern ocean is the El Niño Southern Oscillation (ENSO), which may occasionally be responsible for increasing the depth to the OMZ in the eastern tropical south Pacific during periods of enhanced surface warming (Morales et al., 1999; Escribano et al., 2004).

Ocean deoxygenation is a significant feature of open marine coastal settings today as a consequence of global warming, with the most intense oxygen loss occurring between 100 – 600 m depths in localised offshore zones which are partially disconnected from the influence of nutrient driven productivity (Levin, 2017).

1.5 Rationale of Palaeoredox proxies

In order to translate to the stratigraphic record our knowledge of the influence of redox on modern ecosystems, it is necessary to use proxy methods which are sensitive to redox-controlled changes in elemental concentration or isotopic composition. Distinct redox transitions occur at correspondingly distinct ranges in reduction potential (E_H) and as such, redox proxy sensitivity is defined by the chemical zone at which the associated elemental or isotopic transformation occurs (Figure 1.7, Canfield and Thamdrup, 2009). Studies of long term changes in global ocean redox state rely upon elements and isotopes which have long mean ocean residence times today and are thus well mixed and reflective of the

global ocean inventory. Under specific local depositional redox conditions, (e.g. sediments deposited under locally euxinic waters) or targeting carbonate sediments (in cases where no (or known and constant) isotopic fractionation is associated with elemental incorporation), these proxies may provide a window into the global ocean redox state. In contrast, local-scale studies employing numerous elemental proxies that record relatively rapid redox-associated transformations under distinct E_H can, in theory, distinguish between individual chemical zones pertaining to the position of the local palaeo-redoxcline (e.g. Tostevin et al., 2016b). When incorporated into a sequence stratigraphic framework, this targeted approach proves powerful in reconstructing temporal variations in position and thickness of the redoxcline along a shelf to basin transect. A number of proxies are discussed in this section, in addition to the relative sensitivity to local versus global changes recorded by their redox-dependent transitions.

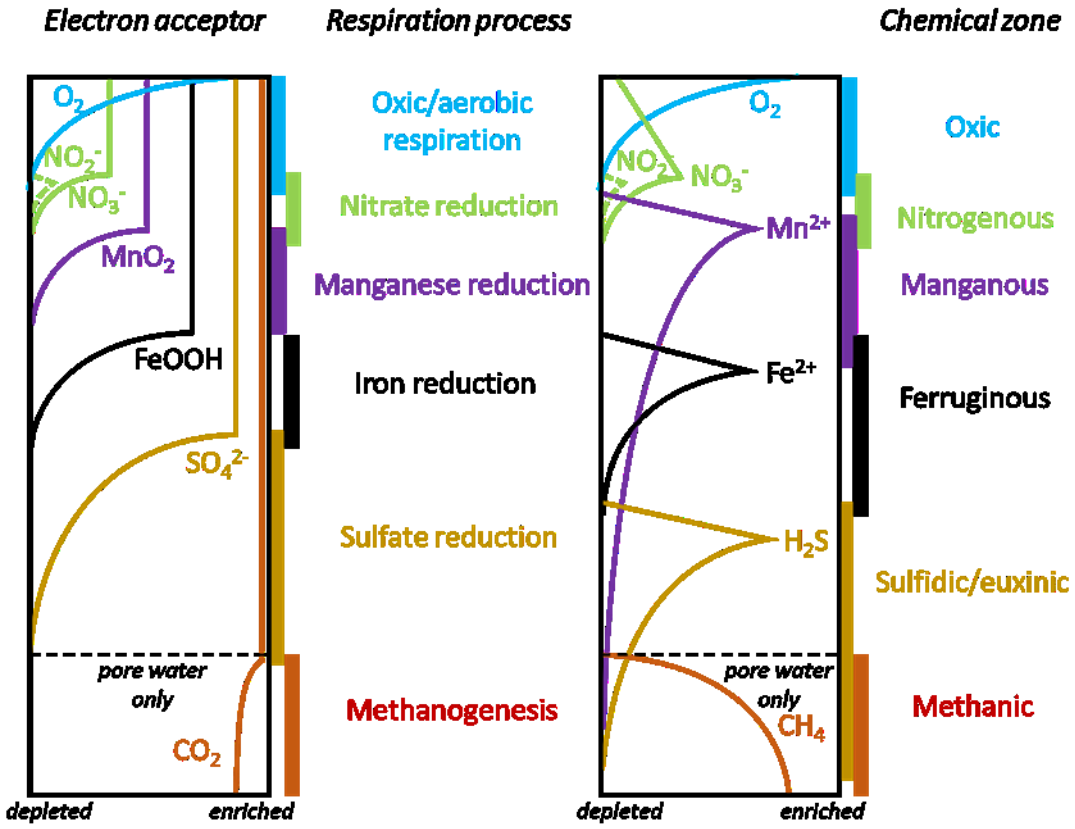

Figure 1.8

Hierarchical electron acceptor zonation, organic matter oxidation pathways, reduced elemental by-products and chemical zonation terminology after Canfield and Thamdrup (2009).

1.6 Global ocean proxies

1.6.1 Redox sensitive elements

Oceanic residence times greatly in excess of the rate of global ocean mixing allow a number of redox sensitive trace elements (RSE) to display globally homogeneous open ocean concentrations today. Examples include molybdenum, uranium and vanadium each of which are commonly enriched in sediments deposited beneath locally anoxic, particularly euxinic, bottom waters. These provide a window for interpretation of the global ocean elemental inventory provided that their residence times have not differed significantly through geological time and that the extent of enrichment has not been impacted by protracted episodes of local basin restriction (Algeo and Lyons, 2006; Scott and Lyons, 2012; Sahoo et al., 2012; Kendall et al., 2015). If these assumptions hold true, expanded global ocean oxygenation results in globally reduced burial of RSE and consequently, elevated RSE concentrations within coeval shales deposited under local-euxinia. In contrast, periods of widespread anoxia are more commonly expressed by lowered shale RSE concentrations due to enhanced burial under widespread bottom water anoxia resulting in reduced global ocean RSE reservoir (Tribovillard et al., 2006; Scott and Lyons, 2012; Sahoo et al., 2012). In this way, extreme enrichments of RSE within organic-rich shales are indicative of local euxinia, whilst maximum values may aid interpretation of the global seawater elemental inventory and thus the degree of global marine anoxia. The relative sensitivity of each element is related to the reduction potential at which accumulation commences in sediments, with V enrichment occurring earliest followed by U enrichment which initiates at E_H characteristic of Fe(III) reduction, and lastly extensive Mo enrichment under euxinic conditions (Tribovillard et al., 2006; Zhang et al., 2016). Anoxic, non-euxinic conditions are associated with a coupling of Mo, U, and V with organic matter flux, however under euxinic conditions this relationship commonly breaks down and (RSE)/TOC tend towards higher values as a consequence of locally enhanced RSE burial (Tribovillard et al., 2006; Och et al., 2015). The productivity-associated burial flux of organic matter may be estimated separately through assessment of elemental enrichments in Ba, Ni and Cu, each of which show high biological affinity and may be indicative of delivery in association with organic matter (Tribovillard et al., 2006).

1.6.2 Redox sensitive isotopic fractionation

In addition to redox sensitive element enrichments, a number of elements display redox associated isotopic fractionation, of which the most commonly utilised in palaeoenvironmental studies are Mo and U. Isotopic fractionation of Mo in seawater relative to composition of the primary riverine source occurs during adsorption of molybdate (MoO_4^{2-}) onto manganese and iron oxides under oxic/suboxic conditions

due to preferential adsorption of the lighter isotope. Enhanced fractionation is associated with incomplete conversion of molybdate to thiomolybdate ($MoO_xS^{2-}_{(4-x)}$, x = 0 to 3) under oxic, anoxic non-sulfidic and weakly euxinic conditions (Siebert et al., 2003; Neubert et al., 2008; Kendall et al., 2015). In the modern oxic ocean, significant fractionation results in average seawater δ^{98}Mo values of 2.34 ± 0.1 ‰ (Siebert et al., 2003; Neubert et al., 2008). In contrast, strongly euxinic conditions are thought to permit quantitative conversion of molybdate to tetrathiomolybdate (MoS_4^{2-}) and consequently result in negligible fractionation between contemporaneous scavenged Mo and seawater, thus preserving seawater δ^{98}Mo in euxinic sediments (Siebert et al., 2003). From this it is possible to quantify the mass balance between contemporaneous oxic and euxinic sedimentation on a global ocean scale. However, the significant isotopic fractionations occurring in weakly euxinic environments (up to 3.0 ‰ lower than oxic ocean waters where H_2S_{aq} < 11 $\mu molL^{-1}$; Neubert et al., 2008; Dahl et al., 2010) and the importance of such environments in past global oceans implies that the Mo isotope record is best interpreted to represent the mass balance between strongly euxinic environments and all other environments of higher redox potential (aerobic to ferruginous) (Neubert et al., 2008; Wille et al., 2008; Kendall et al., 2015). As such, elevated δ^{98}Mo values recorded in euxinic black shales reflect the greater proportion of non-euxinic water masses conducive to molybdenum isotope fractionation, whilst lower δ^{98}Mo values may suggest reduced global ocean molybdenum fractionation as a consequence of enhanced euxinia.

Uranium isotopes are thought to follow a similar pathway of redox-dependent fractionation whereby, during U(VI) reduction, the heavier isotope of uranium (^{238}U) is preferentially incorporated into insoluble U(IV) and buried. As such, a shift towards lighter δ^{238}U of the global ocean during periods of expanded oceanic anoxia is documented in the record of contemporary euxinic sediments (Kendall et al., 2015). The maximum fractionation factor expected between U(VI) and U(IV) retained in the rock record is thought to be approximately -0.6 ‰ and expanded global ocean anoxia is expected to result in δ^{238}U < 0.2 ‰ in unrestricted euxinic sediments (Andersen et al., 2014; Kendall et al., 2015; Hinojosa et al., 2016). Iron and manganese oxide crusts formed under oxic water column conditions contrastingly show depleted δ^{238}U compositions with respect to seawater whilst biologically and abiologically mediated carbonate precipitation is associated with negligible fractionation providing pore water dissolved sulfide is absent (Kendall et al., 2015; Stirling et al., 2015). In this way, extended episodes of global ocean oxygenation will result in elevated δ^{238}U of local organic rich euxinic settings, nearing the average δ^{238}U composition of source uranium as a consequence of reduced ^{238}U removal in limited global marine anoxic settings. However, recent studies highlight the need for better constraining potential drivers of U isotope fractionation which may be independent of redox, such as adsorption onto organic molecules, in addition to understanding controls on the variability in isotopic composition of source U (Hinojosa et al., 2016).

Whilst the records from Mo and U isotopes are continually developed, recent advances in understanding of the cycling and isotopic behaviour of selenium is further expanding knowledge of oceanic redox dynamics in deep time (Pogge von Strandmann et al., 2015; Stüeken et al., 2015b; Mitchell et al., 2016). A gradual, protracted increase in global ocean oxygenation to levels at or above those characteristic of iron oxide reduction has been inferred from compiled Se isotope data which show a decrease in average $\delta^{82/76}$Se from the end-Cryogenian to early Cambrian (Pogge von Strandmann et al., 2015). However, analytical difficulty linked to the large fraction of Se associated with organic matter is thought to mute the signal of redox-derived Se isotope variations (Mitchell et al., 2016). Continued development of extraction and speciation procedures targeting selenium phases in bulk rock samples is expected to significantly enhance our current understanding of the $\delta^{82/76}$Se record.

1.6.3 Sulfur isotope compositions of sulfate and pyrite ($\delta^{34}S_{CAS}$ and $\delta^{34}S_{py}$)

The sulfur cycle is a crucial component in the redox balance of the Earth's surface environment, with the burial of sulfide in the form of pyrite allowing for the long-term build-up of atmospheric (and oceanic) oxygen. Continental weathering and oxidation of sulfur-bearing compounds; predominantly pyrite and evaporites (e.g. gypsum $CaSO_4H_2O$), results in the release of sulfate (SO_4^{2-}) and (via riverine delivery) provides the dominant source of oceanic SO_4^{2-} (Canfield, 2004). Other, less globally important SO_4^{2-} sources include subaerial volcanism and submarine hydrothermal activity (Canfield, 2004). As a result, sulfate is the second most abundant anion in the ocean today and has a modern oceanic residence time of ~ 7 – 14 million years, enabling large perturbations with respect to concentration and isotopic composition of the sulfur cycle to be longstanding in the global ocean today (Shields et al., 2004).

Under anoxic water column (or pore water) conditions, sulfate is used as an electron acceptor during oxidation of organic matter by sulfate reducing bacteria (Canfield, 2001) following the dissimilatory reactions:

$$SO_4^{2-} + 2CH_2O \rightarrow H_2S + 2HCO_3^-$$

$$2H^+ + SO_4^{2-} + 4H_2 \rightarrow H_2S + 4H_2O$$

The proportional pyrite burial flux is dependent upon the global extent of euxinic water column (or sulfidic pore water) conditions in addition to the availability of reactive iron which scavenges the H_2S by-product and leads to pyrite precipitation. Preferential utilisation of the lighter isotope of sulfur (^{32}S) during bacterial sulfate reduction results in a lighter $\delta^{34}S$ composition of generated H_2S and a

corresponding shift towards heavier $\delta^{34}S$ of residual seawater sulfate. Provided the system is closed with respect to sulfate (i.e. restricted basin or pore water disconnect), continued BSR and pyrite formation will result in progressively enriched $\delta^{34}S$ values of H_2S as bacteria successively reduce residual sulfate. This acts to reduce the offset between the sulfur isotopic composition of coeval H_2S and SO_4^{2-}. Further ^{34}S-enrichment of seawater sulfate and depletion of H_2S may indicate additional fractionation via cycles of bacterial disproportionation of sulfur intermediates and subsequent H_2S oxidation back to elemental sulfur (S^0) via scavenging by Fe oxides (Goldberg et al., 2005).

The size of the seawater sulfate reservoir and extent of BSR in ancient oceans is thought to be resolvable through determination of the sulfur isotopic composition of pyrite ($\delta^{34}S_{py}$) in sedimentary rocks alongside determination of sulfate incorporated into the lattice of sedimentary carbonates ($\delta^{34}S_{CAS}$), or carbonate fluorapatite (francolite) in phosphorites (Shields et al., 2004; Fike and Grotzinger, 2008; Och and Shields-Zhou, 2012). Negligible fractionation accompanies substitution of SO_4^{2-} into carbonate precipitates which allows the isotopic composition of carbonate associated sulfate (CAS) to directly represent that of contemporary seawater sulfate ($\delta^{34}S_{SO4}$) (Shields et al., 2004; Goldberg et al., 2005; Fike et al., 2006). It follows that variations in $\delta^{34}S_{CAS}$ record changes to the primary seawater sulfate isotopic composition, with heavier $\delta^{34}S_{CAS}$ resulting from elevated rates of BSR in an organic matter and sulfate-replete water column accompanied by decreasing $\delta^{34}S_{py}$, which in turn drives an increase in the isotopic offset between seawater sulfate and pyrite sulfur ($\Delta^{34}S_{CAS\text{-}py}$). Alternatively, oxidation of isotopically light H_2S or pyrite at the oxic/anoxic interface or in the anoxic water column (or pore water) through reduction of Fe(III) in the presence of H_2O, will act to reduce $\delta^{34}S_{CAS}$ (Goldberg et al., 2005). It is important to note, however that the target lithologies for the isotopic analyses of carbonate associated and pyrite bound sulfur reflect formation under inherently separate depositional regimes which are subject to variable connectivity to the water column. Sulfate limitation in a closed system during extended periods of basin restriction or effective disconnect between pore water and seawater will tend to drive sedimentary $\delta^{34}S_{py}$ towards heavier values through continued BSR of the increasingly isotopically heavy sulfate reservoir, whereas coeval carbonate associated $\delta^{34}S$ will remain constant, effectively leading $\Delta^{34}S_{CAS\text{-}py}$ to approach zero (Gomes and Hurtgen, 2013). As a consequence, evaluation of local environmental factors such as basin restriction and redox allows for comprehensive interpretation of trends in the sulfur isotopic record provided by $\delta^{34}S_{py}$ and $\delta^{34}S_{CAS}$.

1.7 Determining basin restriction

Studies on modern marine basins subject to variable degrees of restriction from the open ocean indicate that the elemental composition of basinal waters is related to the rate of deep-water renewal (Algeo and Lyons, 2006; Gilleaudeau and Kah, 2015). A number of studies have explored the potential for the ratio of molybdenum to total organic carbon (TOC), alongside changes in the size of the local seawater sulfate reservoir as evidenced from sulfur isotopic composition of pyrite and carbonate associated sulfate, as geochemical proxies for basin restriction in sulfidic settings. A Mo pump scenario under restricted or semi-restricted basin conditions has been proposed whereby short-term variations in euxinia result in a peak of Mo removal from the water column. This occurs through the combined effects of Mo adsorption during Fe-Mn-oxyhydroxide formation under oxic to suboxic conditions, followed by Mo release via reductive dissolution during periods of euxinia and scavenging by sulfur-rich organic matter (Algeo and Lyons, 2006; Scott and Lyons, 2012). Long-term restriction under euxinic conditions leads to a decrease in sedimentary Mo relative to TOC as a consequence of depletion of the aqueous Mo (Mo_{aq}) inventory through efficient removal via transformation to particle reactive thiomolybdate and subsequent scavenging and burial, with Mo/TOC values of 10-15 ppm/wt% indicative of Mo_{aq} depletion (Algeo and Lyons, 2006; Scott et al., 2008; Scott and Lyons, 2012). Thus, following an episode of deep water renewal in restricted settings, Mo/TOC is expected to peak due to resupply of aqueous Mo and will subsequently return to lower values during restriction-induced deep water stagnation. In contrast, basins characterised by frequent deep water renewal and aqueous Mo supply will show more elevated, and typically less variable Mo/TOC values on timescales lower than the residence time of Mo in the global ocean (Algeo and Lyons, 2006; Scott et al., 2008).

1.8 Local/regional proxies

1.8.1 The iron shuttle and iron speciation

Iron speciation, using the procedural method of Poulton and Canfield (2005) allows for localized redox reconstructions based on the evaluation of iron phases considered highly reactive to biological/abiological reduction under anoxic conditions (Fe_{HR}) relative to total iron (Fe_T) and the proportion of this Fe_{HR} pool which is contributed as pyrite iron (Fe_{py}). Under oxic conditions, soluble Fe(II) is oxidized to insoluble Fe(III), whilst anoxic conditions permit the water column transport of Fe(II) until precipitation is induced (Figure 1.9) (Raiswell and Canfield, 1998). Water-column Fe(II) may lead to formation of pyrite through reaction with H_2S_{aq} when transported to euxinic settings, or may be precipitated as a range of non-sulfidized minerals (including Fe carbonates and oxides) under anoxic,

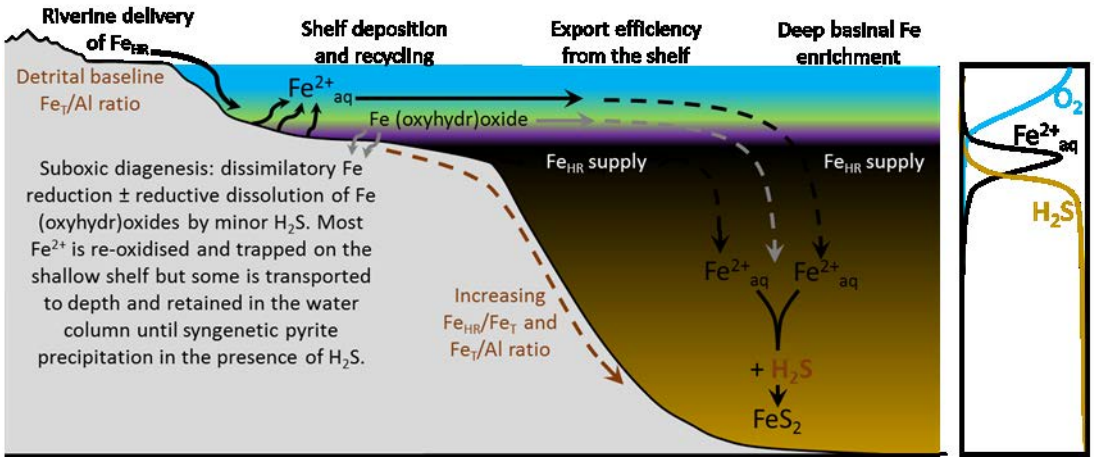

Figure 1.9

Schematic representation of low temperature iron cycling in an anoxic basin after Raiswell and Anderson (2005) and Lyons and Severmann (2006).

non-sulfidic (ferruginous) conditions (Poulton et al., 2004). This augments the detrital influx of $Fe_{HR,}$ resulting in Fe_{HR} enrichments in the deposited sediment. The technique of Poulton and Canfield (2005) subdivides these Fe_{HR} minerals into operationally defined phases, including iron carbonates (e.g. ankerite and siderite), Fe(III) oxyhydroxides (e.g. goethite, lepidocrocite, ferrihydrite, and hematite), mixed valence iron (magnetite), and sulfide-associated iron phases (e.g. pyrite and mackinawite). The sum of Fe_{HR} plus iron bound in poorly reactive or unreactive silicates (geochemically inert on early diagenetic timescales) encompass the total iron (Fe_T) content of modern sediments and ancient marine shales (Raiswell and Canfield, 1998; Poulton and Raiswell, 2002). Sediments deposited under oxic water column conditions record suppressed Fe_{HR}/Fe_T (commonly below 0.22) due to the lack of highly reactive iron accumulation in the water column, whereas under anoxic water column conditions, ratios of Fe_{HR}/Fe_T are typically elevated above 0.38 (Poulton and Canfield, 2005). Where samples have $0.22 < Fe_{HR}/Fe_T < 0.38$, redox interpretation is problematic due to the potential for physical processes such as rapid sedimentation to reduce the preserved signal of Fe_{HR} enrichment under anoxic depositional conditions (Poulton and Canfield, 2011; Lyons and Severmann, 2006). In some instances, alteration of Fe_{HR} to unreactive iron (Fe_U) similarly results in reduced Fe_{HR}/Fe_T, and a false oxic interpretation (Raiswell and Canfield, 1998; Poulton et al., 2004; Raiswell et al., 2008). In these cases, additional consideration of Fe_T/Al ratios (see below) and poorly reactive Fe contents may allow oxic and anoxic samples to be distinguished (see Poulton et al., 2010; Cumming et al., 2013).

Redox proxy	Reduction potential sensitivity	Target lithologies
a) Global ocean redox		
Examples of redox sensitive elements (RSE)		
V	Sedimentary enrichment begins under E_H typical of NO_3^- reduction	Shale and siltstone
U	Significant sedimentary enrichment occurs rapidly under E_H typical of Fe(III) reduction	Organic-rich black shale
Mo	Sequestered by Mn-Fe oxides under aerobic to mildly reducing conditions. Quantitative drawdown through conversion to particle-reactive thiomolybdate in the presence of free $H_2S > 11 \mu mol L^{-1}$	Organic-rich black shale
Isotopic fractionation		
$\delta^{238/235}U$	Preferential incorporation of ^{238}U into insoluble U^{4+} during reduction of U^{6+} and incorporation into organic-rich mudrocks begins under E_H typical of Fe(III) reduction	Organic-rich shale: Elevated $\delta^{238}U$ under anoxic conditions, Carbonate: negligible fractionation during incorporation yielding contemporaneous seawater $\delta^{238}U$ composition
$\delta^{98/95}Mo$	Negligible fractionation during quantitative drawdown of thiomolybdate under highly euxinic conditions. Significant fractionation under weakly euxinic, anoxic non-sulfidic and oxic conditions.	Organic-rich shales: Represent the proportion of euxinic to less reducing conditions which characterize the global ocean
$\delta^{82/76}Se$	Se oxyanion reduction at E_H characterised by Fe(III) reduction	Shale
b) Local/basin-wide redox		
REE(Ce/Ce*)	Ce^{4+} scavenged onto Fe and Mn oxides under aerobic to mildly reducing conditions	Phosphorite, chert, carbonate
Fe speciation	Enrichment of Fe_{HR}/Fe_T allow anoxic conditions to be distinguished from oxic conditions. The degree of sulfidation of Fe_{HR} allows ferruginous and euxinic conditions to be distinguished provided $Fe_{HR}/Fe_T > 0.38$.	Shale and carbonate
I/Ca	Rapid conversion of iodate to iodide under E_H associated with NO_3^- and Mn oxide reduction	Carbonate

The iron speciation proxy has the additional advantage of being able to distinguish between euxinic and ferruginous conditions. Under euxinic conditions the build-up of water column hydrogen sulfide (H_2S_{aq}) results in sulfidation of iron oxides and formation of iron pyrite (FeS_2; Fe_{py}), leading to elevated Fe_{py}/Fe_{HR} (Poulton et al., 2004). Constrastingly, enrichments in Fe_{HR} with low Fe_{py} is considered indicative of ferruginous anoxia (Poulton and Canfield, 2005). Calibration of modern and ancient sediments indicates that, where anoxic conditions are inferred by $Fe_{HR}/Fe_T > 0.38$, correspondingly elevated ratios of $Fe_{py}/Fe_{HR} > 0.7 - 0.8$ are a strong indicator of euxinic water column conditions, whereas $Fe_{py}/Fe_{HR} < 0.7$ are thought to represent ferruginous conditions (Poulton et al., 2004; März et al., 2008; Poulton and Canfield, 2011).

Clarkson et al. (2014) enhanced the application of the iron speciation technique via calibration for use on carbonate-rich sediments. This is of considerable benefit due to the confinement of fossils which represent early calcifiers to carbonate lithologies (Wood, 2011). Clarkson et al. (2014) show that the oxic/anoxic Fe_{HR}/Fe_T thresholds are also valid for carbonates, provided $Fe_T > 0.5$wt%. When $Fe_T < 0.5$ wt%, Fe_{HR}/Fe_T for oxic samples commonly show values greater than 0.38 either as an artefact of diagenetic Fe addition or due to the combination of Fe_{ox} incorporation and very low lithogenic iron. Iron speciation should thus be avoided for samples wherer $Fe_T < 0.5$ wt%, in addition to samples which show evidence for burial dolomitization where late diagenetic iron addition is common.

The average ratio of Fe_T/Al measured from studies of Phanerozoic shales and carbonates (0.53 ± 0.11 and 0.55 ± 0.11, respectively) provides additional support when interpreting iron speciation data, with values greater than the upper threshold strongly suggesting local Fe_{HR} enrichment during deposition under a reducing water column (Lyons and Severmann, 2006; Raiswell et al., 2008; Clarkson et al., 2014). Conditions leading to shale Fe_T/Al values below the calibrated lower threshold are not well understood (Sahoo et al., 2012). However, possible mechanisms for depleted Fe_T/Al may involve an unusual lithogenic source composition, or depletion of Fe_{HR} by reduction of Fe (oxyhydr)oxide minerals and mobilization of Fe^{2+} to the water column (the benthic iron shuttle; Lyons and Severmann, 2006; Severmann et al., 2008). The geochemical expression of oxygen minimum zones with respect to the

---

Table 1.1 (Facing page)**:** Summary of major paleoredox proxies, the redox potentials at which they record transformation, and lithologies targeted for their application. **a)** Examples of elements which, in addition to providing information on local basin-scale redox, also enable inference of the nature and extent of global ocean redox and **b)** examples of techniques which enable evaluation of basin-scale redox state.

benthic Fe shuttle shows that enrichment of Fe_{HR} typically occurs at the oxycline beneath the OMZ, while sediments within the OMZ commonly show reduced Fe_T/Al relative to sediments above and below, indicating a possible source of Fe_{HR} for underlying enrichment (Scholz et al., 2014).

1.8.2 Rare Earth Elements and Cerium anomalies

Distributions of rare earth elements (REE) within authigenic minerals (e.g. carbonates, phosphates, and chert) represent contemporaneous equilibrium between solution complexes and solid phase surface complexes (metal (oxyhydr)oxides, clay and organic matter) provided there has been no deep-burial diagenetic modification (McArthur and Walsh, 1984). Cerium is the only rare earth element prone to substantial transformation as a function of ambient seawater E_H, due to the relatively reduced solubility of oxidized Ce(IV) at neutral to high pH (Pourret and Houben, 2018) and consequent scavenging by Fe-Mn (oxyhydr)oxides, which leaves the seawater REE pool comparatively depleted in Ce in oxic settings (German and Elderfield, 1990). Characteristic REE profiles with associated anomalous Ce depletion (Ce/Ce*) can therefore be a good indicator of oxic conditions, on condition that there has been no signal modification by later reducing fluids (Bau and Dulski, 1996; Shields et al., 2004). As such, the entire REE profile must display a distinguishing pattern of diagnostic relative depletions and enrichments indicative of average seawater, from which depletion of Ce relative to the light rare earth elements (LREE: praseodymium to gadolinium), lanthanum and neodymium indicates likely deposition under oxic water column conditions (Shields et al., 2004; Tostevin et al., 2016a).

1.8.3 Iodine/(Calcium + Magnesium)

Calibration of a proxy based on the ratio of iodine to calcium+magnesium is providing further information into the redox conditions which prevail during carbonate sedimentation. Oxidised iodate (IO_3^-) is the only iodine species incorporated during carbonate mineral formation, and the rapid conversion of iodate to iodide occurs at redox potentials in the range characterised by Mn reduction and denitrification (Lu et al., 2010). With a modern residence time of approximately 300ky, iodine is considered to be well mixed in the ocean and, as a biophilic element, the size of the iodine reservoir in the global ocean is largely controlled by organic carbon burial (Lu et al., 2010). Importantly however, it the oceanic residence time of I may have changed dramatically through geological time and this remains largely unconstrained. Indirect evaluation of local mildly reducing conditions conducive to iodate conversion is therefore possible through determination of the ratio of I/(Ca+Mg) in contemporary carbonate sediments (Lu et al., 2010; Hardisty et al., 2014).

1.8.4 Trace fossils

Studies of modern benthic macrofaunal diversity and complexity under different dissolved oxygen levels imply that traces indicative of motility or active bioturbation, such as *Treptichnus pedum*, are restricted to formation by organisms with active metabolic lifestyles that most likely require elevated dissolved oxygen concentrations (Chang et al., 2006; Wilson et al., 2012). The absence of trace fossil evidence for active motility (Aceñolaza et al., 2009), in addition to a lack of evidence for extensive carnivory and predation (Sperling et al., 2015c), may support geochemical evidence for widespread anoxic, or low oxygen conditions prior to the late Ediacaran. Indeed, one interpretation for the observed increase in trace fossil evidence nearing the Ediacaran-Cambrian boundary, and first appearance of *Treptichnus pedum*, is a trend towards increasing concentration or stability of bottom water oxygen (Sperling et al., 2013b).

1.9 Proxy limitations

A shortfall of most redox proxies has traditionally been associated with their application to a limited range of lithologies, with most proxies originally calibrated to target fine grained siliciclastic sediments such as shale. As discussed above however, recent calibration of iron speciation (Clarkson et al., 2014), alongside redox proxy extraction processes targeting Ce/Ce* (German and Elderfield, 1990; Shields et al., 2004; Tostevin et al., 2016a) within carbonate-rich sediments can significantly aid redox interpretation of mixed carbonate-siliciclastic palaeoenvironments. Differing lithological requirements and proxy sensitivity to different reducing conditions are summarized in Table 1.2.

Furthermore, assessing the proportion of the global ocean characterized by euxinia through the use of RSE and isotopic enrichment in shales deposited under locally euxinic conditions suffers the complication that local environments are subject to variation in the degree of euxinia and connectivity to the global ocean. This leads to the necessity for data collection to be accompanied by an evaluation of local water column redox conditions and restriction (e.g. Algeo and Lyons, 2006; Kendall et al., 2011; Gomes and Hurtgen, 2013). The elemental composition of modern semi-restricted basins is affected by the rate of deep-water renewal (Konovalov et al., 2006; Algeo and Lyons, 2006; Gilleaudeau and Kah, 2015). As noted in section 1.7, the ratio of molybdenum to total organic carbon (TOC), and changes in RSE concentration relative to the size of the local seawater sulfate reservoir are geochemical proxies which inform the degree of basin restriction in anoxic sulfidic settings (Algeo and Lyons, 2006; Scott and Lyons, 2012).

Previous studies have also stressed the relative insensitivity of bulk rock techniques to record rapid fluctuations in water column redox conditions, such as those potentially associated with individual fossil occurrences, since samples often represent a significant period of time. For example, very fleeting oxia and rapid colonization of substrate by opportunistic biota may be preserved as an overall signature of pervasive anoxia, which in fact may only represent the dominant redox condition during sedimentation of the bulk sample (Johnston et al., 2013; Wood et al., 2015; Sperling et al., 2015b, 2015c).

1.10 Methodologies employed in this thesis

1.10.1 Fieldwork and sample preparation

Samples for which new data are presented in this thesis were collected on numerous field excursions led by Rachel Wood to southern Namibia, southeast Siberia and South China. Sedimentary rocks were targeted including shale, fine-grained mudstone, limestone and dolomite. When collecting outcrop material, extensive weathering which typifies surface exposure requires sampling of individual shale fragments of sufficiently large size to ensure complete removal of weathered parting surfaces. As such, samples were taken with a minimum mass of ~40g, weathered surfaces were removed and samples were divided in two with a diamond saw, washed and dried. Samples showing visible veining and alteration were rejected at this point. Once dry, half the sample was crushed and pulverised to a homogeneous powder using a tungsten carbide jaw crusher and disc mill. The other half of each sample was archived. Carbonate samples underwent the same meticulous cleaning, trimming, crushing and powdering procedure and in some instances (e.g. in determination of $\delta^{18}O_{carb}$ and $\delta^{13}C_{carb}$) the archived half was polished, washed and appropriate carbonate cements were targeted for microsampling using a Dremel hand drill fitted with a diamond tipped drill bit. The same cleaning procedure using water, acetone and compressed air was applied to the drill bit as to the crushing and powdering equipment between each sample.

1.10.2 Iron speciation and major element analysis

Iron speciation data documented in this thesis were analysed via the procedure developed by Poulton and Canfield (2005) and follow a 3 step sequential extraction, a total digestion and a sulfide-bound iron extraction. Highly reactive iron (Fe_{HR}) is operationally defined as the portion of the iron pool that is

highly reactive to biological or abiological reduction under anoxic conditions. The original sequential extraction scheme allowed for the chemical leaching of four highly reactive iron fractions bound in carbonates (siderite and ankerite), easily reducible oxides (ferrihydrite and lepidocrocite), reducible oxides (hematite, goethite and akaganéite), and a mixed-valence oxide (magnetite) (Poulton and Canfield, 2005). Further chemical leaches targeted iron sulfides (Fe_{py}, pyrite), poorly reactive sheet silicates (Fe_{PR}) and unreactive silicate-bound iron (e.g. nontronite) (Fe_U) (Canfield et al., 1986; Raiswell and Canfield, 1998; Poulton and Canfield, 2005). Because easily reducible oxides are known to alter to reducible oxides over geological timescales (under sub-prehnite-pumpellyite metamorphic facies conditions, Schwertmann, 1966; Torrent and Cabedo, 1986), the size of the combined iron oxide pool (not including magnetite) for ancient samples can be evaluated by one chemical leach (Poulton and Canfield, 2005, 2011). Reproducibilities for each step are provided in Appendix B.

Sequential extraction procedure (performed on ~0.1g sample powder):

1) Leaching of carbonate-bound iron by a solution of 1 M sodium acetate (82.03gL^{-1} CH_3COONa) buffered to pH 4.5 with acetic acid and agitated for 48 hrs and kept at a constant temperature of 50°C.

2) Leaching of oxide-bound iron using a solution of sodium dithionite (50gL^{-1} $Na_2S_2O_4$) buffered to pH4.8 with acetic (20mlL^{-1}) acid and trisodium citrate (58.82gL^{-1}). This leach was kept at room temperature and left to agitate for 2 hrs.

3) The final leach targeted the remaining sample with an ammonium oxalate (28.42gL^{-1} $C_2H_8N_2O_4.H_2O$) solution buffered with oxalic acid (21.43gL^{-1}) agitated for 6 hrs at room temperature.

All laboratory experiments were carried out at the University of Leeds, School of Earth and Environment, Cohen Laboratories and resultant solutions were analysed for total iron content via atomic absorption spectroscopy (AAS).

Total digestion procedure (performed on ~0.1g sample powder):

Separate to the sequential extraction procedure, all samples were subjected to a trace metal clean total digestion procedure. After ashing samples at 550°C for 12 hours, samples were transferred to PTFE cups using 5 ml concentrated (15.25 M) HNO_3 followed by addition of 2 ml concentrated (27.6 M) HF

and 2-3 drops of concentrated $HClO_4$. Samples were then left to digest completely on a hotplate at a sub-boiling temperature until dry (approximately 12 hours). The residues were then re-dissolved in 2 ml (11.64 M) $B(OH)_3$ to prevent the formation of Al complexes and left to dry on the hotplate for a further 3 hours. Following this, all residues were once more re-dissolved in 2 ml (15.25 M) HNO_3 and left to dry to form a residue of nitrate salts. This final step was carried out to minimise the potential for matrix effects during subsequent analysis via ICP-OES. The resultant residues were once more re-dissolved in 4 ml of (7.63 M) HNO_3 and diluted to 100 ml in ultrapure MilliQ H_2O to create solutions with a final concentration of 0.305 M HNO_3 for ICP-OES analysis.

The preparation of multi-element standards for use on the ICP-OES allowed for determination of a suite of important major elements (e.g. Al, Ti, Ba, Cr, Ca, Na, K) in addition to total iron concentration. All laboratory procedures and ICP-OES analyses were carried out at the University of Edinburgh, School of Geosciences.

Chromium reduction method:

A boiling chromous chloride distillation was used in determination of the fractional contribution of iron bound as pyrite (Fe_{py}) (Canfield et al., 1986). All experiments were conducted under inert conditions through flushing of round-bottomed flasks and condenser columns by N_2. Sample weights varied depending on carbonate content between 4 g (shale) and 6 g (pure carbonate). Samples weighed into round-bottom flasks were initially pre-treated by addition of 8-10 ml concentrated (12.08 M) HCl and brought to boiling in order to remove elemental sulfur and acid volatile monosulfides (AVS). In the extremely rare cases of AVS being present, samples were left to react with the HCl for a further 45 minutes. Following HCl pre-treatment, samples were subjected to addition of 15 ml chromous chloride (533g Cr(III)Cl reduced in 6.04 M HCl and catalysed by Zn shot to a final volume of ~1L). The reaction induced through addition of chromous chloride does not liberate either organic or sulfate sulfur (e.g. sulfur bound in barite) but allows assessment of reduced inorganic sulfur phases (Canfield et al., 1986). The stoichiometric concentrations of AVS and Fe_{py} were determined gravimetrically by precipitation of Ag_2S after reaction of liberated $2H_2S$ with $AgNO_3$ in prepared test tube traps. All steps of the chromous chloride extraction were performed at the University of Edinburgh, School of Geosciences.

1.10.3 Cathodoluminescence microscopy

Highly polished thin sections were examined using a combination of transmitted light and cathodoluminescence microscopy for detailed evaluation of primary carbonate cement zonation prior to targeted electron microprobe analyses (Chapter 4). A Cathodoluminescence Cold Cathode CITL 8200 MK3A mounted on a Nikon optiphot microscope at the University of Edinburgh was used to identify differing luminescence (Habermann et al. 1996; 1998; Mason and Mariano, 1990). Working current and voltage were maintained in the ranges 400 – 600 μA and 15 – 20 kV respectively to avoid damaging carbonate samples via electron bombardment.

1.10.4 Electron Microprobe and X-Ray Diffraction analyses

Highly polished thin sections were carbon coated and carbonate cements were manually targeted for major element concentrations (Fe, Ca, Mg, Mn, Sr) using a Cameca SX100 Electron Microprobe at the University of Edinburgh with an 80 s count time, a beam diameter of 3 μm, an accelerating voltage of 15 kV, and a beam current of 35 nA. Additionally, powdered samples of Nama and Yudoma Group dolomites were subjected to XRD analysis in order to evaluate dolomite stoichiometry and ordering using a weighted mean incident wavelength for CuKα radiation of 1.541838Å and the ^{d}104 peak at a 2θ angle of 30.9°. Results are presented in Chapter 4 and raw data in Appendix C.

1.10.5 Iodine/(Calcium+Magnesium)

Palaeoredox conditions are indeterminable via iron speciation in carbonate samples which contain Fe_T < 0.5 wt% (Clarkson et al., 2014) and were instead analysed via a relatively newly calibrated procedure based on the incorporation of iodate under oxic water column conditions during primary carbonate precipitation (e.g. Lu et al., 2010; Hardisty et al., 2014). Limestone and dolomite subsamples were microdrilled from fresh surfaces which showed no visible indication of secondary alteration or veining and all chemical procedures were undertaken at either the University of California Riverside or Woods Hole Oceanographic Institute by Dalton Hardisty. The extraction method utilised for determination of I/(Ca+Mg) followed that outlined in Lu et al. (2010) and involved a single step digestion in 3% HNO_3 with resultant dilutions analysed on a quadrupole ICP-MS alongside duplicate certified control georeference samples and additional selected duplicate and triplicate samples. Standard curves were

sufficiently reproducible to resolve very low iodine concentrations (~40 parts per trillion) and low values are thus reported with confidence.

1.10.6 Calcium isotopes

A pilot study of $\delta^{44}Ca$ is presented on a subset of carbonate samples from the Nuuchchalakh section deposited on the southeast Siberian Platform in Chapter 5. These data were collected by Sasha Turchyn and Hal Bradbury of the University of Cambridge and are preliminary to ongoing collaborative research. The analytical procedure for Ca isotope analysis followed that outlined in Fantle and DePaolo (2007). Approximately 100-200 µg of carbonate powder was dissolved and an aliquot of approximately 30 µg Ca was separated and spiked with 42-48 Ca double-spike followed by equilibration in 5-8 N HNO_3 (Turchyn and DePaolo, 2011). Following dry-down, samples were loaded in 250µl of 1N HNO_3 onto ion separating columns containing 1.6cm^3 DOWEX® AG 50W-X8 Resin, eluted in 2N HNO_3 and dried. Resultant spiked and chemically-separated samples were loaded onto Re filaments with phosphoric acid (H_3PO_4) and analysed via multi-collector Thermal Ionisation Mass Spectrometry (MC-TIMS) at the University of Cambridge. A minimum of two replicates per sample were analysed and results are provided with error bars representing two standard deviations in Figure 5.5.

1.11 Thesis Aims and Hypotheses

The primary aim of this thesis is to illuminate the nuances of local redox heterogeneity among the currently known Ediacaran and early Cambrian palaeoenvironments. In so doing, this thesis builds upon current understanding in order to evaluate the role that dissolved oxygen availability may have had in early animal ecosystem habitability.

- Provide a comprehensive assessment of fossil occurrence and co-occurring local redox conditions using available published data from palaeoenvironments of the Ediacaran and early Cambrian.

  Hypothesis: The distribution of fossils confidently regarded as early animal representatives correlates with proxy evidence for frequent ventilation or stable oxic water column conditions.

- Attempt to provide a mechanistic interpretation for variability in long-lived local redox conditions based on knowledge of circulation and nutrient-driven productivity dynamics in the modern.

  Hypothesis: Changes in the palaeo-redoxcline depth and thickness of redox-controlled chemical zones identified via proxy methods relate in part to palaeo-hydrodynamic and nutrient-driven palaeoproductivity changes. These are determinable from high resolution sequence stratigraphic reconstruction and palaeoproductivity proxy estimates. Further, long term changes in local redox relate to changing circulation regimes as is the case in the modern.

- Compile a detailed local redox record for the Nama Group from published and new data. Integrate these data with a four-dimensional understanding of changes in relative sea level throughout deposition of the Nama Group and interrogate these records relative to changes in total (and palaeodepth-specific) taxonomic diversity in the final 10 Myrs of the Ediacaran Period.

  Hypothesis: Long term evolution of local shelf-to-basin redox conditions are accompanied by associated changes in the spatial extent of habitable space. It is possible to observe corresponding changes in the distribution of organisms inferred to occupy metabolically active lifestyles.

- Undertake the first high-resolution study of cement stratigraphy for the key *Cloudina* pinnacle reef locality at Driedoornvlakte incorporating cathodoluminescence and cement-specific elemental data in order to interpret the sequence of chemical zones under which skeletal organisms and subsequent carbonate cements grew.

  Hypothesis: The concentrations and distribution of elements within individual generations of cement record precipitation under distinct redox conditions. Dolomite cement in the Nama Group is an early precipitate, the growth of which was mediated under anoxic ferruginous conditions.

- Provide the first assessment of local redox dynamics in the shallow marine environment of the southeast Siberian Craton and additional data from environments of the Yangtze Block. An attempt is made to assess the temporal equivalence of these two environments and the impact of changing redox conditions on local palaeocommunities.

Hypothesis: Local palaeoredox landscapes across the Ediacaran-Cambrian divide are accompanied by corresponding local ecosystem complexity. The boundary between the Ediacaran and Cambrian Periods defined by the appearance of a novel ichnospecies is not only biased by facies but also by habitable ecospace imposed by local palaeoredox.

1.12 Thesis outline

Chapter 2 focuses on a synthesis and review of published local redox proxy data for the Ediacaran Period.

This chapter comprises an updated version of sections 3 to 6 of a paper published in *Geobiology* as: *'Bowyer, F., Wood, R.A., and Poulton, S.W. (2017) Controls on the evolution of Ediacaran metazoan ecosystems: A redox perspective, Geobiology, Vol. 15, Issue 4, pp. 516 – 551.'*

Chapter 3 aims to provide an updated and comprehensive assessment of the co-evolution of palaeontology and redox geochemistry in the late Ediacaran Nama Group, Namibia. The focus of this chapter is on a compilation of iron speciation data and fossil occurrence but also attempts to provide the first assessment of palaeoproductivity utilising excess biogenic barium. Additional data concerned with the ratio of carbonate-bound I/(Ca+Mg) has been collected by, and is the product of ongoing collaboration with Dalton Hardisty (formerly at the University of California, Riverside and currently affiliated with Woods Hole Oceanographic Institution) and Tim Lyons (University of California, Riverside).

Data presented in this chapter are in preparation for submission as: *'Bowyer, F., Wood, R.A., Poulton, S.W., Thomas, A., Butler, I., Hardisty, D.S., Diamond, C. and Lyons, T.W. Constraining the evolution of redox and ecology in the terminal Ediacaran Nama Group, Namibia.'*

Chapter 4 attempts to provide a quantitative assessment of major element concentrations and paragenetic evolution of carbonate cements in the final stages of reef growth at Driedoornvlakte in the northern subbasin of the Nama Group, Namibia. This chapter utilises a combination of electron probe, cathodoluminescence microscopy and X-ray diffraction data of carbonate thin section samples. The findings discussed in this chapter have been published in the journal *Precambrian Research* under the title: *'Wood, R.A., Bowyer, F., Penny, A., and Poulton, S.W. (2018) Did unstable redox terminate Ediacaran benthic communities? Evidence from early diagenesis, Precambrian Research, Vol. 313, pp. 134-147.'*

Chapter 5 provides the first palaeoredox assessment of fossiliferous sediments of the Yudoma-Maya depression, deposited on the southeastern margin of the Siberian Craton in addition to two sections of the Dengying and Zhujiaqing (/Yanjiahe) Formations deposited on the Yangtze Block, South China. This chapter documents iron speciation and major element data from siliciclastic and suitable carbonate samples in addition to data of I/(Ca+Mg) in carbonates (data collected by Dalton Hardisty). The findings presented are in the early stages of manuscript preparation for submission under the title: *'Bowyer, F., Wood, R.A., Poulton, S.W., Thomas, A., Lyons, T., and Hardisty, D.S. Palaeoredox and productivity across the Ediacaran-Cambrian transition: insights from fossiliferous deposits of the Yudoma-Maya depression, southeastern Siberia and Yangtze Platform, South China.'*

Chapter 6 synthesises the data presented in this thesis and attempts to address key questions which remain unanswered. This chapter includes conclusions and suggestions of future directions in the field of Ediacaran palaeoenvironmental research.

1.13 Thesis Contributions

Many of the diagrammatical illustrations provided in this thesis (especially in Chapters 1 and 2) are the product of data compilation from numerous published sources after Bowyer et al. (2017). Original publications from which these primary data have been obtained are directly referenced in appropriate points throughout this thesis.

The application of the iron speciation procedure was largely enabled through inter-laboratory collaboration with the University of Leeds, School of Earth and Environment, Cohen Laboratories. Indeed, the development of iron speciation capability at the University of Edinburgh, Grant Institute would have been substantially more difficult without the technical expertise and advice of S.W. Poulton, A. Connelly, S. Reid and J. Thompson. Expert assistance was also provided by I. Butler of the University of Edinburgh in construction of equipment used in the chemical extraction of acid volatile sulfide and pyrite and by R. Russel and E. McDougall in the safe use of hydrofluoric acid within the University of Edinburgh.

Relevant technical support, supervision and author contributions are given at the start of each chapter and re-use of published figures and photos, or inspiration for updated figures are referenced where appropriate. Sample site information is provided in Appendix A.

Chapter 2

The record of Ediacaran marine redox

Abstract

Detailed geochemical studies of Ediacaran (635–541 Ma) marine successions have provided snapshots into the redox environments that were host to the earliest known metazoans. Whilst numerous compilations have focused on the global evolution of Ediacaran water column palaeeoredox, the inherent chemical heterogeneity evident in paleogeographically distinct Ediacaran environments demands a more dissected approach in order to better understand the nature, interactions and evolution of extrinsic controls on the development of early macro benthic ecosystems. This chapter reviews available data of local-scale redox within a paleogeographic and sequence stratigraphic framework with the aim of exploring the mechanisms controlling water column redox variations and their potential impact on the record of metazoans. Cratonic positioning and migration throughout the Ediacaran Period, in combination with gradually increasing dissolved oxygen loading, may have provided a long-term control on redox evolution through regulating circulation mechanisms in the Mirovian Ocean. Some unrestricted lower slope environments from mid-high latitudes benefited from sustained oxygenation via downwelling, whilst cratonic isolation or transit towards more equatorial positions stifled pervasive ventilation either through ineffective surface ocean mixing, Ekman-induced upwelling, elevated surface ocean productivity or, most likely, a combination of these processes.

Author Contributions: The data presented here were collated from multiple studies and interpreted in a review article published as Bowyer et al. (2017). Text, discussion and figures have been adapted and updated from the Bowyer et al. (2017) manuscript. This chapter benefited from helpful discussions with Rachel Wood, Alex Thomas and Simon Poulton.

2.1 Introduction: The Ediacaran Global Ocean

Seemingly conflicting evidence has been published for the extent of open ocean ventilation during the late Neoproterozoic and early Cambrian. For example, molybdenum isotope data have been variously interpreted to indicate widespread marine oxygenation as early as 700 Ma (Baldwin et al., 2013) or sustained water column redox stratification and continued deep ocean anoxia into to the early Cambrian (Wille et al., 2008; Kurzweil et al., 2015). Elevated $\delta^{238}U$ and temporarily elevated $\delta^{98}Mo$ to near-modern open ocean values reported from the upper Doushantuo Formation (at Jiulongwan, see section 2.2.1), are proposed to reflect well-oxygenated open ocean conditions between 560 and 551 Ma (Kendall et al., 2015). Similarly, elevated concentrations of organic matter-normalised Mo, U, and V recorded from deposits of the Doushantuo Formation (Scott et al., 2008; Sahoo et al., 2012; Kendall et al., 2015), have been suggested to support limited global ocean RSE scavenging, with the onset of deep ocean oxygenation proposed between 663 and 541 Ma (Scott et al., 2008).

Despite apparent ambiguity between initial interpretations, there is an emerging consensus that open ocean conditions during the Ediacaran Period were influenced by periods of widespread but transient oxygenation interrupted by intervals of pervasive anoxia (Kendall et al., 2015; Sahoo et al., 2016). Support for these sporadic, widespread oceanic oxygenation events include compilations of $\delta^{98}Mo$ and Mo/TOC (Kendall et al., 2015) and, more recently, RSE data from open slope euxinic shales of the Doushantuo Formation in addition to collation of RSE data from multiple palaeogeographically distributed sections (Sahoo et al., 2016).

Thus, redox sensitive element concentrations and their isotopic compositions in sediments may hint at dramatic shifts in the extent of global ocean oxygenation in the Ediacaran, rather than a simple unidirectional increase in the volumetric extent of deep ocean oxygen. However, there is some evidence to suggest that these higher frequency, temporary shifts in global ocean redox state were overprinted by an increase in oxygen concentration, culminating in similar-to-modern levels by the early Cambrian (521Ma) as suggested by the observed stepwise increase in $\delta^{98}Mo$ values from the mid-Cryogenian Datangpo Formation to early Cambrian Formations on the Yangtze Block (Chen, X. et al., 2015). Though iron speciation data inherently reflect local/regional redox conditions, extensive compilations from globally distributed shales deposited below wave base may be considered to provide a global redox perspective. Compiling iron speciation data in this way also suggests that the majority of Neoproterozoic settings (but with important exceptions; see below) were characterized by anoxic ferruginous conditions and that these conditions largely persisted into the early Cambrian (Canfield et al., 2008; Guilbaud et al., 2015; Sperling et al., 2015a).

Late Neoproterozoic strata are characterised by an increase in sulfur isotope fractionation between sulfate and pyite (e.g. Canfield and Teske, 1996; Fike et al., 2006) that has been suggested to represent the increased influence of the oxidative sulfur cycle (Fike et al., 2006; Och and Shields-Zhou, 2012). This is further supported by high S/C_{org} ratios in siliciclastic shale that argue for growth of the oceanic sulfate reservoir at this time and a switch from dominantly pyrite to evaporitic sulfate burial (Och and Shields-Zhou, 2012). Conversely, a smaller seawater sulfate reservoir than present (<28mM, Paytan et al., 2004) has also been suggested to account for the localised formation of so-called 'superheavy' pyrite ($\delta^{34}S_{py} > \delta^{34}S_{CAS}$) (e.g. Ries et al., 2009). More recently however, improved chemical extraction procedures for $\delta^{34}S_{CAS}$ which minimise the potential for matrix-bound sulfur contamination have allowed the re-interrogation of 'superheavy' pyrite and suggest that the application of an unsuitable leaching procedure may have been partly responsible for this phenomenon (Tostevin et al., 2017). The correlation of $\delta^{34}S_{CAS}$ profiles between time-equivalent sections in the final 10 Myrs of the Ediacaran indicates an average increase in the sulfur isotopic composition of seawater sulfate to values > 30‰ and may reflect a high pyrite burial flux at this time (Fike and Grotzinger, 2008; Tostevin et al., 2017). Large inter-basin differences in $\Delta^{34}S_{CAS\text{-}py}$ are inferred to be a consequence of the highly heterogeneous local redox landscape at this time, the extensive evidence for which is outlined below (Tostevin et al., 2017).

2.2 Records of local/regional redox in Ediacaran palaeoenvironments

In order to allow direct comparison between numerous Ediacaran sections, iron speciation data have been compiled herein which are based on calibrated iron phase and major element ratios for depositional redox conditions. Data are presented under a conservative framework whereby oxic conditions are indicated by $Fe_{HR}/Fe_T < 0.22$, anoxic ferruginous by $Fe_{HR}/Fe_T > 0.38$ and $Fe_{py}/Fe_{HR} < 0.7$, and euxinic conditions by $Fe_{HR}/Fe_T > 0.38$ and the upper limit of $Fe_{py}/Fe_{HR} > 0.8$. Importantly, where analyses include both siliciclastic and carbonate lithologies, redox variations are shown to be primary and not lithologically determined providing that the total iron concentration of carbonate samples is greater than 0.5 wt% (Clarkson et al., 2014; Wood et al., 2015). Iron speciation is used herein as a redox proxy baseline but where available, additional proxy data are discussed and include redox sensitive trace element concentrations (RSE), and rare earth element (REE) profiles. Due to the difficulty associated with ascertaining an unambiguous mechanism for exceptionally low Fe_T/Al, samples which record values below the lower threshold (0.42) are not considered in this collation unless stated specifically in the text.

Fifty three sections are considered for which accompanying raw iron speciation data are available with the aim of reviewing local water column redox within platform to basin environments of the

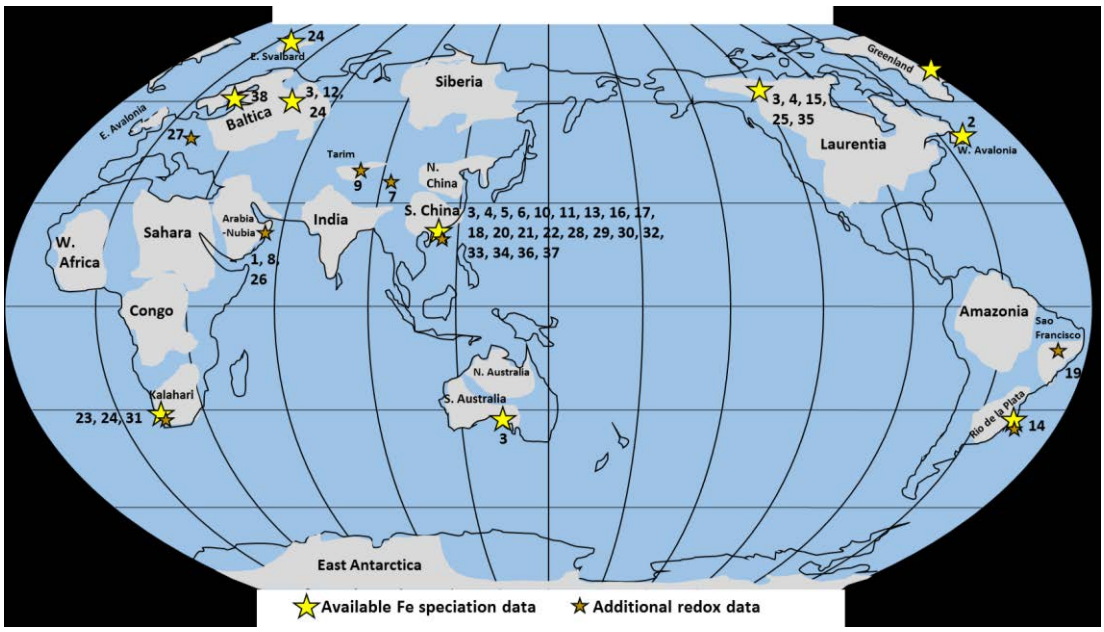

Figure 2.1 Local palaeoredox studies of the terminal Ediacaran and early Cambrian

1 Fike et al. (2006), **2** Canfield et al. (2007), **3** Canfield et al. (2008), **4** Shen et al. (2008), **5** Li, et al. (2010), **6** Dahl et al. (2010), **7** Shen et al. (2010) Ouolongbluq microcontinent, **8** Schroder and Grotzinger (2007), **9** Shen et al. (2011), **10** Sahoo et al. (2012), **11** Wang et al. (2012), **12** Johnston et al. (2012), **13** Och et al. (2013), **14** Frei et al. (2013), **15** Johnston et al. (2013), **16** Fan et al. (2014), **17** Feng et al. (2014), **18** Yuan et al. (2014), **19** Spangenberg et al. (2014) **20** Li, C. et al. (2015b), **21** Kendall et al. (2015), **22** Och et al. (2015), **23** Wood et al. (2015), **24** Sperling et al. (2015a), **25** Sperling et al. (2015b), **26** Osburn et al. (2015), **27** Kurzweil et al. (2015), **28** Han and Fan (2015), **29** Jin et al. (2016), **30** Sahoo et al. (2016), **31** Tostevin et al. (2016b), **32** Huang et al. (2017), **33** Cheng et al. (2017), **34** Xiang et al. (2017), **35** Miller et al. (2017), **36** Li, C. et al. (2017b), **37** Hammarlund et al. (2017), **38** Guilbaud et al. (2018)

Ediacaran to early Cambrian Periods. The environments discussed include the Yangtze Block (South China), Laurentia (western Canada), Kalahari Craton (Namibia), Avalonia (eastern Newfoundland), the East European Platform (western Russia), and the Río de la Plata Craton (Uruguay) (Table 2.1, Figs. 2.1 – 2.5).

2.2.1 Yangtze Block

Richly fossiliferous deposits of the Ediacaran Yangtze Block comprise the Doushantuo and overlying Dengying Formations (and equivalents), together containing multiple examples of possible early Metazoa, from phosphatized animal embryos, soft-bodied *Lantianella*, *Eoandromeda* and *Wutubus* to the biomineralizing tubular forms *Cloudina* and *Sinotubulites* (Xiao et al., 1998; Hua et al., 2003; Zhu et al., 2008; Van Iten et al., 2013; Cai et al., 2014; Chen, Z. et al., 2014). As such, these deposits are key to deciphering the possible environmental requirements of the earliest animal representatives.

Province	Approximate paleolatitude (Li et al., 2013)	Environment and connectivity to Global Ocean	Key biota	Dominant redox environment of habitation
Yangtze Block (South China)	540 Ma: 0–30°N 580 Ma: ~0°N 635 Ma: 30–60°N	Variable connectivity; semi-restricted intra-shelf basins and unrestricted slope-basin environment. Deep siliciclastic facies within intracontinental basins (e.g. Yangtze Gorges), shallow carbonate facies of elevated margins, and deep siliciclastic facies of the open slope to basin.	Early Cambrian Metazoa: articulated sponges, arthropods, motile bilaterian trace-makers, small shelly fossils (SSFs) and stem-lophotrochozoa	Anoxic ferruginous, euxinic and impersistent oxia nearing 520 Ma
			Tubular soft-bodied and biomineralizing metazoans including *Conotubus*, *Cloudina*, *Sinotubulites*, and *Wutubus*. Ediacara-type fossils including *Yangtziramulus*, *Pteridinium*, *Rangea*, and *Charniodiscus* (Dengying Formation)	Anoxic ferruginous, dysoxic to oxic (inferred from Ce/Ce* data, Ling et al., 2013; Duda et al., 2014). Impersistent euxinia of equivalent deep Liuchapo Formation.
			Doushantuo Member IV: Miaohe biota: includes the probable metazoan *Eoandromeda*	Ferruginous
			Doushantuo phosphatized animal embryos and acritarchs Lantian biota: Algae and possible Cnidaria	Ferruginous with euxinia of the open deep slope to basin
Laurentia (North America)	540 Ma: 10–50°S 580 Ma: 30–75°S	Siliciclastic lower slope to basin, shallowing up-section to mixed carbonate-siliciclastic. Freely connected rifting to passive margin, equatorial coast of Laurentia.	Complex multicellular eukaryotes	Anoxic ferruginous, minor oxic intervals
Kalahari Craton (Namibia)	540 Ma: 30–60°S	Mixed carbonate-siliciclastic foreland basin fully connected to Brazilides ocean. Two subbasins shelf-to-basin.	Soft-bodied multicellular eukaryotes & biomineralizing metazoans, *Cloudina* reefs	Variably anoxic ferruginous, manganous and oxic. Progressive oxygenation?
West Avalonia (Newfound-land)	540 Ma: 45-60°S 580 Ma: 30–45°S	Unrestricted lower slope to basin. Dominantly siliciclastic facies.	Complex multicellular eukaryotes	Oxic
East European Platform	540 Ma: 30–60°S 580 Ma: ~30°S	Unrestricted mid-shelf inferred from drill core. Yskemes-Vapol': carbonate dominated. Vychegda-Kotlin: siliciclastic dominated.	Complex multicellular eukaryotes, motile bilaterian metazoans, biomineralizing metazoans	Oxic (inferred- no direct fossil occurrence in drill core section)
Rio de la Plata Craton (Uruguay)	?1000 – 650 Ma: ~60°S	Unrestricted shelf to slope, openly connected to Brazilides Ocean. Mixed carbonate-siliciclastic.	Acritarchs and controversial occurrences of biomineralizing metazoans (*Cloudina*).	Inferred oxic.

Table 2.1: Summary of the six paleogeographic provinces considered in this study with inferred paleolatitude, degree of restriction, associated biota and dominant redox environment during biotic colonization.

Intense study of many Ediacaran to early Cambrian sections of the Yangtze Block have allowed unparalleled detail in paleoredox reconstruction across an array of paleodepth profiles, however difficulty remains in coherent determination of lateral equivalence between some formations and members (Figure 2.2). Basin reconstructions and tentative sequence stratigraphic correlations have been made possible by concerted studies of ash bed dating and detailed $\delta^{13}C$ chemostratigraphy (Figure 2.2) (Condon et al., 2005; Jiang, G., et al., 2006, 2007, 2011; Zhu et al., 2001, 2007, 2013; Compston et al., 2008; Jiang, S.-Y., et al., 2009; Chen, D., et al., 2009, 2015; Cui et al., 2015; Wang et al., 2016).

Recent reassessments of stratigraphic equivalence and completeness between studied sections of the Yangtze Block via analyses of sedimentary facies architecture and chemostratigraphic correlation have enabled a nuanced understanding of the complex paleobathymetry which existed during deposition (Vernhet and Reijmer, 2010; Jiang et al., 2011; Zhu et al., 2013; Cui et al., 2015; Wang et al., 2016). Reconstructions reveal a broad shallow platform to the modern northwest with contemporaneous development of small intra-shelf lagoons and restricted to semi-restricted deeper basins which occupied grabens during initial rifting (e.g. Yangtze Gorges area). The intra-shelf basin environment was bordered by an extensive SW-NE trending elevated shelf margin which gave way down slope to a large, deep basin (Nanhua basin) to the modern southeast which was freely connected to the open ocean (Zhu et al., 2007; Sahoo et al., 2016). Abundant rift-related and block faulted grabens were gradually incorporated into a broad passive continental margin during deposition of Ediacaran sediments and changing relative sea level periodically resulted in restriction of intra-shelf basin envronments (Zhu et al., 2007; Jiang et al., 2011).

Doushantuo Formation (635 to >551 Ma)

Facies of the Doushantuo Formation include shallow peritidal carbonate platform settings (e.g. Xiaofenghe, Baiguoyuan, Liuhuiwan, Jiuqunao, Miaohe), isolated subtidal shales and carbonates of the intra-shelf basin (e.g. Jiulongwan section), mixed carbonate and siliciclastic deposition of the elevated margin rim (e.g. Zhongling) and slope to basinal minor carbonates and shales (e.g. Wuhe, Xiangtan and Lantian) (inset Figure 2.2) (Zhou and Xiao, 2007; Zhu et al., 2007; Vernhet and Reijmer, 2010; Li, C. et al., 2010; Jiang et al., 2011; Sahoo et al., 2012; Xiao et al., 2012; Fan et al., 2014; Cui et al., 2015; Och et al., 2015). With increasing depth, mixed carbonate-siliciclastic environments gradually transition to shale-dominated facies and Doushantuo stratigraphy is reassigned in the deep basin to the Lantian Formation (Shen et al., 2008). Deposition of the Doushantuo Formation is constrained by zircon U-Pb chemical abrasion ID-TIMS ages of 635.2±0.6 Ma and 551.1±0.7 Ma (Condon et al., 2005).

In the Yangtze Gorges area the Doushantuo Formation has classically been subdivided into four

lithostratigraphic members which, in ascending order, comprise the thin basal cap dolostone of Member I, 80 – 120 m of shale with occasional medium-bedded dolostone and chert nodules of Member II, 40 – 60 m of banded and lenticular chert interbeds and dolostone of Member III, and a locally absent 10 m thick black shale unit of Member IV which commonly exhibits large dolomite concretions (Liu, P. et al., 2013).

Doushantuo Members II and III contain a notably diverse suite of large acanthamorphic acritarchs within chert nodules and phosphorites, alongside vase-shaped microfossils, probable phosphatized animal embryos, multicellular algae and cyanobacteria within semi-restricted and shallow shelf settings which together comprise the 'Weng'an biota' (Xiao et al., 1998, 2014; McFadden et al., 2008; Liu, P. et al., 2013). Controversy surrounding fossilized Weng'an embryos has provoked numerous studies (e.g. Huldtgren et al., 2011), however most contributions now support an animal affinity as originally proposed (e.g. Xiao et al., 1998; Schiffbauer et al., 2012). Additional extensive study of acritarch taxonomy as a tool for biostratigraphic correlation of the Doushantuo Formation has been made possible through appreciation of three dimensional morphology via acid maceration of well-preserved specimens entombed within phosphorites at the type section of Weng'an (Guizhou) (Xiao et al., 2014).

Fossiliferous shales of the Lantian Formation Member II contain an assemblage of probable *in situ* multicellular eukaryotes which include *Chuaria circularis*, fan-shaped macroalgal forms and potential conulariid-type Metazoa (Yuan et al., 2011; Van Iten et al., 2013; Wan et al., 2016). Recent systematic description of an expanded Lantian fossil sample set has assigned the proposed medusozoan to the morphospecies *Lantianella laevis* and a further two morphogenera have been assigned to a suite of fossils which share features similarly suggestive of possible stem-group cnidarian affinity (Van Iten et al., 2013; Wan et al., 2016). In sum, putative animal embryos of Doushantuo Members II and III and the 'Lantian biota' of deep water Lantian Member II potentially include examples of the oldest metazoan organisms in the fossil record.

Overlying organic-rich shales at the base of Doushantuo Formation, Member IV (≤580 Ma, >551 Ma) contain an assemblage of carbonaceous compressions which likely represent the fossil remains of green, and potentially red algae alongside possible Metazoa including the eight-armed *Eoandromeda octobrachiata* at shallow shelf Miaohe and Weng'an sections and deep water deposits at Wenghui (Xiao et al., 2002; Condon et al., 2005; Zhu et al., 2008; An et al., 2015). Doushantuo Member IV is thus commonly referred to as the Miaohe Member after the distinctive 'Miaohe biota' assemblage at the type locality and is confidently regarded as distinct from deposits of the overlying Shibantan Member (Xiao et al., 2002, 2017).

A sequence stratigraphic framework across the shelf and basin has been proposed which dissects Formation deposition during two-and-a-half cycles of accommodation change equating to Stages 1 – 3, of which regressive Stage 3 spans the Doushantuo-Dengying boundary (McFadden et al., 2008; Zhu et al., 2013). At Jiulongwan, Stage 1 begins with relative sea level rise during deposition of the basal cap dolostone and shales of lower Member II, followed by subsequent regression represented by sedimentological indicators of facies shallowing (McFadden et al., 2008). The transgressive surface capping Stage 1 lacks signs of exposure and is immediately overlain by deep water facies which show an increase in sedimentological indicators of shallowing during regression throughout Stage 2. Abrupt deepening is re-initiated at the base of Stage 3 correlating to the transgressive surface between members III and IV (McFadden et al., 2008). This repeated sequence is permitted through long-term eustatic sea level rise across the Ediacaran-Cambrian boundary (Haq and Schutter, 2008).

Importantly, recent integrated chemostratigraphic investigation of the Doushantuo Formation suggests regionally variable completeness of $\delta^{13}C$ profiles and infers either stratigraphic truncation in shallow marine settings or a diachronous Doushantuo-Dengying boundary (Cui et al., 2015). Consequently, it is expected that regional paleoenvironmental reconstruction based on equivalence across platform to basin sections may be reinterpreted through future chemostratigraphic studies.

The spatial distribution of local redox observed within the Doushantuo Formation (Figure 2.2) is schematically illustrated in Figure 2.6a and supports localized development and maintenance of a metastable zone of euxinia on the openly connected lower slope at Wuhe (Figure 2.2, section 8), which episodically encroached into the deeper basin as supported by intervals of elevated Fe_{HR}/Fe_T and Fe_{py}/Fe_{HR} at Xiangtan (Figure 2.2, section 12) (Han and Fan, 2015; Sahoo et al., 2016). Intra-shelf basins represented at sections such as Jiulongwan (Figure 2.2, section 4) were only surficially connected to the open ocean and exhibit negligible RSE enrichment and elevated $\delta^{34}S$, suggestive of intervals of sulfate depletion brought on by basin restriction (Bristow et al., 2009; Vernhet and Reijmer, 2010; Jiang, G. et al., 2011; Sahoo et al., 2012; Zhu et al., 2013; Cui et al., 2015; Och et al., 2015). As outlined in Chapter 1 (Section 1.6.3) sulfate limitation in a closed system during extended periods of basin restriction or effective disconnect between pore water and seawater will tend to drive the sulfur isotope composition of sedimentary pyrite ($\delta^{34}S_{py}$) towards heavier values, thus reducing the offset between the isotopic composition of seawater sulfate (preserved in carbonate associated sulfate) and pyrite ($\Delta^{34}S_{CAS\text{-}py}$) through continued BSR of the increasingly isotopically enriched sulfate reservoir (Gomes and Hurtgen, 2013). Sporadic euxinia inferred from intermittently elevated Fe_{py}/Fe_{HR} at Jiulongwan (Li et al., 2010) is thought to be a consequence of episodically low Fe_{HR} supply in the dominantly ferruginous depths of the intrashelf basin during deposition of Doushantuo Members II – III (Och et al., 2015). Yet more proximal

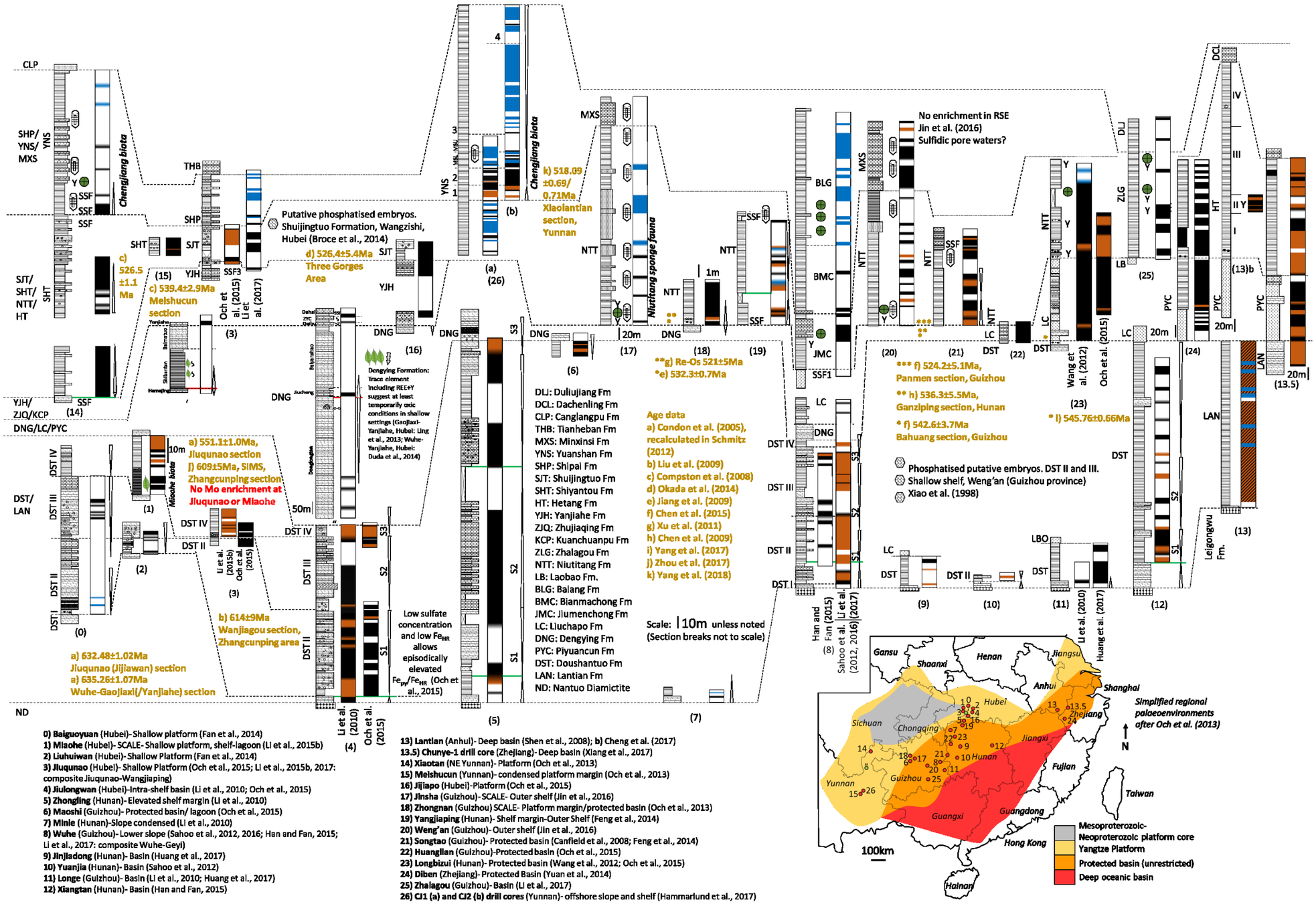

Figure 2.2 Correlation and schematic palaeoredox representation of Ediacaran to early Cambrian age sections in South China. Palaeoredox interpretation based on referenced publications. Legend on reverse.

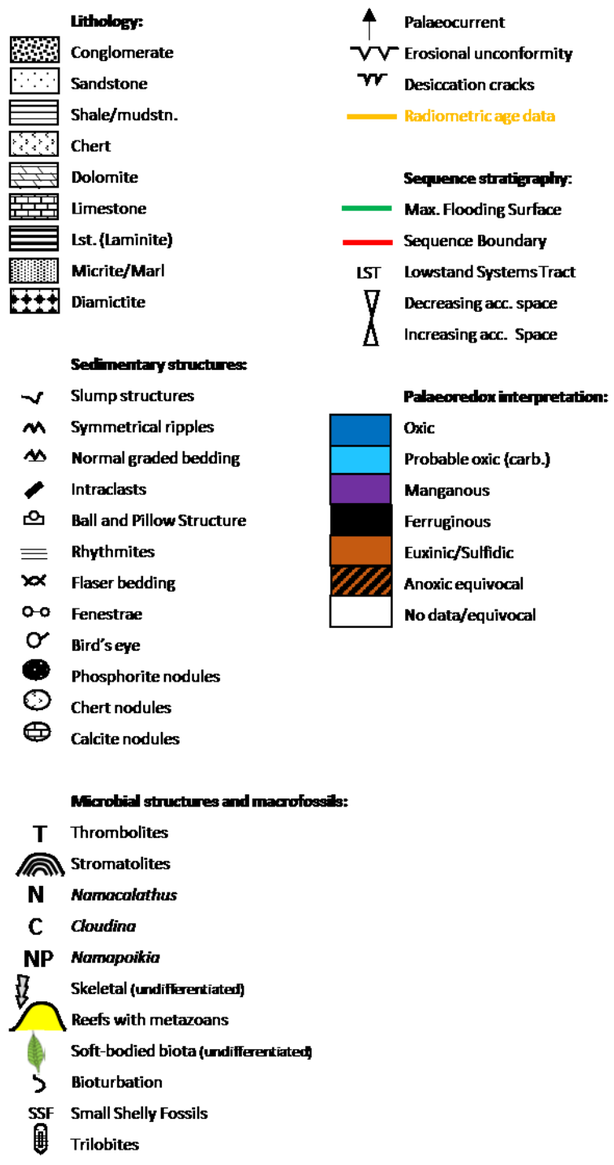
Lithology:
Conglomerate
Sandstone
Shale/mudstn.
Chert
Dolomite
Limestone
Lst. (Laminite)
Micrite/Marl
Diamictite
Sedimentary structures:
Slump structures
Symmetrical ripples
Normal graded bedding
Intraclasts
Ball and Pillow Structure
Rhythmites
Flaser bedding
Fenestrae
Bird's eye
Phosphorite nodules
Chert nodules
Calcite nodules
Microbial structures and macrofossils:
T Thrombolites
Stromatolites
N Namacalathus
C Cloudina
NP Namapoikia
Skeletal (undifferentiated)
Reefs with metazoans
Soft-bodied biota (undifferentiated)
Bioturbation
SSF Small Shelly Fossils
Trilobites
Palaeocurrent
Erosional unconformity
Desiccation cracks
Radiometric age data
Sequence stratigraphy:
Max. Flooding Surface
Sequence Boundary
LST Lowstand Systems Tract
Decreasing acc. space
Increasing acc. Space
Palaeoredox interpretation:
Oxic
Probable oxic (carb.)
Manganous
Ferruginous
Euxinic/Sulfidic
Anoxic equivocal
No data/equivocal

settings on the shallow platform (e.g. Baiguoyuan; Figure 2.2, section 0) show evidence for infrequent ventilation and deposition in oxic water column conditions which were sporadically permitted within a dominantly ferruginous regime (Fan et al., 2014). Variations in thickness of the euxinic zone are thought to be functionally equivalent to spatial variability observed in modern open marine oxygen minimum zones related to highly productive shallow waters stimulated through nutrient upwelling (Li et al., 2010; Och et al., 2015; Sahoo et al., 2016). Sustained euxinic conditions in unrestricted settings such as those that characterized the open slope at Wuhe (Sahoo et al., 2012, 2016; Han and Fan, 2015) require both high levels of organic matter supplied by surface water productivity and at least locally elevated marine sulfate (potentially linked to local evaporite weathering) capable of supporting build-up of H_2S_{aq}, after quantitative sulfidation of available highly reactive iron (Poulton and Canfield, 2011).

Uranium and molybdenum isotope data from euxinic shales of the Yangtze Block have been interpreted to indicate a global increase in the spatial extent of oceanic dissolved oxygen throughout the Ediacaran (Kendall et al., 2015; Chen, X. et al., 2015). Likewise, secular organic matter-normalized RSE enrichment and depletion within euxinic shales of the Doushantuo Formation have been interpreted to support limited global ocean Mo scavenging and temporarily widespread ocean oxygenation (Scott et al., 2008; Sahoo et al., 2012, 2016; Kendall et al., 2015).

A suggested model for the initiation of Mo enrichment and the trend towards more negative $\delta^{34}S_{py}$ during Doushantuo Member IV within the intra shelf basin at Jiulongwan implies progressive landward incursion of the lower slope euxinic wedge into isolated platform environments under a regime of rising sea level (Figure 2.6b, Li, C. et al., 2010; Och et al., 2015). The transgressive surface at the Doushantuo Member III/IV boundary therefore likely represents an increase in sill depth ratio and basin connectivity. Continued local basin restriction of yet more proximal sections, including Jiuqunao, is thought to account for a corresponding lack of RSE enrichment and elevated $\delta^{34}S_{py}$ at this time (Och et al., 2015). Additional iron speciation and RSE data collected at Jiuqunao and nearby Miaohe sections corroborate ferruginous anoxia for the lowermost deposits of Doushantuo Member IV, but also suggest a trend towards more euxinic conditions within overlying shales (Li, C. et al., 2015b). Importantly, however, inception of euxinic conditions at Miaohe is seen to postdate fossil occurrence of the Miaohe biota (Li, C. et al., 2015b). Limited Mo enrichment within both Jiuqunao and Miaohe sections (Li, C. et al., 2015b) is consistent with the model of Och et al. (2015) for continued partial restriction of intra-shelf sections, and accompanying $\delta^{15}N$ data at Jiuqunao have been interpreted as evidence for restriction-induced nitrate limitation which may have precluded the maintenance of euxinia (Och et al., 2015).

Published Ce/Ce* data of the Doushantuo Formation are in broad agreement with iron

speciation at Jiulongwan and support deposition beneath a redox stratified water column (Shields et al., 2004; Zhou et al., 2012; Ling et al., 2013; Cui et al., 2015). There is also some evidence for a trend toward decreasing frequency of ventilated, oxygenated conditions with proximity to the Doushantuo-Dengying boundary in some settings (Zhou et al., 2012; Cui et al., 2015).

Basinal open ocean deposition at Xiangtan is defined by dominantly ferruginous conditions where organic matter was depleted (Li, C. et al., 2015a; Han and Fan, 2015). Under this model, nearshore and distal Fe sources are thought to have been distinct, with the shallow manganous-ferruginous zone permitted through reductive dissolution of detrital Fe and Mn oxides (Li, C. et al., 2015a). In contrast, anoxic deep waters were typically enriched in soluble reduced Fe^{2+} derived from long-term hydrothermal build-up, in addition to reduction of iron oxides and mobilization of Fe to depth (Lyons and Severmann, 2006; Severmann et al., 2008; Li, C. et al., 2015a).

A number of samples in the basinal Lantian section indicate low Fe_{HR}/Fe_T, possibly corresponding to sedimentation under oxic water column conditions. However, the extraction procedure used by Shen et al. (2008) at this locality does not isolate carbonate-bound iron (Poulton and Canfield, 2005; Johnston et al., 2013; Sperling et al., 2015b), and given that inferred oxic samples show Fe_{HR}/Fe_T bordering the upper calibrated threshold for identification of oxic conditions (lowest sample value of 0.19), these data should be treated with caution. Despite methodological issues associated with Fe phase extraction, Fe speciation data of Shen et al. (2008) unambiguously point to a predominantly anoxic water column during Lantian Member II. Additional data of pyrite framboid size, RSE, organic carbon, total sulfur, and $\delta^{34}S_{py}$ of *Chuaria*-bearing strata have helped constrain deposition of Lantian Member II shales under episodically suboxic/oxic conditions (Guan et al., 2016). It has therefore been suggested that, if the physiology of the Lantian biota demanded less reducing conditions, intervals conducive to habitation may have been very brief (Yuan et al., 2011).

Terminal Ediacaran to early Cambrian Formations (551–520 Ma)

Shallowing associated with continued regression during the highstand of Stage 3 resulted in deposition of the widespread dolomitic Dengying Formation (551–541 Ma) in shallow and mid-depth environments. Down slope, the Dengying Formation is reassigned to interbedded cherts and shales of the lower Liuchapo formation (Wang et al., 2012). The Dengying Formation is assigned a minimum age of 539.4 ± 2.9 Ma after SHRIMP U-Pb dating of zircons from deposits of the middle (Zhongyicun) Member of the overlying Zhujiaqing Formation (Compston et al., 2008). Corresponding deposition of the deeper water Liuchapo Formation is corroborated by an upper (zircon U-Pb SHRIMP) age of

536.3 ± 5.5 Ma (Chen et al., 2009). Based on first appearance of *T. pedum* the Ediacaran-Cambrian boundary is conventionally placed at the Daibu/Zhongyicun boundary within the Zhujiaqing Formation (lower Yanjiahe) or deep water equivalent Liuchapo/Niutitang boundary (Zhu et al., 2003). The redox environment of the Dengying and overlying early Cambrian Formations is explored further and new data presented in Chapter 5.

In the Yichang area (Yangtze Gorges), the Dengying Formation is subdivided into the lower, shallow marine Hamajing dolostone Member, middle richly fossiliferous transgressive micritic limestone of the Shibantan Member, and upper regressive Baimatuo dolostone member (Ling et al., 2013; Duda et al., 2014). The Dengying Formation preserves an assemblage of Ediacaran soft-bodied organisms within bituminous limestones of the Shibantan Member, including the frond-like *Paracharnia*, *Rangea*, *Pteridinium*, *Yangtziramulus zhangi*, and the tubular *Wutubus annularis* (Sun, 1986; Xiao et al., 2005; Chen, Z. et al., 2014). All of these fossils are found in association with abundant trace fossils (e.g. *Lamonte trevallis*), indicating the co-occurrence of motile bioturbating organisms that are thought to have actively mined nutrients, and potentially oxygen, from contemporaneous microbial mats (Chen et al., 2013; Duda et al., 2014; Meyer et al., 2014). Specimens of the tubular, biomineralizing organism *Sinotubulites baimatuoensis* are recorded from the overlying Baimatuo Member in western Hubei (Chen, M., et al., 1981; Chen, Z., et al., 2008). *Sinotubulites* and *Cloudina* have also been described from Shibantan and Baimatuo-equivalent shallow platform carbonates of the Gaojiashan and Beiwan Members in southern Shaanxi province, where they immediately overlie strata hosting the soft-bodied tubular organism *Conotubus hemiannulatus* (Hua et al., 2003; Cai et al., 2014; Cui et al., 2016a). To date, no evidence has been presented for reef-building by *Cloudina* in Dengying Formation carbonates and all specimens appear to occupy a 'mat-sticker' mode of life (Cai et al., 2014). Possible borings have also been described in specimens of *Cloudina hartmannae* from shallow platform carbonates of the upper Gaojiashan Member, which may represent the earliest evidence of metazoan predation in the fossil record (Bengtson and Zhao, 1992).

Shallow, high energy facies of the lowermost Dengying Formation at Zhongling show continued euxinia from three samples on the shelf margin (Figure 2.2, section 5) (Li, C. et al., 2010), whilst basinal sections of the equivalent Liuchapo Formation (Huanglian and Longbizui) show predominantly ferruginous anoxia (Wang et al., 2012; Och et al., 2015). On the shallow platform decreasing Ce/Ce* has been suggested to indicate gradually more oxygenated conditions across the Dengying Formation interval (Ling et al., 2013) and additional RSE and Ce/Ce* data from the subtidal Shibantan Member support punctuation of reducing conditions by temporary oxygenation during storm events (Duda et al., 2014). Intermittent increases in local marine sulfate concentration accompanying deposition of the

Dengying Formation at the Wuhe-Yanjiahe section (Hubei) may have been associated with increased salinity and consequent density-driven stratification during periods of intra-shelf basin shallowing and evaporation, similar to conditions suggested during deposition of the underlying Doushantuo Member IV at the shallow Xiaofenghe section (Yangtze Gorges, Hubei) (Duda et al., 2014; Hohl et al., 2015).

Earliest Cambrian deposits which locally overly the Dengying Formation on the shallow platform include the upper Yanjiahe and Zhujiaqing Formations. Yanjiahe Formation deposits occupy present-day Hubei province whilst equivalent deposits in Yunnan are assigned to the Zhujiaqing Formation and consist of three minor shallowing cycles of the Daibu, Zhongyicun, and Dahai Members (Li, D. et al., 2013; Och et al., 2015). Continued contemporaneous deposition of basinal Liuchapo Formation cherts and shales is suggested by a U-Pb age of 536.3 ± 5.5 Ma in the upper Liuchapo Formation at Ganziping (Chen et al., 2009; Och et al., 2015). Iron speciation data of the Yanjiahe Formation and equivalents indicate ferruginous shallow water conditions, whilst time-equivalent deposition of the upper Liuchapo and Piyuancun Formations continued under sustained ferruginous anoxia and sporadic euxinia (Wang et al., 2012; Och et al., 2015; Xiang et al., 2017).

Approximate equivalence between overlying Cambrian Shiyantou and Shuijingtuo Formations is inferred from zircon U-Pb ages of 526.5 ± 1.1 Ma (Compston et al., 2008) and 526.4 ± 5.4 Ma (Okada et al., 2014) respectively. A minimum U-Pb SHRIMP age of 532.3 ± 0.7 Ma has been assigned to the basal Niutitang Formation at Zhongnan (Jiang, S.-Y. et al., 2009) and dating of overlying units of the Niutitang Formation give a U-Pb age of 524.2 ± 5.1 Ma from Panmen section, Guizhou province (Chen, X., et al., 2015) and a composite Re-Os age of 521 ± 5 Ma from 3 sections of Hunan and neighboring Guizhou province (Xu et al., 2011). Together, these ages indicate at least partially contemporaneous deposition of the deeper Niutitang Formation with the shallow marine equivalent Shiyantou and Shuijingtuo Formations.

Global sea level rise during the early Cambrian (Haq and Schutter, 2008) is expressed in deepening deposits of the Shiyantou, Shuijingtuo and lower Niutitang Formations across sections of the Yangtze Platform and basin, with evidence for dominant ferruginous anoxia interrupted by periods of extensive euxinia (Och et al., 2013, 2015; Wang et al., 2012; Canfield et al., 2008; Feng et al., 2014). Equivalent middle and upper Niutitang shales show first evidence from iron speciation for at least episodic oxygenation of the outer shelf and shelf margin at Jinsha and Yangjiaping, and basin at Longbizui which has been attributed to progressive deepening of the oxycline (Wang et al., 2012; Feng et al., 2014; Jin et al., 2016). Chert of the deep basin equivalent Hetang Formation continue to indicate ferruginous conditions at Diben (Yuan et al., 2014). The earliest definitive evidence for oxia inferred from iron speciation within the shallow platform at Xiaotan is found within the upper Yu'anshan Formation, and

is accompanied by continued anoxia of the Minxinsi Formation at Weng'an, implying continued water column redox stratification (Och et al., 2015; Jin et al., 2016).

An effective Fe-Mn oxide shuttle has been proposed as a mechanism for producing observed differences in preserved δ^{98}Mo between sections of the early Cambrian South China Block (Li, C. et al., 2015a; Cheng et al., 2016). Under this model, adsorption of ^{95}Mo onto Mn-oxides in well oxygenated, nearshore surface waters and re-release during reductive dissolution in the underlying zone of Fe-Mn reduction was followed by quantitative scavenging within euxinic levels of the water column consistent with Mo cycling in modern euxinic environments (Algeo and Tribovillard, 2009; Kendall et al., 2015; Li, C. et al., 2015a; Cheng et al., 2016).

Early Cambrian biota of the Yangtze Block include small shelly fossil (SSF) assemblages preserved in shallow and deep water facies of the Zhujiaqing and Kuanchuanpu Formations, succeeded by SSFs of the Shiyantou Formation (Jin et al., 2016). These assemblages give way to early trilobites, articulated sponges and bivalved arthropods of the Niutitang sponge fauna within outer shelf fine grained siliciclastic deposits of the Niutitang Formation (Jin et al., 2016). Weakly phosphatized putative animal embryos have also been documented from the shallow shelf mixed ferruginous/euxinic Shuijingtuo Formation at Wengzishi section, Hubei Province (Broce et al., 2014). The increasing proportion of oxic samples recorded from Cambrian Stage 3 appears to be accompanied by increased ecosystem complexity throughout shallow shelf to outer slope environments of the Yangtze Block. However, these diverse assemblages dominantly comprise motile benthic communities, including trilobites for which occasional exploration of dominantly anoxic deeper slope environments (e.g. Songtao) may have been possible during fleeting oxygenation (Vannier et al., 2009; Feng et al., 2014).

2.2.2 Laurentia

Sediments along the Canadian Cordillera were deposited in a rift setting, with evolution to a passive continental margin and associated subsidence initiated in the mid-Ediacaran (MacNaughton et al., 2000; Macdonald et al., 2013; Yonkee et al., 2014). Ediacaran age deposits of the Windermere Supergroup outcrop at Goz Creek in the Wernecke Mountains of Yukon, Canada (Figure 2.3a) (Johnston et al., 2013) and are complemented by an expansive record from the deeper Sekwi Brook section of the Mackenzie Mountains (Figure 2.3b). Detailed multiproxy analyses of both sections have enabled geochemical scrutiny of the marine environment during deposition of the fossiliferous June Beds and Blueflower Formations (Johnston et al., 2013; Sperling et al., 2015b). Regional carbon isotope chemostratigraphic correlation and reconstruction of relative sea level change within the Gametrail,

Blueflower and Risky Formations suggest deposition along an unrestricted slope to basin environment (Macdonald et al., 2013; MacNaughton et al., 2000).

North Canadian Cordillera: Goz Creek, Wernecke Mountains

Iron speciation at Goz Creek (Figure 2.3a) reveals almost continuous anoxic ferruginous deposition within the Ediacaran Windermere Supergroup, with a brief oxic interval recorded during regression within the deep water upper Sheepbed Formation (Johnston et al., 2013). Oxia of the upper Sheepbed Formation has also been documented at the siliciclastic Shale Lake section (Shen et al., 2008 after stratigraphic re-evaluation by Macdonald et al., 2013). An observed trend towards heavier $\delta^{34}S_{py}$ documented throughout the Sheepbed Formation has been interpreted to represent pore water sulfate limitation (Johnston et al., 2013).

A first order shallowing trend is superimposed upon a number of parasequences within the overlying Blueflower Formation, yet no change in dominant redox is recorded and all iron speciation samples instead suggest continued anoxic ferruginous conditions. Proximal deposition of the shallow water Blueflower Formation is accompanied by the potential for estuarine trapping of iron oxides, which is suggested to account for a shift towards higher ratios of Fe_{HR}/Fe_T, which may preserve a false anoxic signal (Johnston et al., 2013).

Sekwi Brook, Mackenzie Mountains

Stratigraphy at Sekwi Brook records a deeper water environment than that of Goz Creek, with similarly unrestricted access to the open ocean (Sperling et al., 2015b). Iron speciation and trace element analyses of the June Beds and Blueflower Formation (Figure 2.3b) are in broad agreement with the results of Johnston et al. (2013) at Goz Creek, where no clear progression towards more persistent oxygenation across the sampled interval is detected (Sperling et al., 2015b). Outcrops at the base of the section have been tentatively correlated to the deep water Sheepbed Formation deposited during one cycle of relative sea level change and show evidence for intermittently oxic conditions within both the transgressive and highstand systems tracts. Overlying fossiliferous shales of the June Beds show overwhelming evidence for protracted anoxic ferruginous conditions, punctuated by two brief episodes of oxia initially within the middle lowstand systems tract, and again during transgression nearing the top of the June Beds. The exclusively carbonate sequence of the Gametrail Formation was not sampled at Sekwi Brook, however iron speciation of the overlying Blueflower Formation again indicates predominance of anoxic

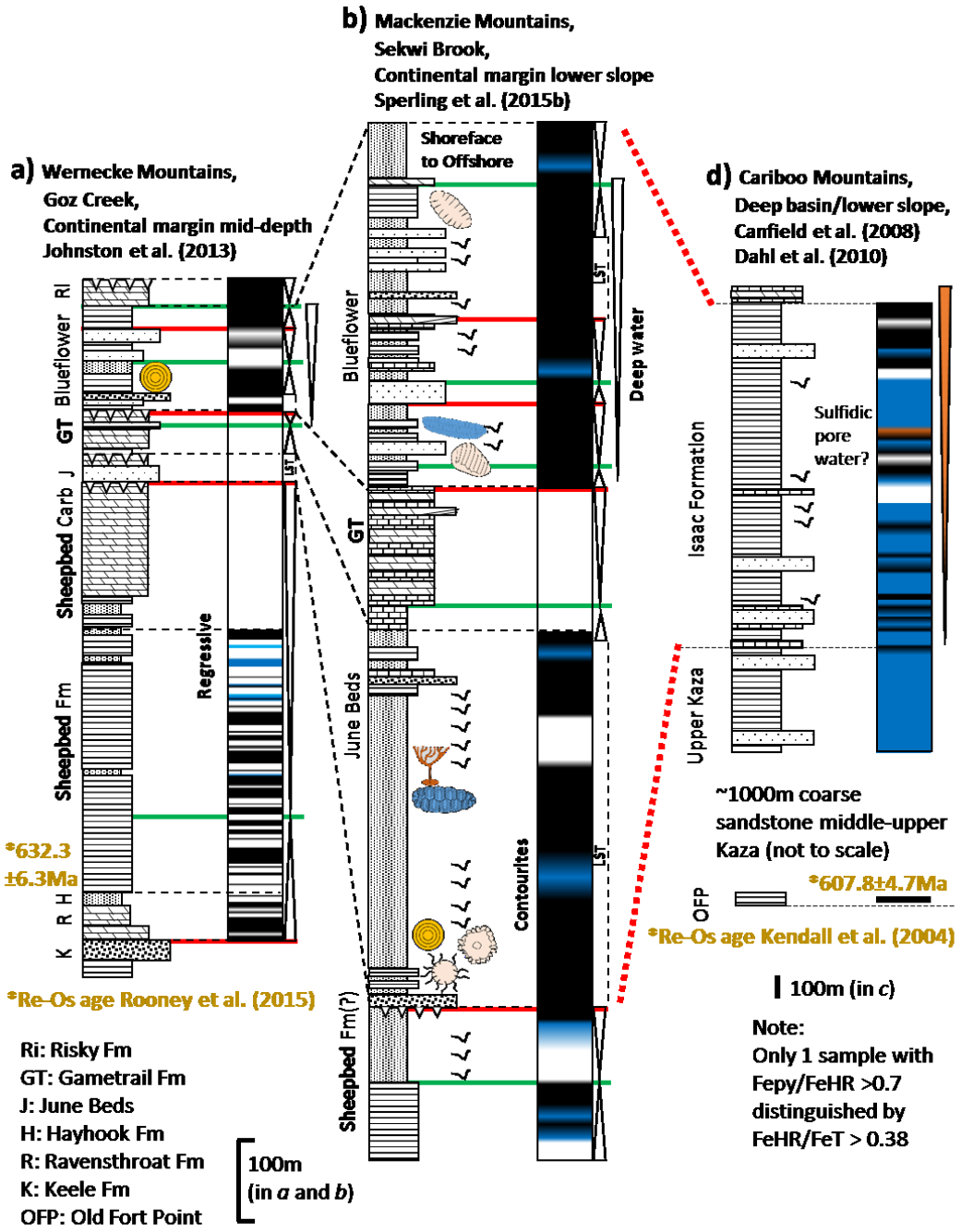

Figure 2.3 (a–c) Local redox from deep-water successions of the Windermere Supergroup deposited on northern margin of Laurentia (sections of Yukon Territory, Northwestern Territories and British Columbia Canada) (~632–540 Ma). See reverse of Figure 2.2 for legend. (red dotted lines: tentative temporal correlation after Yonkee et al., 2014). Fossil symbols detailed in Appendix D.

ferruginous conditions with two minor oxic intervals, both of which immediately follow maximum flooding surfaces (Sperling et al., 2015b).

Fossils of soft-bodied biota which inhabited the Laurentian passive margin outcrop in the June Beds and Blueflower Formations of the Windermere Supergroup at Sekwi Brook and represent an Avalon-type fossil assemblage with abundant rangeomorphs and arboreomorphs, in addition to the erniettamorph *Namalia* (Narbonne et al., 2014; Sperling et al., 2015b). These fossil forms are largely preserved on the soles of mass flow deposits, however some specimens are preserved three-dimensionally, similar to those of the Nama Group, Namibia (Narbonne et al., 2014). This facies control on fossil occurrence complicates identification of first appearance within the June Beds (Sperling et al., 2015b).

Whilst the June Beds biotic assemblage inhabited a deep water lower slope setting, facies of the upper Blueflower Formation represent a lower shoreface to offshore environment and incorporate specimens of the newly described tubular genera *Sekwitubulus annulatus* and the larger flexible *Annulatubus flexuosus*, in addition to a shallow water dickinsonid *Windermeria aitkeni* (Narbonne et al., 2014).

The majority of samples from the Sekwi Brook section have depleted Fe_T/Al below the lower calibrated threshold value expected under Phanerozoic marine deposition (Raiswell et al., 2008), similar to the basal Sheepbed and Blueflower Formations of Goz Creek (Johnston et al., 2013). Whilst previous studies have advised caution in interpretation of shales exhibiting extreme depletions (e.g. Sahoo et al., 2012), one hypothesis provided by Sperling et al. (2015b) concerns the threshold value itself and suggests the potential for significantly different balances of iron and aluminium cycling in the Ediacaran which may be supported by the closer to 'normal' shale Fe/Ti ratios.

South Canadian Cordillera: Cariboo Mountains, British Columbia

Ediacaran deposits of southern Canadian Cordillera outcrop in the Cariboo Mountains of British Columbia and represent post-rift basinal deposition within the Laurentian passive margin (Ross et al., 1995; Schwarz and Arnott, 2007; Canfield et al., 2008). A maximum age of 608±4.7 Ma is given from Re-Os dating of black shales of the Old Fort Point Formation (Kendall et al., 2004) and a Re-Os age of 632.3±6.3 Ma has been documented from the lower Sheepbed Formation (Rooney et al., 2015). Deposition of the upper Kaza and Isaac Formations is tentatively considered to have taken place contemporaneous to deposition of Sheepbed and overlying formations (Macdonald et al., 2013; Yonkee et al., 2014; Rooney et al., 2015). Despite difficulties in correlation, iron speciation data recorded in

Canfield et al. (2008) and Dahl et al. (2010) allow for a snapshot of approximately time-equivalent lower slope to basinal water column conditions (Figure 2.3c) (Ross et al., 1995). Mudstones and shales of the Upper Kaza Formation were deposited in a quiescent basinal environment and indicate exclusively oxic conditions (Canfield et al., 2008; Dahl et al., 2010). In contrast, the overlying Isaac Formation contains abundant rapidly deposited turbidites, debris flows and slumping consistent with lower slope deposition (Schwarz and Arnott, 2007). Ratios of Fe_{HR}/Fe_T which fall below the calibrated upper threshold for oxic conditions may be an expected consequence of rapid deposition, however the mean value of Fe_{HR}/Fe_T in Isaac Formation samples which fall below the threshold of 0.22 is ~0.11, indicating significant Fe_{HR} depletion. At least intermittent oxia is implied in these samples, with a possible trend towards ferruginous anoxia up-section.

Additional sections of the Laurentian passive margin

The Upper Miette Group of the Windermere Supergoup in southeastern British Columbia and Wood Canyon of Death Valley also host Ediacaran fossils of both soft-bodied and biomineralizing organisms. The Upper Miette Group is tentatively considered chronostratigraphically equivalent to shallow marine carbonates of the Cunningham Formation which locally overlies the Isaac Formation of the Southern Canadian Cordillera (Ross et al., 1995). The Byng carbonate platform within the Upper Miette Group contains *Cloudina* and *Namacalathus,* and shallow water siltstones of the potentially coeval Yellowhead carbonate platform preserve soft-bodied forms which include *Cyclomedusa* found in association with stromatolitic mounds (Hofmann and Mountjoy, 2001).

The upper Stirling and lower Wood Canyon Formations of California preserve an assemblage strikingly similar to that of the upper Nama Group within a subtidal, possible-deltaic shallow marine succession with *Cloudina* alongside *Ernietta* and *Swartpuntia* (Corsetti and Hagadorn, 2000). Additionally, the earliest recorded example of the ichnofossil *Zoophycos* is recorded from the overlying lower Cambrian portion of the Wood Canyon Formation (Sappenfield et al., 2012). These additional sections have not yet been evaluated using redox proxy methods and so present an intriguing succession for future geochemical consideration.

2.2.3 Avalonia

Siliciclastic units of the Conception and St. Johns Groups of Newfoundland record deposition in an unrestricted deep water environment with rapid emplacement of volcanic ash preserving a wealth of

body fossils. The Avalon assemblage of Newfoundland includes rangeomorphs (*Rangea, Charnia,* and *Fractofusus*), possible triradialomorphs (e.g. *Triforillonia costellae*), arboreomorphs (*Charniodiscus*), discoidal fossils (*Aspidella* and *Cyclomedusa*) and possible sponges (*Thectardis*) (Sperling et al., 2011; Laflamme et al., 2013; Liu et al., 2015). Ediacaran organisms which thrived in the basinal waters of Avalonia did so well below the photic zone, similar to conditions which persisted during deposition of the June Beds and Blueflower Formation of the Windermere Supergroup (Narbonne et al., 2014).

A strikingly sharp, early transition from ferruginous anoxia of the deep water Mall Bay and Gaskiers axial turbidite sequence to almost continuously uninterrupted oxia of overlying strata is revealed by iron speciation at 11 localities on the Avalon peninsula, which combine to form a 6km snapshot equating to ~15 Myr of Ediacaran deposition transcending the Gaskiers glaciation (Figure 2.4a) (Canfield et al., 2007). The basal Drook Formation defines the boundary for this transition, followed by the first fossil evidence of soft-bodied Ediacara biota in the fossil record within the upper Drook Formation at approximately 570.94 ± 0.38 Ma (Pu et al., 2016). Persistently oxygenated conditions accompanied biotic establishment in these deep basinal sediments throughout deposition of the overlying Briscal, Mistaken Point, Trepassey and Fermeuse Formations, with just two minor periods of ferruginous anoxia recorded from the base and top of deep delta front deposits of the Fermeuse Formation (Canfield et al., 2007). Whilst the rapid emplacement of turbiditic sediments may innately result in reduced Fe_{HR} accumulation beneath an anoxic water column, the upper layers of each turbidite deposit (hemipelagite) were sampled and define the finest sediment emplaced at the slowest rate (Canfield et al., 2007). Shale of the Conception and St. Johns Groups are confidently regarded to record oxic deposition within and above the Drook Formation (Canfield et al., 2007).

Lower rates of bacterial sulfate reduction indicated by low C and S concentrations and persistently elevated $\delta^{34}S_{py}$ nearing the approximated contemporaneous composition of seawater sulfate are seen to have preceded the Gaskiers Formation (Fike et al., 2006; Canfield et al., 2007). A decrease to predominantly negative $\delta^{34}S_{py}$ values is subsequently observed in the Drook Formation, coincident with inferred oxygenation of the deep marine environment, followed by a return to more elevated $\delta^{34}S_{py}$ during deposition of the Fermeuse Formation (Canfield et al., 2007).

2.2.4 East European Platform

Whilst no direct fossil identification beyond microfossil evidence is possible from drill core samples, the stratigraphic succession from which the Kel'tminskaya-1 core was extracted is known to host a richly fossiliferous example of the White Sea assemblage, which may have existed approximately

contemporaneous with the mid-upper Doushantuo Formation, Drook Formation, and June Beds (Boag et al., 2016). Large ornamented microfossil assemblages composed of acanthamorphic acritarchs have made useful biostratigraphic indicators within the Vychegda Formation (Vorob'eva et al., 2009), whilst soft-bodied biota including the probable motile early molluscan organism *Kimberella* are documented from the overlying Redkino Formation (Martin et al., 2000; Fedonkin et al., 2007a; Gehling et al., 2014). The equivalent Ust'-Pinega Formation on the Onega River also hosts *Swartpuntia, Vendoconularia triradiata*, and *Ventogyrus* (Ivantsov and Fedonkin, 2002; Fedonkin and Ivantsov, 2007).

Redox evolution of the unrestricted East European Platform (Figure 2.4b) margin has been evaluated through application of Fe speciation, alongside $\delta^{34}S_{py}$, $\delta^{13}C$ and major element analyses of the Kel'tminskaya 1 drillcore (Johnston et al., 2012). The lower 2000 m of the drillcore comprises mixed

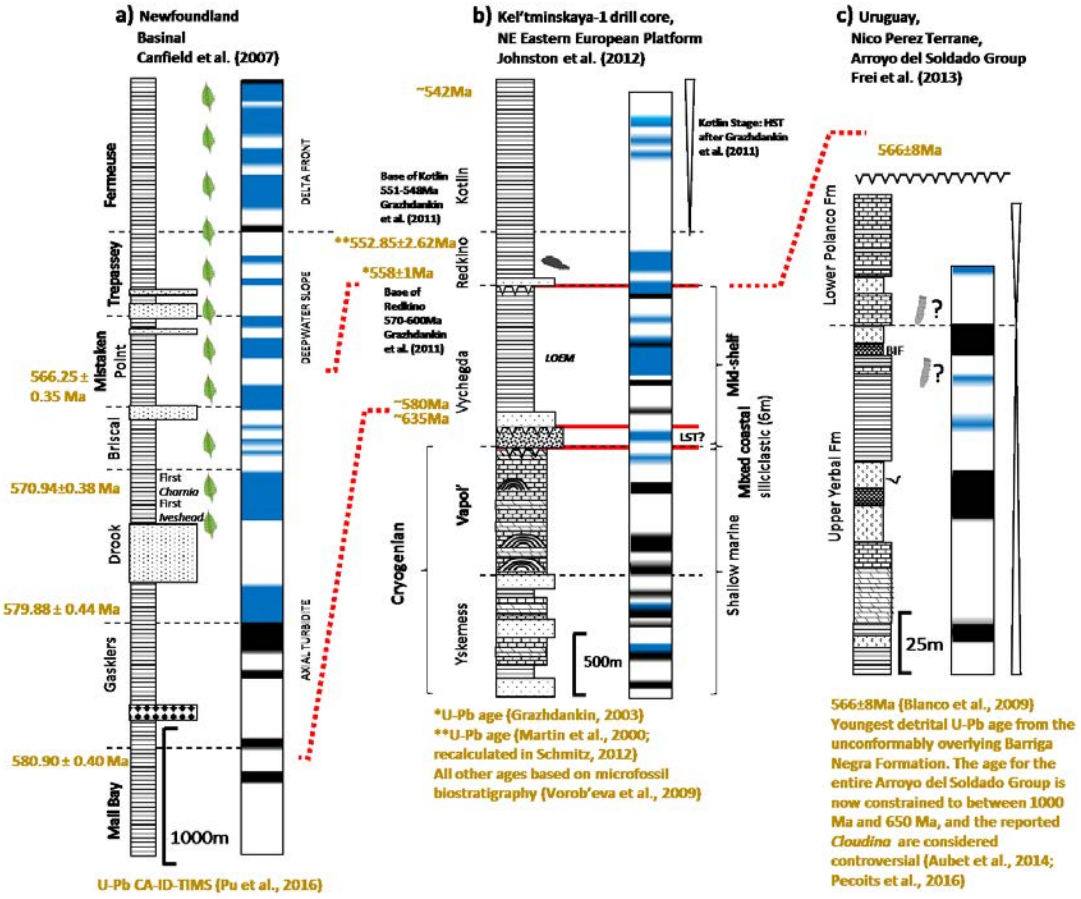

Figure 2.4 a) Local redox of unrestricted lower slope. Western Avalonia, Newfoundland (~584 Ma to <565 Ma) and (b) Local redox of unrestricted mid-outer shelf. East European Platform (EEP), western Russia (>635 Ma to ~542 Ma) and (c) shallow platform deposits of the Río de la Plata Craton, Uruguay (?1000 – 650 Ma). Red dotted line: approximate temporal correlation. See Figure 2.2 for legend and Appendix D for key to fossil symbols.

siliciclastic and shallow marine carbonate platform deposits of the Cryogenian Yskemess and Vapol' Formations, which indicate deposition under dominantly anoxic ferruginous conditions with some evidence for fleeting oxia. Ediacaran siliciclastics of the Vychegda, Redkino, and Kotlin Formations unconformably overlie the Vapol' Formation, with an age constraint dictated by microfossil biostratigraphy of basal Vychegda (Vorob'eva et al., 2009) and U-Pb dating within the upper and lower Redkino Formation (Grazhdankin, 2003; Martin et al., 2000). The lower boundary of the fossiliferous Redkino Formation has since been re-interpreted by Grazhdankin et al. (2011) to be in the range 570 – 600 Ma, thus placing a minimum age in approximate stratigraphic equivalence with the Drook Formation of Newfoundland. The underlying Vychegda Formation occupied a mid-shelf depositional environment and iron speciation measurements suggest predominantly oxygenated conditions during deposition, with minor incursions of ferruginous anoxia (Johnston et al., 2012). Additional $\delta^{34}S_{py}$ data from the Ediacaran Vychegda Formation show generally depleted values and support the existence of an oxidative water column sulfur cycle (Johnston et al., 2012). The overlying 1000 m siliciclastic succession of the Redkino and Kotlin Formations exhibits exclusive oxia, recorded by low Fe_{HR}/Fe_T. Higher $\delta^{34}S_{py}$ values observed in deposits of the Redkino and Kotlin successions are considered to be a consequence of localized sedimentary pore water sulfate limitation (Johnston et al., 2012). These data have been interpreted to represent a shift towards oxygen stability of the local environment reflected in reduced variation of Fe_{HR}/Fe_T about the mean up section (Johnston et al., 2012). This is comparable to deep water sediments of Avalonia which may indicate that oxygen concentration allowed for effective suppression of anoxia in the local water column from as early as 570–600 Ma (Canfield et al., 2007).

2.2.5 Río de la Plata Craton

Outcropping stratigraphy of the Río de la Plata craton in Uruguay constitute the Arroyo del Soldado Group, which was unconformably deposited over Archean and Proterozoic units of the Nico Perez Terrane and includes the Barriga Negra, Yerbal, Polanco, Cerro Espuelitas, Cerros San Francisco and Cerro Victoria Formations (Gaucher, 2000; Gaucher et al., 2009; Blanco et al., 2009). Whilst dating of the Arroyo del Soldado Group has been complicated by the sparsity of zircon-bearing ash beds, stratigraphic reappraisal has positioned deposits of the Barriga Negra Formation below or equivalent to the lower Yerbal Formation (Gaucher et al., 2011). In this framework, a maximum detrital zircon age from the Barriga Negra Formation constrains deposition of the Lower Yerbal Formation to $> 566 \pm 8$ Ma (Gaucher et al., 2008; Blanco et al., 2009). Importantly however, stratigraphic and chronological constraints on deposition of the Arroyo del Soldado Group have recently come under severe scrutiny resulting in extensive reassessment of the equivalence of these strata with other late Ediacaran sections

worldwide (Aubet et al., 2014). This prompted a detailed study of detrital zircon geochronology which supports a new conservative age range for the Arroyo del Soldado and overlying Arroyo de la Pedrera Groups of 1000 – 650 Ma and also questions the affinity of previously reported *Cloudina* specimens of the Yerbal and Polanco Formations (Aubet et al., 2014; Pecoits et al., 2016). Future fossil prospecting is required to confirm or deny the affinity of Arroyo del Soldado *Cloudina*, however the present status of this Group remains controversial and the data reviewed below may instead pertain to strata of Tonian-Cryogenian age.

Fossils described from the Arroyo del Soldado Group include two distinct acritarch assemblages, in addition to putative representatives of *Cloudina* (Gaucher, 2000). Examples of *in situ* hematized *Cloudina riemkeae* reportedly outcrop in upper Yerbal Formation siltstones and reworked fragments of *C. riemkeae* have been described from within storm deposits of the overlying Polanco Formation (Gaucher, 2000; Gaucher and Poiré, 2009; but see Aubet et al., 2014).

Iron speciation analyses of the Yerbal and Polanco Formations (Figure 2.4c) indicate the predominance of anoxic ferruginous water column conditions with some evidence for occasional deposition in oxic waters (Frei et al., 2013). Additional RSE and Ce/Ce* anomaly data of the Arroyo del Soldado Group are consistent with iron speciation and are interpreted to indicate a water column with suboxic to anoxic non-sulfidic depths, overlain by an oxygenated surface layer (Pecoits, 2010; Aubet et al., 2012).

2.2.6 Kalahari Craton

This section provides an overview of the stratigraphic architecture and local redox of Nama Group sediments, however more detailed information including exact fossil position and compiled published and raw data are provided in Chapter 3.

Exceptional exposure along two shelf to basin transects has permitted sequence stratigraphic reconstruction, geochemical analysis and fossil distribution of a substantial portion of the Nama Group to parasequence level (Figure 2.5) (Saylor et al., 1995, 1998; Saylor, 2003; Dibenedetto and Grotzinger, 2005; Wood et al., 2015). The Nama foreland basin formed on the Kalahari Craton as a consequence of convergence along the Damara and Gariep orogenic belts to the present-northeast and southwest respectively during closure of the Brazilides Ocean and amalgamation of southwest Gondwana (Gaucher et al., 2009). The Nama basin was subdivided into northern Zaris, and southern Witputs subbasins by a zone of depositional thinning across the 'Osis Arch' paleobathymetric high (Germs, 1983). Correlative

formations of fluvial to shallow marine siliciclastic and carbonate sediments within both subbasins have been mapped extensively across the Osis Arch and support basin connectivity during deposition, with a general paleodepth increase to the northwest in the Zaris subbasin and southwest in the Witputs subbasin (Germs, 1983). Deposits of both subbasins are subdivided into the lower Kuibis Subgroup, and the upper Schwarzrand Subgroup, with diachronous deposition of lower Nama Group sediments recording a marine transgression onto the underlying Proterozoic basement. Whilst thinning across the Osis Arch during deposition of the Kuibis Subgroup may suggest the possibility for minor independence of local water column conditions between the two subbasins, the extent of thinning gradually decreased with deposition of the overlying Schwarzrand Subgroup indicating a trend towards more pronounced connectivity corresponding to an overall marine transgression nearing the Ediacaran-Cambrian boundary (Germs, 1983; Saylor et al., 1995).

Unrestricted connection of the Nama basin with the Brazilides Ocean to the present west is implied by a near-primary record of $\delta^{13}C_{carb}$ which presents major features in agreement with other time-equivalent sections globally. Values begin as low as -7.40‰ in deposits of the Kanies Member (Dabis Formation, Kuibis Subgroup) and show a gradually increasing trend to positive values during deposition of the lower Omkyk Member (Zaris Formation, Kuibis Subgroup) (Chapter 3 and Appendix A; Kaufman et al., 1991; Saylor et al., 1998; Wood et al., 2015). This trend is thought to reflect the transitional recovery from the Shuram-Wonoka negative $\delta^{13}C_{carb}$ anomaly and is succeeded by stable positive values up to the inferred position of the Ediacaran-Cambrian boundary (Saylor et al., 1998; Wood et al., 2015).

Uranium-lead geochronology of four volcanic ash beds has constrained the duration of Nama Group deposition, with a lower Hoogland member (upper Kuibis Subgroup) age of 547.32±0.65 Ma, and an age of 540.61±0.67 Ma for the upper Spitskop Member of the Urusis Formation (Schwarzrand Subgroup), coincident with the first appearance datum (FAD) of the trace fossil *Streptichnus narbonnei* (Grotzinger et al., 1995; Jensen and Runnegar, 2005; Bowring et al., 2007; Schmitz, 2012). Strata of the Dabis and lower Zaris Formations which were deposited prior to the lowermost ash bed rest atop crystalline basement along a dramatic, readily identifiable angular unconformity with a contact age inferred at ~550 – 553 Ma (Saylor et al., 1998), whilst conglomeratic and fluvial to shallow marine siliciclastic facies of the Nomtsas Formation unconformably overlie the Urusis Formation with an intercalated ash bed dated at 538.18±1.11 Ma immediately below deposits containing *Treptichnus pedum* (Grotzinger et al., 1995; Schmitz, 2012). Total stratigraphic coverage of the Nama Group below the Cambrian Fish River Formation spans the final 10-12 million years of the Ediacaran Period (Figure 2.5).

More recently, additional U-Pb ages based on the chemical abrasion ID-TIMS method were presented at the International Symposium on the Ediacaran-Cambrian Transition in St. John's,

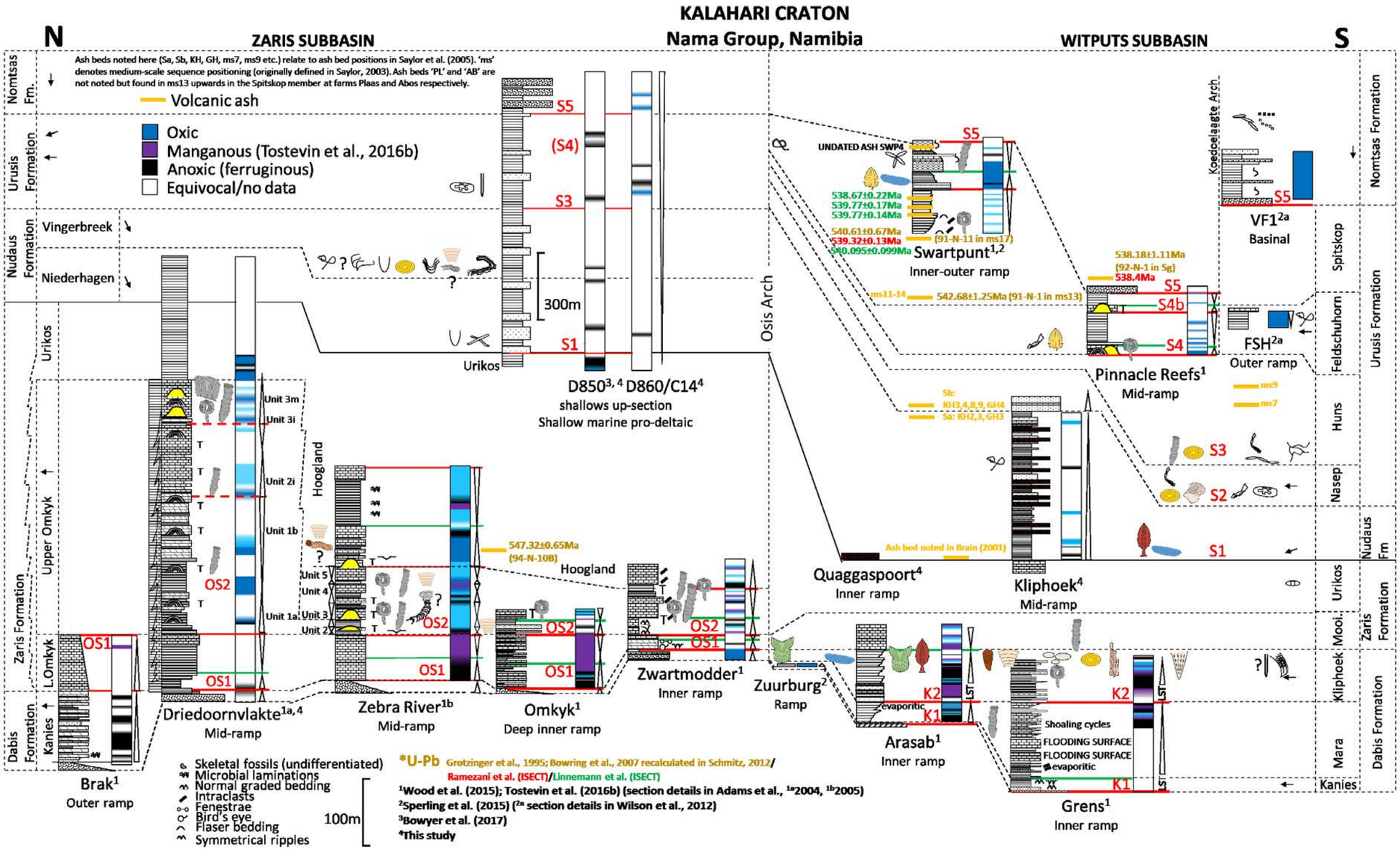

Figure 2.5 Correlation and schematic palaeoredox representation of sections from the Kalahari Craton (Nama Group). Iron speciation data from cited publications and new data. See Apppendix D for fossil key.

Newfoundland (Linnemann et al., 2017). These ages remain unpublished to date, however they apply to four silicified ash layers collected from medium-scale sequence 17 of Saylor (2003) from the Spitskop Member on Farm Swartpunt and reduce the age of the upper Spitskop Member to 538.67 ± 0.22 Ma (in green on Figure 2.5, discussed in Appendix A; Linnemann et al., 2017).

First appearance of soft-bodied Ediacara biota belonging to the Nama assemblage are documented from proximal sandstones of the Kanies Member, Dabis Formation (Bouougri et al., 2011). Subsequent likely-*in situ* occurrence of *Ernietta, Rangea*, and *Nemiana* (/*Beltanelliformis*) are documented within layers of the upper Kliphoek (Aar) Member at Arasab and Grens Farm sections (Hall et al., 2013; Wood et al., 2015). Nama assemblage fossils are recorded throughout the overlying Schwarzrand Subgroup of the Witputs subbasin and include the Erniettamorpha *Pteridinium, Rangea* and *Paramedusium*, in addition to discoidal *Cyclomedusa* in the lower Schwarzrand Subgroup (Germs, 1995). *Pteridinium*, *Swartpuntia*, *Aspidella*, and one possible example of *Bradgatia* are also recorded within the Spitskop Member at Swartpunt section (Grotzinger et al., 1995; Narbonne et al., 1997; Darroch et al., 2015). The published range of soft-bodied fossils within contemporaneous deposits of the Zaris subbasin is restricted to the Nudaus Formation of the lower Schwarzrand Subgroup and include recently documented occurrences of *Aspidella* and *Shaanxilithes* (Darroch et al., 2016, thought the latter may in fact be *Palaeopasichnus*, Zhuravlev, A.Y. pers. com.), in addition to mention of possible *Pteridinium* (Grotzinger et al., 1995). Palaeontological records of the Nama Group and associated reference data is given in full in Chapter 3 and Appendix D.

The Omkyk and Hoogland Members of the Zaris Subgroup and the Huns and Feldschuhhorn Members of the Urusis Formation host prominent thrombolite-stromatolite reefs, including the thick transgressive pinnacle reef succession at Driedoornvlakte, mid-ramp bioherms and biostromes of the highstand systems tract at Zebra River and pinnacle reefs which formed during transgression of the upper Huns and middle Felschuhorn Members (Saylor et al., 1995; Grotzinger, 2000). The earliest documented occurrences of *Cloudina hartmannae, Cloudina riemkeae* and *Namacalathus hermanastes* in the Nama Group are found in association with thrombolitic-stromatolitic microbial reefs of the lower Omkyk Member (though *Cloudina* have also been noted from the underlying Mara Member in the Witputs Subbasin, Germs, 1983) and the possible first appearance of active reef-building by a metazoan is found in the high energy mid-ramp setting at Driedoornvlakte (Grotzinger, 2000; Penny et al., 2014; Wood and Curtis, 2015; but see Mehra and Maloof, 2018). Driedoornvlakte also exhibits the only known occurrence of the neptunian dyke-dwelling, robust skeletal *Namapoikia rietoogensis* of probable poriferan affinity (Wood et al., 2002; Wood and Penny, 2018). Associated *Cloudina* and *Namacalathus* have also been found within shallower facies of the upper Omkyk and lower Hoogland members at Zwartmodder

(Wood et al., 2015) and ichnofossil-rich strata immediately overlying a soft-bodied Nama assemblage horizon in the middle Spitskop Member at Swartpunt (Narbonne et al., 1997; Wood et al., 2015; Darroch et al., 2015).

A wealth of trace fossil evidence recorded throughout the Nama Group initially enabled its interpretation as a terminal Ediacaran (/Vendian) succession (Crimes and Germs, 1982). Of particular note are vertical trace fossils within the lower Nudaus Formation of the Zaris sub basin and basal Huns Member of Urusis Formation in the Witputs, *Treptichnus*-like trace fossil of the basal Huns Member, and *Streptichnus narbonnei* from the Upper Spitskop Member (Jensen et al., 2000; Jensen and Runnegar, 2005; Wilson et al., 2012). In addition, an array of enigmatic tubular compression fossils have been noted from the lowermost Nudaus Formation and Feldschuhhorn Member of the Witputs subbasin (Cohen et al., 2009), and a diverse assemblage of organic walled microfossils has been noted from the Schwarzrand Subgroup of the Witputs subbasin including leiosphaerid acritarchs and *Vendotaenia* (Germs et al., 1986).

Recent, extensive redox analyses utilizing iron speciation of shales, silts and carbonates and Fe_T/Al ratios of nine study sections within the Nama Group, have enabled reconstruction of three distinct time-equivalent shelf to basin transects. Positioning these data in association with paleoecological information has enabled interpretation of the relationship between redox hospitability and sustained ecological presence (Figure 2.5) (Wood et al., 2015; Sperling et al., 2015a). The first transect incorporates data of the Dabis Formation from three sections of the Witputs subbasin at Arasab, Grens and Zuurburg, and two sections of the Zaris subbasin at Zwartmodder and Brak. Shallow water oxia persisted throughout deposition of the Kanies Member (Zwartmodder) and lower Mara Member (Zuurburg) coincident with considerable redox heterogeneity between the moderately deeper Arasab and Grens sections which record probable oxic conditions (inferred from extremely low Fe_T of carbonate sediments) and ferruginous anoxia (Wood et al., 2015; Sperling et al., 2015a). Deep water deposition within the Zaris subbasin (Brak) is seen to have been exclusively anoxic and ferruginous (Wood et al., 2015). Three shallowing-upward cycles are associated with deposition of the Dabis Formation within the Witputs subbasin, whilst only one transgressive unit comprising the Kanies Member is recognized within the Dabis Formation of the Zaris subbasin.

The second transect includes sections comprising time-equivalent carbonate platform deposits of the Omkyk, Hoogland and Urikos Members of the Zaris Formation (Zaris subbasin) on farms Zwartmodder, Omkyk, Zebra River, and Driedoornvlakte. Throughout the Omkyk and Hoogland Members a highly heterogeneous redox environment is evident with shallow waters at Omkyk characterized by repeated establishment of ferruginous anoxia punctuating dominant probable oxic conditions (Wood et al., 2015). Extensive growth of the mid-ramp microbial-metazoan reef at

Driedoornvlakte occupied a transgressive systems tract of the upper Omkyk Member (Unit 3m, OS2, Figure 2.5) (Adams et al., 2004). Additional new data suggest that the termination of reef growth at Driedoornvlakte, which was likely brought on by inundation of the reef by Urikos Member sediments, was accompanied by development of reducing conditions whilst the reef framework was still in contact with sea water (Chapters 3 and 4). Similarly, oxic conditions which appear to have dominated time-equivalent deposition during the second major cycle of the Omkyk Member at Zebra River, are accompanied by growth of microbial-metazoan biostromes which dominantly grew during highstands (Adams et al., 2005). Pulsed ferruginous conditions are recorded during OS2 at Zebra River, which may either reflect development of sluggish circulation within a more proximal and productive inner ramp position, or may imply upwelling of anoxic deep water during transgression (Wood et al., 2015). Indeed, ferruginous conditions which accompanied deposition of transgressive Urikos Member shales during Unit 3m on the deep, outer shelf at Driedoornvlakte are also seen to have developed at Zebra River. However, whilst the carbonate factory at Driedoornvlakte was terminated through inundation by high clastic flux of the Urikos Member, contemporaneous ventilated and likely oligotrophic conditions at Zebra River were accompanied by successful repetitive development of thrombolitic-stromatolitic biostromes, in addition to both *Namacalathus* and *Cloudina*. Equivalent (/slightly older) deposits of the lowermost Zaris Formation in the Witputs subbasin were sampled on Farm Arasab and similarly suggest probable oxic water column conditions during deposition of the Mooifontein Member (Wood et al., 2015).

The third transect incorporates three sections of the Feldschuhhorn and Spitskop Members of the upper Urusis Formation at the mid-ramp pinnacle reefs locality, outer ramp FSH section, and variable depth deposits at Swartpunt (Wilson et al., 2012; Wood et al., 2015; Sperling et al., 2015a). Additional redox data of Nomtsas Formation deposits at the distal Sonntagsbrunn section are also considered herein (Wilson et al., 2012; Sperling et al., 2015a). All sections of transect 3 show a dominantly oxic marine environment within the Witputs subbasin across the Precambrian-Cambrian boundary, however, two brief intervals of ferruginous anoxia recorded from the Spitskop Member at Swartpunt (Wood et al., 2015) may be suggestive of continued water column redox stratification. Accommodation increase during transgression appears to have favoured growth of pinnacle reefs capping the Huns Member on Swartkloofberg Farm similar to conditions at Driedoornvlakte, though there is little indication of anoxic stress present within the Witputs subbasin at this time, and cessation of reef growth is seen to coincide with repeated drowning by siliciclastic deposits of the Feldschuhhorn Member (Saylor et al., 1995; Grotzinger, 2000; Wood et al., 2015).

Recent complimentary data supporting redox stratification of the Nama Basin have enabled nuanced interpretation of intermediate redox states through identification of unusual REE(+Y) profiles

(Tostevin et al., 2016b). This has also allowed infilling of data gaps, where low Fe_T (< 0.5 wt%) of some carbonate samples previously impeded analysis via Fe speciation. Where iron speciation indicates surface water oxia, these data are corroborated by negative Ce anomalies. However, where highly reactive iron enrichments indicate anoxic ferruginous conditions, REE patterns either show the absence of, or expression of positive, Ce anomalies (Tostevin et al., 2016b). In the latter case, positive Ce anomalies are interpreted to indicate the presence of an intermediate layer of dissolved oxygen ≤ ~10μM immediately overlying ferruginous deeper waters (Tostevin et al., 2016b). Within this layer, the reductive dissolution of Mn (oxyhydr)oxides likely resulted in release to the water column of Ce(IV), leading to Ce accumulation and resultant enrichment in Ce relative to neighboring rare earth elements in carbonate sediments (Tostevin et al., 2016b). In the Nama Group, Ce anomaly data indicate episodic incursion of the manganous zone at shallow water Arasab, Grens, Zwartmodder and Omkyk sections and intermediate depth at Zebra River. However, an absence of, or negative Ce anomalies at Driedoornvlakte, the Pinnacle Reefs and Swartpunt sections support sediment deposition at these localities under predominantly oxic conditions (Figures 2.5 and 2.6d, e) (Tostevin et al., 2016b).

Whilst almost exclusive oxia recorded within the upper Urusis Formation of the Witputs subbasin may suggest progressive oxygenation of the Nama Group towards the Ediacaran Cambrian boundary (Chapter 3, Wood et al., 2015), additional sampling of Urusis Formation strata of the Zaris subbasin appears to complicate this development. Fine-grained, olive green and purple-red mudstones are interbedded with channelized sandstones of the Schwarzrand Subgroup in the Zaris subbasin and yield iron speciation data which indicate exclusive formation under anoxic ferruginous water column conditions. Ratios of Fe_T/Al suggest normal marine deposition within the calibrated range of 0.53 ± 0.11, with the exception of 5 outliers indicating significant iron enrichment and supporting deposition under an anoxic water column (Figure 2.5). In depth discussion of these and additional complementary data are further presented in Chapter 3.

Redox evolution accompanying the Driedoornvlakte skeletal community

The majority of sampled sections within the Kuibis Subgroup represent shallow to mid-ramp marine facies above storm wave base (with the exception of the most distal section at Brak), and as such introduction of oxygen via diffusion and surficial mixing from the overlying atmosphere is expected to have been pervasive. Riverine input of oxic freshwater may also have been an important vector for the introduction of O_2 into nearshore environments, with paleocurrent data supporting dominantly westward-directed effluent sediment transport from the Kalahari Craton, evident from trough cross-

stratification in siliciclastic lowstand systems tract deposits of the Kanies and lower Kliphoek Members (Germs, 1983; Saylor et al., 1995).

During deposition of the Dabis Formation, two cycles of marine transgression show repetitive shoaling of the oxycline (Figure 2.5), with switching between ferruginous and probable oxic signatures at Arasab and Grens which may represent retrogradational stacking during higher order parasequences leading to deposition above the oxycline. If soft-bodied organisms found in Dabis Formation deposits of the Witputs subbasin required oxygen, short-lived oxic episodes may have been transiently habitable in these environments, or alternatively, metabolically active forms were restricted to shallowest environments where oxia was more stable (see Chapter 3). Distal dolomites, limestones and shales at Brak record uninterrupted deposition below the oxycline and represent anoxic ferruginous conditions which dominated the deep marine environment at this time.

Throughout the overlying Zaris Formation, frequent occurrence of anoxia in the most proximal sampled environments has been interpreted as a consequence of upwelling anoxic ferruginous deep water, which is supported by progressively decreasing Fe_T/Al in shallower sections (Wood et al., 2015). Though shallow waters of the exposed mid-ramp are thought to have been subject to active physical mixing and effective oxygenation, frequent incursions of anoxia are also thought to correspond to upwelling. However, relatively quiescent conditions at proximal Zwartmodder and Omkyk sections may represent an environment prone to high surface water productivity fuelled by riverine nutrient input. Efficient remineralization of the resultant elevated organic matter via aerobic respiration within shallow waters may have reduced dissolved oxygen concentration, followed by reduction of readily available iron oxides leading to thickening of the zone of Fe-Mn reduction (Figure 2.6d) (Tostevin et al., 2016b).

Meter-scale reefs constructed through mutual attachment of *Cloudina* have so far been noted solely from the thrombolite-stromatolite reef at Driedoornvlakte and grew exclusively during transgression of the Upper Omkyk Member (Penny et al., 2014; Wood and Curtis, 2015; but see Mehra and Maloof, 2018). Laterally extensive thrombolite-stromatolite biostromes of the upper Omkyk and lower Hoogland Members at the more proximal Zebra River locality are associated with solitary mat-sticking *Cloudina* and *Namacalathus*. These biostrome horizons record pulsed incursion of anoxic ferruginous deeper waters into a dominantly oxic/probable oxic water column (Wood et al., 2015). It has been suggested that unconsolidated seafloor conditions relating to a proximal siliciclastic influx from the Damara orogen to the north may have prevented early cementation conducive to formation of relief-structures during platform development of the Hoogland Member (Dibenedetto and Grotzinger, 2005) which was deposited following drowning of the Driedoornvlakte reef by sediments of the Urikos Member (Figure 2.5). This may imply a favourable combination of sustained oxic conditions and low

sediment influx of the mid-ramp at Driedoornvlakte, which supported greater diversity of calcifying ecologies. Indeed, successful colonization of shallow marine environments by diverse calcifying paleocommunities was likely facilitated during periods of relatively stable oxygenation, and larger body size association in both *Namacalathus* and *Cloudina* is observed exclusively under prolonged, stable oxic water-column conditions throughout the Nama Group (Wood et al., 2015).

Iron speciation results of the Schwarzrand Subgroup north of Osis at first appear entirely incongruent with fully oxic, unrestricted water column conditions within the connected Witputs subbasin to the south, where the overall paucity of anoxic conditions may suggest deepening of the oxycline. The Nudaus Formation of the Schwarzrand Subgroup within the Zaris subbasin represents a sequence of prodeltaic (Niederhagen Member) to low-energy shoreline (Vingerbreek Member) mudstones and laminated and channelized sandstones, with deposition in increasingly shallower water towards the east, nearing the top of the sampled section (Germs, 1983; Grotzinger et al., 1995). Analysis of the Niederhagen Member, which locally overlies Hoogland and Urikos sediments, indicates provenance from a relict volcanic island arc within the Damara Belt, which divided the Congo and Kalahari Cratons to the present-day north/northwest of the Nama Group (Germs, 1983; Blanco et al., 2011). The axis of the carbonate platform within the overlying Urusis Formation was shifted to the deeper, shallow marine environment to the southwest of Osis, and equivalent facies of the smaller Zaris subbasin represent proximal siliciclastic deposition (Germs, 1983). The depocenter of the Zaris subbasin gradually shifted southwards associated with diminishing influence of the Osis Arch throughout deposition of the upper Schwarzrand Subgroup (Germs, 1983). A potential scenario for some elevated Fe_{HR}/Fe_T within the Nudaus and Urusis Formations in the Zaris subbasin may follow a simple Fe-trap mechanism, whereby Fe_{HR} is effectively retained within this proximal deltaic environment (Figure 2.6e) (Johnston et al., 2013). Such a setting would subsequently act as a source for Fe_{HR} via reductive remobilization to the subjacent water column via oxic or anoxic iron shuttle processes (Lyons and Severmann, 2006; Severmann et al., 2008). This may be supported by a significantly greater contribution of oxide-bound iron within the highly reactive iron pool of the Schwarzrand subgroup north of Osis, when compared to contemporaneous siliciclastic deposits of the Witputs subbasin, and accompanied by 'normal shale' values of Fe_T/Al. Further data collected from transects of the Zaris subbasin which aid palaeoenvironmental reconstruction are discussed in Chapter 3.

Whilst diverse soft-bodied and skeletonizing biota thrived within the upper Urusis Formation, as well as motile metazoans evident from the ichnofossil record at the oxic Swartpunt locality, the Schwarzrand Subgroup in the Zaris subbasin lacks evidence for a comparatively significant biotic presence but for possible *Pteridinium* (Grotzinger et al., 1995) and recently recorded *Aspidella* and *Shaanxilithes*

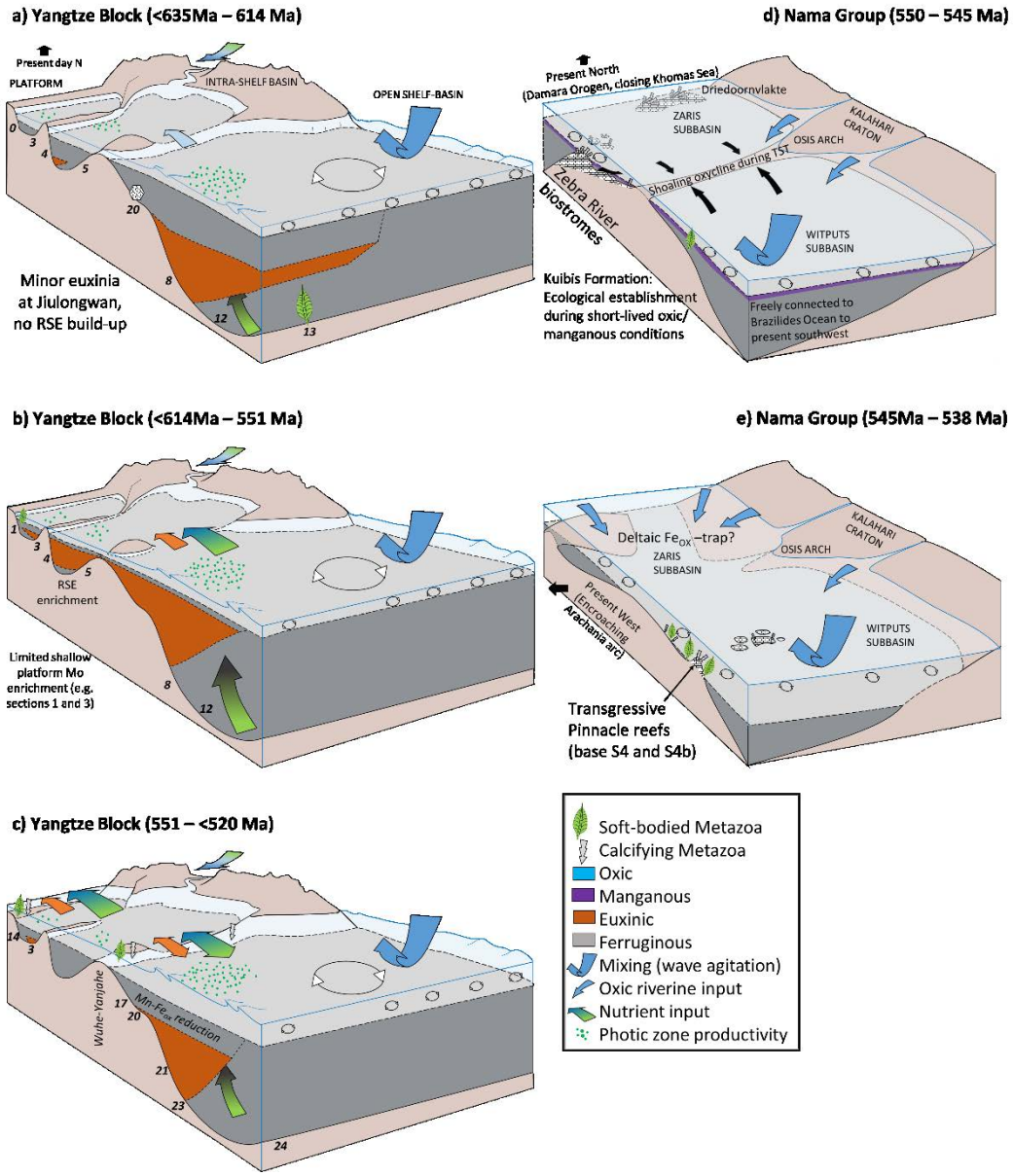

Figure 2.6 (a–e) Basin-scale reconstructions of redox conditions for key successions of the Ediacaran-Cambrian **(a–c)** Yangtze Block, South China and **(d, e)** Nama Group, Namibia. A key to section numbers of the Yangtze Block is provided in Figure 2.2. **(a)** Doushantuo/Lantian Formations Members I-III (<635 Ma to 614 Ma): Deep-water restriction of the Yangtze Gorges intrashelf basin, and euxinia of the unrestricted slope at Wuhe. **(b)** Miaohe Member (<614 Ma to 551 Ma): Sea-level rise and reduced restriction of the Yangtze Gorges intrashelf basin. Semi-restricted conditions are sustained at more proximal sections (e.g., Jiuqunao) evident from continued lack of Mo enrichment (Li, C. et al., 2015b; Och et al., 2015). **(c)** Dengying to early Cambrian Formations (<551 Ma to <520 Ma): Deposition during continued eustatic sea-level rise resulted in reduced restriction of proximal intrashelf basins. Whilst euxinia continued to intermittently characterise platform and slope settings, there is some evidence to suggest deepening of the chemocline with first appearance of episodic oxia recorded in deposits of the upper Niutitang Formation at basinal Longbizui. **(d)** Kuibis Subgroup (550 Ma to <547 Ma): Deposits of the Witputs sub-basin initially record heterogeneous redox with dominantly anoxic ferruginous conditions

(/*Palaeopasichnus*, Zhuravlev, A.Y. pers. com.) within the Nudaus Formation (Darroch et al., 2016). This may simply be a consequence of comparatively poor stratal exposure of the Schwarzrand Subgroup north of Osis farm which has, until recently, impeded extensive body fossil recovery. If the interpretation of an episodic prodeltaic iron-trap within this formation is correct, original water column conditions may in fact have been at least intermittently oxic (Chapter 3).

2.3 Discussion

2.3.1 Palaeogeographic context

The beginning of the Ediacaran saw the waning stages of breakup of the supercontinent Rodinia and climatic recovery following the global Marinoan glaciation, and the ensuing 95 million years witnessed substantial migration of isolated cratons across a wide variety of latitudinal ranges during assembly of Gondwana (Figure 2.7). Consideration of the dominant redox conditions recorded within each environment, alongside the extent of local restriction, allows speculation as to the possible control of latitudinal position on paleoredox evolution throughout this interval.

Gradual equatorial migration of the South China Block (Li, Z.-X. et al., 2013; Zhang et al., 2015) is associated with little change in dominant redox, with anoxia documented into the early Cambrian (Figure 2.2). In fact, sections of the Yangtze Block are exceptional in that they include the only documented development of spatially extensive and sustained euxinia (Figure 2.6 a–c). This implies elevated seawater sulfide relative to reactive iron which has been variably attributed to local hydrothermal activity, riverine delivery and elevated productivity – induced anoxia on a sulfate replete open shelf (Chen et al., 2009; Wang et al., 2012; Och et al., 2015; Sahoo et al., 2016).

The evolution of redox within intra-shelf basins of the Yangtze Block was likely associated with the combined effects of variable sulfate supply, nutrient delivery and local water column stagnation. However, maintenance of euxinia on the freely connected slope requires persistently elevated productivity. Primary fluid inclusion analyses of halite from the Dengying Formation indicate an approximate paleo-seawater temperature close to that of the modern tropics during the final 10 million

---

Figure 2.6 continued: followed by subsequent reef growth confined to transgressive systems tract of the Zaris sub-basin and skeletal metazoan ecology influenced by incursions of anoxia during shoaling of the chemocline. Manganous zone suggested after regional Ce/Ce* study of Tostevin et al. (2016b). **(e)** Schwarzrand Subgroup (<547 Ma to 538 Ma): Oxia is documented from the Witputs sub-basin and ferruginous anoxia in the Zaris sub-basin potentially due to the deltaic trapping of Fe oxides.

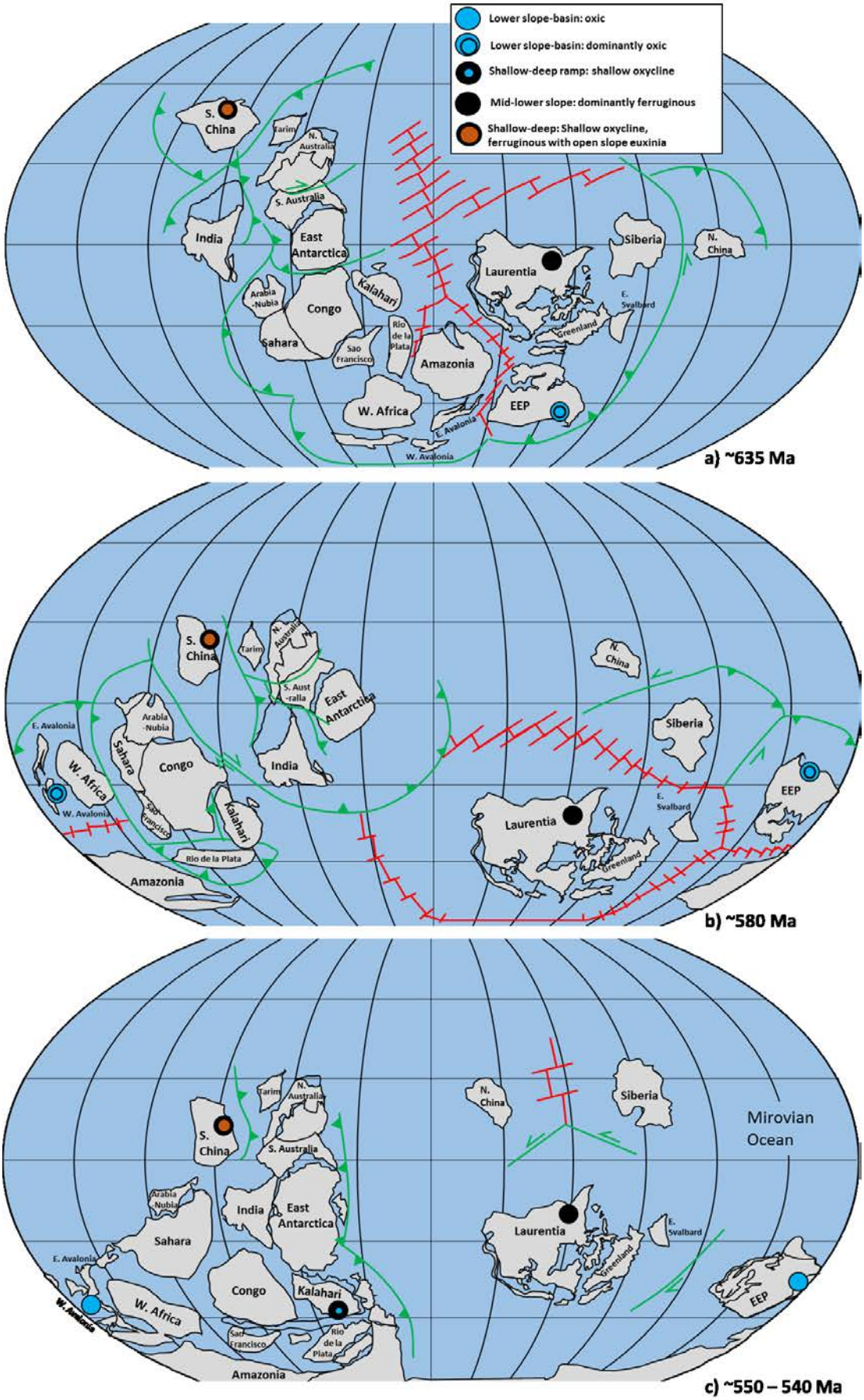
Lower slope-basin: oxic
Lower slope-basin: dominantly oxic
Shallow-deep ramp: shallow oxycline
Mid-lower slope: dominantly ferruginous
Shallow-deep: Shallow oxycline, ferruginous with open slope euxinia
S. China
Tarim
N. Australia
S. Australia
India
East Antarctica
Arabia -Nubia
Congo
Kalahari
Sahara
Rio de la Plata
Sao Francisco
Amazonia
W. Africa
EEP
E. Avalonia
W. Avalonia
Laurentia
Siberia
N. China
E. Svalbard
Greenland
a) ~635 Ma
b) ~580 Ma
c) ~550 – 540 Ma
Mirovian Ocean

years of Ediacaran deposition (Meng et al., 2011). With lowered solubility of dissolved O_2 under higher water temperatures, the approximately equatorial paleo-latitude of the South China Block at 550–540 Ma may in itself have been less susceptible to extensive water column oxygenation under the lower atmospheric oxygen concentrations of the Ediacaran Period. Though there is some evidence for increased oxygenation across the Yangtze Block, oxic conditions recorded in Ediacaran sections (e.g. Baiguoyuan) are largely confined to shallow platform sediments intermittently deposited within the oxygenated surface mixed layer.

Deep slope deposits of Laurentia also record persistent anoxia within the lower Sheepbed Formation at ~635 Ma, with only intermittent oxic influence documented through to the terminal Ediacaran upper Risky Formation (Johnston et al., 2013; Sperling et al., 2015b). A low latitude favorable to Ekman-induced surface water transport away from the Laurentian continental margin may have resulted in persistent upwelling which sustained deep water anoxia through elevated surface productivity at ~635 Ma. Subsequent migration of Laurentia to occupy mid-high latitude in the southern hemisphere is represented in Figure 2.7b, however Li, Z.-X. et al. (2013) caution that this constitutes the reconstruction of least reliability. Occasional, short-lived oxia recorded within the overlying upper Sheepbed, June Beds and Blueflower formations may be a product of deposition above the oxycline and/or an effect of lateral transport of subjacent oxygenated bottom water currents, similar to those which are inferred to have dominated the depositional environment of the distal Isaac Formation.

Both Avalonia and the East European Platform, which shared a similar latitudinal position to Laurentia at ~580 Ma, show contrasting evolution from ferruginous anoxia towards dominantly persistent oxygenation of the deep slope environment as early as ~579–575 Ma (Canfield et al., 2007; Johnston et al., 2012; Pu et al., 2016). Migration of the East European Platform to occupy a mid-high latitude position close to western Avalonia during the final ~40 Myrs of the Ediacaran Period alongside

---

Figure 2.7 (page 99) Schematic illustration of evolving local redox and palaeogeography throughout the Ediacaran (635–540 Ma). Modified after Li et al. (2013). **(a)** 635 Ma. Sections of the Yangtze platform and basin (South China) indicate predominance of anoxia with euxinia restricted to mid-lower slope. Lower slope of the Laurentian passive margin (Northwest Canada) shows ferruginous anoxia and the lower Vychegda Formation (East European Platform) shows oxia with occasional ferruginous anoxia. **(b)** 580 Ma. Avalonia and the East European Platform occupy similar mid-latitude position. Iron speciation data from Western Avalonia (Newfoundland) show predominantly oxic conditions on the lower slope. Short-lived oxia recorded from sections of Laurentia. South China Block continues to migrate to low latitude (Zhang et al., 2015). **(c)** 540 Ma. Shallow to mid-depth sections of the Kalahari (Namibia) indicate continued intermittent ferruginous anoxic incursions.

their corresponding shift towards more stable oxygenation, may reasonably be interpreted to suggest a similar mechanism. The stable oxygenated conditions accompanying deep marine deposition of the Conception and St John Groups and neighboring deposits of the Vychegda and Redkino Formations require a well-established hydrographic system. It is possible that surface water cooling in this region may have stimulated density-induced deep water development in the aftermath of the regional Gaskiers deglaciation (Laflamme et al., 2013). Under these conditions, oxygen-rich water from the well-mixed surface ocean would be drawn to depth in a similar manner to present day North Atlantic Deep Water formation (Broecker, 1997). Importantly, deep water formation in the modern ocean is location specific and dependent on factors including local bathymetry, freshwater input and evaporation (Bruce, 1983; Broecker, 1997). Whilst the key conditions conducive to deep water formation continued to characterize the vicinity of Avalonia and the EEP, cratonic positioning of the Laurentian passive margin likely favored a regime of continued upwelling.

The Nama basin occupied a mid-high latitude position freely connected to the narrowing Brazilides Ocean in the southern hemisphere in the final 10–12 million years of the Ediacaran. Mixed carbonate-siliciclastic deposition in a ramp environment, occupying shallower levels of the water column than sections of Avalonia and the East European Platform, alongside surrounding assembly of Gondwanaland may have restricted development of effective deep water formation and maintained continued stratification with ferruginous anoxic depths (Figure 2.6d). A transition from dominantly anoxic and ferruginous water column conditions during deposition of the Kuibis Subgroup to long-lasting oxia of the Urusis Formation, particularly of the Witputs subbasin, may also suggest a progressive deepening of the oxycline toward the Ediacaran-Cambrian boundary. Meanwhile, contemporaneous closure of the intra-cratonic seaway, encroachment of the Arachania arc and differential sediment flux affecting the two subbasins may have led to the preservation of distinct geochemical signatures within a predominantly oxic shallow marine environment (Figure 2.6e).

The stratified redox model proposed for the Arroyo del Soldado Group (Pecoits, 2010; Aubet et al., 2012) is consistent with that described from the Nama Group. However, with poor temporal constraint on deposition of the Yerbal and Polanco Formations, stratigraphic equivalence between units of these two groups is now considered highly unlikely. Indeed, the age range of these deposits and fossil specimens reported continue to be the subject of debate (Aubet et al., 2014; Pecoits et al., 2016).

In summary, whilst a gradual increase in global ocean oxygenation may have occurred during the Ediacaran Period (e.g. Kendall et al., 2015; Chen, X. et al., 2015), cratonic positioning likely influenced mechanisms for local oxygenation resulting in regions characterized by continued dominance of anoxia. Recent detailed geochemical analyses employed on drill-core samples from a shelf-to-basin

transect of the early Cambrian Baltic basin indicate that this environment was characterised by long-lived mid-depth anoxia, the spatial extent of which was governed by changing productivity, similar to modern oxygen minimum zones (Guilbaud et al., 2018). It is important to take into account the (likely significant) effect of sampling bias associated with the deposition and preservation of fine-grained sediments within versus above/below such metastable OMZs. Sediments from Ediacaran environments largely deposited within such OMZ settings would record dominantly anoxic conditions (e.g. lower Nama Group, Wernecke and Mackenzie Mountains of Laurentia and South China), whereas those deposited below (e.g. western Avalonia and Cariboo Mountains of Laurentia) and above (upper Nama Group, East European Platform and middle Cambrian of South China) would be represented by dominantly oxic palaeoredox signatures.

2.3.2 Complex multicellular eukaryotes

Whilst some regions indicate a distinct trend towards local oxygenation accompanied by first fossil appearance of complex multicellular eukaryotes (e.g. Avalonia, the EEP and the Kalahari Craton) assemblages including the Avalon assemblage of the Laurentian passive margin, and Lantian and Miaohe biotas of the Yangtze Block, are seen to have occupied dominantly anoxic ferruginous bottom water environments. Therefore, if dissolved oxygen above a threshold concentration was necessary to support such communities, benthic colonization occurred during short-lived oxic episodes indistinguishable by current proxy methods.

Potential benefits of inhabiting an environment prone to dissolved oxygen depletion may be associated with nutrient demand. For instance, upwelling or continental nutrient delivery and elevated primary production might conceivably have favored organisms such as rangeomorphs which may have fed via osmotrophic absorption of labile DOC or active fluid endocytosis during periods of less active vertical mixing (Laflamme et al., 2009).

With the exception of *Eoandromeda* which is recorded from ferruginous deposits of the Miaohe Member (Li, C. et al., 2015b), soft-bodied fossils considered to represent probable Metazoa including *Thectardis* and *Kimberella* have so far been noted only from stratigraphic sections known to have been deposited beneath oxygenated bottom waters. This may be considered to support the inference of relatively high physiological oxygen demand suggested for motile *Kimberella* (Sperling et al., 2015c).

2.3.3 Benthic sulfide stress in Yangtze Block environments

Semi-restricted intra-shelf basins of the Yangtze Block were prone to protracted anoxic intervals typified by free water column hydrogen sulphide and quantitative trace metal drawdown (Li, C. et al., 2010; Och et al., 2015; Sahoo et al., 2016). Whilst localized hypoxia in the modern ocean reduces macrofaunal biodiversity, the additional deleterious effects of elevated H_2S_{aq} on aerobic benthic communities is also well documented, with accelerated mortality during anoxic periods in the presence of H_2S_{aq} due to the enzymatic disruption of oxygen carrying cytochrome *c* oxidase at the terminus of the mitochondrial electron transport chain (Complex IV of Figure 1.6) (Vaquer-Sunyer and Duart, 2010). The toxic effects of hydrogen sulfide are experienced by bivalve and annelid species in the modern ocean at $\mu molL^{-1}$ concentrations below those expected to result in quantitative scavenging of Mo such as that recorded from black shales of the Doushantuo Formation and overlying terminal Ediacaran and Cambrian formations of the Yangtze Block (Vaquer-Sunyer and Duart, 2010). As such, under conditions of elevated aqueous H_2S, body plans which exhibit higher surface area to volume ratios are expected to suffer greater losses (Sperling et al., 2015c).

Extensive benthic sulfide stress of Yangtze Block environments following transgression and flooding of intra-shelf basins during deposition of Doushantuo Member IV is likely to have been severe, with long-lived 'patchy' water column euxinia persisting into the early Cambrian when sessile benthic communities were likely restricted to inner shelf platform settings (Och et al., 2015). Despite the extreme environmental conditions, a diverse macrofaunal assemblage developed within basins of the Yangtze Block. Repetitive flooding by reducing waters may have been accompanied by repeated local community die-off. This may also have irrigated shallower depths through nutrient recycling from the deeper water environment in preparation for recolonization during subsequent ventilation. It may be reasonable to assume that, although we know little about the physiological requirements of the Miaohe biota, fossil representatives of probable animals such as *Eoandromeda* may have suffered considerably under anoxic conditions with elevated H_2S. Interestingly, iron speciation data of lower fossiliferous units of the Doushantuo Member IV at the type locality of Miaohe (Hubei) show dominantly ferruginous anoxic conditions, with elevated proportions of pyrite indicative of euxinia restricted to overlying shales which are devoid of fossils (Li et al., 2015b). Similar high resolution geochemical sampling may benefit physiological discussions of the fossiliferous Lantian Formation. Whilst the early Cambrian saw continued euxinia in environments of the Yangtze Block, there is evidence to suggest a gradual progression towards more oxygenated inner shelf environments and restriction of euxinic conditions to the lower slope and basin (Wang et al., 2012; Yuan et al., 2014; Feng et al., 2014; Och et al., 2015; Hammarlund et al., 2017).

2.3.4 Skeletal metazoans

Benthic *Sinotubulites* and *Cloudina* recognized across the Yangtze Block dominantly outcrop in shallow marine carbonate facies of the Gaojiashan and Beiwan Members (and equivalents) of the middle and upper Dengying Formation (Figure 2.6c). However, specimens of *Sinotubulites* are also noted from deeper ramp limestones deposited above storm wave base of the Gaojiashan-equivalent Shibantan Member (Cai et al., 2014). During deposition of the Dengying Formation, proxy evidence supports a temporarily oxic shallow shelf (Duda et al., 2014; Ling et al., 2013) which perched above a dominantly anoxic deeper water environment within which periods of euxinia may have been detrimental to calcification. Dominant anoxia and encroachment of the euxinic wedge into shallow inner platform environments typified the water column during deposition of the underlying Doushantuo Member IV, which may have restricted colonization of calcifying communities along the shelf and within the anoxic intra-shelf basins until intermittent ventilation during deposition of the middle Dengying Formation, potentially as a consequence of occasional deeper water mixing by mass-flow events, permitted transient habitation by mat-sticking *Cloudina* (Cai et al., 2014). Geochemical and paleontological investigations of Dengying Formation shallow platform carbonates at Gaojiashan (Shaanxi Province) suggest that the observed transition from soft-bodied to calcareous biomineralization represented by successive appearance of *Cloudina* after *Conotubus* may have been related to an increase in continental weathering-derived sulfate and alkalinity (Cui et al., 2016a). In this scenario, initially more oxidizing conditions supported soft-bodied and bioturbating communities, whilst subsequently enhanced continental weathering associated with elevated water column alkalinity and carbonate saturation not only led to reinforced water column redox stratification but may, alongside the advent of predation, have promoted the necessity for biocalcifying communities inhabiting shallow oxic waters through instigating the requirement for a mode of Ca removal from newly developed circulatory systems (Cui et al., 2016a).

Shallow, inner-ramp carbonate and siliciclastic sediments of the Omkyk and lower Hoogland Members of the Nama Group host *Cloudina and Namacalathus* within transient oxic/ferruginous conditions dominantly attributed to the short-lived incursion of anoxic deeper water (Figure 2.6d) (Wood et al., 2015). However, water column anoxia induced via primary productivity and organic matter oxidation, as may have occurred in shallowest settings influenced by riverine nutrient influx, results in the by-product of substantial dissolved CO_2 and lowered *p*H conducive to enhanced $CaCO_3$ dissolution (Sperling et al., 2015c). Therefore, under lowered pO_2 of the Ediacaran Period, long-lived productivity-induced anoxia as seen in modern OMZs is unlikely to have supported immobile, benthic, strongly-calcifying organisms such as *Namapoikia*. Intervals associated with protracted oxia both throughout, above and below biomineralizing fossil horizons, in shallow to mid-ramp settings are

accompanied by thicker walled and larger individuals reflective of the ease of metabolically demanding calcification within these stable oxic, oligotrophic, carbonate-saturated waters (Wood et al., 2015).

If skeletal fragments reported from the Arroyo del Soldado Group are representative of *Cloudina* (requiring that recent geochronological and/or stratigraphic reconsideration is incorrect), partial redox reconstruction (Figure 2.4 c) lends further support to this proposed biotic response, with alleged *Cloudina riemkeae* recorded from the upper Yerbal Formation bracketed by oxic siliciclastic deposits (Gaucher and Sprechmann, 1999; Gaucher and Poiré, 2009; Frei et al., 2013). However, further high-resolution geochemical sampling within the Arroyo del Soldado Group is required within a paleontological and paleo-ecological remit to support protracted oxygen stability as a prerequisite for extensive skeletonisation. Future integrated studies incorporating sections of the Upper Miette Group (Rocky Mountains), Wood Canyon (California), Dengying Formation (Yangtze Block), Itapucumi Group (Paraguay), Yudoma Group (Siberian Platform), lower Ara Group (Oman), Puerto Blanco Formation (Mexico), Bambuí and Corumbá Groups (Brazil), and Ibor and nivel de Fuentes Groups (Spain) may help establish this as a globally identifiable condition (Corsetti and Hagadorn, 2000; Hofmann and Mountjoy, 2001; Hua et al., 2003; Cortijo et al., 2010; Sour-Tovar et al., 2007; Zhuravlev et al., 2012; Warren et al., 2014; Cui et al., 2016a).

2.3.5 Earliest metazoan reefs

The only documented occurrence of active reef-building by *Cloudina hartmannae* and *C. riemkeae* alongside dyke-dwelling *Namapoikia* is recorded within mid-ramp positions typified by inferred persistent oxygenation of the Nama Group, Namibia (Penny et al., 2014; Wood et al., 2015; but see Mehra and Maloof, 2018). Prerequisite conditions for effective, long-lived reef building in the modern include stable substrate, low sediment influx, readily available Ca^{2+} and CO_3^- ions and relatively well oxygenated conditions above the contemporaneous carbonate compensation depth (James and Jones, 2015). Under these ideal conditions Ediacaran *Cloudina* reefs grew and there is some evidence for confinement of reef growth to exclusively oxic intervals of the mid-ramp at Driedoornvlakte (see Chapter 3). Establishment of a pelagic-benthic link was likely enabled in such ecosystems through proficient suspension feeding by *Cloudina* and *Namacalathus*. This may have resulted in rapid and effective redistribution of organic matter to depth thereby supporting a model of biological ventilation of shallow and mid-depth environments via reduced oxygen consumption in surface waters towards the end of the Ediacaran (Butterfield, 2009; Lenton et al., 2014; Meyer et al., 2016).

2.4 Conclusions

Through development and application of varied geochemical proxies, the past decade has witnessed a revolution in our understanding of global and local redox heterogeneity which accompanied the evolution of ecosystems containing potential candidates for the earliest animals. Although earlier studies suggested that oxygen stabilization may have characterized the global ocean as early as the late Ediacaran (Canfield et al., 2007; Johnston et al., 2012), continued local redox heterogeneity is evident from multiple shallow to deep marine environments well into the Cambrian. While increase beyond a low pO_2 concentration threshold within the shallow marine environment may have enabled a step-change in complexity of middle Ediacaran ecosystems, in some areas this facultative threshold may have been surpassed only transiently. Currently available bulk rock redox proxy methods are unable to resolve short-term oxygenation which may have permitted opportunistic colonization of the substrate by organisms with higher oxygen demand. However, high resolution geochemical sampling conducted in a comprehensive paleontological and paleoecological framework, despite the inherent complications associated with taphonomic and facies biases, enables appreciation of changing provincial ecosystem structure together with the extent of accompanying local water column oxygenation through the Ediacaran (Sperling et al., 2015b; Liu et al., 2015). Placing such studies in relative sea- level and paleogeographic framework will enable appreciation of the nuances of marine redox heterogeneity which characterized environments on the kilometre scale, similar to those that exist in modern shelf to basin environments.

A decrease in the volumetric proportion of euxinic mid-depths during the Tonian is suggested to have removed a toxic barrier to evolutionary diversification of aerobic eukaryotes (Guilbaud et al., 2015) and oxygen concentrations in shallow waters was likely sufficient to support evolution of the earliest Metazoa represented by crown group demosponges (Sperling et al., 2013a). Subsequently, environments of the Ediacaran witnessed the proliferation of probable animals which appear to have opportunistically colonized habitable substrates. This may, in part, have been defined by the availability of dissolved oxygen under oxic/dysoxic conditions, with greatest diversity permitted in environments subject to effective, stable ventilated conditions. Once developmental barriers to biomineralization were surpassed at the end of the Ediacaran, local ecosystem feedbacks associated with biological ventilation of the water column were reinforced. Such feedbacks likely incorporated efficient filtration of rapidly sinking, large organic particles via suspension feeding within high surface area to volume ratio, multi-tiered reefal ecosystems, substrate bioturbation and efficient sedimentary phosphorus retention (Lenton et al., 2014; Penny et al., 2014; Wood and Curtis, 2015).

The Ediacaran Earth saw extensive cratonic migration during the formation of Gondwana and associated alterations in available niche space. The geographic positioning of paleoenvironments within the global ocean, alongside their relative paleodepth, likely influenced mechanisms controlling redox in open shelf environments. Particularly significant however, is that our record of local redox suffers from sampling of sediments that are not truly basinal. It is likely that a failure to recognise this will result in wildly different interpretations of the mechanisms for variability in the distribution of oxic and anoxic water masses (Guilbaud et al., 2018).

When viewed together, geochemical, paleogeographic and paleoenvironmental data suggest local ecosystem dynamics constrained by dissolved oxygen availability, nutrient provision, stable substrate for colonization and the evolution of predation. Continued environmental proxy development and utilization in high-resolution biostratigraphic and paleoecological studies across shelf-to-basin transects will aid clarification of compelling issues associated with Ediacaran ecosystem development. In particular, novel geochemical proxies that record near-instantaneous transitions sensitive to minor changes in dissolved oxygen concentration may shed light on the absolute oxygen requirements for shallow marine colonization at ecologically meaningful timescales in the earliest calcifying invertebrate communities.

Chapter 3

Enhancing the palaeoredox record of the Nama Group, Namibia

Abstract

Marine ecosystems in the final 30 million years of the Ediacaran Period (~571 – 541 million years ago, Ma) witnessed a notable increase in complexity and diversity, the cause for which remains under debate. Significantly, lower than present atmospheric and oceanic oxygen concentrations enabled some shallow marine environments to remain poised at iron reduction until well into the Cambrian and likely influenced regional-scale ecosystem structure and stability. This chapter provides a four-dimensional reconstruction of local redox dynamics and associated biotic establishment in the Ediacaran Nama Group of southern Namibia. This is made possible through collation of previously published fossil occurrence and palaeoredox proxy data, in addition to new data of iron speciation alongside major element and carbonate-bound iodine concentrations. We find that a marked shift in oxycline depth from shallow to deeper levels in the water column and correspondingly reduced frequency of anoxic incursions onto the shallow shelf approximately coincided with the first appearance and subsequent diversification of novel sediment bioturbators in the Lower Urusis Formation (~547-542 Ma). Additionally, the persistent spatial separation of anoxic deep waters from habitable ecospace implied by the fossil distribution of phylogenetically-enigmatic soft-bodied forms, supports the inference that at least minor oxygen concentrations were a metabolic requirement of these organisms.

Author Contributions: This chapter benefited from enlightening discussions with Rachel Wood, Alex Thomas, Simon Poulton and Raja Ganeshram in addition to inspiring email correspondence with Gerard Germs. Additional invaluable advice was provided by Ian Butler and Andy Connelly in construction of the iron speciation laboratory at the University of Edinburgh. Complementary data of iodine/(calcium + magnesium) for selected samples were analysed by Dalton Hardisty at UC Riverside and are a product of ongoing collaboration with Dalton Hardisty (Woods Hole) and Timothy Lyons (University of California Riverside).

3.1 Introduction

Sedimentary deposits of the Ediacaran Period (635-541 Ma) contain impressions of large, complex multicellular eukaryotes which include likely representatives of the first animals in the fossil record (Xiao and Laflamme, 2009). One of the key questions which remains contentious is the relative importance of genomic development and changes in the chemical state of the marine environment to the rapid emergence and diversification of animal-grade organisms at this time. Particular attention has been paid to the hypothesis that an increase in the dissolved oxygen concentration of marine environments across this crucial interval enabled the rise of metabolically active ecologies, large body size and active biomineralisation (Chapters 1 and 2; Runnegar, 1991; Lyons et al., 2014; Sperling et al., 2013, 2015c). Numerous studies have aimed to better constrain the timing of global deep ocean ventilation through a variety of proxies which relate to patterns in redox sensitive trace element accumulation and isotopic fractionation (e.g. Kendall et al., 2015; Sahoo et al., 2016). Whilst this remains an ongoing and crucial focus of attention, the key to clarifying the relationship between redox and ecosystem habitability in these early animal environments lies in high resolution studies of local redox and investigations of palaeontological and palaeoecological association.

Individual Ediacaran to early Cambrian marine basins have shown substantial regional disparity in patterns and persistence of dominant local-scale redox on million year timescales (Chapter 2; Canfield et al., 2007, 2008; Och et al., 2015; Wood et al., 2015; Sperling et al., 2015b; Bowyer et al., 2017; Guilbaud et al., 2018). Whilst some mid-shelf to lower slope environments appear to indicate an early transition to deposition under persistently oxygenated waters (Canfield et al., 2007; Johnston et al., 2012), other lower slope settings were characterised by continued anoxic and ferruginous water column conditions (Johnston et al., 2013; Sperling et al., 2015b; Miller et al., 2017). Indeed, highly reactive iron enrichments typical of ferruginous water column conditions are also recorded from shallow marine sediments deposited above fair weather wave base in the final 10 million years of the Ediacaran (Wood et al., 2015; Tostevin et al., 2016b). Furthermore, some time-equivalent sections record the repeated development of productivity-induced water column euxinia in lower slope and basin environments which are inferred to have been freely connected to the open ocean (Sahoo et al., 2016; Xiang et al., 2017). It is possible that these differing local redox regimes correspond to the combined effects of relative position from, and spatial extent of oxygen minimum zones (OMZs) which developed as a consequence of local shallow water productivity and vertical distribution in electron acceptor zonation during downward transport and oxidation of organic matter (Chapters 1 and 2; Canfield and Thamdrup, 2009; Guilbaud et al., 2018).

Herein, a multi-proxy approach is used to better constrain the redox evolution of one of the most important terminal Ediacaran palaeoenvironments, the Nama Group of southern Namibia. In addition to application of iron speciation to infill crucial gaps in knowledge of fossiliferous siliciclastic deposits, data are presented of I/(Ca+Mg) from carbonate sediments which add to the basin-wide multi-proxy redox framework. Previous redox studies of the Nama Group have clearly shown the limitation imposed on early calcifying animals by low oxygen waters (Wood et al., 2015; Tostevin et al., 2016b), however the considerable trace and soft-bodied fossil records have been largely neglected in such studies primarily due to preservation within coarse siliciclastic sedimentary deposits unsuitable for geochemical scrutiny. This gap in knowledge is particularly apparent when considering the potentially significant detrimental effects of ferruginous incursion into this shallow ecospace. However, the construction of variable-depth geochemical transects within the well-defined sequence stratigraphic architecture of the Nama Group has enabled delineation of relative oxycline position through time across the basin. This allows for a semi-quantitative assessment of incursion frequency of anoxic waters onto the shallow inner ramp over the last ~10 million years of the Ediacaran. In order to clarify the relationship between stability of the chemical environment and substrate colonisation, iron speciation and major element data are discussed herein and these data are integrated with details of the spatial distribution and palaeodepth of habitation for all organisms represented in the Nama Group fossil record.

As such, the primary aims of this study are to:

1) Compile the first holistic dataset of published palaeontological information for the Nama Group and clarify the spatial distribution and palaeodepth of fossil ecosystems.

2) Infill crucial gaps in the palaeoredox record of the Nama Group and quantitatively assess the degree to which water column redox conditions evolved over the ~10 million year duration of Nama Group sedimentation.

3) Fully integrate palaeontological and geochemical data into the robustly constrained sequence stratigraphic architecture of Nama sediments. This will aid an integrated assessment of the degree to which changes in the chemical environment of the Nama basin influenced, or were influenced by, the evolution and diversification of the large, enigmatic organisms preserved in the fossil record.

3.2 The Nama Group: Geological and Palaeontological overview

Extensive sedimentary deposits of the Nama Group preserve a richly fossiliferous archive of one of the most geologically well constrained terminal Ediacaran to early Cambrian palaeoenvironments. The Nama Group represents a mixed carbonate and siliciclastic succession deposited within a foreland basin on the Kalahari Craton during convergence along two orogenic belts; the Damara to the north and the Gariep to the southwest (Germs, 1983; Germs and Gresse, 1991; Gresse and Germs, 1993). Zircon within silicified air-fall tuff deposits yield air and chemical abrasion ID-TIMS U-Pb ages which constrain deposition of Nama sediments between approximately 547 and 538 Ma (see discussion in Appendix A; Grotzinger et al., 1995; Bowring et al., 2007; Schmitz, 2012; Linnemann et al., 2017; Ramezani et al., 2017). An approximate age for the base of the Nama Group of 550-553 Ma is based on inferred rates of sedimentation (Saylor et al., 1998; discussed further in Section 3.6).

This study concerns the Nama Group in southern Namibia wherein Formations and Members are best correlated with respect to sequence stratigraphy and chemostratigraphy (Germs, 1983; Saylor et al., 1995, 1998; Saylor, 2003). The primary research area outcrops over ~30000 km^2 south of Rehoboth, north of the Orange River and west of Keetmanshoop (Figure 3.1). Sediments were deposited in two subbasins, the Zaris and the Witputs which deepened to the northwest and southwest respectively with distance from a basement forebulge (the Osis Arch) in the vicinity of Farm Osis (Figure 3.1). Though partial separation was imposed by the Osis Arch, numerous studies indicate that subbasin connectivity increased as a consequence of transgression during deposition of the upper Nama Group and gradual infill of the Zaris subbasin (Germs, 1983; Saylor et al., 1995). Ediacaran to early Cambrian deposits of the Nama Group are divided into the Kuibis and Schwarzrand Subgroups, which are further subdivided into Formations and Members based on regional facies and sequence stratigraphic mapping (Germs, 1974, 1983, 1995; Germs and Gresse, 1991; Gresse and Germs, 1993; Saylor et al., 1995; Saylor, 2003). In some cases, detailed mapping of individual Members have enabled parasequence level correlation across distances of up to 100km (Saylor, 2003; Adams et al., 2005; Dibenedetto and Grotzinger, 2005).

Deposition of the Nama Group was not restricted to the map area of Figure 3.1 but extends in part to the north, east and south (Shown as black blobs on inset map of Figure 3.1; Germs, 1974, 1983; Germs and Gresse, 1991; Germs et al., 2009). These areas are not discussed in detail in the present study but are briefly described here for regional context. In the Gobabis – Witvlei area to the northeast of Farm Driedoornvlakte, large northeast – southwest trending anticlines and synclines expose a mixed carbonate and clastic succession comprising the Weissberg, Zenana and Grünental Members which were deposited in the Zaris subbasin and are correlatable to the Kuibis Subgroup (Hegenberger, 1993; Germs

et al., 2009). Sediments of the Grünental Member (equivalent to the Zaris Formation) locally contain *Cloudina* and *Namacalathus* (Germs et al., 2009). To the east and south of Farm Sonntagsbrunn, fluvial to shallow marine sediments of the Kuibis and Schwarzrand Subgroups locally extend into northwestern South Africa and have been mapped as far east as Charliesputs (Appendix D; Germs, 1974, 1983).

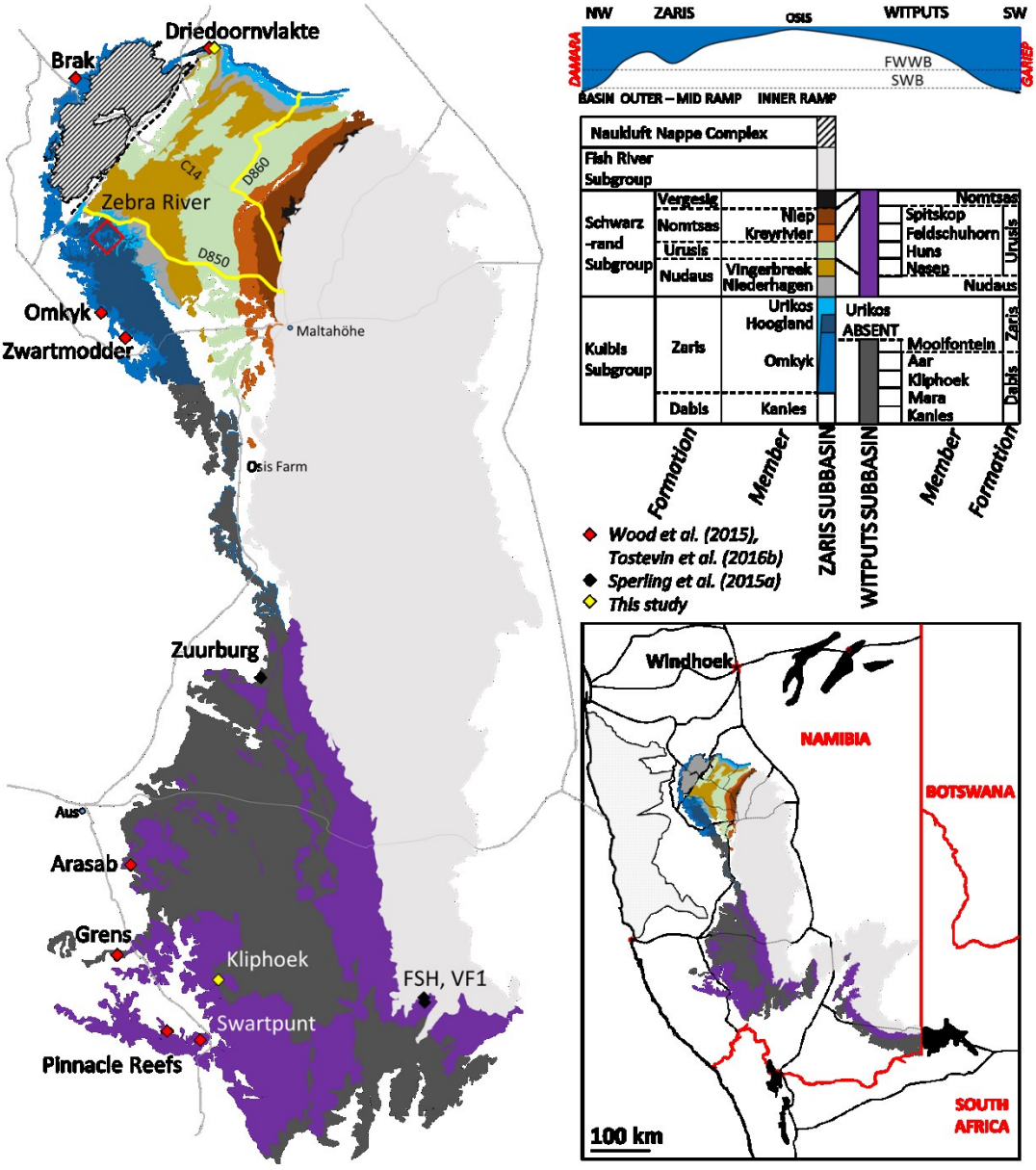

Figure 3.1 Geological map of the Nama Group and stratigraphy with studied localities. Map redrawn using the: 1:1000000, 1963, 1978, and revised 1980 editions, and 1:250000 map of Mariental area (2416), Geological Survey of Namibia, Ministry of Mines and Energy. Inset shows schematic of subbasin architecture.

Eastern deposits largely comprise coarse clastics and contain examples of the soft-bodied organism *Paramedusium africanum* (considered synonymous with *Aspidella*, Gehling et al., 2000) and the enigmatic form *Archaeichnium haughtoni* in units which are likely correlative to the Nasep Member (Gurich, 1933; Glaessner, 1963, 1978; Germs, 1995; Pickford, 1995). Sediments of the Witputs subbasin are further exposed in northwest South Africa and individual formations are stratigraphically correlatable on the Neint Nababeep Plateau as far south as Springbok (Germs, 1983; Germs and Gresse, 1991; Gresse and Scheepers, 1993). Recent discoveries near Springbok of *Cloudina* and *Namacalathus* in the Zaris Formation, alongside trilobozoan soft-bodied impressions in deposits inferred to be correlative to the Vingerbreek Member (Taylor et al., 2017) have spurred further investigation into this part of the Witputs subbasin which has, until now, been relatively understudied. South of Springbok, a second palaeobathymetric high (the Kamieskroon Ridge) separated sedimentation of the Nama Group to the north from contemporaneous deposition of the Vanrhynsdorp Group in the Vanrhynsdorp subbasin to the present southeast (Germs and Gresse, 1991; Gresse and Scheepers, 1993; Germs et al., 2009).

Connection to the open ocean during deposition of the Nama Group is corroborated by strontium isotope values, carbon isotope values which are globally correlatable and record recovery from the Shuram excursion, in addition to carbonates which show normal marine rare earth element profiles (Kaufman et al., 1991, 1993; Saylor et al., 1998; Wood et al., 2015; Tostevin et al., 2016b).

Almost 90 years of palaeontological study in the Nama Group has uncovered a diverse body and trace fossil record with representatives of the Nama Assemblage (Waggoner, 2003) which include *Pteridinium*, *Rangea*, *Ernietta*, *Nasepia*, *Namalia* and *Swartpuntia* (Germs, 1973a, 1995; Narbonne et al., 1997). In addition, sediments host the skeletal invertebrates *Namacalathus* and *Cloudina*, the robustly calcified *Namapoikia*, a rich suite of ichnofossils, microbially induced sedimentary structures, stromatolites, thrombolites and organic walled microfossils, including leiosphaerid acritarchs (Germs, 1972b; Crimes and Germs, 1982; Germs et al., 1986; Jensen et al., 2000; Grotzinger, 2000; Wood et al., 2002; Jensen and Runnegar, 2005; Wilson et al., 2012; Penny et al., 2014, 2017; Zhuravlev et al., 2015; Wood and Penny, 2018).

Previous geochemical studies utilising Fe-S-C systematics and rare earth element profiles have revealed a highly heterogeneous palaeoredox environment for the Kuibis Subgroup and constrain deposition under variably oxic, intermediate manganous and ferruginous waters in inner to outer-ramp facies (reviewed in Chapter 2; Wood et al., 2015; Sperling et al., 2015a; Tostevin et al., 2016b). Repetitive incursion of ferruginous anoxia into inner shelf environments are considered to reflect changes in the position of the chemocline which were, in large part, passively controlled by changing relative sea level. The results of

these studies further suggested a possible progressive trend towards more stable oxygenated conditions typical of mid-outer ramp sediments of the upper Nama Group (Schwarzrand Subgroup), however a more balanced sampling strategy with particular focus on Schwarzrand Subgroup deposits was required to substantiate this hypothesis (Wood et al., 2015; Sperling et al., 2015a; Tostevin et al., 2016b; Bowyer et al., 2017).

3.3 Samples and Methods

In this study, sampling transects were chosen with the aim of infilling major stratigraphic gaps in published geochemical records of the Nama Group. These include downdip deposits at the prominent *Cloudina* pinnacle reef locality of Driedoornvlakte, the Nudaus Formation of the Witputs subbasin exposed on Farm Kliphoek and deposits of the Schwarzrand subgroup of the Zaris subbasin. Associated raw geochemical data are provided in Appendix B. Sample materials for which data are presented in this chapter were collected on field excursions by R. Wood and A. Curtis in 2015 and by F. Bowyer, R. Wood, A. Curtis, A. Penny, S. Curtis-Walcott and S. Iipinge in July 2016.

In order to analyse major shifts in the redox state of the Nama basin as a whole, recognise redox independence between the two subbasins and directly relate the stratigraphic position of fossil occurrences, it is necessary to confidently correlate relative sample position across the subbasin divide. During deposition of the Schwarzrand Subgroup, major depositional sequences have been defined within both the Zaris and Witputs subbasins which indicate increasing subbasin connectivity nearing the Ediacaran-Cambrian boundary unconformity (Germs, 1983; Gresse and Germs, 1993). In contrast, deposition of the underlying Kuibis subgroup shows distinct patterns of preserved systems tracts between the two subbasins (Saylor et al., 1995, 1998). Discrete trends in carbonate carbon isotopes ($\delta^{13}C_{carb}$) across individual sections have previously been used in the Nama Group as a chemostratigraphic tool (Kaufman et al., 1991; Saylor et al., 1998). Based on this framework, published $\delta^{13}C_{carb}$ data (Smith, 1998; Wood et al., 2015) are compiled for each studied section for use in construction of a composite $\delta^{13}C_{carb}$ curve tied to major sequence boundaries in order to aid section correlation of the Kuibis subgroup across the Osis Arch (see Appendix A for discussion relating to construction of $\delta^{13}C$ curve).

All published iron speciation data have been positioned within this relative framework and partitioned into three broad facies groups based on sedimentary depth indicators (Germs, 1983; Saylor et al., 1995; Wood et al., 2015; Sperling et al., 2015a). These data are supplemented by available information on body fossil and ichnofossils occurrence throughout the Nama Group (see Appendix D for

full details).

The Kanies Member represents diachronous deposition upon a transgressive surface which unconformably separates Nama sediments from the underlying crystalline Proterozoic basement (Germs, 1983). Chemostratigraphic correlation of two dimensional sections requires consideration of the inherent variation in $\delta^{13}C_{carb}$ with depth in the water column from which $CaCO_3$ precipitation occurred. Autotrophic C fixation in the photic zone preferentially incorporates the light isotope (^{12}C) during organic matter formation, resulting in elevated $^{13}C/^{12}C$ of shallow waters whereas organic matter remineralisation during downward transport in the water column liberates ^{12}C and may therefore result in decreasing $^{13}C/^{12}C$ with depth until all organic matter has been oxidised (e.g. Broecker and Peng, 1982). Therefore, the most negative $\delta^{13}C_{carb}$ recorded in deposits of the early Nama Group may be expected in sections where the deepest facies are preserved. However, whilst carbonates of the deepest and oldest section in the Zaris subbasin, represented by outer ramp deposits at Brak, do record increasingly negative $\delta^{13}C_{carb}$, shallow inner and mid-ramp carbonates immediately overlying the transgressive surface in the Witputs subbasin at Arasab and Grens also record correspondingly negative values (Wood et al., 2015). Integrated chemostratigraphic and sequence stratigraphic assessment provides a robust toolkit for scrutinizing the relative ages of sampled sections across both Zaris and Witputs subbasins in the lower Nama Group.

Major and trace element concentrations were evaluated through a multi-step digestion procedure after ashing at 550°C for 8 hours. Samples were quantitatively dissolved in trace metal grade HNO_3, HF, and $HClO_4$ heated in open PTFE cups (at sub-boiling temperature) and left to dry fully over a period of 24 hours before addition of H_3BO_3. The addition of H_3BO_3 was employed to prevent formation of Al complexes. Dry residues were then dissolved in concentrated HNO_3, fully dried and re-dissolved in concentrated HNO_3 and diluted with ultrapure 18MΩ water. Resultant solutions were analysed on a Varian Vista-Pro CCD simultaneous ICP-OES at the University of Edinburgh, Grant Institute with replicate analyses yielding a RSD of <5% (reference materials and RSDs in Appendix B).

We applied the calibrated sequential extraction procedure of Poulton and Canfield (2005) in determination of the fractional contribution of iron carbonates (Fe_{carb}), iron (oxyhydr)oxides (Fe_{ox}) and magnetite (Fe_{mag}). An initial leach targeting Fe_{carb} employed Na-acetate buffered to pH4.5 with acetic acid and agitated at 50°C for 48hrs. This was followed by a 2hr Fe_{ox} extraction in Na-dithionite buffered to pH 4.8 and a final extraction of Fe_{mag} with ammonium oxalate for 6 hrs. All steps of the sequential leach were performed at the Cohen Laboratories, Leeds University, School of Earth and Environment and resultant solutions were analysed for Fe using a Thermo Scientific iCE-3000 series flame atomic

absorption spectrometer with replicate extractions for each step yielding RSDs of <5%.

The concentration of pyrite iron (Fe_{py}) was determined by a boiling chromous chloride distillation with a pre-leach of boiling 6M HCl to quantitatively extract acid volatile sulfide (AVS) after the method of Canfield et al. (1986). Weight percent AVS and Fe_{py} were determined gravimetrically after stoichiometric precipitation of Ag_2S (RSD = 2%, replicate values in Appendix B).

Additional chemical extractions have been performed on selected interbedded carbonates with the aim of characterising water column redox conditions through the relative enrichment of iodine (Hardisty et al., 2017). Laboratory experiments targeting iodine uptake in carbonates have clearly shown that oxidised iodate (IO_3^-) is the only form which is not actively excluded from incorporation during growth of the carbonate lattice (Lu et al., 2010). Recent attention has consequently focused upon the potential application for enrichments and depletions in iodine relative to calcium + magnesium in shallow marine limestones and dolostones as a proxy for palaeoredox (Lu et al., 2010, 2016; Hardisty et al., 2014, 2017; Zhou et al., 2017). Despite an oceanic residence time for iodine of ~300 kyrs today, the I/(Ca+Mg) proxy is sensitive to both local dissolved oxygen concentration in addition to the relative proximity of the sedimentary environment to anoxic waters (Hardisty et al., 2014, 2017).

Limestone and dolomite powders were microdrilled from fresh surfaces which showed no visible indication of secondary alteration or veining and all chemical procedures were undertaken at either the University of California Riverside or Woods Hole Oceanographic Institute by Dalton Hardisty. The extraction method utilised for determination of I/(Ca+Mg) followed that outlined in Lu et al. (2010) and involved a single step digestion in 3% HNO_3 with resultant dilutions analysed on a quadrupole ICP-MS alongside duplicate certified control georeference samples and additional selected duplicate and triplicate samples. Standard curves were sufficiently reproducible to resolve very low iodine concentrations (~50 parts per trillion) and replicate samples yielded a RSD of ≤ 15% (Appendix B).

Finally, a number of proxies are classically applied in the assessment of palaeoproductivity which focus on augmentation of elements with biological affinity such as total organic carbon (TOC), phosphorus and barium (Schoepfer et al., 2015). Variability in marine redox conditions are not only a potential consequence of local productivity but also largely control early diagenetic elemental recycling and the extent to which biogenic enrichment is preserved in the rock record. Therefore, it is of prime importance to compile a multi proxy record of redox and palaeoproductivity indicators when interpreting trends in enrichment of elements with biogenic affinity. In order to assess the degree to which redox conditions in the Nama Group were influenced by changes in marine productivity, a

preliminary assessment of changes in total phosphorus and barium concentrations is undertaken in association with iron speciation data and relative sedimentation rates.

Details of replicate analyses and standard values for total digestion, sequential iron extraction steps and I/(Ca+Mg) are provided in Appendix B and, where error bars are absent, data point sizes on all figures incorporate relative standard deviation.

3.4 Section Details

3.4.1 Farm Omkyk: Omkyk Member

The section at Farm Omkyk represents deposition in a deep to shallow inner ramp setting. The lower ~73m of section is composed of thinly bedded lime mudstone interbedded by turbiditic calcisiltite, grainstone and minor shale of the Lower Omkyk Member. The Upper Omkyk Member is characterised by a basal unit of interbedded green shale and sandstone overlain by dark limestone grainstone and minor thrombolites with thin dolomite interbeds. The Lower Omkyk Member at this section represents deposition in a deeper inner ramp environment during a widespread marine transgression, followed by shallower deposition of the Upper Omkyk Member in an inter- to supra-tidal environment. At the base of the Upper Omkyk Member, an ~20cm thick quartzite bed contains specimens of *Palaeopasichnus gracilis* (personal observation) and overlying this unit are found minor thrombolites and abundant *Namacalathus* and *Cloudina hartmannae* in grainstone beds (Wood et al., 2015).

Previously reported iron speciation and cerium anomaly data of the basal ~100 m of the Omkyk Member at Farm Omkyk are illustrated in Figure 3.2 (Wood et al., 2015; Tostevin et al., 2016b). Where $Fe_T > 0.5$ wt %, interbedded dolomite, limestone and minor siliciclastic samples show iron speciation values in agreement with anoxic and ferruginous water column conditions ($Fe_{HR}/Fe_T > 0.38$ and $Fe/Al > 0.66$) with the exception of one limestone sample from the Upper Omkyk Member which supports short-lived oxia ($Fe_{HR}/Fe_T = 0.17$) (Wood et al., 2015). Cerium anomaly data for a suite of carbonate samples support the anoxic iron speciation interpretation, however, where $Fe_T < 0.5$ wt %, samples are commonly characterised by Ce enrichment and positive Ce/Ce* in the Lower Omkyk Member, interpreted to represent carbonate precipitation under intermediate, manganous redox conditions (Tostevin et al., 2016b). Together, these data support dominantly reducing conditions during carbonate deposition of the Lower Omkyk Member that transiently gave way to intervals of water column oxia recorded in the Upper Omkyk Member conducive to habitation by calcified metazoans (Wood et al., 2015; Tostevin et al., 2016b; Penny et al., 2017).

3.4.2 Farm Driedoornvlakte: Omkyk Member

Isolated carbonate platform deposits with capping microbial-metazoan pinnacle reefs grew in a mid-ramp position during deposition of the Omkyk Member and are today exposed on Farm Driedoornvlakte (Figure 3.3; Germs, 1972b; Smith, 1998; Grotzinger, 2000; Adams et al., 2004). *Cloudina* individuals are found throughout the upper Omkyk Member at this locality, however the mutually calcifying, reef-building ecology is restricted to the pinnacle cap of transgressive Unit 3m (Germs, 1972b, 1983; Adams et al., 2004; Penny et al., 2014; Wood and Curtis, 2015). Previously published palaeoredox data from farm Driedoornvlakte have been largely restricted to analyses of carbonate reef material (Wood et al., 2015; Tostevin, 2016b). Here, the combination of low total iron concentrations (<0.5 wt%) accompanied by intermittently negative Ce/Ce* values have been interpreted as evidence for oxic conditions during reef growth (Wood et al., 2015; Tostevin et al., 2016b). The combination of these data and reef construction by *Cloudina* at this locality have supported the hypothesis that locally stable, long-lived oxia may have been a prerequisite for this unique ecological habit.

Carbonate clinoforms of the Omkyk Member interfinger with down-dip fine grained mudstones and shales at the northeast flank of the Driedoornvlakte carbonate platform (pink slope deposits on Figure 3.3a) (Adams et al., 2004). Structural dip of the carbonate platform and overlying stratigraphy varies between 40° and 45° to SSE, resulting in siliciclastic sediments of the overlying Urikos Member and Nudaus Formation to be poorly exposed across the planate topography to the south. For this study, a total of 31 shale samples were taken along a transect from the base of the Upper Omkyk Member Unit 1a, through Units 2 and 3 and, where exposed, from overlying shale of the Urikos Member and Niederhagen Member (lower Nudaus Formation) to the south of the carbonate platform (Figure 3.3). Siliciclastic samples of the Omkyk Member were collected from between clinoform terminations. Shale of the Omkyk and Urikos Members was deposited below wave base and as such, represent the deepest sampled environment during growth of *Cloudina* at Driedoornvlakte (Germs, 1983; Germs et al., 1986; Smith, 1998; Adams et al., 2004; Wood et al., 2015; Tostevin et al., 2016b).

3.4.3 Farm Kliphoek: Nudaus Formation

The Nudaus Formation represents a thick siliciclastic sedimentary succession of sandstone and shale which blankets deposits of the Zaris Formation across both the Zaris and Witputs subbasins. Deposits of the Nudaus Formation have been largely neglected in previous redox studies due to the apparent paucity in recorded fossil occurrence. However, in addition to abundant tubular macrofossils (Germs et al.,

1986; Cohen et al., 2009), this succession is known to host fossils of soft bodied organisms including *Pteridinium* and *Rangea* in the Witputs subbasin (Germs, 1995).

In order to examine this gap in the redox record, 18 shale samples were recovered from an approximately 220m thick exposure of the Nudaus Formation, immediately overlying the undulate and locally erosive palaeotopography of the carbonate Mooifontein Member at Farm Kliphoek (Figure 3.4). As this section represents one of the most westerly exposures of the Nudaus Formation in the Witputs subbasin, prograding shoreline deposits of the highstand systems tract (Niederhagen Member) are absent and siliciclastics are instead representative of the distal, transgressive Vingerbreek Member (Saylor et al., 1995; Grotzinger and Miller, 2008; Cohen et al., 2009).

Olive green to dark red shales of the Vingerbreek Member (upper Nudaus Formation) on Farm Kliphoek are interpreted to represent deposition in an outer shelf environment, with upward – coarsening shoaling sequences, the tops of which represent deposition above fair weather wave base (Saylor et al., 1995; Saylor, 1996; Grotzinger, 2002; Cohen et al., 2009).

3.4.4 Zaris subbasin road transects: Schwarzrand Subgroup

Fossils of soft-bodied forms including *Shaanxilithes* (or, more likely, *Palaeopasichnus delicatus/linearis*, Zhuravlev, A.Y. pers. com.) and *Aspidella* have recently been reported from shallow marine sediments of the lower Schwarzrand Subgroup north of Osis (Darroch et al., 2016). These finds have re-emphasised the importance of largely-neglected Zaris Subbasin deposits for accurate palaeoenvironmental reconstruction of the Upper Nama Group across the Nama basin.

During deposition of the Schwarzrand Subgroup, siliciclastic sediments gradually infilled the Zaris Subbasin and the locus of carbonate sedimentation shifted to occupy a position in the shallow marine environments south of the Osis arch (Gresse and Germs, 1993; Germs, 1983). The Schwarzrand Subgroup north of Osis covers an almost entirely planate areal expanse of approximately 8000km^2, however the combined lack of relief and burial beneath deeply weathered regolith results in a scarcity of vertically exposed sections. Where exposed, sedimentary features are commonly representative of prodeltaic and shoreline shallow marine deposition above storm wave base, frequently interrupted by channelized sandstones. However, some areas continue to record sedimentation in offshore settings of low-intermediate hydrodynamic energy conducive to microbial mat growth (e.g. Noffke et al., 2002). Prior to subbasin infill, relative palaeodepth is thought to have increased with distance north from the Osis Arch and west from the Kalahari Craton and as such, sequential exposure of higher stratigraphic

units towards the southeast also corresponds to a relative shallowing (Germs and Gresse, 1991; Gresse and Germs, 1993).

Shale samples were collected along three road transects north of Osis (D860, C14 and D850, Figures 3.5 – 3.6) which bisect Member boundaries at known distances across a total sampling interval spanning the Urikos Member of the upper Kuibis Subgroup to the Niep Member (Nomtsas Formation) of the Schwarzrand Subgroup. The relative positions of sampling localities were measured by GPS and plotted using Google Earth overlain by the 1:250000 Geological Survey of Namibia (Ministry of Mines and Energy) map of Mariental (2416) and samples were placed into their relative stratigraphic position (Figure 3.5a). This sampling was conducted with the aim of supplementing the preliminary redox study of Bowyer et al. (2017) and as such, the combined dataset is discussed herein.

3.5 Results and Interpretation

3.5.1 Palaeoredox of the Omkyk Member. New insight from I/(Ca+Mg)

Carbonate-bound iodine concentration at Farm Omkyk are between 0.42 – 5.38 μmolmol^{-1} (mean = 1.50 μmolmol^{-1}). Whilst there is little variation between sample values throughout the lower Omkyk Member, there is a clear and abrupt increase in concentration at the sequence boundary separating OS1 from OS2 at approximately 73 m. At this level, I/(Ca+Mg) increases to a maximum of 5.38 μmolmol^{-1} before immediately declining to 2.78 μmolmol^{-1}, whereafter values remain low for the remaining ~30 m with the exception of one bioclastic dolomite sample where I/(Ca+Mg) = 2.97 μmolmol^{-1}.

When examined in isolation, values of I/(Ca+Mg) at Omkyk fall within the range considered characteristic of carbonate sediments deposited in close proximity to an oxygen minimum zone (Lu et al., 2016). However, a number of features exhibited by these proxy data require consideration in combination with pre-existing palaeoredox and major element data.

The sample which yields the highest value of I/(Ca+Mg) (OMK1/1) has previously undergone iron speciation and REE+Y analayses, the results of which indicate highly reactive iron enrichment and a negligible Ce/Ce* anomaly, together supporting deposition under ferruginous conditions (Fe_T = 2.09 wt%, Fe_{HR}/Fe_T = 1, Ce/Ce* = 1.26). This is in apparent contradiction to the assumption that carbonate-bound iodine is a direct consequence of dissolved oxygen availability. One possible reason for iodine enrichment in shallow inner ramp deposits may be related to minor leaching of clays during sample digestion, however, based on the absence of covariation between I/Ca and Al/Ca, the dissolution method employed is not thought to leach clay minerals (Lu et al., 2010). Furthermore, Fe_{HR}/Fe_T = 1

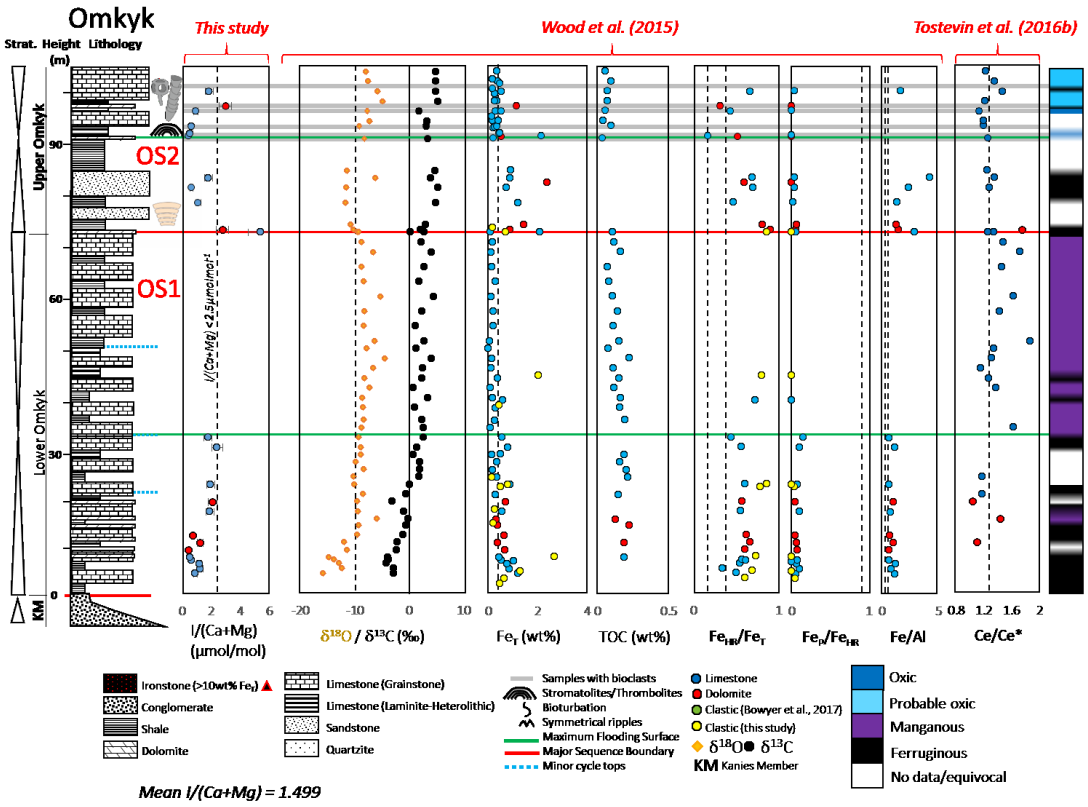

Figure 3.2: Farm Omkyk

Stratigraphic log and accompanying published and unpublished chemical data of the Omkyk Member on Farm Omkyk (Zaris subbasin). Section redrawn after Wood et al. (2015) with additional data from Tostevin et al. (2016). See Appendix D for key to fossil symbols.

in this sample argues against significant silicate-bound iron and thus clay contribution. Additional contamination may result from iodine hosted in organic carbon (Lu et al., 2010), however, where data are available, TOC < 0.5 wt % and no trend is observed in I/TOC.

The presence of iodine in all samples indicates the presence of IO_3^- in the water column and by extension, oxygen. It is known that quantitative iodate reduction precedes iron reduction (Rue et al., 1997) and consequently, I/(Ca+Mg) should be negligible in a sample which yields values typical of anoxia from iron speciation. However, elevated I/(Ca+Mg) and elevated Fe_{HR}/Fe_T (and Fe/Al) may instead allude to a depositional environment above which the water column was oxic but which was transiently impinged upon by anoxic bottom waters. A stratigraphic position immediately above a sequence boundary within the lower transgressive systems tract for the above mentioned sample is indicative of a period of relative sea level rise during which time the sedimentary environment may still have been relatively shallow. In this scenario, the mass balance for Fe/Al during anoxic incursions is significantly tilted in favour of an anoxic interpretation and during this time carbonate-bound iodine would in turn

be significantly diluted. This interpretation is also consistent with the range of values observed for I/(Ca+Mg), which are characteristic of an oxic water column environment in close proximity to anoxic waters (e.g. within or immediately adjacent to an OMZ) (Glock et al., 2014; Lu et al., 2016).

3.5.2 Slope sediments at Driedoornvlakte

Compiled major element and iron speciation data for the Driedoornvlakte bioherm are presented as yellow markers in Figure 3.3 and absolute values are provided in Appendix B. During growth of the carbonate platform, Fe_T of down-dip shales is relatively invariant, from 4.15 to 5.70 wt%. The stratigraphically lowest sample shows an anomalously elevated Fe_{HR}/Fe_T value of 0.47 but following samples are characterised by Fe_{HR}/Fe_T and Fe/Al values from 0.06 to 0.33 and 0.45 to 0.64 respectively. The relative proportion of the highly reactive iron pool contributed by pyrite is negligible throughout, with a maximum Fe_{py}/Fe_{HR} of 0.03. Shales of the overlying Urikos and Niederhagen Members are characterised by Fe_T in the range 1.77 to 6.63 wt%, Fe_{HR}/Fe_T between 0.06 and 0.42 and Fe/Al from 0.49 to 0.71. These overlying sediments are similarly pyrite-deficient, with a maximum Fe_{py}/Fe_{HR} of 0.01. Sample colour varies from grey to green – brown and shows no clear correlation with interpreted redox.

Chromium concentrations range from depleted to slightly enriched relative to Phanerozoic marine shale (Cr = 90 ppm and Cr/Ti = 0.020; Turekian and Wedepohl, 1961) with values between 35 and 111 ppm (mean = 83.55 ppm, Cr/Ti = 0.023 – 0.037).

There is a notable increase in Mn/Ti (and Mn/Al) upsection from OS2 Units 1b-3i (0.004 – 0.025) to Unit 3m (0.14) with no significant Al or Ti depletion which may otherwise imply redox-independent augmentation of relative Mn enrichment.

Iron speciation data of all siliciclastic samples equivalent to OS2 Units 1b – 3m firmly corroborate previous interpretations of locally stable oxia at Driedoornvlakte (Wood et al., 2015; Tostevin et al., 2016b; Bowyer et al., 2017). In this interval, 12 samples record oxic iron speciation values and two samples fall in the equivocal range of Fe_{HR}/Fe_T = 0.22 – 0.38 (Poulton and Canfield, 2011). Additionally, all samples show values of Fe/Al in the normal range for oxic Phanerozoic shale of between 0.42 – 0.64 (Lyons and Severmann, 2006; Raiswell et al., 2008).

The water column remained dominantly oxic during deposition of Urikos sediment following drowning of the Driedoornvlakte carbonate platform, however some evidence exists for intermittent

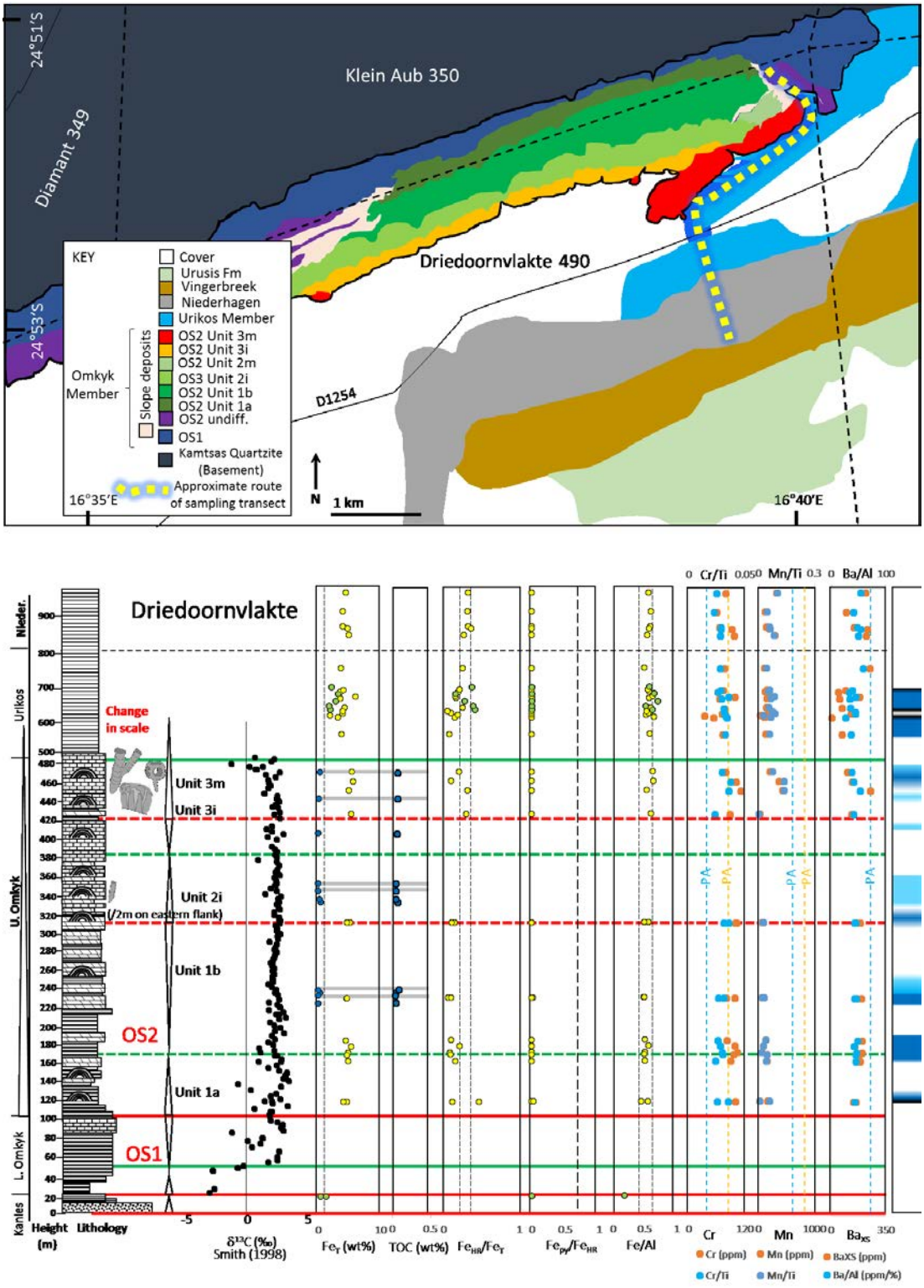

Figure 3.3: Farm Driedoornvlakte

a) Geological map of Driedoornvlakte reef and overlying siliciclastic deposits. Map redrawn after Adams et al. (2004) and 1:250000 map of Rehoboth area (2316), Geological Survey of Namibia, Ministry of Mines and Energy, **b)** (Lower) Stratigraphic log and geochemical data of composite section on Farm Driedoornvlakte (blue and green markers correspond to published

deposition under fleeting ferruginous water column conditions in the middle Urikos Member. Two samples in this interval record moderate iron enrichment ($Fe_{HR}/Fe_T = 0.38 – 0.41$) and one sample is typified by muted highly reactive iron enrichment ($Fe_{HR}/Fe_T = 0.28$) but an elevated Fe/Al value of 0.71. Regional sequence stratigraphic studies of the upper Omkyk Member confidently place deposits of the Urikos Member overlying Unit 3m at Driedoornvlakte in an equivalent downdip position to upper Unit 3 – Urikos Member deposits in more proximal, shallower environments such as Zebra River (Adams et al., 2004, 2005). This supports correlation of the anoxic episode overlying OS2 Unit 3m at Driedoornvlakte with anoxia at the maximum flooding surface of OS2 or the Hoogland Member at Zebra River (Wood et al., 2015; Bowyer et al., 2017). These samples may thus record deposition at or near the major maximum flooding surface and proximity to ferruginous deep waters which persisted in the deeper outer ramp environment, however this remains difficult to confirm due to the lack of preserved outer ramp deposits of the upper Omkyk Member (Bowyer et al., 2017).

Minor chromium enrichments do not correspond with ferruginous anoxic values and may instead reflect detrital variability or additional Cr contributed in organic matter, however Cr/Ti is not seen to correlate with biogenic Ba or P/Ti, and in the absence of available TOC data, this hypothesis is difficult to verify.

Two samples deposited subjacent to the carbonate reef of Unit 3m record the most elevated Mn/Ti in the entire profile (Mn/Ti = 0.14) and yield Fe speciation data consistent with oxic or equivocal redox conditions. Average Mn/Ti of Phanerozoic marine shale is 0.185 (Turekian and Wedepohl, 1961) and as such, these values are relatively depleted, however the clear up-section increase in Mn concentration may be significant at Driedoornvlakte. Whilst iron speciation and Fe/Al are sensitive proxies to E_H typical of iron reduction, oxygen levels above this boundary remain conducive to Mn oxide reduction until this boundary E_H is exceeded. As such, relatively elevated Mn in samples of Unit 3m which record low Fe_{HR}/Fe_T may be indicative of the precipitation of insoluble manganese oxides in fully oxygenated shallow waters. This is supported by relatively elevated values of Mn/Fe (0.006 – 0.009) compared to underlying and overlying deposits at Driedoornvlakte.

Early marine cements which precipitated directly within reef cavities of Unit 3m have been tentatively suggested to indicate a relatively rapid incursion of ferruginous conditions into the open

---

Figure 3.3 continued: data in Wood et al. (2015) and Bowyer et al. (2017) respectively). Change in scale occurs at ~490 m. Section redrawn after Adams et al. (2004) and Wood et al. (2015). See Figure 3.2 for full key (fossil symbols in Appendix D). PA = Phanerozoic average.

Cloudina framework prior to disconnect from the water column by burial beneath sediment (detailed further in Chapter 4 and Wood et al., 2018). The apparent conflicting proxy records from oxic sediment deposition from iron speciation and anoxic precipitation of early marine cements may either reflect the higher precipitation rate of marine cements primed to capture high frequency changes in redox or simply that siliciclastic samples recording this short-lived ferruginous interval were missed as a consequence of poor exposure. It is notable that the redox chemistry of those shales sampled from immediately subjacent to the reef build-up of Unit 3m point to deposition at E_H conditions adequate to fully oxidise ferrous iron and possibly manganese. However, at the maximum flooding surface, the reef may have been subjected to ferruginous conditions which typified deeper waters and possibly resulted in the precipitation of iron-rich, pore-lining isopachous dolomite cement (discussed in Chapter 4).

3.5.3 The Nudaus Formation at Farm Kliphoek

Total iron concentrations of the Kliphoek section range from 4.94 – 29.77 wt% and of these samples, only those with $Fe_T < 10$ wt% have been subjected to the iron speciation procedure. Samples with $Fe_T > 10$ wt% are invariably characterised by elevated Fe/Al of up to 4.59 and these samples are herein categorised as ironstones. Extreme iron enrichments of up to 41.57 wt% have previously been reported from shallow water deposits of the lower Aar Member (Wood et al., 2015). Ironstones at Farm Kliphoek are interbedded with shale ($Fe_T < 10$ wt%) exhibiting values of Fe_{HR}/Fe_T in the range 0.10 – 0.67. Where $Fe_{HR}/Fe_T > 0.38$, then $Fe/Al > 0.64$ and, as in all other analysed samples from the Nama Group, the contribution of pyrite is minimal ($Fe_{py}/Fe_{HR} < 0.05$). Two samples with robustly oxic iron speciation signatures in the lower half of the succession also record minor enrichments in Fe/Al which may support partial Fe_{HR} depletion via transformation to Fe_{PR} during diagenesis (Poulton and Raiswell, 2002; Cumming et al., 2013).

In most samples, Cr concentration values are near world average Phanerozoic marine shale composition (Turekian and Wedepohl, 1961), with minor enrichments of up to 107 ppm. However, one sample near the top of the section records Cr depletion of 38 ppm. In ironstones, there is a weak positive correlation between Cr and Fe concentration which may point to Cr^{4+} reduction and adsorption onto iron oxides which constitute the bulk iron phase in these sediments (see below).

Redox interpretation from iron speciation on Farm Kliphoek samples show some correlation with sample colour such that samples with $Fe_{HR}/Fe_T > 0.38$ (anoxic) are pale to dark red whilst those with $Fe_{HR}/Fe_T < 0.22$ (oxic) are invariably olive green. Colouration is dependent on the fractional contribution of iron oxide, with $Fe_{ox}/Fe_T = 0.44 – 0.62$ for anoxic samples and 0.03 – 0.13 for oxic

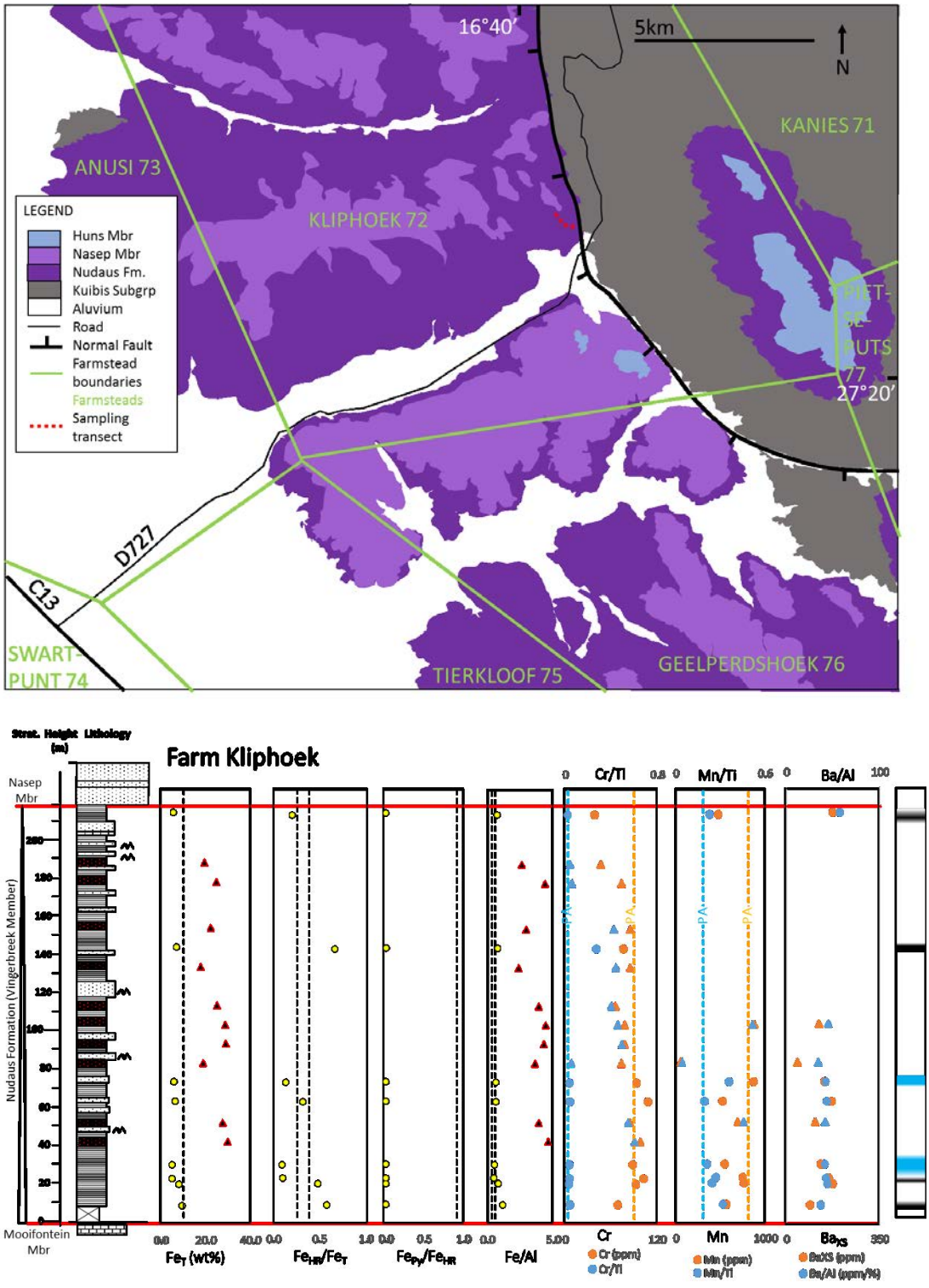

Figure 3.4: Farm Kliphoek

a) (Upper) Geological map of Nudaus Formation deposits at Farm Kliphoek showing position of sampling transect. Map drawn using a combination of Figure 5 of Saylor et al. (1998) and GoogleEarth, **b)** (Lower) Stratigraphic log and accompanying chemical data of the Vingerbreek Member, Farm Kliphoek. PA = Phanerozoic average.

(green) samples which contain a larger proportion of Fe_{HR} in the form of iron carbonates and magnetite. The darkest red-brown shales correspond to ironstones with (where measured) total dithionite-reducible iron oxide concentrations in the range 15.77 – 22.44 wt%.

Iron speciation and major element concentrations at Farm Kliphoek are consistent with deposition under dominantly ferruginous conditions. However, samples with extreme iron enrichment alongside those showing low Fe_{HR}/Fe_T provide additional information on variability of the local chemical environment.

Accumulation of sediments with elevated iron concentrations in the observed range either requires a mechanism by which ferrous iron is rapidly and quantitatively removed from the anoxic water column at a rate greater than background deposition, or early diagenetic recycling and build-up of iron oxides on the shallow shelf. The former mechanism may point to hyperpycnal penetration of the chemocline by dense, oxygenated riverine water, intermittently resulting in acute sedimentary iron enrichment as a product of instantaneous water column Fe^{2+} oxidation. If this is the case, variable iron enrichment throughout the section may either reflect parasequence-scale shoaling of the sedimentary environment or channel avulsion and associated changes in proximity to the source of oxidation. A similar mechanism has been proposed for the genesis of Sturtian ironstones (Lechte and Wallace, 2015).

A second, and perhaps more probable scenario may simply relate to extensive and complex shallow marine sedimentary reworking via pore water sulfide oxidation coupled to iron reduction and re-oxidation, similar to physical irrigation processes operating on rapidly deposited inner shelf muds of the Amazon delta today (Aller et al., 1986). Solid phase iron was likely supplied from both riverine input and intermittent shoaling of ferruginous deep waters into the oxic surface layer, however the aforementioned processes likely resulted in secondary augmentation of sedimentary iron concentrations and consequently extreme iron enrichments and iron speciation data of these samples are not considered informative of prevailing water column redox. This process can also be applied to samples of extreme iron concentration reported from the underlying lower Aar Member of the Nama Group at Farm Arasab (Wood et al., 2015, supplementary data).

3.5.4 The Schwarzrand Subgroup, Zaris Subbasin

Diachronous deposition of Urikos Member sediments incrementally swamped shallow carbonate production of the Omkyk and overlying Hoogland Members during long-lived transgression of the upper Zaris Formation in the Zaris subbasin (Dibenedetto and Grotzinger, 2005). The Urikos Member

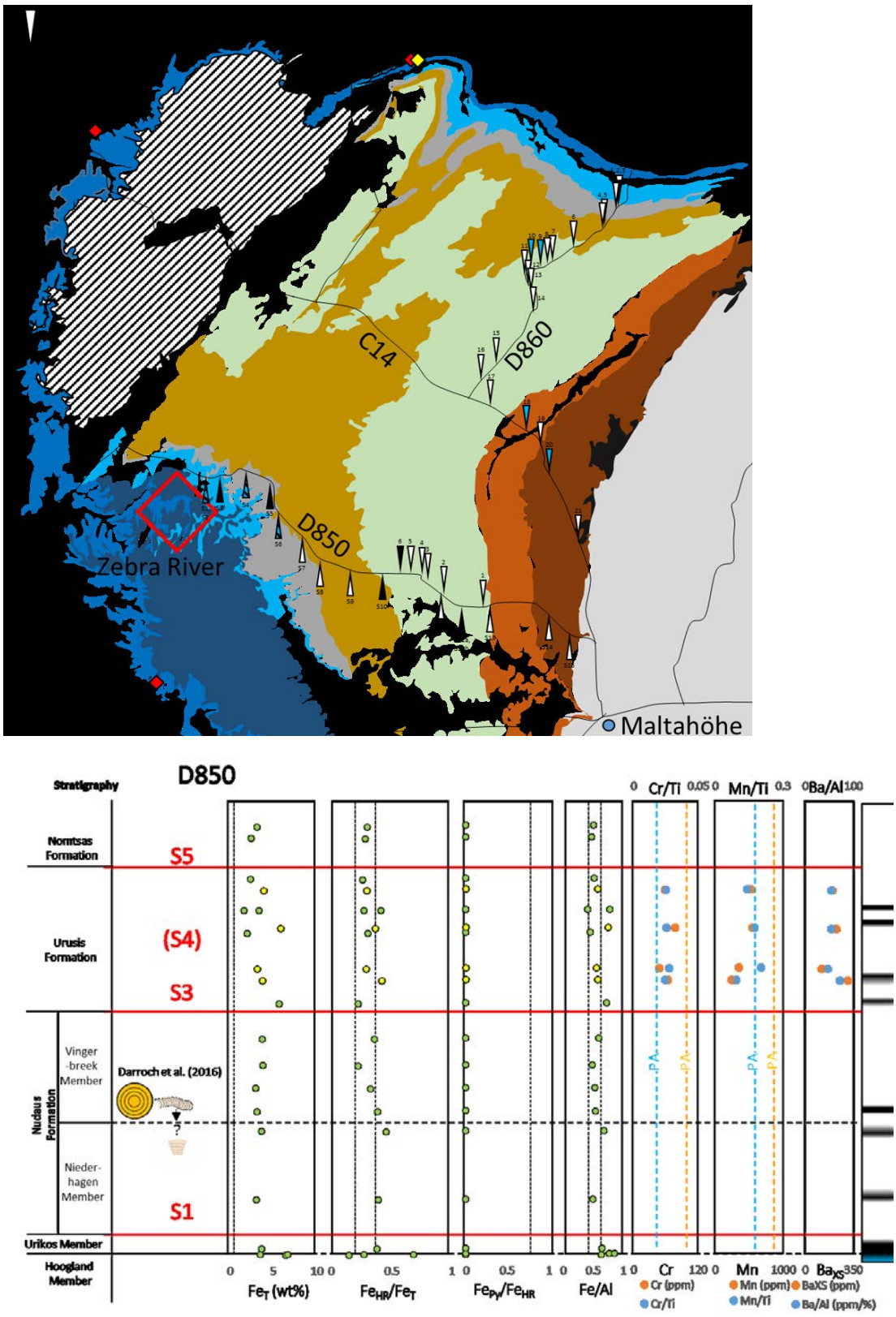

Figure 3.5 The Schwarzrand Subgroup north of Osis

represent the structurally lowest unit and deepest palaeoenvironment sampled along these road transects. Total iron concentrations range from 3.56 to 6.68 wt% (mean = 5.11 wt%), Fe_{HR}/Fe_T values are in the range 0.15 to 0.69 (mean = 0.37) and Fe/Al is between 0.64 to 0.86 (mean = 0.73). Only where $Fe_{HR}/Fe_T > 0.27$ is iron enrichment corroborated by Fe/Al > 0.64.

The overlying Niederhagen and Vingerbreek Members (Nudaus Formation) have total iron concentrations in the range 2.58 to 4.42 wt% and Fe_{HR}/Fe_T between 0.22 and 0.45. However, of the four samples where $Fe_{HR}/Fe_T > 0.38$, only one shows significantly elevated Fe/Al > 0.64. Where proxies appear to disagree in this way, Fe_{HR}/Fe_T does not exceed 0.39. One possible reason for muted Fe enrichment from Fe/Al coupled with elevated Fe_{HR}/Fe_T in samples of the Niederhagen Member is a weathered detrital source material of unusually iron-depleted composition (e.g. Clarkson et al., 2016). However, detailed petrographic study of Niederhagen Member deposits suggest a dominantly metapelitic siliciclastic provenance, with minor input from a relic volcanic island arc to the present northwest, evident from chemical characteristics of detrital chromian spinels (Germs, 1983; Blanco et al., 2009, 2011).

Shales of the Urusis Formation have Fe_T between 1.64 and 5.87 wt% and Fe_{HR}/Fe_T from 0.14 to 0.42. Five samples with Fe_{HR}/Fe_T in the range 0.22 – 0.38 are accompanied by elevated Fe/Al (0.67 – 0.78) which may suggest late stage conversion of highly reactive to poorly reactive sheet silicate-bound iron.

Finally, distal fluvial to shallow marine sediments of the Nomtsas Formation (Kreyrivier and Niep Members) have Fe_T between 2.50 and 5.23 wt%, and Fe_{HR}/Fe_T and Fe/Al in the range 0.21 – 0.30 and 0.47 – 0.62 respectively. In the Nomtsas Formation, 'normal oxic' Fe/Al data corroborate low Fe_{HR}/Fe_T (< 0.22) in two samples and imply negligible water column iron enrichment for the remaining three. Sampled sediments throughout the Schwarzrand Subgroup vary in colour between grey, dark

---

Figure 3.5: a) Geological map of the Schwarzrand Subgroup north of Osis showing relative positions of individual sampling localities. GPS coordinates for sampled points are given in Appendix B. Map redrawn using a combination of GoogleEarth and geological maps (1:1000000, 1963, 1978, and revised 1980 editions, and map of Mariental area, 2416, Geological Survey of Namibia, Ministry of Mines and Energy), **b)** Compiled section for samples collected along the D850 road transect. Data from samples in green are published in Bowyer et al. (2017) and those in yellow constitute as yet unpublished data. See Appendix D for key to fossil symbols. PA = Phanerozoic average.

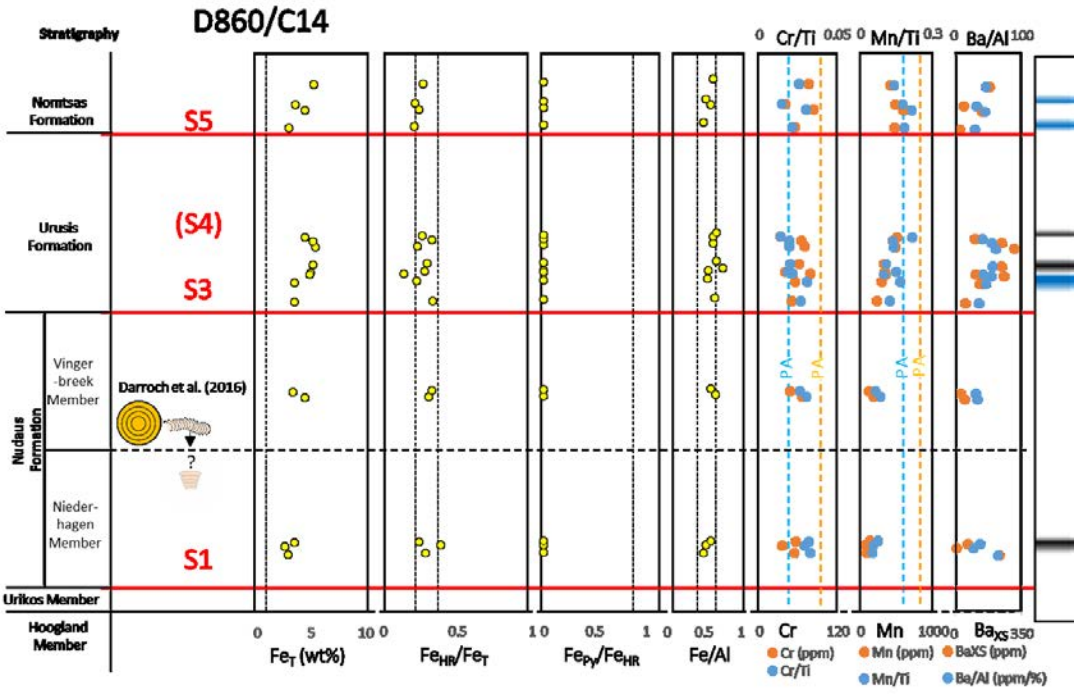

Figure 3.6: D860/C14

Composite section for samples taken along the D860/C14 road transect. See Appendix D for key to fossil symbols. PA = Phanerozoic average.

green and pale red and colour shows no clear correlation with observed patterns in iron enrichment or dominant iron species.

Water column iron enrichment implied by $Fe_{HR}/Fe_T > 0.38$ is not accompanied by significant Cr enrichment.All samples are relatively depleted in total Cr concentration with respect to typical Phanerozoic marine shale concentrations and fall in the range 35 to 83 ppm. However, Cr/Ti (0.015 – 0.032) shows occasional enrichment above the Phanerozoic average (Turekian and Wedepohl, 1961).

An additional feature concerns the stratigraphic trend in relative Mn concentration in samples of the Schwarzrand Subgroup. Values of Mn/Ti and Mn/Al are almost all below average shale values (Turekian and Wedepohl, 1961), however there is a notable shift in Mn concentrations (reflected also in Mn/Ti and Mn/Al) up-section (Figure 3.7). Initially, manganese is extremely depleted, with a minimum concentration of 62 ppm (Mn/Ti = 0.052) in the Niederhagen Member and concentrations progressively increase to a maximum of 590 ppm (Mn/Ti = 0.21) in the lower Nomtsas Formation, before decreasing slightly to a final value of 418ppm in the upper Nomtsas Formation. There is a positive correlation between Mn/Ti ($r^2 = 0.544$), P/Ti ($r^2 = 0.564$) and Fe/Ti ($r^2 = 0.648$) in samples of the Schwarzrand

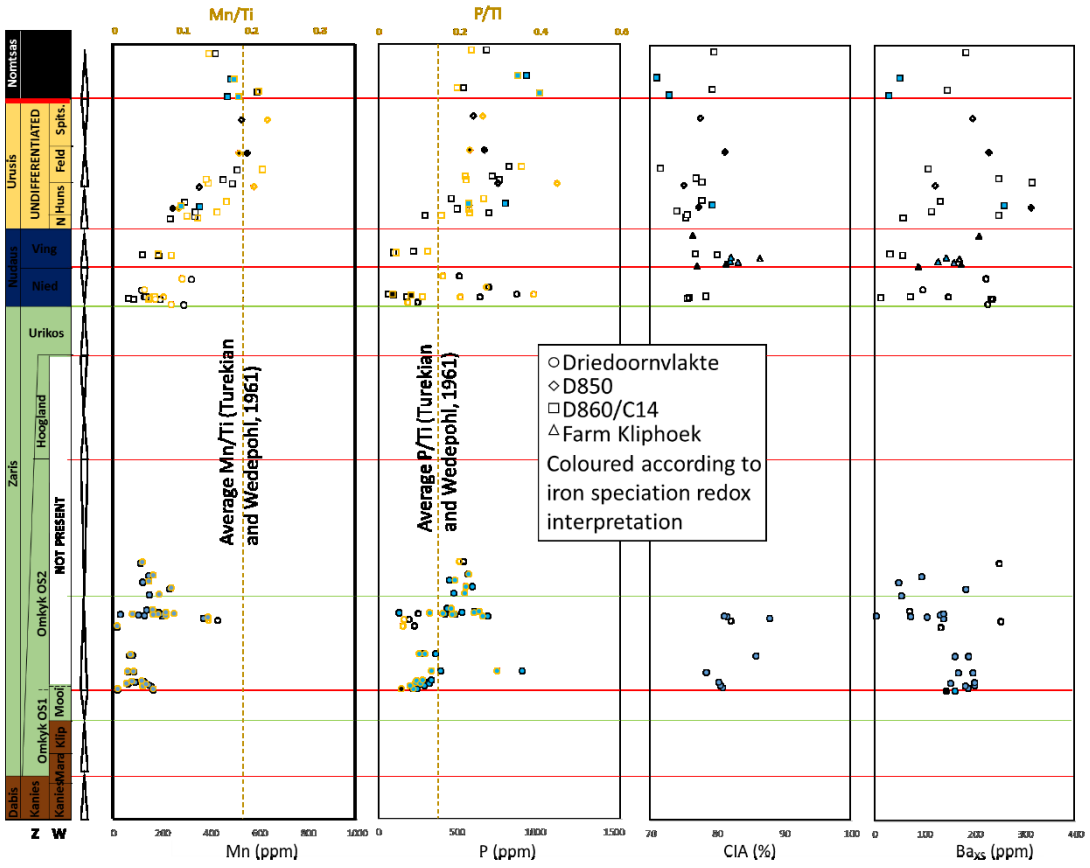

Figure 3.7

Compiled data of Mn, Mn/Ti, P, P/Ti, CIA and BaXS for samples collected in July 2016. Symbols correspond to sampling localities and are coloured according to redox interpretation based on iron speciation and Fe/Al. Blue: oxic, Black: Ferruginous, White: equivocal. Note, composite stratigraphic log is not to scale.

Subgroup, each of which reflect the dominantly detrital source component for these elements. However the positive up-section trends in Mn/Ti and P/Ti (Figure 3.7) and negligible covariation with Ti/Al support a mechanism for relative sedimentary Mn and P enrichments (/retention) which are disconnected from detrital input and bulk contribution from clay minerals. Additionally, there is a pronounced increase in Mn/Fe upsection through the Schwarzrand Subgroup with no associated trend in Fe concentration or Fe/Al (Appendix B, Figure AB4).

Samples of the Schwarzrand Subgroup in the Zaris subbasin display relatively invariant iron speciation signatures which are largely confined between the calibrated threshold ratios of $0.22 < Fe_{HR}/Fe_T < 0.38$. In the upper Schwarzrand subgroup, the freely-connected Witputs subbasin to the

south shows unequivocally stable oxic water column conditions (Wood et al., 2015). At this time, shale interbeds of the Zaris subbasin represent deposition in a mildly productive inner ramp environment with abundant siliciclastic biolaminites, organic walled microfossils, *Vendotaenia* and burgeoning evidence for primitive burrowing organisms (Crimes and Germs, 1982; Germs et al., 1986; Bouougri and Porada, 2007; Darroch et al., 2016). Under lower Ediacaran atmospheric and marine oxygen concentrations, organic matter remineralisation in shallow, stagnant and moderately productive inner ramp environments likely resulted in occasional anoxia, promoting ferric (oxyhydr)oxide reduction from pore waters and allowing short-term build-up of ferrous iron in the water column. This is most obvious in the case of 5 samples of the Nudaus and Urusis Formations which show $Fe_{HR}/Fe_T > 0.38$. However, the observed positive trend in Mn/Ti towards an apex in Schwarzrand Subgroup, with values in the range typical for Phanerozoic oxic shale (0.185, Turekian and Wedepohl, 1961), supports a gradual increase in reduction potential (or decrease in frequency of anoxic incursions) to a level conducive to sedimentary Mn oxide retention.

An alternative interpretation of the combined data would be to view the majority of samples in the Schwarzrand Subgroup north of Osis which fall in the equivocal range of Fe_{HR}/Fe_T, and the normal marine range for Fe/Al, as predominantly reflecting dilution of an anoxic signal by rapid deposition (Lyons and Severmann, 2006; Raiswell et al., 2018). The inherent difficulty in disentangling these processes is particularly apparent during infill of the Zaris subbasin in the lower Nomtsas Formation. However, the noted positive shift in Mn/Fe towards the top of the Schwarzrand Subgroup likely attests to trapping of manganese oxides in the oxic portion of the water column which became more efficient up-section as a consequence progressive shallowing of the depositional environment.

3.6 Sedimentation rate, primary elemental retention and an updated age estimate for the base of the Nama Group

Higher rates of sedimentation lead to enhanced preservation of elements including total organic carbon, phosphorus and barite, whereas low sedimentation rates increase the exposure time of these elements to prevailing water column redox conditions. Enhanced exposure to oxygenated conditions results in effective remineralisation of organic carbon and a reduction in the resulting organic carbon content of sediment. In contrast, both P and Ba are more effectively preserved in oxic pore waters (Canfield, 1994; Schoepfer et al., 2015). Consequently, rapid burial effectively masks the deleterious effect of differential preservation caused by prevailing water column redox. Sediment accumulation rate is therefore a major factor to account for in the interpretation of palaeoproductivity.

Studies investigating palaeoredox and productivity commonly benefit from Phanerozoic sample sets where microfossil biozonation or high resolution oxygen isotope records are able to inform reasonably high resolution estimates of sedimentation rate (e.g. Shen et al., 2015; Schoepfer et al., 2015). Though targeted efforts are continuously improving geochronological resolution, the Ediacaran Period suffers from a dearth of biozonal (and other) chronological tie-points. Despite this shortfall, the bulk accumulation rate (BAR) in the Nama Group can be roughly approximated, based on the estimated maximum thickness of sedimentary deposits and the time intervals represented by intervening ash bed ages in the lower Hoogland Member and lower and upper Spitskop Member. Previous accumulation rate estimates for the Nama Group have also aimed to approximate the basal age of the Nama Group through correlation of carbon isotope records in distal, time-equivalent sections where radiometric ages are present such as Oman and Western Canada (Saylor et al., 1998). Based on updated U-Pb ages for the Nama Group and approximate siliciclastic thicknesses as represented in Saylor et al. (1998), the minimum bulk accumulation rate for sediments of the upper Nama Group is calculated as follows:

$$BAR = 1400 / (548.01 - 538.45) = \underline{146.44\ m/Myrs}$$

The age of 548.01 Ma is a maximum age for the lower Hoogland ash (94-N-10B, Grotzinger et al., 1995; Bowring et al., 2007, recalculated in Schmitz, 2012), 538.45 Ma is the proposed minimum age of the upper Spitskop ash (Linnemann et al., 2017) and 1400 is the approximate stratigraphic thickness between the lower Hoogland and upper Spitskop ash beds (Saylor et al., 1998). This accumulation rate value is a almost a third of that approximated by Saylor et al. (1998) largely as a consequence of the considerably younger age now realised for the upper Spitskop ash and the consequently longer duration for accumulation of the total sediment package. A maximum bulk accumulation rate can similarly be estimated based upon the minimum age of the Hoogland ash (546.71 Ma) and the maximum age of the upper Spitskop ash (538.89 Ma), yielding a BAR of 179.03m/Myrs. Extrapolating these sedimentation rate estimates to the maximum thickness between the lower Hoogland Member and the basal Proterozoic unconformity (~550m, Saylor et al., 1998) allows an updated approximation of the age of the base of the Nama Group from 551.77 Ma to 549.78 Ma. This is similar to the estimate of Saylor et al. (1998) and conforms to the most robust radiometric age constraint currently available for carbon isotopic recovery from the Shuram-Wonoka excursion in South China (Condon et al., 2005). However, these accumulation rate estimates are based upon $^{206}Pb/^{238}U$ dates only and do not take into account the larger possible age ranges provided by $^{207}Pb/^{206}Pb$ dates of the same zircon samples. Extrapolating changes in accumulation rate between some intervening ash beds of the Nama Group would need to account for a number of uncertainties associated with different laboratory methodologies employed in dating (for example) the lower Spitskop (91-N-1, Grotzinger et al., 1995) and lower Hooogland (94-N-10B,

Bowring et al., 2007) ash beds (discussed further in Appendix A). Finally, the base of the Brak section (Wood et al., 2015) likely records the oldest carbon isotopic values during initial transgression onto Proterozoic basement of the Kalahari craton and may capture the local nadir of the Shuram excursion.

Crucially however, sedimentation rates undoubtedly varied widely with proximity to effluent sources. This is especially significant in the case of the Schwarzrand Subgroup north of Osis during gradual infilling of the Zaris subbasin and also at periodic intervals when relative accommodation space was reduced, such as late highstand systems tracts.

3.7 A preliminary assessment of palaeoproductivity

3.7.1 Phosphorus

It is widely accepted that phosphorus is the main limiting nutrient for marine primary productivity on geological timescales (Tyrrell, 1999) and resultant organic matter is the dominant source of P to marine sediments (Schoepfer et al., 2015). The concentration of phosphorus in marine sediments is dependent upon a complex interplay between P and local depositional redox conditions. Sedimentary retention of P is enhanced in sediments bathed under oxic waters, whilst remineralisation and re-release to the water column is promoted under anoxic pore water conditions through dissolution of iron oxides onto which P is commonly adsorbed (Ingall and Jahnke, 1994; Schoepfer et al., 2015; Reinhard et al., 2017; Poulton, 2017). However, ferruginous water column conditions may also promote P scavenging and sedimentary enrichment through crystallisation of vivianite (a hydrated iron phosphate) and mixed valence (FeII/FeIII) iron minerals (e.g. carbonated green rust and magnetite) (Zegeye et al., 2012; Derry, 2015; Reinhard et al., 2017).

Figure 3.8 shows the ratio of phosphorus to the detrital baseline represented by concentrations of aluminium and titanium. The ratios of P/Al, P/Ti, are highly variable in sediments of the Nama Group and P shows no significant correlation with these refractory detrital elements. It has been shown that post-depositional complexation of organic P with iron and manganese (oxyhydr)oxides is a dominant pathway for P retention under oxic conditions. Whilst there is no significant correlation between P/Fe_{ox} in any sampled section, there are very weak positive correlations between P and Fe_T and also between P and Fe_{mag} in samples of the Schwarzrand Subgroup ($r^2 = 0.185$ and 0.1544 respectively). The slight positive correlation observed between P and Fe_{mag} may relate to a small proportion of P originally bound in the lattice of green rust which diagenetically alters to magnetite over geological timescales (Sumoondur et al., 2008; Zegeye et al., 2012). In contrast, there is a strong positive correlation between P and Mn

concentrations ($r^2 = 0.7351$) in addition to P/Ti and Mn/Ti ($r^2 = 0.6436$) in samples of the Schwarzrand subgroup north of Osis which may point to a combination of elevated sedimentation rate at this time and P adsorption onto Mn oxides under oxic-nitrogenous water column conditions both of which would favour sedimentary P retention.

Whilst productive conditions may be expected to result in build-up of sedimentary P, water column or pore water anoxia is likely to mute enrichment through effective dissolution of Fe or Mn

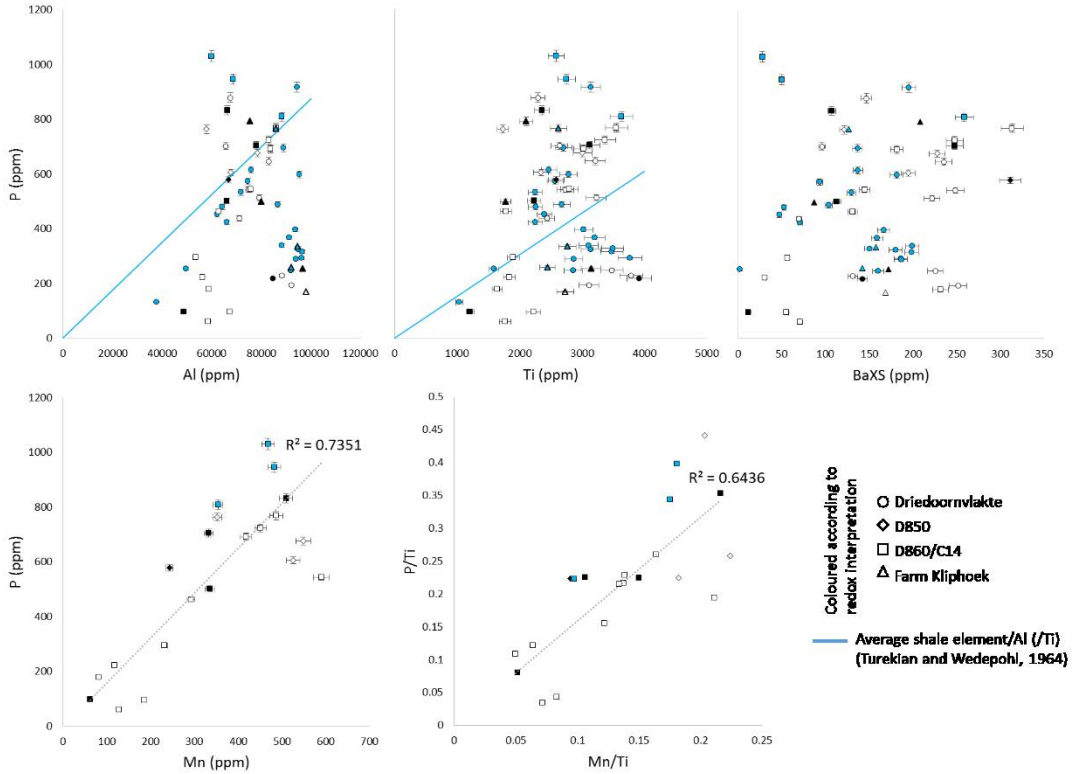

Figure 3.8

Elemental crossplots showing the absence of correlation between P concentration and detrital background (Al and Ti), inferred productivity (Ba_{XS}), but a positive correlation between Mn and P concentrations in addition to P/Ti and Mn/Ti.

oxides and release of adsorbed P. Therefore, samples which yield anoxic iron speciation signatures may be more likely to have correspondingly lower P/Ti, however no correlation is observed between P/Ti and Fe_{HR}/Fe_T (Appendix B, Figure AB8). Indeed some low P/Ti values correspond to Urikos Member sediments at Driedoornvlakte where Fe_{HR}/Fe_T is consistently < 0.22. The complex signal of P preservation in the Nama Group is most likely a combination of variable water column redox conditions and changing sedimentation rate with enhanced burial rate in the Schwarzrand subgroup north of Osis allowing more effective preservation of Mn oxide-bound P.

3.7.2 Excess Barium

The application of excess Ba (Ba_{XS}) as a palaeoproductivity indicator is based on the assumption that Ba enrichments above detrital baseline values are principally indicative of biogenic Ba loading as a consequence of barite precipitation during organic matter degradation in the water column (Dymond et al., 1992; Ganeshram et al., 2003; Tribovillard et al., 2006; Shen et al., 2012, 2015; Zhou et al., 2015; Liu, K. et al., 2017). This biogenic Ba component is commonly derived as:

$$Ba_{XS} = Ba_{sam} - Al_{sam} \times (Ba/Al)_{det}$$

where Ba_{sam} and Al_{sam} are the sample concentrations of Ba (ppm) and Al (wt%) respectively (Dymond et al., 1992). It has been shown that local terrigenous baseline ratios of Ba/Al vary considerably between sedimentary basins, thereby necessitating the determination of local detrital $(Ba/Al)_{det}$ as opposed to average crustal or marine shale Ba/Al (Klump et al., 2000; Eagle et al., 2003). The $(Ba/Al)_{det}$ baseline derived for the Nama Group is 26 ppm/% based on the minimum Ba/Al ratio of the sample set. In the Nama Group, Ba and Al exhibit a strong positive correlation (Appendix B, Figure AB9), as do Ba and Ti suggesting that the major source of Ba is of detrital origin and this is corroborated by low values of Ba_{XS} in the range 0 to 313 ppm (averaging ~150 ppm). There is no significant correlation between Ba and the chemical index of alteration (see section 3.4.6.2) suggesting that Ba concentration is not controlled by changing weathering intensity. The observed range in Ba_{XS} is comparable to that recorded from early Cambrian sediments of the Yanjiahe Formation which were deposited under oxic – dysoxic water column conditions of inferred low productivity (Liu, K. et al., 2017). However, a number of factors are known to affect the preservation of biogenic Ba and these are considered below.

Highly productive, sulfate reducing pore water conditions are likely to mask enrichment processes as a consequence of Ba dissolution (van Os et al., 1991; Tribovillard et al., 2006). Sulfidic pore waters are a common feature in nearshore sedimentary environments and the sealing effect of microbial mats which blanketed some siliciclastic deposits of the Nama Group likely provided the perfect environment for localised build-up of pore water H_2S (Canfield, 1994, 2014; Noffke et al., 2002; Bouougri and Porada, 2007; Gomes et al., 2018). Whilst both very small framboidal pyrite aggregates and pyrite pseudomorphs have been noted from the Nama Group (Germs et al., 1986), vanishingly small contributions of Fe_{py}/Fe_{HR} are a consistent feature throughout Nama sediments. Oxidative weathering which typifies surficial exposure of Nama Group deposits likely resulted in partial oxidation of pyrite bound iron thus lowering the Fe_{py}/Fe_{HR}, however a significantly elevated proportion of the highly reactive iron pool is composed of iron carbonates (>20% Fe_{carb}/Fe_{HR} pool in ~62% of anoxic samples) which

argues against pervasive diagenetic iron remobilisation (Wood et al., 2015). Despite these features, the loss of a fraction of authigenic barite through anoxic pore water dissolution is possible.

It has also been noted that the calculation of Ba_{XS} commonly overestimates the fractional contribution of biogenic barite due to the additional component of Ba adsorb onto Fe-Mn (oxyhydr)oxides which may similarly be decoupled from detrital input (Eagle et al., 2003). However, there is no observable correlation between Ba_{XS} and Fe_{ox} or Ba_{XS} and Mn concentration which supports a dominantly biogenic contribution for excess Ba. In sum, the data presented herein argue for a relatively stable, low productivity marine environment with little evidence for temporary spikes in Ba_{XS} associated with observed anoxia. This is consistent with the dearth of iron speciation data for euxinic conditions which are commonly attributable to high levels of productivity. Even in the extreme and unlikely case that all dithionite-extractable iron oxide is a product of pyrite oxidation, only ~18% of anoxic samples would yield a euxinic speciation signature.

However, biogenic Ba accumulation in the modern ocean displays a characteristic depth profile such that deep waters commonly exhibit higher Ba concentrations than those of the shallow mixed layer due to the both the coupling of organic decay and barite formation with downward transport in the water column, in addition to barite formation in deeper micro-environments (Van Beek et al., 2007). Consequently barite is expected to be preferentially preserved in deeper waters and low Ba_{XS} may simply be an artefact of the shallow depositional environment above storm wave base for the majority of Nama Group deposits.

A more nuanced interpretation of Nama Group productivity would distinguish between redox-dominated and productivity-dominated signals. Under a redox-dominated scenario, elemental preservation is dependent upon dominant water column redox following the assumption that anoxic conditions are conducive to organic matter preservation but deleterious to the preservation of both P and Ba, whilst the opposite is true in the presence of oxygen (Tyson, 2005; Schoepfer et al., 2015). Conversely, productivity-dominated conditions are preserved as covariation of TOC, P and Ba_{XS} as a product of the overwhelming flux of organic matter under highly productive conditions, regardless of dominant redox state (Tyson, 2005). Preservation is also impacted by increasing rate of sediment accumulation which results in higher burial efficiencies of TOC and Ba (Dymond et al., 1992; Canfield, 1994; Schoepfer et al., 2015). Future work focusing on productivity estimates of Nama Group deposits should build upon the Ba and P data presented herein through incorporation of TOC data and, ideally, P speciation with the aim of distinguishing the dominant phase responsible for observed P accumulation.

3.8 Note on elemental characteristics of sampled deposits

3.8.1 Titanium, Aluminium and Chromium

The compiled major element dataset reveals a number of broader characteristics which relate to the depositional environment of the Nama basin. Firstly, Ti/Al ratios (0.022 – 0.046, mean = 0.033) are consistently below the Phanerozoic average range (0.052 – 0.057, Turekian and Wedepohl, 1961; Li and Schoonmaker, 2003), similar to those noted in older deposits of Northwest Canada (Miller et al., 2017). Both Al (3.70 – 9.82 wt%, mean = 7.54 wt%) and Ti (0.10 – 0.39 wt%, mean = 0.25 wt%) concentrations commonly plot below Phanerozoic marine shale average values (Al = 8 – 8.8 wt%, Ti = 0.46 wt%, Turekian and Wedepohl, 1961; Li and Schoonmaker, 2003). Depleted Ti/Al is likely a product of the dominantly felsic weathered material supplied from the Kalahari craton to the east. Minor contributions of material supplied by the volcanic island arc which is inferred to have been present to the northwest during deposition of the lower Nudaus and upper Nomtsas Formations were insufficient to significantly alter this ratio in the fine grained sediments sampled (Germs, 1983; Young and Nesbitt, 1998; Blanco et al., 2009, 2011; Miller et al., 2017). An apparent trend toward higher (but still depleted) average Ti/Al in the uppermost Nama Group may directly relate to a relative increase in sedimentation rate in shallow upper Urusis – Nomtsas Formation deposits (Bertrand et al., 1996; Murphy et al., 2000). The dominance of relative Ti-depletion results in spuriously elevated Fe/Ti values above average Phanerozoic marine shale, which is in contrast to Fe/Al, where relative iron enrichments above the range typical of oxic Phanerozoic marine shale are often corroborated by elevated Fe_{HR}/Fe_T supporting water column iron enrichment under anoxic conditions.

Finally, mildly reducing conditions conducive to the onset of denitrification are sufficient for the reduction of chromate (CrO_4^{2-}) from Cr(VI) to Cr(III) and sedimentary Cr enrichment may subsequently occur, partly as a consequence of adsorption of the resultant complexes to Mn and Fe oxides (Algeo and Maynard, 2004; Tribovillard et al., 2006). As such, sedimentary chromium enrichments do not require euxinic conditions (Algeo and Maynard, 2004). The average Phanerozoic shale chromium concentration of 90 ppm and Cr/Ti of 0.020 (Turekian and Wedepohl, 1961) are similar or enriched relative to the majority of samples analysed herein (Cr = 32.55 – 111.68 ppm, mean = 74.35, Cr/Ti = 0.01 – 0.04, mean = 0.03). The low average Cr concentration in samples of the Nama Group is similar to concentrations recorded from older Ediacaran sections in Northwest Canada (Miller et al., 2017). In the Nama Group, there is a weak positive correlation between Cr and Ti for the majority of samples which supports a dominantly detrital source for Cr. However, ironstones at Farm Kliphoek show notably elevated Cr/Ti (0.04 – 0.06, mean = 0.05) which may allude either to enrichment under dominantly

reducing conditions, or shallow water recycling similar to that inferred for build-up of iron in these sediments.

3.8.2 The Chemical Index of Alteration

Chemical weathering plays a major role in controlling the mineralogical composition of fine grained siliciclastic rocks and is therefore a key metric in understanding compositional changes in their major element distribution, particularly in relation to the maturity of terrigenous clay. During chemical weathering, labile elements are preferentially removed, resulting in elevated ratios of immobile elements (Al, Ti) to alkalis (Na, Ca, K) (Nesbitt and Young, 1982). The chemical index of alteration (CIA) (Nesbitt and Young, 1982) has long been used to assess the degree of chemical weathering required for an observed suite of major elements and is derived as:

$$CIA = [Al_2O_3/(Al_2O_3 + CaO^* + Na_2O + K_2O)] \times 100$$

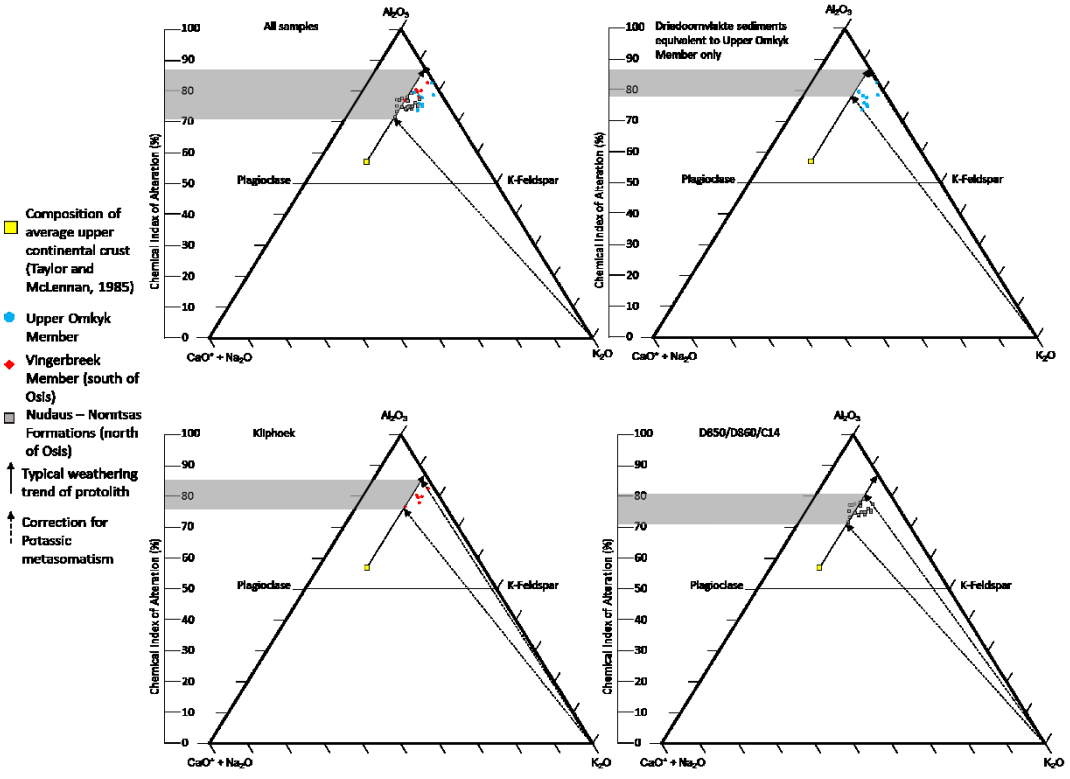

Figure 3.9

Calculated values of the chemical index of alteration and the relative positions of sampled areas in A-CN-K space. For raw data see Appendix B.

When calculating CIA, the CaO concentration in silicates (CaO*) is evaluated by correcting for Ca contribution in carbonate and apatite (Nesbitt and Young, 1984). Available P_2O_5 data was used in order to first correct for Ca in apatite ($CaO_{corr} = CaO - 10/3 \times P_2O_5$, concentrations in mol%) (Fedo et al., 1995; Zhai et al., 2017). Where resultant CaO_{corr} in moles was less than Na_2O, CaO_{corr} was used as CaO*. Conversely, where $CaO_{corr} > Na_2O$, the CaO* value was determined through equivalence with the average CaO/Na_2O ratio of the sample set (McLennan, 1993; Zhai et al., 2017). The majority of Nama Group samples display very low ratios of CaO/Na_2O (~0.15), which may reflect the higher weathering rate of anorthite (Ca-rich) relative to albite (Na-rich) and sediment supplied from a moderately to heavily weathered source rock (Nesbitt et al., 1996).

An additional concern is the diagenetic accumulation of K via potassic metasomatism, which may be corrected for by projecting observed K excess onto a theoretical weathering trend in A-CN-K ($Al_2O_3 - [CaO^* + Na_2O] - K_2O$) space (Fedo et al., 1995; Tosca et al., 2010; Johnston et al., 2013; Blanco et al., 2011; Zhai et al., 2017). It has been suggested that Nama Group strata have undergone no greater than zeolite facies metamorphism (thermal alteration in the range 170 – 200°C, Germs et al., 1986), therefore deviation from the weathering trend toward the K_2O apex may reflect K contruibuted during clay diagenesis rather than K enrichment via metasomatism. The resulting range of CIA values fall betwen ~71 – 88% with the highest values confined to the Kuibis and lower Schwarzrand subgroup as previously observed (Figure 3.9) (Blanco et al., 2011). The overlapping range of CIA values in samples of the Upper Omkyk Member at Driedoornvlakte and the Vingerbreek Member at Kliphoek reflect their provenance from the Kalahari craton to the present east (Germs, 1983). In contrast, the narrower range and lower average value of samples of the Schwarzrand Subgroup of the Zaris subbasin are likely a product of sediment input from the less heavily weathered protolith to the north in addition to that supplied from the east, consistent with published palaeocurrent and heavy mineral data (Germs, 1983; Blanco et al., 2011).

Sedimentary samples from the Nama Group show no correlation between Fe_{HR}/Fe_T and CIA which suggests that major shifts in the terrestrial weathering regime and the associated maturity of contributed terrigenous material is not responsible for the observed changes in redox from iron speciation. This is an important factor to constrain, as clay minerals provide a crucial role in organic matter adsorption and preservation post-burial and organic matter burial is one of the most efficient mechanisms for environmental oxygenation (Keil et al., 1994; Kennedy et al., 2006; Rothman and Forney, 2007; Tosca et al., 2010).

3.9 Discussion

3.9.1 Redox evolution and fossil occurrence

The consistency of carbon isotope values and trends in the Nama Group relative to records from palaeogeographically distant areas has been suggested to support a sedimentary environment which was freely connected to the global ocean (Kaufman et al., 1991; Saylor et al., 1998). This is most clearly evident from a gradual transition to positive values following a significantly negative $\delta^{13}C_{carb}$ excursion which is partially preserved in deposits of the Dabis Formation across the subbasin divide at sections including Brak, Grens and Arasab (Wood et al., 2015). The nadir of the $\delta^{13}C_{carb}$ anomaly in the Nama Group reached values of -7.4 ‰ (Figure 3.10 a), comparable in magnitude to the globally identifiable Shuram-Wonoka excursion (Wood et al., 2015). The inference that basal carbonates reflect the positive recovery from the Shuram excursion is further supported by the reconcilable age of these deposits with other globally-recognised Shuram-equivalent deposits (see Figure 1.1). In the Nama Group, a minimum age for deposits which post-date the negative excursion is constrained by a chemical abrasion ID-TIMS U-Pb age of 547.36 ± 0.65 Ma from an ash layer in the overlying Hoogland Member (Bowring et al., 2007; Schmitz, 2012) and an inferred age for the base of the Nama Group (549.8 – 551.8 Ma) approximates the age of the most negative recorded values (Section 3.6; Saylor et al., 1998).

Where anoxia is indicated by $Fe_{HR}/Fe_T > 0.38$, ratios of Fe_{py}/Fe_{HR} are ubiquitously < 0.3, characteristic of a ferruginous water column and consequently, ratios of Fe_{py}/Fe_{HR} are omitted from Figure 3.10. Shallow inner ramp conditions of time interval 1 (Figure 3.10 b,c) were typified by oxic water column conditions at Zuurburg and Zwartmodder (Figures 3.1 and 3.11) with evidence in the

---

Figure 3.10 Composite figure highlighting relative changes in carbon isotopes, redox and fossil occurrences. Note that this stratigraphic reconstruction is not to scale. **a)** Composite $\delta^{13}C_{carb}$ profile for the Nama Group using unpublished data from Smith (1998) and published data from Wood et al. (2015), **b)** Time intervals pinned to major points on the composite carbon isotope curve or major stratigraphic subdivisions. These time bins are used to aid discussion and are referenced in the text, **c-e)** Compiled Fe speciation and Fe/Al data, separated according to relative depth from inner to outer ramp. Data are compiled from Wood et al. (2015), Bowyer et al. (2017) and the present study, **f)** Published ranges for fossil occurrences in the Nama Group. Ichnofossil, soft-bodied, skeletal and probable microbial fossils are separated. Thrombolites and stromatolites are not differentiated. Breakdown of fossil occurrence on reverse (pg 144). Full information pertaining to published fossil occurrence and fossil symbols is compiled in Appendix D.

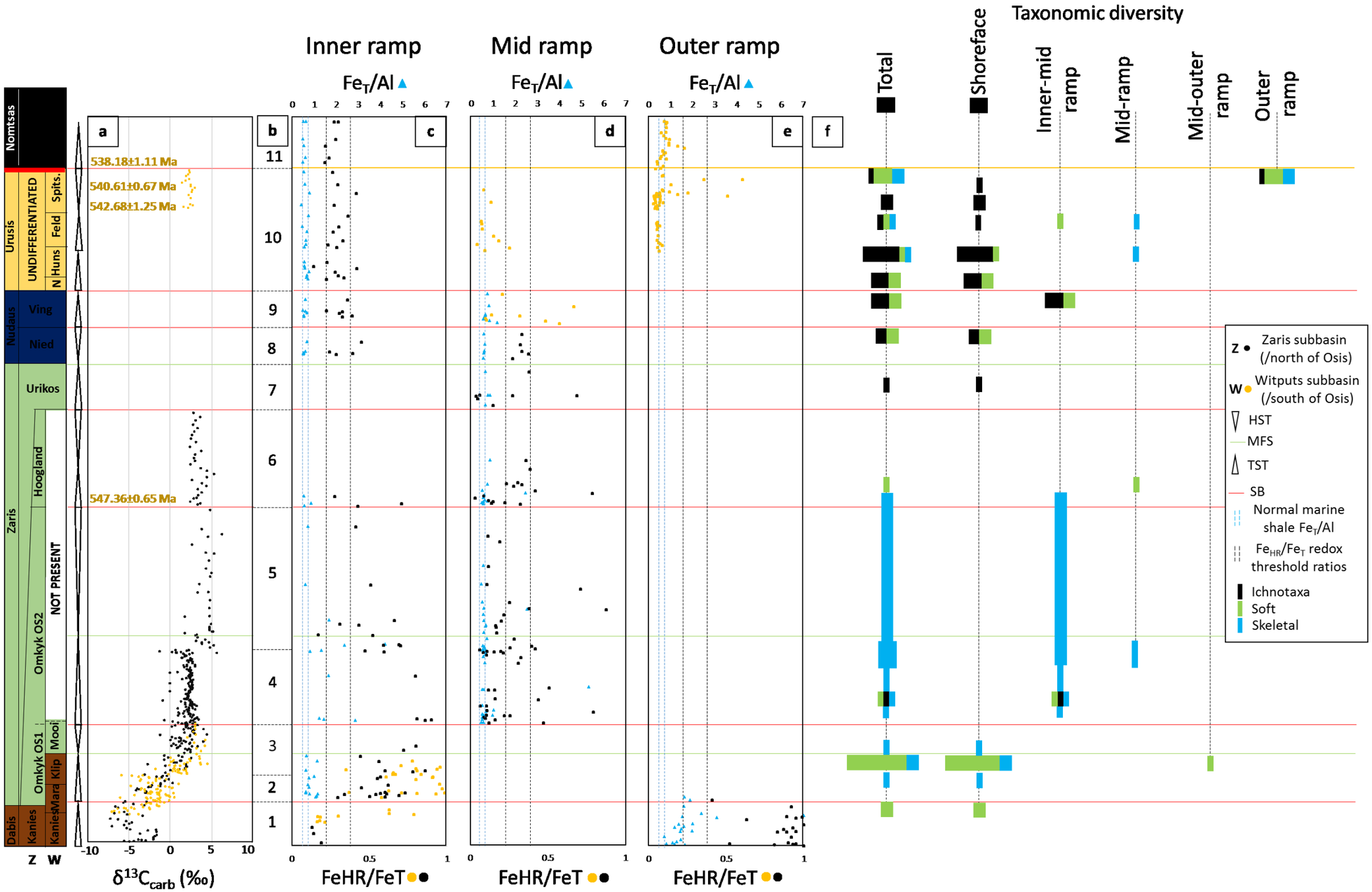
Inner ramp
Mid ramp
Outer ramp
Fe$_T$/Al
Taxonomic diversity
Total
Shoreface
Inner-mid ramp
Mid-ramp
Mid-outer ramp
Outer ramp
538.18±1.11 Ma
540.61±0.67 Ma
542.68±1.25 Ma
547.36±0.65 Ma
Nomtsas
Urusis
UNDIFFERENTIATED
Spits.
Feld
Huns
Nudaus
Ving
Nied
Urikos
Hoogland
Zaris
Omkyk OS2
NOT PRESENT
Omkyk OS1
Mooi
Klip
Mara
Dabis
Kanies
Z
W
δ^{13}C$_{carb}$ (‰)
FeHR/FeT
Zaris subbasin (/north of Osis)
Witputs subbasin (/south of Osis)
HST
MFS
TST
SB
Normal marine shale Fe$_T$/Al
Fe$_{HR}$/Fe$_T$ redox threshold ratios
Ichnotaxa
Soft
Skeletal

Figure 3.10

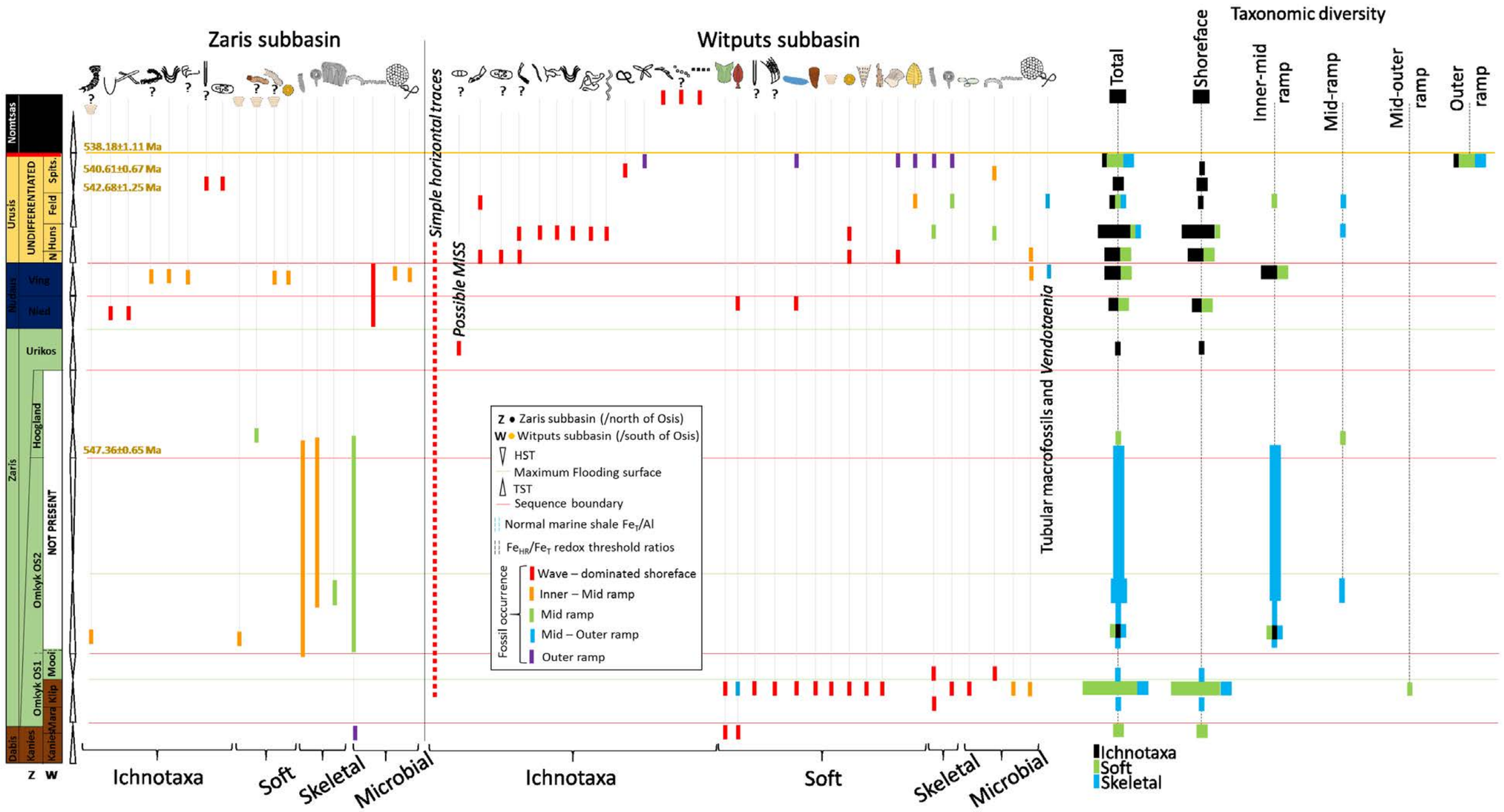
Zaris subbasin
Witputs subbasin
Taxonomic diversity
Total
Shoreface
Inner-mid ramp
Mid-ramp
Mid-outer ramp
Outer ramp
Nomtsas
Unusis
UNDIFFERENTIATED
Spits
Feld
Huns
Ving
Nied
Urikos
Hoogland
Omkyk OS2
NOT PRESENT
Mooi
Omkyk OS1
Klip
Kanies
Mara
Dabis
538.18±1.11 Ma
540.61±0.67 Ma
542.68±1.25 Ma
547.36±0.65 Ma
Simple horizontal traces
Possible MISS
Tubular macrofossils and Vendotaenia
Z ● Zaris subbasin (/north of Osis)
W ● Witputs subbasin (/south of Osis)
HST
Maximum Flooding surface
TST
Sequence boundary
Normal marine shale FeT/Al
FeHR/FeT redox threshold ratios
Fossil occurrence
Wave – dominated shoreface
Inner – Mid ramp
Mid ramp
Mid – Outer ramp
Outer ramp
Z W
Ichnotaxa
Soft
Skeletal
Microbial
Ichnotaxa
Soft
Skeletal
Microbial
Ichnotaxa
Soft
Skeletal

Zaris subbasin for deep ferruginous waters established in the outer ramp (Figure 3.10 e) (Wood et al., 2015; Sperling et al., 2015a). At this time, wave-influenced shoreface sandstones in close proximity to the sampling site of Zuurburg (Sperling et al., 2015a) contain 3-dimensionally preserved specimens of *Ernietta* in life position (Bouougri et al., 2011), whilst facies across the Zaris and deeper Witputs subbasins lack similar fossil evidence (Figure 3.10 f).

Continued marine transgression during deposition of the Kliphoek and lower Omkyk Members (intervals 2-3; Figures 3.10 b and 3.11) led to shoaling of the chemocline and permitted frequent incursions of anoxic deep water into shallow settings in both subbasins (Wood et al., 2015; Tostevin et al., 2016b). This interval has been notably prolific with regards to soft bodied fossils including *Ernietta*, *Rangea*, *Pteridinium*, *Ausia*, *Namalia*, *Buchholzbrunnichnus* and *Orthogonium*, the occurrences of which are constrained to intertidal to shallow subtidal sandstones of the Witputs subbasin (Gurich, 1930; Pflug, 1966; Germs, 1968, 1973a, 1973b, 1983; Jenkins, 1985; Vickers-Rich et al., 2013; Elliot et al., 2011, 2016). In contrast to these shoreface deposits, which were likely oxygenated through frequent wave-action, carbonates of the Upper Kliphoek (Aar) Member host depauperate assemblages of weakly calcified *Namacalathus* in the deeper inner ramp, wherein very low $Fe_T < 0.5$ wt% has been interpreted to represent briefly oxygenated benthic conditions suitable for opportunistic colonisation (Wood et al., 2015). Additionally, organic walled microfossils, including the possible cyanobacterium *Bavlinella faveolata* have been recovered from borehole material corresponding to shale of the Kliphoek Member (Mansuy and Vidal, 1983; Germs et al., 1986).

The Upper Omkyk and Hoogland Members and correlative deeper water clastics of the Urikos Member span time intervals 4 – 6 (corresponding to sequence K3 of Saylor et al., 1998) which are absent in the Witputs subbasin. Whilst *Cloudina* and *Namacalathus* are abundant across inner-outer ramp environments of the Zaris subbasin, large microbial-metazoan reefs grew unimpeded in persistently oxic mid-ramp positions and supported the most diverse calcifying community in the Nama Group (Penny et al., 2014; Wood and Curtis, 2015; Penny et al., 2017; Wood et al., 2017; Wood and Penny, 2018). This interval is also characterised by the first supposedly complex surface traces recorded from the Nama Group in shallow – mid depth facies (Macdonald et al., 2014). However, these apparent ichnofossils may in fact represent impressions of the body fossil *Palaeopasichnus gracilis* (Zhuravlev, A.Y. pers. com.), an additional specimen of which has been discovered in the upper Omkyk Member (OS2) on Farm Omkyk (own observation).

Overlying Schwarzrand subgroup deposits (time intervals 9 – 11) of the Zaris subbasin predominantly represent shallow, inner ramp facies which were host to a low diversity assemblage largely consisting of *Aspidella*, *Shaanxilithes* (/*Palaeopasichnus delicatus*/*linearis*, Zhuravlev A.Y. pers. com.) and

various trace makers in addition to acritarchs and filamentous *Vendotaenia* (Crimes and Germs, 1982; Germs et al., 1986; Germs, 1995; Cohen et al., 2009; Darroch et al., 2016). Proximity of this environment to riverine nutrient input likely promoted shallow water productivity and organic matter oxidation, leading to reduced water column oxygen concentrations. However, reducing conditions were only occasionally sufficient to solubilise riverine derived Fe (oxyhydr)oxides and lead to water column iron enrichment. The peak in the observed Mn trend is attained in the upper Urusis Formation, during which time the fossil record of the Zaris subbasin is limited to possible representatives of the putative sponge *Brooksella* and the enigmatic, possibly-cyanobacterial fossils formerly ascribed to *Skolithos* (Crimes and Germs, 1982; Pickford, 1995; Ciampaglio et al., 2006; Acenolaza et al., 2009).

In the Witputs subbasin, Schwarzrand subgroup deposits document a shift in dominant water column redox and deepening of the oxycline. Here, suitable fine grained siliciclastic deposits of the Vingerbreek Member record both oxic and ferruginous iron speciation signatures indicating continued redox stratification. Whilst shallow transgressive deposits of the conformable Niederhagen Member yield complex soft bodied fossils such as *Rangea*, these deeper Vingerbreek Member deposits are solely host to simple tubular macrofossils superficially resembling *Vendotaenia* and organic walled microfossils including *Bavlinella faveolata* (Germs, 1973a; Germs et al., 1986; Cohen et al., 2009). In fact, the relatively depauperate fossil assemblage may be a direct by-product of the prevailing redox state in the Nama basin at this time, whereby algal and cyanobacterial blooms were fertilised during transgression by nutrient and Fe^{2+} -rich deep waters (Mansuy and Vidal, 1983; Germs et al., 1986; Cohen et al., 2009; Frei et al., 2013).

In contrast, overlying deposits of the Urusis Formation reveal an assemblage of higher diversity including body fossils of *Nasepia*, *Swarpuntia* and *Pteridinium*, *Aspidella*, possible *Bradgatia*, biomineralising *Cloudina* and *Namacalathus* and abundant trace fossils (Germs, 1972a, b; Narbonne et al., 1997; Jensen et al., 2000; Jensen and Runnegar, 2005; Wood et al., 2015, 2017; Darroch et al., 2015; Penny et al., 2017; Buatois et al., 2018). As in examples from the lower Nama Group, the majority of soft-bodied forms inhabited well ventilated shoreface environments in the Witputs subbasin and are commonly preserved in redeposited coarse clastic units. Interbedded deeper, mid to outer-ramp shales preserve a record of stable, oxic water column conditions (Wood et al., 2015; Sperling et al., 2015a).

3.9.2 Oxygen requirements and Nama organisms

It must be stressed that the vast majority of Ediacaran macrofossils cannot be confidently assigned to the Metazoa and therefore the assumption that significant dissolved oxygen was required by many

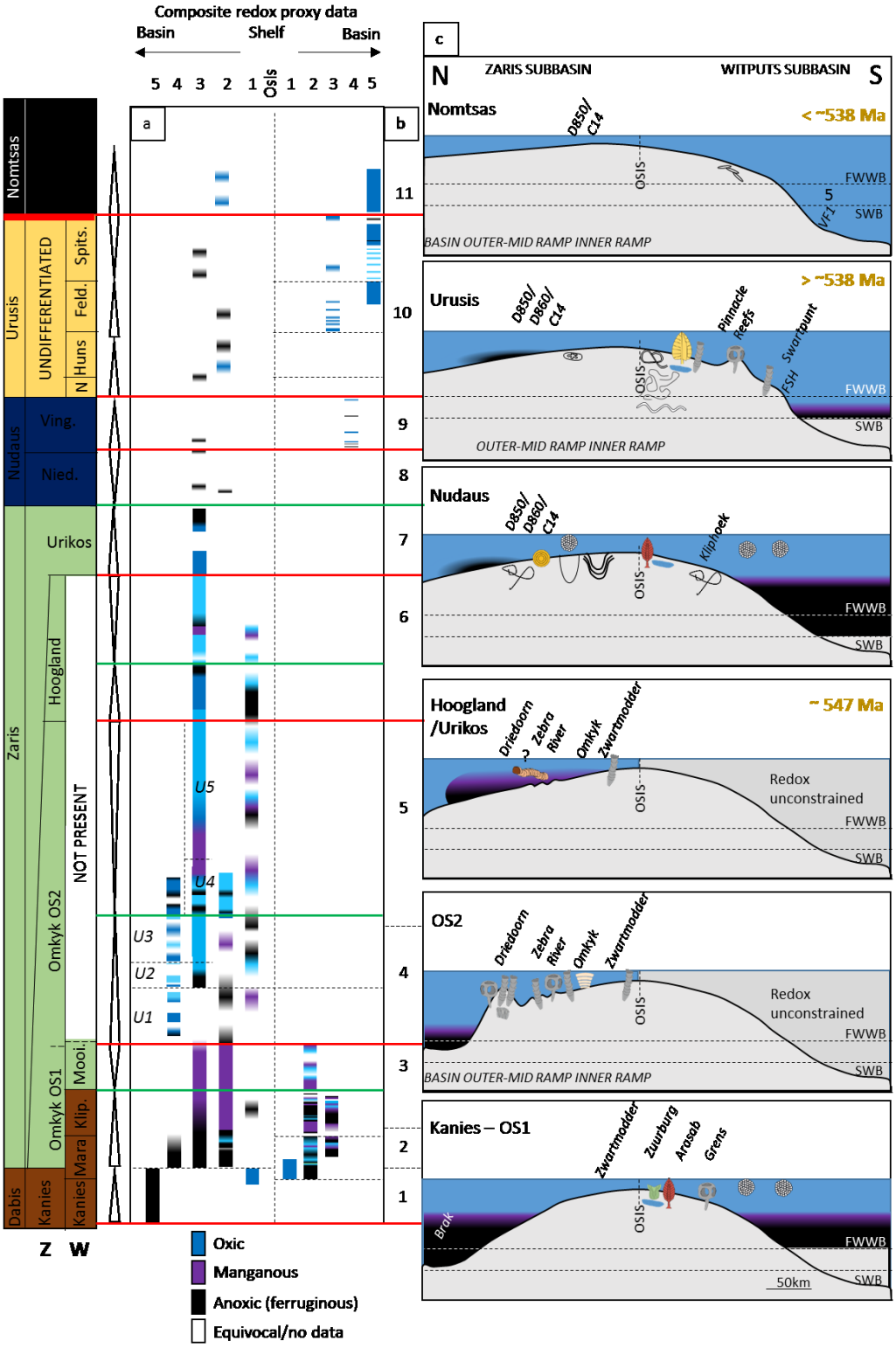

Figure 3.11

Schematic representation of redox and biotic evolution during deposition of the Nama Group. Colours represent dominant redox. Blue: oxic, Black: ferruginous, White: equivocal/no data. A key to fossil symbols is provided in Appendix D.

representatives of the Nama assemblage is questionable (Xiao and Laflamme, 2009; Droser and Gehling, 2015; Muscente et al., 2017). A prime example of the danger in over-interpreting Ediacaran Period fossils concerns recent biomarker evidence indicating that the widespread macrofossil *Nemiana* (a junior synonym of *Beltanelliformis*, Ivantsov et al., 2014), once thought to correspond to complex soft-bodied organisms, more likely represent colonial cyanobacteria (Bobrovskiy et al., 2018). Indeed, of all the organisms represented in the Ediacaran body fossil record only a handful share attributes representative of animal-grade complexity, most notably the motile bilaterians *Kimberella* and *Dickinsonia* both of which are confined to siliciclastics of the preceding White Sea assemblage (Fedonkin and Waggoner, 1997; Ivantsov, 2009; Evans et al., 2017; Hoekzema et al., 2017). Whilst likely animal representatives including the calcifying forms *Cloudina*, *Namacalathus* and *Namapoikia* are thought to have required at least moderate levels of oxygen to sustain a skeletonising growth habit (Sperling et al., 2013, 2015c; Wood et al., 2015; Tostevin et al., 2016b; Penny et al., 2017), inferring habitable oxygen thresholds for the enigmatic soft-bodied assemblage preserved in Nama sediments may currently be considered phylogenetically unsubstantiated. Of all soft-bodied representatives in the Nama Group, only *Pteridinium*, *Rangea*, *Ausia* and one tentative specimen interpreted as *Gaojiashania* have been proposed to represent possible stem-group animals and, even then, phylogenetic interpretations remain highly controversial (Dzik, 2002; Weber et al., 2007; Fedonkin et al., 2012; Meyer et al., 2014b; Smith et al., 2017). In contrast, it is widely acknowledged that active lifestyles maintained by bilaterian ichnofossil trace makers are more robustly interpreted as having required elevated levels of dissolved O_2 (Chang et al., 2006; Wilson et al., 2012; Sperling et al., 2013, 2015c).

The current redox database for the Nama Group supports a progressive ventilation of mid – depth environments in the final ~10 Ma of the Ediacaran Period which is accompanied by a concurrent, clear increase in diversity of the ichnofossil record (Figure 3.10 f). Inner shelf environments of the Kuibis subgroup were intermittently subject to upwelling of ferruginous deep waters and impressions which were initially considered to represent trace fossils such as *Buchholzbrunichnus* and *Skolithos* were restricted to the very shallow inner shelf (Figures 3.11 and 3.12) (Germs, 1973b; Crimes and Germs, 1982). However, these two occurrences are now largely considered to represent body fossils of unknown affinity (Acenolaza et al., 2009) and the ichnofossil record of the Kuibis Subgroup is thus restricted to primitive horizontal traces (Germs, 1972a; Crimes and Fedonkin, 1996; Jensen et a., 2000; Jensen and Runnegar, 2005; Xiao and Kaufman, 2006; Acenolaza et al., 2009). The earliest relatively complex ichnofossil representative in strata of the Nama Group may be a single specimen proposed to relate to an under-mat mining habit recorded from siliciclastics deposited above wave base in the upper Omkyk Member at Hauchabfontein Farm (Macdonald et al., 2014, but see Buatois and Mangano, 2016). However, this form may instead represent the body fossil of *Palaeopasichnus gracilis* (Zhuravlev, A.Y.

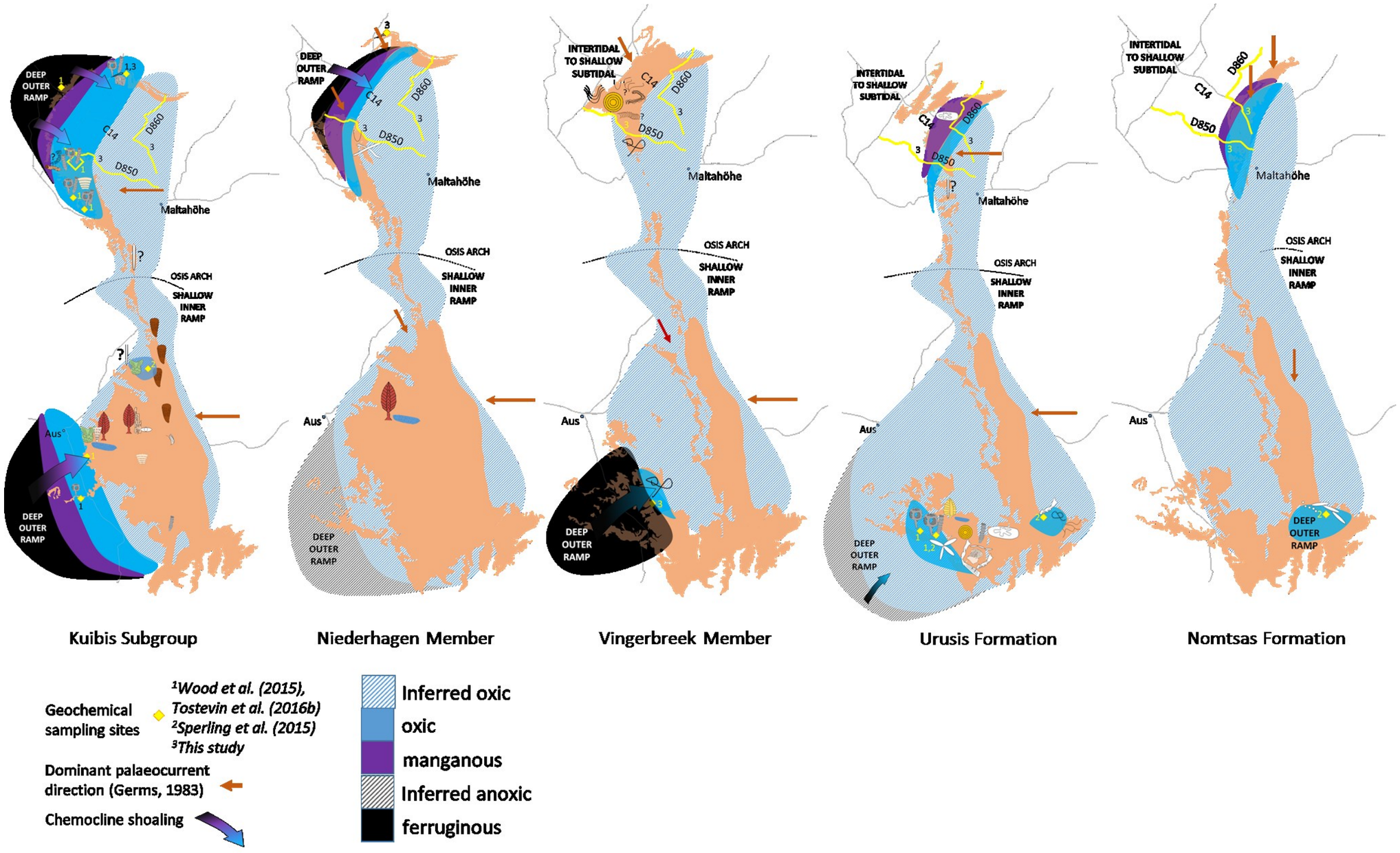

Figure 3.12 Schematic diorama representing the plan-view evolution of redox in the Nama Group and corresponding published fossil occurrences for each time interval. Full information pertaining to published fossil occurrence and fossil symbols is compiled in Appendix D.

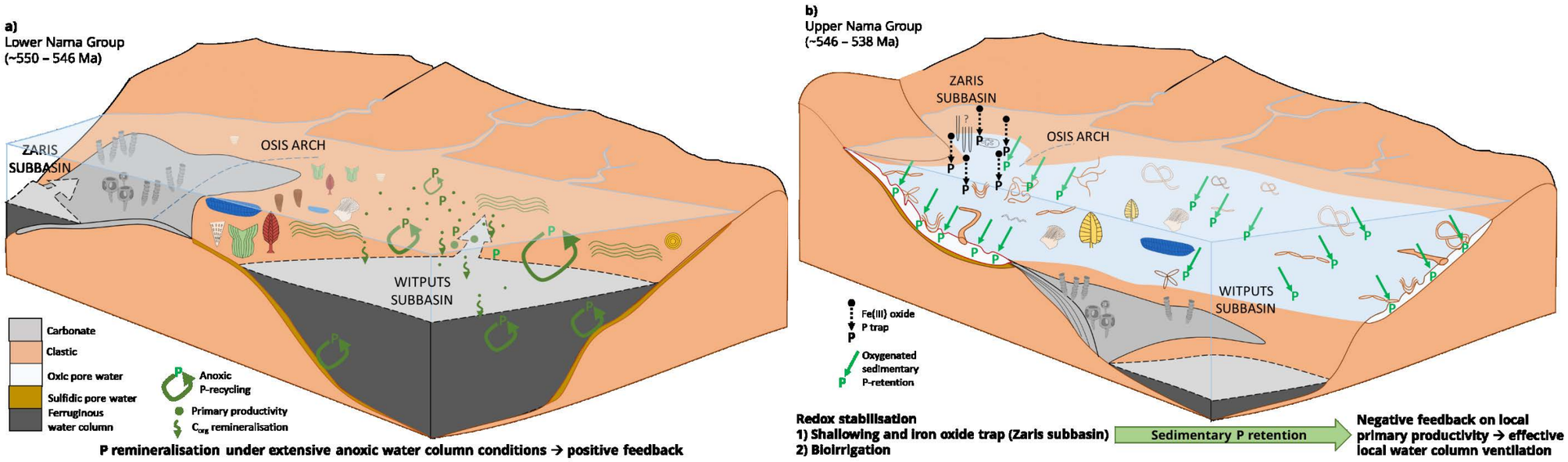

Figure 3.13 Proposed model for the combined impact of regional facies evolution and bioturbation on changes to the P cycle and the potential feedbacks on the evolution of local water column redox. **A)** Lower Nama Group (~550 – 546 Ma) and **B)** Upper Nama Group (~546 – 538 Ma).

pers. com.). During this time, shallow – intermediate depth environments record at least temporarily well oxygenated conditions (Figures 3.11 and 3.12). Abundant trace fossils are subsequently noted from the Schwarzrand Subgroup of the Zaris subbasin (Darroch et al., 2016), approximately coincident with a shift to lower and more stable Fe_{HR}/Fe_T and Fe_T/Al values of the inner-ramp environment. This trend continues in overlying deposits with an increase in diversity and complexity of ichnotaxa (Crimes and Germs, 1982; Jensen et al., 2000; Jensen and Runnegar, 2005; Buatois et al., 2018) that may in part have favoured the regional shift towards shallow water oxygen stability.

An integrated model incorporating regional facies, the diversity of ichnotaxa, nutrient availability and water column redox is herein proposed (illustrated in Figure 3.13). It is known that water column anoxia promotes the efficient remineralisation and release of phosphorus from sediments, thereby providing a strong feedback on local primary productivity (Ingall and Jahnke, 1994; Lenton et al., 2014). In this way, extensive ferruginous water column conditions recorded from deposits of the Kuibis Subgroup may have resulted in a positive feedback on productivity-induced anoxia (Figure 3.13a). However, progressive infill of the Zaris subbasin promoted shallow marine trapping of iron oxides (section 3.4.5), which may have resulted in a regional P sink, due to adsorption of P onto iron oxides. Similarly, phosphorus retention under oxygenated pore water conditions was likely promoted through progressively efficient bioirrigation in the Schwarzrand Subgroup (Aller, 1994; Ziebis et al., 1996; Meysman et al., 2006; McIlroy and Logan, 1999; Canfield and Farquhar, 2009; Macdonald et al., 2014; Tarhan, 2018). Sedimentary phosphorus retention brought on by iron oxide trapping and bioirrigation supports a two-stage model for reduced water column productivity in the upper Nama Group (Figure 3.13b). This model suggests that progressive oxygenation of mid-outer shelf environments in the Nama Group through time was directly linked to the distribution of shallow shelf facies and the evolution of redox and bioturbating organisms. Substantiation of this hypothesis would require P speciation and N isotope analyses to constrain the evolution of the nutrient cycle.

The rise of a widespread sediment-disturbing life habit may also have had negative implications for pre-existing benthic and immobile suspension feeding fauna largely associated with a loss of stable substrate and obstruction of filter feeding appendages (Buatois et al., 2018). It has previously been proposed that the possible semi-infaunal life habit exploited by some organisms of the Nama assemblage, including *Ernietta* (/*Namalia*) and *Pteridinium* may thus have been largely abandoned as a consequence of the significant substrate impact of emerging bioturbators (Germs, 1968; Grazhdankin and Seilacher, 2002; Bottjer et al., 2000). This would be particularly pertinent following the development of shallow-infaunal burrowing such as that represented by the recently-described *Parasammichnites pretzeliformis* in lower Spitskop Member sediments of the Witputs subbasin (Buatois et al., 2018). While at first glance,

this may be corroborated by the apparent loss of *Ernietta* (/*Namalia*) from sediments of the Schwarzrand Subgroup; *Pteridinium* is seen to have persisted up to the Ediacaran – Cambrian boundary where the effects of bioturbation were likely significant (Narbonne et al., 1997; Jensen et al., 2000; Jensen and Runnegar, 2005). Indeed, a number of soft-bodied and skeletal organisms, including proposed filter feeding forms are recorded from the latest Ediacaran Spitskop Member, however this is overshadowed by an apparent shift to lower diversity of soft-bodied forms associated with a concurrent diversity increase in ichnotaxa (Figure 3.10) (Buatois et al., 2018). It seems equally plausible that bilaterian organisms capable of actively disrupting the sediment may be responsible for obliteration of any post-mortem impression left by soft-bodied forms. As such, the suggestion that diversification of sediment disrupting organisms resulted in out-competition of soft-bodied forms within the ecosystem is problematic.

3.10 Conclusions

The sparsity of Ediacaran-aged deep ocean deposits precludes direct proxy reconstruction of truly basinal palaeoredox. Rather, inference on the global extent of anoxic deep waters has been assembled from trace metal enrichments in organic matter rich sediments deposited under locally anoxic water column conditions (e.g. Chen, X. et al., 2015; Kendall et al., 2015). If the Ediacaran deep ocean experienced a transition to dominantly oxic conditions as suggested by some studies (Holland, 2006; Canfield et al., 2007; Johnston et al., 2012), continued ferruginous anoxia documented in some inner – outer shelf environments (e.g. the Kalahari craton and Yangtze Block) may simply preserve prevailing development of oxygen minimum zones along productive continental margins (Hammarlund et al., 2017; Guilbaud et al., 2018).

The predominantly intertidal to shallow subtidal niche space occupied by soft-bodied organisms throughout deposition of the Nama Group and the pattern observed in their distribution on the shallow shelf through time reflects in part the initially dynamic constraint of proximal deep water anoxia. Similarly, stable and long-lived oxia in shallow refugia supported the most diverse skeletal communities (Wood et al., 2015; Tostevin et al., 2016b). A gradual shift towards oxygen stability of the inner – outer ramp during deposition of the upper Schwarzrand Subgroup may also be accompanied by a decline in organic walled microfossil diversity and, if this is the case, it may reflect reduced fertilization by upwelling anoxic, dissolved iron and nutrient-rich deeper waters. Widespread oxygen stability was also accompanied by invasion of the Nama basin by active, motile trace makers which thrived in shallow to mid-ramp transgressive clastic interbeds between highstand carbonate horizons which host *Cloudina*, *Namacalathus* and mid to outer ramp clastics containing the last of the soft-bodied Nama assemblage

(Jensen et al., 2000; Jensen and Runnegar, 2005; Buatois et al., 2018). Whilst rising marine oxygen levels likely supported the proliferation of motile organisms, active bioturbation would have effectively ventilated the sediment, resulting in significant feedbacks on trace metal and nutrient retention. This hypothesis warrants a detailed and integrated study of nutrient cycling, redox and bioturbation in the Nama Group through modelling of Fe and P speciation in addition to N isotopes. However, the conclusion that a rise in sediment disruption by bioturbating ichnotaxa is the root cause of the disappearance of soft-bodied organisms and skeletal filter feeders remains tenuous and requires further investigation.

Chapter 4

The paragenetic sequence of carbonate cements at Driedoornvlakte: inferring water column palaeoredox

Abstract

The Ediacaran oceanic redox landscape was heterogeneous, where many basins had a shallow and highly dynamic chemocline above anoxic (ferruginous or euxinic) or low oxygen (manganous) waters. Seawater mMg/Ca ratio was also high, promoting early diagenetic dolomitisation. How the benthos responded to these conditions is fundamental to understanding their ecological dynamics. This chapter focuses on redox sensitive elements in early marine carbonate cements to investigate possible water column redox controls on the distribution and growth of one of the oldest metazoan communities.

Skeletal invertebrate taxa in the Zaris Sub-Basin of the Nama Group, Namibia (~550-547 Ma), grew in shallow waters where fine-grained carbonate sediment often shows evidence of early dolomitisation. Mid-ramp *Cloudina* reefs (< 20 m in diameter) are composed of open, highly porous structures that formed multiple, successive assemblages. Each assemblage is terminated by thin (< 1 mm), layers of dolomitised sediment and dolomite cement. All dolomitic lithologies in the Nama Group analysed via Fe speciation suggest precipitation under anoxic ferruginous water column conditions.

Reef cements show a paragenetic sequence from synsedimentary to early marine cement and final burial, which were precipitated under dynamic redox conditions. First, botryoidal pseudomorphed aragonite cement formed under oxic conditions (low Fe and Mn). Next, the presence of iron-rich dolomitised sediment, often associated with a recrystallised ferroan dolomite crust, suggests that originally aragonitic or calcitic sediment and a high-Mg precursor cement were preferentially dolomitised. Dolomitisation may have been enhanced via upwelling of deeper water, anoxic, ferruginous seawater, or by later fluid remobilisation from adjacent shales. A following Mn-rich calcite cement is

inferred to be early marine due to its inclusion-rich, fibrous form and well-preserved CL zonation. The final blocky cement precipitated under oxic conditions, probably during shallow burial.

The cements likely record a general shallow to deeper water transect, from oxic shallow waters to low oxygen manganous waters, then to oxic, shallow burial conditions. Transient incursions of upwelled, anoxic, ferruginous and dolomitising waters may have occurred during short-term, transgressive cycles, although the timing for this is poorly constrained. Such incursions may have terminated Ediacaran benthic communities that grew close to the chemocline.

Author Contributions: This chapter benefited from extensive discussions with Rachel Wood, Amelia Penny, Simon Poulton, Tony Dickson and Ashleigh van Smeerdijk Hood and was substantially improved after helpful critique by Ashleigh van Smeerdijk Hood and one anonymous reviewer. Electron microprobe data were collected with technical assistance from Chris Hayward and technical experience provided by John Craven in the use of the cathodoluminescence microscope. X-ray diffraction data was collected with the technical assistance of Nic Odling and thanks go to Nick Tosca for helpful comments on the interpretation of the XRD spectra in relation to dolomite ordering. Thanks also goes to Mike Hall for creation of highly polished thin sections examined in this chapter.

The bulk of this chapter is published as Wood et al. (2018) in the Journal of *Precambrian Research* under the title: 'Did unstable redox conditions terminate Ediacaran benthic communities? Evidence from early diagenesis'. Much of the text and discussion is adapted from and expands on the Wood et al. (2018) manuscript.

4.1 Introduction

Ediacaran skeletal macrobiota were restricted to well-oxygenated waters above the chemocline (Chapters 2 and 5; Wood et al., 2015; Tostevin et al., 2016b). The role of dynamic redox conditions in relation to the nature of the earliest metazoan benthos is fundamental to understanding the ecological dynamics of the first metazoan communities. However, most bulk-rock geochemical techniques provide an indication of the dominant redox condition during sedimentation over geological rather than ecological timescales, and thus rapid fluctuations in water column redox conditions are seldom recorded.

The unusual chemical state of Ediacaran oceans will be manifest in the record of early marine cements (Nothdurft et al., 2004; Hood and Wallace, 2015; Wallace et al., 2017; Della Porter et al., 2015). The petrography, trace element and stable isotope composition of varied carbonate cements in metazoan reefs are here considered from the late Ediacaran Nama Group, Namibia. The use of early marine cements allows high resolution reconstruction of the evolution of seawater-sourced pore fluids in shallow carbonate settings, where Ediacaran skeletal metazoan biodiversity was highest. Dolomite is also common in the Nama Group, and the majority of dolomite samples processed for iron speciation show highly reactive iron primarily incorporated into carbonate phases, though a significant proportion is contributed as iron oxides in proximal, shallow environments and magnetite in deeper settings (Appendix B, Figures AB1 and AB3; Wood et al., 2015). All dominantly-dolomitic lithologies indicate precipitation under ferruginous water column conditions (Wood et al., 2015). Therefore, it is also considered that dolomitisation may preserve a record of transient anoxic seawater conditions, which in turn may have influenced the ecological structure of Ediacaran skeletal communities.

4.1.2 Background: The dolomite dilemma

Dolomite ($CaMg(CO_3)_2$) is a carbonate mineral with a rhombohedral form and is characterised by replacement of Ca to varying degree by Mg cations (Figure 4.1). Stoichiometric, well-ordered dolomite is defined by equal proportions of Ca^{2+} and Mg^{2+} which are distributed evenly between lattice planes of carbonate (CO_3^{2-}) anions within the crystal structure (Figure 4.1b) (e.g. Gregg et al., 2015). In contrast, cations in non-stoichiometric dolomite are dominated by Ca^{2+}, with some lattice planes exhibiting Mg^{2+} incorporation which results in a structure that is commonly less well ordered.

Primary dolomite cementation and dolomitisation of carbonate precursors (resulting in secondary/replacement dolomite) is considered to be thermodynamically favoured in solutions of high Mg/Ca, high carbonate alkalinity and high temperature (which acts to reduce the requirement for

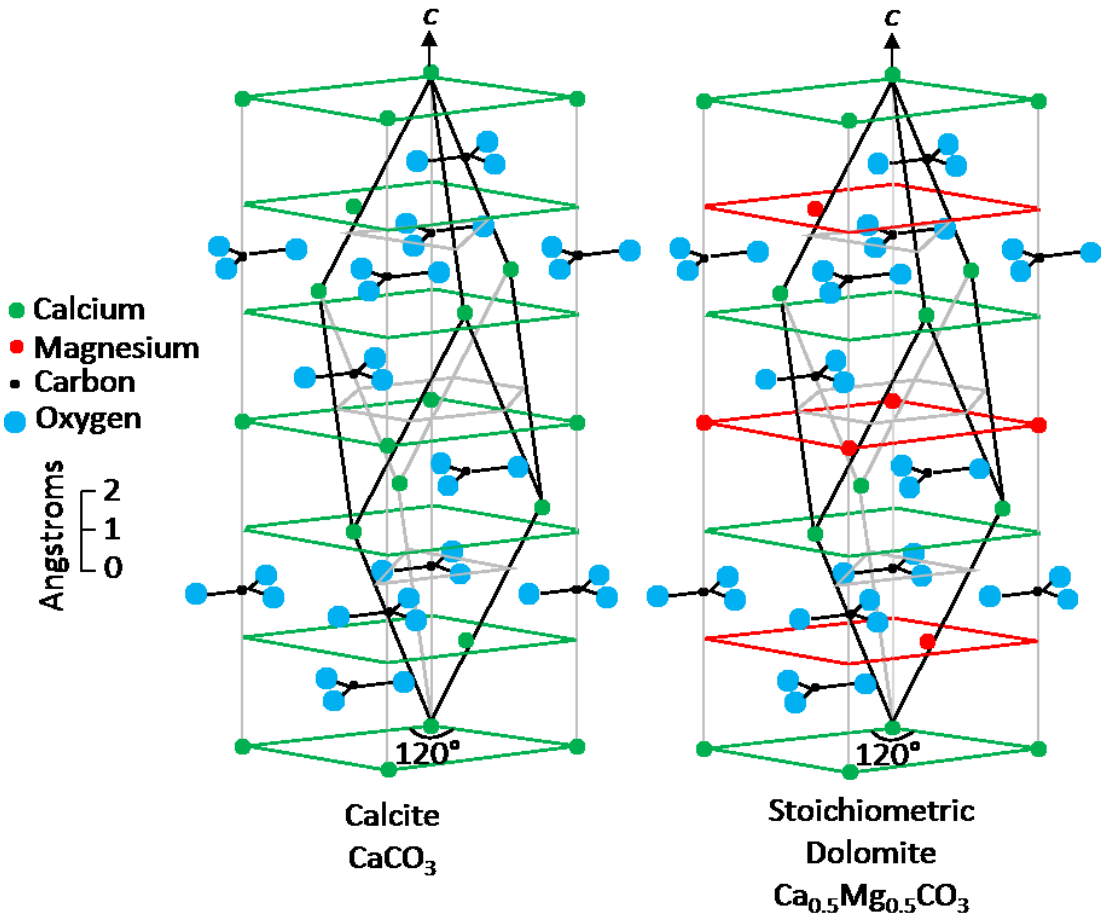

Figure 4.1 Structure of calcite relative to stoichiometric dolomite (well ordered). Hexagonal and rhombohedral unit cells are superimposed. Adapted from Gregg et al. (2015) after original model in Lippmann (1973).

elevated Mg^{2+} during dolomitisation) (Katz and Mathews, 1977; Gaines, 1980; Sibley et al., 1987, 1994; Arvidson and MacKenzie, 1999). Dolomitisation of a carbonate precursor proceeds via a series of dissolution-reprecipitation reactions and can be simplified by the following two equations:

1) $2CaCO_3\ (s) + Mg^{2+}\ (aq) \rightarrow CaMg(CO_3)_2\ (s) + Ca^{2+}\ (aq)$

2) $CaCO_3\ (s) + Mg^{2+}\ (aq) + CO_3^{2-}\ (aq) \rightarrow CaMg(CO_3)_2\ (s)$

Where (s) represents a solid, and (aq) an aqueous state (Machel, 2004). The reactions differ in their requirement for Ca^{2+} removal and CO_3^{2-} supply from/to the reaction site (Machel, 2004). In contrast, dolomite cementation follows the reaction:

3) $Ca^{2+}\ (aq) + Mg^{2+}\ (aq) + 2CO_3^{2-}\ (aq) \rightarrow CaMg(CO_3)_2\ (s)$

The inhibition of dolomitization in the presence of elevated sulfate (Baker and Kastner, 1981) is not always considered to be a significant controlling factor under low temperature diagenetic conditions (Morrow and Abercrombie, 1994; Machel, 2004; Sánchez-Román et al., 2009). However, substantial evidence has been presented for dolomite formation in organic-rich seawater and catalysed in the presence of microbial processes, particularly sulfate reducing or methanogenic metabolisms which act to increase pore fluid pH, total alkalinity and CO_3^{2-} concentrations (Vasconcelos et al., 1995; Mazzullo, 2000; Warthmann et al., 2000; Roberts et al., 2004, 2013). It has been stressed that laboratory experiments which purport to have achieved the growth of dolomite in the presence of bacteria have instead almost ubiquitously presented evidence for poorly ordered very high-magnesium calcite (VHMC) (Kaczmarek et al., 2017). However, VHMC is confidently regarded as a viable precursor for recrystallisation via Ostwald-ripening to ordered and stoichiometric dolomite at temperatures < 220°C (and possibly sea surface temperatures given sufficient time) (Rodriguez-Blanco et al., 2015; Kaczmarek et al., 2017).

Despite supersaturation in seawater, dolomite does not form as a cement under normal marine conditions in modern environments but instead precipitates within restricted shallow, evaporitic environments including sabkhas and hypersaline lakes (Illing et al., 1965; von der Borch, 1976; Last, 1990). In evaporitic environments, limestone alteration may occur via reflux dolomitisation whereby dense, Mg-rich and CO_2-poor brines percolate slowly through pore waters and readily replace Ca^{2+} by Mg^{2+} (Adams and Rhodes, 1960). In sabkha settings this is supplemented by significant evaporative pumping and increased carbonate alkalinity as a consequence of extensive sulfate reduction under anoxic pore water conditions (McKenzie et al., 1980; Müller et al., 1990; Machel, 2004). However a variety of ancient dolomite deposits display no evidence for an evaporitic environment of deposition and are instead variably considered to represent late replacement of an original calcite or aragonite precursor mineralogy or primary marine dolomite cement precipitation during times of elevated seawater Mg/Ca (Mackenzie and Morse, 1992; Budd, 1997; Holland and Zimmermann, 2000; Machel, 2004; Hood and Wallace, 2012, 2015, 2018; Wood et al., 2017a).

4.1.3 Petrographic and paragenetic evidence for penecontemporaneous marine dolomite cements in the Precambrian

In order to distinguish cements as penecontemporaneous, they must fulfil certain criteria which clearly indicate that they were precipitated in the marine environment. These include 1) an isopachous, pore-lining fabric where fibrous and inclusion-rich crystals are oriented normal to cavity walls, 2)

cements which are directly overlain by marine geopetal sediments or other early marine features, and 3) cements which are clearly truncated by other early-forming features such as neptunian fractures (Davies, 1977; Hood and Wallace, 2012, 2018). Additionally, the original mineralogy of marine cements which may have undergone later neomorphism may be determined through observations of a number of petrological characteristics outlined below.

The crystal form, the orientation at which crystals are cleaved (Figure 4.2b) and the shape of the substrate to which the crystals nucleate are just some of the things that contribute to the observed character of inorganically-precipitated carbonate cements in thin section (Dickson, 1983, 1993). Descriptions of crystallographic character for carbonate cements include 'length-fast' and 'length-slow' which relate to the degree of angular separation between the crystal c-axis and the greatest growth vectors (Figure 4.2a) (Dickson, 1983). A higher angle results in obtuse crystal terminations and the resulting crystal shape is length-slow, whereas a lower angle will generate acute terminations corresponding to a length-fast character (Dickson, 1983, 1993). Carbonate cements precipitated in

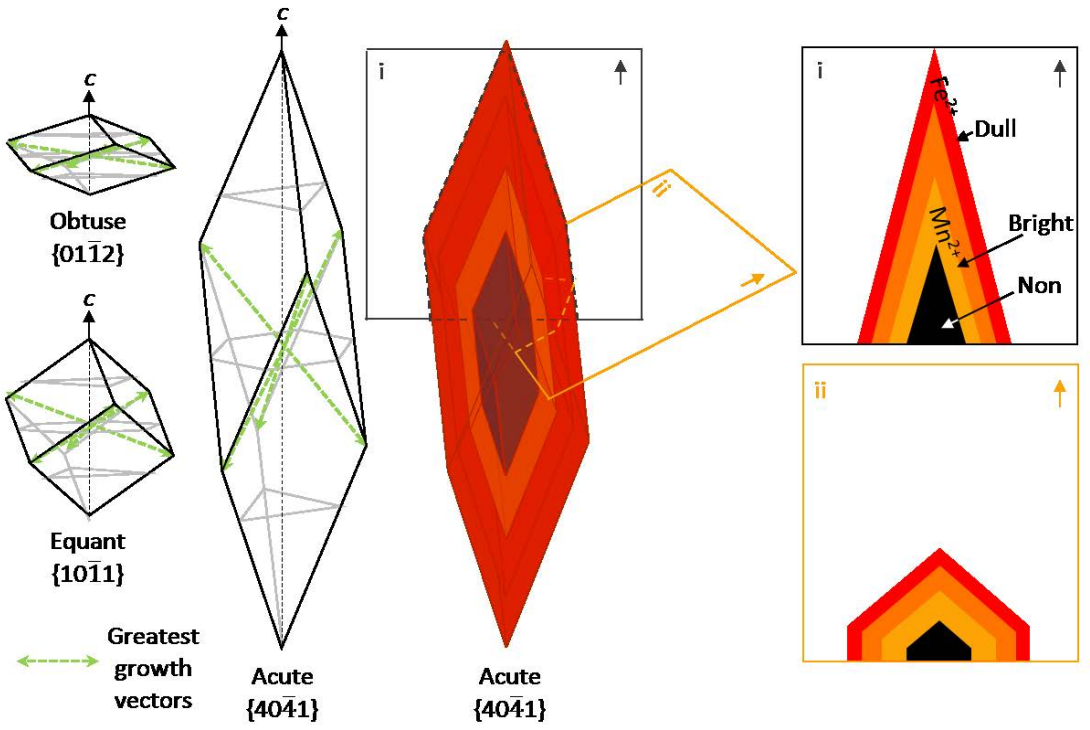

Figure 4.2: a) Crystallographic diagrams for rhombic carbonates with associated Miller-Bravais indices (after Dickson, 1983 and Hood and Wallace, 2018), **b)** A carbonate crystal with acute form showing luminescence zonation relating to changing elemental composition during burial (after Barnaby and Rimstidt, 1989). Length fast character when sectioned parallel to c-axis. Apparent length-slow character represented when sectioned at greater angles from the c-axis.

seawater (where Mg^{2+} is elevated relative to fresh water) will rapidly grow as acicular, length-fast aragonite (orthorhombic) crystals with blunt terminations or, more slowly as calcite (trigonal) crystals, also of length-fast character which show acute rhombohedral (Figure 4.2a), or scalenohedral form (Folk, 1974; Berner, 1975). Sparry calcite with length-slow character is most commonly precipitated as late stage pore-occluding cement where low Mg/Ca solutions and negligible contamination by Mg^{2+} ions does not inhibit growth perpendicular to the c-axis (Folk, 1974; Folk and Land, 1975). In contrast, marine dolomite cements (which do not naturally occur in seawater today, see above) always show length-slow character and commonly conform to three crystal forms termed 'radial slow', 'radiaxial slow' and 'fascicular slow' dolomite (Hood et al., 2011; Hood and Wallace, 2012, 2015, 2018).

The justification that some late Neoproterozoic carbonate cements represent original marine dolomite rests upon well-defined relationships between crystallographic character and knowledge of the nature by which dolomite replacement modifies pre-existing carbonate fabrics. For example, dolomitisation of a calcite cement precursor will be syntaxial and preserve the original character and optical continuity of calcite as a consequence of the common crystal form shared by both dolomite and calcite (trigonal rhombohedra, Figure 4.1) (Hood and Wallace, 2012). In contrast, dolomitisation of an aragonite precursor will only crudely preserve the original aragonitic fabric due to the contrast in crystal form between aragonite (orthorhombic) and dolomite (trigonal) (Hood and Wallace, 2012). As such, primary marine dolomite is represented by an isopachous and inclusion-rich cavity-lining cement which retains its original length-slow character (Hood and Wallace, 2012, 2018).

Mimetic preservation by dolomite (i.e., retention of original crystallographic orientation) of original aragonite and/or high-Mg calcite (HMC) grains (Tucker, 1982; Corsetti et al., 2006), as well as the presence of well-preserved dolomite cements, suggests that early marine dolomite precipitation dominated Cryogenian to early Ediacaran oceans (ca. 740 to ca. 630 Ma; Hood and Wallace, 2015, 2018) and was also a local feature in the terminal Ediacaran (~550 Ma; Wood et al., 2017a). This has been suggested to reflect widespread low-oxygen or redox-stratified oceans which were organic carbon rich and characterised by high Mg/Ca (Tucker, 1992; Hardie, 2003; Hood et al., 2011; Hood and Wallace, 2012, 2018). The combination of high iron (ferroan) concentrations in early dolomite cements (Hood and Wallace, 2015), ferroan dolomite concretions in shales and iron speciation data from shales further indicate that these oceans were anoxic and ferruginous (Canfield et al., 2008; Planavsky et al., 2011; Poulton and Canfield, 2011; Spence et al., 2016). Dramatically enhanced continental weathering occurred during the Neoproterozoic to early Cambrian which is inferred to have resulted in significant Ca^{2+} supply to seawater and permitted a marked increase in carbonate deposition (Hardie, 2003; Peters and Gaines, 2012). Fluid inclusion data confirm that seawater Ca^{2+} increased markedly and Mg^{2+} declined

slightly during the Ediacaran to early Cambrian, so progressively lowering seawater mMg/Ca by the early Cambrian (Brennan et al., 2004).

4.2 Redox and ecology during deposition of the Omkyk Member

This chapter considers mixed microbial-metazoan reefs from the Upper Omkyk Member of the Kuibis Subgroup which grew in the far north of the Zaris sub-basin in the late Ediacaran and are exposed on Farm Driedoornvlakte (Figures 4.3 and 4.4). Chemical abrasion ID-TIMS uranium-lead chronology of zircons (using the EARTHTIME double spike) from an ash bed in the immediately overlying lower Hoogland Member (upper Kuibis Subgroup) yield an age of 547.32 ± 0.65 Ma (Bowring et al., 2007; Schmitz, 2012).

During deposition of the Omkyk Member, the Zaris subbasin increased in depth with distance northwest from the Osis ridge and the deepest facies of the lower Omkyk Member are preserved at Brak, northwest of the Nauklufte Nappe Complex (Germs, 1974, 1983; Saylor et al., 1998; Wood et al., 2015). Palaeomarine redox conditions during deposition of the Lower and Upper Omkyk Member (OS1 and OS2 respectively) in the Zaris subbasin have been well constrained through a combination of iron speciation, cerium anomaly and carbonate-bound iodine data (Chapters 2 and 3, Wood et al., 2015; Tostevin et al., 2016b). The very shallow redoxcline which persisted throughout deposition of shelf grainstones of OS1 is evident from invariably anoxic ferruginous waters during transgression, to manganous conditions during the highstand systems tract at positions up to and including those represented by the shallowest deposits at Zwartmodder (see Figure 2.5). The deepest environment at Brak yields only one sample, where Ce/Ce* values indicate manganous waters (Tostevin et al., 2016b). Neither soft-bodied nor skeletal fossils have been noted from the Lower Omkyk Member to date.

In contrast, Upper Omkyk Member sediments (lower OS2) record a transition to well oxygenated conditions and reef growth at Driedoornvlakte took place during an interval of stable oxia (Chapter 3, Section 3.5.2). Similarly, oxic water column conditions dominated time-equivalent deposition at more proximal mid-ramp sites, including Zebra River where reefs also formed (Wood et al., 2015). The Upper Omkyk Member was accompanied by an abundant skeletal macrofauna and the earliest proposed evidence for complex bioturbation in the Nama Group (Figures 2.5 and 3.10, Germs, 1972b; Grotzinger et al., 2000; Adams et al., 2004; Penny et al., 2014, 2017; Macdonald et al., 2014; Wood et al., 2015, 2017b; Tostevin et al., 2016b). Brief intervals of ferruginous anoxia post-date the microbial-metazoan reef at Driedoornvlakte and are approximately contemporaneous across the subbasin, recorded in shales of the Urikos Member and more proximal deposits of OS2 Unit 3 – lower

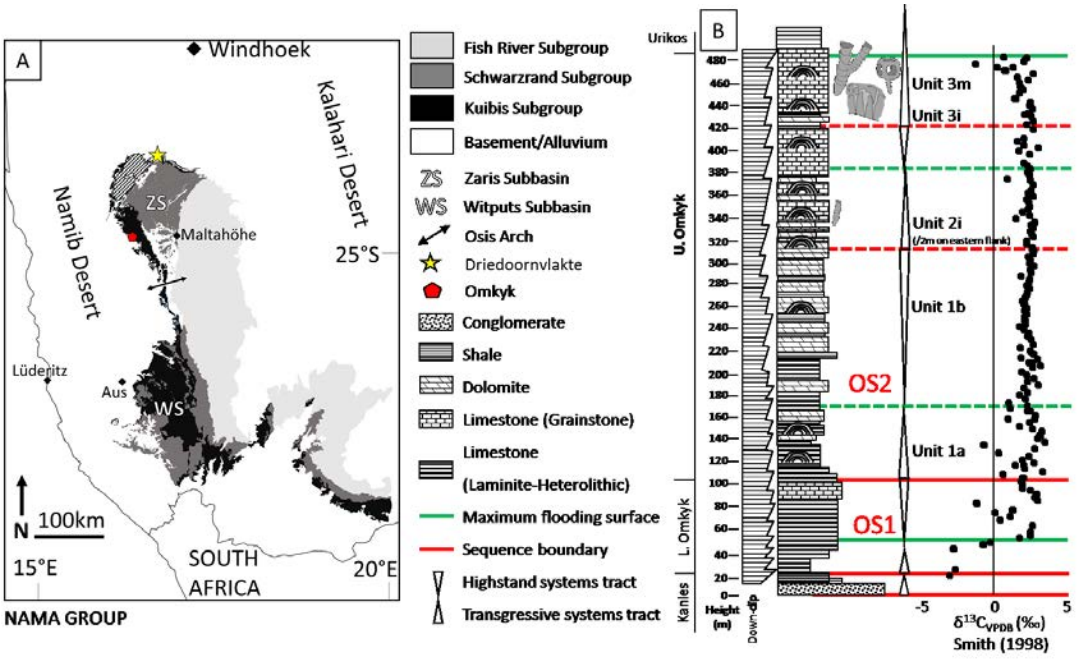

Figure 4.3 a) Location and stratigraphic setting of the Nama Group, Namibia. Simplified map showing geological setting, subgroups, and sub-basins of the late Ediacaran to early Cambrian Nama Group of southern Namibia, with the location of Farms Driedoornvlakte and Omkyk. **B)** Stratigraphic log of the Omkyk Member at the Driedoornvlakte isolated carbonate platform showing concurrent slope and basinal shale and overlying shale of the Urikos Member (after Adams et al., 2004) with carbon isotope chemostratigraphy (Smith, 1998).

Unit 4 (Chapter 3, Bowyer et al., 2017). Short-lived ferruginous intervals, variably associated with transgressive upwelling and shallow marine productivity-associated organic carbon oxidation continue to punctuate the palaeoredox record for the remainder of Kuibis Subgroup deposition and, to a lesser extent, the overlying Schwarzrand Subgroup (Chapters 2 and 3, Wood et al., 2015).

4.2.2 Architecture of the Driedoornvlakte Reef Complex

An isolated carbonate platform approximately 10 km in length and now exposed on Farm Driedoornvlakte grew in the far north of the Zaris subbasin less than 5km northeast of the easternmost extent of the Naukluft Nappe Complex (Figure 4.3a). The structural evolution, palaeontology and palaeoecology at Driedoornvlakte have been well studied over the past 46 years (Germs, 1972b, 1983; Grant, 1990; Smith, 1998; Grotzinger et al., 2000; Wood et al., 2002, 2017b; Adams et al., 2004,

2005; Penny et al., 2014, 2017; Wood and Curtis, 2015; Wood and Penny, 2018). The extremely expanded stratigraphic thickness of the Upper Omkyk Member at Driedoornvlakte (~500m) relative to shallower sections such as Zebra River (~160m) is inferred to relate to foreland basin subsidence in more northerly areas with proximity to the Damara orogen (Smith, 1998; Grotzinger and Miller, 2008). At Driedoornvlakte, growth of the carbonate platform kept-up with this subsidence-induced relative sea level increase during deposition of the Upper Omkyk Member but was eventually drowned by fine, basinal siliciclastics of the Urikos Member which were deposited equivalent to ongoing carbonate production of OS2 Units 4 and 5 in shallower sections to the south (Smith, 1998; Adams et al., 2004, 2005; Dibenedetto and Grotzinger, 2005).

Carbonate build-up of OS2 at Driedoornvlakte is interpreted to record 3 cycles of relative sea level change (Units 1 – 3) each of which are represented by sequentially expanded stratigraphic horizons as a consequence of increasing subsidence during deposition (Figure 4.3b and 4.4) (Adams et al., 2004). Microbial-metazoan reefs at Driedoornvlakte grew in association with coalesced thrombolite mounds of the final cycle of reef growth (Unit 3m), representing an ~50m thick transgressive succession which formed in a shallow subtidal setting immediately prior to drowning by Urikos Member sediments (Grotzinger et al., 1995; Adams et al. 2004). *Cloudina* reefs are associated with *Namacalathus*, and

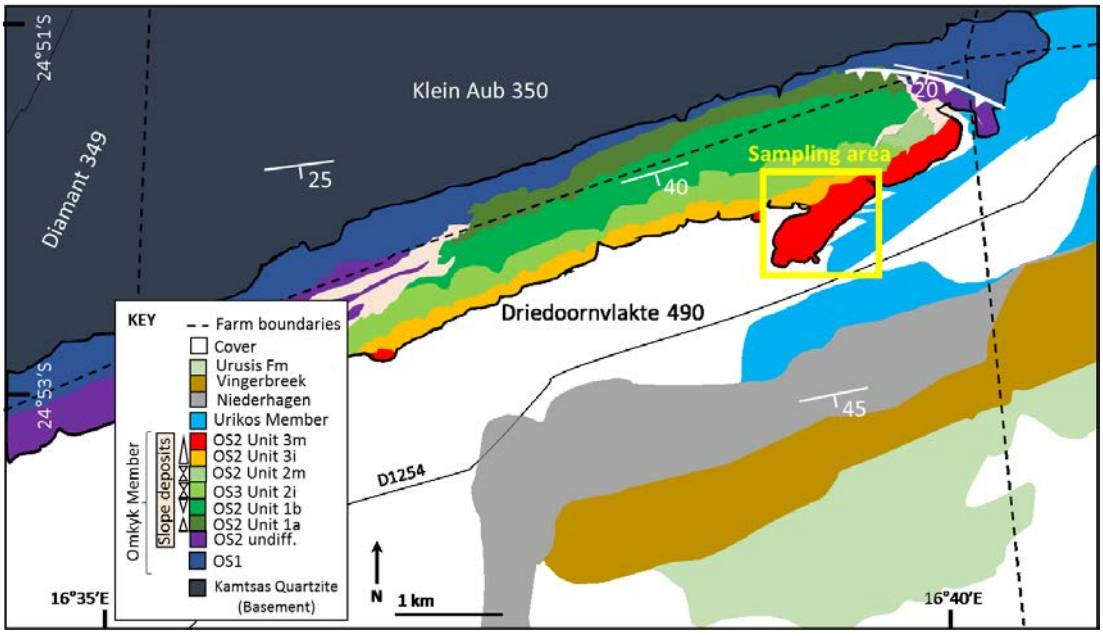

Figure 4.4 Geological map of the Driedoornvlakte isolated carbonate platform with the position of the sampling area in Unit 3m highlighted by the yellow box (after Adams et al., 2004).

Namapoikia, which preferentially inhabited synsedimentary fissures. There have been no recorded occurrences of evaporite pseudomorphs, karstification or any other features indicative of subaerial exposure or evaporitic conditions. The inferred accommodation increase during deposition of Unit 3m is based upon an observed increase in size of coalesced thrombolite-stromatolite mounds and formation of synsedimentary fissures and collapse breccias (Adams et al., 2004).

In Unit 3m, *Cloudina* formed reefs by mutual attachment either to each other or to diffuse, micro-clotted, thrombolite (Penny et al., 2014; Wood and Curtis, 2015). Reefs have been interpreted as composite, composed of up to 20 repeated lens-shaped units or assemblages, 10-30 cm in height and up to 3 m in length (Figure 4.5a, Wood and Curtis, 2015; Wood et al., 2017b). The upper part of these units grades into a layer 5-32 mm thick, which is preferentially dolomitised and composed of an increasing density of microthrombolitic clots, stromatolitic laminae, or thin (< 1 mm) discontinuous to highly laterally continuous layers of sediment with dolomite cement crusts (Figure 4.5a). The final layers, commonly composed of geopetal micrite sediment, mark a sharp boundary before growth of the

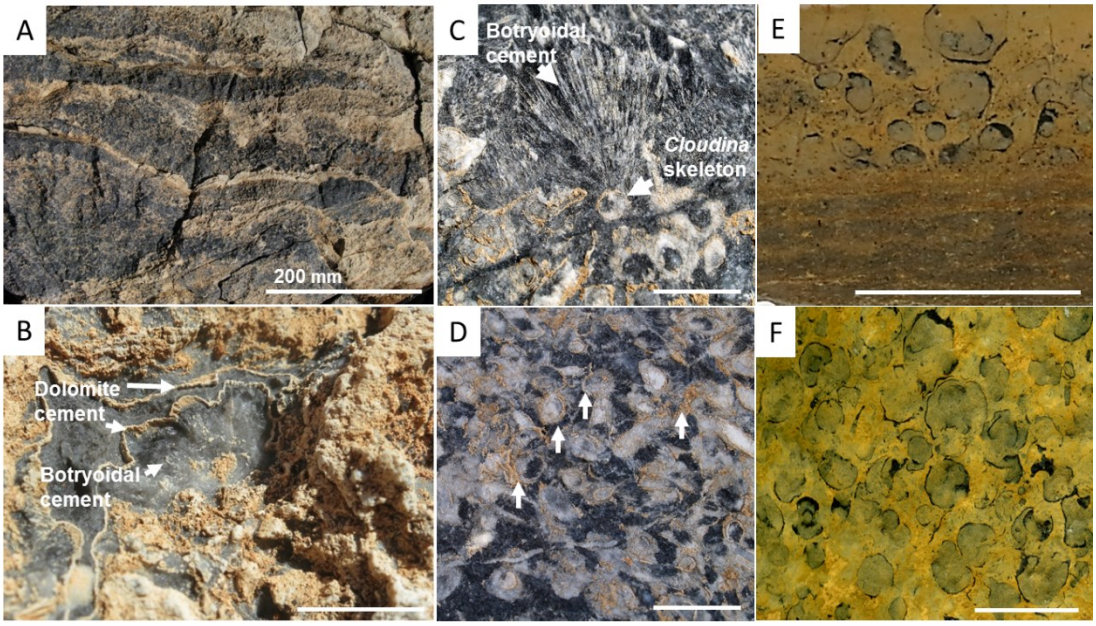

Figure 4.5 Field photographs of *Cloudina* reef in Unit 3m. **A)** Repeated assemblages of *Cloudina* reef terminated by light brown dolomitised sediment. **B)**, Reef void filled with botryoidal cement encrusted by dolomite cement. **C)** Recrystallised *Cloudina* individual encrusted by botryoidal cement, **D)** Recrystallised *Cloudina* skeletons showing localised dolomitisation of some shell walls **E, F)** Inner ramp *Namacalathus* assemblage showing dolomitisation of surrounding micritic sediment, but retention of limestone within the *Namacalathus* cups. **E**, Longitudinal polished section. **F**, Bedding plane surface. Scale bars 10 mm unless noted.

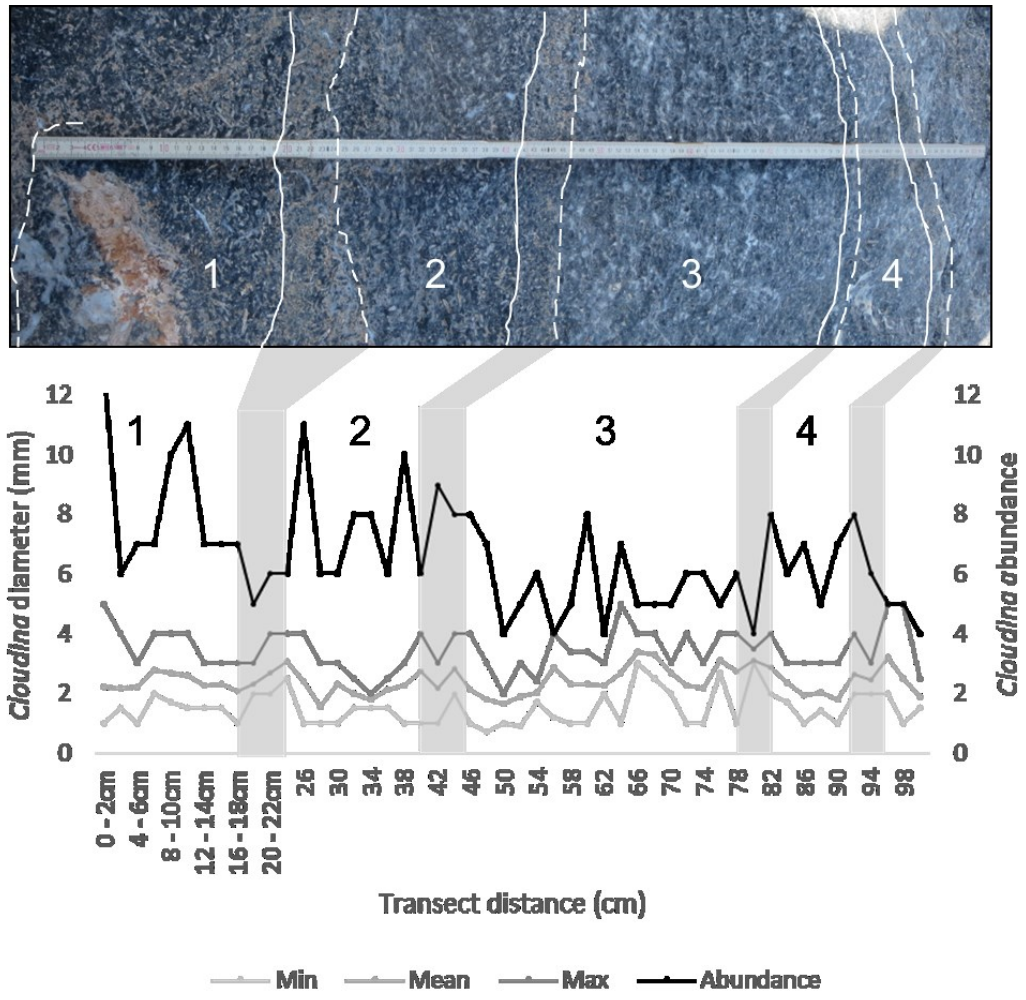

Figure 4.6 Size distribution and abundance of *Cloudina* through Driedoornvlakte reef. Diameter (grey lines, scale on left) and abundance (black lines, scale on right) of *Cloudina* at 2 cm increments along a tangential ~100 cm transect (modified after Wood et al., 2017b). Shaded areas are dolomitised layers at the top of each assemblage.

succeeding unit, and may be erosionally-truncated (Wood et al., 2017b). *Cloudina* in the Nama Group are known to have been only weakly mineralised (Germs, 1972b; Wood and Curtis, 2015) and a recent, impressive three-dimensional reconstruction of *Cloudina* 'thicket' material at Driedoornvlakte has shown that some lenses are partially composed of detrital shell hash material (Mehra and Maloof, 2018). However there is clear evidence that other portions of the pinnacle reef of Unit 3m preserve mutually-cemented *Cloudina* individuals which formed framework structures (Penny et al., 2014) and the overall paragenetic sequence of cements appears to be uniform throughout Unit 3m (see below).

Reefs were highly porous structures, with pore space between adjacent individuals and within large enclosed cavities (up to 300 mm diameter) being filled dominantly with carbonate cements, and a

small volume of microbialite and geopetal sediment (Grotzinger et al., 2000; Penny et al., 2014; Wood and Curtis, 2015). As such, full communication with the overlying seawater was maintained prior to shallow burial.

Abundant dolomite cement is also recognised in the field, often noted to encrust pseudomorphed aragonitic botryoids within voids in addition to *Cloudina* individuals (Figure 4.5b-d) (Figures 3b-d of Wood and Curtis, 2015). Dolomite cement increases in volume from the base to the top of each assemblage, and field observations suggest that its occurrence was controlled by the available pore space for precipitation after synsedimentary growth of botryoidal cement. The size of *Cloudina* varies through each successive community, including an increase in *Cloudina* diameter towards the top of each assemblage (Wood et al., 2017b). Abundance (density), however, shows no correlation with successive position within a community, but does show an overall general decrease through the ~ 1 m vertical transect measured for this study (Figure 4.6). Environmental controls on *Cloudina* size are unknown, and may include cyclical changes in nutrient levels, water depth, hydrodynamic energy, space availability, or carbonate supersaturation.

4.3 Reconstructing cement stratigraphy of *Cloudina* reef carbonates

4.3.1 Methods

Sampling of palaeontological specimens from the Driedoornvlakte pinnacle reef was conducted across a number of field expeditions led by Rachel Wood between 2002 and 2016. Sample material commonly consists of large specimens wherein the palaeo-horizontal has been confidently defined based on micritic geopetal sediments within and around *Cloudina* individuals. The sample collection analysed in the following study consists of specimens collected from multiple areas of the ~ 50m thick mixed microbial-metazoan pinnacle reef of Unit 3m which outcrops on the southeast flank of the carbonate build-up on Farm Driedoornvlakte (Figure 4.4).

Selected hand samples from the *Cloudina* reef TST at Driedoornvlakte were sliced and areas targeted from which large thin sections were made (75 x 50 mm). Thin sections were etched with 0.06 M hydrochloric acid for 10 s followed by staining with a mixed solution of Alizarin Red S and Potassium ferricyanide in 0.06 M HCl for approximately 30 s before rinsing with deionised water after the method outlined by Dickson (1965). The acidified solution preferentially dissolves (and thus more effectively stains) calcite which throws dolomite into sharp definition as a colourless cement in a mass of pink-stained recrystallized calcite.

Twenty-three highly polished thin sections were examined under transmitted light and cathodoluminescence microscopy. Differing luminescence was observed through use of a Cold Cathode CITL 8200 MK3A mounted on a Nikon optiphot microscope (Habermann et al. 1996; 1998; Mason and Mariano, 1990). Seven highly polished thin sections were further analysed and all cements targeted for major element concentrations (Fe, Ca, Mg, Mn, Sr) using a Cameca SX100 Electron Microprobe at the University of Edinburgh with an 80 s count time, a beam diameter of 3 μm, an accelerating voltage of 15 kV, and a beam current of 35 nA (see Appendix C for maps of electron probe sampling transects).

Powders of sample size 0.03-0.20 mg were removed for isotope analysis from thin sections using a tungsten steel needle under a Leica 240 microscope. Powders were dissolved at 25°C with 100% phosphoric acid followed by conventional mass spectrometry using a Thermo Electron Delta+ Advantage stable isotope ratio mass spectrometer. Results are reported as deviations from the Vienna PeeDee Belemnite (VPDB) standard (‰) and precision was measured at a level better than 0.1‰ for $\delta^{13}C$ and $\delta^{18}O$.

Dolomite stoichiometry was obtained on one sample via the 104 peak shift XRD method (Lumsden and Chimahusky, 1980), using a weighted mean incident wavelength for CuKα radiation of 1.541838Å and the $^{d}104$ peak at a 2θ angle of 30.9° (See Appendix C for details of this method).

4.3.2 Results

Samples show a diagenetic paragenetic sequence of six successive cement generations upon a *Cloudina* skeletal reef framework (Figure 4.7), each with distinct cathodoluminescence characteristics and Fe and Mn concentrations (see Table 4.1 and Appendix C). *Cloudina* skeletons (CS) are preserved as neomorphic calcite or finely crystalline calcite, in some cases with microdolomite inclusions, or can be completely dolomitised (Figure 4.8e). Where not dolomitised, Mn concentrations are up to 1130 ppm (mean 160 ppm; n = 48), and Fe concentrations reach 630 ppm (mean 140 ppm; n= 48). Sr concentrations reach up to 1600 ppm (mean 480 ppm; n= 48).

Facing Page: Table 4.1 (top) Elemental concentrations (ppm) of Fe, Mn, and Sr, and Mg/Ca and Mn/Sr for un-dolomitised *Cloudina* and each cement type. **Figure 4.7 (bottom)** Proposed paragenetic sequence of cements in the Driedoornvlakte reef of Unit 3m (b-e coloured according to CL characteristics).

Component	Mg/Ca				Mn				Fe				Sr				Mn/Sr			
	Min	Max	Mean	Standard Deviation	Min (ppm)	Max (ppm)	Mean (ppm)	Standard Deviation	Min (ppm)	Max (ppm)	Mean (ppm)	Standard Deviation	Min (ppm)	Max (ppm)	Mean (ppm)	Standard Deviation	Min	Max	Mean	Standard Deviation
Acicular Cement (AC)																				
Cloudina Skeleton (CS)																				
Dolomitised Sediment (DS)																				
Dolomite 1 (D1)																				
Dolomite 2 (D2)																				
Calcite 1 (C1a)																				
Calcite 1 (C1b)																				
Calcite 1 (C1c)																				
Calcite 2 (C2)																				

Large, volumetrically abundant acicular cements (AC) (Figure 4.8b) that reach up to 50 mm in radius and exhibit square crystal terminations appear to have dominantly nucleated upon *Cloudina* skeletons (Figures 4.8b) or grew during deposition of geopetal sediment (Figure 4.8a). Acicular cements are mainly non-luminescent (Figure 4.9c, arrowed) and are volumetrically most abundant in the lower to middle parts of each assemblage where they may occlude most or all pore space. Mn concentrations for the acicular cements are below detection limits (BDL) and Fe concentrations are close to detection limits (150 ppm) whilst Sr concentrations are up to 6900 ppm (mean 1890 ppm) (n= 21).

At the top of assemblages, thin (< 1 mm) layers of dolomite geopetal, internal micritic sediment (DS) appear, commonly with a nonplanar texture (Sibley and Gregg, 1987; Figures 4.8a, f). The sediment appears only in the upper parts of each assemblage and often, but not always, terminates growth of acicular cement (Figure 4.8a). Geopetal sediments also commonly infill *Cloudina* individuals (Figure 4.9a), and ranges in elemental composition of these sediments are indistinguishable from those which overlie acicular cements and *Cloudina* shells. The dolomite geopetal sediment fill has elevated Fe (up to 6850 ppm, mean 1980 ppm), and slightly elevated Mn (up to 1000 ppm, mean 220 ppm) whilst Sr has a maximum concentration of 720 ppm, mean (150 ppm) (n = 52).

The microcrystalline shell structure of some *Cloudina* individuals has been partially or completely dolomitised and, where this material has been targeted, it is noted as dolomite 1 (D1). D1 is mid-brown and inclusion-rich, with poorly preserved, often patchy, CL zonation. Pervasive recrystallisation of individual D1 crystals commonly obscures grain boundaries and original crystal width is consequently difficult to accurately estimate but is certainly < 20μm (Figure 4.8e). There then follows a thin isopachous, dolomite cement crust (D2) which is paler brown, inclusion-rich, with poor (patchy), but occasionally well-preserved CL zonation of usually dull zones that do not extend across crystal boundaries (Figures 4.8d, e, 4.10). Under cross-polarised light and where best preserved, individual

---

Figure 4.8 Transmitted light photomicrographs of cements in plane polarised light. Fibrous botryoidal cement nucleating on dolomitised sediment (**A**), and *Cloudina* skeleton (**B**). Dolomitised geopetal sediment commonly overlies botryoidal cement and *Cloudina* skeleton fragments (**A, B, C, F**). Inclusion-rich generation of isopachous dolomite cement encrusts a recrystallized *Cloudina* skeleton (**D, F**), succeeded by the second generation of dolomite cement (**A, C, D-F**) sometimes showing evidence for dissolution (**D**). (**G**) Clearly shows the order of cement generations up to and including D2. CS: *Cloudina* skeleton, AC: Acicular fibrous cement, DS: Dolomitised sediment, D1: Dolomite cement 1, D2: Dolomite cement 2, C1: Calcite cement 1, C2: Calcite cement 2.

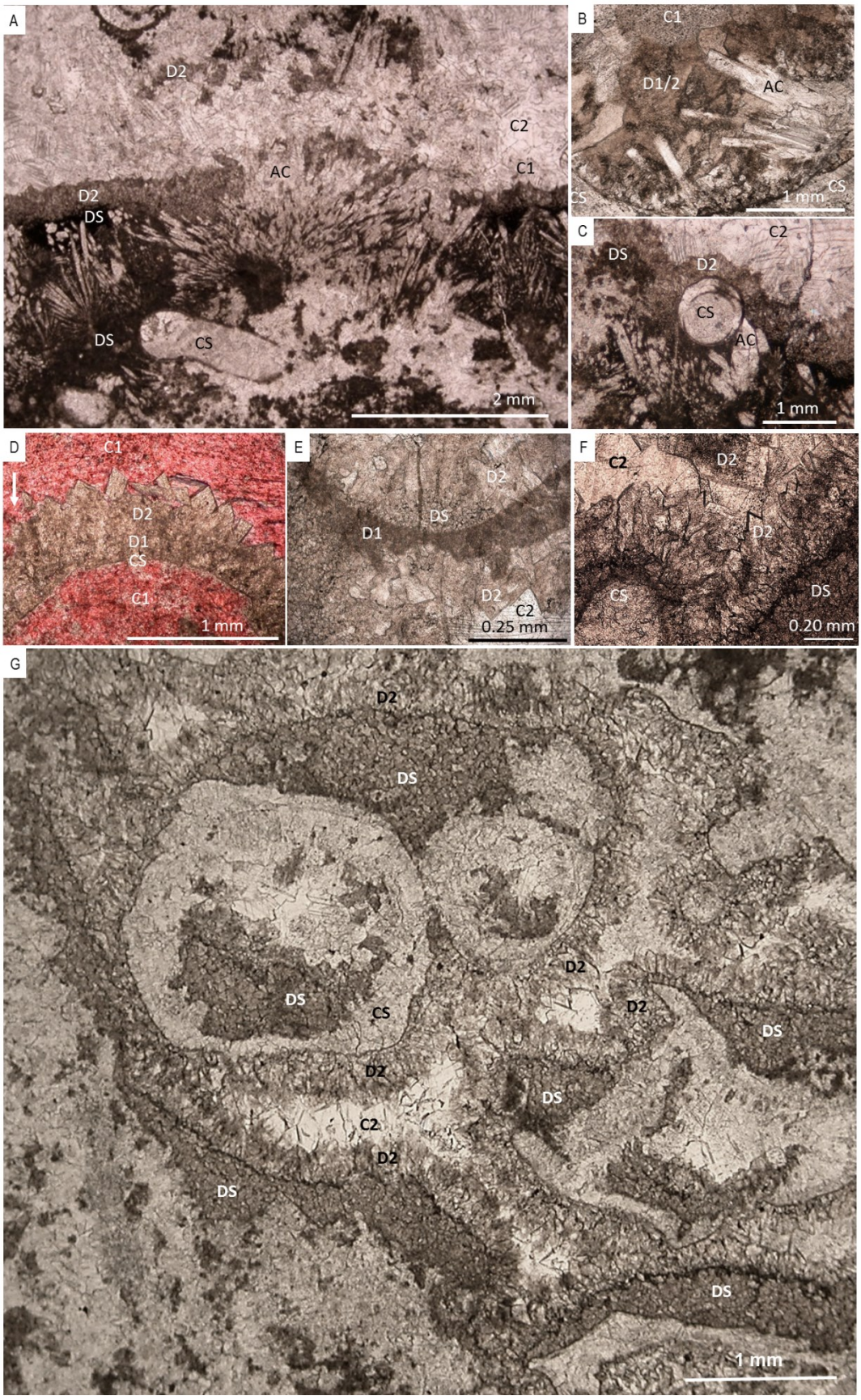
A
D2
C2
AC
C1
D2
DS
DS
CS
2 mm
B
C1
D1/2
AC
CS
CS
1 mm
C
C2
DS
D2
CS
AC
1 mm
D
C1
D2
D1
CS
C1
1 mm
E
D2
DS
D1
D2
C2
0.25 mm
F
C2
D2
D2
CS
DS
0.20 mm
G
D2
DS
D2
DS
CS
D2
D2
DS
DS
C2
D2
DS
DS
1 mm

Figure 4.8

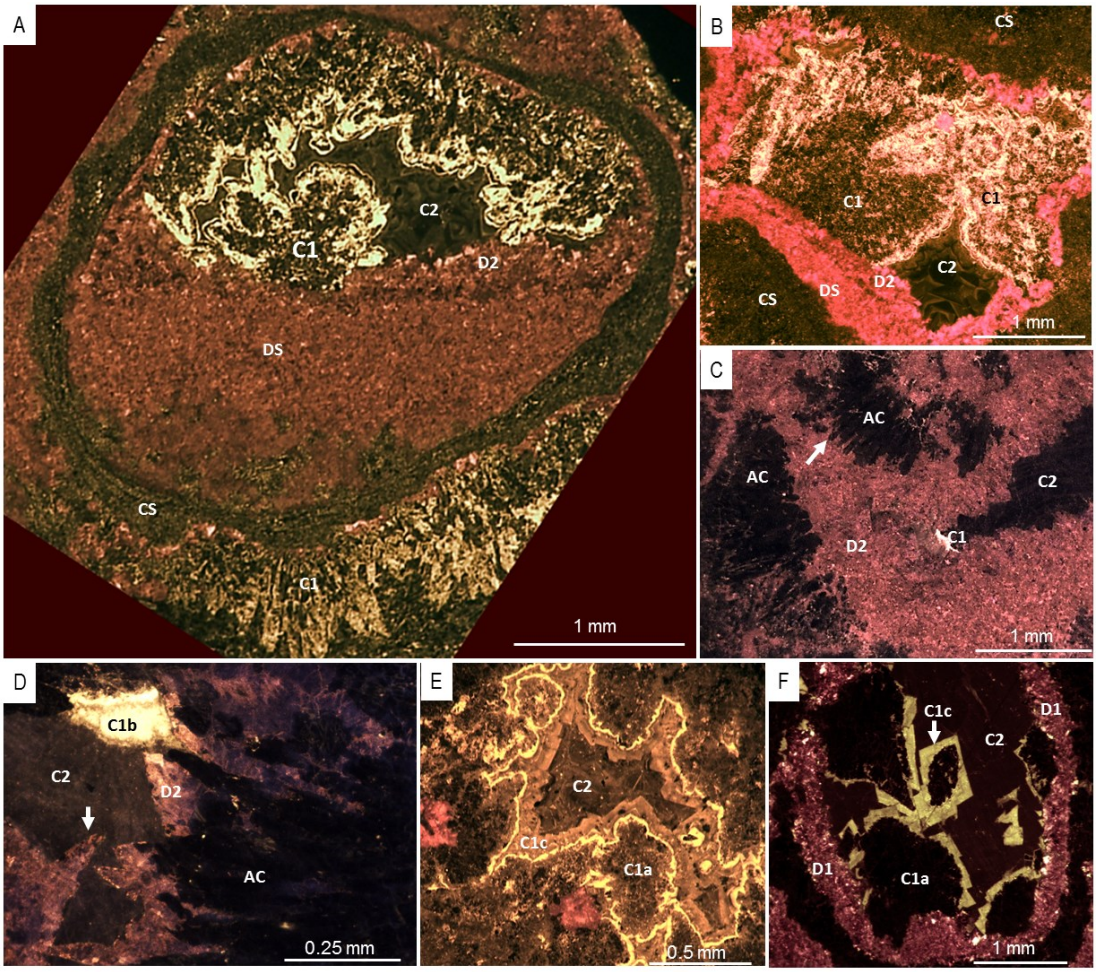

Figure 4.9 Cathodoluminescence photomicrographs of cements. **A**, Recrystallised *Cloudina* skeleton partially filled with dull luminescent dolomitised geopetal sediment, which is successively encrusted by dolomite cement and brightly luminescent fibrous calcite cement. The remaining pore space is occluded by dull luminescent calcite. **B**, Successive cements within pore space invariably follow the sequence: dull luminescent isopachous dolomite cement (Fe-rich, Mn-poor), non to bright luminescent fibrous calcite cement (Mn-rich, Fe poor), and finally dull luminescent blocky calcite (Fe and Mn-poor). **C**, Non-luminescent fibrous acicular cement (Fe and Mn poor) is encrusted by an isopachous, heavily altered dolomite cement (Fe rich, Mn poor), the remaining pore space is lined by a thin, brightly luminescent Mn-rich calcite and finally non-luminescent Fe and Mn-poor calcite. **D**, Fibrous acicular cement locally shows evidence for partial dolomitization (arrowed). **E**, Fibrous C1 cement is locally overgrown by limpid cement of moderate luminescence (C1c) prior to pore occlusion by non-luminescent block calcite (C2). **F**, Where present, C1c commonly precipitated about C1(a/b) epitaxially.

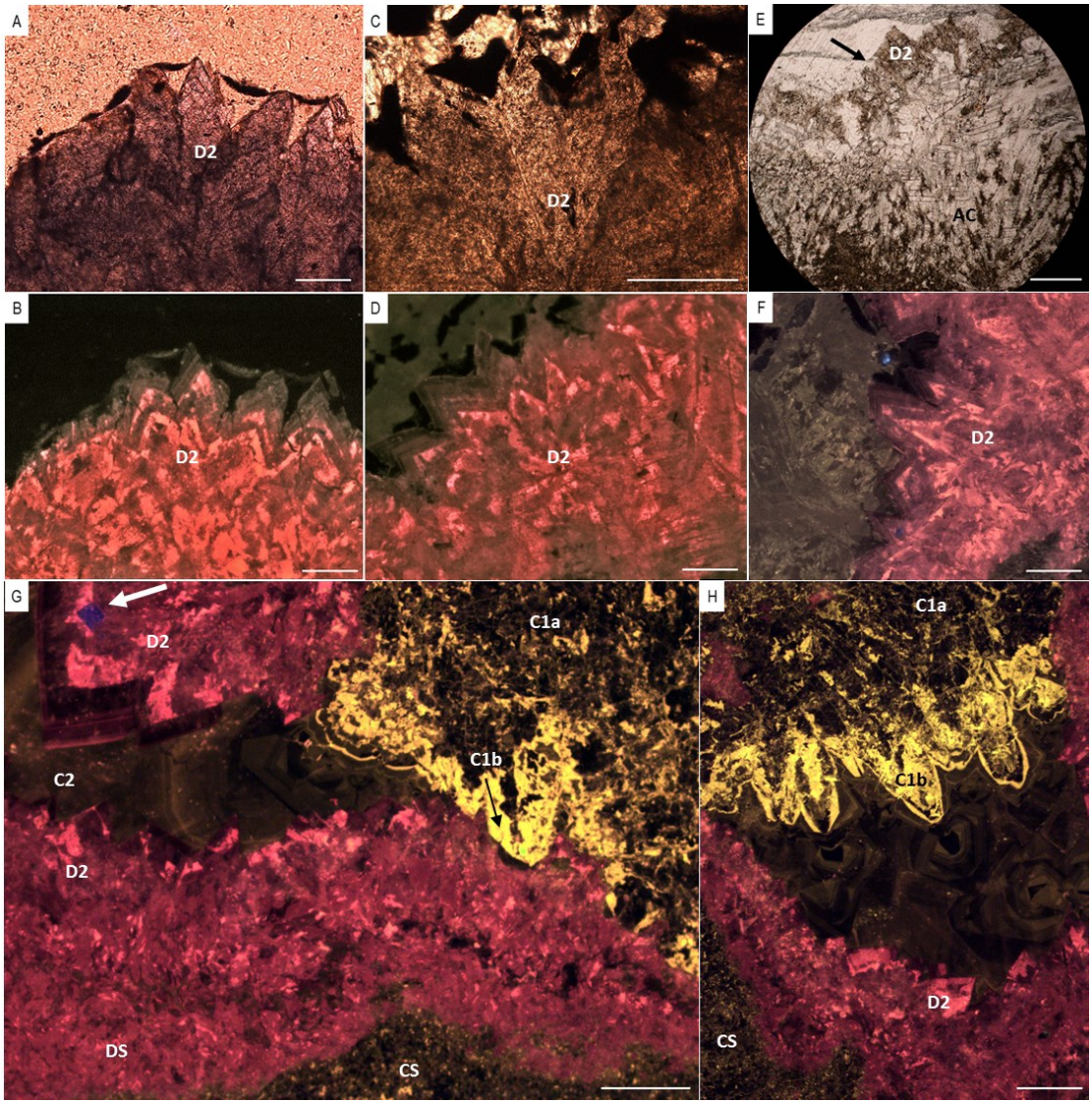

Figure 4.10 Selected photomicrographs to show the petrographic characteristics of D2 and C1 cement generations. Where best preserved, D2 cement exhibits fine CL zonation (**B, D, F, G**) with the final growth zones commonly the dullest (**G**). **A** and **C** are plane polarised light images of **B** and **D** respectively. Dissolution of crystal terminations is common in D2 (**E**). Acute rhombic terminations typical of high-Mg calcite are exhibited when the plane of the thin section bisects the D2 cement parallel (/near-parallel) to the c-axis (**F**). Fluorite is rarely present as an accessory mineral within D2 cement (white arrow in **G**). **H**, Fibrous columnar, scalenohedral nature of C1 is best exhibited when plane of thin section bisects the crystal parallel to the c-axis. All scale bars are 0.1 mm.

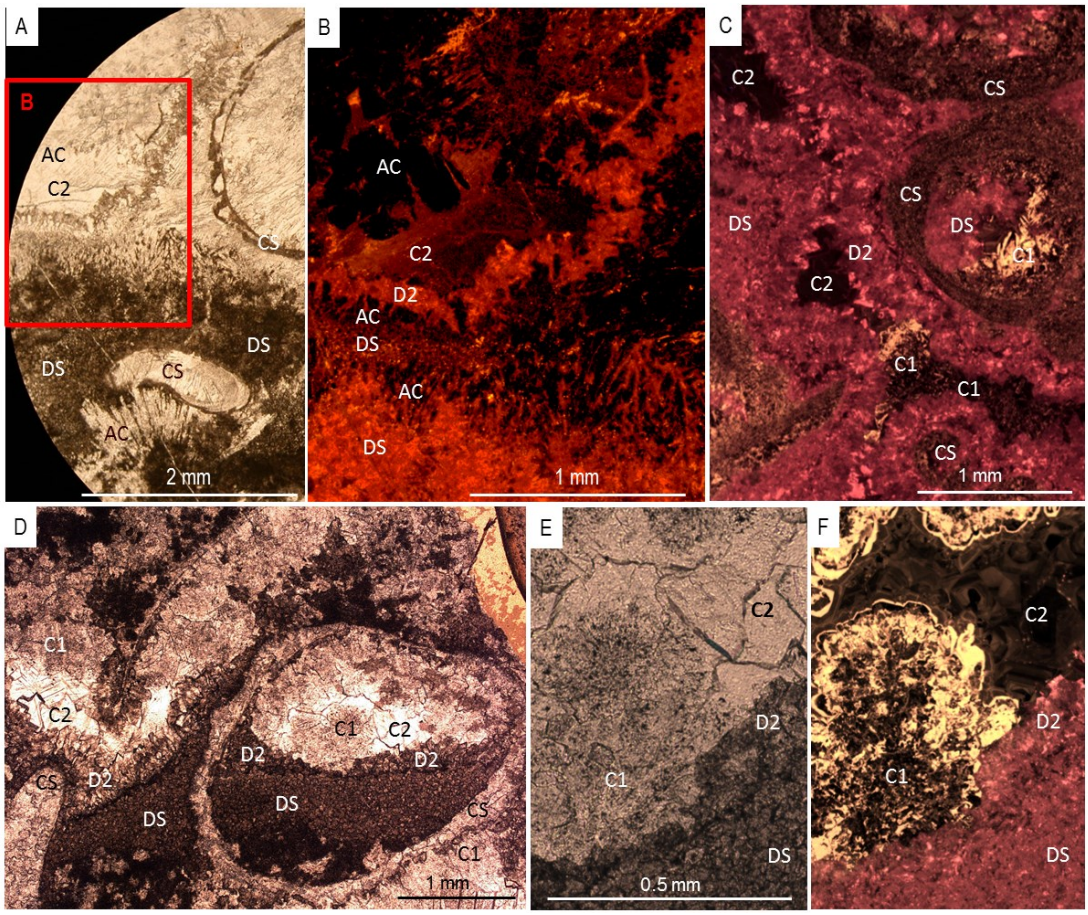

Figure 4.11 Photomicrographs of cements. **A**, Transmitted light photomicrograph of cements in plane polarised light. Image clearly shows cement stratigraphy with repeated burial of acicular cement (inferred aragonitic precursor) cement by dolomitised sediment, which is then capped by a crust of dolomite cement with length-fast character. **B**, enlarged cathodoluminescence image of boxed area in **A**. Early acicular marine cement repeatedly nucleates on top of dolomitised sediment and is finally encrusted by an isopachous dolomite cement (D2). Final pore space is occluded by non-luminescent calcite cement. **C**, Cathodoluminescence photomicrograph showing well-developed isopachous dolomite cement (D2) encrusting *Cloudina* skeletons. Remaining pore space is occluded successively by non-brightly luminescing fibrous calcite (C1) and finally non-luminescent blocky calcite (C2). **D**, Transmitted light photomicrograph in plane polarised light. *Cloudina* reef framework with dolomitised geopetal sediment fill encrusted by dolomite cement (D2). Remaining pore space is occluded by two generations of calcite cement, inclusion-rich C1 and blocky, inclusion-poor C2. **E**, Transmitted light photomicrograph in plane polarised light showing turbid, inclusion-rich nature of fibrous, brightly luminescing, Mn-rich calcite cement (C1), **F**, Cathodoluminescence photomicrograph of (**E**).

crystals of D2 cement show unit extinction. The D2 cement precipitates either vertically upon geopetal sediment (Figures 4.8a, g), radially around *Cloudina* skeletons (Figures 4.8c-g), or directly upon acicular cements (Figures 4.9c, d) and crystals largely show a unimodal size distribution (length = 250 μm, max width = 200 μm), suggestive of a single cementation event (Machel, 2004). Fibrous D2 cements appear to regularly show a radial length-slow character (Figures 4.9 and 4.10) with obtuse rhombic crystal terminations, however in other areas D2 clearly exhibits acute terminations indicative of a length-fast character (Figure 4.10f) (Dickson, 1983, 1993; Hood and Wallace, 2012, 2018). This difference in inferred crystallographic character may simply be a consequence of perspective whereby the plane of the thin section bisects length fast crystals at angles divergent from the c-axis (Dickson, 1983). D2 shows evidence for multiple phases of dissolution, particularly near crystal terminations (arrowed in Figures 4.8d, and 4.10e). The dolomite crust becomes most abundant in the upper parts of each assemblage where more pore space was available (i.e. less occlusion by acicular cements) but is also well developed in localised areas of shelter porosity beneath or within *Cloudina* individuals (e.g. Figure 4.8g). Dolomite 1 shows elevated Fe (up to 9750 ppm, mean 880 ppm), low Mn (up to 820 ppm, mean 120 ppm) and Sr reaches up to 720 ppm (mean 150 ppm) (n= 38). Dolomite 2 also shows elevated Fe (up to 7020 ppm, mean 1440 ppm) and low Mn (up to 850 ppm, mean 230 ppm) and Sr has a maximum value of 670 ppm (mean 130 ppm) (n = 143).

In some rare instances, D2 cements contain cubic crystals with a maximum diameter of 20 μm which display blue-violet luminescence under CL (white arrow in Figure 4.10g). These features are consistent with fluorite, which is not uncommon as an accessory mineral in dolomite as a consequence of increasing Ca^{2+} and decreasing Mg^{2+} (resulting in displacement of MgF^{+} complexes) in pore solutions during dolomitisation (Dickson, 1980; Möller et al., 1980).

X-ray diffraction was undertaken on one sample of mixed composition (calcite, dolomite and dolomitised cement) wherein the relative positions and intensities of characteristic dolomite peaks suggest a dolomite composition which is non-stoichiometric and calcic 47.33 mole% $MgCO_3$ but is likely relatively well ordered (see Appendix C for discussion of XRD data). Electronprobe data reveal a range of Mg/Ca from 0.40 to 0.66 (n = 184). There do not appear to be any uniform trends in Mg/Ca through individual dolomite cements from nucleation point of D1 to crystal termination of D2 (see Appendix C).

A cloudy, inclusion-rich low-Mg calcite cement (C1) follows, forming as scalenohedra with an initial non-luminescent columnar portion (C1a), followed by a dominantly brightly luminescing zone (C1b) (Figures 4.9a, b; Figure 4.11e-f). These columnar scalenohedral cements invariably radiate from single points, forming bundles which, when cut perpendicular to the plane of the thin section, appear as rosettes with non-luminescent to patchy bright luminescent cores (C1a) and brightly luminescing rims

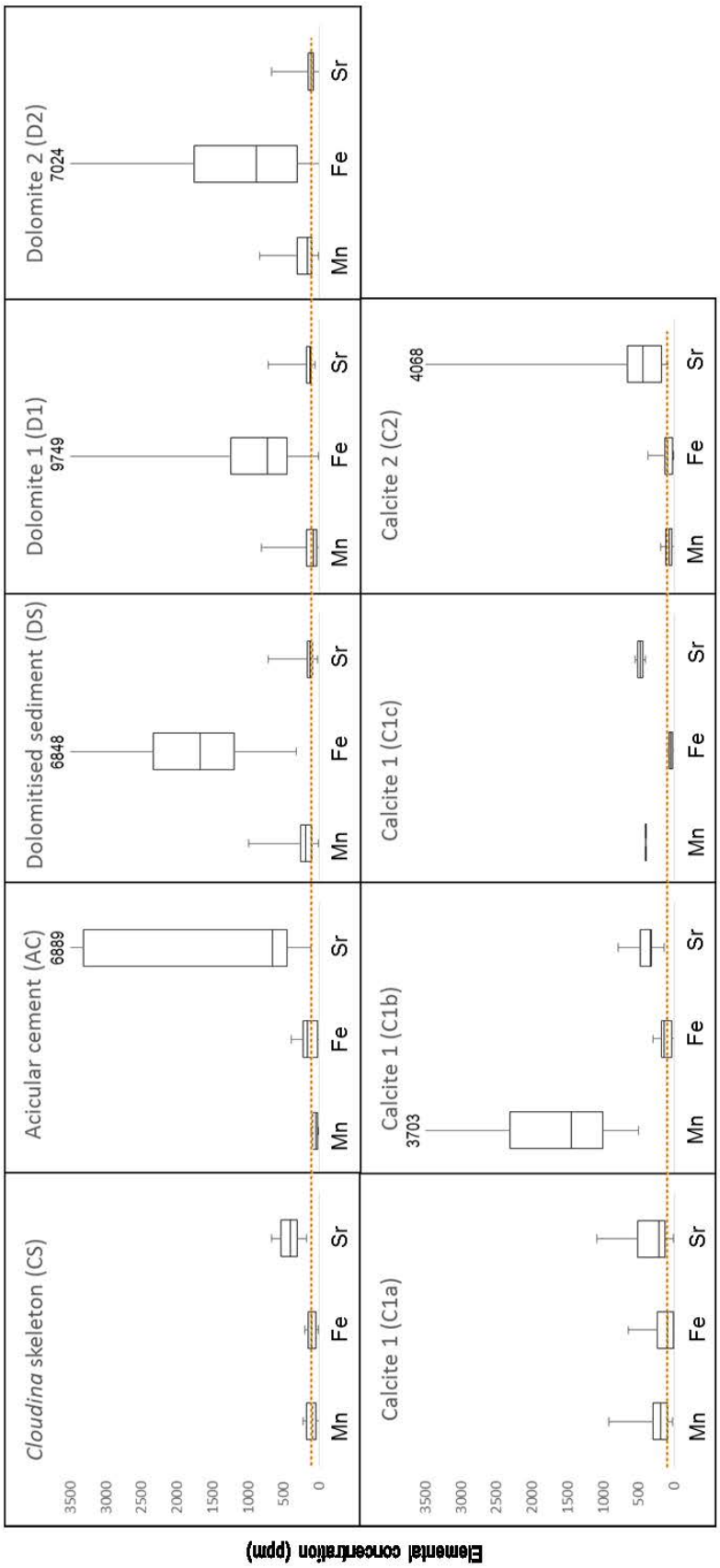

Figure 4.12. Box and whisker plots of basic statistics and ranges in elemental concentration between *Cloudina* skeleton and different cements. Red dotted line is detection limit for Fe; Yellow dotted line is detection limit for Mn.

(C1b). These cements are not isopachous but may grow vertically upward or suspended from cavity ceilings and directly nucleate upon D2, skeletal *Cloudina* material or AC cements. There are no noted incidents of C1 cements being overgrown by D2 and this cement is robustly interpreted as postdating growth of D2. These cements differ from later pore-occluding cements by being inclusion-rich with a length-fast character and individual crystals exhibit an average length-width ratio of 5:1 when the plane of the thin section bisects the crystal parallel to the c-axis (e.g. Figure 4.10h). In C1a, Fe is low (up to 650 ppm, mean 180 ppm), as is Mn (up to 930 ppm, mean 240 ppm) and Sr is up to 1100 ppm, (mean 340 ppm) (n = 21). In C1b, Fe is low (up to 300 ppm, mean 120 ppm), Mn is notably elevated (up to 3700 ppm, mean 1600 ppm) and Sr is up to 800 ppm, (mean 400 ppm) (n = 14). The non-luminescing zones of C1a and C1b are etched by dissolution (Figure 4.11f).

In some rare instances, C1 is overgrown by a euhedral calcite precipitate of moderate luminescence (C1c) (brighter than D1 and D2 but duller than C1b) which lacks inclusions but preserves fine CL zonation with only very minor variability in luminescence between growth zones. This precipitate sometimes appears as an epitaxial overgrowth of C1 (Figure 4.9e) and invariably lacks evidence for dissolution at crystal terminations. C1c clearly postdates all other carbonate components with the exception of the final pore occluding calcite precipitate discussed below and is characterised by iron below detection, low Mn (max 405 ppm, mean 400 ppm) and low Sr (max 550 ppm, mean 480 ppm) (n = 2).

All remaining pore space is occluded by a low-Mg blocky calcite (C2) which most commonly shows straight extinction in cross polars but may occasionally show twinning (Appendix C, Figure AC3a) and invariably shows non- to dull-luminescence (Figure 4.11f). Both Fe and Mn are below detection in C2 whilst Sr is up to 4070 ppm (mean 790 ppm) (n = 15). An additional volumetrically sparse component is represented by patchy non- to dull luminescent rhombic dolomite crystals of up to 250 μm in maximum length which appear to float within C2 or aggregate about zones of complex dissolution which display moderate luminescence similar to C1c.

Summarised elemental data reveal the distinctive elemental composition of the cements (Figure 4.12). Acicular cements (AC) have high Sr concentrations, but low Fe and Mn. Non-dolomitised *Cloudina* skeleton (CS) has slightly elevated Sr concentrations, but low Fe and Mn. Dolomitised sediment (DS), dolomitised *Cloudina* skeleton (D1) and dolomite cement (D2) have notably high Fe and low Mn and Sr. Calcite cement 1a (C1a) has low Fe, Mn and Sr, but calcite cement 1b (C1b) has low Fe and Sr but high Mn. The few sampled areas of calcite 1c (C1c) indicate low Mn, Fe and Sr and final pore occlusion by calcite 2 (C2) records low Fe and Mn but slightly elevated Sr.

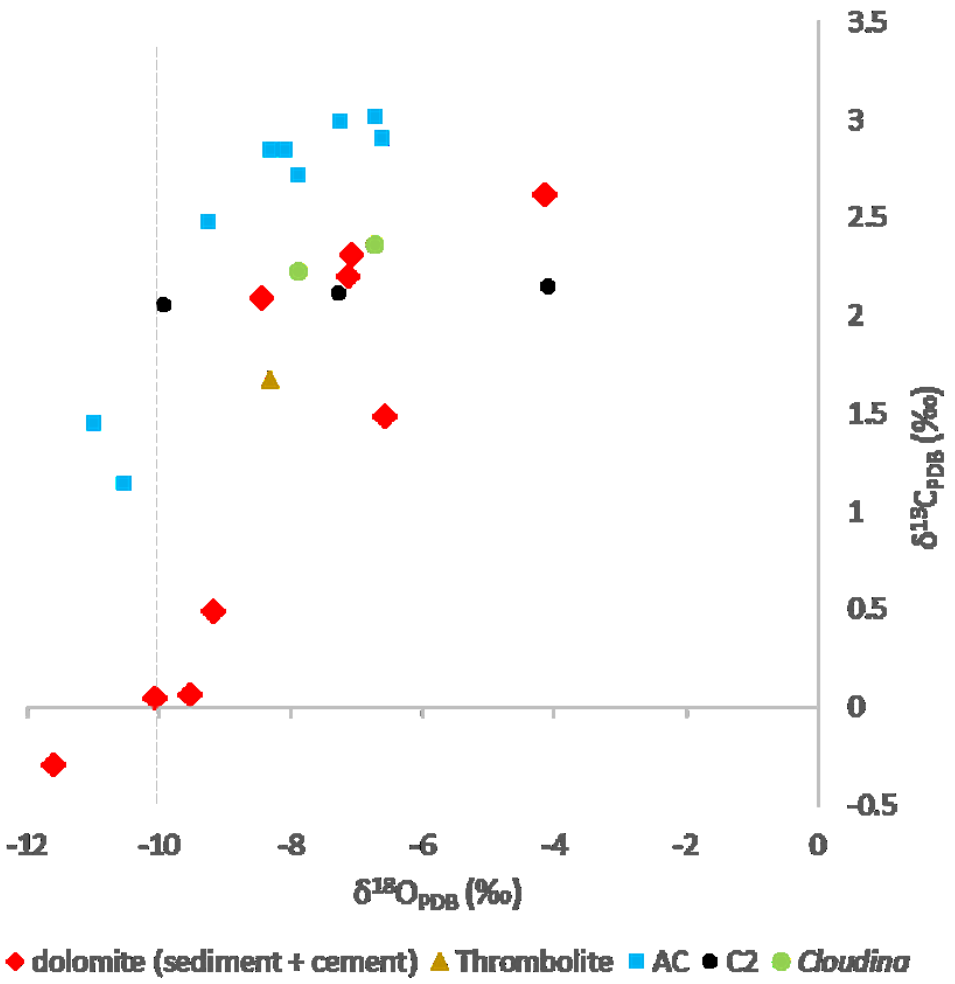

Figure 4.13 $\delta^{13}C_{carb}$ and $\delta^{18}O_{carb}$ cross plot for separated skeletal, calcite and dolomite cements. To left of dash are values where $\delta^{18}O_{carb}$ < -10 ‰.

Cloudina skeleton, thrombolite, acicular cement and calcite spar cement show a narrow range of $\delta^{13}C_{carb}$ from 1.15 to 3.02‰ (mean 2.28‰), and $\delta^{18}O_{carb}$ from -10.99 to -4.09‰ (mean -8.02‰). Combined dolomitised sediment and dolomite cements show a slightly wider range of $\delta^{13}C_{carb}$ from -0.29 to 2.62‰ (mean 1.22‰), and a similar range of $\delta^{18}O_{carb}$ from -11.60 to -4.15‰ (mean -8.19‰) (Figure 4.13). There is a notable positive correlation between $\delta^{13}C_{carb}$ and $\delta^{18}O_{carb}$ for each carbonate component with the exception of the late stage pore-occluding C2.

4.4 Discussion

4.4.1 Interpreting combined visual microscopy and electronprobe data

Iron and manganese concentrations influence cathodoluminescence in marine carbonate cements, so providing constraints on the redox conditions for the pore fluids (Barnaby and Rimstidt, 1989; Hood and Wallace, 2015). Electronprobe measurements support the following CL interpretations: non-luminescent cements have low Fe and Mn; bright luminescent cements have high (activating) Mn values, but low Fe; and dull luminescent cements have moderate values of both Fe (quenching) and Mn. A non-luminescent, through bright, to dull luminescent stratigraphic progression is caused by carbonate precipitation in waters with decreasing E_H that are in equilibrium with poorly crystalline Fe–Mn oxides (Barnaby and Rimstidt, 1989). The overall Fe–Mn and cathodoluminescence behaviour of the Driedoornvlakte reef cements are similar to that observed in burial cements from Phanerozoic carbonate sequences (e.g. Grover and Read, 1983).

Cathodoluminescence may also reveal fine growth zones within cements, which correspond to variable redox chemistry (Barnaby and Rimstidt, 1989). Recrystallisation or replacement by another mineral will destroy original cathodoluminescence zonation. The preservation of delicate zonation, which does not extend beyond crystal boundaries, indicates that cements are a product of primary growth (Hood and Wallace, 2012, 2018). Zonation patterns are controlled by the crystal form of each cement type, and so also reveal pore-filling crystal growth away from a substrate.

The acicular cement (AC) is interpreted to represent early marine precipitation of originally aragonitic mineralogy, as this shows a fibrous crystallographic texture and is inclusion-rich. The interpretation of an originally aragonitic mineralogy for AC is further supported by its elevated Sr content (up to 6900 ppm). It is well understood that the wider lattice spacing in the crystallographic structure of aragonite relative to calcite is more permissive to incorporation of the large atomic radius of strontium (Sandberg, 1984). An originally aragonitic interpretation for acicular cements of high Sr content at Driedoornvlakte has previously been reported by Grant (1990). The acicular, aragonite-precursor cement (AC) is commonly overlain by both marine geopetal sediment and by *Cloudina* individuals which either grew or were deformed about cement botryoids (Figure 4.11a).

The general absence of clear CL zonation in the dolomite cement (D1 and D2) suggests recrystallisation after a precursor, but these cements are nonetheless distinct from burial cements and coarsely recrystallised, dolomitic replacements (Whittaker et al., 1994; Corsetti et al., 2006). However, there are localised instances where the dolomite cement shows fine zonation, revealing a crystal form very similar to short, wedge-shaped marine dolomite cements of the older Karibib Formation (northern

Namibia) (Figure 8H of Hood and Wallace, 2018) which also show greater definition of growth zonation towards rhombic terminations (supplementary information of Hood and Wallace, 2018). This is also clearly represented in the best preserved examples of dolomite cements at Driedoornvlakte, however in most instances the primary dolomite fabric is unfortunately obscured by significant alteration and crystal terminations are also notable for their considerable dissolution, both in D1 and D2.

The interpretation of the C1 cement as having had an original high magnesium calcite mineralogy is corroborated by the columnar length-fast character and scalenohedral form of crystals when bisected parallel to the c-axis (e.g. Figure 4.10h). As detailed in section 4.3.1, the length-fast character of high-Mg calcite crystals require elevated Mg/Ca supplied in seawater. Whilst there are no documented occurrences of C1 cements overlain by geopetal sediment, this length-fast and inclusion-rich character argue for growth of this cement within shelter porosity where pore space was in open contact with seawater.

In contrast to the inferred precipitation from seawater of AC and C1(a and b), sparry calcite or length-slow, equant growth character is typical for carbonate crystal precipitated in pore waters where Mg/Ca is low. The localised presence of a limpid C1c cement prior to pore occlusion by C2, is occasionally represented by an epitaxial form whereby C1c was seeded upon the active substrate of C1(a/b) (Figure 4.9f) (Dickson, 1993). Negligible alteration in C1c and C2 may indicate that pervasive alteration of all preceding carbonate components (including CS and AC) occurred prior to precipitation of C1c, or alternatively, that the fluid from which C1c precipitated was itself responsible for dissolution of prior cements. Alternatively, multiple fluid generations may have promoted alteration prior to growth of C1c within the shallow burial environment. If the latter case is preferred, current data do not adequately distinguish between individual episodes of alteration. However the observation that pervasively recrystallized *Cloudina* skeletons (CS) are occasionally characterised by patchy bright luminescence (see Appendix C, Figure AC3b) indicative of activation by at least moderately elevated Mn may support the inference that CS was altered by fluids which were responsible for precipitation of C1b or later alteration of C1b and Mn remobilisation.

The final blocky calcite (C2) occludes all remaining pore space and is interpreted to represent a shallow burial cement from pore fluid which was likely disconnected from seawater and where Mg/Ca was low. The Sr concentration in C2 is significantly elevated, similar to the inferred early aragonite cement, but for C2 this likely reflects the relatively low degree of alteration to which this cement was subjected following total pore occlusion and the consequently negligible remobilisation of Sr.

In summary the CL and Fe-Mn abundance data indicate that cements were precipitated under

variable water column redox conditions: originally non-luminescent aragonitic botryoids (AC) in oxic conditions, and then non to brightly luminescent fibrous and columnar, inclusion-rich calcite (C1) first precipitated under low Fe and Mn, dominantly oxic (C1a), and then low Fe and elevated Mn, dominantly low oxygen manganous (C1b) conditions. The patchy luminescence of particularly C1a suggests some recrystallization, possibly from an aragonitic or HMC precursor. The non-luminescent blocky calcite (C2) grew under oxic conditions probably during shallow burial.

4.4.2 Origin for dolomite cements

It is clear that the elevated iron concentration of geopetal micrite sediment, and cements D1 and D2 was introduced during the dolomitisation process and was not a pre-existing feature of the precursor HMC. This is best recognised by elevated iron concentrations in dolomitised *Cloudina* individuals which could not possibly have been originally iron rich when grown under oxic conditions. Therefore, constraining the timing of dolomitisation is key to understanding the sequence of redox conditions to which the system was subjected.

As a result of the slow kinetics of dolomite formation at temperatures less than 40°C (Arvidson and Mackenzie, 1999), it has been proposed that under near-normal sea water conditions unstable, precursor, Ca–Mg carbonate phases form, such as very high-Mg calcite (VHMC). Prior to dolomite formation this VHMC, over decades or more, may become more ordered dolomite through dissolution and re-precipitation (Kaczmarek et al., 2017). Recrystallization from VHMC to ordered dolomite is common in natural settings where higher surface temperatures and longer time periods overcome kinetic barriers to dolomite formation (Kaczmarek et al., 2017). High magnesium calcite has previously been inferred for the mineralogy of original *Cloudina* shell material at Driedoornvlakte and has similarly been suggested to provide a localised source of Mg^{2+} required during subsequent diagenetic dolomitisation (e.g. D1) (Grant, 1990). Early dolomitisation of a HMC precursor cement is similarly inferred for D2, as neither the preceding botryoidal cement, nor later cements, are dolomitised. This is supported by the observation that some of the D2 cement crystals exhibit the classic high-Mg calcite form with a length-fast character and acute rhombic crystal terminations (Figures 4.9d arrowed and 4.10f). The presence of considerable dissolution suggests that precipitation took place under variable conditions which may have included multiple fluid alteration stages accompanied by changing carbonate saturation state or possibly just one progressive change in carbonate saturation state and pore fluid alteration during burial.

Low oceanic oxygen levels in the Neoproterozoic might provide a control on marine dolomite

precipitation by promoting microbial reactions such as methanogenesis or sulfate reduction (Burns et al., 2000). Stable carbon isotope data from the dolomitised sediment plus cement have slightly lighter carbon isotopic compositions (from -0.29 to 2.62‰) compared to the calcitic components (from 1.15 to 3.02‰) (Figure 4.13). This could indicate that some component of organic carbon (perhaps of microbial origin) is involved in the dolomitization process. Oxygen isotope data are very similar for both calcitic and dolomitic components, but the wide range (from -11.60 to -4.09‰) probably reflects the varying degrees of diagenetic alteration. There is a notable positive correlation between $\delta^{13}C_{carb}$ and $\delta^{18}O_{carb}$ within each individual carbonate component analysed, with the exception of the late stage pore-filling C2. This strongly suggests that diagenetic alteration progressively lowered $\delta^{13}C_{carb}$ when open pore space permitted fluid flow prior to occlusion by C2.

The most depleted $\delta^{13}C_{carb}$ and $\delta^{18}O_{carb}$ values are associated with dolomitised components (Figure 4.13). The carbon isotopic composition of dolomite may reveal the degree to which dolomitization was controlled by bacterial processes under anoxic pore fluids. Bacterial sulfate reduction proceeds via oxidation of organic matter utilising sulfate as the terminal electron acceptor and results in hydrogen sulfide and bicarbonate as by-products. This bicarbonate is therefore isotopically light with respect to $\delta^{13}C$. Using carbon isotope signatures, both sulfate reduction and methanogenesis have been evoked to explain precipitation of transient dolomite cements in Holocene shallow marine carbonate platforms (Teal et al., 2000) and for marine dolomite cements of the Cryogenian Oodnaminta Reef complex (Hood et al., 2011; Hood and Wallace, 2012).

Notwithstanding the very low quantities of pyrite in bulk carbonate samples at Driedoornvlakte (< 0.1 wt%), there are some localised instances where euhedral and opaque crystals which may represent oxidised pyrite are present within the micritic geopetal sediment (see Appendix C, Figure AC3e). The light carbon isotope signature of some combined dolomite sediment and dolomite cement samples relative to all other components supports a role for bicarbonate produced by a variety of early diagenetic organic matter remineralization reactions.

As outlined in section 4.1.2, dolomitisation and dolomite formation in the modern is largely restricted to shallow sediments which are frequently subject to evaporative conditions and provide the perfect environment for dissolution-reprecipitation reactions by encouraging the build-up of Mg^{2+} and removal of Ca^{2+} (Machel, 2004). Though reef growth of Unit 3m is inferred to have occurred above fair weather wave base, there are no features representative of subaerial exposure or evaporative conditions present (Adams et al., 2004). Instead, detailed sequence stratigraphic mapping indicates the transition to

a deeper environment during transgression and swamping by basinal shales of the Urikos Member (Adams et al., 2004).

Given the high porosity of the reef system, pore spaces were likely connected to the overlying water column prior to inundation by Urikos sediments. Circulation through the sediment of considerable volumes of seawater is required for dolomite formation, driven by tidal plumbing, wind generated currents and storms. In light of this, it is inferred that sediment porosity was high enough to have maintained interstitial seawater circulation and dolomite precipitation. Furthermore, precipitation of the dolomite cement was likely promoted by sustained, elevated pore water alkalinity, where Mg was sourced from seawater and possibly aragonite neomorphism (although this would most likely have occurred mainly during burial), as well as localised sulfate reduction. Elevated Fe also supports a role for anoxia. These conditions, coupled with unstable and reactive precursor phases such as HMC, would further enhance the dolomitization potential of fluids sourced from seawater (Corsetti et al., 2006).

There is evidence to suggest that the micritic geopetal sediment acted as a permeable conduit for the distribution of ferrous iron mobilised under anoxic pore water conditions. This is most apparent in one analysed sample (Appendix C, Figure AC3c and AC3d), where shelter porosity within a *Cloudina* individual was locally breached and infilled with geopetal sediment. In this case, the dolomite cement abutting the fracture are now high in iron, whilst those more distant have correspondingly low iron. This is clearly evident from cathodoluminescence characteristics of dull and non-luminescence respectively (Appendix C, Figure AC3d), and corroborated by electronprobe analyses. The patchy dull luminescence of these iron-rich cements and the absence of CL zonation clearly indicates that these crystals underwent pervasive fabric-destructive alteration as it the case for much of the D2 cement.

The timing of dolomitisation of the geopetal sediment, HMC *Cloudina* individuals and inferred HMC precursor cement is difficult to constrain. Dolomitisation may have been enhanced, either very early via upwelling of deeper, ferruginous seawater prior to inundation by Urikos sediments, or potentially later by fluid remobilisation from adjacent and overlying Urikos Member shales during shallow burial. Dolomitisation would, however, have occurred prior to final occlusion of porosity within the reefs, i.e. prior to the precipitation of the final cement (C2) and the preceding localised epitaxial cement (C1c).

If the latter case is preferred and dolomitisation proceeded during shallow burial, anoxic pore water ferric oxide reduction and remobilisation from overlying shales would have supplied ferrous iron which was incorporated into the dolomite lattice. The question remains as to whether such shallow burial conditions would have been permissive to growth of the length-fast character represented by C1(a/b),

where elevated Mg/Ca and good connection with overlying seawater is strongly implied. More to the point, if growth of the C1 cement predated dolomitisation then why was this cement not also dolomitised?

Iron speciation and Ce/Ce* data strongly suggest local water column conditions to have been variably ferruginous, manganous and oxic (Chapters 2 and 3; Wood et al., 2015; Tostevin et al., 2016b;

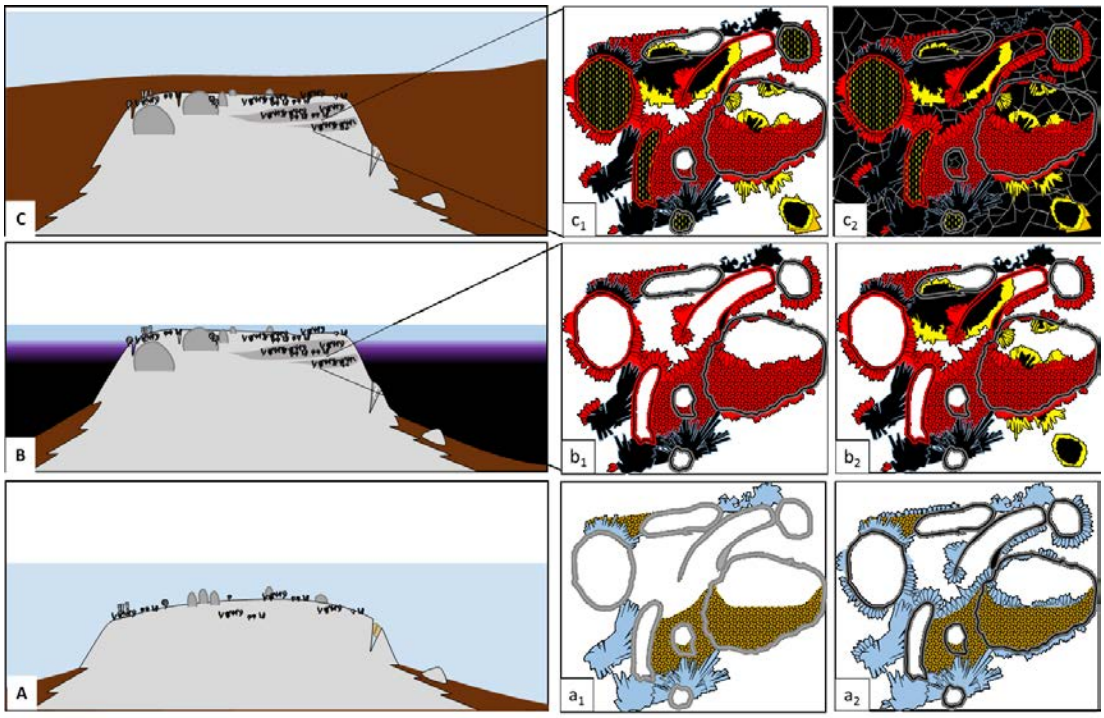

Figure 4.14 Schematic illustration of Omkyk Member during reef growth of Unit 3m and relative chronology of paragenetic sequence. **A)** *Cloudina* grow under oxic water column conditions, accompanied by botryoidal aragonite marine cement and geopetal sediment (a_1). the lack of geopetal sediment overlying inclusion-rich, length-fast high-Mg calcite cement (precursor to D2 cement) suggests that this precipitated within sheltered but open pore space. **B)** Anoxic conditions accompanied dolomitisation of D2 cement, geopetal sediment and occasionally *Cloudina* skeletons within seawater-derived pore fluids (b_1). Iron may have been sourced directly from ferruginous seawater. Seawater-sourced pore fluids are responsible for precipitation of non-brightly luminescent fibrous, scalenohedral calcite cement (b_2). **C)** Burial of Unit 3m reef by shale of the Urikos Member resulted in effective pore disconnect and consequently, latest cement generations (c_1 = C1c, c_2 = C2) are length slow, reflecting low Mg/Ca of pore fluids.

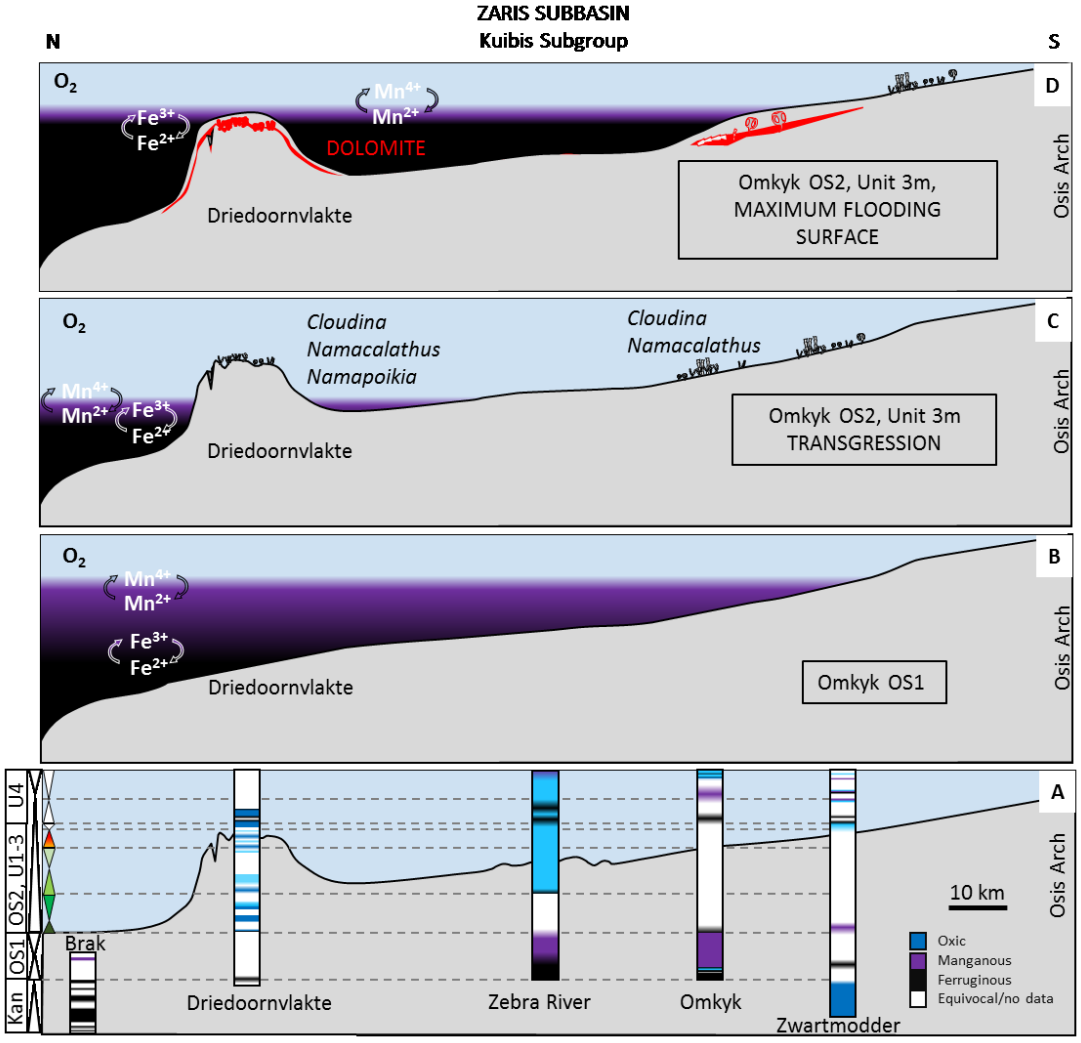

Figure 4.15 Simplified cross section of water column palaeoredox in the Zaris Sub-basin during deposition of the Omkyk Member, Kuibis Formation, showing the position of Brak, Driedoornvlakte, Zebra River, Omkyk and Zwartmodder (Wood et al., 2015). Suggested regional correlation of major interval of ferruginous upwelling during deposition of the Upper Omkyk Member which may have been partially responsible for iron supply during cement growth. **A**, The evolution of redox structure through the Omkyk Member (from Wood et al., 2015; Tostevin et al., 2016b; Bowyer et al., 2017), and the position of the iron-rich dolomite which can be correlated across the basin. Systems tracts for OS1 and OS2 (Units 1-3) are colour coded according to Figure 4.4 after Adams et al. (2004). **B**, Lower Omkyk (OS1), showing expansion of anoxic waters across the ramp, with no benthic biota. **C**, Upper Omkyk (OS2) transgressive systems tract. *Cloudina*, *Namacalathus* and *Namapoikia* grew within the oxic portion of the water column but close to the chemocline at Driedoornvlakte, Zebra River and Omkyk. **D**, Upper Omkyk (OS2) maximum flooding surface, showing shoaling of the chemocline at the end of transgression, causing termination of benthic community growth and dolomitisation of host sediment and calcite precursor to iron-rich dolomite cement.

Bowyer et al., 2017). In light of this, the simplest explanation for the sequence of inferred redox conditions and associated crystallographic character of carbonate cements is the permeation of pore space by seawater of changing reduction potential prior to pore water disconnect by deposition of the Urikos Member (Figure 4.14b). In this case, dolomitisation is inferred to have been early and catalysed in the presence of ferruginous waters of elevated Mg/Ca, in addition to anoxic microbial activity.

4.4.3 Regional dolomitisation in the Nama basin through time

If dolomitisation of Driedoornvlakte cements did take place under the influence of short-term ferruginous water column conditions, it stands to reason that some dolomitised horizons elsewhere in the Nama basin at this time may also reflect the presence of water column anoxia. Preferential dolomitisation of thrombolitic patch reefs of the Upper Omkyk Member and Lower Hoogland Member are well described from a mid-ramp position at Zebra River (Grotzinger et al., 2000; Dibenedetto and Grotzinger, 2005; Adams et al., 2005), however detailed petrographic and elemental analyses distinguishing the paragenetic sequence at Zebra River is yet to be undertaken. Dolomite is also present on Farms Omkyk and Zwartmodder of the inner ramp during the Omkyk Member and Outer ramp at Farm Brak during deposition of the underlying Kanies Member (Wood et al., 2015). The presence of dolomitized sediment and ferruginous anoxia approximately contemporaneous with the major maximum flooding surface of the Upper Omkyk Member in other mid-ramp (Zebra River) and inner-ramp (Omkyk and Zwartmodder) localities supports the interpretation that dolomitisation at this time may have been related to relative shoaling of ferruginous waters (Figure 4.15d). For example, at the inner ramp site Omkyk (Figure 4.3a), the in-situ *Namacalathus* assemblages on bedding planes show dolomitisation of surrounding micrite sediment, but retention of limestone within the *Namacalathus* cups (Figures 4.5e, f). This coincides with a short-lived anoxic event as revealed by Fe speciation at the MFS of the Upper Omkyk Member (OS2) (Chapters 2 and 3; Wood et al., 2015; Bowyer et al., 2017).

Indeed, a similar paragenetic sequence, including pore-lining dolomite cement has also been briefly described from thrombolitic pinnacle reefs of the Huns Member limestone in the Witputs subbasin (Pinnacle reef locality of Chapters 2 and 3) (Grotzinger et al., 2000). Interbedded stromatolitic dolostones and dolomitised flat-pebble conglomerate are noted throughout deposition of Huns Member shale prior to the major transgression responsible for pinnacle reef development (Saylor et al., 1995). However, it has been noted that these thin dolostone interbeds commonly show potholes and karstic features and are iron stained by overlying shales and may thus represent a situation akin to modern dolomitising environments (Saylor et al., 1995; Saylor, 2003). If short-term upwelling of anoxic

ferruginous water from depth was a contributing factor in dolomitisation of other carbonate cements in the Nama Group, particularly in deeper sections that show no evidence for subaerial exposure or evaporative conditions, a similar paragenetic sequence for cavity cements as documented at Driedoornvlakte may be expected at these localities, however this remains to be tested.

4.5 Conclusions

Ediacaran oceans were probably of high Mg/Ca with a shallow and fluctuating oxic chemocline compared to most of the Phanerozoic. The succession of early marine cements in the open reef system at Driedoornvlakte likely represents precipitation at either successively deeper positions in the water column or during changes in pore water chemistry due to transgression and/or upwelling, from shallow oxic (AC, C1a) through to manganous (C1b). The dolomitisation of sediment (DS), some *Cloudina* shell material (D1) and associated dolomite cement (D2) may have occurred as a result of a temporary incursion of Mg-rich, anoxic ferruginous waters, combined microbial activity and possibly sulfate reduction, but this hypothesis remains to be tested.

These cement data are consistent with the interpretation that Nama Group Ediacaran skeletal communities grew in oxic waters but were occasionally impinged upon by low oxygen, manganous waters that shoaled during late transgressive to early highstand cycles and lowered the reduction potential of framework pore space. Encroachment of anoxic, ferruginous waters in shallow environments may have dolomitised sediment and a HMC cement precursor. Dissolution is also common in the paragenetic succession of cements, suggesting changes in the mean carbonate saturation state. A model of dynamic redox changes through the Omkyk Member is proposed to account for the observed features (Figure 4.15). The Lower Omkyk (OS1) shows expansion of anoxic waters across the ramp with no recorded benthic biota, but during the Upper Omkyk (OS2), the chemocline occupied a position lower in the water column and skeletal communities grew at Driedoornvlakte, Zebra River and Omkyk within the oxic portion of the water column. At the maximum flooding surface, there was a shoaling of the chemocline, causing termination of communities at Driedoornvlakte and dolomitisation of host sediment and replacement of a HMC cement by iron-rich dolomite.

Growth of major Ediacaran communities in the Nama Group was likely terminated by low-oxygen or anoxic incursions which may have also resulted in extensive dolomitisation. Such communities may therefore have experienced regular devastation, leading to both an observed patchy distribution and limited longevity.

Chapter 5

Redox geochemistry and biostratigraphy of Precambrian-Cambrian sections of the south-eastern Siberian craton and Yangtze Block

Abstract

The boundary between the Ediacaran and Cambrian has been defined by the first appearance of the ichnofossil *Treptichnus pedum*, however a number of other marker fossil markers were originally propsed. The choice of a single defining marker fossil has proven controversial among researchers, primarily due to the effect of facies bias. The *T. pedum* ichnofossil represents the trace of an active bilaterian burrower which undoubtedly required significant dissolved oxygen concentrations to fuel its metabolism. Marine redox conditions which characterised individual basins in the late Ediacaran and early Cambrian were highly heterogeneous, thereby introducing further bias associated with inhospitable environmental conditions. This chapter aims to assess the relative timing of first and last appearance of originally proposed boundary marker fossils and changing redox conditions across the Ediacaran – Cambrian boundary through study of four sections across two palaeogeographic provinces. Despite dramatically variable palaeomarine redox conditions, we find that the timing of marker fossil last and first appearances overlap between individual regions within geochronological error. This strongly supports the notion that shallow marine oxic refugia were sufficiently widespread to enable utility of these fossils as markers in inter-regional correlation, providing that shallow deposits are also correlatable through sequence stratigraphic mapping.

Author Contributions: Data of I/(Ca+Mg) were collected by Dalton Hardisty and $\delta^{44}Ca$ data were collected by Alexandra Turchyn and Harold Bradbury. This chapter greatly benefited from discussions with Rachel Wood and Alex Thomas.

5.1 Introduction: The Basal Cambrian Conundrum

The transition between uppermost Ediacaran and basal Cambrian strata is bracketed by the widespread disappearance (/extinction?) of the skeletal invertebrate *Cloudina* but defined by the first appearance datum of the distinctive bilaterian trace fossil *Treptichnus pedum* (Brasier et al., 1994; Xiao et al., 2016). The early 1980s saw extensive geological and palaeontological deliberation centred upon agreement of a global stratotype section and point (GSSP) to represent the boundary and three candidates were successful in being selected for final consideration. These were Meishucun in Yunnan Province, South China (see inset Figure 2.2), Ulukhan-Sulugur on the banks of the Aldan River of southeastern Siberia (Figure 5.2b) and various sections on the southwest coast of the Burin Peninsula, Newfoundland (Magaritz, 1989; Landing, 1992; Brasier et al., 1994; Geyer and Landing, 2017).

Initial discussion was focused upon the utility of small shelly fossil (SSF) biozones in inter-regional stratigraphic correlation, however the efficacy of SSF first appearance as a marker horizon was questioned largely as a consequence of problems relating to facies biases, species endemism and the recognition of a significant erosional unconformity immediately below the Tommotian boundary at Ulakhan-Sulugur (then considered to represent the base of the Cambrian in Siberia) (Landing et al., 1989; Qian and Bengtson, 1989; Geyer and Landing, 2017). Another option was to define the boundary at the first appearance datum (FAD) of a particular ichnospecies. After years of deliberation and intensive scrutiny of the candidate formations, a type section was chosen at Fortune Head on the Burin Peninsula of Newfoundland. This section represents a shallow-intermediate depth monofacial, predominantly siliciclastic sequence of the Chapel Island Formation wherein the rather dramatic first appearance of *T. pedum* is readily distinguishable stratigraphically below carbonate beds which yield early Cambrian (Nemakit-Daldynian equivalent) SSFs, including hyoliths and *Anabarites* (Myrow and Hiscott, 1991,1993; Gehling et al., 2001; Droser et al., 2002; Herringshaw et al., 2017).

The absolute age of the Ediacaran-Cambrian boundary at Fortune Head is poorly constrained due to sparsity of ash beds for radiometric dating and the unreliability of carbon isotope values obtained from the thin and widely separated carbonate interbeds (Figure 5.1) (Brasier et al., 1992). Indeed, at present, the boundary age of ~ 541 Ma is defined based on high precision U-Pb dating of ash bed zircons in Oman which bracket the last appearance of *Cloudina* and *Namacalathus* and co-occurrence of a globally identifiable significant negative carbonate carbon isotope excursion termed the basal Cambrian carbon isotope excursion (BACE) (Amthor et al., 2003; Zhu et al., 2006; Bowring et al., 2007). The correspondence of the ratified GSSP to this ash bed age is further complicated by the absence of *T. pedum* in the Oman stratigraphy, which necessitates correlation of the *Cloudina* 'extinction' horizon to presumed equivalent and radiometrically constrained strata where *T. pedum* is present. Fortunately, suitable

fossiliferous deposits are found in the upper Nama Group, below and above the basal Cambrian unconformity, however this erosional event has eradicated any evidence for a negative $\delta^{13}C$ trough which would otherwise be assigned to the BACE. In fact, in Namibia, recent high precision radiometric ages have been presented which constrain the interval represented by the erosional unconformity and the last appearance datum of *Cloudina* to between 538.67 ± 0.22 and 538.18 ± 1.24 Ma, which are significantly younger than the Oman age (Linnemann et al., 2017; Ramezani et al., 2017). Therefore, based on the first appearance of *T. pedum*, the absolute boundary age should now be reduced to ~538 – 539.4 Ma (Figure 5.1).

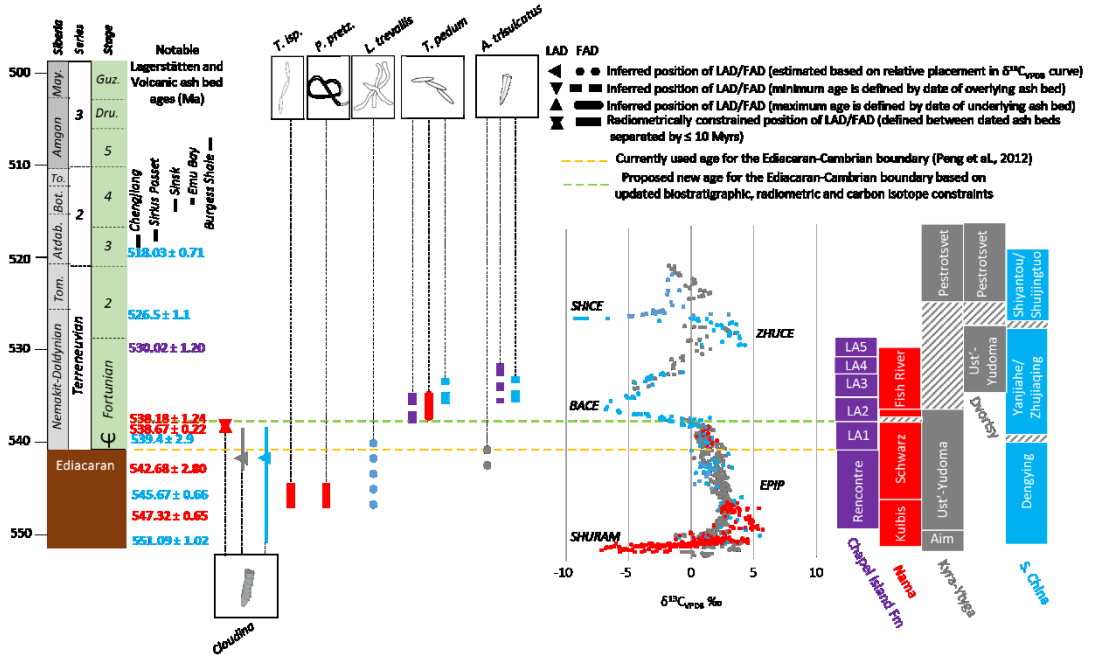

Figure 5.1 Current understanding of the series of events marking the Ediacaran-Cambrian transition in regions discussed in detail in this thesis relative to the basal Cambrian GSSP at Fortune Head (Newfoundland). Noted biotic events include the extinction of *Cloudina*, earliest treptichnid traces below the boundary unconformity in Namibia, notable complex trace fossils below the FAD of *Treptichnus pedum*, FAD of *Treptichnus pedum* and earliest small shelly fossils (SSFs) of the *Anabarites trisulcatus* – *Protohertzina anabarica* zone. Carbon isotope correlation between sections discussed in the text in addition to early Cambrian (Fortunian – Stage 3) $\delta^{13}C_{VPDB}$ profile of drill core study of the Yangtze Gorges area (Ishikawa et al., 2008) and $\delta^{13}C_{VPDB}$ profile of the Dvortsy section on the Aldan River southeast Siberia (Magaritz et al., 1986). Note that the precise age for the nadir of the BACE may be as old as ~ 538 -539.4 Ma, however this is not well constrained. Carbon isotope values are colour coded according to stratigraphy (noted at right). Approximate relative position of the Ust'-Yudoma Formation between the Aldan and Yudoma Rivers is discussed in the text.

There is evidence for restricted ecological niche space in environments of the Ediacaran Period associated with prevailing local redox conditions (Chapters 2 and 3). It is possible then, that the first appearance of *T. pedum* is not only facies restricted but also biased by the presence of persistently unfavourable redox conditions in some areas which further limits the use of this ichnospecies as a regional marker for the Ediacaran-Cambrian boundary. This chapter will focus upon mixed siliciclastic and carbonate strata from key sections of the southeast Siberian Platform and the Yangtze Block of South China which were deposited within the transitionary interval of the uppermost Ediacaran and basal Cambrian Periods. Carbon isotope chemostratigraphy and iron speciation (where possible) are interpreted alongside iodine and major element data which are holistically integrated with fossil occurrence in an attempt to constrain the palaeoenvironmental conditions which typified the local shallow marine realm in these two regions.

5.2 Sample collection and Methods

Data are presented in this chapter for samples which were collected during two separate field seasons to Yunnan Province and Hubei Province, South China (2014) and along the Maya and Yudoma Rivers of remote southeast Siberia (August-September, 2015). Samples from South China were collected by Rachel Wood and Aihua Yang and Siberian samples were collected by Rachel Wood on an international research expedition with colleagues from Russia and China including Andrey Zhuravlev, Andrey Ivantsov, Sergei Sukhov, Fangchen Zhao and Maoyan Zhu. Details of individual sampling sites are discussed in the relevant sections below and precise GPS coordinates are provided in Appendix A.

New carbon and oxygen isotope data are presented for samples of the Dengying and Zhujiaqing Formations of the Yangtze Block. Fresh surfaces were exposed and polished using a diamond saw and diamond lap and prepared surfaces were washed and dried. Microsamples were drilled from the prepared surfaces and 1 – 3 mg of the resultant powders were loaded into an ISOCARB preparation device and reacted at 90°C with concentrated orthophosphoric acid (H_3PO_4). Resultant CO_2 was analysed on a VG Isogas PRISM III stable isotope ratio mass spectrometer at the School of Geosciences, University of Edinburgh. The standard deviation (n = 15) of a powdered laboratory coral standard (COR1D, $\delta^{13}C$= -0.668 ‰, $\delta^{18}O$= -4.920 ‰) analysed alongside samples was ±0.05 ‰ for $\delta^{13}C$ and ±0.08 ‰ for $\delta^{18}O$. Additional unpublished carbon isotope data for the Nuuchchalakh section were provided by Maoyan Zhu. Data are presented in standard delta notation relative to the Vienna Pee Dee Belemnite (VPDB).

Standard sample preparation procedures were undertaken to remove weathered surfaces and visible signs of alteration and samples were subsequently washed and dried and pulverised to powder. Samples were then quantitatively dissolved following a multi-stage HNO_3-$HClO_4$-HF-H_3BO_3 hot acid digestion. Resultant solutions were analysed for major element concentrations on a Varian VistaPro ICP-OES at the University of Edinburgh, Grant Institute.

Where total iron was greater than 0.5 wt%, further chemical dissolutions were carried out following the iron speciation method (Poulton and Canfield, 2005) which partitions total iron into operationally defined iron pools via a sequential chemical extraction protocol. Specifically, the procedure targets carbonate, oxide and magnetite –bound iron alongside a separate, boiling chromous chloride distillation which isolates the fraction bound as iron pyrite through quantitative precipitation of Ag_2S (Canfield et al., 1986). Resultant solutions of the sequential extraction step were analysed via flame AAS at the University of Leeds, School of Earth and Environment, Cohen Laboratories.

Additional analyses for selected samples of the Nuuchchalakh section include I/(Ca+Mg) and $\delta^{44}Ca$. These were undertaken by Dalton Hardisty of Woods Hole Oceanographic Institute and Sasha Turchyn and Harold Bradbury of the University of Cambridge respectively and constitute preliminary data in ongoing collaborative research. The analytical methods by which these data were obtained are outline in Chapter 1 sections 1.10.5 and 1.10.6. All raw data presented in this chapter are provided in Appendix B.

Inferring primary marine isotopic composition from carbonate-rich lithologies requires confident, robust assessment of preservational quality. Classic geochemical criteria used in determining the degree of alteration include interpretation of the $\delta^{18}O$ record, the ratio of major elements and $\delta^{13}C_{carb}$ to $\delta^{18}O$ and the ratio of Mn/Sr. Progressive alteration via meteoric diagenesis and hydrothermal fluid interaction will tend to decrease the strontium concentration and $\delta^{18}O$ and increase the elemental concentrations of, for example, manganese, iron and zinc (Brand and Veizer, 1980; Kaufman and Knoll, 1995). Consequently, negligible covariance between Fe and $\delta^{13}C_{carb}$ or $\delta^{18}O$, low Mn/Sr (< 10), $\delta^{18}O > -10$ ‰ and high Sr concentration are commonly accepted as evidence to support adequate preservation for reliable interpretation of primary conditions during carbonate precipitation (Kaufman and Knoll, 1995). Crucially however, the use of Mn/Sr as an alteration proxy is based on observations of Phanerozoic carbonates precipitated under oxic marine conditions where water column Mn concentrations are inherently low. Ediacaran marine conditions are typified by local anoxia and, in many cases, Mn concentrations in the water column were likely elevated leading to higher primary Mn/Sr in marine carbonates.

5.3 Introduction to the Siberian Platform Ediacaran-Cambrian boundary problem

The vast expanse of the Siberian Platform is host to a large number of key late Neoproterozoic to early Phanerozoic fossiliferous sedimentary sequences. These include exposures of the Khorbusuonka Group (Mastakh, Khatyspyt, Turkut and Kessyusa Formations) of the Olenek uplift on the banks of the Olenek and Khorbusuonka Rivers in the northeast (e.g. Sokolov and Fedonkin, 1984; Knoll et al., 1995a; Nagovitsin et al., 2015), the Sukharika River (Sukharika Formation) in the west (Rowland et al., 1998; Kouchinsky et al., 2007), the Kotuikan River (Staraya Rechka, Manykai, Medvezhya and Kyndyn Formations) in the central north (Knoll et al., 1995b; Kaufman et al., 1996) and the Aldan, Selinde, Yudoma and Maya Rivers in the south and southeast (including the Aim, Ust'-Yudoma and Pestrotsvet Formations) (Figures 5.2a, 5.3) (Magaritz et al., 1986; Brasier et al., 1993; Khomentovsky and Karlova, 1993, 2002, 2005; Kouchinsky et al., 2005; Khomentovsky, 2008; Zhuravlev et al., 2009; Wood et al., 2017a; Zhu et al., 2017).

In order to best understand Siberian stratigraphic subdivision for this time interval, it is first necessary to recognise that there has been (and still exists to some degree) disagreement between researchers in the placement of the Nemakit-Dalynian Stage with respect to the Cambrian and preceding Vendian Systems (e.g. Khomentovsky, 2008). The base of the Nemakit-Daldynian is defined by the first appearance of small shelly fossils including *Anabarites trisulcatus* and *Purella antiqua* and the subsequent Tommotian Stage is demarcated by the first appearance of hyoliths, gastropods and archaeocyaths of the *Nochoroicyathus* (/*Aldanotreta*) *sunnaginicus* zone (Khomentovsky and Karlova, 1993; Peng et al., 2012). Traditionally, the base of the Tommotian in Siberia has defined the base of the Cambrian at the contact between the Ust'-Yudoma and Pestrotsvet Formations at the type sections of Dvortsy and Ulakhan-Sulugur on the Aldan River (relative position to southwest of Figure 5.2b, Figure 5.3) (e.g. Cowie and Rozanov, 1984; Magaritz et al., 1986; Magaritz, 1989). This assigns the Nemakit-Daldynian to the latest Stage of the Upper Vendian System of the Precambrian (Khomentovsky and Karlova, 1993;

Figure 5.2 a) Map of Siberia with major structural units (after Rozanov and Zhuravlev, 1992 and Khomentovsky, 2008), (I) Igarka-Norilsk Uplift, (II) Anabar Shield, (III) Olenek Uplift, (IV) Kharaulakh Uplift, (V) Yenisei-Angara Structural Facies Region, (VI) Baikal-Patom Structural Facies Region, (VII) Lena River sections, (VIII) Uchur-Maya Plate, (IX) Yudoma-Maya Belt, (X) Okhotsk microcontinent, **b)** Enlarged map showing Uchur-Maya facies region subdivided into Aldan Shield, Uchur-Maya Plate and Yudoma Maya Belt (Khomentovsky, 2008) Drawn using the Geological Map of the Siberian Platform and Adjoining Areas 1:1 500 000 and the State Geological Map of the USSR 0-53-V (1984) 1: 200 000.

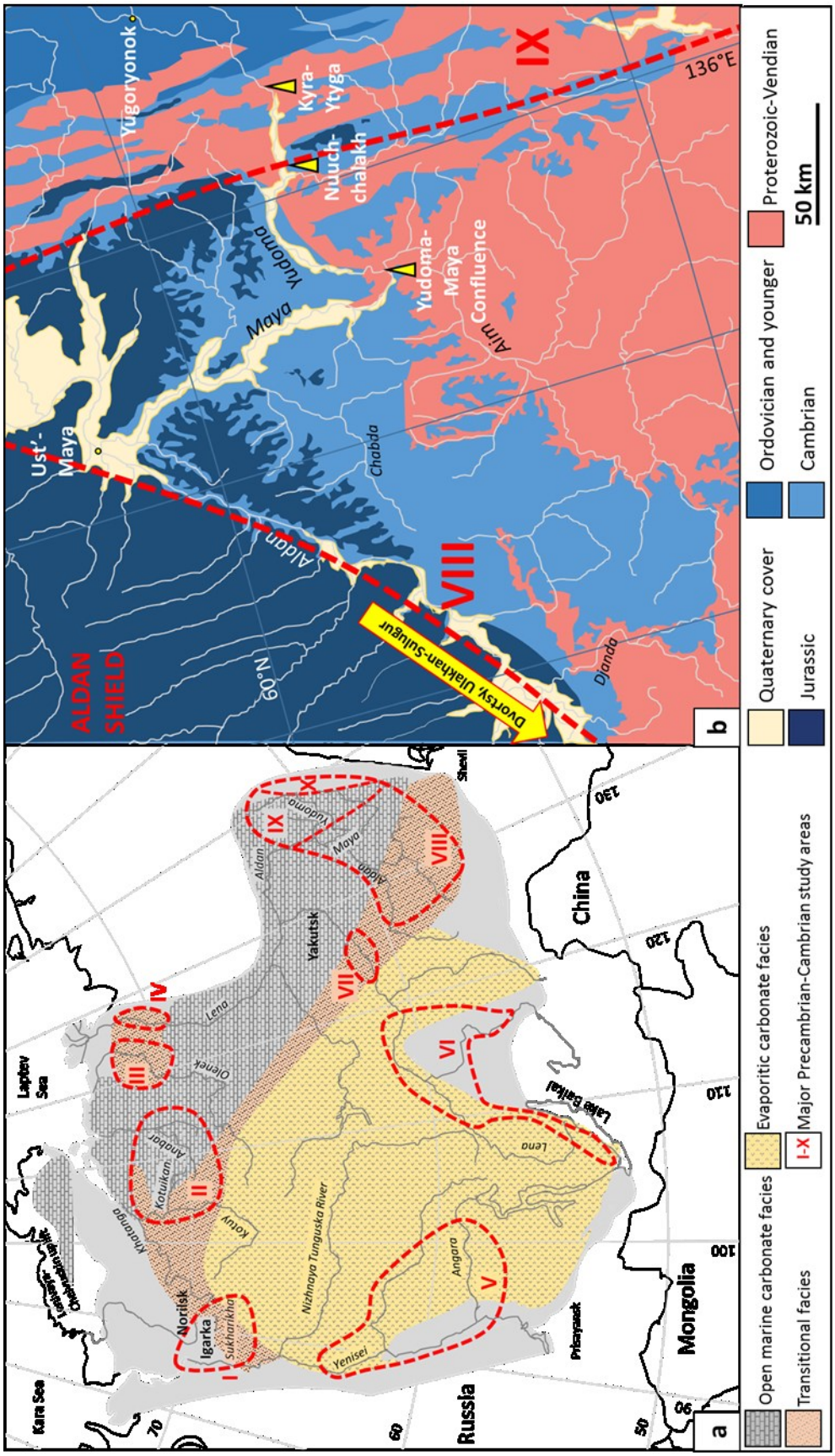
Yugoryonok
Kyra-Ytyga
Nuuchchalakh
Yudoma-Maya Confluence
Aim
Yudoma
Maya
Ust'-Maya
Chabda
Aldan
ALDAN SHIELD
Dvortsy Ulakhan-Sulugur
Djanda
60°N
136°E
IX
VIII
b
Proterozoic-Vendian
Ordovician and younger
Cambrian
Quaternary cover
Jurassic
50 km
Shevli
China
Yakutsk
Lena
Olenek
Laptev Sea
Anabar
Kotuikan
Khatanga
Kotuy
Nizhnaya Tunguska River
Angara
Lake Baikal
Norilsk
Igarka
Sukharikha
Yenisei
Kara Sea
Russia
Mongolia
Prisayansk
I
II
III
IV
V
VI
VII
VIII
IX
X
XI
a
Open marine carbonate facies
Transitional facies
Evaporitic carbonate facies
I-X Major Precambrian-Cambrian study areas

Figure 5.2

Khomentovsky, 2008). However, the base of the Cambrian has now been repositioned to the base of the Nemakit-Daldynian Stage in accordance with the relative positions of the ichnofossil and small shelly fossil records of the Chapel Island Formation GSSP (Landing et al., 1989; Kouchinsky et al., 2007; Peng et al., 2012; Geyer and Landing, 2017).

The majority of sections in southeast Siberia suffer from a significant gap in the geological record (termed the sub-Tommotian unconformity) which further complicates interpretation of section correlation (Knoll et al., 1995b; Kaufman et al., 1996). This erosional event is widely considered to have locally eradicated much of early Cambrian Stage 1 (Fortunian) and lower Stage 2 stratigraphy, exemplified by high resolution $\delta^{13}C_{carb}$ studies undertaken across the Siberian Platform (Magaritz, et al., 1986, 1991; Kirschvink et al., 1991; Brasier et al., 1993; Knoll et al., 1995a, b; Kaufman et al., 1996; Kouchinsky et al., 2001, 2005, 2007). A composite $\delta^{13}C_{carb}$ profile of the Sukharikha River section has been suggested to correlate with an almost identical carbon isotope record from Morocco which benefits from accompanying radiometric age constraints (Maloof et al.,. 2010b). Though many in the scientific community are sceptical of potential stratigraphic repetition within the Sukharikha River section (Wood, R.A. pers.com.), this correlation has remained undisputed in the published literature. The result is a composite chemostratigraphic profile which suggests that the base of the Nemakit-Daldynian (defined by the first appearance of *Anabarites* in Mongolia and Siberia below a major negative $\delta^{13}C_{carb}$ excursion (BACE) but above the last appearance of *Cloudina*) can be placed at approximately 542.37 $\pm$ 0.63 Ma within the terminal Ediacaran (Bowring et al., 2007; Maloof et al., 2010b; Schmitz, 2012). Similarly, the base of the Tommotian defined by first appearance of archaeocyaths corresponds to a prominent negative $\delta^{13}C_{carb}$ excursion at approximately 525.23 $\pm$ 0.61 Ma (Maloof et al., 2005, 2010a, b; Schmitz, 2012).

Recent work in southeast Siberia at the Kyra-Ytyga section of the Yudoma-Maya depression (Figure 5.2b) has revealed a previously undocumented co-occurrence of *Anabarites* and *Cloudina* in the Ust'-Yudoma Formation beneath the sub-Tommotian unconformity and beneath a negative carbon isotope excursion interpreted as the BACE (Zhu et al., 2017). Small shelly fossils and archaeocyathans representative of the Tommotian are not noted from the Uchur-Maya structural facies zone (VII and VIII of Figure 5.2) prior to the overlying basal Pestrotsvet Formation (Khomentovsky, 2008). Therefore, based on biozonation, the upper Ust'-Yudoma Formation at Kyra-Ytyga can be placed in both the terminal Ediacaran and the Nemakit-Daldynian (earliest Cambrian), whilst it is chemostratigraphically restricted to the terminal Ediacaran by the position of the BACE. Pinning the upper Ust'-Yudoma Formation immediately beneath the BACE and firmly correlating the Pestrotsvet Formation with the Tommotian Stage necessitates acknowledgement of the astonishingly long duration of the intervening

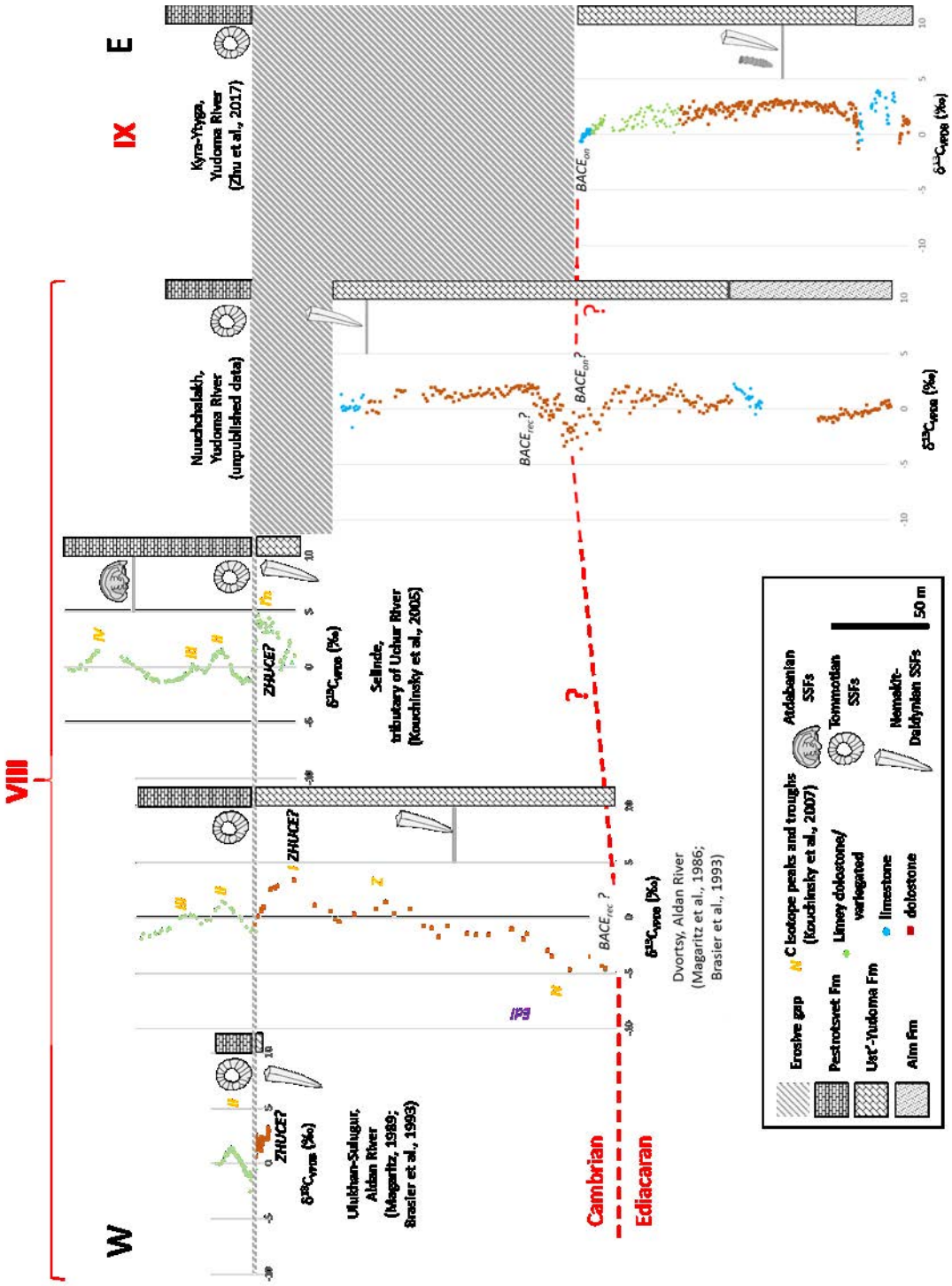

Figure 5.3 Chemostratigraphic relationships between sections along the Aldan, Uchur and Yudoma Rivers of the Uchur-Maya region, southeast Siberia (regions VIII and IX of Figure 5.2a). Section and $\delta^{13}C_{carb}$ data (Magaritz et al., 1986; Magaritz, 1989; Brasier et al., 1993; Kouchinsky et al., 2005; Zhu et al., 2017) and data from Nuuchchalakh (Zhu, unpublished). Red dashed lined indicates approximate position of the Ediacara – Cambrian boundary tied to the BACE, red erotemes denote uncertainty in correlation. Black italicised acronyms

gap, which may have been up to 12 million years according to placement of the Tommotian lower boundary in the internationally recognised Geological Time Scale (Peng et al., 2012). This position also draws down the base of the Nemakit-Daldynian (FAD of *Anabarites*) into the upper Ediacaran as suggested by the BACE and the presence of *Cloudina* and suggests both that classical separation of these biota is flawed and that the BACE is likely not attributable to a consequence of extensive mass extinction of Ediacaran organisms (Zhu et al., 2017).

5.3.1 The Yudoma-Maya Depression

The following discussion concerns data obtained from two sampled sections of the Aim and Ust'-Yudoma Formations which outcrop on the banks of the Yudoma River in southeastern Siberia, namely Nuuchalakh and Kyra-Ytyga (Figures 5.2b, 5.4-5.6). Samples were collected by Professor Rachel Wood during an extensive international field expedition. In addition to positioning of the Ust'-Yudoma Formation with respect to biostratigraphic and chemostratigraphic data (Zhu et al., 2017), this expedition identified well-preserved early dolomite cements and allowed novel interpretation of water column redox conditions in the shallow marine environment across this interval (Wood et al., 2017a).

The Uchur-Maya structural facies region of southeast Siberia is the southernmost facies region of the Yudoma-Anabar facies province and constitutes the Uchur-Maya Plate to the west and the Yudoma-Maya belt to the east (Figure 5.2) (Khomentovsky, 1986). The boundary between these two structural regions is defined along strike of the Nel'kan thrust fault complex (Khomentovsky and Karlova, 2002; Khomentovsky, 2008). In this region, mixed siliciclastic and carbonate sedimentary deposits of the Aim and Ust'-Yudoma Formations unconformably rest atop various pre-Ediacaran age units, of which the youngest is the Ust'-Kirbi Formation (Khomentovsky, 1986). Thrust faulting within the Nel'kan complex has resulted in some stratigraphic repetition within the Ust'-Yudoma Formation which is observable in outcrop.

The only published radiometric age constraint for deposits of the Yudoma Group is a Pb-Pb age from carbonate samples of the upper Aim Formation which were screened via combined U-Pb and Rb-Sr systematics as having undergone the least alteration (Semikhatov et al., 2003). These samples

---

Figure 5.3 continued: (e.g. Zhujiaqing carbon isotope excursion 'ZHUCE') represent suggested correspondence of regionally identified isotopic excursions to global excursions as defined by Zhu et al. (2006).

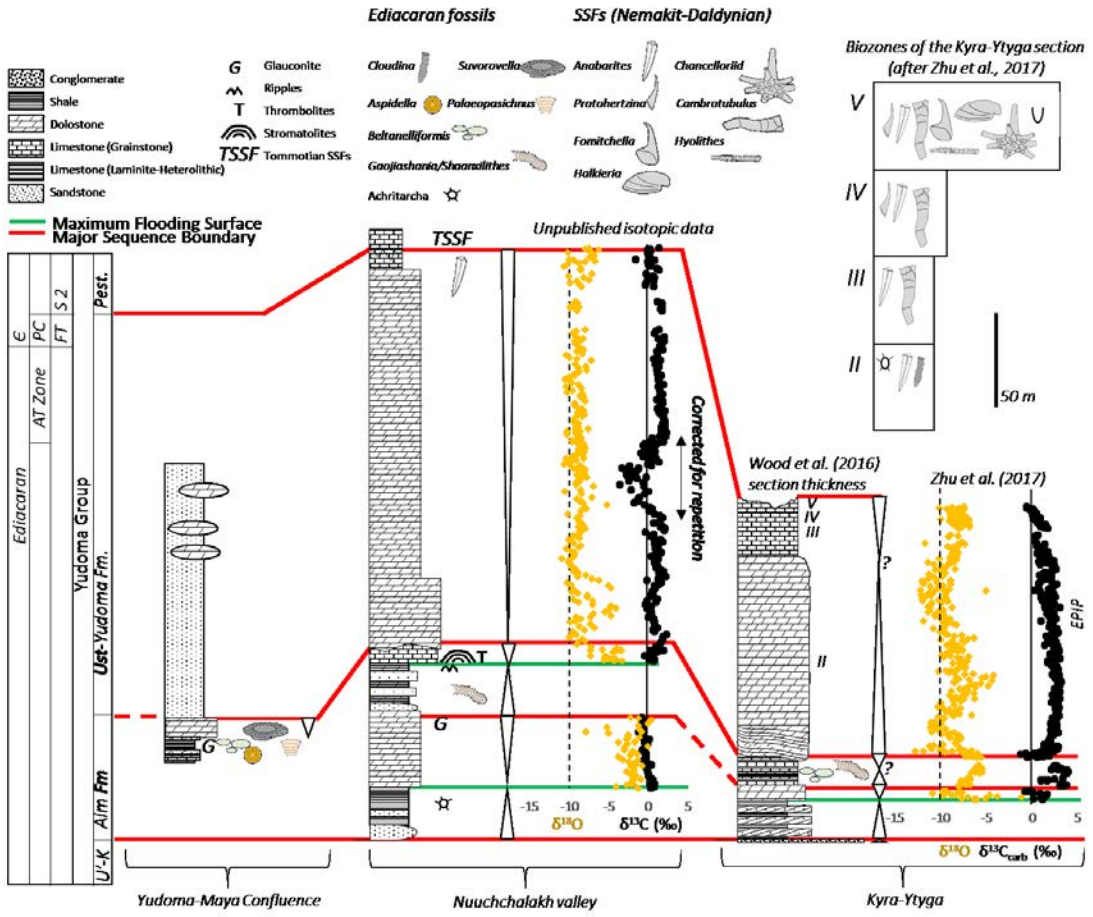

Figure 5.4 Stratigraphic relationship of sections from west to east (left to right) along the Yudoma River, including carbon isotope data for Kyra-Ytyga (Zhu et al., 2017) and Nuuchchalakh (Zhu, unpublished data). Biostratigraphic information from Zhu et al. (2017)

were retrieved from the Kyra-Ytyga section (noted in publication as Ulakhan-Yatygy) and give an age of 553 ± 23 Ma (Semikhatov et al., 2003). Considering the large error in this estimate, the approximate age of the Yudoma Group relies heavily on a combination of carbon isotope chemostratigraphy and the relative positions of classic Ediacaran and small shelly fossils which together suggest deposition in the latest Ediacaran (~550-538 Ma, Figure 5.1) (Zhu et al., 2017).

The three sections of the Yudoma Group discussed above have been reconstructed as an inner to outer shelf transect, with deposition in a proximal shoreface environment at the Yudoma-Maya confluence and increasing depth of exposed sections to the northeast along the Yudoma River (Wood et al., 2017a). Despite a distinct increase in relative depth between the Yudoma-Maya confluence and

Nuuchchalakh and Kyra-Ytyga, deposition in the deepest exposed stratigraphy is still representative of relatively shallow marine conditions above wave base (Wood et al., 2017a; Zhu et al., 2017).

5.3.2 Yudoma-Maya Confluence

The shallowest facies in outcropping strata exposed along the Yudoma River were deposited on the Uchur-Maya Plate near the confluence with the Maya River (Figure 5.2b). One representative section, the Yudoma-Maya Confluence (Figures 5.2b, 5.4), is composed of 25 m of limestone, dolomitised sandstone and highstand systems tract dolomites of the Aim Formation followed by 125 m of coarse sandstone with dolomite nodules of the Ust'-Yudoma Formation (Figure 5.4) (Wood et al., 2017a). Classic Ediacaran Period fossils of soft-bodied biota are abundant in sandstones of the Aim Formation and include *Palaeopasichnus* and the discoidal holdfast *Aspidella* in addition to the cyanobacterial impressions of *Beltanelliformis* (Wood et al., 2017a, c; Ivantsov, 2017; Zhu et al., 2017; Bobrovskiy et al., 2018). Dolomitised shelly packstones of the Aim Formation at this locality are also host to the skeletal organism *Suvorovella aldanica* (/ *Majaella verkhojanica*) (Vologdin and Maslov, 1960; Wood et al., 2017a, c; Ivantsov, 2017; Zhu et al., 2017). The bed within which *Suvorovalla* is found is laterally extensive to over 1 km and contains broken shell fragments and microbial oncoids (Wood et al., 2017c).

Though sample material was collected from this section, the proximal nature of course grained siliciclastic and very low Fe_T (< 0.5 wt%) carbonate lithologies has precluded robust geochemical analyses (Appendix B). Though no new data for this section are presented herein, its palaeontological and facies relationship to the following two sections is significant and aids a holistic understanding of the shelf environment.

5.3.3 Nuuchchalakh

The Nuuchchalakh valley section is located approximately 80 km up-river from the Yudoma-Maya confluence. At Nuuchchalakh, the lower ~100 m are composed of variably dolomitised clastics and carbonates of the Aim Formation which were deposited during two full cycles of relative sea level change. Siliciclastic deposits of the Aim Formation occupy transgressive systems tracts whilst carbonates prograded over these deposits during sea level highstands (Figure 5.5). Cross-bedded and laminated dolostones of the lower cycle are capped by a sequence boundary containing glauconitic grains (Wood et al., 2017a). Mixed dolomitised siltstones and dark red shales occupy the TST of the second cycle and are

interpreted as having been deposited during a series of shallowing upward parasequences. A thick, undolomitised red shale package marks the maximum flooding surface (MFS) which is subsequently overlain by dolomitised siltstone with green shale interbeds of the highstand systems tract (HST) (Wood et al., 2017a). Siliciclastic deposits in the second depositional cycle of the Aim Formation at Nuuchchalakh contain *Shaanxilithes* (previously ascribed to *Gaojiashania*, Zhuravlev et al., 2009; Ivantsov, 2017) and various acritarch species (Pyatiletov, 1988; Zhu et al., 2017). The HST of the upper Aim Formation includes a unit of dark, laminated stromatolitic and thrombolitic limestone which is overlain by shallow water deposits of prograding light grey dolomite of the Ust'-Yudoma Formation, deposited during the late HST.

The Ust'-Yudoma Formation deposits are described as 'sucrosic dolograinstones, packstones and wackestones, with cement-filled sheet-like cavities' and contain high concentrations of quartz sand (Wood et al., 2017a). The uppermost 10 – 70 m of the Ust'-Yudoma Formation are composed of limestone and this transition is not accompanied by any significant change in facies (Wood et al., 2017a). Fossils of the shallow water Ust'-Yudoma Formation at Nuuchchalakh are restricted to *Anabarites* recorded in limestones deposited in the uppermost 10 m (Wood et al., 2017a). The regional sub-Tommotian unconformity separates these deposits from overlying limestone of the Pestrotsvet Formation which contains Tommotian SSFs (Figure 5.5).

5.3.3.2 Nuuchchalakh geochemistry

Figure 5.5 shows compiled geochemical data for Nuuchchalakh and, in addition to iron speciation, includes $\delta^{13}C_{carb}$ (Zhu, unpublished data), carbonate-bound iodine concentrations and $\delta^{44}Ca$ (Figure 5.5). Carbon isotope data of highstand dolostones in sequence 1 of the Aim Formation show a gradual decreasing trend from values as high as +1‰ to a nadir of approximately -1.22‰. Highstand limestone of the second sequence in the Upper Aim Formation record a recovery to positive values up to +2.26‰ followed by values which remain within the range -0.36 to +2.17‰ within the lower Ust'-Yudoma Formation. At approximately 147m, $\delta^{13}C_{carb}$ begin a notable negative excursion culminating in a nadir of -3.59‰ at ~165m, followed by a recovery to positive values at 188m which remain stable around a mean value of +1.6‰ for the following ~75m. This prominent negative $\delta^{13}C_{Carb}$ excursion is not accompanied by $\delta^{18}O_{Carb}$ below -10‰ and instead likely records preservation of primary carbon isotopic composition. Values decrease once more at the top of the section to ~0‰ but this trend is unrelated to the changing lithology.

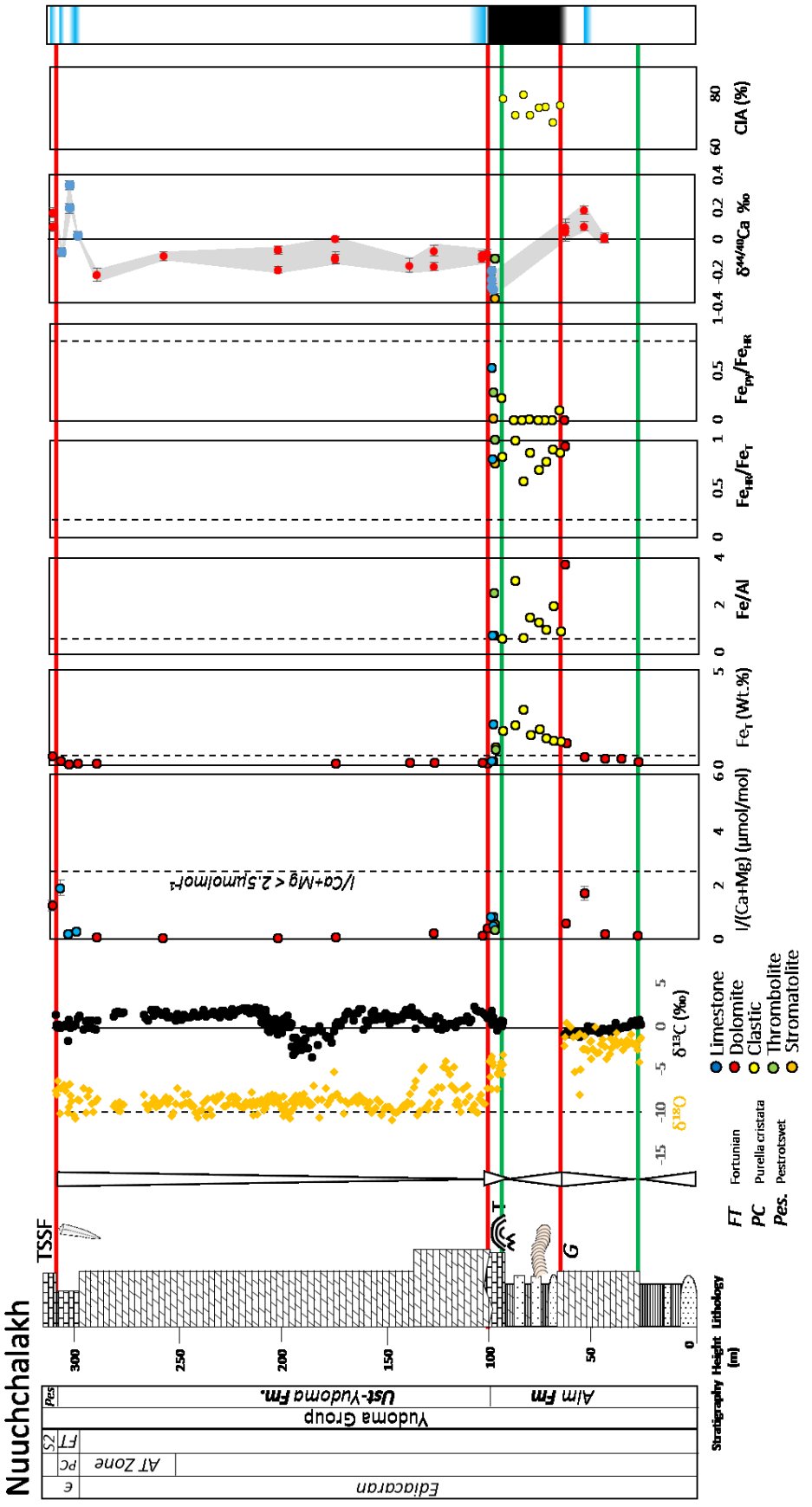

Figure 5.5 Stratigraphic log and geochemical data of the Nuuchchalakh valley section. $\delta^{13}C_{carb}$ provided by M. Zhu (unpublished data). 'AT' and 'PC' zones, *Anabarites trisulcatus* and *Purella cristata* biozones respectively. 'FT', Fortunian, 'S2', Stage 2. TSSF, Tommotian Small Shelly Fossils. Key to lithological and biostratigraphic symbols provided in Figure 5.4.

Total iron concentrations range from below detection in some dolomite samples to 2.96 wt% in shale samples of the Upper Aim Formation. Whilst dolomite cements of the Yudoma Group have been shown via electron microprobe analyses to contain relatively elevated iron concentrations (Wood et al., 2017a), bulk sample digestion indicates that total iron is less than 0.5wt% in all dolomite analysed with the exception of one sample at the inferred sequence boundary separating the lower and upper sequences of the Aim Formation where Fe_T = 1.12 wt% (Figure 5.5). The apparent discrepancy between bulk digestion and targeted cement analysis is likely due to homogenisation of low and high iron zones during bulk rock dissolution. Upper Aim Formation siliciclastic deposits contain 0.94 to 2.96 wt% iron and highstand stromatolitic and thrombolitic limestones of the Upper Aim Formation have Fe_T in the range 0.80 to 2.17 wt%. One sample of micritic limestone of the Upper Aim HST has a significantly reduced Fe_T concentration of 0.17 wt% which may reflect relatively rapid carbonate precipitation.

Where carbonate samples contain $Fe_T < 0.5$ wt%, iodine is present at very low concentrations relative to calcium+magnesium (< 2.5μmolmol^{-1}), however there are clear trends in I/(Ca+Mg) which are unrelated to lithology (Figure 5.5). Particularly, with the exception of one outlier at ~50 m, I/(Ca+Mg) values increase during regression in the late highstand systems tracts within the upper Aim and Ust'-Yudoma Formations (but values remain < 2.5μmolmol^{-1}). A maximum of 1.90 μmolmol^{-1} is reached immediately below the erosional unconformity which separates the Ust'-Yudoma Formation from the overlying Pestrotsvet.

Iron speciation of all samples with $Fe_T > 0.5$ wt% yield $Fe_{HR}/Fe_T > 0.38$ in the range 0.57 – 1.00 and $Fe_{py}/Fe_{HR} < 0.7$ in the range 0 – 0.53. The most elevated Fe_{py}/Fe_{HR} data correspond to two thrombolitic and micritic limestone samples of the Upper Aim Formation HST. With the exception of two siliciclastic samples which fall within the normal marine range of Fe/Al (0.42 – 0.64, Lyons and Severmann, 2006; Raiswell et al., 2008), all samples display significant iron enrichment where Fe/Al is between 0.68 and 3.70.

A pilot study of $\delta^{44/40}$Ca has been undertaken for selected samples at Nuuchchalakh and these data are also presented (alongside replicate analyses) in Figure 5.5. Data are given relative to the calcium isotopic composition of seawater. Dolomite samples of the Lower Aim Formation are characterised by δ^{44}Ca values which deviate about 0 ‰ with a possible minor positive excursion to 0.182 ‰ immediately followed by a return to ~0 ‰ at the Lower/Upper Aim Formation sequence boundary. This is followed by a trend to negative δ^{44}Ca values in the Aim Formation HST and values remain negative, between -0.21 and ~0 ‰, throughout dolomite of the Ust'-Yudoma Formation. The distinct negative excursion documented in the Upper Aim Formation HST corresponds to a change in lithology and reaches a nadir

of -0.362 ‰ within a sample of stromatolitic limestone. A trend towards positive $\delta^{44}Ca$ values is recorded with a change in lithology to limestones of the upper Ust'-Yudoma Formation and values reach a maximum of 0.336 ‰, however this change is not facies related (Wood et al., 2017a) and, following a short-lived negative excursion (-0.078 ‰), positive values are restored in dolomitic limestones of the lower Pestrotsvet Formation (0.080 – 0.165 ‰).

5.3.4 Kyra-Ytyga

The Kyra-Ytytga section outcrops near the Kyra-Ytyga creek mouth on the Yudoma River ~45 km up-river from Nuuchchalakh and approximately 50 km down river from the remote settlement of Yugoryonok (Figure 5.2b). Recent integrated bio- and chemostratigraphic study of this section strongly supports its position as latest Ediacaran in age (Zhu et al., 2017). At Kyra-Ytyga, the Aim Formation rests unconformably upon coarse conglomeratic sandstones of the Ust'-Kirbi Formation and, as at Nuuchchalakh, sediments of the Aim Formation were deposited during two cycles of accommodation change (Figure 5.6). Here, the Aim Formation constitutes an unfossiliferous lower sequence of

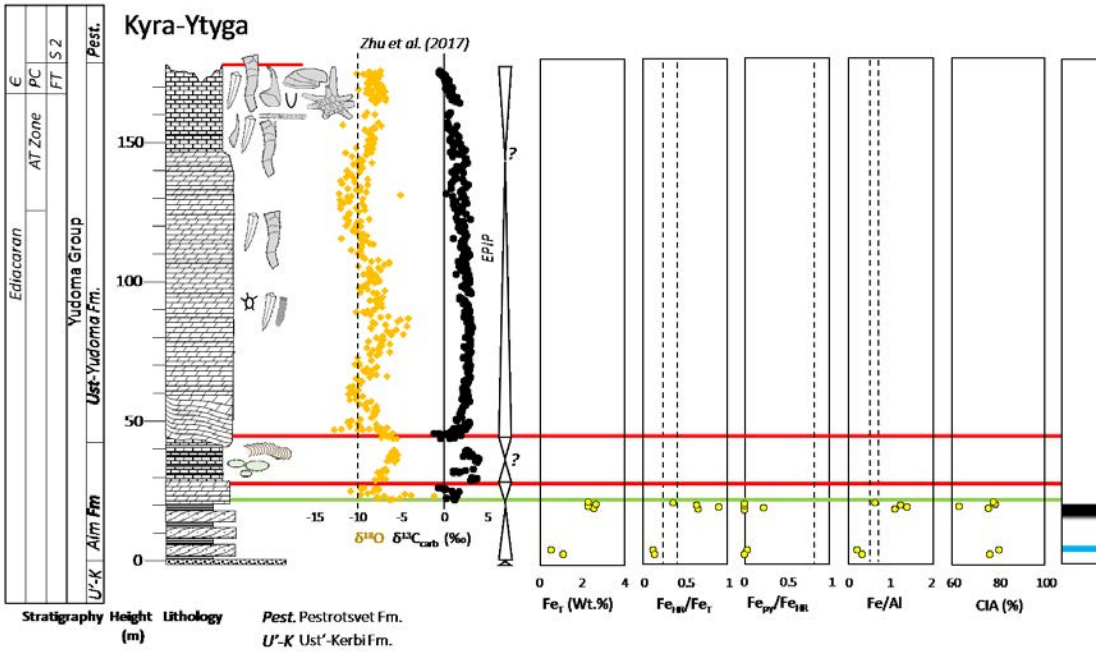

Figure 5.6 Stratigraphic log and geochemical data of the Kyra-Ytyga section with $\delta^{13}C_{carb}$ and biostratigraphic information after Zhu et al. (2017). Yellow markers represent siliciclastic samples. 'AT' and 'PC', *Anabarites trisulcatus* and *Purella cristata* biozones respectively. 'FT', Fortunian, 'S2', Stage 2. TSSF, Tommotian Small Shelly Fossils. Key to lithological and biostratigraphic symbols provided in Figure 5.4.

transgressive cross-bedded grey sandstones with red shale interbeds and highstand calcitic dolostones and an upper sequence of dark laminated limestones with black shale interbeds containing abundant soft-bodied fossils including *Shaanxilithes* and *Beltanelliformis* (Zhu et al., 2017). The overlying Ust'-Yudoma Formation is composed of shallow marine dolostones which transition to mixed dolomitic limestones and an upper unit of dolomitic limestone laminite (Zhu et al., 2017). The Kyra-Ytyga section terminates with the regional sub-Pestrotsvet unconformity and Tommotian variegated limestones of the Pestrotsvet Formation are absent at this section (Khomentovsky, 2008; Wood et al., 2017a; Zhu et al., 2017).

The Ust'-Yudoma Formation at Kyra-Ytyga is host to both *Cloudina* and *Anabarites* which co-occur in dolostone stratigraphically beneath numerous Nemakit-Daldynian small shelly fossils of the *Anabarites trisulcatus – Protohertzina anabarica* and *Purella cristata* zones (summarised in Figures 5.4 and 5.6) (Zhu et al., 2017). Abundant small shelly fossil associations noted from carbonate deposits of the Ust'-Yudoma Formation are peculiarly absent from correlative deposits of the nearby Nuuchchalakh section and are seen to predate a negative trend in $\delta^{13}C_{VPDB}$ inferred to relate to the BACE (Zhu et al., 2017).

5.3.4.2 Kyra-Ytyga geochemistry

Recently published carbonate carbon isotope values (Zhu et al., 2017) are displayed alongside new Fe/Al and iron speciation data for the Kyra-Ytyga section in Figure 5.6. Only suitable siliciclastic samples of the lower Aim Formation at Kyra-Ytyga were analysed for major element concentrations and iron speciation (Figure 5.6). In these samples, total iron concentration falls in the range 0.56 to 2.65 wt%. Values of Fe_{HR}/Fe_T increase up-section from 0.11 at the base to 0.88 nearing the MFS of the lower Aim Formation, with the stratigraphically highest sample at 29m yielding a Fe_{HR}/Fe_T value of 0.34 (Figure 5.6). The contribution of pyrite iron to the Fe_{HR} pool remains low throughout, with a maximum Fe_{py}/Fe_{HR} value of 0.23 corresponding to the sample with the highest Fe_{HR}/Fe_T. There is a positive correlation between Fe_T and Fe/Al whereby samples in the lower Aim Formation are distinctly depleted in Fe_T which is reflected in Fe/Al below the range of average marine shale (0.19 – 0.32). Similarly samples with $Fe_{HR}/Fe_T > 0.38$ are accompanied by $Fe/Al > 0.64$ near the MFS.

5.3.5 Southeast Siberia synthesis

Highstand systems tract deposits of the lower Aim Formation at Nuuchchalakh show a negative trend in $\delta^{13}C_{carb}$ which is comparable in magnitude to that observed from equivalent dolostones of the lower Aim Formation at Kyra-Ytyga (Figure 5.4 to 5.6) (Zhu et al., 2017 and unpublished data). Clastics

occupy transgressive deposits of the upper Aim Formation at Nuuchchalakh, however deeper limestone deposits at Kyra-Ytyga record a stepwise increase in $\delta^{13}C_{carb}$ to maximum values of ~4 ‰ (Zhu et al., 2017). The prominent negative $\delta^{13}C_{carb}$ excursion reported from the sequence boundary separating the Aim and Ust'-Yudoma Formations at Kyra-Ytyga (Zhu et al., 2017) either occupies a position equivalent to uppermost clastic deposits or is extremely attenuated at Nuuchchalakh (Figure 5.5). However, a minor trend to positive $\delta^{13}C_{carb}$, with a maximum of 2.26 to 2.83 ‰ is recorded at the base of the Ust'Yudoma Formation at Nuuchchalakh and Kyra-Ytyga respectively (Figure 5.4). Mean positive carbon isotope values of the Ust'-Yudoma Formation are 1.14 ‰ at Nuuchchalakh relative to 1.89‰ at Kyra-Ytyga. Most notably, the negative trend in $\delta^{13}C_{carb}$ in the middle Ust'-Yudoma Formation at Nuuchchalakh is absent at Kyra-Ytyga until uppermost limestones which preserve a richly fossiliferous SSF assemblage (Zhu et al., 2017). Such an abundance of SSFs is, in turn, absent at Nuuchchalakh, complicating section correlation within the Ust'-Yudoma Formation.

Iron speciation data at both Nuuchchalakh and Kyra-Ytyga indicate a predominantly anoxic and ferruginous shallow marine environment throughout deposition of the Aim Formation. Low Fe_{HR}/Fe_T analysed in siliciclastics of the lower Aim Formation at Kyra-Ytyga may suggest a very shallow marine environment above the oxycline, however these data must be treated with caution due to their unusually low Fe/Al below Phanerozoic average values (Lyons and Severmann, 2006; Raiswell et al., 2008). Highly reactive iron is predominantly contributed in carbonate phases in analysed samples from both sections and, even if all oxide-bound iron was ultimately contributed from the oxidation of pyrite, re-apportioned values of Fe_{py}/Fe_{HR} would not support deposition under euxinic water column conditions.

This redox interpretation is supported by very low values of I/(Ca+Mg). The presence of iodine within carbonate samples (even at vanishingly low concentrations) implies the existence of iodate and thus oxygen in the contemporary water column (e.g. Hardisty et al., 2017). However, concentrations of I/(Ca+Mg) are restricted to $< 2.5 \mu mol mol^{-1}$ indicative of deposition in close proximity to oxygen-depleted waters (Glock et al., 2014; Lu et al., 2016; Hardisty et al., 2017). Average I/(Ca+Mg) at Nuuchchalakh is significantly depleted relative to shallow deposits of the Omkyk Member of the Nama Group (Chapter 3, Section 3.4.1) and this likely reflects substantial dilution of iodate at Nuuchchalakh and closer proximity to, or more frequent interaction with, an anoxic water mass. A very shallow chemocline during deposition of the sections of southeast Siberia has previously been invoked as a mechanism promoting the formation of co-occurring iron-rich primary dolomite cements (Wood et al., 2017a). Furthermore, prominent glauconitic horizons in the Aim Formation at the Yudoma-Maya confluence and Nuuchchalakh also support this interpretation, as glauconite has been shown to precipitate at or near the redoxcline associated with iron reduction (e.g. Tang et al., 2017).

Major element analyses of Yudoma Group siliciclastics have also allowed for the calculation of the chemical index of alteration (CIA, Figure 5.7). Preliminary analyses reveal that these samples exhibit evidence for extensive potassic metasomatism which is likely related to the production of illite and/or the replacement of Ca or Na in plagioclase by K during metamorphism (Figure 5.7) (Fedo et al., 1995; Tosca et al., 2010). Correcting for metasomatism and using a primary source rock composition of late Proterozoic granite (Condie et al., 1993) yields a lower limit for the chemical index of alteration (Figure 5.7). Corrected values of CIA fall in the range 62.5 – 80.3% and there is a negative correlation between Fe_{HR}/Fe_T and CIA in samples of both Nuuchchalakh ($r^2 = 0.53$) and Kyra-Ytyga ($r^2 = 0.51$) (Appendix B, Figure AB12), indicating that changes in the composition of weathered source material, particularly increased contribution of clay minerals and associated organic matter burial may have aided brief periods of oxygenation. The degree to which samples have undergone metasomatism may suggest cause for concern in interpretation of redox from iron speciation, as higher metamorphic temperatures lead to the redistribution of Fe_{HR} and formation of poorly reactive silicate- bound iron (Raiswell and Canfield, 1998). However, in a closed system this only acts to reduce Fe_{HR}/Fe_T leaving the ratio of Fe/Al

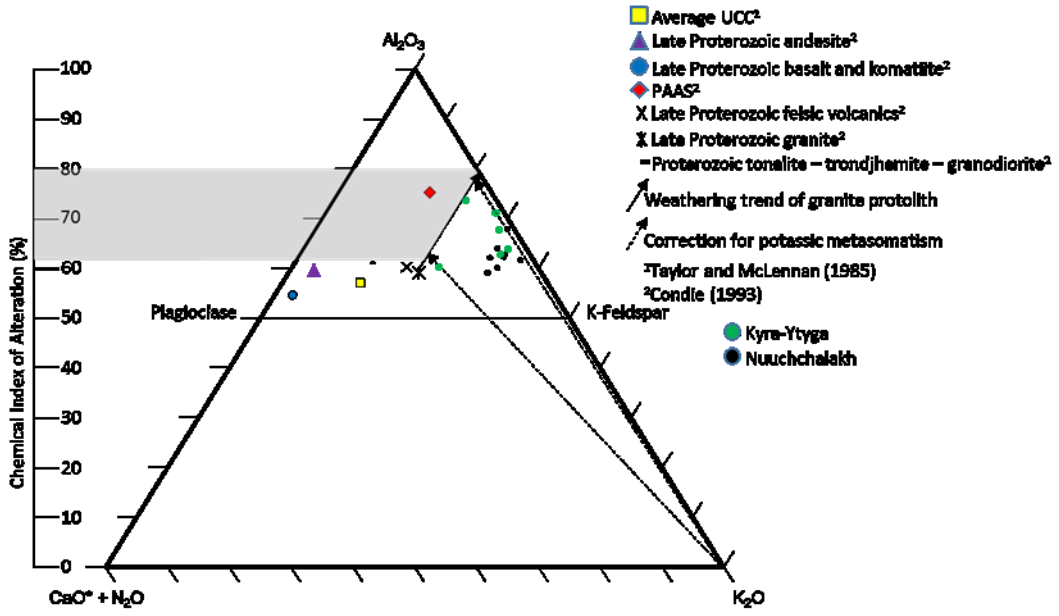

Figure 5.7 Ternary diagram showing variability in the chemical index of alteration (CIA) between siliciclastic samples of the Yudoma River.

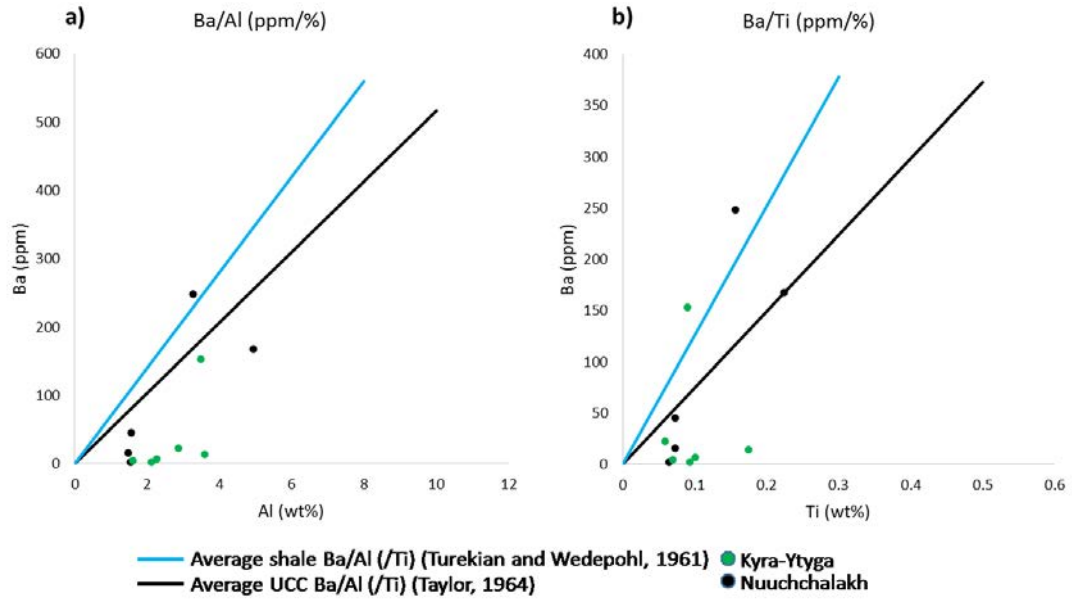

Figure 5.8 a) Ba/Al (ppm/%) and **b)** Ba/Ti (ppm/%) for samples of the Yudoma River. Graphs show the difficulty involved in assessment of local baseline Ba/Al (and Ba/Ti).

unchanged and as such, the interpretation of anoxia from elevated Fe/Al remains robust. Furthermore, diagenesis and metamorphic alteration are only known to reduce the iodine concentration of carbonates and therefore, data of I/(Ca+Mg) represent minimum values (Hardisty et al., 2017).

Data of Ba/Al and Ba/Ti for siliciclastic samples of Nuuchchalakh and Kyra-Ytyga are presented in Figure 5.8. Average Ba/Al and Ba/Ti are unusually low in the Aim Formation, with a minimum value of Ba/Al = 1.1 ppmwt%$^{-1}$. Barium depletion may be related to post-depositional barite dissolution under sulfidic pore water conditions and fluid migration (van Os et al., 1991) and as such, it is difficult to assess whether apparent Ba enrichments relate to primary water column biogenic production or simply post-depositional element remobilisation in these samples.

5.4 The Dengying and Zhujiaqing Formations of the Yangtze Block

The redox record of the Dengying Formation is conspicuously sparse, especially when considering the fact that it comprises one of the most fossiliferous late Ediacaran Formations deposited on the Yangtze platform. This gap in knowledge is largely a consequence of the predominantly carbonate lithologies deposited on the shallow shelf, which have classically been considered unfavourable for iron speciation.

However, recent calibration of iron speciation for carbonate-rich samples (Clarkson et al., 2014) unveiled these deposits for further study, prompting a field excursion by Rachel Wood and Aihua Yang in August 2014 to two sections; Yinchangpo in Yunnan Province and Wuhe in Hubei which contain deposits of the Dengying Formation. Here, new carbon and oxygen isotopic data are presented from carbonate-rich sediments (including early diagenetic dolomites and phosphorites) of both sections in addition to major element and, where possible, iron speciation data.

5.4.1 Yinchangpo, Yunnan

Stratigraphy of Ediacaran-Cambrian age in northeast Yunnan Province is exposed approximately 10km northwest of Huize County town, with deposits at Yinchangpo representing one of the most intact shallow marine sections on the Yangtze Platform. This section closely corresponds to the Laolin section described in Li, D. et al. (2009), with the addition of the lower Dengying Formation (Donglongtan Member). The Donglongtan Member is an approximately 450m thick succession of micritic dolomite with minor stromatolites and fenestral limestone in upper layers (Figure 5.9a). The overlying Jiucheng Member is approximately 37m thick and composed of interbedded dark green dolomitic shale and quartz-rich black siltstone. Zircons in ash beds of the basal and middle Jiucheng Member have recently been analysed via SIMS U-Pb geochronology at the Xiaolantian and Yinchangpo sections and yield a lower age (from Xiaolantian section) of 553.6 ± 2.7 Ma and an upper age (from Yinchangpo section) of 546.3 ± 2.7 Ma) (Yang et al., 2016).

The Jiucheng Member is conformably overlain by highstand systems tract deposits of the Baiyanshao Member (Upper Dengying Formation) which are represented by ~245m of thick-bedded grey dolostone. An uppermost unit of beige siliceous dolostone in the Baiyanshao Member has previously been ascribed to the lower unit of the Xiaowaitoushan Member (Luo et al., 1991), however this classification has since been rejected and is consequently not used in this study (Qian et al., 1996; Zhu et al., 2001; Li, D. et al., 2009).

The Zhujiaqing Formation overlies the Dengying Formation deposits at Yinchangpo and constitutes, in ascending order the Daibu, Zhongyicun and Dahai Members. The Daibu Member is composed of interbedded limestone, siltstone, and chert representing a 20m thick transgressive systems tract (TST) (Qian et al., 1996; Zhu et al., 2001). The following 9m of grey laminated phosphorites have been assigned to the Zhongyicun Member and contain small shelly fossils characteristic of the *Anabarites trisulcatus – Protohertzina anabarica* zone in addition to bioturbation traces (Zhu et al., 2001; Steiner et al., 2007). A transitional boundary gives way to 17m of phosphatic dolostone and minor black shale of the

Dahai Member. The transitional boundary which separates the Daibu Member from the maximum flooding surface of Zhongyicun Member phosphorite is taken to represent the Precambrian/Cambrian boundary at the Yinchangpo section (Li, D. et al; 2009), with first appearance of SSFs postdating the boundary. It is important to note that the Zhujiaqing Formation at Yinchangpo section exhibits a high degree of tectonic compression which has distorted the Daibu, Zhongyicun, and Dahai Members evident from severe, occasionally isoclinal folding.

5.4.1.2 Yinchangpo geochemistry

At Yinchangpo, $\delta^{13}C_{carb}$ values at the base of the Donglongtan Member begin at 1.95 ‰ and, with the exception of one sample at the base of the Donglongtan Member (-0.94 ‰), values remain positive throughout the Dengying Formation in the range 0.73 – 3.25 ‰ (Figure 5.9a). Geochemical results of the Zhujiaqing Formation at Yinchangpo are enlarged in Figure 5.9b. The upper Daibu Member of the Zhujiaqing Formation records the onset of a distinctly negative carbon isotope excursion reaching values as low as -8.04 ‰ in the Upper Zhongyicun Member. Previous isotopic studies undertaken at Meishucun and Laolin sections record onset of this negative $\delta^{13}C_{carb}$ excursion in the uppermost Baiyanshao Member of the Dengying Formation (Brasier et al., 1990; Li, D. et al., 2009). It is likely that corresponding isotopically depleted samples of the Upper Baiyanshao Member were missed during sampling at Yinchangpo and the expected interval of the BACE is marked in Figure 5.9b. Samples of the Zhujiaqing Formation are typified by a positive trend between $\delta^{13}C_{carb}$ and $\delta^{18}O_{carb}$ and low $\delta^{18}O_{carb}$ (< -10 ‰) with the exception of 2 samples, one from the lower Daibu Member and the second from the middle Dahai Member (samples Daibu 0 and 9 respectively). Positive $\delta^{13}C_{carb}$ values are restored in the Dahai Member as previously reported at Meishucun and Laolin (Brasier et al., 1990; Li, D. et al., 2009) and reach values as high as 3.69 ‰.

Diagenetic overprinting of elemental concentrations may be a cause for concern in carbonates from Yinchangpo, especially in samples of the Zhujiaqing Formation where dolomitic phosphorites of the Zhongyicun Member display pronounced negative $\delta^{18}O$ < -10 ‰. As such, carbon isotope values of the Zhongyicun Member have previously been suggested to reflect the influence of meteoric or deep burial diagenesis rather than global seawater DIC (Brasier et al., 1990). These negative $\delta^{13}C_{carb}$ have been omitted from the compilation represented in Figure 5.1. The majority of samples from Yinchangpo are characterised by Mn/Sr in the range 1.52 to 13.88, however three samples have Mn/Sr > 20 (lower Donglongtan, middle Jiucheng and upper Dahai Members) and the final sample, taken from phosphatic dolostone of the Dahai Member, has as value of 53.73 associated with significant Mn enrichment.

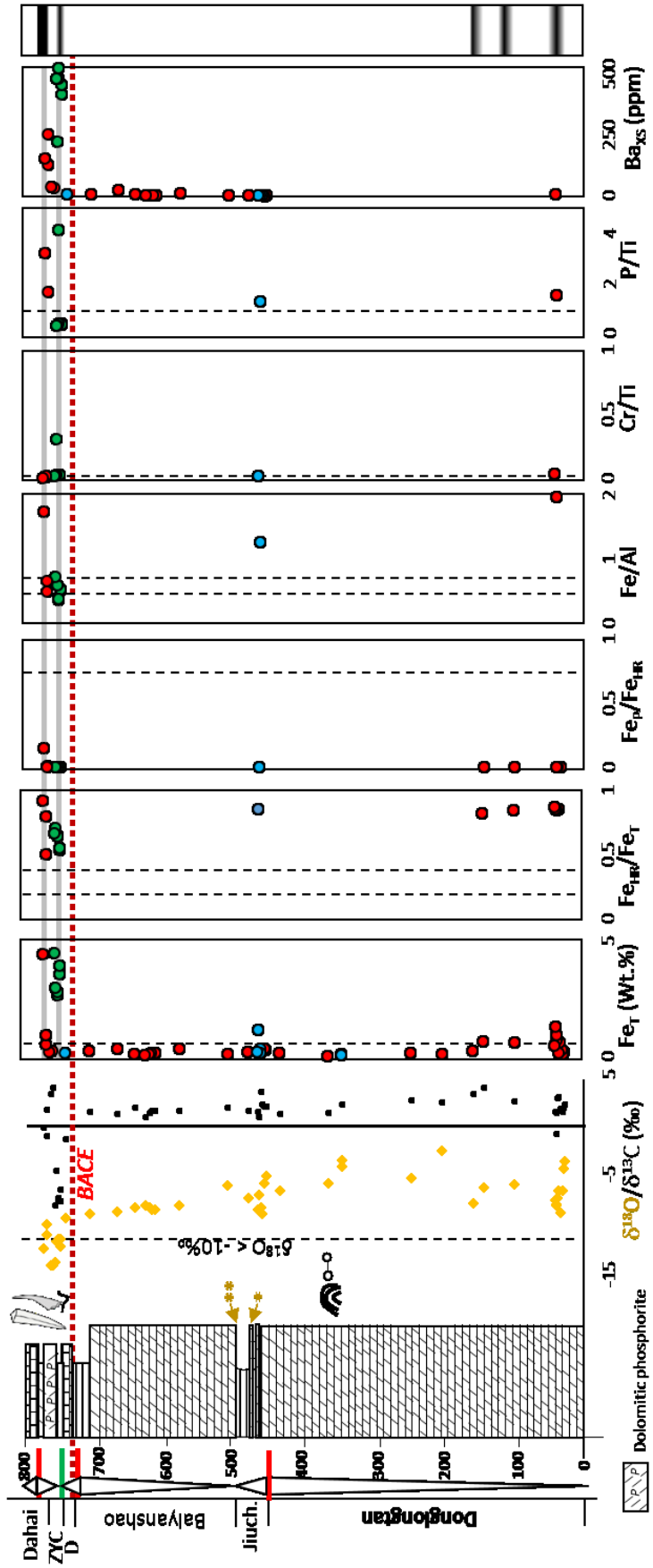

Figure 5.9a
Stratigraphic log and geochemical data of Yinchangpo section, Yunnan Province, South China. Section location and schematic redox interpretation also noted in Chapter 2, Figure 2.2 and accompanying inset map. Note that the nadir position of the BACE is in the Daibu Formation, immediately below diagenetically altered negative $\delta^{13}C_{carb}$ of the Zhongyicun Member. D = Daibu, ZYC = Zhongyicun.

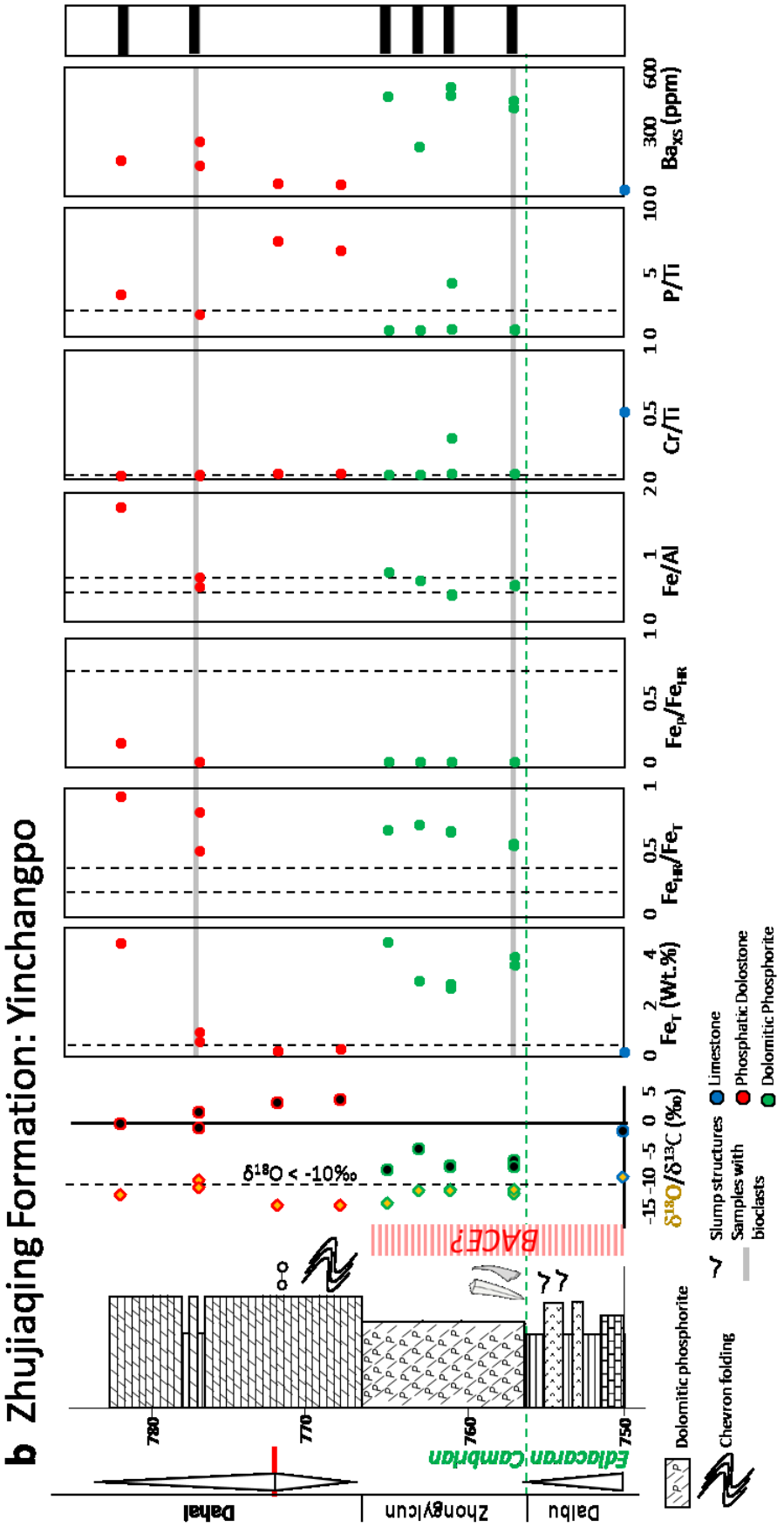

Figure 5.9b
Enlarged view of the proposed Ediacaran-Cambrian boundary in the depositional interval between the upper Baiyanshao to Dahai Members. Green dashed line indicates the classically defined boundary between the Ediacaran and Cambrian at the MFS separating the Daibu from Zhongyicun Members of the Zhujiaqing Formation.

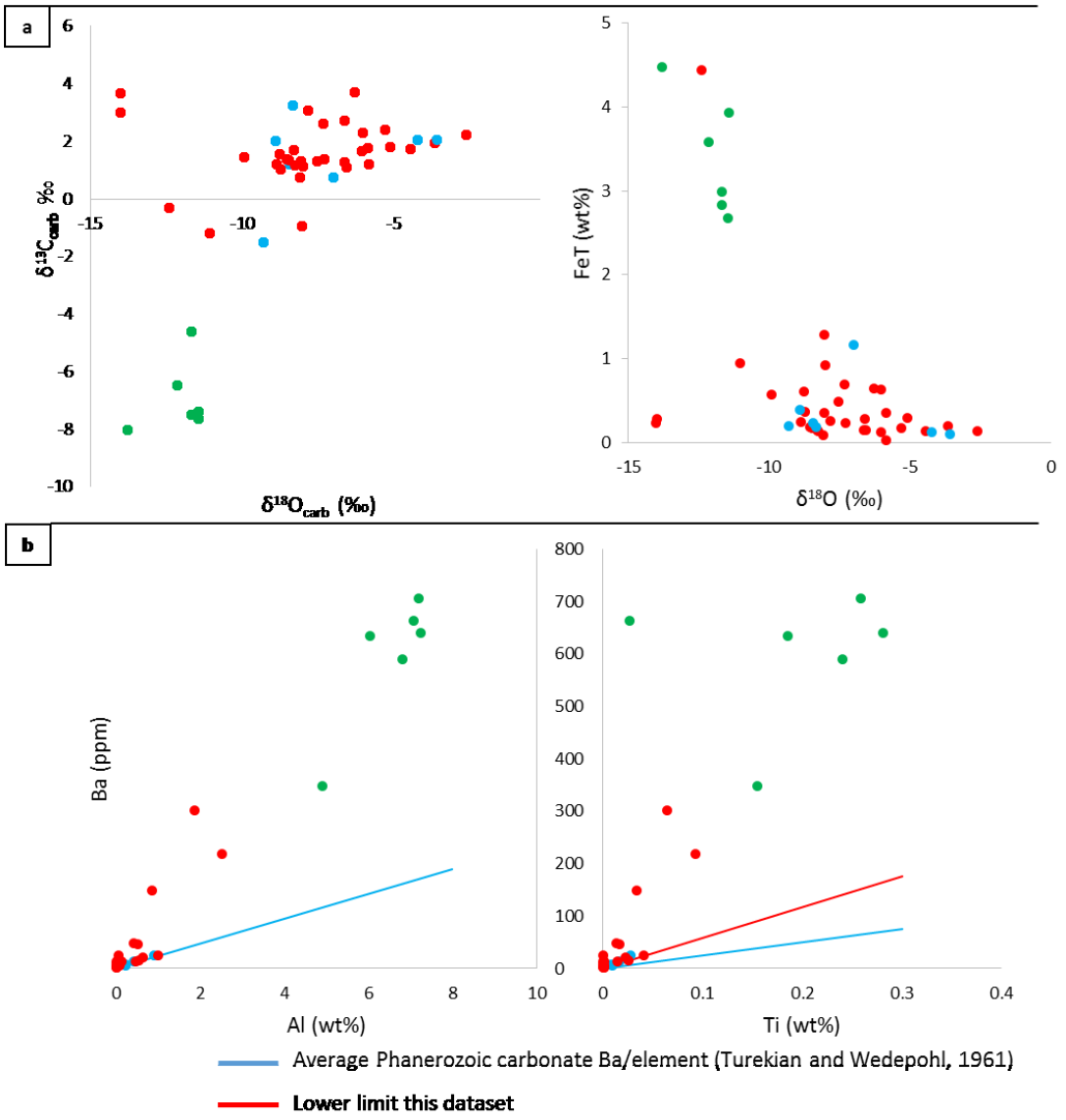

Figure 5.10

Proxies for degree of alteration including **a)** covariation of $\delta^{13}C$ and $\delta^{18}O$ and the relationship between depleted $\delta^{18}O$ and Fe_T enrichment at Yinchangpo, **b)** The relationship between Ba and detrital elements (Al and Ti) and determination of the local Ba/Al baseline ratio. Red: dolomite/phosphatic dolostone, blue: limestone, green: dolomitic phosphorite.

Manganese enrichment may reflect elevated concentrations of Mn in the water column during primary carbonate precipitation or late stage enrichment during diagenesis under anoxic pore water conditions. Whereas $\delta^{13}C_{carb}$ of the Dengying Formation likely reflect primary values, the three samples of Mn/Sr > 20 may have undergone significant open-system elemental exchange, however, as discussed above this

interpretation is complicated by the likelihood of water column anoxia during deposition of carbonate sediments.

In carbonate samples of the Dengying Formation, total iron is predominantly lower than the minimum threshold concentration suitable for iron speciation (0.5 wt%), however there are a number of horizons where samples contain sufficient iron including the lower Donglongtan Member and one sample of the Jiucheng Member (Figures 5.9a). In contrast, numerous samples of the Zhujiaqing Formation contain $Fe_T > 0.5$wt%, with a maximum concentration in dolomitic phosphorites of the Zhongyicun Member where Fe_T reaches 4.48wt% (Figure 5.9b). However, the most negative $\delta^{18}O_{carb}$ values in Zhongyicun Member samples are associated with the highest Fe_T (Figure 5.10a), suggesting possible anoxic pore water iron remobilisation and enrichment during carbonate diagenesis and as such, these data must be treated with caution.

Iron speciation data for suitable samples at Yinchangpo are invariably characterised by $Fe_{HR}/Fe_T > 0.38$ and $Fe_{py}/Fe_{HR} < 0.7$ consistent with ferruginous water column conditions throughout deposition (Figure 5.9a). The highly reactive iron pool is concentrated predominantly in iron carbonates throughout the Dengying Formation, with a significant contribution from iron oxides and negligible magnetite or pyrite bound iron (see Appendix B). In contrast, highly reactive iron in samples of the Zhongyicun Member is primarily concentrated in the iron oxide pool with a significantly reduced proportion divided approximately-equally between carbonate phases and magnetite. Overlying phosphatic dolostones of the Dahai Member contain a significantly greater proportion of iron in carbonates relative to the Zhongyicun Member.

Iron enrichments inferred from Fe/Al in a limited number of samples from the Dengying Formation are significant relative to the range of Phanerozoic oxic carbonates (Clarkson et al., 2014), with two samples of $Fe_T > 0.5$ wt% with Fe/Al from 1.27 to 1.99. Contrastingly, iron enrichments are only significant in a small number of samples from the overlying Zhujiaqing Formation wherein Fe/Al values are in the range 0.38 to 1.76. Low average Fe/Al and elevated Fe_{HR}/Fe_T may suggest weathered source rock of unusually low Fe_T which would be consistent with exposure and erosion of low iron carbonates of the underlying Dengying Formation carbonates during sea level lowstands.

Two samples of the Zhujiaqing Formation exhibit Cr/Ti values of 0.31 and 0.51which are significantly enriched relative to average Phanerozoic carbonates (Cr/Ti = 0.028, Turekian and Wedepohl, 1961), however in all other samples of the Zhujiaqing Formation, a mean Cr/Ti value of 0.026 approximates average carbonate composition. Zhujiaqing Formation samples also show highly variable P/Ti, with the most depleted values (at first glance counterintuitively) corresponding to

dolomitic phosphorite of the Zhongyicun Member. However, the majority of these dolomitic phosphorites contain extremely elevated Ti concentrations due to their siliciclastic content (up to 0.28 wt%) which swamp the ratio of P/Ti (and Cr/Ti) leading to values closer to average shale composition.

Samples of the Yinchangpo section display a positive correlation between Ba and Al (/Ti) implying that Ba was predominantly sourced in detrital material (Figure 5.10b). However, there are distinct local baseline ratios for both Ba/Al and Ba/Ti (blue lines in Figure 5.10b) from which Ba enrichments are quantifiable. Using a local baseline Ba/Al at Yinchangpo of 24.8 ppmwt%$^{-1}$ yields stable and low Ba_{XS} throughout the Dengying Formation with a mean of just 5.12 ppm (variability near the detrital background composition), however there is a notable positive excursion associated with dolomitic phosphorite of the Zhongyicun Member where Ba_{XS} attains a maximum value of 528.19 ppm (Figure 5.9b). The Ba_{XS} peak in the Zhujiaqing Formation is comparable in magnitude to previously reported values for correlative deposits of the lower Yanjiahe Formation phosphorites at Luojiacun section (Yangtze Gorges, Hubei) (Liu et al., 2017). However, there is a positive correlation between Ba_{XS} and Fe_{ox} in samples of the Zhongyicun Member ($r^2 = 0.67$) which may allude to Ba delivery via adsorption onto iron oxides rather than organic matter.

5.4.2 Wuhe, Hubei

The Wuhe (/Gaojiaxi) section is exposed in the Huangling anticline south of Sandouping, in the Yangtze Gorges area, Hubei Province (Figure 5.11). Strata here are correlative to those exposed at Yinchangpo, with Hamajing, Shibantan, and Baimatuo Members comprising the Dengying Formation, and lowermost Yanjiahe Formation (early Cambrian) equivalent to Zhongyicun and Dahai Members of the Zhujiaqing Formation at Yinchangpo.

At Wuhe, the Hamajing Member is approximately 20m thick and composed of undulating beds of peritidal intraclastic and oolitic dolomitic grainstone containing oncolites characteristic of shallow water and high energy (Zhu et al., 2007; Duda et al. 2014). The lower Hamajing Member also contains karstic features and tepee structures indicative of a significant fall in relative sea level (Shen et al., 2009). Over 120m of carbon-rich, bituminous, micritic limestone constitutes the overlying Shibantan Member which is interpreted as having been deposited between fair weather and storm wave base (Chen, Z. et al., 2014). Abundant fossils of soft-bodied organisms are preserved in the Shibantan Member and include the tubular *Wutubus annularis*, the frondose *Paracharnia dengyingensis*, discoidal *Hiemalora*, a possible palaeopasichnid *Curviacus ediacaranus*, *Yangtziramulus zhangi* and forms reputed to represent *Rangea*, *Pteridinium*, and *Charniodiscus* (Sun, 1986; Xiao et al., 2005; Shen et al., 2009, 2017; Chen, Z. et al.,

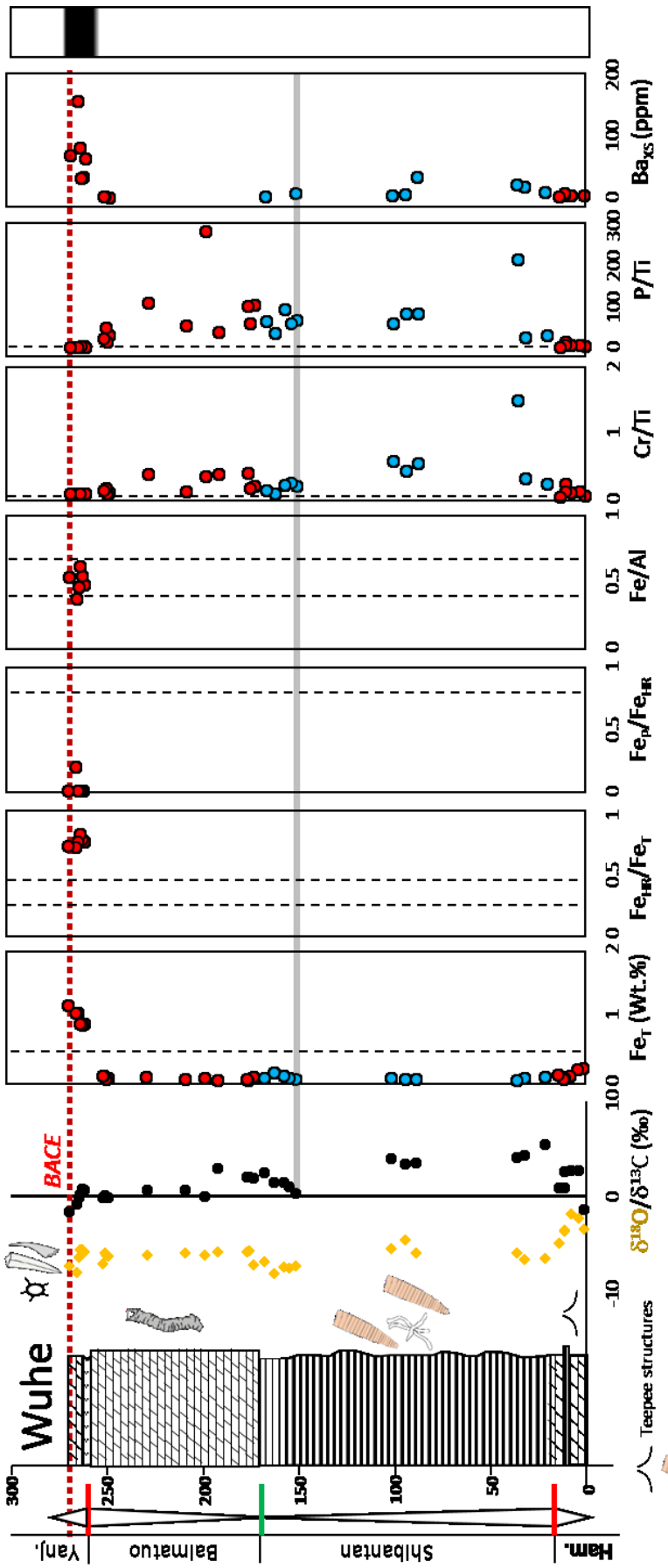

Figurer 5.11
Stratigraphic log and geochemical data of the Wuhe section, Yangtze Gorges area, Hubei Province, South China. Section location and schematic redox interpretation also noted in Chapter 2, Figure 2.2 and accompanying inset map.

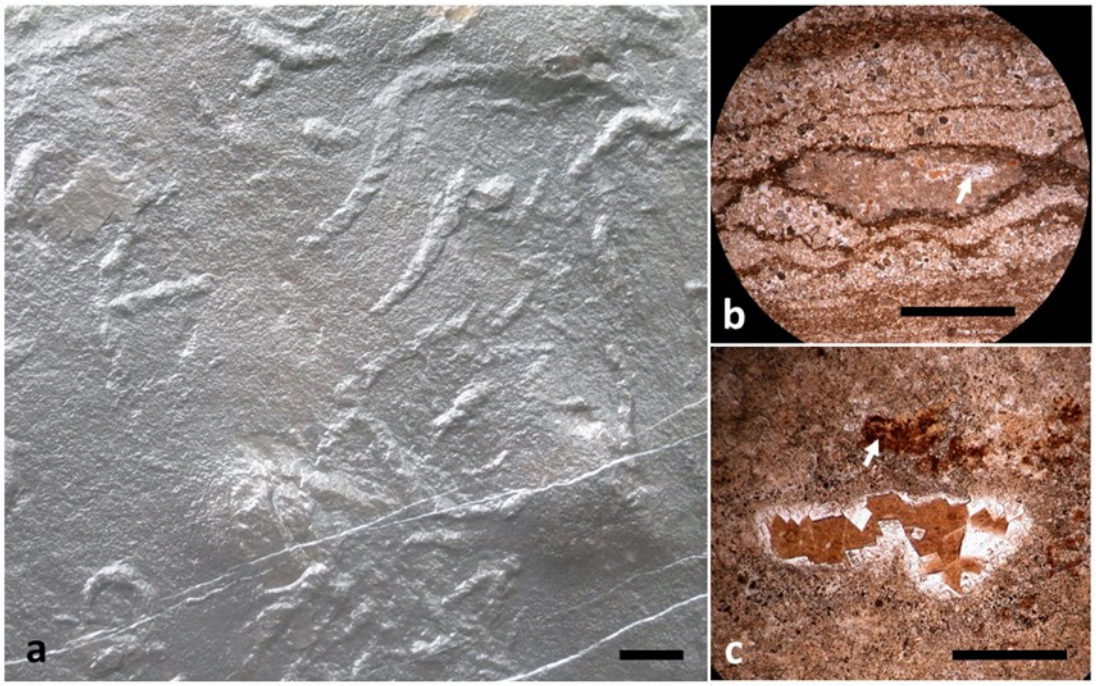

Figure 5.12

a) Outcrop photograph of ichnofossils from the middle Shibantan Member including complex radial elements with right-handed helical morphology similar to *Streptichnus narbonnei* (Jensen and Runnegar, 2005), Scale bar = 1 cm (photograph provided by Rachel Wood), **b)** Transmitted light photomicrograph of small burrow cross-section from Shibantan Member limestones, defined by crinkled, organic-rich microlaminae. Burrow infill is composed of micritic sediment and dolomite cement (white arrow), Scale bar = 2.5 mm, **c)** Magnified transmitted light photomicrograph of diagenetic rhombic dolomite cement which preferentially infills permeability within burrows (white arrow denotes possible bitumen) Scale bar = 0.5 mm.

2014). Sediments of the Shibantan Member were deposited in a distal, off-shore environment within a protected intra-shelf basin (Shen et al., 2009, 2017; Duda et al., 2014). Abundant microbial mat fabrics, *Vendotaenia* and trace fossils including *Lamonte trevallis*, *Planolites*, *Palaeophycus*, *Helminthoidichnites* and *Torrowangea* are found in deposits of the Shibantan Member in association with the aforementioned soft-bodied assemblage (Figure 5.12a) (Weber et al., 2007; Meyer et al., 2014).

The upper Shibantan Member is chert-rich and grades into the Baimatuo Member, composed of massively bedded micritic dolomite deposited in a peritidal environment (Zhu et al., 2007; Duda et al., 2014). The Baimatuo Member contains fossil representatives of the skeletal *Sinotubulites baimatuoensis* (Chen et al., 1981). A disconformable contact separates the Baimatuo from overlying sediments of the

basal Cambrian Yanjiahe Formation which is composed of interlayered chert and grey dolostone. The Yanjiahe Formation of the Yangtze Gorges area also contains a prominent phosphorite horizon considered equivalent to that of the Zhongyicun Member in Yunnan Province (e.g. Shen et al., 2009), however this unit was not sampled for the present study. Earliest Cambrian acanthomorphic acritarchs of the *Asteridium – Comasphaeridium – Heliosphaeridium* (AHC) assemblage and small shelly fossils of the *Anabarites trisulcatus – Protohertzina anabarica* zone occur in cherts and phosphorites of the lower Yanjiahe Formation horizon which together support a stratigraphic position equivalent to Nemakit-Daldynian deposits of the Siberian Platform (Chen, 1984; Dong et al., 2009). Furthermore, recent assessment of the spatiotemporal association of the AHC assemblage to other markers, including the *Anabarites trisulcatus – Prrotohertzina anabarica* zone and the BACE have confirmed its utility as a biostratigraphic marker for the basal Cambrian in South China (Ahn and Zhu, 2017).

5.4.2.2 Wuhe geochemistry

Carbon isotope chemostratigraphy of the Dengying and lower Yanjiahe Formations at Wuhe are presented alongside geochemical data in Figure 5.11. In contrast to aforementioned significant $\delta^{18}O_{carb}$ depletion in shallow shelf deposits at Yinchangpo, the oxygen isotopic record at Wuhe records an initial decrease from -1.71 to -6.32 ‰ in the Hamajing to lower Shibantan Members. Following this, values remain relatively stable, with $\delta^{18}O_{carb}$ between -7.91 and -4.47 ‰ throughout the Shibantan and Baimatuo Members and the overlying lower Yanjiahe Formation (Figure 5.11).

Carbon isotopes of Hamajing Member dolomites at Wuhe display a positive trend from negative values as low as -1.29 ‰ at the base to a maximum of 2.77 ‰ (Figure 5.11). Values of $\delta^{13}C_{carb}$ reach a maximum of 5.51‰ in lower Shibantan limestones and remain positive throughout deposition of the Shibantan Member with variability between 0.38 and 4.38 ‰. In the overlying Baimatuo Member at 190-200m, $\delta^{13}C_{carb}$ decrease from 2.95 ‰ to 0.08 ‰ after which values linger about 0‰ for the remaining ~50m of Baimatuo deposition with two minor negative excursions near the top of the Member to a minimum value of -0.06 ‰. The overlying Yanjiahe Formation shows a distinct negative $\delta^{13}C_{carb}$ excursion from 0.73 ‰ to -1.54 ‰. In contrast to the record at Yinchangpo, there is no covariation between $\delta^{18}O_{carb}$ and $\delta^{13}C_{carb}$ and the majority of samples are characterised by Mn/Sr < 5 (average Mn/Sr= 3.8) (Figure 5.13a).

Total iron concentrations are consistently below 0.5wt% throughout carbonates of the Dengying Formation (mean Fe_T = 0.06 wt%), precluding palaeoredox analysis via iron speciation.

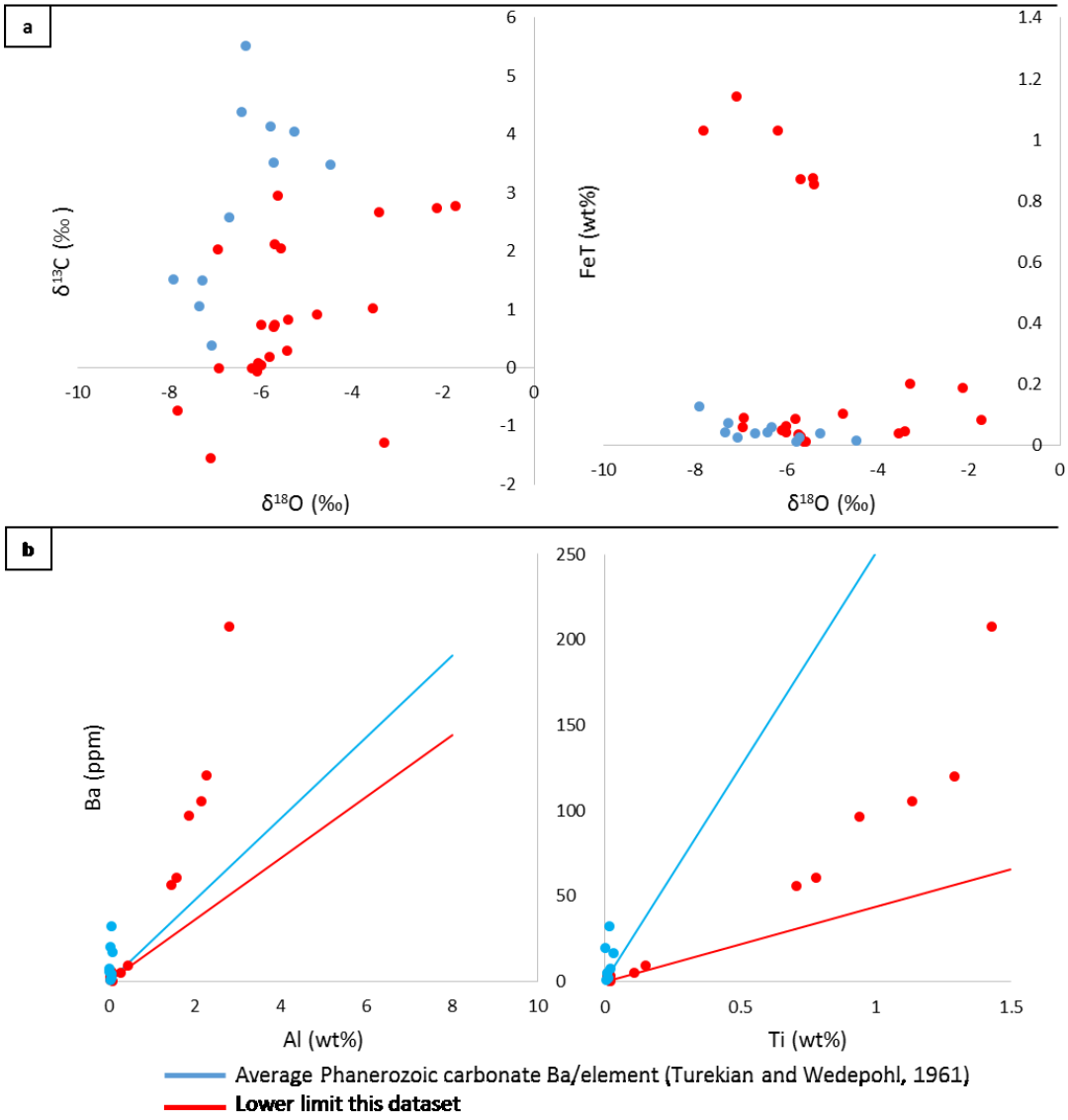

Figure 5.13

a) Proxies for degree of alteration including covariation of $\delta^{13}C$ and $\delta^{18}O$ and the relationship between depleted $\delta^{18}O$ and Fe_T enrichment at Wuhe, **b)** The relationship between Ba and detrital elements (Al and Ti) and determination of the local Ba/Al baseline ratio. Red: dolomite, blue: limestone.

Transmitted light photomicrographs of samples containing ichnofossil traces indicate that diagenetic dolomite preferentially grew in regions of higher permeability within burrow interiors (Figure 5.12b, c). Inspection of the same specimens under CL indicates that these non-luminescent, rhombic dolomite cements were precipitated by pore fluids depleted in iron, likely due to correspondingly iron-depleted

carbonates which constitute the surrounding sediment. In contrast total iron concentrations of the Yanjiahe dolostone are markedly elevated (mean = 0.97 wt%). The absence of a correlation between Fe_T and $\delta^{18}O_{carb}$ or Fe_T and Mn/Sr in samples collected at Wuhe suggest minimal elemental remobilisation during diagenesis (Figure 5.13a and Appendix B).

Iron speciation data for samples of the Yanjiahe Formation where $Fe_T > 0.5$ wt% cluster about a mean Fe_{HR}/Fe_T value of 0.78, with Fe_{py}/Fe_{HR} consistently below 0.7 (mean = 0.04). Iron speciation data therefore strongly support ferruginous conditions during deposition of the lower Yanjiahe Formation, in agreement with a decrease in oxygen concentration inferred from Ce/Ce* data (Ling et al., 2013). Samples of the Yanjiahe Member display Fe/Al between 0.37 and 0.61 supporting negligible iron enrichment, however it is inferred that local detrital baseline Fe/Al was lower in this area of the Yangtze Platform during deposition of the Yanjiahe Formation due to a broad hinterland predominantly composed of low iron carbonates (Dengying Formation) which provided weathered material during sea level lowstands.

Throughout much of the section, ratios of Cr/Ti and P/Ti are slightly enriched relative to Phanerozoic average carbonate composition (Cr/Ti = 0.03 and P/Ti = 1, Turekian and Wedepohl, 1961) and are lowest during deposition of the Hamajing Member and Yanjiahe Formation. However, sporadic Cr and P enrichment is evident during deposition of the Shibantan and Baimatuo Members (Figure 5.11). Chromium enrichment reaches a maximum in the lower Shibantan Member where Cr/Ti = 1.49 (with correspondingly elevated P/Ti = 214.70) and the maximum value of P/Ti (285.80) is found in a dolomite sample of the Baimatuo Member. However, maximum Cr and P enrichments occur in samples characterised by significant Ti depletion and consequently are unlikely to reflect changes in water column elemental concentrations but may instead reflect differential carbonate precipitation rate and/or relative distance from detrital source material. Furthermore, highly variable concentrations of Cr and P in Shibantan carbonates are likely complicated by the compounding effects of variable organic carbon content and elemental retention resulting from patchily distributed microbial mat material.

For the majority of samples at Wuhe, there is a positive correlation between Ba and Al (/Ti) (Figure 5.13b), indicating that the dominant source for Ba was associated with detrital material, similar to samples at Yinchangpo. Discounting one unusually depleted sample in the Hamajing Member (Hamajing 2, see Appendix B) yields a baseline Ba/Al ratio of 18.23 $ppmwt\%^{-1}$ from which values of Ba_{XS} correspond to enrichment above this ratio (Figure 5.11). Excess Ba remains extremely low throughout carbonates of the Dengying Formation with values of 0.06 – 31.74 ppm, however there is a distinct positive trend towards more elevated (but still modest) concentrations in the Yanjiahe Formation where Ba_{XS} attains a maximum value of 157.41 ppm. In contrast to samples from Yinchangpo, those of

the Yanjiahe Formation show no correlation between Ba_{XS} and Fe_{ox} or Mn, and enrichment in the Yanjiahe Formation are instead consistent with enhanced Ba delivery in association with organic matter.

5.4.3 Yangtze Block synthesis

The positive trend of $\delta^{13}C_{carb}$ in the lower Donglongtan Member at Yinchangpo and the Hamajing member at Wuhe likely records recovery from the underlying Doushantuo negative carbon isotope excursion (or 'DOUNCE') which is considered correlatable to the Shuram-Wonoka anomaly (Zhu and Li, 2017). As such, lower Dengying Formation carbonates are approximately time correlative to deposits of the Omkyk Member in Namibia and possibly the upper Aim or lowermost Ust'-Yudoma Formation of the southeast Siberian Platform. Overlying relatively stable and positive $\delta^{13}C_{carb}$ values throughout the Dengying Formation are considered characteristic of the late Ediacaran positive carbon isotope plateau (EPIP), approximately equivalent to values recorded from the Ust'-Yudoma Formation of the southeast Siberian Platform and the Upper Kuibis and Schwarzrand Subgroups of the Nama Group, Namibia (Figure 5.1) (Zhu et al., 2017). Following this, a negative $\delta^{13}C_{carb}$ excursion recorded in the Yanjiahe Formation can be correlated with the onset of the BACE.

Iron speciation data presented herein point towards infrequent ferruginous water column conditions during deposition of the Dengying Formation at Yinchangpo, however extremely iron depleted carbonates which constitute the bulk of deposition throughout the Dengying Formation at both sections may either reflect the dominance of oxic waters (e.g. Wood et al., 2015) or be the product of rapid carbonate precipitation. Previous geochemical studies of palaeoredox are sparse for the Dengying Formation and have predominantly targeted RSEs, REEs and Ce anomalies in carbonates of the Gaojiashan and Beiwan Members of southern Shaanxi Province and correlative deposits of the Shibantan Member of Hubei Province (Ling et al., 2013; Zhang, P. et al., 2014; Duda et al., 2014; Chen, X. et al., 2015). In both areas, intermittent redox stratification has been inferred with ferruginous depths overlain by oxic surface waters. Indeed, previous Ce anomaly data of the Dengying Formation at Wuhe have been interpreted to represent deposition under an intermittently redox-stratified water column influenced by frequent storm ventilation (Duda et al., 2014). A trend towards more oxygenated conditions (or a decrease in frequency of anoxic incursion) has further been suggested for water column conditions during deposition of the Baimatuo Member (Ling et al., 2013).

There is evidence to suggest that some carbonate-rich samples of the Zhujiaqing Formation at Yinchangpo have undergone pervasive open-system element and isotopic remobilisation during diagenesis. This has previously been inferred to account for a corresponding negative carbon isotope

excursion in dolomitic phosphorites of the Zhongyicun Member (Brasier et al., 1990). As such, iron speciation data of the Zhongyicun Member may have been significantly altered from depositional values as a consequence of secondary iron addition, possibly during later dolomitisation. However, considering the fact that highly reactive iron in samples of the Zhongyicun Member is primarily contributed as oxide rather than iron carbonate, these Fe_{HR}/Fe_T data may instead represent primary depositional water column conditions. If this is the case, the Zhongyicun Member was likely deposited in the presence of a dominantly ferruginous water column. This is in agreement with iron speciation data for time-equivalent deposits of the Yanjiahe Formation at Wuhe, Jijiapo (Och et al., 2013) and Jiuqunao (Li, C. et al., 2017b) where ferruginous conditions are similarly inferred (Chapter 2, Figure 2.2).

The early Cambrian Zhujiaqing and Yanjiahe Formations were deposited atop carbonates of the Dengying Formation on the Yangtze Platform during an interval of marine transgression. The Upper Liuchapo Formation is considered correlative to the Dengying Formation based on SHRIMP (/SIMS) U-Pb dating (Chen, D. et al., 2009, 2015) and was deposited in deeper environments on the outer slope of the Yangtze Block in the Nanhua Basin. Iron speciation of the Liuchapo Formation indicates persistently ferruginous conditions during deposition (Wang et al., 2012; Och et al., 2015). During marine transgression, ferruginous deeper waters were introduced to shallow environments and protected basins on the Yangtze Platform (e.g. Yinchanpo and Wuhe), due to a landward shift in the position of the anoxic wedge possibly related to the accompaniment of upwelling nutrients and enhanced productivity (Chapter 2, Section 2.2.1).

The causal mechanism for phosphogenesis in environments of the Yangtze Block has been interpreted to relate to enhanced upwelling of anoxic deep waters which were rich in dissolved organic carbon, followed by remineralisation in oxic surface waters and resulting in $\delta^{13}C_{carb}$ depletion in carbonates of the inner shelf (Cook and Shergold, 1984; Gao et al., 2018). This mode of formation is supported both by the sequence stratigraphic information and iron speciation data presented herein for the Zhongyicun Member dolomitic phosphorites. Elevated Ba_{XS} in Zhongyicun Member samples may be partially attributable to adsorption onto primary iron oxides, however this is difficult to constrain as enrichment resulting from Ba delivery in association with organic matter may also be expected to covary with iron enrichment as a consequence of ferruginous anoxia.

Future attempts at constraining a mechanism for Ba enrichment in samples of the Zhongyicun Member would benefit from measurements of total organic carbon content and relative changes in sediment accumulation rate (Schoepfer et al., 2015). Estimating palaeoproductivity and testing hypotheses relating to the genesis of early Cambrian phosphorites on the Yangtze Block would further benefit from phosphorus speciation experiments enabling identification of the primary phases for

phosphorus delivery to sediments. A comparable dataset has clarified the mechanism for phosphorus enrichment in carbonate-rich early Cambrian sediments of Australia and revealed the combined importance of iron-bound P delivery and organic carbon shuttling (Creveling et al., 2015).

5.5 Discussion: Shallow habitable space, fossil affinities and oxygen requirements

5.5.1 The southeast Siberian Platform

Palaeoredox data for sections of the Aim Formation in southeast Siberia attest to a persistently shallow redoxcline with anoxic and iron-rich deeper waters but how does this redox stratification relate to the inferred complexity represented by contemporary fossil organisms?

The taxonomic affinity of the organic-walled body fossil *Shaanxilithes* remains contentious (Meyer et al., 2012; Tarhan et al., 2014), however their relatively simple serial and modular construction do not definitively demonstrate a metabolically active life habit requiring elevated environmental oxygen. Similarly, the suggestion that *Palaeopasichnus* may represent a possible xenophyophore (Antcliffe et al., 2011) and the recent biomarker evidence which supports a colonial cyanobacterium affinity for *Beltanelliformis* (Bobrovkiy et al., 2018) do not attest to metabolic requirements for high pO_2 . The only soft-bodied fossil representative in deposits of the Aim Formation for which an affinity remains truly problematic is *Aspidella*. In sum, soft-bodied fossils within transgressive siliciclastic deposits of the Upper Aim Formation (Figures 5.4 and 5.14a) may represent forms which did not require significantly elevated (or stable) dissolved oxygen levels.

In contrast, the laterally extensive *Suvorovella* shell hash in highstand dolostone of the upper Aim Formation at the Yudoma-Maya confluence is indicative of the ease of biomineralisation in this environment and likely required relatively elevated, stable water column oxia (Chapter 3, Wood et al., 2015, 2017c; Tostevin et al., 2016b). It is noteworthy that the environment of highest diversity (including biomineralised representatives) in the Aim Formation is also the shallowest (Yudoma-Maya confluence) and likely represents a position where physical ventilation mechanisms were permissive for occasional biotic establishment (Figure 5.14a). Abundant biomineralising forms including *Cloudina* and SSFs within dolomitised limestone of the overlying Ust'-Yudoma Formation are similarly considered to represent forms which required appreciable local dissolved oxygen concentration (Wood et al., 2017c). The redox stratified architecture distinguished by a very shallow oxycline in environments of the southeast Siberian platform is consistent with previously proposed models for the genesis of early marine

dolomite cements in anoxic, ferruginous deep waters (Hood et al., 2011; Hood and Wallace, 2012, 2014, 2018; Wood et al., 2017a).

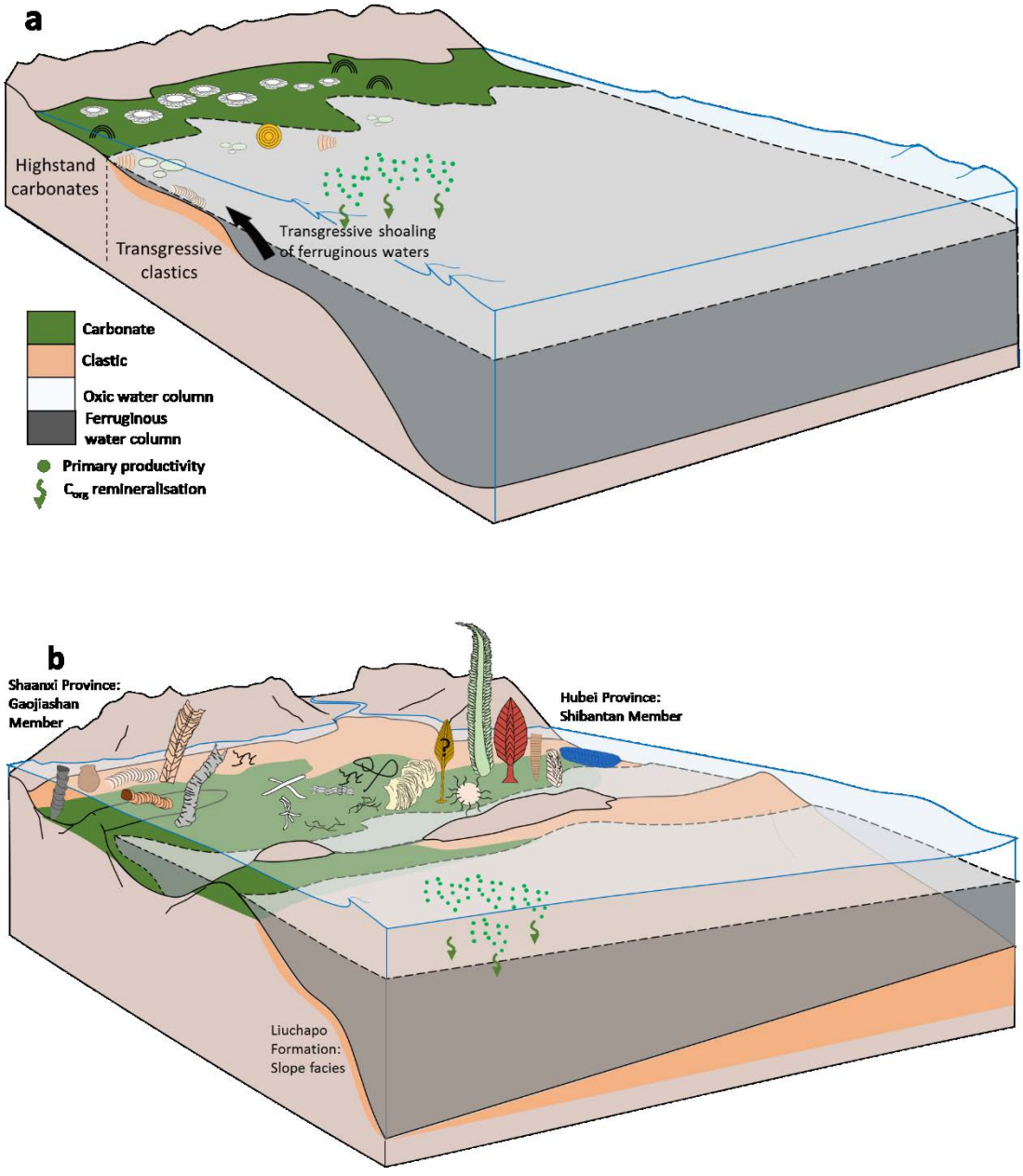

Figure 5.14

Dioramas of inferred redox and biotic distribution for the terminal Ediacaran **a)** Aim Formation along the Yudoma River sections, southeast Siberian Platform and, **b)** middle Dengying Formation on the Yangtze Block. See Appendix D for key to fossil symbols.

5.5.2 The Yangtze Block

The Dengying Formation records evidence for a diverse biotic presence across shallow platform and intra-platform basin carbonates of the Yangtze Block. Diverse tubular soft-bodied and skeletonising forms including *Gaojiashania*, *Shaanxilithes*, *Conotubus*, *Cloudina* and *Sinotubulites* are present in the shallowest environments of the Gaojiashan Member exposed in southern Shaanxi Province, whilst frondose soft-bodied forms predominate in the deeper Yangtze Gorges environment of Hubei (Figure 5.14b). In addition to a rich body fossil record, specific intervals of the Dengying Formation contain abundant ichnofossils occasionally characterised by relatively complex morphologies (e.g. Figure 12a) (Weber et al., 2007; Meyer et al., 2014).

Despite their relative morphological complexity, it is difficult to argue for metabolically active life habits for frond-like soft-bodied forms preserved in the Shibantan Member (e.g. *Rangea*, *Charniodiscus* and *Paracharnia*). Contrastingly however, their co-occurrence with overwhelming evidence for motile bilaterian trace makers demands local dissolved oxygen levels permissive to relatively high energy ecologies. Positive carbonate carbon isotopes of the Shibantan Member have previously been suggested to relate to the efficient burial of ^{12}C by primary producers in coexisting microbial mats (Duda et al., 2014). The high density of microbial mat fabrics in the Shibantan Member likely supported some active bioturbating communities (particularly represented by *Lamonte trevallis*) by acting both as a nutrient source and providing photosynthetic oxygen (during the day) to the under-mat benthic microenvironment (Gingras et al., 2011; Meyer et al., 2014). Whilst mining of these microbial 'oxygen oases' may have occasionally supported organisms responsible for complex traces (e.g. *Lamonte trevallis*), other ichnofossils which are not restricted to a microbial mat association were more likely created by organisms which required intervals of relatively well oxygenated water column conditions. Deeper sections of the correlative Liuchapo Formation are devoid of ichnofossils but do show evidence for microbial mat fabrics and strong evidence for permanent water column anoxia (Weber et al., 2007; Wang et al., 2012; Och et al., 2015).

Unlike ichnofossil and palaeoredox trends observed in the Upper Nama Group, extensive bioturbation traces in deposits of the Shibantan Member do not clearly accompany a trend towards stable regional oxygenation. Instead, this shallow oxygenation event is reported from overlying middle Cambrian Formations of the Yangtze Block (Jin et al., 2016; Li, C. et al., 2017b; Hammarlund et al., 2017). As such, late Ediacaran bioirrigation on the Yangtze Platform was likely restricted to infrequent episodes of oxic water column conditions, the short duration of which precluded sedimentary phosphorus retention and maintained elevated water column productivity fuelled in the photic zone by nutrient-charged upwelling waters.

The biomineralising organism *Sinotubulites baimatuoensis* inhabited shallow waters during deposition of the overlying Baimatuo Member in the Yangtze Gorges and microbial mat-sticking *Cloudina* and *Sinotubulites* are found in correlative shallow water carbonates of the Gaojiashan Member in Shaanxi Province (Figure 5.14b). Cerium anomaly data indicate a local environment of higher oxygen concentration during deposition of the Baimatuo Member relative to the underlying Shibantan (Ling et al., 2013), which was likely permissive to the energetically costly process of precipitating a carbonate skeleton and may be one reason for the restriction of this ecology to the shallowest environments represented in Dengying Formation deposits on the Yangtze Platform.

Finally, early Cambrian deposits on the Yangtze Platform preserve characteristic Terreneuvian small shelly fossils and ichnotaxa. No appreciable shift in dominant local redox towards more oxygenated water column conditions is evident in South China across the Ediacaran-Cambrian boundary which is likely due to extremely productive surface waters which maintained anoxia beneath a shallow redoxcline.

5.6 Conclusions

All fossil associations which were originally considered as potential markers for the boundary between the Ediacaran and Cambrian Periods suffer from shortfalls associated with facies bias (e.g. Ahn and Zhu, 2017; Zhu and Li, 2017). These include the FAD of *Treptichnus pedum*, the LAD of *Cloudina* and the basal Cambrian negative carbon isotope excursion (BACE). The FAD of small shelly fossils of the *Anabarites trisulcatus – Protohertzina anabarica* zone suffers the additional complication of associated species endemism. Furthermore, recent evidence has been presented for the co-existence of *Cloudina* and *Anabarites* at Kyra-Ytyga on the southeast Siberian Platform and the inferred temporal position of their co-occurrence would negate the use of the FAD of this SSF zone and LAD of *Cloudina* as together representative of the lower Cambrian (Zhu et al., 2017).

A further, underappreciated complication in pinpointing the Ediacaran-Cambrian boundary in some sections is related to palaeoenvironmental suitability. Both *Cloudina* and *T. pedum* represent organisms (or the presence of organisms) with metabolically demanding ecologies requiring relatively enriched local marine dissolved oxygen concentrations. Palaeoredox studies imply that many shallow marine environments across the Ediacaran-Cambrian transition continued to suffer the influence of low oxygen conditions and anoxic incursions. Where stable oxygenated conditions prevailed, such as the upper Nama Group (Chapter 3), a diverse ichnofossil and skeletal fossil assemblage flourished, whereas environments of unstable redox or persistent anoxia were intermittently occupied by opportunistic colonisation during short-lived oxic episodes. Whilst the evolution of skeletonisation may have been

related in part to increasing marine Ca^{2+} and decreasing Mg/Ca (Wood et al., 2017c), future work employing palaeoredox proxies which specifically target carbonates will enable a quantitative assessment of the influence of redox on the stepwise habitation of deposits of, for example, the Ust'-Yudoma Formation by SSF taxa.

Integrated proxy methods are able to distinguish palaeoredox heterogeneity between and within early animal ecosystems and test the influence of anoxia on ecosystem structure. The first and last appearances of *Cloudina* and *T. pedum* respectively show no identifiable range overlap in any sections analysed in this study (Figure 5.1). Furthermore, all of the stratigraphic sections described in this Chapter, in addition to those of the Nama Group, constrain the first appearance of *T. pedum* to a range currently indistinguishable from the inferred first appearance at the Fortune Head GSSP (Figure 5.1). This suggests that the first appearance of the organism responsible for characteristic *T. pedum* traces may have been approximately contemporaneous (within current chronological error) in oxic habitable refuges of all regions in this study regardless of the prevalence of long-lived anoxic water column conditions which persisted in coeval deeper environments.

Pinpointing the Ediacaran-Cambrian boundary in sections where *T. pedum* traces are not preserved due to facies bias is best surmounted through a combination of *Cloudina* last appearance and the position of the BACE. However, it is acknowledged that this may underestimate the absolute age of the boundary as defined by *T. pedum*. The combined use of the BACE and the *Anabarites trisulcatus – Protohertzina anabarica* zone is problematic as this SSF zone is locally present below and above the BACE, however, a *Cloudina* and *Anabarites* association may be indicative of a terminal Ediacaran age if this assemblage is confined below the BACE (Zhu et al., 2017). For this interpretation to be substantiated, the relative timing of last and first appearances of *Cloudina* and *T. pedum* relative to the BACE within mixed siliciclastic-carbonate successions must be determined within a single region. In this regard, the Nama Group offers a tantalising, yet frustrating glimpse into the co-occurrence of treptichnids and *Cloudina* below the BACE, however no carbonate strata have yet been identified in the Nama Group which record the BACE or the FAD of SSFs that may have co-occurred with shallow siliciclastic strata hosting *T. pedum* itself. Continued detailed study of fossiliferous terminal Ediacaran mixed sedimentary sequences may help clarify this series of events.

Chapter 6

Discussion and Conclusions

6.1 A biotic response to redox in the Ediacaran

The most basal animals likely evolved as early as ~850 Ma (dos Reis et al., 2015) and classical hypotheses suggest that a driving factor for their emergence was associated with a rise in oxygen concentration beyond a critical threshold (e.g. Nursall, 1959; Runnegar et al., 1991). In contrast, more recent studies propose that the delayed emergence of animals may have been primarily associated with the evolution of genetic or developmental innovations which permitted cellular survival under increasing levels of toxic environmental oxygen (Hammarlund et al., 2018). The latter line of thought argues that, whilst the energetic benefit of metabolising aerobically permits large size and active ecologies, oxygenated conditions are inherently inhospitable due to their promoting cellular maturity rather than permitting the maintenance of a viable store of stem cells (Hammarlund et al., 2018). If this is the case, it provides an evolutionary answer to the large temporal separation between the early ventilation of the surface ocean and the first appearance of large, complex macrofossils in the middle Ediacaran Period (~571 Ma, Pu et al., 2016).

Though the phylogenetic affinities of almost all soft-bodied macrofossils of the Avalon, White Sea and Nama assemblages in the Ediacaran remain enigmatic, a small number have been ascribed, with some degree of confidence, to the Metazoa (Dunn et al., 2017). The most recent experimental studies suggest that oxygen requirements of early, primitive animals may have been very low (Mills et al., 2014, 2018), however the subsequent appearance of motile animals, macropredation and biomineralisation in uppermost Ediacaran and basal Cambrian strata are more confidently hypothesised to represent a metabolic revolution brought on by an increase in marine dissolved oxygen concentration (e.g. Sperling et al., 2015c). Active ecologies conducive to sediment disruption and biocalcification demand at least intermittently elevated local dissolved oxygen to fuel aerobic respiration. In order to better understand the nature of early animal environments and to test the 'oxygen revolution' hypothesis, the past 30 years have witnessed intense geochemical study of fossiliferous Ediacaran sedimentary sequences.

Geochemical proxies that are well characterised with respect to elemental and isotopic cycling in the modern are our only hope for reconstructing chemical environments in deep time. In Chapter 2, we attempt to characterise local palaeoredox environments of the Ediacaran Period through collation of published proxy data in association with biotic occurrence and sequence stratigraphic information. This study integrates a large number of iron speciation datasets pertaining to local water column redox conditions and, where possible, correlates stratigraphic section in a framework of relative palaeodepth. Employing sequence stratigraphic information is critical to understanding the mechanisms that act to

modify the position of the redoxcline and thus to recognise the spatial distribution of habitable space represented by the distribution of associated fossil forms.

The extent of water column oxygenation within individual shallow marine to deep slope environments of the Ediacaran was controlled by a combination of local nutrient loading, productivity and physical ventilation mechanisms (e.g. Canfield et al., 2007; Och et al., 2015; Wood et al., 2015; Bowyer et al., 2017). Patterns of ocean circulation, which are controlled in large part by cratonic positioning, act either as a nutrient source or aid in efficient redistribution of oxygen to depth and are thus inferred to have influenced the long-term evolution of regional marine redox conditions.

Ediacaran palaeoenvironments were typified by pronounced redox variability both between and within basins and some shallow environments above wave base experienced the influence of anoxic and iron-rich water column conditions throughout the latest Ediacaran and early Cambrian (Wood et al., 2015; Och et al., 2013, 2015). Recent high resolution geochemical studies of early Cambrian shelf-to-basin sequences suggest that variability in recorded palaeoredox conditions reflect changes in the position of metastable oxygen-minimum zones along productive continental margins (Hammarlund et al., 2017; Guilbaud et al., 2018). It is possible that this reconstruction similarly applies to the spatial distribution of anoxia in the preceding Ediacaran and, if so, may support the interpretation of widespread early deep ocean ventilation as reported from some of the deepest analysed deposits (Figure 6.1a, Canfield et al., 2007). However, a number of other lines of evidence, including iron isotope ratios of submarine basalt (Stolper and Keller, 2018) and data of sedimentary δ^{98}Mo (Dahl et al., 2010) suggest that extensive deep ocean ventilation was a Palaeozoic phenomenon.

The recognition of spatial heterogeneity in palaeomarine redox at this time is crucial to our understanding of trace element and nutrient cycling and informs interpretations of observed changes in the isotopic ratios of (for example) carbon, nitrogen and sulphur. In the Ediacaran, this is best exemplified by the magnitude and temporal extent of the Shuram-Wonoka negative carbonate carbon isotope excursion which is widely considered to represent the oxidation of a deep oceanic store of isotopically light organic carbon (Rothman et al., 2003; Fike et al., 2006, but see e.g. Bjerrum and Canfield, 2011; Swart and Kennedy, 2012). If this is the case, it remains unclear as to whether a return to positive $\delta^{13}C_{carb}$ values in the last ~10 Myrs of the Ediacaran corresponds to exhaustion of the organic carbon reservoir and subsequent progressive oxygenation of the global deep ocean, or whether the oxidant source was itself consumed, allowing re-expansion of the organic carbon reservoir. Notwithstanding significant uncertainties in temporal correlation of the Shuram excursion, recent modelling efforts emphasize that partial oxidation may have proceeded heterogeneously between basins

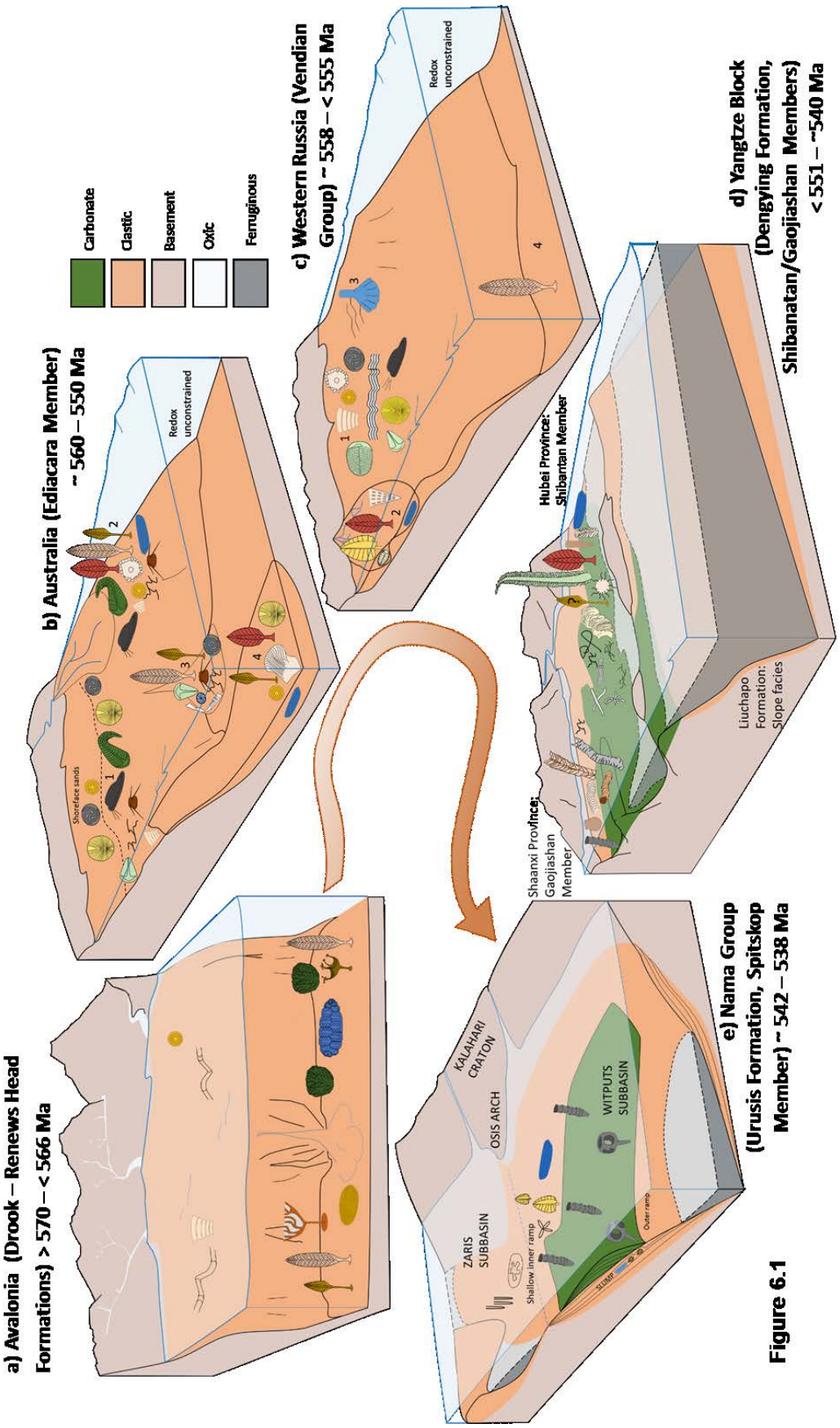
Carbonate
Clastic
Basement
Oxic
Ferruginous
a) Avalonia (Drook – Renews Head Formations) > 570 – < 566 Ma
b) Australia (Ediacara Member) ~ 560 – 550 Ma
Redox unconstrained
Shoreface sands
c) Western Russia (Vendian Group) ~ 558 – < 555 Ma
Redox unconstrained
d) Yangtze Block (Dengying Formation, Shibanatan/Gaojiashan Members) < 551 – ~540 Ma
Hubei Province: Shibantan Member
Shaanxi Province: Gaojiashan Member
Liuchapo Formation: Slope facies
e) Nama Group (Urusis Formation, Spitskop Member) ~ 542 – 538 Ma
KALAHARI CRATON
OSIS ARCH
ZARIS SUBBASIN
WITPUTS SUBBASIN
Shallow inner ramp
Outer ramp
SLUMP

Figure 6.1

as a consequence of strong local controls on the availability of organic carbon and oxidant supply (Li, C. et al., 2017; Shi et al., 2017).

From a biotic perspective, it is suggested that local redox conditions were of prime importance in the structuring of local benthic communities of the Ediacaran and dominant palaeoredox conditions may have influenced the degree to which biotic assemblages differed between and within regions (Figure 6.1). However, the inability of the current proxy toolkit to distinguish periods of rapid oxygenation conducive to short-lived environmental habitability results in an incomplete understanding of the oxygen requirements of most soft-bodied forms (particularly the deep marine Lantian biota of the Yangtze Block, deep slope biota of the Laurentian passive margin and biota of the upper Aim Formation of the southeast Siberian Platform discussed in Chapter 5).

6.2 Redox evolution and biodiversity of the Nama Group

Chapter 3 focuses on providing an integrated assessment of palaeoredox, sequence stratigraphy and biotic change in the Ediacaran Nama Group of Namibia which preserves a diverse mixed skeletal and soft-bodied biota. Previous multi-proxy investigations have successfully reconstructed the stratified redox architecture of the water column which accompanied deposition of (particularly) the lower Nama Group (Wood et al., 2015; Tostevin et al., 2016b). Integrated palaeoecological studies show that early

---

Figure 6.1 (Facing page)

Schematic dioramas representing biotic assemblages for selected environments of the Ediacaran Period and the associated interpretations of water column palaeoredox conditions. All reconstructions equate to single, conformable sequences in **a)** Avalonia, **b)** Australia, **c)** Western Russia (White Sea Region), **d)** the Yangtze Block, South China and **e)** Namibia. Redox conditions of **b)** and **c)** remain unconstrained. Each depiction includes the relative depth of biotic assemblages, however, scale between dioramas is not relative. See Appendix D for key to fossil symbols. Numerals in **b)** relate to facies association of biota after Gehling and Droser (2013) and Tarhan et al. (2017) and include **1**) Oscillation-rippled sandstone, **2**) Flat-laminated to linguoid-rippled sandstone, **3**) Planar-laminated and rip-up sandstone, and **4**) Channelised sandstone and sandstone-breccia**.** Likewise, numerals in **c)** correspond to facies association of biota after Grazhdankin (2004) and include **1**) Upper shoreface prodelta, **2**) Distributary mouth bar – middle shoreface, **3**) Lower energy shoreface and **4**) Storm influenced middle shoreface. Figure adapted after Wood et al. (in prep.).

calcifying forms such as *Cloudina*, *Namacalathus* and *Namapoikia* were likely sensitive to high frequency changes in water column redox conditions whilst the success of long-lived communities and biomineralisation of thicker-walled individuals was supported under stable oxic conditions (Wood et al., 2015; Tostevin et al., 2016b; Penny et al., 2017; Wood and Penny, 2018).

The study presented in Chapter 3 builds upon the palaeoredox and palaeontological framework for the Nama Group by infilling gaps in understanding of the long-term redox evolution of the basin through geochemical analyses of new sampling intervals and holistic integration of the extensive soft-bodied and ichnofossil records. The Kuibis Subgroup was host to a soft-bodied ('Nama') assemblage biota which were restricted to the shallowest facies where frequent physical ventilation may have played a role in maintaining a habitable environment which was spatially separated from deeper ferruginous waters. The subsequent redox stabilisation to dominantly oxic conditions recorded in the overlying Schwarzrand Subgroup is inferred to represent a deepening of the redoxcline and was accompanied both by a notable increase in ichnofossil diversity and the apparent expansion in habitable ecospace of soft-bodied forms which are recorded for the first time from outer-ramp deposits in the upper Spitskop Member at Swartpunt. This is tantalising evidence supporting the hypothesis that the spatial distribution of enigmatic soft-bodied forms in the Nama basin may have been constrained by the depth of the ferruginous redoxcline.

It is suggested that stabilisation of oxic conditions on the shallow shelf in the Schwarzrand Subgroup contributed to the diversification of metabolically active organisms as exemplified by the burgeoning ichnofossil record. It is further hypothesised that the stabilisation of oxic conditions in the upper Schwarzrand Subgroup may have been the direct consequence of bioirrigation and sedimentary phosphorus retention which imposed a first order limitation upon primary productivity, however this remains to be tested.

6.3 Through the veil of diagenesis

High frequency changes in palaeoredox conditions (e.g. less than ~1000 years) are largely irresolvable due to time averaging of proxy records associated with bulk sample analyses. In contrast, marine carbonate cements grow within the water column and targeted analyses may thus provide an archive of short-term chemical change on ecologically meaningful timescales. Identifying primary water column chemistry from the sedimentary rock record crucially relies upon first accurately distinguishing the degree of alteration to which these sediments have been subjected. This is particularly important in

carbonate sediments and cements which are prone to elemental redistribution during early diagenetic pore fluid dissolution and reprecipitation.

A mixed microbial-metazoan reef complex in the Nama Group (Namibia) which outcrops on Farm Driedoornvlakte provides the earliest evidence for reef-building by skeletal animals and is the only *Cloudina* reef known (to date) in strata of the late Ediacaran Period. Redox sensitive element concentrations in carbonate cements which co-precipitated within the reef framework provide the potential to capture short-term changes in water column redox conditions. In Chapter 4 we investigate the paragenetic sequence of carbonate cements at Driedoornvlakte and attempt to disentangle the compounding effects of primary versus diagenetic elemental enrichment. This has been achieved through detailed petrographic study of numerous samples incorporating traditional transmitted light and cathodoluminescence microscopy. Primary precursor mineralogies have been determined through interpreting the petrographic form and character of carbonate cements. The distribution of redox sensitive elements (Mn and Fe) revealed by CL and quantified through targeted electron microprobe analyses show a discrete pattern between cement generations. This combined approach of petrographic and elemental analysis allows the critical distinction of primary fluid composition from which these carbonate cements precipitated versus secondary pore fluid remobilisation during carbonate diagenesis.

Elemental concentration data have been integrated with an assessment of local *Cloudina* ecology and together suggest that successful reef growth at Driedoornvlakte was permitted under stable oxic shallow water conditions. However, it is possible that this reef-building ecology was sensitive to intermediate redox conditions where low oxygen levels were conducive to manganese oxide reduction but E_H was above that required for the reduction of iron oxides (Chapter 4; Tostevin et al., 2016b). This study supports the presence of a metastable manganous zone previously inferred from data of positive Ce/Ce* in the Nama Group (Tostevin et al., 2016b). Furthermore, ferruginous conditions which are known to have persisted in neighbouring deeper waters of the Zaris subbasin may also have promoted the early dolomitisation of high-Mg calcite precursor cements and micritic sediment at Driedoornvlakte. This study adds to an increasing body of evidence which argues for anactualistic water column chemistry in the Neoproterozoic with mMg/Ca sufficiently high to permit early dolomitisation without the requirement for evaporitic conditions (Hood et al., 2011; Hood and Wallace, 2012, 2018; Wood et al., 2017a).

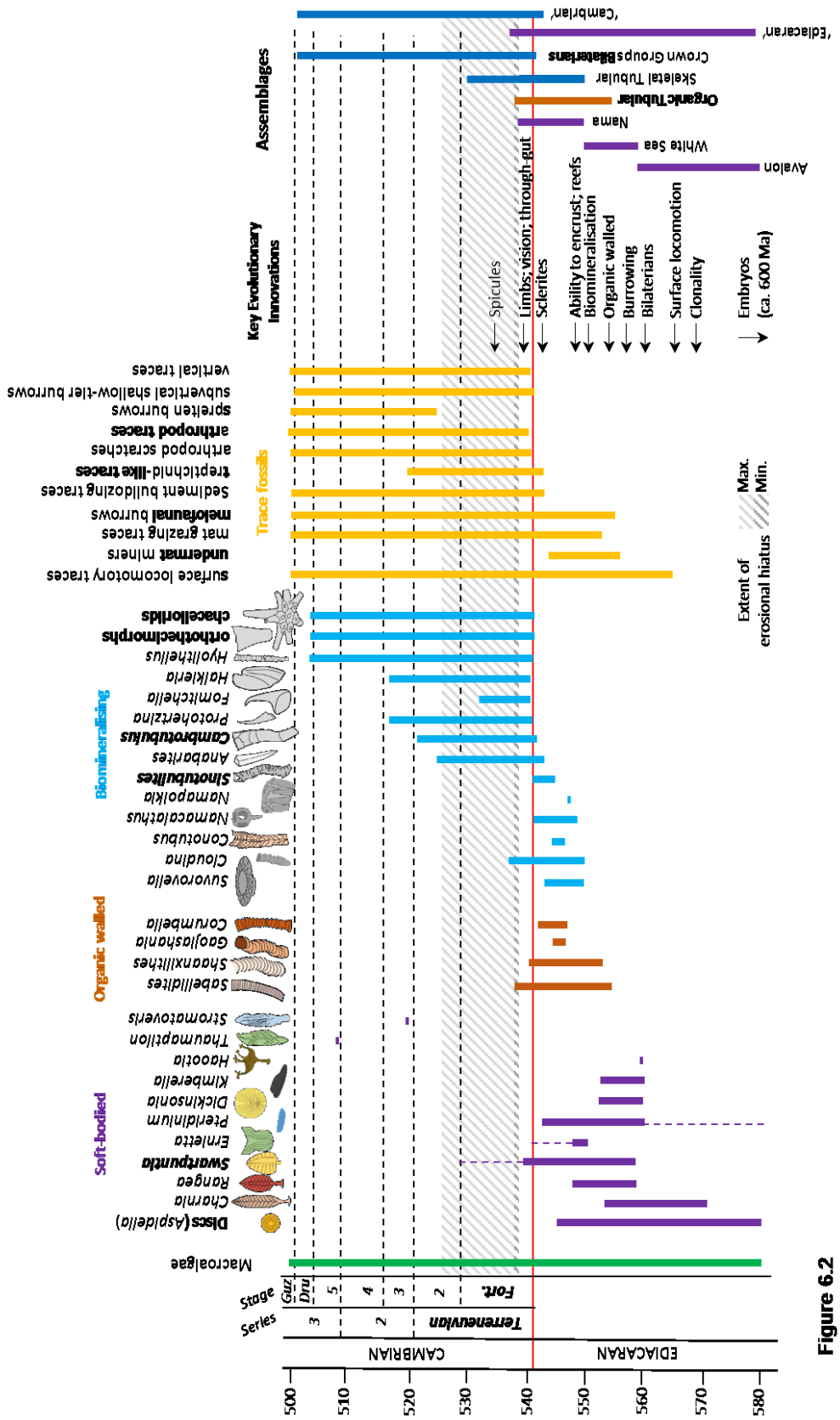
'Cambrian'
'Ediacaran'
Crown Group Bilaterians
Skeletal Tubular
Organic Tubular
Nama
White Sea
Avalon
Assemblages
Key Evolutionary Innovations
Spicules
Limbs; vision; through-gut
Sclerites
Ability to encrust; reefs
Biomineralisation
Organic walled
Burrowing
Bilaterians
Surface locomotion
Clonality
Embryos (ca. 600 Ma)
Max.
Min.
Extent of erosional hiatus
vertical traces
subvertical shallow-tier burrows
sprelten burrows
arthropod traces
arthropod scratches
trepltichnid-like traces
Sediment bulldozing traces
melofaunal burrows
mat grazing traces
undermat miners
surface locomotory traces
Trace fossils
chaeteliorlids
orthothecimorphs
Hyolithellus
Halkieria
Formitchella
Protohertzina
Cambrotubulus
Anabarites
Sinotubulites
Namapoikia
Namacalathus
Conotubus
Cloudina
Suvorovella
Gourmbella
Gaojiashania
Shaanxilithes
Sabellidites
Stromatoverls
Thaumaptilon
Haootia
Kimberella
Dickinsonia
Pertidilnum
Ernietta
Swartpuntia
Rangea
Charnia
Discs (Aspidella)
Biomineralising
Organic walled
Soft-bodied
Macroalgae
Stage
Series
Guz
Dru
5
4
3
2
Fort.
Terreneuvian
CAMBRIAN
EDIACARAN
500
510
520
530
540
550
560
570
580

Figure 6.2

6.4 How distinct were the Ediacaran and Cambrian?

The nature of biotic change at the Ediacaran-Cambrian boundary, whether it represents transition or competitive replacement and the extent to which taphonomic bias vs palaeoenvironmental change is implicated in the apparent disappearance of soft-bodied Ediacaran forms remains one of the most heavily debated topics in the study of early animal palaeoecology (Laflamme et al., 2013; Darroch et al., 2015; Geyer and Landing, 2017; Zhu et al., 2017; Muscente et al., 2017). Firstly, it is important to recognise that soft-bodied and early calcifying invertebrates co-existed with motile bioturbating organisms in most regions but often occupied different facies (Figure 6.1; Grazhdankin, 2004; Gehling and Droser, 2015; Budd and Jensen, 2017). For example, in the Nama Group and the Yangtze Block, burrowing organisms conspicuously lived alongside soft-bodied and skeletal forms for at least 2-10 Myrs prior to the Ediacaran – Cambrian boundary (Chapters 2, 3 and 5, Figure 6.2; Meyer et al., 2014; Buatois et al., 2018). Additionally, frondose organisms superficially similar to Ediacaran soft-bodied forms are noted from as high as Cambrian Stage 5 (Figure 6.2; Conway Morris, 1993; Shu et al., 2006). In this regard, the model of biotic replacement suffers and instead, integrated palaeontological data support successive taxonomically discrete assemblages which transcend the boundary (Figure 6.2; Wood et al., in prep).

Secondly, an increase in taxonomic diversity in the early Cambrian is not seen to reflect a unidirectional evolution in palaeomarine redox conditions, with the majority of shallow to deep environments clearly indicating the continued influence of water column anoxia well into the Cambrian (e.g. Chapters 2 and 5; Wang et al., 2012; Och et al., 2013, 2015). However, whilst unstable redox conditions persisted on the Yangtze Platform, a number of studies have implicated the gradual stabilisation and expansion of oxic shallow waters during the early to middle Cambrian, in the stepwise diversification of complex animals and associated increases in ecosystem complexity (e.g. Chapter 3; Jin et al., 2016; Li, C. et al., 2017b; Hammarlund et al., 2017; Zhang, J. et al., 2017; Zhao et al. in press).

Factors implicated in the evolution of calcareous biomineralisation at the end of the Ediacaran are numerous and include a rise in oxygen of the marine environment and a decrease in the mMg/Ca of seawater driven by enhanced continental weathering (Brennan et al., 2004; Peters and Gaines, 2012; Wood et al., 2017c). Predation pressure was likely important in the ecological arms race that followed

---

Figure 6.2 (Facing page)

The temporal ranges of fossil taxa across the Ediacaran – Cambrian boundary including so-called 'transitional' biota. Key to fossil symbols is provided in Appendix D. Figure adapted after Wood et al. (in prep.)

during the early Cambrian (Knoll, 2003). However, active biomineralisation is metabolically costly and so, when under biological control, requires oxygen (Rhoads and Morse, 1971; Sperling et al., 2015c). Multi-proxy reconstructions of the Nama Group (Chapters 2 – 4) show clear evidence for the ecological pressure imposed by ferruginous waters upon the earliest calcifying invertebrates *Cloudina*, *Namacalathus* and *Namapoikia* (Wood et al., 2015; Tostevin et al., 2016b; Penny et al., 2017; Wood et al., 2017b; Wood and Penny, 2018). There is similar evidence to suggest that low oxygen conditions were detrimental to early biomineralisers elsewhere at this time, including the restriction of *Suvorovella* to the shallowest facies of southeast Siberia (Chapter 5; Wood et al., 2017a, c). However, the hypothesis that stable oxia was a prerequisite for early biomineralisation would benefit from further geochemical and palaeoecological investigations in Ediacaran strata elsewhere and suitable candidate sections for study are numerous (e.g. Zhuravlev et al., 2012).

It has been suggested that unstable redox conditions may encourage morphological novelty in benthic soft-bodied biota and result in the subsequent innovation of skeletal forms and evolutionary diversification once stable oxygenated conditions are established (Wood and Erwin, 2017). We find support for this hypothesis at the Ediacaran-Cambrian boundary, albeit at differing temporal scales between basins.

6.5 Future work

Ferruginous water column conditions were a common feature affecting ecosystems of the earliest animals. Though modern ferruginous environments are limited, those that exist (e.g. Lake Matano, Indonesia) provide extremely informative analogues for the study of element and nutrient cycling, in addition to microbial ecology (e.g. Crow et al., 2008; Zegeye et al., 2012). Ongoing research of geochemical proxy signatures in modern ferruginous settings will be of great value for their interpretation in deep time.

Recent studies have shown that multiproxy palaeoredox records are, in certain circumstances, capable of distinguishing intermediate redox conditions above the E_H conducive to iron oxidation (Tostevin et al., 2016b). Such an approach is key to understanding the subtleties of early animal oxygen requirements and is warranted in all mixed carbonate and clastic fossiliferous sedimentary sequences. In addition, the development of proxies which are able to track high frequency changes on environmentally significant timescales, whilst particularly challenging, is an extremely laudable pursuit to robustly characterise the ecological requirements of these organisms.

All future Ediacaran palaeoenvironmental reconstructions should consider the benefits of integrating a multi-proxy geochemical toolkit with detailed palaeoecological analyses of associated fossil assemblages in a manner exemplified by recent studies of the Nama Group (Wood et al., 2015, 2017b; Tostevin et al., 2016b; Penny et al., 2017). This is particularly crucial in the Ediacaran where phylogenetic affinities for the majority of fossil representatives remain enigmatic. Furthermore, local nutrient cycling is intimately tied to both water column redox and benthic community structure. As such, the most holistic characterisation of early animal ecosystem dynamics will also employ proxies which illuminate aspects of the nutrient cycle such as phosphorus speciation and nitrogen isotopes (e.g. Creveling et al., 2014; Cremonese et al., 2014; Xiang et al., in press).

One particular area where significant uncertainty remains is the link between late Ediacaran and early Cambrian small skeletal fossils and local palaeoenvironmental change, especially in exceptionally fossiliferous sections of the Siberian craton where longstanding debate persists with respect to stratigraphic equivalence and completeness (e.g. Knoll et al., 1995b; Kouchinsky et al., 2015; Zhu et al., 2017). Studies which focus on palaeoseawater pH and alkalinity of fossiliferous sections through use of boron and calcium isotopes will likely bolster our understanding of the drivers for widespread biomineralisation. Ideally, such studies will be performed in combination with assessments of palaeoredox and nutrient cycling.

Though efforts are continually being made to infill gaps in knowledge of Ediacaran ecosystems, almost a century of palaeontological exploration has unveiled a prodigious amount for geochemical scrutiny. Fossiliferous regions which remain vastly understudied with respect to palaeoredox include (but are not limited to) almost all of the Siberian Platform, exposures of the Nama Group in northwest South Africa, the Byng carbonate platform of the Miette Group (British Columbia) and the Corumbá Group of Brazil. Other areas where dominant lithology or metamorphic overprinting currently preclude detailed interpretations of the primary geochemical palaeoenvironment include the Rawnsley Quartzite of Australia, the Charnian Supergroup (England) and shallow fossiliferous deposits of Podolia (Ukraine).

Finally, of paramount importance to all studies of Proterozoic palaeontology and biogeochemistry are ongoing efforts to accurately correlate stratigraphic sections through time via high resolution, standardised geochronological methods of radiometric dating tied to carbon and strontium isotope chemostratigraphy. Continued construction of a detailed geochronological scaffold for stratigraphic correlation is essential when attempting to determine the duration of unconformities, rates of evolutionary diversification and the local versus global nature of biogeochemical changes. This framework may eventually aid the establishment of regional and global Ediacaran biozones for fossiliferous strata where both carbonates and ash beds are lacking (Xiao et al., 2016; Zhu and Li, 2017).

References

Aceñolaza, G.F., Germs, G.J.B. and Aceñolaza, F.G. (2009) Trace Fossils and the Agronomic Revolution at the Neoproterozoic-Cambrian Transition in Southwest Gondwana. Chapter 9.3 in: Gaucher, C., Sial, A.N., Halverson, G.P., Frimmel, H.E. (Eds.), *Neoproterozoic to Cambrian Tectonic, Global Change and Evolution: a Focus on Southwestern Gondwana*. *Developments in Precambrian Geology*, Vol. 16, pp.339–347.

Adams, E.W. Schroder, S., Grotzinger J.P. and McCormick D.S. (2004) Digital reconstruction and stratigraphic evolution of a microbial-dominated, isolated carbonate platform (terminal Proterozoic, Nama Group, Namibia). *Journal of Sedimentary Research*, Vol. 74, pp.479–497.

Adams, E.W., Grotzinger, J.P., Watters, W.A., Schroder, S., McCormick, D.S., and Al-Siyabi, H.A. (2005) Digital characterization of thrombolite-stromatolite reef distribution in a carbonate ramp system (terminal Proterozoic, Nama Group, Namibia), *AAPG bulletin*, Vol. 89, no. 10, pp.1293-1318.

Adams, J.E., and Rhodes, M.L. (1960) Dolomitization by seepage refluxion. *Bulletin of the American Association of Petroleum Geologists*, Vol. 44, No. 12, pp. 1912-1920.

Ahn, S.Y. and Zhu, M. (2017) Lowermost Cambrian acritarchs from the Ynajiahe Formation, South China: implications for defining the base of the Cambrian in the Yangtze Platform. *Geological Magazine*, Vol. 154, no. 6, pp. 1217 - 1231.

Alberts, B., Johnson, A., Lewis, J., Raff, M., Roberts, K. and Walter, P. (2002) Molecular Biology of the Cell. *New York: Garland Science*.

Algeo, T.J. and Lyons, T.W. (2006) Mo-total organic carbon covariation in modern anoxic marine environments: Implications for analysis of paleoredox and paleohydrographic conditions. *Paleoceanography*, Vol. 21, Issue 1.

Algeo, T.J. and Maynard, J.B. (2004) Trace-element behavior and redox facies in core shales of Upper Pennsylvanian Kansas-type cyclothems. *Chemical Geology*, Vol. 286, pp. 289-318.

Algeo, T.J., and Tribovillard, N. (2009) Environmental analysis of paleoceanographic systems based on molybdenum–uranium covariation, *Chemical Geology*, Vol. 268, pp. 211-225.

Aller, R.C. (1994) Bioturbation and remineralization of sedimentary organic matter: effects of redox oscillation. *Chemical Geology*, Vol. 114, No. 3-4, pp. 331-345.

Aller, R.C., Mackin, J.E. and Cox Jr, R.T. (1986) Diagenesis of Fe and S in Amazon inner shelf muds: apparent dominance of Fe reduction and implications for the genesis of ironstones. *Continental Shelf Research*, Vol. 6, No. 1-2, pp. 263-289.

Amthor, J.E., Grotzinger, J.P., Schroder, S., Bowring, S.A., Ramezani, J., Martin, M.W. and Matter, A. (2003) Extinction of *Cloudina* and *Namacalathus* at the Precambrian-Cambrian boundary in Oman. *Geology*, Vol. 31, No. 5, pp. 431-434.

An, Z., Jiang, G., Tong, J., Tian, L., Te, Q., Song, H. and Song H. (2015) Stratigraphic position of the Ediacaran Miaohe biota and its constrains on the age of the upper Doushantuo ??13C anomaly in the Yangtze Gorges area, South China. *Precambrian Research*, Vol. 271, pp.243–253.

Andersen, M.B., Romaniello, S., Vance, D., Little, S.H., Herdman, R. and Lyons, T.W. (2014) A modern framework for the interpretation of 238U/235U in studies of ancient ocean redox. *Earth and Planetary Science Letters*, Vol. 400, pp.184–194.

Anderson, J.J. and Devol, A.H. (1973) Deep water renewal in Saanich Inlet, an intermittently anoxic basin. *Esturiane and Coastel Marine Science*, Vol. 1, Issue 1, pp.1–10.

Antcliffe, J.B., Gooday, A.J. and Brasier, M.D. (2011) Testing the protozoan hypothesis for Ediacaran fossils: a developmental analysis of *Palaeopascichnus*. *Palaeontology*, Vol. 54, No. 5, pp. 1157-1175.

Arvidson, R.S. and Mackenzie, F.T. (1999) The dolomite problem: control of precipitation kinetics by temperature and saturation state: *American Journal of Science*, Vol. 299, pp. 257-288.

Aubet, N.R., Pecoits, E., Bekker, A., Gingras, M.K., Zwingmann, H., Veroslavsky, G., de Santa Ana, H., and Konhauser, K.O. (2012) Chemostratigraphic constraints on early Ediacaran carbonate ramp dynamics, Río de la Plata craton, Uruguay. *Gondwana Research*, Vol. 22, pp. 1073-1090.

Aubet, N.R., Pecoits, E., Heaman, L.M., Veroslavsky, G., Gingras, M.K., and Konhauser, K.O. (2014) Ediacaran in Uruguay: Facts and controversies, *Journal of South American Earth Sciences*, Vol. 55, pp. 43 - 57.

Azmy, K., Stouge, S., Brand, U., Bagnoli, G. and Ripperdan, R. (2014) High-resolution chemostratigraphy of the Cambrian–Ordovician GSSP: enhanced global correlation tool. *Palaeogeography, Palaeoclimatology, Palaeoecology*, Vol. 409, pp. 135-144.

Baker, P.A., and Kastner, M. (1981) Constraints oon the formation of sedimentary dolomite. *Science*, Vol. 213, No. 4504, pp. 214-216.

Baldwin, G.J., Nagler, T.F., Greber, N.D., Turner, E.C. and Kamber, B.S. (2013) Mo isotopic composition of the mid-Neoproterozoic ocean: An iron formation perspective. *Precambrian Research*, Vol. 230, pp.168–178.

Barnaby, R.J. and Rimstidt, J.D. (1989) Redox conditions of calcite cementation interpreted from Mn and Fe contents of authigenic calcites: *Geological Society of America Bulletin*, Vol. 101, pp. 795-804.

Bau, M. and Dulski, P. (1996) Distribution of yttrium and rare-earth elements in the Penge and Kuruman iron-formations, Transvaal Supergroup, South Africa. *Precambrian Research*, Vol. 79, Issues 1-2, pp.37–55.

Becker-Kerber, B., Pacheco, M.L.A.F., Rudnitzki, I.D., Galante, D., Rodrigues, F. and de Moraes Leme, J. (2017) Ecological interactions in *Cloudina* from the Ediacaran of Brazil: implications for the rise of animal biomineralization. *Scientific reports*, Vol. 7, No. 1, pp. 5482.

Bengtson, S. Cooper, B.J., Jell, P.A., and Runnegar, B.N. (1990) Early Cambrian fossils from South Australia, *Memoirs of the Association of Australian Palaeontologists*, Vol. 9, pp. 364.

Bengtson, S. and Zhao, Y. (1992) Predatorial borings in late precambrian mineralized exoskeletons. *Science,* Vol. 257, Issue 5068, pp.367–369.

Bengtson, S., and Hou, X. (2001) The integument of Cambrian chancelloriids, *Acta Palaeontologica Polonica*, Vol. 46, issue pp. 1-22.

Berg, J.M., Tymoczko, J.L. and Stryer, L. (2002) Biochemistry (5th Edition). *New York: WH Freeman*. ISBN- 10: 0-7167-3051-0

Berner, R.A. (1975) The role of magnesium in the crystal growth of calcite and aragonite from sea water. *Geochimica et Cosmochimica Acta*, Vol. 39, pp. 489-504.

Berner, R.A. (1980) Early diagenesis: a theoretical approach (No. 1). *Princeton University Press.*

Bertrand, P., Shimmield, G., Martinez, P., Grousset, F., Jorissen, F., Paterne, M., Pujol, C., Bouloubassi, I., Menard, P.B., Peypouquet, J.P. and Beaufort, L. (1996) The glacial ocean productivity hypothesis: the importance of regional temporal and spatial studies. *Marine Geology*, Vol. 130, pp. 1 – 9.

Bjerrum, C.J. and Canfield, D.E. (2011) Towards a quantitative understanding of the late Neoproterozoic carbon cycle, *Proceedings of the National Academy of Sciences of the United States of America,* vol. 108, no. 14, pp.5542–5547.

Blamey N.J.F., Brand U., Parnell J., Spear N., Lécuyer C., Benison K., Meng F. and Ni P. (2016) Paradigm shift in determining Neoproterozoic atmospheric oxygen, *Geology*, Vol. 44, Issue 8, pp. 651-654.

Blanco, G., Rajesh, H.M., Gaucher, C., Germs, J.G.B., and Chemale, F.Jr. (2009) Provenance of the Arroyo del Soldado Group, (Ediacaran to Cambrian, Uruguay): Implications for the paleogeographic evolution of southwest Gondwana, *Precambrian Research*, Vol. 171, pp. 57-73.

Blanco, G., Germs G.J.B., Rajesh H.M., Chemale Jr, F., Dussin, I.A. and Justino D. (2011) Provenance and paleogeography of the Nama Group (Ediacaran to early Palaeozoic, Namibia): Petrography, geochemistry and U-Pb detrital zircon geochronology. *Precambrian Research*, Vol. 187, Issues 1-2, pp.15–32.

Boag, T.H., Darroch, S.A.F., Laflamme, M. (2016) Ediacaran distributions in space and time: testing assemblage concepts of earliest macroscopic body fossils. *Paleobiology*, Vol. 42, Issue 4, pp. 574-594.

Bobrovskiy, I., Hope, J.M., Krasnova, A., Ivantsov, A., and Brocks, J.J. (2018) Molecular fossils from organically preserved Ediacara biota reveal cyanobacterial origin for *Beltanelliformis*. *Nature ecology and evolution*, Vol. 1

Bottjer, D.J., Hagadorn, J.W. and Dornbos, S.Q. (2000) The Cambrian substrate revolution. *GSA today*, Vol. 10, No. 9, pp. 1 – 7.

Bouougri, E.H., and Porada, H. (2007) Siliciclastic biolaminites indicative of widespread microbial mats in the Neoproterozoic Nama Group of Namibia, *Journal of African Earth Sciences*, Vol. 48, pp. 38-48.

Bouougri, E.H., Porada, H., Weber, K. and Reitner, J. (2011) Sedimentology and palaeoecology of *Ernietta*-bearing Ediacaran deposits in southern Namibia: implications for infaunal vendobiont communities. In *Advances in Stromatolite Geobiology* (pp. 473-506). Springer Berlin Heidelberg.

Bowring, S.A., Grotzinger, J.P., Condon, D.J., Ramezani, J., Newall, M.J., Allen, P.A., (2007) Geochronologic constraints on the chronostratigraphic framework of the Neoproterozoic Huqf Supergroup, Sultanate of Oman. *American Journal of Science*, Vol. 307, no. 10, pp. 1097-1145.

Bowyer, F., Wood, R.A., and Poulton, S.W. (2017) Controls on the evolution of Ediacaran metzoan ecosystems: A redox perspective. *Geobiology*, Vol. 15, Issue 4, pp. 516 - 551.

Boyle, R.A., Clark, J.R., Poulton S.W., Shields-Zhou, G., Canfield, D.E. and Lenton, T.M. (2013) Nitrogen cycle feedbacks as a control on euxinia in the mid-Proterozoic ocean. *Nature communications*, Vol. 4, p.1533.

Boynton, H.E., Ford, T.D. (1996) Ediacaran fossils from the Precambrian (Charnian Supergroup) of Charnwood Forest, Leicestershire, England. *Mercian Geologist*, Vol. 13, pp. 165–182.

Brain, C.K. (2001) Some observations on *Cloudina*, a terminal Proterozoic index fossil from Namibia. *Journal of African Earth Sciences*, Vol. 33, Issues 3-4, pp. 475-480.

Brand, U. and Veizer, J. (1980) Chemical diagenesis of a multicomponent carbonate system--1: Trace elements. *Journal of Sedimentary Research*, Vol. 50, No. 4, pp. 1219-1236.

Brasier, M.D., Magaritz, M., Corfield, R., Huilin, L., Xiche, W., Lin, O., Zhiwen, J., Hamdi, B., Tinggui, H. and Fraser, A.G. (1990) The carbon-and oxygen-isotope record of the Precambrian–Cambrian boundary interval in China and Iran and their correlation. *Geological Magazine*, Vol. 127, No. 4, pp. 319-332.

Brasier, M.D., Anderson, M.M. and Corfield, R.M. (1992) Oxygen and carbon isotope stratigraphy of the Cambrian carbonates in southeastern Newfoundland and England. *Geological Magazine*, Vol. 129, pp. 265-279.

Brasier, M.D., Khomentovsky, V.V. and Corfield, R.M. (1993) Stable isotopic calibration of the earliest skeletal fossil assemblages in eastern Siberia (Precambrian-Cambrian boundary). *Terra Research*, pp. 225-232.

Brasier, M., Cowie, J. and Taylor, M. (1994) Decision on the Precambrian-Cambrian boundary stratotype. *Episodes*, Vol. 17, No. 1-2, pp. 3-8.

Brasier, M.D., and Antcliffe, J. (2009) Evolutionary relationships in the Avalonian Ediacara biota: new insights from laser analysis. *Journal of the Geological Society, London*, Vol. 166, pp. 361 – 384.

Brennan, S.T., Lowenstein, T. K., and Horita, J. (2004) Seawater chemistry and the advent of calcification: *Geology*, Vol.32, pp. 473-476.

Bristow, T.F., Kennedy, M.J., Derkowski, A., Droser, M.J., Jiang, G. and Creaser, R.A. (2009) Mineralogical constraints on the paleoenvironments of the Ediacaran Doushantuo Formation. *Proceedings of the National Academy of Sciences of the United States of America*, Vol. 106, no. 32, pp.13190–13195.

Broce, J., Schiffbauer, J.D., Sen Sharma, K., Wang, G. and Xiao, S. (2014) Possible Animal Embryos from the Lower Cambrian (Stage 3) Shuijingtuo Formation, Hubei Province, South China. *Journal of Paleontology*, Vol. 88, Issue 2, pp.385–394.

Brocks, J.J., Jarrett, A.J., Sirantoine, E., Hallmann, C., Hoshino, Y. and Liyanage, T. (2017) The rise of algae in Cryogenian oceans and the emergence of animals. *Nature*, Vol. 548, No. 7669, pp. 578.

Broecker, W.S., and Peng, T.-H. (1982) Tracers in the Sea. Eldigio Press, New York, N.Y., pp. 690.

Broecker, W.S. (1997) ThermohalineCirculation, the Achilles Heel of Our Climate System; Will Man-Made CO2 Upset the Current Balance, *Science*, VOl. 278, pp. 1582-1588.

Bruce, W.A., (1983) Why is no deep water formed in the North Pacific? *Journal of Marine Research*, Vol. 41, pp. 327-347.

Buatois, L.A. and Mángano, M.G. (2016) Ediacaran ecosystems and the dawn of animals. *In: The trace-fossil record of major evolutionary events* (pp. 27-72). Springer, Dordrecht.

Buatois, L.A., Narbonne, G.M., Mángano, M.G., Carmona, N.B. and Myrow, P. (2014) Ediacaran matground ecology persisted into the earliest Cambrian. *Nature Communications*, Vol. 5, pp. 3544.

Buatois, L.A., Almond, J., Mángano, M.G., Jensen, S., and Germs, G.J.B. (2018) Sediment disturbance by Ediacaran bulldozers and the roots of the Cambrian explosion, *Nature Scientific Reports*, Vol. 8, No. 4514, pp. 1 – 9.

Budd, D.A. (1997) Cenozoic dolomites of carbonate islands: their attributes and origin. *Earth-Science Reviews*, Vol. 42, pp. 1-47.

Budd, G.E. and Jensen, S. (2017) The origin of the animals and a 'Savannah' hypothesis for early bilaterian evolution. *Biological Reviews*, Vol. 92, no. 1, pp. 446-473.

Butterfield, N.J. (2009) Macroevolutionary turnover through the Ediacaran transition: ecological and biogeochemical implications. *Geological Society, London, Special Publications*, Vol. 326, pp.55–66.

Burns, S.J., and Matter A. (1993) Carbon isotopic record of the latest Proterozoic from Oman. *Eclogae, Geologicae, Helvetiae* 86, pp.595–607.

Burns, S.J., Mckenzie, J.A. and Vasconcelos, C. (2000) Dolomite formation and biogeochemical cycles in the Phanerozoic. *Sedimentology*, Vol. 47, pp. 49-61.

Cai, Y., Schiffbauer, J.D., Hua, H., Xiao, S. (2011) Morphology and paleoecology of the late Ediacaran tubular fossil *Conotubus hemiannulatus* from the Gaojiashan Lagerstatte of southern Shaanxi Province, South China, *Precambrian Research*, Vol. 191, pp. 46-57.

Cai, Y., Hua, H. and Zhang, X. (2013) Tube construction and life mode of the late Ediacaran tubular fossil *Gaojiashania cyclus* from the Gaojiashan Lagerstätte. *Precambrian Research*, Vol. 224, pp. 255-267.

Cai, Y., Hua, H., Schiffbauer, J.D., Sun, B., Yuan, X. (2014) Tube growth patterns and microbial mat-related lifestyles in the Ediacaran fossil *Cloudina*, Gaojiashan Lagerstätte, South China. *Gondwana Research*, 25(3), pp.1008–1018.

Cai, Y., Xiao, S., Hua, H., Yuan, X. (2015) New material of the biomineralizing tubular fossil *Sinotubulites* from the late Ediacaran Dengying Formation, South China. *Precambrian Research*, Vol. 261, pp. 12–24.

Cai, Y., Cortijo, I., Schiffbauer, J.D., and Hua, H. (2017) Taxonomy of the late Ediacaran index fosil *Cloudina* and a new similar taxon from South China. *Precambrian Research*, Vol. 298, pp. 146-156.

Calver, C.R. (2000) Isotope stratigraphy of the Ediacarian (Neoproterozoic III) of the Adelaide Rift Complex, Australia, and the overprint of water column stratification. *Precambrian Research*, Vol. 100, 1-3, pp. 121-150.

Canfield, D.E. (1994) Factors influencing organic carbon preservation in marine sediments. *Chemical Geology*, Vol. 114, No. 3-4, pp. 315-329.

Canfield, D.E. (2001) Biogeochemistry of sulfur isotopes. *Reviews in Mineralogy and Geochemistry*, Vol. 43, No. 1, pp. 607–636.

Canfield, D.E. (2004) The Evolution of the Earth Surface Sulfur Reservoir, *American Journal of Science,* Vol. 304, pp. 839-861.

Canfield, D.E. (2006) Models of oxic respiration, denitrification and sulfate reduction in zones of coastal upwelling. *Geochimica et Cosmochimica Acta*, Vol. 70, Issue 23, pp.5753–5765.

Canfield, D.E. (2014). *Oxygen: a four billion year history*. Princeton University Press. ISBN: 9781400849888

Canfield, D.E., Raiswell, R., Westrich, J.T., Reaves, C.M. and Berner, R.A. (1986) The use of chromium reduction in the analysis of reduced inorganic sulfur in sediments and shales. *Chemical geology*, Vol. 54, No. 1-2, pp.149-155.

Cnafield, D.E. and Teske, A. (1996) Late Proterozoic rise in atmospheric oxygen concentration inferred from phylogenetic and sulphur-isotope studies. *Nature*, Vol. 382, pp. 127-132.

Canfield, D.E., Poulton, S.W. & Narbonne, G.M. (2007) Late-Neoproterozoic deep-ocean oxygenation and the rise of animal life. *Science*, Vol. 315, Issue 5808, pp.92–5.

Canfield, D.E., Poulton, S.W., Knoll, A.H., Narbonne, G.Y., Ross, G., Goldberg, T. and Strauss, H. (2008) Ferruginous conditions dominated later neoproterozoic deep-water chemistry. *Science*, Vol. 321, Issue 5891, pp.949–52.

Canfield, D.E. and Farquhar, J. (2009) Animal evolution, bioturbation, and the sulfate concentration of the oceans. *Proceedings of the National Academy of Sciences*, Vol. 106, No. 20, pp. 8123-8127.

Canfield, D.E. and Thamdrup, B. (2009) Towards a consistent classification scheme for geochemical environments, or, why we wish the term "suboxic" would go away. *Geobiology*, Vol. 7, Issue 4, pp.385–92.

Caron, J.B. and Jackson, D.A. (2008) Paleoecology of the greater phyllopod bed community, Burgess Shale. *Palaeogeography, Palaeoclimatology, Palaeoecology*, Vol. 258, no. 3, pp. 222-256.

Chang, A.J., Chronis, N., Karow, D.S., Marletta, M.A., and Bargmann, C.I. (2006) A Distributed Chemosensory Circuit for Oxygen Preference in *C. elegans*, *PLoS Biol*, Vol. 4, no. 9, p.e274.

Chang, C., Hu, W., Wang, X., Yu, H., Yang, A., Cao, J. and Yao, S. (2017) Carbon isotope stratigraphy of the lower to middle Cambrian on the eastern Yangtze Platform, South China. *Palaeogeography, Palaeoclimatology, Palaeoecology*, Vol. 479, pp. 90-101.

Chen, D., Wand, J., Qing, H., Yan, D. and Li, R. (2009) Hydrothermal venting activities in the Early Cambrian, South China: Petrological, geochronological and stable isotopic constraints. Chemical Geology, Vol. 258, Issues 3-4, pp.168–181.

Chen, D., Zhou, X., Fu, Y., Wang, J. and Yan, D. (2015) New U-Pb zircon ages of the Ediacaran-Cambrian boundary strata in South China. Terra Nova, Vol. 27, pp.62–68.

Chen, M.E., Chen, Y., and Qian, Y. (1981) Some tubular fossils from Sinian–Lower Cambrian boundary sequences, Yangtze Gorge. *Tianjin Institute of Geology and Mineral Resources Bulletin*, Vol. 3, p. 117–124.

Chen, P. (1984) Discovery of Lower Cambrian small shelly fossils from Jijiapo, Yichang, west Hubei and its significance. *Professional Papers on Stratigraphy and Palaeontology*, Vol. 13, pp. 49–66.

Chen, X., Ling, Hong-F., Vance, D., Shields-Zhou, G., Zhu, M., Poulton, S., Och, L.M., Jiang, Shao-Y., Li, D., Cremonese, L. and Archer, C. (2015) Rise to modern levels of ocean oxygenation coincided with the Cambrian radiation of animals. *Nature communications*, 6, 7142.

Chen, Z., Bengtson, S., Zhou, C.M., Hua, H., Yue, Y. (2008) Tube structure and original composition of *Sinotubulites*: shelly fossils from the late Neoproterozoic in southern Shaanxi, China. *Lethaia*, Vol. 41, pp. 37–45.

Chen, Z., Zhou, C., Meyer, M., Xiang, K., Schiffbauer, J.D., Yuan, X., and Xiao, S. (2013) Trace fossil evidence for Ediacaran bilaterian animals with complex behaviors. *Precambrian Research*, Vol. 224, pp. 690-701.

Chen, Z., Zhou, C., Xiao, S., Wang, W., Guan, C., Hua, H. and Yuan, X. (2014) New Ediacara fossils preserved in marine limestone and their ecological implications. *Scientific reports*, 4, 4180.

Cheng, M., Li, C., Zhou, L., Algeo, T.J., Zhang, F., Romaniello, S., Jin, Cheng-S., Lei, Li-D., Feng, Lian-J. and Jiang, Shao-Y. (2016) Marine Mo biogeochemistry in the context of dynamically euxinic mid-depth waters: A case study of the lower Cambrian Niutitang shales, South China. *Geochimica et Cosmochimica Acta*, Vol. 183, pp.79-93.

Cheng, M., Li, C., Zhou, L., Feng, L., Algeo, T.J., Zhang, F., Romaniello, S., Jin, C., Ling, H. and Jiang, S. (2017) Transient deep-water oxygenation in the early Cambrian Nanhua Basin, South China. *Geochimica et Cosmochimica Acta*, Vol. 210, pp. 42-58.

Ciampaglio, C.N., Babcock, L.E., Wellman, C.L., York, A.R., Brunswick, H.K. (2006) Phylogenetic affinities and taphonomy of *Brooksella* from the Cambrian of Georgia and Alabama, USA, *Palaeoworld*, Vol. 15, pp. 256 – 265.

Clarkson, E.N.K. (1979) *Invertebrate Palaeontology and Evolution*, John Wiley and Sons.

Clarkson, M.O., Poulton, S.W., Guilbaud, R. and Wood, R.A. (2014) Assessing the utility of Fe/Al and Fe-speciation to record water column redox conditions in carbonate-rich sediments. *Chemical Geology*, Vol. 382, pp.111-122.

Clarkson, M.O., Wood, R.A., Poulton, S.W., Richoz, S., Newton, R.J., Kasemann, S.A., Bowyer, F. and Krystyn, L. (2016) Dynamic anoxic ferruginous conditions during the end-Permian mass extinction and recovery. *Nature communications*, 7.

Clites, E.C., Droser, M.L. and Gehling, J.G. (2012) The advent of hard-part structural support among the Ediacara biota: Ediacaran harbinger of a Cambrian mode of body construction. *Geology*, Vol. 40, no. 4, pp.307–310.

Cohen, P.A., Bradley, A., Knoll, A.H., Grotzinger, J.P., Jensen, S., Abelson, J., Hand, K., Love, G., Metz, J., McLoughlin, N., Meister, P., Shepard, R., Tice, M. and Wilson, J.P. (2009) Tubular Compression Fossils from the Ediacaran Nama Group, Namibia. *Journal of Paleontology*, Vol. 83, Issue 1, pp.110-122.

Cohen, P.A., Schopf, J.W., Butterfield N.J., Kudryavtsev A.B. and MacDonald, F. (2011) Phosphate biomineralization in mid-neoproterozoic protists. *Geology*, Vol. 39, no. 6, pp.539–542.

Cole, D.B., Reinhard, C.T., Wang, X., Gueguen, B., Halverson, G.P., Gibson, T., Hodgskiss, M.S.W., McKenzie, N.R., Lyons, T.W. and Planavsky, N. (2016) A shale-hosted Cr isotope record of low atmospheric oxygen during the Proterozoic. *Geology*, Vol. 44, no. 7, pp.1–4.,

Compston, W., Zhang, Z., Cooper, J.A., Ma, G. and Jenkins, R.J.F. (2008) Further SHRIMP geochronology on the early Cambrian of South China. *American Journal of Science*, Vol. 308, no. 4, pp.399–420.

Condie, K.C. (1993) Chemical composition and evolution of the upper continental crust: Contrastinng results from surface samples and shales. *Chemical Geology*, Vol. 104, pp. 1-37.

Condon, D., Zhu, M., Bowring, S., Wang, W., Yang, A. and Jin, Y. (2005) U-Pb ages from the neoproterozoic Doushantuo Formation, China. *Science*, Vol. 308, Issue 5718 pp.95–8.

Condon, D.J., McLean, N., Noble, S.R. and Bowring, S.A. (2010) Isotopic composition ($^{238}U/^{235}U$) of some commonly used uranium reference materials. *Geochimica et Cosmochimica Acta*, Vol. 74, pp. 7127-7143.

Condon, D.J., Schoene, B., McLean, N.M., Bowring, S.A. and Parrish, R.R. (2015) Metrology and traceability of U-Pb isotope dilution geochronology (EARTHTIME Tracer Calibration Part I). *Geochimica et Cosmochimica Acta*, Vol. 164, pp. 464 - 480.

Conway Morris, S., and Peel, J.S. (1990) Aritculated halkieriids from the Lower Cambrian of north Greenland, *Nature*, Vol. 345, pp. 802-805.

Conway Morris, S. (1993) Ediacaran-like fossils in Cambrian Burgess shale-type faunas of North America, *Palaeontology*, Vol. 36, Part 3, pp. 593-635.

Cook, P.J. and Shergold, J.H. (1984) Phosphorus, phosphorites and skeletal evolution at the Precambrian—Cambrian boundary. *Nature*, Vol. 308, No. 5956, pp. 231.

Corsetti, F.A., Kidder, D.L. and Marenco, P.J. (2006) Trends in oolite dolomitization across the Neoproterozoic–Cambrian boundary: A case study from Death Valley, California. *Sedimentary Geology*, Vol. 191, pp. 135-150.

Corsetti, F.A. and Hagadorn, J.W. (2000) Precambrian-Cambrian transition: Death Valley, United States. *Geology*, 28(4), pp.299–302.

Cortijo, I., Martí Mus, M., Jensen, S. and Palacios, T. (2010) A new species of Cloudina from the terminal Ediacaran of Spain. *Precambrian Research*, Vol. 176, pp.1–10.

Cowie J.W. and Rozanov, A.Y. (1983) Precambrian-Cambrian boundary candidate, Aldan River, Yakutia, U.S.S.R. *Geological Magazine*, Vol. 120, No. 2, pp. 129-139.

Cremonese, L., Shields-Zhou, G.A., Struck, U., Ling, H.F. and Och, L.M. (2014) Nitrogen and organic carbon isotope stratigraphy of the Yangtze Platform during the Ediacaran–Cambrian transition in South China. *Palaeogeography, Palaeoclimatology, Palaeoecology*, Vol. 398, pp.165-186.

Creveling, J.R., Johnston, D.T., Poulton, S.W., Kotrc, B., März, C., Schrag, D.P. and Knoll, A.H. (2014) Phosphorus sources for phosphatic Cambrian carbonates. *GSA Bulletin*, Vol. 126, No. 1-2, pp.145-163.

Crimes, T.P. and Germs, G.J.B. (1982) Trace Fossils from the Nama Group (Precambrian-Cambrian) of Southwest Africa (Namibia). *Journal of Paleontology*, Vol. 56, no. 4, pp.890-907.

Crimes, T.P. (1989) Trace Fossils. *In*: J.W. Cowie and M.D. Brasier (Eds) The Precambrian-Cambrian Boundary, 166-185, Clarendon Press, Oxford.

Crimes, T.P., and Fedonkin, M.A. (1996) Biotic changes in platform communities across the Precambrian Phanerozoic boundary, *Revista Italiana di Paleontologia e Stratigrafia*, Vol. 102, No. 3, pp. 317 – 332.

Cui, H., Kaufman A.J., Xiao S., Zhu M., Zhou C., Liu X.-M. (2015) Redox architecture of an Ediacaran ocean margin: Integrated chemostratigraphic (δ13C–δ34S–87Sr/86Sr–Ce/Ce*) correlation of the Doushantuo Formation, South China. *Chemical Geology*, Vol. 405, pp. 48–62.

Cui, H., Kaufman A.J., Xiao S., Peek S., Cao H., Min X., Cai Y., Siegel Z., Liu X.M., Peng Y., Schiffbauer J.D., Martin A.J. (2016a) Environmental context for the terminal Ediacaran biomineralization of animals. *Geobiology*, Vol. 14, 344–363.

Cui, H., Xiao, S., Zhou, C., Peng, Y., Kaufman, A.J., and Plummere, R. (2016b) Phosphogenesis associated with the Shuram Excursion: Petrographic and geochemical observations from the Ediacaran Doushantuo Formation of South China. *Sedimentary Geology*. Vol. 341, pp. 134-146.

Cumming, V.M., Poulton, S.W., Rooney, A.D., Selby, D. (2013) Anoxia in the terrestrial environment during the late Mesoproterozoic. *Geology*, Vol. 41, Issue 5, pp. 583–586.

Cunningham, J.A., Liu, A.G., Bengtson, S. and Donoghue, P.C. (2017a) The origin of animals: Can molecular clocks and the fossil record be reconciled? *BioEssays*, Vol. 39, No. 1, pp. 1-12.

Dahl, T.W., Hammarlund, E.U., Andbar, A.D., Bond, D.P.G., Gill, B.C., Gordon, G.W., Knoll, A.H., Nielsen, A.T., Schovsbo, N.H. and Canfield, D.E. (2010) Devonian rise in atmospheric

oxygen correlated to the radiations of terrestrial plants and large predatory fish. *Proceedings of the National Academy of Sciences of the United States of America*, Vol. 107, no. 42, pp.17911–17915.

Danovaro, R., Dell'Anno, A., Pusceddu, A., Gambi, C., Heiner, I. and Kristensen, R.M. (2010) The first metazoa living in permanently anoxic conditions. *BMC biology*, Vol. 8, No. 1, pp. 30.

Darroch, S.A.F., Sperling, E.A., Boag, T.H., Racicot, R.A., Mason, S.J., Morgan, A.S., Tweedt, S., Myrow, P., Johnston, D.T., Erwin, D.H. and Laflamme, M. (2015) Biotic replacement and mass extinction of the Ediacara biota. *Proceedings of the Royal Society B*, Vol. 282, Issue 3. pp. 20151003.

Darroch, S.A.F., Boag, T.H., Racicot, R.A., Tweedt, S., Mason, S.J., Erwin, D.H. and Laflamme, M. (2016) A mixed Ediacaran metazoan assemblage from the Zaris sub-basin, Namibia. *Palaeogeography, Palaeoclimatology, Palaeoecology*, Vol. 459, pp. 198-208.

Davies, G.R. (1977) Former magnesian calcite and aragonite submarine cements in upper Paleozoic reefs of the Canadian Arctic: a summary. *Geology*, Vol. 5, pp. 11-15

Della Porta, G., Webb, G.E. and McDonald, I. (2015) REE patterns of microbialcarbonate and cements from Sinemurian (Lower Jurassic) siliceous sponge mounds (Djebel Bou Dahar, High Atlas, Morocco). *Chemical Geology*, Vol. 400, pp. 65-86.

Derry, L.A (2010) A burial diagenesis origin for the Ediacaran Shuram–Wonoka carbon isotope anomaly. *Earth and Planetary Science Letters*, Vol. 294, Issues 1-2, pp.152–162.

Derry, L.A. (2015) Causes and consequences of mid-Proterozoic anoxia. *Geophysical Research Letters*, Vol. 42, No. 20, pp. 8538-8546.

Dibenedetto, S., and Grotzinger, J. (2005) Geomorphic evolution of a storm-dominated carbonate ramp (c. 549 Ma), Nama Group, Namibia, *Geol. Mag.*, Vol. 142(5), pp.583-604.

Dickson, J.A.D. (1965) A modified staining technique for carbonates in thin section. *Nature*, Vol. 205, pp. 587-587

Dickson, J.A.D. (1980) Aritificial colouration of fluorite by electron bombardment. *Mineralogical Magazine*, Vol. 43, pp. 820-822.

Dickson, J.A.D. (1983) Graphical Modelling of Crystal Aggregates and its Relevance to Cement Diagnosis. *Philosophical Transactions of the Royal Society of London, Series A, Mathematical and Physical Sciences*, Vol. 309, No. 1509, pp. 465-502.

Dickson, J.A.D. (1993) Crystal growth diagrams as an aid to interpreting the fabrics of calcite aggregates. *Journal of Sedimentary Petrology*, Vol. 63, No. 1, pp. 1-17.

Dohrmann, M. and Wörheide, G. (2017) Dating early animal evolution using phylogenomic data. *Scientific reports*, Vol. 7, No. 1, pp. 3599.

Dong, L., Xiao, S., Shen, B., Zhou, C., Li, G. and Yao, J. (2009) Basal Cambrian microfossils from the Yangtze Gorges area (South China) and the Aksu area (Tarim block, northwestern China). *Journal of Paleontology*, Vol. 83, No. 1, pp. 30-44.

Dorland, H.C., 1999. Paleoproterozoic Laterites, Red Beds and Ironstones of the Pretoria Group With Reference to the History of Atmospheric Oxygen. *Rand Afrikaans University, Johannesburg, South Africa*, pp. 1-147.

dos Reis, M., Thawornwattana, Y., Angelis, K., Telford, M.J., Donoghue, P.C.J., and Yang, Z. (2015) Uncertainty in the Timing of Origin of Animals and the Limits of Precision in Molecular Timescales, *Current Biology*, Vol. 25, Issue 22, pp. 2939-2950.

Droser, M.L., and Gehling, J.G. (2013) How well do fossil assemblages of the Ediacara biota tell time? *Geology*, Vol. 41, No. 4, pp. 447-450.

Droser, M.L. and Gehling, J.G., (2015) The advent of animals: the view from the Ediacaran. *Proceedings of the National Academy of Sciences*, Vol. 112, pp. 4865-4870.

Droser, M.L., Jensen, S., Gehling, J.G., Myrow, P.M. and Narbonne, G.M. (2002) Lowermost Cambrian Ichnofabrics from the Chapel Island Formation, Newfoundland: Implications for Cambrian Substrates. *Palaios*, Vol. 17, pp. 3-15.

Droser, M.L., Gehling, J.G., Dzaugis, M.E., Kennedy, M.J., Rice, D., and Allen, M.F. (2015) A new Ediacaran fossil with a novel sediment displacive life habit, *Journal of Paleontology*, Vol. 88, no. 1, pp. 145-151.

Duda, J.-P., Blumenberg, M., Thiel, V., Simon, K., Zhu, M. and Reitner, J. (2014) Geobiology of a palaeoecosystem with Ediacara-type fossils: The Shibantan Member (Dengying Formation, South China). *Precambrian Research*, Vol. 255, pp.48–62.

Dunn, F.S., Liu, A.G. and Donoghue, P.C.J. (2017) Ediacaran Developmental Bioology. *Biological Reviews*.

Dymond, J., Suess, E. and Lyle, M. (1992) Barium in deep-sea sediment: A geochemical proxy for paleoproductivity. *Paleoceanography*, Vol. 7, No. 2, pp. 163 – 181.

Dzik, J. (1999) Organic membranous skeleton of the Precambrian metazoans from Namibia. *Geology*, Vol. 27, No. 6, pp. 519-522.

Dzik, J. (2002) Possible ctenophoran affinities of the Precambrian "Sea – Pen" *Rangea*, *Journal of Morphology*, Vol. 252, pp. 315 – 334.

Eagle, M., Paytan, A., Arrigo, K.R., van Dijken, G. and Murray, R.W. (2003) A comparison between excess barium and barite as indicators of carbon export. *Paleoceanography*, Vol. 18, Issue 1, 1021.

Elliott, D.A., Vickers-Richer, P., Trusler, P., and Hall, M. (2011) New Evidence on the Taphonomic Context of the Ediacaran Pteridinium. *Acta Palaeontologica Polonica*, Vol. 56, No. 3, pp. 641-650.

Elliott, D.A., Trusler, P.W., Narbonne, G.M., Vickers-Rich, P., Morton, N., Hall, M., Hoffmann, K.-H., and Schneider, G.I.C. (2016) Ernietta from the late Ediacaran Nama Group, Namibia. Journal of Paleontology, Vol. 90, no. 6, pp. 1017-1026.

Escribano, R., Daneri, G., Farías, L., Gallardo, V.A., González, H.E., Gutiérrez, D., Lange, C.B., Morales, C.E., Pizarro, O., Ulloa, O. and Braun, M. (2004) Biological and chemical consequences

of the 1997–1998 El Niño in the Chilean coastal upwelling system: a synthesis. *Deep Sea Research Part II: Topical Studies in Oceanography*, Vol. 51, No. 20-21, pp. 2389-2411.

Evans, S.D., Droser, M.L. and Gehling, J.G. (2017) Highly regulated growth and development of the Ediacara macrofossil *Dickinsonia costata*. *PloS one*, Vol. 12, No. 5, p.e0176874.

Fan, H., Zhu, X., Wen, H., Yan, B., Li, J. and Feng, L. (2014) Oxygenation of Ediacaran Ocean recorded by iron isotopes. *Geochimica et Cosmochimica Acta*, Vol. 140, pp.80–94.

Fanning, C.M., Link, P.K. (2008) Age constraints for the Sturtian Glaciation; data fromthe Adelaide Geosyncline, South Australia and Pocatello Formation, Idaho, USA. *In*: Gallagher, S.J., Wallace, M.W. (Eds.), *Selwyn Symposium 2008 Neoproterozoic Extreme Climates and the Origin of Early Metazoan Life*. Geological Societyof Australia, Victoria Division, Melbourne, p. 57.

Fantle, M.S. and DePaolo, D.J. (2007) Ca isotopes in carbonate sediment and pore fluid from ODP Site 807A: the Ca 2+(aq)–calcite equilibrium fractionation factor and calcite recrystallization rates in Pleistocene sediments. *Geochimica et Cosmochimica Acta*, Vol. 71, No. 10, pp. 2524-2546.

Fedo, C.M., Nesbitt, H.W., Young, G.M. (1995) Unraveling the effects of potassium metasomatism in sedimentary rocks and paleosols, with implications for paleoweathering conditions and provenance. *Geology*, Vol. 23, pp. 921 – 924.

Fedonkin, M.A. (1981) White Sea biota of the Vendian. *Trudy Geologicheskiy Institut, Akademiya Nauk SSSR*, 342, 1-100. [In Russian]

Fedonkin, M. A. (1983) Non-skeletal fauna of Podoloia, Dniester River valley, *In* Velikanov, V. A.; Asse]eva, E. A.; Fedonkin, M.A. *The Vendian of the Ukraine* (in Russian). Kiev: Naukova Dumka. pp. 128–139.

Fedonkin, M.A., Gehling, J.G., Grey, K., Narbonne, G.M., and Vickers-Rich, P. (2007a) The Rise of Animals: Evolution and Diversification of the Kingdom Animalia, JHU Press.

Fedonkin, M.A., Simonetta, A. and Ivantsov, A.Y. (2007b) New data on *Kimberella*, the Vendian mollusc-like organism (White Sea region, Russia): palaeoecological and evolutionary implications. *Geological Society, London, Special Publications*, 286, pp.157–179.

Fedonkin, M.A., Vickers-Rich, P., Swalla, B.J., Trusler, P., and Hall, M. (2012) A New Metazoan from the Vendian of the White Sea, Russia, with Possible Affinities to the Ascidians, *Paleontological Journal*, Vol. 46, No. 1, pp. 1 – 11.

Fedonkin, M.A., and Ivantsov, A.Y. (2007) *Ventogyrus*, a possible siphonophore – like trilobozoan coelenterate from the Vendian Sequence (late Neoproterozoic), northern Russia. *In*: Vickers – Rich, P., and Komarower, P. (eds) The Rise and Fall of the Ediacaran Biota. *Geological Society, London, Special Publications*, Vol. 286, pp. 187 – 194.

Fedonkin, M.A., and Waggoner, B.M. (1997) The Late Precambrian fossil *Kimberella* is a mollusc – like bilaterian organism, *Nature*, Vol. 388, pp. 868 – 871.

Feng, L., Li, C., Huang, J., Chang, H. and Chu, X. (2014) A sulfate control on marine mid-depth euxinia on the early Cambrian (ca. 529-521Ma) Yangtze platform, South China. *Precambrian Research*, Vol. 246, pp.123–133.

Fike, D.A., Grotzinger, J.P., Pratt, L.M. and Summons, R.E. (2006) Oxidation of the Ediacaran ocean. *Nature*, Vol. 444, pp.744–7.

Fike, D.A. and Grotzinger, J.P. (2008) A paired sulfate-pyrite $\delta^{34}S$ approach to understanding the evolution of the Ediacaran - Cambrian sulfur cycle. *Geochimica et Cosmochimica Acta*, Vol. 72, pp. 2636-2648.

Flude, L.I., Narbonne, G.M. (2008) Taphonomy and ontogeny of amultibranched Ediacaran fossil: *Bradgatia* from the Avalon Peninsula of Newfoundland. *Canadian Journal of Earth Sciences*, Vol. 45, pp. 1095–1109.

Folk, R.L. (1974) The natural history of crystalline calcium carbonate: effect of magnesium content and salinity. *Journal of Sedimentary Research*, Vol. 44, pp. 40-53.

Folk, R.L. and Land, L.S. (1975) Mg/Ca ratio and salinity: two controls over crystallization of dolomite. *AAPG bulletin*, Vol. 59, pp. 60-68.

Ford, T.D. (1958) Precambrian fossils fromCharnwood Forest. *Proceedings of the Yorkshire Geological Society*, Vol. 31, pp. 211–217.

Frei, R., Gaucher, C., Stolper, S. and Canfield, D.E. (2013) Fluctuations in late Neoproterozoic atmospheric oxidation - Cr isotope chemostratigraphy and iron speciation of the late Ediacaran lower Arroyo del Soldado Group (Uruguay). *Gondwana Research*, Vol. 23, pp.797–811.

Fuenzalida, R., Schneider, W., Garcés-Vargas, J., Bravo, L. and Lange, C. (2009) Vertical and horizontal extension of the oxygen minimum zone in the eastern South Pacific Ocean. *Deep-Sea Research II*, Vol. 56, Issue 16, pp.992–1003.

Gaines, A.M. (1980) Dolomitization kinetics: recent experimental studies. *SEPM special publications*, No. 28, pp. 81-86.

Ganeshram, R.S., François, R., Commeau, J. and Brown-Leger, S.L. (2003) An experimental investigation of barite formation in seawater. *Geochimica et Cosmochimica Acta*, Vol. 67, No. 14, pp. 2599 – 2605.

Gao, Y., Zhang, X., Zhang, G., Chen, K. and Shen, Y. (2018) Ediacaran negative C-isotopic excursions associated with phosphogenic events: Evidence from South China. *Precambrian Research*, Vol. 307, pp. 218-228.

Gaucher, C., and Sprechmann, P. (1999) Upper Vendian skeletal fauna of the Arroyo del Soldado Group, Uruguay, *Beringeria*, Vol. 23, pp. 55-91

Gaucher, C., (2000) Sedimentology, paleontology and stratigraphy of the Arroyo del Soldado Group (Vendian to Cambrian; Uruguay). *Beringeria* 26, 1–120.

Gaucher, C., Finney, S.C., Poiré, D.G., Valencia, V.A., Grove, M., Blanco, G., Pamoukaghlián, K., and Peral, L.G. (2008) Detrital zircon ages of Neoproterozoic sedimentary successions in Uruguay and Argentina: Insights into the geological evolution of the Río de la Plata Craton. *Precambrian Research*, Vol. 167, pp. 150-170.

Gaucher, C., Frimmel, H.E. and Germs, G.J.B. (2009) Tectonic Events and Palaeogeographic Evolution of Southwestern Gondwana in the Neoproterozoic and Cambrian, Chapter 8 in: Gaucher, C., Sial, A.N., Halverson, G.P., Frimmel, H.E. (Eds.), *Neoproterozoic to Cambrian Tectonic, Global Change and Evolution: a Focus on Southwestern Gondwana.* Developments in Precambrian Geology, 16, Elsevier, pp. 103-114 Elsevier.

Gaucher, C., and Poiré, D. (2009) Biostratigraphy. Chapter 4.3.1 in: Gaucher, C., Sial, A.N., Halverson, G.P., Frimmel, H.E. (Eds.), Neoproterozoic to Cambrian Tectonic, Global Change and Evolution: a Focus on Southwestern Gondwana. *Developments in Precambrian Geology*, 16, Elsevier, pp. 103-114 Elsevier.

Gaucher, C., Frei, R., Sial, A.N., Cabrera, J., (2011). Contrasting Sr isotope composition of Paleo- and Neoproterozoic high-Sr limestone successions from the Nico Pérez Terrane, Uruguay. *Gondwana*, Vol. 14, p. 165.

Gaucher, C., Poiré, D.G., Bossi, J., Bettucci, L.S., and Beri, A. (2013) Comment on "Bilaterian Burrows and Grazing Behaviour at > 585 Million Years Ago", *Science*, Vol. 339, Issue 6122, pp. 906.

Gehling, J.G., and Rigby, J.K. (1996) Long Expected Sponges from the Neoproterozoic Ediacara Fauna of South Australia, *Journal of Paleontology*, Vol. 70, No. 2, pp. 185 – 195.

Gehling, J.G., Narbonne, G.M., and Anderson, M.M. (2000) The first named Ediacaran body fossil, *Aspidella terranovica*. *Palaeontology*, Vol. 43, Part 3, pp. 427-456.

Gehling, J.G., Jensen, S., Droser, M.L., Myrow, P.M. and Narbonne, G.M. (2001) Burrowing beneath the basal Cambrian GSSP, Fortune Head, Newfoundland. *Geological Magazine*, Vol. 138, No. 2, pp. 213-218.

Gehling, J.G., Narbonne, G.M., and Anderson, M.M. (2007) Spindle-shaped Ediacara fossils from the Mistaken Point assemblage, Avalon Zone, Newfoundland, *Canadian Journal of Earth Sciences*, Vol. 44, pp. 367 – 387.

Gehling, J.G. and Droser, M.L. (2009) Textured organic surfaces associated with the Ediacara biota in South Australia. *Earth-Science Reviews*, 96(3), pp.196–206.

Gehling, J.G., and Droser, M. (2013) How well do fossil assemblages of the Ediacara Biota tell time? *Geology*, Vol. 41, no. 4, pp.447-450.

Gehling, J.G., Runnegar, B.N., and Droser, M.L. (2014) Scratch Traces of Large Ediacaran Bilaterian Animals. *Journal of Paleontology*, Vol. 88, Issue, 2, pp. 284-298.

German, R. and Elderfield, H. (1990) Application of the Ce anomaly as a paleoredox indicator: The Ground Rules. *Paleoceanography*,Vol. 5, Issue 5, pp.823–833.

Germs, G.J.B. (1968) Discovery of a New Fossil in the Nama System, South West Africa. *Nature*, Vol. 219, pp. 53-54.

Germs, G.J.B. (1972a) Trace fossils from the Nama Group, South-West Africa. *Journal of Paleontology*, Vol. 46, no. 6, pp. 864-870.

Germs, G.J.B. (1972b) New shelly fossils from the Nama Group, South West Africa. *American Journal of Science*, Vol. 272, pp. 752-761.

Germs, G.J.B. (1973a) A reinterpretation of *Rangea schneiderhoehni* and the discovery of a related new fossil from the Nama Group, South West Africa. *Lethaia*, Vol. 6, issue 1, pp. 1-9.

Germs, G.J.B. (1973b) Possible Sprigginid Worm and a New Trace Fossil from the Nama Group, South West Africa. *Geology*, Vol. 1, No. 2, pp. 69-70.

Germs, G.J.B. (1974) The Nama Group in South West Africa and Its Relationship to the Pan – African Geosyncline, *The Journal of Geology*, Vol. 82, No. 3, pp. 301 – 317.

Germs, G.J.B. (1983) Implications of a sedimentary facies and depositional environmental analysis of the Nama Group in South West Africa/Namibia. *Special Publications of the geological Society of South Africa*, Vol. 11, pp.89–114.

Germs, G.J.B. (1995) The Neoproterozoic of southwestern Africa, with emphasis on platform stratigraphy and paleontology. *Precambrian Research*, Vol. 73, Issues 1-4, pp.137–151.

Germs, G.J.B., Knoll, A.H. and Vidal, G. (1986) Latest proterozoic microfossils from the Nama Group, Namibia (south west Africa). *Precambrian Research*, Vol. 32, Issue 1, pp.45–62.

Germs, G.J., Miller, R.M., Frimmel, H.E. and Gaucher, C. (2009) Chapter.4: Syn-to Late-Orogenic Sedimentary Basins of Southwestern Africa. *In:* Gaucher, C., Sial, A.N., Halverson, G.P., Frimmel, H.E. (Eds.), *Neoproterozoic to Cambrian Tectonic, Global Change and Evolution: a Focus on Southwestern Gondwana.Developments in Precambrian Geology*, Vol. 16, pp. 183-203.

Germs, G.J.B., and Gresse, P.G. (1991) The foreland basin of the Damara and Gariep orogens in Namaqualand and southern Namibia: stratigraphic correlations and basin dynamics, South African Journal of Geology, Vol. 94, pp. 159 – 169.

Gerstenberger, H. and Haase, G. (1997) A highly effective emitter substance for mass spectrometric Pb isotope ratio determinations. *Chemical Geology*, Vol. 136, pp. 309.

Geyer, G. and Uchman, A. (1995) Ichnofossil assemblages from the Nama Group (Neoproterozoic-Lower Cambrian) in Namibia and the Proterozoic-Cambrian boundary problem revisited. *Beringeria Special Issue*, Vol. 2, pp. 175-202.

Geyer, G., Peel, J.S., Streng, M., Voigt, S., Fischer, J. and Preusse, M. (2014a) A remarkable Amgan (Middle Cambrian, Stage 5) fauna from the Sauk Tanga, Madygen region, Kyrgyzstan. *Bulletin of Geosciences*, Vol. 89, no. 2, pp. 375-400.

Geyer, G., Buschmann, B. and Elicki, O. (2014b) A new lowermost middle Cambrian (Series 3, Stage 5) faunule from Saxony (Germany) and its bearing on the tectonostratigraphic history of the Saxothuringian domain. *Paläontologische Zeitschrift*, Vol. 88, no. 3, pp. 239-262.

Geyer, G. and Landing, E. (2017) The Precambrian-Phanerozoic and Ediacaran-Cambrian boundaries: a historical approach to a dilemma. *In:* Brasier, A. T., McIlroy, D. &McLoughlin, N. (eds) 2017. Earth System Evolution and Early Life: A Celebration of the Work of Martin Brasier. *Geological Society, London, Special Publications,* Vol. 448, pp. 311–349.

Gibson, G.G., Teeter, S.A., and Fedonkin, M.A. (1984) Ediacarian fossils from the Carolina slate belt, Stanley County, North Carolina, *Geology*, Vol. 12, pp. 387-390.

Gill, B.C., Lyons, T.W., Young, S.A., Kump, L.R., Knoll, A.H. and Saltzman, M.R. (2011) Geochemical evidence for widespread euxinia in the Later Cambrian ocean. *Nature*, Vol. 469, no. 7328, pp. 80.

Gilleaudeau, G.J., Frei, R., Kaufman, A.J., Kah, L.C., Azmy, K., Bartley, J.K., Chernyavsky, P. and Knoll, A.H. (2016) Oxygenation of the mid-Proterozoic atmosphere: clues from chromium isotopes in carbonates. *Geochemical Perspectives Letters*, Vol. 2, pp. 178-187.

Gilleaudeau, G.J. and Kah, L.C. (2015) Heterogeneous redox conditions and a shallow chemocline in the Mesoproterozoic ocean: Evidence from carbon-sulfur-iron relationships. *Precambrian Research*, Vol. 257, pp.94–108.

Gingras, M., Hagadorn, J.W., Seilacher, A., Lalonde, S.V., Pecoits, E., Petrash, D. and Konhauser, K.O. (2011) Possible evolution of mobile animals in association with microbial mats. *Nature Geoscience*, Vol. 4, No. 6, pp. 372.

Glaessner, Martin F. (1958) New Fossils from the Base of the Cambrian in South Australia. *Transactions of the Royal Society of South Australia*. Vol. 81, pp. 185–188.

Glaessner, M.F., Daily, B. (1959) The geology and Late Precambrian fauna of the Ediacara fossil reserve. *Records of the South Australian Museum*, Vol. 13, pp. 369–407.

Glaessner, M.F. (1963) Zur Kenntnis der Nama-Fossilien Südwest-Afrikas. *Ann. Naturhistor. Mus. Wien.*, Vol. 66, pp. 113-120.

Glaessner, M.F. (1978) Re-examination of *Archaeichnium*, a fossil from the Nama Group. *Annals of the South African Museum*, Vol. 74, Issue 13, pp. 335-342.

Glaessner, M.F. (1979) An echiurid worm from the late Precambrian. *Lethaia*, Vol. 12, No. 2, pp. 121 - 124.

Glaessner, M.F., and Wade, M. (1966) The late Precambrian fossils from Ediacara, South Australia: *Palaeontology*, Vol. 9, pp. 599–628.

Glock, N., Liebetrau, V., and Eisenhauer, A. (2014) I/Ca ratios in benthic foraminifera from the Peruvian oxygen minimum zone: analytical methodology and evaluation as a proxy for redox conditions. *Biogeosciences*, Vol. 11, pp. 7077-7095.

Goldberg, T., Poulton, S. and Strauss, H. (2005) Sulphur and oxygen isotope signatures of late Neoproterozoic to early Cambrian sulphate, Yangtze Platform, China: Diagenetic constraints and seawater evolution. *Precambrian Research*, Vol. 137, Issues 3-4, pp.223–241.

Gomes, M.L., and Hurtgen, M.T. (2013) Sulfur isotope systematics of a euxinic, low-sulfate lake: Evaluating the importance of the reservoir effect in modern and ancient oceans. *Geology*, Vol. 41., no. 6, pp. 663-666.

Gomes, M.L., Fike, D.A., Bergmann, K.D., Jones, C. and Knoll, A.H. (2018) Environmental insights from high-resolution (SIMS) sulfur isotope analyses of sulfides in Proterozoic microbialites with diverse mat textures. *Geobiology*, Vol. 16, No. 1, pp. 17-34.

Gradstein, F.M., Ogg, J.G., Schmitz, M. and Ogg, G. eds. The geologic time scale 2012. *Elsevier*.

Grant, S.W.F. (1990) Shell structure and distribution of Cloudina, a potential index fossil for the terminal Proterozoic. *American Journal of Science*, Vol. 290 A, pp.261–294.

Grazhdankin, D.V. (2003) Structure and Depositional Environment of the Vendian Complex in the Southeastern White Sea Area. *Stratigraphy and Geological Correlation*, Vol. 11, no. 4, pp.313–331.

Grazhdankin, D. (2004) Patterns of distribution in the Ediacaran biotas: facies versus biogeography and evolution, *Paleobiology*, Vol. 30, No. 2, pp. 203-221.

Grazhdankin, D. (2014) Patterns of Evolution of the Ediacaran Soft-Bodied Biota, *Journal of Paleontology*, Vol. 88, Issue 2, pp. 269-283.

Grazhdankin, D. and Seilacher, A. (2002) Underground Vendobionta from Namibia. *Palaeontology*, Vol. 45, No. 1, pp. 57 – 78.

Grazhdankin, D. V., Marusin, V.V., Meert, J., Krupenin, M.T. and Maslov, A.V. (2011) Kotlin regional stage in the South Urals. *Doklady Earth Sciences*, Vol. 440, no. 2, pp.1222–1226.

Gregg, J.M., Bish, D.L., Kaczmarek, S.E., and Machel, H.G. (2015) Mineralogy, nucleation and growth of dolomite in the laboratory and sedimentary environment: A review. *Sedimentology*, Vol. 62, pp. 1749-1769.

Gresse, P.G., and Germs, G.J.B. (1993) The Nama foreland basin: sedimentation, major unconformity bounded sequences and multisided active margin advance, *Precambrian Research*, Vol. 63, pp. 247 – 272.

Gresse, P.G., and Scheepers, R. (1993) Neoproterozoic to Cambrian (Namibian) rocks of South Africa: a geochronological and geotectonic review. *Journal of African Earth Sciences*, Vol. 16, No. 4, pp. 375-393.

Grotzinger, J.P. (2000) Facies and paleoenvironmental setting of Thrombolite-Stromatolite Reefs , Terminal Proterozoic Nama Group (ca. 550-543 Ma), central and southern Namibia. *Commun. Geol. Surv. Namib*, 12, pp.251–264.

Grotzinger, J. P. (2002) Stratigraphy, facies, and paleoenvironmental setting of a terminal Proterozoic carbonate ramp, Nama Group (ca. 550–543 Ma), Namibia: Johannesburg, South Africa, 16th International Sedimentological Congress, Field Guide, 71 p.

Grotzinger, J.P., Bowring, S.A., Saylor, B.Z. and Kaufman, A.J. (1995) Biostratigraphic and Geochronologic Constraints on Early Animal Evolution. *Science*, Vol. 270, Issue 5236, pp.598–604.

Grotzinger, J.P., Watters, W.A., Knoll, A.H. (2000) Calcified metazoans in thrombolite-stromatolite reefs of the terminal Proterozoic Nama Group, Namibia, *Paleobiology*, Vol. 26, no. 3, pp. 334-359.

Grotzinger, J.P, Adams, E.W. and Schroeder, S. (2005) Microbial–metazoan reefs of the terminal Proterozoic Nama Group (c. 550–543 Ma), Namibia. *Geological Magazine*, Vol. 142, Issue 5, pp. 499–517.

Grotzinger, J.P., and Miller, R. McG. (2008) The Nama Group. *In*: The Geology of Namibia, Vol. 2 (ed. Miller, R. McG). Geological Survey of Namibia, pp. 13.229-13.272.

Grotzinger J.P., Fike D.A., Fischer W.W. (2011) Enigmatic origin of the largest-known carbon isotope excursion in Earth's history. *Nature Geoscience*, Vol. 4, pp. 285–292.

Grover, G., and Read, J. (1983) Paleoaquifer and deep burial related cements defined by regional cathodoluminescent patterns, Middle Ordovician carbonates, Virginia. *American Association of Petroleum Geoscientist Bulletin*. Vol. 67, pp. 1275–1303.

Guan, C., Wang, W., Zhou, C., Muscente, A.D., Wan, B., Chen, X., Yuan, X., Chen, Z. and Ouyang, Q. (2016) Controls on fossil pyritization : Redox conditions , sedimentary organic matter content , and Chuaria preservation in the Ediacaran Lantian Biota. *Palaeogeography, Palaeoclimatology, Palaeoecology*. Vol. 474, pp. 26-35.

Guilbaud, R., Poulton, S.W., Butterfield, N.J., Zhu, M. and Shields-Zhou, G. (2015) A global transition to ferruginous conditions in the early Neoproterozoic oceans. *Nature Geoscience*, 8, pp.466–470.

Guilbaud, R., Slater, B.J., Poulton, S.W., Harvey, T.H.P., J.J., Nettersheim, B.J., and Butterfield, N.J. (2018) Oxygen minimum zones in the early Cambrian ocean, *Geochemical Perspective Letters*, Vol. 6, pp. 33 - 38.

Gurich, G. (1930a) Die bislang altesten Spuren von Ofganismen in Sudafrika. *Int. Geol. Congr. S. Africa*, 1929, Vol. 15, pp. 670-680.

Gurich, G. (1930b) Uber den Kuibisquarzit in Sudwest-afrika. Z. Deutsch. *Geos. Ges.*, Vol. 82, pp. 637

Gurich, G. (1933) Die Kuibis-Fossillien der Nama-Formation von Südwest-Afrika. *Paläontologische Zeitschrift*, Vol. 15, No. 2, pp. 137-154.

Habermann, D., Neuser, R.D., and Richter, D.K. (1996) REE-activated cathodoluminescence of calcite and dolomite: high-resolution spectrometric analysis of CL emissions (HRS-CL). *Sedimentary Geology*, Vol. 101, pp. 1-7.

Habermann, D., Neuser, R.D. and Richter, D.K. (1998) Low limit of Mn2+-activated cathodoluminescence of calcite: state of the art. *Sedimentary Geology*, Vol. 116, No. 1-2, pp. 13-24.

Hackstein, J.H., Akhmanova, A., Boxma, B., Harhangi, H.R. and Voncken, F.G. (1999) Hydrogenosomes: eukaryotic adaptations to anaerobic environments. Trends in microbiology, Vol. 7, No. 11, pp. 441-447.

Hagadorn, J.W., and Waggoner, B. (2000) Ediacaran Fossils from the southwestern Great Basin,United States, *Journal of Paleontology*, Vol. 74, No. 2, pp. 349-359.

Hahn, G., Hahn, R., Leonardos, O.H., Pflug, H.D., and Walde, D.H.G. (1982) Körperlich erhaltene Scyphozoen-Reste aus dem Jungpräkambrium Brasiliens: *Geologia et Paleontologia*, Vol. 16, pp. 1–18.

Hahn, G., and Pflug, H. (1985) Polypenartige Organismen aus dem Jung-Präkambrium (Nama-Gruppe) von Namibia. *Geologica et Palaeontologica*, Vol. 19, pp. 1–13.

Hall, P.A. (2012) Elemental, isotopic and molecular signatures of early Cambrian marine sediments and a phantom petroleum system in south Australia. *Unpublished PhD thesis*, School of Earth and Environmental Science, Faculty of Science, University of Adelaide.

Hall, M., Kaufman, A.J., Vickers-Rich, P., Ivantsov, A., Trusler, P., Linnemann, U., Hofmann, M., Elliott, D., Cui, H., Fedonkin, M., Hoffmann, K.-H., Wilson, S.A., Schneider, G. and Smith, J. (2013) Stratigraphy, palaeontology and geochemistry of the late Neoproterozoic Aar Member, southwest Namibia: Reflecting environmental controls on Ediacara fossil preservation during the terminal Proterozoic in African Gondwana. *Precambrian Research*, Vol. 238, pp.214–232.

Halverson, G.P., Hoffman, P.F., Schrag, D.P., Maloof, A.C., Hugh, A., and Rice, N. (2005) Toward a Neoproterozoic composite carbon-isotope record. *GSA Bulletin*, Vol. 117, no. 9, pp. 1181-1207

Hamdi, B., Brasier, M.D. and Zhiwen, J., (1989) Earliest skeletal fossils from Precambrian–Cambrian boundary strata, Elburz Mountains, Iran. *Geological Magazine*, Vol. 126, no. 3, pp. 283-289.

Hammarlund, E.U., Gaines, R.R., Prokopenko, M.G., Qi, C., Hou, X.G. and Canfield, D.E. (2017) Early Cambrian oxygen minimum zone-like conditions at Chengjiang. *Earth and Planetary Science Letters*, Vol. 475, pp. 160-168.

Hammarlund, E.U., Stedingk, K.v. and Pahlman, S. (2018) Refined control of cell stemness allowed animal evolution in the oxic realm. *Nature Ecology and Evolution*, Vol. 2, pp. 220-228.

Han, T. and Fan, H. (2015) Dynamic evolution of the Ediacaran ocean across the Doushantuo Formation, South China. *Chemical Geology*, Vol. 417, pp.261–272.

Haq, B.U. and Schutter, S.R. (2008) A Chronology of Paleozoic Sea-Level Changes. *Science*,Vol. 322, Issue 5898, pp.64–68.

Hardie, L.A. (2003) Secular variations in Precambrian seawater chemistry and the timing of Precambrian aragonite seas and calcite seas. *Geology*, Vol. 31, pp. 785-788.

Hardisty, D.S., Lu, Z., Planavsky, N.J., Bekker, A., Philippot, P., Zhou, X. and Lyons, T.W. (2014) An iodine record of Paleoproterozoic surface ocean oxygenation. *Geology*, Vol. 42, No. 7, pp. 619-622.

Hardisty, D.S., Lu, Z., Bekker, A., Diamond, C.W., Gill, B.C., Jiang, G., Kah, L.C., Knoll, A.H., Loyd, S.J., Osburn, M.R., Planavsky, N.J., Wang, C., Zhou, X., and Lyons, T. (2017) Perspectives on Proterozoic surface ocean redox from iodine contents in ancient and recent carbonate. *Earth and Planetary Science Letters*, Vol. 463, pp. 159-170.

Hegenberger, W. (1993) Stratigraphy and sedimentology of the late Precambrian Witvlei and Nama Groups, East of Windhoek. *Memoirs of the Geological Survey of Namibia*, Vol. 17., pp. 1-82.

Helly, J.J. and Levin, L.A. (2004) Global distribution of naturally occurring marine hypoxia on continental margins. *Deep-Sea Research Part I: Oceanographic Research Papers*, Vol. 51, Issue 9, pp.1159–1168.

Herringshaw, L.G., Callow, R.H. and McIlroy, D. (2017) Engineering the Cambrian explosion: the earliest bioturbators as ecosystem engineers. *Geological Society, London, Special Publications*, Vol. 448, No. 1, pp. 369-382.

Hinojosa, J.L., Stirling, C.H., Reid, M.R., Moy, C.M. and Wilson, G.S. (2016) Trace metal cycling and 238U/235U in New Zealand's fjords: Implications for reconstructing global paleoredox conditions in organic-rich sediments. *Geochimica et Cosmochimica Acta*, Vol. 179, pp. 89-109.

Hinz, I.(1987) The Lower Cambrian microfauna of Comley and Rushton, Shropshire/England. *Palaeontographica Abteilung A*, pp. 41-100.

Ho, T.Y., Taylor, G.T., Astor, Y., Varela, R., Müller-Karger, F. and Scranton, M.I. (2004) Vertical and temporal variability of redox zonation in the water column of the Cariaco Basin: implications for organic carbon oxidation pathways. *Marine Chemistry*, Vol. *86*, Issues 1-2, pp.89-104.

Hoekzema, R.S., Brasier, M.D., Dunn, F.S. and Liu, A.G. (2017) Quantitative study of developmental biology confirms *Dickinsonia* as a metazoan. *Proceedings of the Royal Society B*, Vol. 284, No. 1862, p. 20171348.

Hofmann, H.J. and Mountjoy, E.W. (2001) *Namacalathus-Cloudina* assemblage in Neoproterozoic Miette Group (Byng Formation), British Columbia: Canada's oldest shelly fossils. *Geology*, Vol. 29, no. 12, pp.1091–1094.

Hoffmann, K.-H., Condon, D.J., Bowring, S.A., Crowley, J.L., (2004) U-Pb zircon date from the Neoproterozoic Ghaub Formation, Namibia: Constraints on Marinoan glaciation. *Geology*, Vol. 32, pp. 817-820.

Hofmann, H.J., O'Brien, S.J., King, A.F. (2008) Ediacaran biota on Bonavista Peninsula, Newfoundland, Canada. *Journal of Paleontology*, Vol. 82, pp. 1–36.

Hohl, S. V., Becker, H., Gamper, A., Jiang, S.-Y., Wiechert, U., Yang, J.-H. and Wei, H.-Z. (2015) Secular changes of water chemistry in shallow-water Ediacaran ocean: Evidence from carbonates at Xiaofenghe, Three Gorges area, Yangtze Platform, South China. *Precambrian Research*, Vol. 270, pp.50–79.

Holland, H.D., and Zimmermann, H. (2000) The dolomite problem revisited. *International Geology Review*, Vol. 42, pp. 481-490.

Holland, H.D. (2006) The oxygenation of the atmosphere and oceans. Philosophical Transactions of the Royal Society of London B: Biological Sciences, Vol. 361, No. 1470, pp. 903 – 915.

Holmes, J.D., García-Bellido, D.C. and Lee, M.S. (2018) Comparisons between Cambrian Lagerstätten assemblages using multivariate, parsimony and Bayesian methods. *Gondwana Research*, Vol. 55, pp. 30-41.

Hong, H., Zhe, C., and Xunlai, Y. (2007) The advent of mineralized skeletons in Neoproterozoic Metazoa- new fossil evidence from the Gaojiashan Fauna. *Geological Journal*, Vol. 42, pp. 263-279.

Hood, A. v.S., Wallace, M.W., and Drysdale, R.N. (2011) Neoproterozoic aragonite dolomite seas? Widespread marine dolomite precipitation in Cryogenian reef complexes. *Geology*, Vol. 39, pp. 871-874.

Hood, A.v.S. and Wallace, M.W. (2012) Synsedimentary diagenesis in a Cryogenian reef complex: ubiquitous dolomite precipitation. *Sedimentary Geology*, Vol. 255-256, pp. 56-71.

Hood, A.v.S. and Wallace, M.W. (2015) Extreme ocean anoxia during the Late Cryogenian recorded in reefal carbonates of Southern Australia. *Precambrian Research*, Vol. 261, pp.96–111.

Hood, A.v.S. and Wallace, M.W. (2018) Neoproterozoic marine carbonates and their paleoceanographic significance. *Global and Planetary Change*, Vol. 160, pp. 28-45.

Hua, H., Pratt, B.R. and Zhang, L.-Y. (2003) Borings in Cloudina Shells: Complex Predator-Prey Dynamics in the Terminal Neoproterozoic. *Palaios*, Vol. 18, no. 4-5, pp.454–459.

Huang, J., Feng, L., Chu, X., Sun, T., Wen, H., Qin, L. and Shen, Y. (2017) A predominantly ferruginous condition in the Ediacaran deep ocean: Geochemistry of black shales in the Ediacaran Doushantuo Formation, South China. *Precambrian Research*, Vol. 295, pp. 12-23.

Huldtgren, T., Cunningham, J.A., Yin, C., Stampanoni, M., Marone, F., Donoghue, P.C.J., and Bengtson, S. (2011) Fossilized Nuclei and Germination Structures Identify Ediacaran "Animal Embryos" as Encrusting Protists, *Science*, Vol. 334, Issue 6063, pp. 1696-1699.

Husson, J.M., Maloof, A.C. and Schoene, B. (2012) A syn-depositional age for Earth's deepest $\delta^{13}C$ excursion required by isotope conglomerate tests. *Terra Nova*, Vol. 24, Issue 4, pp.318–325.

Husson, J.M., Maloof, A.C., Schoene, B., Chen, C.Y. and Higgins, J.A. (2015) Stratigraphic expression of Earth's deepest δ13C excursion in the Wonoka Formation of South Australia. *American Journal of Science*, 315, 1, pp. 1-45.

Illing, L.V., Wells, A.J., and Taylor, J.C.M. (1965) Penecontemporary dolomite in the Persian Gulf. *The Society of Economic Paleontologists and Mineralogists (SEPM)*, SP13, pp. 89-111.

Ingall, E. and Jahnke, R. (1994) Evidence for enhanced phosphorus regeneration from marine sediments overlain by oxygen depleted waters. *Geochimica et Cosmochimica Acta*, Vol. 58, No. 11, pp. 2571-2575.

Isachsen, C.E., Bowring, S.A., Landing, E. and Samson, S.D. (1994) New constraint on the divisionn of Cambrian time. *Geology*, Vol. 22, pp. 496 - 498.

Ishikawa, T., Ueno, Y., Komiya, T., Sawaki, Y., Han, J., Shu, D., Li, Y., Maruyama, S. and Yoshida, N. (2008) Carbon isotope chemostratigraphy of a Precambrian/Cambrian boundary section in the Three Gorge area, South China: prominent global-scale isotope excursions just before the Cambrian Explosion. *Gondwana Research*, 14, 1-2, pp. 193-208.

Ishikawa, T., Ueno, Y., Shu, D., Li, Y., Han, J., Guo, J., Yoshida, N., Maruyama, S. and Komiya, T. (2014) The $\delta^{13}C$ excursions spanning the Cambrian explosion to the Canglangpuian mass extinction in the Three Gorges area, South China. *Gondwana Research*, Vol. 25, no. 3, pp. 1045-1056.

Ivantsov, A.Y. (1999) A New Dickinsonid from the Upper Vendian of the White Sea Winter Coast (Russia, Arkhangelsk Region). *Paleontological Journal*, Vol. 33, No. 3, pp. 233–241.

Ivantsov, A.Y. (2009) New reconstruction of *Kimberella*, problematic Vendian metazoan. *Paleontological Journal*, Vol. 43, No. 6, pp. 601 – 611.

Ivantsov, A.Y. (2011) Feeding traces of proarticulata—the Vendian metazoa. *Paleontological Journal*, Vol. 45, No. 3, pp. 237-248.

Ivantsov, A.Y. (2017) Finds of Ediacaran-Type fossils in Vendian deposits of the Yudoma Group, Eastern Siberia. *Doklady Earth Sciences*, Vol. 472, Part 2, pp. 143-146.

Ivantsov, A.Y., and Grazhdankin, D.V. (1997) A New Representative of the Petalonamae from the Upper Vendian of the Arkhangelsk Region, *Paleontological Journal*, Vol. 31, No. 1, pp. 1 – 16.

Ivantsov, A.Y. and Fedonkin, M.A. (2002) Conulariid-like fossil from the Vendian of Russia: A metazoan clade across the Proterozoic/Palaeozoic boundary. *Palaeontology*, Vol. 45, pp.1219–1229.

Ivantsov, A.Y.; Malakhovskaya, Y.E.; Serezhnikova, E.A. (2004) Some Problematic Fossils from the Vendian of the Southeastern White Sea Region, *Paleontological Journal*, Vol. 38, No. 1, pp. 1–9.

Ivantsov, A.Y., Gritsenko, V.P., Konstantinenko, L.I., Zakrevskaya, M.A. (2014) Revision of the Problematic Vendian Macrofossil *Beltanelliformis* (=*Beltanelloides*, *Nemiana*). *Paleontological Journal*, Vol. 48, no. 13, pp. 1415-1440.

James, N.P. and Jones, B. (2015) *Origin of Carbonate Sedimentary Rocks*, Wiley Press, American Geophysical Union, ISBN: 978-1-118-65270-1

Janussen, D., Steiner, M., and Zhu, M. (2002) New well-preserved scleritomes of chancelloridae from the early Cambrian Yuanshan Formation (Chengjiang, China) and the Middle Cambrian Wheeler Shale (Utah, USA) and paleobiological implications. *Journal of Paleontology*, Vol. 76, issue 4, pp. 596-606.

Jenkins, R.J.F., (1985) The enigmatic Ediacaran (late Precambrian) genus *Rangea* and related forms. *Paleobiology*, Vol. 11, issue 3, pp. 336-355

Jensen, S.M. (2003) The Proterozoic and Earliest Cambrian Trace Fossil Record; Patterns, Problems and Perspectives. *Integrative and Comparative Biology*, Vol. 43, Issue 1, pp. 219-228.

Jensen, S.M., Saylor, B.Z., Gehling, J.G., Germs, G.J.B. (2000) Complex trace fossils from the terminal Proterozoic of Namibia, *Geology*, Vol. 28, Issue 2, pp. 143-146.

Jensen, S.M. and Runnegar, B.N. (2005) A complex trace fossil from the Spitskop Member (terminal Ediacaran–? Lower Cambrian) of southern Namibia. *Geological Magazine*, Vol. 142, Issue 5, pp.561–569.

Jiang, G., Kennedy, M.J., Christie-Blick, N., Wu, H. and Zhang, S. (2006) Stratigraphy, Sedimentary Structures, and Textures of the Late Neoproterozoic Doushantuo Cap Carbonate in South China. *Journal of Sedimentary Research*, Vol. 76, no. 7, pp.978–995.

Jiang, G., Kaufman, A.J., Christie-Blick, N., Zhang, S., and Wu, H. (2007) Carbon isotope variability across the Ediacaran Yangtze platform in South China: Implications for a large surface-to-deep ocean $\delta^{13}C$ gradient, *Earth and Planetary Science Letters*, Vol. 261, pp. 301-320.

Jiang, G., Shi, X., Zhang, S., Wang, Y. and Xiao, S. (2011) Stratigraphy and paleogeography of the Ediacaran Doushantuo Formation (ca. 635-551Ma) in South China. *Gondwana Research*, Vol. 19, Issue 4, pp.831–849.

Jiang, S.-Y., Pi, D.-H., Heubeck, C., Frimmel, H., Liu, Y.-P., Deng, H.-L., Ling, H.-F. and Yang, J.-H. (2009) Early Cambrian ocean anoxia in South China. *Nature*, Vol. 459, Issue 7248, pp.E5–E6; discussion E6.

Jin, C., Li, C., Algeo, T.J., Planavsky, N.J., Cui, H., Yang, X., Zhao, Y., Zhang, X. and Xie, S. (2016) A highly redox-heterogeneous ocean in South China during the early Cambrian (~529-514 Ma): Implications for biota-environment co-evolution. *Earth and Planetary Science Letters*, Vol. 441, pp.38–51.

Johnson, B.W., Poulton, S.W. and Goldblatt, C. (2017) Marine oxygen production and open water supported an active nitrogen cycle during the Marinoan Snowball Earth. *Nature Communications*, Vol. 8, No. 1, pp.1316.

Johnston, D.T., Poulton, S.W., Dehler, C., Porter, S., Husson, J., Canfield, D.E. and Knoll, A.H. (2010) An emerging picture of Neoproterozoic ocean chemistry: Insights from the Chuar Group, Grand Canyon, USA. *Earth and Planetary Science Letters*, Vol. 290, Issues 1-2, pp.64–73.

Johnston, D.T., Poulton, S.W., Goldberg, T., Sergeev, V.N., Podkovyrov, V., Vorob'eva, N.G., Bekker, A. and Knoll, A.H. (2012) Late Ediacaran redox stability and metazoan evolution. *Earth and Planetary Science Letters*, Volumes 335-336, pp.25–35.

Johnston, D.T., Poulton, S.W., Tosca, N.J., O'Brien, T., Halverson, G.P., Schrag, D.P. and Macdonald, F.A. (2013) Searching for an oxygenation event in the fossiliferous Ediacaran of northwestern Canada. *Chemical Geology*, Vol. 362, pp.273–286.

Kaczmarek, S.E., Gregg, J.M., Bush, D.L., Machel, H.G. and Fouke, B.W. (2017) Dolomite, Very High-Magnesium Calcite, and Microbes – Implications for the Microbial Model of Dolomitization. *SEPM Special Publications*, Vol. 109: Characterization and Modeling of Carbonates - Mountjoy Symposium 1

Katz, A., and Matthews, A. (1977) The dolomitization of $CaCO_3$: and experimental study att 252-295°C. *Geochimica et cosmochimica acta*, Vol. 41, pp, 297-308.

Kaufman, A.J., Hayes, J.M., Knoll, A.H. and Germs, G.J.B. (1991) Isotopic compositions of carbonates and organic carbon from upper Proterozoic successions in Namibia: stratigraphic variation and the effects of diagenesis and metamorphism. *Precambrian Research*, Vol. 49, pp.301–327.

Kaufman, A.J., Jacobsen, S.B. and Knoll, A.H. (1993) The Vendian record of Sr and C isotopic variations in seawater: implications for tectonics and paleoclimate. *Earth and Planetary Science Letters*, Vol. 120, Issue 3-4, pp.409-430.

Kaufman, A.J. and Knoll, A.H. (1995) Neoproterozoic variations in the C-isotopic composition of seawater: stratigraphic and biogeochemical implications. *Precambrian research*, Vol. 73, No. 1-4, pp. 27-49.

Kaufman, A.J., Knoll, A.H., Semikhatov, M.A., Grotzinger, J.P., Jacobsen, S.B. and Adams, W. (1996) Integrated chronostratigraphy of Proterozoic-Cambrian boundary beds in the western Anabar region, nortthern Siberia. *Geological Magazine*, Vol. 133, No. 5, pp. 509-533.

Kaufman A.J., Corsetti F.A., and Varni M.A. (2007) The effect of rising atmospheric oxygen on carbon and sulfur isotope anomalies in the Neoproterozoic Johnnie Formation, Death Valley, USA. *Chemical Geology*, Vol. 237, pp. 47–63.

Kaufman, A.J., Peek, S., Aaron, J., Cui, H., Grazhdankin, D., Rogov, V., Xiao, S., Buchwaldt, R., Bowring, S. (2012) A Shorter Fuse for the Cambrian Explosion?, 2012 *GSA Annual Meeting*. The Geological Society of America, Charlotte, North Carolina, USA.

Keil, R.G., Montluçon, D.B., Prahl, F.G. and Hedges, J.I. (1994) Sorptive preservation of labile organic matter in marine sediments. *Nature*, Vol. 370, No. 6490, pp. 549.

Kendall, B.S., Creaser, R.A., Ross, G.M., and Selby, D. (2004) Constraints on the timing of Marinoan "Snowball Earth" glaciation by ^{187}Re-^{187}Os dating of a Neoproterozoic, post-glacial black shale in Western Canada, *Earth and Planetary Science Letters*, Vol. 222, pp. 729-740.

Kendall, B., Gordon, G.W., Poulton, S.W., and Anbar, A.D. (2011) Molybdenum isotope constraints on the extent of late Paleoproterozoic ocean euxinia, *Earth and Planetary Science Letters*, Vol. 307, Issues 3-4, pp. 450-460.

Kendall, B., Komiya, T., Lyons, T.W., Bates, S.M., Gordon, G.W., Romaniello, S.J., Jiang, G., Creaser, R.A., Xiao, S., McFadden, K., Sawaki, Y., Tahata, M., Shu, D., Han, J., Li, Y., Chu, X. and Anbar, A.D. (2015) Uranium and molybdenum isotope evidence for an episode of widespread ocean oxygenation during the late Ediacaran Period. *Geochimica et Cosmochimica Acta*, Vol. 156, pp.173–193.

Kennedy, M., Droser, M., Mayer, L.M., Pevear, D. and Mrofka, D. (2006) Late Precambrian oxygenation; inception of the clay mineral factory. *Science*, Vol. 311, No 5766, pp. 1446-1449.

Kershaw, S. (2015) Modern Black Sea oceanography applied to the end-Permian extinction event. *Journal of Palaeogeography*, Vol. 4(1), pp.52–62.

Khomentovsky, V.V. (1986) The Vendian System of Siberia and a standard stratigraphic scale. *Geological Magazine*, Vol. 123, No. 4, pp. 333-348.

Khomentovsky, V.V. (2008) The Yudomian of Siberia, Vendian and Ediacaran Systems of the International Stratigraphic Scale. *Stratigraphy and Geoological Correlation*, Vol. 16, No. 6, pp. 581-598.

Khomentovsky, V.V. and Karlova, G.A. (1993) Biostratigraphy of the Vendian-Cambrian beds and the lower Cambrian boundary in Siberia. *Geological Magazine*, Vol. 130, No. 1, pp. 29-45.

Khomentovsky, V.V. and Karlova, G.A. (2002) The boundary between Nemakit-Daldynian and Tommotian Stages (Vendian-Cambrian Systems) of Siberia. *Stratigraphy and Geological Correlation*, Vol. 10, No. 3, pp. 217-238.

Khomentovsky, V.V. and Karlova, G.A. (2005) The Tommotian Stage Base as the Cambrian lower boundary in Siberia. *Stratigraphy and Geological Correlation*, Vol. 13, No. 1, pp. 21-34.

Kirschvink, J.L., Magaritz, M., Ripperdan, R.L., Zhuravlev, A.Y. and Rozanov, A.Y. (1991) The Precambrian/Cambrian boundary: Magnetostratigraphy and Carbon Isotopes Resolve Correlation Problems Between Siberia, Morocco, and South China. *GSA Today*, Vol. 1, No. 4, pp. 69-91.

Klump, J., Hebbeln, D., Wefer, G. (2000) The impact of sediment provenance on barium – based productivity estimates, *Marine Geology*, Vol. 169, pp. 259 – 271.

Knauth, L.P. and Kennedy, M.J. (2009) The late Precambrian Greening of the Earth. *Nature*, Vol. 460, pp.728-732.

Knoll, A.H. (2003) Biomineralisation and evolutionary history. *Reviews in mineralogy and geochemistry*, Vol. 54, pp. 329 - 356.

Knoll, A.H., Grotzinger, J.P., Kaufman, A.J. and Kolosov, P. (1995a) Integrated approaches to terminal Proterozoic stratigraphy: an example from the Olenek Uplift, northeastern Siberia. *Precambrian Research*, Vol. 73, pp. 251-270.

Knoll, A.H., Kaufman, A.J., Semikhatov, M.A. and Grotzinger, J.P. (1995b) Sizing up the sub-Tommotian unconformity in Siberia. *Geology*, Vol. 23, No. 12, pp. 1139-1143.

Knoll, A., Walter, M., Narbonne, G. and Christie-Blick, N. (2006) The Ediacaran Period: a new addition to the geologic time scale. *Lethaia*, Vol. 39, No. 1, pp. 13-30.

Konovalov, S.K., Murray, J.W., Luther, G.W. and Tebo, B.M. (2006). Processes controlling the redox budget for the oxic/anoxic water column of the Black Sea. *Deep Sea Research Part II: Topical Studies in Oceanography*, Vol. *53*, Issue 17, pp.1817-1841.

Kouchinsky, A., Bengtson, S., Missarzhevsky, V.V., Pelechaty, S., Torssander, P. and Val'kov, A.K. (2001) Carbon isotope stratigraphy and the problem of a pre-Tommotian Stage in Siberia. *Geological Magazine*, Vol. 138, No. 4, pp. 387-396.

Kouchinsky, A., Bengtson, S., Pavlov, V., Runnegar, B., Val'kov, A. and Young, E. (2005) Pre-Tommotian age of the lower Pestrotsvet Formation in the Selinde section on the Siberian platform: carbon isotopic evidence. *Geological Magazine*, Vol. 142, No. 4, pp. 319-325.

Kouchinsky, A., Bengtson, S., Pavlov, V., Runnegar, B., Torssander, P., Young, E., Ziegler, K. (2007) Carbon isotope stratigraphy of the Precambrian-Cambrian Sukharikha River section, northwestern Siberian Platform. *Geological Magazine*, Vol. 144, No. 4, pp. 609-618.

Kouchinsky, A., Bengtson, S., Feng, W., Kutygin, R. and Val'kov, A. (2009) The Lower Cambrian fossil anabaritids: affinities, occurrences and systematics. *Journal of Systematic Palaeontology*, Vol. 7, no. 3, p.241.

Kouchinsky, A., Bengtson, S., Clausen, S., Gubanov, A., Malinky, J.M. and Peel, J.S. (2011) A Middle Cambrian fauna of skeletal fossils from the Kuonamka Formation, northern Siberia. *Alcheringa*, Vol. 35, no. 1, pp. 123-189.

Kumar, S.P. and Narvekar, J. (2005) Seasonal variability of the mixed layer in the central Arabian Sea and its implication on nutrients and primary productivity. *Deep-Sea Research Part II: Topical Studies in Oceanography*, Vol. 52, pp.1848–1861.

Kurzweil, F., Drost, K., Pasava, J., Wille, W., Taubald, H., Schoeckle, D. and Schoenberg, R. (2015) Coupled sulfur, iron and molybdenum isotope data from black shales of the Teplá-Barrandian unit argue against deep ocean oxygenation during the Ediacaran. *Geochimica et Cosmochimica Acta*, Vol. 171, pp.121–142.

Laflamme, M., Narbonne, G.M., and Anderson, M.M. (2004) Morphometric analysis of the Ediacaran frond *Charniodiscus* from the Mistaken Point Formation, Newfoundland. *Journal of Paleontology*, Vol. 78, pp. 827–37.

Laflamme, M., Xiao, S., and Kowalewski, M., (2009) Osmotrophy in modular Ediacara organisms: *Proceedings of the National Academy of Sciences*, USA, Vol. 106, p. 14438–14443.

Laflamme, M., Flude, L.I., and Narbonne, G.M. (2012) Ecological tiering and the evolution of a stem: the oldest stemmed frond from the Ediacaran of Newfoundland, Canada. *Journal of Paleontology*, Vol. 86, pp. 193–200.

Laflamme, M., Darroch, S.A.F., Tweedt, S.M., Peterson, K.J. and Erwin, D.H. (2013) The end of the Ediacara biota: Extinction, biotic replacement, or Cheshire Cat? *Gondwana Research*, 23, Issue 2, pp.558–573.

Landing, E. (1991) Upper Precambrian through Lower Cambrian of Cape Breton Island: Faunas, Paleoenvironments, and Stratigraphic Revision. *Journal of Paleontology*, Vol. 65, no. 4, pp. pp. 570 - 595.

Landing, E. (1992) Lower Cambrian of southeastern Newfoundland: Epeirogeny and Lazarus faunas, lithofacies-biofacies linkages, and the myth of a global chronostratigraphy. In: Lipps, J.H., Signor, P.W. (Eds.), *Origin and Early Evolution of Metazoa. Plenum Press, New York*, pp. 283 – 309.

Landing, E. (1994) Precambrian-Cambrian boundary global stratotype ratified ad a new perspective of Cambrian time. *Geology*, Vol. 22, pp. 179 - 182.

Landing, E. (1995) Upper Placentian—Branchian series of mainland Nova Scotia (middle-upper Lower Cambrian): Faunas, paleoenvironments, and stratigraphic revision. *Journal of Paleontology*, Vol. 69, no. 3, pp. 475-495.

Landing, E., Myrow, P., Benus, A.P., and Narbonne, G.M. (1989) The Placentian Series: Appearance of the Oldest Skeletalized Faunas in Southeastern Newfoundland. *Journal of Paleontology*, Vol. 63, No. 6, pp. 739-769.

Last, W.M. (1990) Lacustrine dolomite - an overview of modern, Holocene, and Pleistocene occurrences. *Eartth-Science Reviews*, Vol. 27, pp. 221-263.

Lechte, M.A., and Wallace, M.W. (2015) Sedimentary and tectonic history of the Holowilena Ironstone, a Neoproterozoic iron formation in South Australia, *Sedimentary Geology*, Vol. 329, pp. 211 – 224.

Le Guerroué, E., Allen, P.A. and Cozzi, A. (2006) Chemostratigraphic and sedimentological framework of the largest negative carbon isotopic excursion in Earth history: The Neoproterozoic Shuram Formation (Nafun Group, Oman). *Precambrian Research*, Vol. 146, Issues 1-2, pp.68–92.

Lenton, T.M., Boyle, R.A., Poulton, S.W., Shields-Zhou, G.A. and Butterfield, N.J. (2014) Co-evolution of eukaryotes and ocean oxygenation in the Neoproterozoic era. *Nature Geoscience*, 7, pp.257–265.

Levin, L.A., Ekau, W., Gooday, A.J., Jorissen, F., Middelburg, J.J., Naqvi, S.W.A., Neira, C., Rabalais, N.N., and Zhang, J. (2009) Effects of natural and human-induced hypoxia on coastal benthos, *Biogeosciences*, Vol. 6, no. 10, pp.2063-2098.

Levin, L.A. (2017) Manifestation, Drivers, and Emergence of Open Ocean Deoxygenation. *Annual review of marine science*, (0).

Li, C., Love, G.D., Lyons, T.W., Fike, D.A., Sessions, A.L. and Chu, X. (2010) A stratified redox model for the Ediacaran ocean. *Science*, Vol. 328, Issue 5974, pp.80–3.

Li, C., Love, G.D., Lyons, T.W., Scott, C.T., Feng, L., Huang, J., Chang, H., Zhang, Q. and Chu, X. (2012) Evidence for a redox stratified Cryogenian marine basin, Datangpo Formation, South China. *Earth and Planetary Science Letters*, Voumes 331–332, pp. 246–256.

Li, C., Meng, C., Algeo, T.J. and ShuCheng, X. (2015a) A theoretical prediction of chemical zonation in early oceans (>520 Ma). *Science China Earth Sciences*, Vol. 58, pp.1901–1909.

Li, C., Planavsky, N.J., Shi, W., Zhang, Z., Zhou, C., Cheng, M., Tarhan, L.G., Luo, G., and Xie, S. (2015b) Ediacaran Marine Redox Heterogeneity and Early Animal Ecosystems. *Scientific Reports*, Vol. 5, 17097.

Li, C., Hardisty, D.S., Luo, G., Huang, J., Algeo, T.J., Cheng, M., Shi, W., An, Z., Tong, J., Xie, S. and Jiao, N. (2017a) Uncovering the spatial heterogeneity of Ediacaran carbon cycling. *Geobiology*, Vol. 15, No. 2, pp. 211-224.

Li, C., Jin, C., Planavsky, N.J., Algeo, T.J., Cheng, M., Yang, X., Zhao, Y. and Xie, S. (2017b) Coupled oceanic oxygenation and metazoan diversification during the early–middle Cambrian?. *Geology*, Vol. 45, No. 8, pp. 743-746.

Li, D., Ling, H.-F., Jiang, S.-Y., Pan, J.-Y., Chen, Y.-Q., Cai, Y.-F., and Feng, H.-Z. (2009) New carbon isotope stratigraphy of the Ediacaran-Cambrian boundary interval from SW China: implications for global correlation, *Geological Magazine*, Vol. 146, No. 4, pp. 465 - 484.

Li, D., Ling, H.F., Shields-Zhou, G.A., Chen, X., Cremonese, L., Och, L., Thirlwall, M. and Manning, C.J. (2013) Carbon and strontium isotope evolution of seawater across the Ediacaran–Cambrian transition: evidence from the Xiaotan section, NE Yunnan, South China. *Precambrian Research*, Vol. 225, pp.128-147.

Li, X., Taylor, G.T., Astor, Y., Varela, R. and Scranton, M.I. (2012) The conundrum between chemoautotrophic production and reductant and oxidant supply: A case study from the Cariaco basin. *Deep-Sea Research Part I: Oceanographic Research Papers*, Vol. 61, pp.1–10.

Li, Y.-H., and Schoonmaker, J.E. (2003) Chemical Composition and Mineralogy of Marine Sediments. *In*: Holland, H.D., and Turekian, K.K. *Treatise on Geochemistry*, Vol. 7, pp. 1-35. Elsevier pergamon.

Li, Z.-X., Evans, D.A.D. and Halverson, G.P. (2013) Neoproterozoic glaciations in a revised global palaeogeography from the breakup of Rodinia to the assembly of Gondwanaland. *Sedimentary Geology*, Vol. 294, pp.219–232.

Lin, J.P., Gon III, S.M., Gehling, J.G., Babcock, L.E., Zhao, Y.L., Zhang, X.L., Hu, S.X., Yuan, J.L., Yu, M.Y. and Peng, J. (2006) A *Parvancorina*-like arthropod from the Cambrian of South China. *Historical Biology*, Vol. 18, No. 1, pp. 33-45.

Lin, S., Zhang, Y., Zhang, L., Tao, X., Wang, M. (1986) Body and trace fossils of metazoa and algal macrofossils from the upper Sinian Gaojiashan Formation in southern Shaanxi. *Geology of Shaanxi*, Vol. 4, pp. 9–17.

Ling, H.-F., Chen, X., Li, D., Wang, D., Shields-Zhou, G.A. and Zhu, M. (2013) Cerium anomaly variations in Ediacaran-earliest Cambrian carbonates from the Yangtze Gorges area, South China: Implications for oxygenation of coeval shallow seawater. *Precambrian Research*, Vol. 225, pp.110–127.

Linnemann, U., Ovtcharova, M., Schaltegger, U., Vickers-Rich, P., Gärtner, A., Hofmann, M., Zieger, J., Krause, R., Kriesfeld, L., and Smith, J. (2017) New geochronological and stratigraphic constraints on the Precambrian-Cambrian boundary (Swartpunt section, South Namibia), *In: International Symposium on the Ediacaran-Cambrian Transition*. At Memorial University, St. Johns, Newfoundland. June 2017

Lippmann, F. (1973) *Sedimentary Carbonate Minerals*, Springer-Verlag, Berlin, 228 pp.

Liu, A.G., McIlroy, D., and Brasier, M.D. (2010) First evidence for locomotion in the Ediacara biota from the 565 Ma Mistaken Point Formation, Newfoundland. *Geology*, Vol. 38, No2., pp. 123 - 126.

Liu, A.G., McIlroy, D., Antcliffe, J.B., and Brasier, M.D. (2011) Effaced preservation in the Ediacara biota and its implications for the early macrofossil record. *Palaeontology*, Vol. 54, part 3, pp. 607 – 630.

Liu, A.G., McIlroy, D., Matthews, J.J. and Brasier, M.D. (2012) A new assemblage of juvenile Ediacaran fronds from the Drook Formation, Newfoundland. *Journal of the Geological Society*, Vol. 169, No. 4, pp. 395-403.

Liu, A.G., Matthews, J.J., Menon, L.R., McIlroy, D., and Brasier, M.D. (2014) *Haootia quadriformis* n. gen., n. sp., interpreted as a muscular cnidarian impression from the Late Ediacaran period (approx. 560 Ma). *Proceedings of the Royal Society, B*, Vol. 281, 20141202.

Liu, A.G., Kenchington, C.G. and Mitchell, E.G. (2015) Remarkable insights into the paleoecology of the Avalonian Ediacaran macrobiota. *Gondwana Research*, 27(4), pp.1355–1380.

Liu, A.G., Matthews, J.J., and McIlroy, D. (2016) The *Beothukis/Culmofrons* problem and its bearing on Ediacaran macrofossil taxonomy: evidence from an exceptional new fossil locality. *Palaeontology*, Vol. 59, Part 1, pp. 45 – 58

Liu, A.G. (2016) Framboidal pyrite shroud confirms the 'Death Mask' model for moldic preservation of Ediacaran soft-bodied organisms. *Palaios*, v.31, pp.259–274.

Liu, K., Feng, Q., Shen, J., Khan, M. and Planavsky, N.J. (2017) Increased productivity as a primary driver of marine anoxia. *Palaeogeography, Palaeoclimatology, Palaeoecology*, Vol. 491, pp. 1-9.

Liu, P., Yin, C., Gao, L., Tang, F. and Chen, S. (2009) New material of microfossils from the Ediacaran Doushantuo Formation in the Zhangcunping area, Yichang, Hubei Province and its zircon SHRIMP U-Pb age. *Chinese Science Bulletin*, Vol. 54, pp.1058–1064.

Liu, P., Yin, C., Chen, S., Tang, F. and Gao, L., (2013). The biostratigraphic succession of acanthomorphic acritarchs of the Ediacaran Doushantuo Formation in the Yangtze Gorges area, South China and its biostratigraphic correlation with Australia. *Precambrian Research*, Vol. 225, pp.29-43.

Love, G.D.,Grosjean, E., Stalvies, C., Fike D.A., Grotzinger, J.P., Bradley, A.S., Kelly, A.E., Bhatia, M., Meredith, W., Snape, C.E., Bowring, S.A., Condon, D.J. and Summons, R.E. (2009) Fossil steroids record the appearance of Demospongiae during the Cryogenian period. *Nature*, 457(7230), pp.718–21.

Lu, Z., Jenkyns, H.C. and Rickaby, R.E. (2010) Iodine to calcium ratios in marine carbonate as a paleo-redox proxy during oceanic anoxic events. *Geology*, Vol. 38, No. 12, pp. 1107-1110.

Lu, Z., Hoogakker, B.A.A., Hillenbrand, C.-D., Zhou, X., Thomas, E., Gutchess, K.M., Lu, W., Jones, L. and Rickaby, R.E.M. (2016) Oxygen depletion recorded in upper waters of the glacial Southern Ocean. *Nature communications*, Vol. 7, pp. 11146.

Lumsden, D.N., and Chimahusky, J.S. (1980) Relationship between dolomite nonstoichiometry and carbonate facies parameters. *SEPM special publication*, No. 28, pp. 123-137.

Luo, H-L., Wu, X.-C., and Ouyang, L. (1991) Facies changes and transverse correlation of the Sinian-Cambrian boundary strata in eastern Yunnan. *Sedimentary Facies and Palaeogeography*, Vol. 4, p. 27 - 35 (in Chinese with English abstract)

Lyons, T.W. and Severmann, S. (2006) A critical look at iron paleoredox proxies: New insights from modern euxinic marine basins. *Geochimica et Cosmochimica Acta*, Vol. 70, Issue 23, pp.5698–5722.

Lyons, T.W., Reinhard, C.T., and Planavsky, N. J. (2014) The rise of oxygen in Earth's early ocean and atmosphere. *Nature*, Vol. 506, pp. 307-315.

Macdonald, F.A., Jones, D.S., and Schrag, D.P. (2009) Stratigraphic and tectonic implications of a newly discovered glacial diamictite–cap carbonate couplet in southwestern Mongolia. *Geology*, Vol. 37, No. 2, pp.123-126.

Macdonald, F.A., Schmitz, M.D., Crowley, J.L., Roots, C.F., Jones, D.S., Maloof, A.C., Strauss, J.V., Cohen, P.A., Johnston, D.T. and Schrag, D.P. (2010) Calibrating the cryogenian. *Science*, Vol. 327, No. 5970, pp. 1241-1243.

Macdonald, F.A., Strauss, J.V., Sperling, E.A., Halverson, G.P., Narbonne, G.M., Johnston, D.T., Kunzmann, M., Schrag, D.P. and Higgins, J.A. (2013) The stratigraphic relationship between the Shuram carbon isotope excursion, the oxygenation of Neoproterozoic oceans, and the first

appearance of the Ediacara biota and bilaterian trace fossils in northwestern Canada. *Chemical Geology*, Vol. 362, pp.250–272.

Macdonald, F.A., Pruss, S.B., and Strauss, J.V. (2014) Trace fossils with spreiten from the late Ediacaran Nama Group, Namibia: complex feeding patterns five million years before the Precambrian – Cambrian boundary, *Journal of Paleontology*, Vol. 88, No. 2, pp. 299 – 308.

Machel, H.G. (2004) Concepts and models of dolomitization: a critical reappraisal. *Geological Society, London, Special Publications*, Vol. 235, pp. 7-63.

Mackenzie, F.T., and Morse, J.W. (1992) Sedimentary carbonates through Phanerozoic time. *Geochimica et Cosmochimica Acta*, Vol. 56, pp. 3281-3295.

MacNaughton, R.B., Narbonne, G.M., and Dalrymple, R.W. (2000) Neoproterozoic slope deposits, Mackenzie Mountains, northwestern Canada: implications for passive-margin development and Ediacaran faunal ecology, *Canadian Journal of Sciences*, Vol. 37(7), pp. 997-1020.

Magaritz, M. (1989) ^{13}C minima follow extinction events: A clue to faunal radiation. *Geology*, Vol. 14, pp. 337-340.

Magaritz, M., Holser, W.T., and Kirschvink, J.L. (1986) Carbon-isotope events across the Precambrian/Cambrian boundary on the Siberian Platform. *Nature*, Vol. 320, pp. 258-259.

Magaritz, M., Kirschvink, J.L., Latham, A.J., Zhuravlev, A.Y. and Rozanov, A.Y. (1991) Precambrian/Cambrian boundary problem: Carbon isotope correlations for Vendian and Tommotian time between Siberia and Morocco. *Geology*, Vol. 19, pp. 847-850.

Maloof, A.C., Schrag, D.P., Crowley, J.L. and Bowring, S.A. (2005) An expanded record of early Cambrian carbon cycling from the Anti-Atlas Margin, Morocco. *Canadian Journal of Earth Sciences*, Vol. 42, pp. 2195-2216.

Maloof, A.C., Ramezani, J., Bowring, S.A., Fike, D.A., Porter, S.M. and Mazouad, M. (2010a) Constraints on early Cambrian carbon cycling from the duration of the Nemakit-Daldynian - Tommotian boundary $\delta^{13}C$ shift, Morocco. *Geology*, Vol. 38, No. 7, pp. 623-626.

Maloof, A.C., Porter, S.M., Moore, J.L., Dudas, F.O., Bowring, S.A., Higgins, J.A., Fike, D.A. and Eddy, M.P. (2010b) The earliest Cambrian record of animals and ocean geochemical change. *GSA Bulletin*, Vol. 122, No. 11/12, pp. 1731-1774.

Mángano, M.G. and Buatois, L.A.(2017) The Cambrian revolutions: trace-fossil record, timing, links and geobiological impact. *Earth-Science Reviews*, Vol. 173, pp. 96-108.

Mansuy, C., and Vidal, G. (1983) Late Proterozoic Brioverian microfossils from France: taxonomic affinity and implications of plankton productivity, *Nature*, Vol. 302, pp. 606 – 607.

Martin, M.W., Grazhdankin, D.V., Bowring, S.A., Evans, D.A.D., Fedonkin, M.A. and Kirschvink, J.L. (2000) Age of Neoproterozoic bilatarian body and trace fossils, White Sea, Russia: implications for metazoan evolution. *Science*, Vol. 288, Issue 5467, pp.841–845.

März, C., Poulton, S.W., Beckmann, B., Küster, K., Wagner, T., and Kasten, S. (2008) Redox sensitivity of P cycling during marine black shale formation: Dynamics of sulfidic and anoxic, non-sulfidic bottom waters, *Geochimica et Cosmochimica Acta*, Vol. 72, pp. 3703-3717.

Mason, R.A., and Mariano, A.N. (1990) Cathodoluminescence activation in manganese-bearing and rare earth-bearing synthetic calcites. *Chemical Geology*, Vol. 88, pp. 191-206.

Mattinson, J.M. (2005) Zircon U-Pb chemical abrasion ("CA-TIMS") method: Combined annealing and multi-step partial dissolution analysis for improved precision and accuracy of zircon ages. *Chemical Geology*, Vol. 220, pp. 47-66.

Mattinson, J.M. (2010) Analysis of the relative decay constants of ^{235}U and ^{238}U by multi-step CA-TIMS measurements of closed-system natural zircon samples. *Chemical Geology*, Vol. 275, pp. 186-198.

Mazzullo, S.J. (2000) Organogenic dolomitization in peritidal to deep-sea sediments. *Journal of Sedimentary Research*, Vol. 70, No. 1, pp. 10-23.

McArthur, J.M. and Walsh, J.N. (1984) Rare-earth geochemistry of phosphorites. *Chemical Geology*, Vol. 47, pp.191–220.

McFadden, K.A., Huang, J., Chu, X., Jiang, G., Kaufman, A.J., Zhou, C., Yuan, X. and Xiao, S. (2008) Pulsed oxidation and biological evolution in the Ediacaran Doushantuo Formation. *Proceedings of the National Academy of Sciences of the United States of America*, Vol. 105, no. 9, pp.3197–3202.

McIlroy, D. and Logan, G.A. (1999) The impact of bioturbation on infaunal ecology and evolution during the Proterozoic-Cambrian transition. *Palaios*, Vol. 14, No. 1, pp. 58-72.

McIlroy, D. and Brasier, M.D. (2017) Ichnological evidence for the Cambrian explosion in the Ediacaran to Cambrian succession of Tanafjord, Finnmark, northern Norway. *Geological Society, London, Special Publications*, Vol. 448, no. 1, pp. 351-368.

McKenzie, J.A., Hsu, K.J., and Schneider, J.F. (1980) Movement of subsurface waters under the sabkha, Abu Dhabi, UAE, and its relation to evaporative dolomite genesis. *SEPM Special Publications*, No. 28, pp. 11-30.

McLean, N.M., Condon, D.J., Schoene, B. and Bowring, S.A. (2015) Evaluating uncertainties in the calibration of isotopic reference materials and multi-element isotopic tracers (EARTHTIME Tracer Calibration Part II). *Geochimica et Coosmochimica Acta*, Vol. 164, pp. 481-501.

McLennan, S.M. (1993) Weathering and Global Denudation, *The Journal of Geology*, Vol. 101, No. 2, 100th Anniversary Symposium: Evolution of the Earth's Surface (Mar., 1993), pp. 295 – 303.

Meert, J.G., Gibsher, A.S., Levashova, N.M., Grice, W.C., Kamenov, G.D. and Ryabinin, A.B., (2011) Glaciation and ~770 Ma Ediacara (?) fossils from the lesser Karatau microcontinent, Kazakhstan. *Gondwana Research*, Vol. 19, no. 4, pp. 867-880.

Mehra, A. and Maloof, A. (2018) Multiscale approach reveals that *Cloudina* aggregates are detritus and not in situ reef constructions. *Proceedings of the National Academy of Sciences*, pp. 201719911.

Meng, F., Ni, P., Schiffbauer, J.D., Yuan, X., Zhou, C., Wang, Y. and Xia, M. (2011) Ediacaran seawater temperature: Evidence from inclusions of Sinian halite. *Precambrian Research*, Vol. 184, Issues 1-4, pp.63–69.

Menon, L.R., McIlroy, D., and Brasier, M.D. (2016) '*Intrites*' from the Ediacaran Longmyndian Supergroup, UK: a new form of microbially-induced sedimentary structure (MISS). *Geological Society, London, Special Publications*, Vol. 448, pp. 271 – 283.

Meyer, M., Schiffbauer, J.D., Xiao, S., Cai, Y. and Hua, H. (2012) Taphonomy of the upper Ediacaran enigmatic ribbonlike fossil *Shaanxilithes*. *Palaios*, Vol. 27, No. 5, pp. 354-372.

Meyer, K.M., Ridgwell, A. and Payne, J.L. (2016) The influence of the biological pump on ocean chemistry: Implications for long-term trends in marine redox chemistry, the global carbon cycle, and marine animal ecosystems. *Geobiology*, Vol. 14, pp.207–219.

Meyer, M., Xiao, S., Gill, B.C., Schiffbauer, J.D., Chen, Z., Zhou, C., and Yuan, X. (2014a) Interactions beween Ediacaran animals and microbial mats: Insights from *Lamonte trevallis*, a new trace fossil from the Dengying Formation of South China. *Palaeogeography, Palaeoclimatology, Palaeoecology*, Vol 396, pp. 62-74.

Meyer, M., Elliott, D., Wood, A.D., Polys, N.F., Colbert, M., Maisano, J.A., Vickers-Rich, P., Hall, M., Hoffman, K.H., Schneider, G., and Xiao, S. (2014b) Three – dimensional microCT analysis of the Ediacara fossil Pteridinium simplex sheds new light on its ecology and phylogenetic affinity, *Precambrian Research*, Vol. 249, pp. 79 – 87.

Meysman, F.J., Middelburg, J.J. and Heip, C.H. (2006) Bioturbation: a fresh look at Darwin's last idea. *Trends in Ecology &Evolution*, Vol. 21, No. 12, pp. 688-695.

Michiels, C.C., Darchambeau, F., Roland, F.A., Morana, C., Llirós, M., García-Armisen, T., Thamdrup, B., Borges, A.V., Canfield, D.E., Servais, P. and Descy, J.P. (2017) Iron-dependent nitrogen cycling in a ferruginous lake and the nutrient status of Proterozoic oceans. *Nature Geoscience*, Vol. 10, No. 3, pp. 217-221.

Miller, A.J., Strauss, J.V., Halverson, G.P., Macdonald, F.A., Johnston, D.T. and Sperling, E.A., (2017) Tracking the onset of Phanerozoic-style redox-sensitive trace metal enrichments: new results from basal Ediacaran post-glacial strata in NW Canada. *Chemical Geology*, Vol. 457, pp. 24-37.

Mills, D.B., Ward, L.M., Jones, C., Sweeten, B., Forth, M., Treusch, A. and Canfield, D.E. (2014) Oxygen requirements of the earliest animals. *Proceedings of the National Academy of Sciences*, Vol. 111, no. 11, pp.4168–4172.

Mills, D.B., Francis, W.R., Vargas, S., Larsen, M., Elemans, C.P.H., Canfield, D.E., and Worheide, G. (2018) The last common ancestor of animals lacked the HIF pathway and respired in low-oxygen environments, *eLife*, Vol. 7, e31176.

Missarzhevsky, V.V. and Mambetov, A.M. (1981) Stratigraphy and fauna of Cambrian and Precambrian boundary beds of Maly Karatau. *Trudy Akademii Nauka SSSR*, Moscow, Vol. 326.

Missarzhevsky, V.V. (1989) Drevnejshie skeletnye okamenelosti i stratigrafiya pogranichnykh tolshch dokembriya i kembriya. [The oldest skeletal fossils and stratigraphy of the Precambrian–Cambrian boundary beds.]. *Trudy Geologicheskogo Instituta AN SSSR*, Vol. 443, pp. 1-237. [In Russian].

Mitchell, K., Mansoor, S.Z., Mason, P.R., Johnson, T.M. and Van Cappellen, P. (2016) Geological evolution of the marine selenium cycle: Insights from the bulk shale δ82/76Se record and isotope mass balance modeling. *Earth and Planetary Science Letters*, Vol. 441, pp. 178-187.

Möller, P., Schulz, S. and Jacob, K.H. (1980) Formation of fluorite in sedimentary basins. *Chemical Geology*, Vol. 31, pp. 97-117.

Morales, C.E., Hormazábal, S.E. and Blanco, J. (1999) Interannual variability in the mesoscale distribution of the depth of the upper boundary of the oxygen minimum layer off northern Chile (18–24S): Implications for the pelagic system and biogeochemical cycling. *Journal of Marine Research*, Vol. 57, No. 6, pp. 909-932.

Morrow, D.W. and Abercrombie, H.J. (1994) Rates of dolomitization: the influence of dissolved sulphate. *Spec. Publs Int. Ass. Sediment*, Vol. 21, pp. 377-386.

Mostler, H., and Mosleh-Yazdi, A. (1976) Neue Poriferen aus oberkambrischen Gesteinen der Milaformation in Elburzgebirge (Iran). *Geologische und Paläontologische Mitteilungen Innsbruck*, Vol. 5, pp. 1-36. [In German]

Muller, D.W., McKenzie, J.A., Mueller, P.A. (1990) Abu Dhabi sabkha, Persian Gulf, revisited: Application of strontium isotopes to test an early dolomitization model. *Geology*, Vol. 18, pp. 618-621.

Murphy, A.E., Sageman, B.B., Hollander, D.J., Lyons, T.W., and Brett, C.E. (2000) Black shale deposition and faunal overturn in the Devonian Appalachian basin: Clastic starvation, seasonal water – column mixing, and efficient biolimiting nutrient recycling, *Paleoceanography*, Vol. 15, No. 3, pp. 280 – 291.

Muscente, A.D., Boag, T.H., Bykova, N. and Schiffbauer, J.D. (2017) Environmental disturbance, resource availability, and biologic turnover at the dawn of animal life. *Earth-Science Reviews*, Vol. 48, pp. 164 – 188.

Myrow, P.M. and Hiscott, R.N. (1991) Shallow-water gravity-flow deposits, Chapel Island Formation, southeast Newfoundland, Canada. *Sedimentology*, Vol. 38, pp. 935-959.

Myrow, P.M. and Hiscott, R.N. (1993) Depositional history and sequence stratigraphy of the Precambrian-Cambrian boundary stratotype section, Chapel Island Formation, southeast Newfoundland. *Palaeogeography, Palaeoclimatology, Palaeoecology*, Vol. 104, pp. 13-35.

Nagovitsin, K.E., Rogov, V.I., Marusin, V.V., Karlova, G.A., Kolesnikov, A.V., Bykova, N.V. and Grazhdankin, D.V. (2015) Revised Neoproterozoic and Terreneuvian stratigraphy of the Lena-Anabar Basin and north-western slope of the Olenek Uplift, Siberian Platform. *Precambrian Research*, Vol. 270, pp. 226-245.

Naimark, E. B.; Ivantsov, A. Yu. (2009). Growth variability in the late Vendian problematics *Parvancorina Glaessner*. *Paleontological Journal*, Vol. 43, No. 1, pp. 12–18.

Narbonne, G.M., Myrow, P.M., Landing, E. and Anderson, M.M. (1987) A candidate stratotype for the Precambrian–Cambrian boundary, Fortune head, Burin Peninsula, southeastern Newfoundland. *Canadian Journal of Earth Sciences*, Vol. 24, No. 7, pp. 1277-1293.

Narbonne, G.M., Saylor, B.Z. and Grotzinger, J.P. (1997) The youngest Ediacaran fossils from southern Africa. *Journal of paleontology*, 71(6), pp.953–967.

Narbonne, G.M., and Gehling J.G. (2003) Life after snowball: the oldest complex Ediacaran fossils. *Geology*, Vol. 31, pp. 27-30.

Narbonne, G.M. (2005) The Ediacara Biota: Neoproterozoic Origin of Animals and Their Ecosystems, *Annu. Rev. Earth Planet Sci.*, vol. 3, pp. 421-442.

Narbonne, G.M., Laflamme, M., Greentree, C., and Trusler, P. (2009) Reconstructing a Lost World: Ediacaran Rangeomorphs from Spaniard's Bay, Newfoundland, *Journal of Paleontology*, Vol. 83, Issue 4, pp. 503 – 523.

Narbonne, G.M., Laflamme, M., Trusler, P.W., Dalrymple, R.W. and Greentree, C. (2014) Deep-Water Ediacaran Fossils from Northwestern Canada: Taphonomy, Ecology, and Evolution. *Journal of Paleontology*, 88, Issue 2, pp.207–223.

Nesbitt, H.W., and Young, G.M. (1982) Early Proterozoic climates and plate motions inferred from major element chemistry of lutites, *Nature*, Vol. 299, pp. 715 – 717.

Nesbitt, H.W., Young, G.M. (1984) Prediction of some weathering trends of plutonic and volcanic rocks based on thermodynamic and kinetic considerations. *Geochimica et Cosmochimica Acta*, Vol. 48, pp. 1523–1534.

Nesbitt, H.W., Young, G.M., McLennan, S.M. and Keays, R.R. (1996) Effects of chemical weathering and sorting on the petrogenesis of siliciclastic sediments, with implications for provenance studies. *The Journal of Geology*, Vol. 104, No. 5, pp. 525 – 542.

Neubert, N., Nagler, T.F. and Bottcher, M.E. (2008) Sulfidity controls molybdenum isotope fractionation into euxinic sediments: Evidence from the modern Black Sea. *Geology*, Vol. 36, no. 10, pp.775–778.

Noble, S.R., Condon, D.J., Carney, J.N., Wilby, P.R., Pharaoh, T.C. and Ford, T.D. (2015) U-Pb geochronology and global contet of the Charnian Supergroup, UK: Constraints on the age of key Ediacaran fossil assemblages. *GSA Bulletin*, Vol. 127, no. 1/2, pp. 250 - 265.

Noffke, N., Knoll, A.H., and Grotzinger, J.P. (2002) Sedimentary Controls on the Formation and Preservation of Microbial Mats in Siliciclastic Deposits: A Case Study from the Upper Neoproterozoic Nama Group, Namibia. *Palaios*, Vol. 17, no. 6, pp. 533-544.

Nothdurft, L.D., Webb, G.E. and Kamber, B.S. (2004) Rare earth element geochemistry of Late Devonian reefal carbonates, Canning Basin, Western Australia: confirmation of a seawater REE proxy in ancient limestones. *Geochimica et Cosmochimica Acta*, Vol. 68, pp. 263-283.

Novozhilova, N.V. (2013) *Spinitheca* gen. nov. – A New Orthothecimorph Hyolith Genus from the Lower Cambrian of the Siberian Platform, *Paleontological Journal*, Vol. 47, No. 2, pp. 136-138.

Nursall, J.R. (1959) Oxygen as a prerequisite to the origin of the Metazoa. Nature, Vol. 183, No. 4669, pp. 1170-1172

Och, L.M. and Shields-Zhou, G.A. (2012) The Neoproterozoic oxygenation event: Environmental perturbations and biogeochemical cycling. *Earth-Science Reviews*, Vol. 110, Issues 1-4, pp.26–57.

Och, L.M., Shields-Zhou, G.A., Poulton, S.W., Manning, C., Thirlwall, M.F., Li, D., Chen, X., Ling, H., Osborn, T. and Cremonese, L. (2013) Redox changes in Early Cambrian black shales at Xiaotan section, Yunnan Province, South China. *Precambrian Research*, Vol. 225, pp.166–189.

Och, L.M., Cremonese, L., Shields-Zhou, G.A., Poulton, S.W., Struck, U., Ling, H., Li, D., Chen , X., Manning, C., Thirlwall, M., Strauss, H. and Zhu, M. (2015) Palaeoceanographic controls on spatial redox distribution over the Yangtze Platform during the Ediacaran-Cambrian transition. *Sedimentology*, Vol. 63, Issue 2, pp. 378-410.

Okada, Y., Sawaki, Y., Komiya, T., Hirata, T., Takahata, N., Sano, Y., Han, J. and Maruyama, S. (2014) New chronological constraints for Cryogenian to Cambrian rocks in the Three Gorges, Weng'an and Chengjiang areas, South China. *Gondwana Research*, Vol. 25, Issue 3, pp.1027–1044.

Osburn, M.R., Owens, J., Bergmann, K.D., Lyons, T.W. and Grotzinger, J.P. (2015) Dynamic changes in sulfate sulfur isotopes preceding the Ediacaran Shuram Excursion. *Geochimica et Cosmochimica Acta*, Vol. 170, pp.204–224.

Palmer, T.I.M. (1982) Cambrian to Cretaceous changes in hardground communities. *Lethaia*, Vol. 15, no. 4, pp. 309-323.

Parry, L.A., Boggiani, P.C., Condon, D.J., Garwood, R.J., Leme, J.deM., McIlroy, D., Brasier, M.D., Trindade, R., Campanha, G.A.C., Pacheco, M.L.A.D., Diniz, C.Q.C., and Liu, A.G. (2017) Ichnological evidence for meiofaunal bilaterians from the terminal Ediacaran and earliest Cambrian of Brazil. *Nature Ecology and Evolution*.

Paulmier, A. and Ruiz-Pino, D. (2009) Oxygen minimum zones (OMZs) in the modern ocean. *Progress in Oceanography*, Vol. 80, Issues 3-4, pp.113–128.

Paytan, A., Kastner, M., Campbell, D. and Thiemens, M.H. (2004) Seawater sulfur isotope fluctuations in the Cretaceous. *Science*, Vol. 304, pp. 1663-1665.

Pecoits, E. (2010) Ediacaran iron formations and carbonates of Uruguay: palaeoceanographic, palaeoclimatic and palaeobiologic implications. Unpublished PhD thesis, University of Alberta, p. 190-192

Pecoits, E., Konhauser, K.O., Aubet, N.R., Heaman, L.M., Veroslavsky, G., Stern, R.A., and Gingras, M.K. (2012) Bilaterian Burrows and Grazing Behavior at >585 Million Years Ago, *Science*, Vol. 336, Issue 6089, pp. 1693-1696.

Pecoits, E., Konhauser, K.O., Aubet, N.R., Heaman, L.M., Veroslavsky, G., Stern, R.A., and Gingras, M.K. (2013) Response to Comment on "Bilaterian Burrows and Grazing Behaviour at > 585 Million Years Ago", *Science*, Vol. 339, Issue 6122, pp. 906.

Pecoits, E., Aubet, N.R., Heaman, L.M., Philippot, P., Rosière, C.A., Veroslavsky, G. and Konhauser, K.O. (2016) U-Pb detrital zircon ages from some Neoproterozoic successions of Uruguay:

Provenance, stratigraphy and tectonic evolution. *Journal of South American Earth Sciences*, Vol. 71, pp. 108-130.

Pegel, T.V. (2000) Evolution of trilobite biofacies in Cambrian basins of the Siberian Platform. *Journal of Paleontology*, Vol. 74, No. 6, pp. 1000-1019.

Pelechaty, S.M. (1998) Integrated chronostratigraphy of the Vendian System of Siberia: implications for a global stratigraphy. *Journal of the Geological Society*, Vol. 155, no. 6, pp. 957-973.

Peng, S., Babcock, L.E., and Cooper, R.A. (2012) The Cambrian Period. In The Geological Timescale 2012 (eds: Gradstein, F.M., Ogg, J.G., Schmitz, M.D., and Ogg, G.M.). Elsevier, Boston, pp. 437 – 488.

Penny, A.M. Wood, R.A., Curtis, A., Bowyer, F.T., Tostevin, R. and Hoffman, K.-H. (2014) Ediacaran metazoan reefs from the Nama Group, Namibia. *Science*, Vol. 344, Issue 6191, pp.1504-1506.

Penny, A.M., Wood, R.A., Zhuravlev, A.Y., Curtis, A., Bowyer, F., and Tostevin, R. (2017) Intraspecific variation in an Ediacaran skeletal metazoan: *Namacalathus* from the Nama Group, Namibia, *Geobiology*, Vol. 15, Issue 1, pp. 81-93.

Peters, S.E., and Gaines, R. R. (2012) Formation of the 'Great Unconformity' as a trigger for the Cambrian explosion. *Nature*, Vol. 484, pp. 363-366.

Petsch, S.T. (2003) The Global Oxygen Cycle. In *Treatise on Geochemistry*, Vol. 8, pp. 515-555. Editor: Schlesinger, W.H., Executive Editors: Holland, H.D. and Turekian, K.K. pp. 682. ISBN 0-08-043751-6, Elsevier, 2003.

Pflug, H. D. (1966) Neue Fossilreste aus den NamaSchichten in Südwest-Afrika. *Paläontologische Zeitschrift*, Vol. 40, pp. 14-25.

Pflüg, H.D. (1970) Zur fauna der Nama–Schichten in Südwest–Afrika; I. *Pteridinia*, bau und systematische zugehörigkeit. *Palaeontographica Abteilung A*, Vol. 134, pp. 226–262.

Pickford, M.H.L. (1995) Review of the Riphean, Vendian and early Cambrian palaeontology of the Otavi and Nama Groups, Namibia. *Communs geol. Surv. Namibia*, Vol. 10, pp. 57-81.

Planavsky, N.J., McGoldrick, P., Scott, C.T., Li, C., Reinhard, C.T., Kelly, A.E., Chu, X., Bekker, A., Love, G.D. and Lyons, T.W. (2011) Widespread iron-rich conditions in the mid-Proterozoic ocean. *Nature*, Vol. 477, pp. 448.

Planavsky, N.J., Reinhard, C.T., Wang, X., Thomson, D., McGoldrick, P., Rainbird, R.H., Johnson, T., Fischer, W.W. and Lyons, T.W. (2014) Low Mid-Proterozoic atmospheric oxygen levels and the delayed rise of animals. *Science*, Vol. 346, pp.635-638.

Pogge von Strandmann, P.A., Stüeken, E.E., Elliott, T., Poulton, S.W., Dehler, C.M., Canfield, D.E. and Catling, D.C. (2015) Selenium isotope evidence for progressive oxidation of the Neoproterozoic biosphere. *Nature communications*, Vol. 6, pp. 10157.

Porter, S.M. (2004) Halkieriids in Middle Cambrian phosphatic limestones from Australia. *Journal of Paleontology*, Vol. 78, No. 3, pp. 574-590.

Porter, S.M. (2016) Tiny vampires in ancient seas: evidence for predation via perforation in fossils from the 780-740 million-year-old Chuar Group, Grand Canyon, USA. *Proceedings of the Royal Society B,* Vol. 283, No. 1831.

Poulton, S.W. (2017) Biogeochemistry: Early phosphorus redigested. *Nature Geoscience*, Vol. 10, No. 2, pp. 75.

Poulton, S.W. and Canfield, D.E. (2005) Development of a sequential extraction procedure for iron: implications for iron partitioning in continentally derived particulates. *Chemical Geology*, Vol. 214, Issues 3-4, pp.209–221.

Poulton, S.W. and Canfield, D.E. (2011) Ferruginous Conditions: A Dominant Feature of the Ocean through Earth's History. *Elements,* Vol. 7, pp. 107-112.

Poulton, S.W. and Raiswell, R. (2002) The low-temperature geochemical cycle of iron: from continental fluxes to marine sediment deposition. *American Journal of Science*, Vol. 302, No. 9, pp. 774-805.

Poulton, S.W., Fralick, P.W., and Canfield, D.E. (2004) The transition to a sulphidic ocean ~1.84 billion years ago, *Nature*, Vol. 431, pp. 173-177.

Poulton, S.W., Fralick, P.W., and Canfield, D.E. (2010) Spatial variability in oceanic redox structure 1.8 billion years ago, *Nature Geoscience*, Vol. 3, pp. 486-490.

Pourret, O. and Houben, D. (2018) Characterization of metal binding sites onto biochar using rare earth elements as a fingerprint. *Heliyon*, Vol. 4, Issue 2, p.e00543.

Pu, J., Bowring, S.A., Ramezani, J., Myrow, P., Raub, T.D., Landing, E., Mills, A., Hodgin, E., and Macdonald, F.A. (2016) Dodging snowballs: Geochronology of the Gaskiers glaciation and the first appearance of the Ediacaran biota, *Geology*, Vol. 44, no. 11, pp.955-958.

Pyatiletov, V.G. (1988) Late Precambrian microfossils of the Uchur-Maya Region. *In:* Khomentovsky, V.V., and Shenfil', V.Yu., eds., Late Precambrian and Early Palaeozoic of Siberia, Riphean and Vendian, Collection of Scientific Papers: Institute of Geology and Geophysics, Siberian Branch, USSR Academy of Sciences, Novosibirsk, pp. 47–104 [in Russian].

Qian, Y., and Bengtson, S. (1989) Palaeontology and biostratigraphy of the Early Cambrian Meishucunian Stage in Yunnan, South China, Fossils and Strata, Vol. 24, pp. 156

Qian, Y., Zhu, M., He, T.-G., and Jiang, Z.-W. (1996) New investigation of Precambrian-Cambrian boundary sections in eastern Yunnan, *Acta Micropalaeontologica Sinica*, Vol. 13, No. 3, pp. 225 - 240 (In Chinese with English abstract).

Raiswell, R., Anderson, T.F. (2005) Reactive iron enrichment in sediments deposited beneath euxinic bottom waters: constraints on supply by shelf recycling. In: McDonald, I., Boyce, A.J., Butler, I.B., Herrington, R.J., Polya, D.A. (Eds.), *Mineral Deposits and Earth Evolution*, *Geological Society Special Publication* Vol. 248, pp. 179–194.

Raiswell, R. and Canfield, D.E. (1998) Sources of iron for pyrite formation in marine sediments. *American Journal of Science*, vol. 298, no. 3, pp. 219-245.

Raiswell, R., Newton, R., Bottrell, S.H., Coburn, P.M., Briggs, D.E.G., Bond, D.P.G. and Poulton, S.W. (2008) Turbidite depositional influences on the diagenesis of Beecher's Trilobite Bed and the Hunsrück Slate; sites of soft tissue pyritization. *American Journal of Science*, Vol. 308, pp.105–129.

Raiswell, R., Hardisty, D.S., Lyons, T.W., Canfield, D.E., Owens, J.D., Planavsky, N.J., Poulton, S.W. and Reinhard, C.T. (2018) The iron paleoredox proxies: A guide to the pitfalls, problems and proper practice. *American Journal of Science*. in press.

Ramezani, J., Pu, J., Tsukui, K., Zhu, M., Macdonald, F.A., and Bowring, S.A. (2017) New insights into the Ediacaran-Cambrian transition from high-precision U-Pb geochronology. *In: International Symposium on the Ediacaran-Cambrian Transition*. At Memorial University, St. Johns, Newfoundland. June 2017

Reinhard C.T., Planavsky N.J., Olson S.L., Lyons T.W. and Erwin D.H. (2016) Earth's oxygen cycle and the evolution of animal life, *Proceedings of the National Academy of Sciences of the United States of America*. Vol. 113, no. 32, pp. 8933-8938.

Reinhard, C.T., Planavsky, N.J., Gill, B.C., Ozaki, K., Robbins, L.J., Lyons, T.W., Fischer, W.W., Wang, C., Cole, D.B. and Konhauser, K.O. (2017) Evolution of the global phosphorus cycle. *Nature*, Vol. 541, No. 7637, pp. 386.

Richter, R. (1932) Arthropoda (Trilobitae). N*eues Jahrbuch für Geologie und Paläontologie*, Referate 111, Heft 1, 138-156, 181-188.

Roberts, J.A., Bennet, P.C., Gonzalez, L.A., Macpherson, G.L., and Milliken, K.L. (2004) Microbial precipitation of dolomite in methanogenic groundwater. *Geology*, Vool. 32, No. 4, pp. 277-280.

Roberts, J.A., Kenward, P.A., Fowle, D.A., Goldstein, R.H., Gonzalez, L.A., and Moore, D.S. (2013) Surface chemistry allows for abiotic precipitation of dolomite at low temperature. *Proceedings of the National Academy of Sciences*, Vol. 110, No. 36, pp. 14540-14545.

Rodriguez-Blanco, J.D., Shaw, S., and Benning, L.G. (2015) A route for the direct crystallization of dolomite. *American Mineralogist*, Vol. 100, pp. 1172-1181.

Rogov, V., Marusin, V., Bykova, N., Goy, Y., Nagovitsin, K., Kochnev, B., Karlova, G. and Grazhdankin, D. (2012) The oldest evidence of bioturbation on Earth. *Geology*, Vol. 40, no. 5, pp. 395-398.

Rooney, A.D., Strauss, J.V., Brandon, A.D. and Macdonald, F.A. (2015) A Cryogenian chronology: Two long-lasting synchronous neoproterozoic glaciations. *Geology*, Vol. 43, no. 5, pp.459–462.

Ross, G.M., Bloch, J.D. and Krouse, H.R. (1995) Neoproterozoic strata of the southern Canadian Cordillera and the isotopic evolution of seawater sulfate. *Precambrian Research*, Vol. 73, Issues 1-4, pp.71–99.

Rowland, S.M., Luchinina, V.A., Korovnikov, I.V., Sipin, D.P., Tarletskov, A.I., and Fedoseev, A.V. (1998) Biostratigraphy of the Vendian-Cambrian Sukharikha River section, northwestern Siberian Platform. *Canadian Journal of Earth Sciences*, Vol. 35, pp. 339-352.

Rozanov, A.Y. and Zhuravlev, A.Y. (1992) The Lower Cambrian Fossil Record of the Soviet Union. *In:* Lipps. J.H. and Signor, P.W. (eds) Origin and Early Evolution of the Metazoa. Topics in Geobiology, Vol. 10. Springer, Boston, Ma. ISBN 978-1-4899-2429-2.

Rothman, D.H., Hayes, J.M. and Summons, R.E. (2003) Dynamics of the Neoproterozoic carbon cycle. *Proceedings of the National Academy of Sciences*, Vol. 100, no. 14, pp. 8124-8129.

Rothman, D.H. and Forney, D.C. (2007) Physical model for the decay and preservation of marine organic carbon. *Science*, Vol. 316, No. 5829, pp. 1325-1328.

Rozanov, A.Yu., Missarževskij, V.V., Volkova, N.A., Voronova, L.G., Krylov, I.N., Keller, B.M., Korolûk, I.K., Lendzion, K., Michniak, R., Pykhova, N.G., and Sidorov, A.D. (1969) The Tommotian Stage and the Cambrian lower boundary problem [in Russian]. *GeologiČeskij Institut, Akademiâ Nauk SSSR*, Trudy 206: pp. 1–380.

Rozanov, A.Y., and Zhuravlev, A.Y. (1992) The Lower Cambrian fossil record of the Soviet Union. *In: Origin and evolution of the Metazoa*. Edited by J.H. Lipps and P.W. Signor. *Plenum Press, New York*, pp. 205 – 282.

Rudge, J.F., Reynolds, B.C. and Bourdon, B. (2009) The double spike toolbox. *Chemical Geology*, Vol. 265, pp. 420-431.

Rudnick, R.L., Gao, S. (2003) Composition of the Continental Crust. *In: Treatise on Geochemistry*, Vol. 3, pp. 1-66. Edited by R.L. Rudnick, Ex Eds: H.D.Holland, and K.K. Turekian. ISBN 0-08-043751-6. Elsevier, 2003.

Runnegar, B. (1991) Precambrian oxygen levels estimated from the biochemistry and physiology of early eukaryotes. *Global and Planetary Change*, 5, pp.97–111.

Sahoo, S.K., Planavsky, N.J., Kendall, B., Wang, X., Shi, X., Scott, C., Anbar, A.D., Lyons, T.W. and Jiang, G. (2012) Ocean oxygenation in the wake of the Marinoan glaciation. *Nature*, Vol. 489, pp.546–549.

Sahoo, S.K., Planavsky, N.J., Jiang, G., Kendall, B., Owens, J.D., Wang, X., Shi, X., Anbar, A.D. and Lyons, T.W. (2016) Oceanic oxygenation events in the anoxic Ediacaran ocean. *Geobiology*. Vol. 14, Issue 5, pp. 457-468.

Saltzman, M.R., Runnegar, B. and Lohmann, K.C. (1998) Carbon isotope stratigraphy of Upper Cambrian (Steptoean Stage) sequences of the eastern Great Basin: Record of a global oceanographic event. *Geological Society of America Bulletin*, Vol. 110, 3, pp. 285-297.

Saltzman, M.R., Ripperdan, R.L., Brasier, M.D., Lohmann, K.C., Robison, R.A., Chang, W.T., Peng, S., Ergaliev, E.K. and Runnegar, B. (2000) A global carbon isotope excursion (SPICE) during the Late Cambrian: relation to trilobite extinctions, organic-matter burial and sea level. *Palaeogeography, Palaeoclimatology, Palaeoecology*, Vol. 162, 3-4, pp. 211-223.

Sandberg, P.A. (1984) Recognition criteria for calcitized skeletal and non-skeletal aragonites. *Palaeontographica Americana*, Vol. 54, pp. 272-281.

Sánchez-Román, M., McKenzie, J.A, Wagener, A.d.L.R., Rivadeneyra, M.A., and Vasconcelos, C. (2009) Presence of sulphate does not inhibit low-temperature dolomite precipitation. *Earth and Planetary Science Letters*, Vol. 285, pp. 131-139.

Sappenfield, A., Droser, M., Kennedy, M. and McKenzie, R. (2012) The oldest Zoophycos and implications for Early Cambrian deposit feeding. *Geological Magazine*, Vol. 149, pp.1118–1123.

Saylor, B.Z. (1996) Sequence stratigraphic and chemostratigraphic constraints on the evolution of the terminal Proterozoic to Cambrian Nama Basin, Namibia. *Unpublished PhD thesis*, Massachusetts Institute of Technology, September 1996.

Saylor, B.Z. (2003) Sequence stratigraphy and carbonate-siliciclastic mixing in a terminal Proterozoic foreland basin, Urusis Formation, Nama Group, Namibia. *Journal of Sedimentary Research*, Vol. 73, no. 2, pp.264–279.

Saylor, B.Z. and Grotzinger, J.P. (1996) Reconstruction of important Proterozoic-Cambrian boundary exposures through the recognition of thrust deformation in the Nama Group of southern Namibia. *Communications of the Geological Survey of Namibia*, Vol. 11, pp. 1-12.

Saylor, B.Z., Grotzinger, J.P. and Germs, G.J.B. (1995) Sequence stratigraphy and sedimentology of the Neoproterozoic Kuibis and Schwarzrand Subgroups (Nama Group), southwestern Namibia. *Precambrian Research*, Vol. 73, pp.153–171.

Saylor, B.Z., Kaufman, A.J., Grotzinger, J.P. and Urban, F. (1998) A composite reference section for terminal proterozoic strata of southern Namibia. *Journal of sedimentary research. Section B.* Vol. 68, no. 6, pp. 1223-1235.

Schoepfer, S.D., Shen, J., Wei, H., Tyson, R.V., Ingall, E., and Algeo, T.J. (2015) Total organic carbon, organic phosphorus, and biogenic barium fluxes as proxies for paleomarine productivity. *Earth-Science Reviews*, Vol. 149, pp. 23-52.

Schiffbauer, J.D., Xiao, S., Sharma, K.S., and Wang, G. (2012) The origin of intracellular structures in Ediacaran metazoan embryos. *Geology*, Vol. 40, No. 3, pp. 223-226.

Schmitz, M.D. (2012) Radiogenic isotope geochronology. *In* The Geologic Time Scale 2012 (*eds* Gradstein, F.M., Ogg, J.G., Schmitz, M.D., Ogg, G.M.). Elsevier, Boston, pp. 115–126

Scholz, F., Severmann, S., McManus, J. and Hensen, C. (2014) Beyond the Black Sea paradigm: The sedimentary fingerprint of an open-marine iron shuttle. *Geochimica et Cosmochimica Acta*, Vol. 127, pp.368–380.

Schrag, D.P., Higgins, J.A., Macdonald, F.A. and Johnston, D.T. (2013) Authigenic carbonate and the history of the global carbon cycle. *Science,* Vol. 339, Issue 6119, pp.540–3.

Schroder, S. and Grotzinger, J.P. (2007) Evidence for anoxia at the Ediacaran-Cambrian boundary: the record of redox-sensitive trace elements and rare earth elements in Oman. *Journal of the Geological Society*, Vol. 164, pp.175–187.

Schwarz, E. and Arnott, R.W.C. (2007) Anatomy and Evolution of a Slope Channel-Complex Set (Neoproterozoic Isaac Formation, Windermere Supergroup, Southern Canadian Cordillera):

Implications for Reservoir Characterization. *Journal of Sedimentary Research*, Vol.77, no. 2, pp.89–109.

Schwertmann, U. (1966) Inhibitory effect of soil organic matter on the crystallization of amorphous ferric hydroxide. *Nature*, Vol. 212, No. 5062, pp.645.

Scott, C., Lyons, T.W., Bekker, A., Shen, Y., Poulton, S.W., Chu, X. and Anbar, A.D. (2008) Tracing the stepwise oxygenation of the Proterozoic ocean. *Nature*, Vol. 452, pp.456–459.

Scott, C. and Lyons, T.W. (2012) Contrasting molybdenum cycling and isotopic properties in euxinic versus non-euxinic sediments and sedimentary rocks: Refining the paleoproxies. *Chemical Geology*, Volumes 324-325, pp.19–27.

Semikhatov, M.A., Obchinnikova, G.V., Gorokhov, I.M., Kuznetsov, A.B., Kaurova, O.K. and Petrov, P.Y. (2003) Pb-Pb Isochron Age and Sr-Isotopic Signature of the Upper Yudoma Carbonate Sediments (Vendian of the Yudoma-Maya Trough, Eastern Siberia). *Doklady Earth Sciences*, Vol. 393, No. 8, pp. 1093-1097.

Serezhnikova, E.A. (2007) *Palaeophragmodictya spinosa* sp. nov., a Bilateral Benthic Organism from the Vendian of the Southeastern White Sea Region. *Paleontological Journal*, Vol. 41, No. 4, pp. 360 – 369.

Severmann, S., Lyons, T.W., Anbar, A.D., McManus, J. and Gordon, G. (2008) Modern iron isotope perspective on the benthic iron shuttle and the redox evolution of ancient oceans. *Geology*, Vol. 36, no. 6 , pp.487–490.

Shen, B., Xiao, S., Zhou, C., and Yuan X. (2009) *Yangtziramulus zhangi* new genus and species, a carbonate-hosted macrofossil from the Ediacaran Dengying Formation in the Yangtze Gorges area, South China. *Journal of Paleontology*, Vol. 83, no. 4, pp. 575-587.

Shen, B., Xiao, S., Zhou, C., Kaufman, A.J. and Yuan, X. (2010) Carbon and sulfur isotope chemostratigraphy of the Neoproterozoic Quanji Group of the Chaidam Basin, NW China: Basin stratification in the aftermath of an Ediacaran glaciation postdating the Shuram event? *Precambrian Research*, Vol. 177, pp. 241–252.

Shen, B., Xiao, S., Bao, H., Kaufman, A.J., Zhou, C. and Yuan, X. (2011) Carbon, sulfur, and oxygen isotope evidence for a strong depth gradient and oceanic oxidation after the Ediacaran Hankalchough glaciation. *Geochimica et Cosmochimica Acta*, Vol. 75, pp. 1357-1373.

Shen, B., Xiao, S., Zhou, C., Dong, L., Chang, J., and Chen, Z. (2017) A new modular palaeopasichnid fossil *Curviacus ediacaranus* new genus and species from the Ediacaran Dengying Formation in the Yangtze Gorges area of South China. *Geological Magazine*, Vol. 154, Issue 6, pp. 1257-1268.

Shen, J., Algeo, T.J., Zhou, L., Feng, Q., Yu, J. and Ellwood, B. (2012) Volcanic perturbations of the marine environment in South China preceding the latest Permian mass extinction and their biotic effects. *Geobiology*, Vol. 10, No. 1, pp. 82-103.

Shen, J., Schoepfer, S.D., Feng, Q., Zhou, L., Yu, J., Song, H., Wei, H. and Algeo, T.J. (2015) Marine productivity changes during the end-Permian crisis and Early Triassic recovery. *Earth-Science Reviews*, Vol. 149, pp. 136-162.

Shen, Y., Zhang, T. and Hoffman, P.F. (2008) On the coevolution of Ediacaran oceans and animals. Proceedings of the National Academy of Sciences of the United States of America, Vol. 105, no. 21, pp.7376–81.

Shi, W., Li, C. and Algeo, T.J. (2017) Quantitative model evaluation of organic carbon oxidation hypotheses for the Ediacaran Shuram carbon isotopic excursion. *Science China Earth Sciences*, Vol. 60, No. 12, pp. 2118-2127.

Shi, W., Li, C., Luo, G., Huang, J., Algeo, T.J., Jin, C., Zhang, Z. and Cheng, M. (2017) Sulfur isotope evidence for transient marine-shelf oxidation during the Ediacaran Shuram Excursion. *Geology*, Vol. 46, no. 3, pp. 267 - 270.

Shields, G.A. (2005) Neoproterozoic cap carbonates: a critical appraisal of existing models and the plumeworld hypothesis. *Terra Nova*, Vol. 17, No. 4, pp. 299-310.

Shields, G., Kimura, H., Yang, J. and Gammon, P. (2004) Sulphur isotopic evolution of Neoproterozoic-Cambrian seawater: New francolite-bound sulphate δ34S data and a critical appraisal of the existing record. *Chemical Geology*, Vol. 204, pp.163–182.

Shields-Zhou GA, Porter S, Halverson GP (2016) A new rock-based definition for the Cryogenian Period (circa 720–635 Ma). *Episodes*, 39, 3-8.

Shu, D.-G., Conway Morris, S., Han, J., Li, Y., Zhang, X.-L., Hua, H., Zhang, Z.-F., Liu, J.-N., Guo, J.-F., Yao, Y., and Yasui, K. (2006) Lower Cambrian Vendobionts from China and Early Diploblast Evolution. *Science*, Vol. 312, pp. 731-734.

Sibley, D.F., and Gregg, J.M. (1987) Classification of dolomite rock textures. *Journal of Sedimentary Research*, Vol. 57, pp. 967–975.

Sibley, D.F., Dedoes, R.E., and Bartlett, T.R. (1987) Kinetics of Dolomitization. *Geology*, Vol. 15, pp. 1112-1114.

Sibley, D.F., Nordeng, S.H., and Borkowski, M.L. (1994) Dolomitization kinetics in hydrothermal bombs and natural settings. *Journal of Sedimentary Research*, Vol. A64, No. 3, pp. 630-637.

Siebert, C., Nagler, T.F., von Blankenburg, F. and Kramers, J.D. (2003) Molybdenum isotope records as a potential new proxy for paleoceanography. *Earth and Planetary Science Letters*, Vol. 211, Issues 1-2, pp.159–171.

Skovsted, C.B., and Peel, J.S. (2011) *Hyolithellus* in Life Position from the Lower Cambrian of North Greenland. *Journal of Paleontology*, Vol. 85, no. 1, pp. 37-47.

Smith, E.F., Macdonald, F.A., Petach, T.A., Bold, U. and Schrag, D.P. (2016) Integrated stratigraphic, geochemical, and paleontological late Ediacaran to early Cambrian records from southwestern Mongolia. *Bulletin*, Vol. 128, No. 3-4, pp.442-468.

Smith, E.F., Nelson, L.L., Tweedt, S.M., Zeng, H., and Workman, J.B. (2017) A cosmopolitan late Ediacaran biotic assemblage: new fossils from Nevada and Namibia support a global biostratigraphic link. *Proceedings of the Royal Society, B*, Vol. 284, no. 1858, pp. 20170934.

Smith, O.A. (1998) Terminal Proterozoic Carbonate Platform Development: Stratigraphy and Sedimentology of the Kuibis Subgroup (ca. 550 – 548 Ma), Northern Nama Basin, Namibia. *Unpublished Masters Thesis*, Massachusetts Institute of Technology.

Sokolov, B.S., and Fedonkin, M.A. (1984) The Vendian as the terminal system of the Precambrian. *Episodes*, Vol. 7, No. 1, pp. 12-19

Sour-tovar, F., Hagadorn, J.W. and Huitron-Rubio, T. (2007) Ediacaran and Cambrian index fossils from Sonora, Mexico. *Palaeontology*, Vol. 50, Issue 1, pp.169–175.

Spangenberg, J.E., Bagnoud-Velásquez, M., Boggiani, P.C., and Gaucher, C. (2014) Redox variations and bioproductivity in the Ediacaran: Evidence from inorganic and organic geochemistry of the Corumbá Group, Brazil. *Gondwana Research*, Vol. 26, pp. 1186-1207.

Spence, G. H., Le Heron, D. P., and Fairchild, I. J. (2016) Sedimentological perspectives on climatic, atmospheric and environmental change in the Neoproterozoic Era. *Sedimentology*, Vol. 63, pp. 253-306.

Sperling, E.A., Peterson, K.J. and Laflamme, M. (2011) Rangeomorphs, Thectardis (Porifera?) and dissolved organic carbon in the Ediacaran oceans. *Geobiology*, 9, pp.24–33.

Sperling, E.A., Halverson, G.P., Knoll, A.H., Macdonald, F.A. and Johnston, D.T. (2013a) A basin redox transect at the dawn of animal life. *Earth and Planetary Science Letters*, Volumes 371-372, pp.143–155.

Sperling, E.A., Frieder, C.A., Raman, A.V., Girguis, P.R., Levin, L.A. and Knoll, A.H. (2013b) Oxygen, ecology, and the Cambrian radiation of animals. *Proceedings of the National Academy of Sciences of the United States of America*, Vol. 110, no. 33, pp.13446–51.

Sperling, E. a., Wolock, C.J., Morgan, A.S., Gill, B.C., Kunzmann, M., Halverson, G.P., Macdonald, F.A., Knoll, A.H. and Johnston, D.T. (2015a) Statistical analysis of iron geochemical data suggests limited late Proterozoic oxygenation. *Nature*, Vol. 523, pp.451–454.

Sperling, E.A., Carbone, C., Carbone, C., Strauss, J.V., Johnston, D.T., Narbonne, G.M. and Macdonald, F.A. (2015b) Oxygen, facies, and secular controls on the appearance of Cryogenian and Ediacaran body and trace fossils in the Mackenzie Mountains of northwestern Canada. *Bulletin of the Geological Society of America*, Vol. 128, no. 3-4, pp.558–575.

Sperling, E.A., Knoll, A.H. and Girguis, P.R. (2015c) The Ecological Physiology of Earth's Second Oxygen Revolution. *Annual Review of Ecology, Evolution, and Systematics*,Vol. 46, pp. 215-235.

Sprigg, R. C. (1947) Early Cambrian (?) jellyfishes from the Flinders Ranges, South Australia. *Philos.Trans.R. Soc. S. Aust*. Vol. 71, pp. 212–224.

Steiner, M., Li, G., Qian, Y., Zhu, M. and Erdtmann, B.D. (2007) Neoproterozoic to early Cambrian small shelly fossil assemblages and a revised biostratigraphic correlation of the Yangtze Platform (China). *Palaeogeography, Palaeoclimatology, Palaeoecology*, Vol. 254, No. 1-2, pp. 67-99.

Stirling, C.H., Andersen, M.B., Warthmann, R. and Halliday, A.N. (2015) Isotope fractionation of 238U and 235U during biologically-mediated uranium reduction. *Geochimica et Cosmochimica Acta*, Vol. 163, pp.200–218.

Stolper, D.A. and Keller, C.B. (2018) A record of deep ocean dissolved O_2 from the oxidation state of iron in submarine basalts. *Nature*, Vol. 553, pp. 323.

Stüeken, E.E., Buick, R., Bekker, A., Catling, D., Foriel, J., Guy, B.M., Kah, L.C., Machel, H.G., Montañez, I.P. and Poulton, S.W. (2015) The evolution of the global selenium cycle: secular trends in Se isotopes and abundances. *Geochimica et Cosmochimica Acta*, Vol. 162, pp. 109-125.

Sumoondur, A., Shaw, S., Ahmed, I. and Benning, L.G. (2008) Green rust as a precursor for magnetite: an in situ synchrotron based study. *Mineralogical Magazine*, Vol. 72, No. 1, pp. 201-204.

Sun, W. (1986) Late Precambrian pennatulids (Sea Pens) from the eastern Yangtze Gorge, China: *Paracharnia* Gen. Nov., *Precambrian Research*, Vol. 31, pp. 361-375.

Swart, P.K. and Kennedy, M.J. (2012) Does the global stratigraphic reproducibility of δ13C in neoproterozoic carbonates require a marine origin? A Pliocene- Pleistocene comparison. *Geology*, Vol. 40, no. 1, pp.87–90.

Tahata, M., Ueno, Y., Ishikawa, T., Sawaki, Y., Murakami, K., Han, J., Shu, D., Li, Y., Guo, J., Yoshida, N. and Komiya, T. (2013) Carbon and oxygen isotope chemostratigraphies of the Yangtze platform, South China: decoding temperature and environmental changes through the Ediacaran. *Gondwana Research*, Vol. 23, no. 1, pp. 333-353.

Tang, F., Yin, C., Bengtson, S., Liu, P., Wang, Z., and Gao, L. (2008) Octoradiate Spiral Organisms in the Ediacaran of South China. *Acta Geologica Sinica*, Vol. 82, No. 1, pp. 27 – 34.

Tang, D., Shi, X., Ma, J., Jiang, G., Zhou, X. and Shi, Q. (2017) Formation of shallow-water glaucony in weakly oxygenated Precambrian ocean: an example from the Mesoproterozoic Tieling Formation in North China. *Precambrian Research*

Tarhan, L.G., Hughes, N.C., Myrow, P.M., Bhargava, O.N., Ahluwalia, A.D. and Kudryavtsev, A.B. (2014) Precambrian–Cambrian boundary interval occurrence and form of the enigmatic tubular body fossil *Shaanxilithes ningqiangensis* from the Lesser Himalaya of India. *Palaeontology*, Vol. 57, No. 2, pp. 283-298.

Tarhan, L.G. Droser, M.L., Gehling, J.G. and Dzaugis, M.P. (2017) Microbial mat sandwiches and other anacualistic sedimentary features of the Ediacara Member (Rawnsley Quartzite, South Australia): Implications for interpretation of the Ediacaran sedimentary record. *Palaios*, Vol. 32, pp. 181 - 194.

Tarhan, L.G. (2018) The early Paleozoic development of bioturbation—Evolutionary and geobiological consequences. *Earth-Science Reviews.*

Taylor, S.R. and McLennan, S.M. (1985) The Continental Crust: Its Composition and Evolution. Blackwell, Oxford, 312 pp.

Taylor, W.L., Almond, J.D., Jensen, S., Högström, A., Gresse, P., Harrison, B., Agic, H., Høyberget, M., Ebbestad, J.O.R., Meinhold, G. and Palacios, T. (2017) Possible trilobozoans with internal structures from the Late Ediacaran Nama Group, Northern Cape, South Africa. *In International Symposium on the Ediacaran-Cambrian Transition*, At Memorial University, St. Johns, Newfoundland. Memorial University, St. Johns. June 2017

Teal, C.S., Mazzullo, S.J., and Bischoff, W.D. (2000) Dolomitization of Holocene shallow-marine deposits mediated by sulphate reduction and methanogenesis in normal-salinity seawater, northern Belize. *Journal of Sedimentary Research*, Vol. 70, No. 3, pp. 649-663.

Tomczak, M. and Godfrey, J.S., (2001) *Regional oceanography: an introduction*. Elsevier.

Torrent, J. and Cabedo, A. (1986) Sources of iron oxides in reddish brown soil profiles from calcarenites in southern Spain. *Geoderma*, Vol. 37, No. 1, pp. 57-66.

Tosca, N.J., Johnston, D.T., Mushegian, A., Rothman, D.H., Summons, R.E. and Knoll, A.H. (2010) Clay mineralogy, organic carbon burial, and redox evolution in Proterozoic oceans. *Geochimica et Cosmochimica Acta*, Vol. 74, No. 5, pp. 1579 – 1592.

Tostevin, R. (2015) Developing proxies to constrain redox gradients in terminal Ediacaran oceans (Doctoral dissertation, UCL (University College London)).

Tostevin, R., Shields, G.A., Tarbuck, T.M., He, T., Clarkson, M.O., and Wood, R.A. (2016a) Effective use of cerium anomalies as a redox proxy in carbonate-dominated marine settings. *Chemical Geology*, Vol. 438, pp. 146-162.

Tostevin, R., Wood, R.A., Shields, G.A., Poulton, S.W., Guilbaud, R., Bowyer, F., Penny, A.M., He, T., Curtis, A., Hoffmann, K.-H., and Clarkson, M.O. (2016b) Low-oxygen waters limited habitable space for early animals. *Nature communications*, 7, 12818.

Tostevin, R., He, T., Turchyn, A.V., Wood, R.A., Penny, A.M., Bowyer, F., Antler, G. and Shields, G.A. (2017) Constraints on the late Ediacaran sulfur cycle from carbonate associated sulfate. *Precambrian Research*, Vol. 290, pp. 113-125.

Tribovillard, N., Algeo, T.J., Lyons, T.W. and Riboulleau, A. (2006) Trace metals as paleoredox and paleoproductivity proxies: An update. *Chemical Geology*, Vol. 232, Issues 1-2, pp.12–32.

Tucker, M. E. (1982) Precambrian dolomites: Petrographic and isotopic evidence that they differ from Phanerozoic dolomites. *Geology*, Vol. 10, pp. 7-12.

Tucker, M.E. (1986) Carbon isotope excursions in Precambrian/Cambrian boundary beds, Morocco. *Nature*, Vol. 319, pp. 48-50.

Turekian, K.K., and Wedepohl, K.H. (1961) Distribution of the elements in some major units of the Earth's crust, *Geological Society of America Bulletin*, Vol. 72, pp. 175 – 192.

Turchyn, A.V. and DePaolo, D.J. (2011) Calcium isotope evidence for suppression of carbonate dissolution in carbonate-bearing organic-rich sediments. *Geochimica et Cosmochimica Acta*, Vol. 75, No. 22, pp. 7081-7098.

Tyrrell, T. (1999) The relative influences of nitrogen and phosphorus on oceanic primary production. *Nature*, Vol. 400, No. 6744, pp. 525.

Tyson, R.V. (2005) The "productivity versus preservation" controversy; cause, flaws, and resolution. In: Harris, N.B. (Ed.), Deposition of Organic-carbon-rich Sediments: Models, Mechanisms, and Consequences. *Society for Sedimentary Geology (SEPMSSG) Special Publication*, Vol. 82, pp. 17–33.

Van Beek, P., François, R., Conte, M., Reyss, J.L., Souhaut, M. and Charette, M. (2007) $^{228}Ra/^{226}Ra$ and $^{226}Ra/Ba$ ratios to track barite formation and transport in the water column. *Geochimica et cosmochimica acta*, Vol. 71, No. 1, pp. 71-86.

Van Iten, H., Leme, J., Marques, A.C. and Simoes, M.G. (2013) Alternative interpretations of some earliest Ediacaran fossils from China. *Acta Palaeontologica Polonica*, Vol. 58(1), pp.111–113.

van Os, B.J., Middelburg, J.J. and de Lange, G.J. (1991) Possible diagenetic mobilization of barium in sapropelic sediment from the eastern Mediterranean. *Marine Geology*, Vol. 100(1-4), pp. 125-136.

Vannier, J., García-Bellido, D., Hu, S.-X., Chen, A.-L., (2009). Arthropod visual predators in the early pelagic ecosystem: evidence from the Burgess Shale and Chengjiang biotas. *Proc. R. Soc. Lond. B Biol. Sci.* Vol. 276, pp. 2567–2574.

Vaquer-Sunyer, R. and Duarte, C.M. (2010) Sulfide exposure accelerates hypoxia-driven mortality. *Limnology and Oceanography*, Vol. 55, Issue 3, pp.1075–1082.

Vasconcelos, C., McKenzie, J.A., Bernasconi, S., Grujic, D., and Tiens, A.J. (1995) Microbial mediation as a possible mechanism for natural dolomite formation at low temperature. *Nature*, Vol. 377, pp. 220-222.

Vernhet, E. and Reijmer, J.J.G. (2010) Sedimentary evolution of the Ediacaran Yangtze platform shelf (Hubei and Hunan provinces, Central China). *Sedimentary Geology*, Vol. 225. Issues 3-4, pp.99–115.

Vickers-Rich, P., Ivantsov, A.Y., Trusler, P.W., Narbonne, G.M., Hall, M., Wilson, S.A., Greentree, C., Fedonkin, M.A., Elliott, D.A., Hoffmann, K.-H., and Schneider, G.I.C. (2013) Reconstructing *Rangea*: New Discoveries from the Ediacaran of Southern Namibia. *Journal of Paleontology*, Vol. 87, no. 1, pp. 1-15.

Vologdin, A.G, Maslov, A.B. (1960) On a new group of fossil organisms from the lower Yudoma Formation of the Siberian Platform. *Doklady Akad. nauk SSSR*, Vol. 134, pp. 691–693. [In Russian.]

von der Borch, C.C. (1976) Stratigraphy and formation of Holocene dolomitic carbonate deposits of the Coorong area, South Australia. *Journal of Sedimentary Petrology*, Vol. 46, No. 4, pp. 952-966.

Vorob'eva, N.G., Sergeev, V.N. and Knoll, A.H. (2009) Neoproterozoic microfossils from the margin of the East European Platform and the search for a biostratigraphic model of lower Ediacaran rocks. *Precambrian Research*, Vol. 173, Issues 1-4, pp.163–169.

Wade, M. (1972) Hydrozoa and Scyphozoa and other Medusoids from the Precambrian Eiacara Fauna, South Australia. *Palaeontology*, Vol. 15, pp. 197-229.

Waggoner, B. (2003) The ediacaran biotas in space and time. *Integrative and comparative biology*, 43, pp.104–113.

Walcott, C.D. (1920) Cambrian geology and paleontology IV:6—Middle Cambrian Spongiae, *Smithsonian Miscellaneous Collections*, Vol. 67, pp. 261–364

Wallace, M.W., vS Hood, A., Woon, E.M., Giddings, J.A. and Fromhold, T.A. (2015) The Cryogenian Balcanoona reef complexes of the Northern Flinders Ranges: implications for Neoproterozoic ocean chemistry. *Palaeogeography, Palaeoclimatology, Palaeoecology*, Vol. 417, pp. 320-336.

Wallace, M.W., Shuster, A., Greig, A., Planavsky, N.J. and Reed, C.P. (2017) Oxygenation history of the Neoproterozoic to early Phanerozoic and the rise of land plants. *Earth and Planetary Science Letters*, Vol. 466, pp. 12-19.

Wan, B., Yuan, X., Chen, Z., Guan, C., Pang, K., Tang, Q. and Xiao, S. (2016) Systematic description of putative animal fossils from the early Ediacaran Lantian Formation of South China. *Palaeontology*, Vol. 59, Issue 4, pp.1–18.

Wang, J., Chen, D., Yan, D., Wei, H. and Xiang, L. (2012) Evolution from an anoxic to oxic deep ocean during the Ediacaran–Cambrian transition and implications for bioradiation. *Chemical Geology*, Volumes 306-307, pp.129–138.

Wang, X., Jiang, G., Shi, X. and Xiao, S. (2016) Paired carbonate and organic carbon isotope variations of the Ediacaran Doushantuo Formation from an upper slope section at Siduping, South China. *Precambrian Research*, Vol. 273, pp.53–66.

Warren, L.V., Pacheco, M.L.A.F., Fairchild, T.R., Simoes, M.G., Riccomini, C., Boggiani, P.C., and Caceres, A.A. (2012) The dawn of animal skeletogenesis: Ultrastructural analysis of the Ediacaran metazoan *Corumbella werneri*. *Geology*, Vol. 40, pp. 691-694.s.2015.12.010

Warren, L.V., Quaglio, F., Riccomini, C., Simoes, M.G., Poiré, D.G., Strikis, N.M., Anelli, L.E., and Strikis, P.C. (2014) The puzzle assembled: Ediacaran guide fossil *Cloudina* reveals an od proto-Gondwana seaway. *Geology*, vol. 42, no. 5, pp. 391-394.

Warthmann, R., Lith, Y.v., Vasconcelos, C., McKenzie, J.A., and Karpoff, M.A. (2000) Bacterially induced dolomite precipitation in anoxic culture experiments. *Geology*, Vol. 28, no. 12, pp. 1091-1094.

Watters, W.A. (2000) Digital Reconstructions of Fossil Morphologies, Nama Group, Namibia. Submitted to the Department of Earth, Atmospheric, and Planetary Science in partial fulfilment of the requirements for the degree of Master of Science in Earth & Planetary Science at the Massachusetts Institute of Technology. January, 2000.

Weber, B., Steiner, M., and Zhu, M.-Y. (2007) Precambrian-Cambrian trace fossils from the Yangtze Platform (South China) and the early evolution of bilaterian lifestyles. *Palaeogeography, Palaeoclimatology, Palaeoecology*, Vol. 254, pp. 328-349.

Whittaker, S.G., James, N.P., and Kyser, T.K. (1994) Geochemistry of synsedimentary cements in Early Cambrian reefs. *Geochimica et Cosmochimica Acta*, Vol. 58, No. 24, pp. 5567-5577.

Wilby, P.R., Carney, J.N. and Howe, M.P.A. (2011) A rich ediacaran assemblage from eastern avalonia: Evidence of early widespread diversity in the deep ocean. *Geology*, Vol. 39, no. 7, pp.655–658.

Wille, M., Nagler, T.F., Lehmann, B., Schroder, S. and Kramers, J.D. (2008) Hydrogen sulphide release to surface waters at the Precambrian/Cambrian boundary. *Nature*, Vol. 453, pp.767–769.

Wilson, J.P., Grotzinger, J.P., Fischer, W.W., Hand, K.P., Jensen, S., Knoll, A.H., Abelson, J., Metz, J.M., McLoughlin, N., Cohen, P.A. and Tice, M.M. (2012) Deep-Water Incised Valley Deposits At the Ediacaran-Cambrian Boundary in Southern Namibia Contain Abundant Treptichnus Pedum. *Palaios*, Vol. 27, pp.252–273.

Wood, R.A. (2011) Paleoecology of the earliest skeletal metazoan communities: Implications for early biomineralization. *Earth-Science Reviews*, Vol. 106, Issues 1-2, pp.184–190.

Wood, R.A. and Curtis, A. (2015) Extensive metazoan reefs from the Ediacaran Nama Group, Namibia: The rise of benthic suspension feeding. *Geobiology*, Vol. 13, Issue 2, pp.112–122.

Wood, R.A. and Erwin, D.H. (2017) Innovation not recovery: dynamic redox promotes metazoan radiations. *Biological Reviews*, Vol. 93, pp. 863 - 873.

Wood, R.A. and Penny, A. (2018) Substrate growth dynamics and biomineralisation of an Ediacaran encrusting poriferan. *Proc. R. Soc. B*, Vol. 285, 20171938

Wood, R.A, Grotzinger, J.P. and Dickson, J.A.D. (2002) Proterozoic modular biomineralized metazoan from the Nama Group, Namibia. *Science*, Vol. 296, Issue 5577, pp.2383–6.

Wood, R.A., Poulton, S.W., Prave, A.R., Hoffmann, K.-H., Clarkson, M.O., Guilbaud, R., Lyne, J.W., Tostevin, R., Bowyer, F., Penny, A.M., Curtis, A. and Kasemann, S.A. (2015) Dynamic redox conditions control late Ediacaran metazoan ecosystems in the Nama Group, Namibia. *Precambrian Research*, Vol. 261, pp.252–271.

Wood, R.A., Zhuravlev, A.Y., Sukhov, S.S., Zhu, M., and Zhao, F. (2017a) Demise of Ediacaran dolomitic seas marks widespread biomineralization on the Siberian Platform. *Geology*, Vol. 45, pp. 27-30.

Wood, R.A., Curtis, A., Penny, A., Zhuravlev, A.Y., Curtis-Walcott, S., Iipinge, S., and Bowyer, F. (2017b) Flexible and responsive growth strategy of the Ediacaran skeletal *Cloudina* from the Nama Group, Namibia. *Geology*, Vol. 45, No. 3, pp. 259-262.

Wood, R.A., Ivantsov, A.Y., and Zhuravlev, A.Y. (2017c) First macrobiota biomineralization was environmentally triggered. *Proc. R. Soc. B*, Vol. 284, 20170059.

Wood, R.A., Liu, A.G., Bowyer, F., Wilby, P.R., Dunn, F.S., Kenchington, C.G., Hoyal Cuthill, J.F., Mitchell, E.G., and Penny, A.M. (in prep) The rise of early metazoan ecosystems: challenging the 'Cambrian Explosion', *Nature Ecology and Evolution.*

Wu N., Farquhar J., and Fike D.A. (2015) Ediacaran sulfur cycle: Insights from sulfur isotope measurements (Δ33S and δ34S) on paired sulfate–pyrite in the Huqf Supergroup of Oman. *Geochimica et Cosmochimica Acta*, Vol. 164, pp. 352-364.

Xiang, L., Schoepfer, S.D., Shen, S.-z., Cao, C.-q. and Zhang, H. (2017) Evolution of oceanic molybdenum and uranium reservoir size around the Ediacaran–Cambrian transition: Evidence from western Zhejiang, South China. *Earth and Planetary Science Letters*, Vol. 464, pp. 84-94.

Xiang, L., Schoepfer, S.D., Zhang, H., Cao, C.-q. and Shen, S.-z. (in press) Evolution of primary producers and productivity across the Ediacaran-Cambrian transition. *Precambrian Research*. Available at: https://doi.org/10.1016/j.precamres.2018.05.023.

Xiao, S. and Kaufman, A.J. eds. (2006) Neoproterozoic geobiology and paleobiology, Vol. 27. Berlin: Springer.

Xiao, S., Zhang, Y., and Knoll, A.H. (1998) Three-dimensional preservation of algae and animal embryos in a Neoproterozoic phosphorite, *Nature*, Vol. 391, pp. 553-558.

Xiao, S. and Laflamme, M. (2009) On the eve of animal radiation: phylogeny, ecology and evolution of the Ediacara Biota. *Trends in Ecology and Evolution*, Vol. 24, No. 1, pp. 31 – 40.

Xiao, S., Yuan, X., Steiner, M., and Knoll, A. (2002) Macroscopic carbonaceous compressions in a terminal Proterozoic shale: A systematic reassessment of the Miaohe biota, South China. *Journal of Paleontology*, Vol 76, Issue 2, pp. 347-376.

Xiao, S., Shen, B., Zhou, C., Xie, G., and Yuan, X. (2005) A uniquely preserved Ediacaran fossil with direct evidence for a quilted bodyplan. *Proceedings of the National Academy of Sciences of the United States of America*, Vol. 102, no. 29, pp. 10227-10232.

Xiao, S., Mcfadden K.A., Peek S., Kaufman A.J., Zhou C., Jiang G., Hu J. (2012) Integrated chemostratigraphy of the Doushantuo Formation at the northern Xiaofenghe section (Yangtze Gorges, South China) and its implication for Ediacaran stratigraphic correlation and ocean redox models. *Precambrian Research*, Volumes 192–195, pp. 125–141.

Xiao, S., Zhou, C., Liu, P., Wang, D., and Yuan, X. (2014) Phosphatized acanthomorphic acritarchs and related microfossils from the Ediacaran Doushantuo formation at Weng'an (South China) and their implications for biostratigraphic correlation, *Journal of Paleontology*, Vol. 88, Issue 1, pp. 1-67.

Xiao, S., Narbonne, G.M., Zhou, C., Laflamme, M., Grazhdankin, D.V., Moczydlowska-Vidal, M. and Cui, H. (2016) Towards an Ediacaran Time Scale: Problems, Protocols, and Prospects. *Episodes*, Vol. 39, no. 4.

Xiao, S., Bykova, N., Kovalick, A. and Gill, B.C. (2017) Stable carbon isotopes of sedimentary kerogens and carbonaceous macrofossils from the Ediacaran Miaohe Member in South China: Implications for stratigraphic correlation and sources of sedimentary organic carbon. *Precambrian Research*, Vol. 302, pp. 171-179.

Xing, Y.-S., Ding, Q.-X., Luo, H.-L., He, T.-G., Wang, Y.-G. (1984) The Sinian–Cambrian boundary of China. *Bulletin of the Institute of Geology of the Chinese Academy, Special Issue*, Vol. 10, pp. 182–183 (in Chinese with English Abstr.).

Xu, L., Lehmann, B., Jingwen, M., Wenjun, Q., and Andao, D. (2011) Re-Os age of polymetallic Ni-Mo-PGE-Au mineralization in early Cambrian black shales of South China- A reassessment. *Economic Geology*, Vol. 106, pp. 511-522.

Yang, A., Zhu, M., Zhang, J. and Li, G. (2003) Early Cambrian eodiscoid trilobites of the Yangtze Platform and their stratigraphic implications. *Progress in Natural Science*, Vol. 13, no. 11, pp. 861-866.

Yang, C., Li, X.-H., Zhu, M. and Condon, D.J. (2016) SIMS U-Pb zircon geochronological constraints on upper Ediacaran stratigraphic correlations, South China. *Geological Magazine*, Vol. 154, No. 6, pp. 1202-1216.

Yang, C., Zhu, M., Condon, D.J. and Li, X.H. (2017) Geochronological constraints on stratigraphic correlation and oceanic oxygenation in Ediacaran-Cambrian transition in South China. *Journal of Asian Earth Sciences*, Vol. 140, pp. 75-81.

Yang, C., Li, X.-H., Zhu, M., Condon, D.J., and Chen, J. (2018) Geochronological constraint on the Cambrian Chengjiang biota, South China. *Journal of the Geological Society*, pp.jgs2017-103.

Yang, X. and He, T. (1984) New small shelly fossils from Lower Cambrian Meishucun Stage of Nanjiang Area, northern Sichuan. *Professional papers of Stratigraphy and Palaeontology*, Vol. 13, pp. 35-47 [in Chinese].

Yonkee, W.A. Dehler, C.D., Link, P.K., Balgord, E.A., Keeley, J.A., Hayes, D.S., Wells, M.L., Fanning, C.M. and Johnston S.M. (2014) Tectono-stratigraphic framework of Neoproterozoic to Cambrian strata, west-central U.S.: Protracted rifting, glaciation, and evolution of the North American Cordilleran margin. *Earth-Science Reviews*, Vol. 136, pp.59–95.

Young, G.M., and Nesbitt, H.W. (1998) Processes controlling the distribution of Ti and Al in weathering profiles, siliciclastic sediments and sedimentary rocks. *Journal of Sedimentary Research*, Vol. 68, No. 3, pp. 448 – 455.

Yuan, X., Chen, Z., Xiao, S., Zhou, C. and Hua, H. (2011) An early Ediacaran assemblage of macroscopic and morphologically differentiated eukaryotes. *Nature*, 470(7334), pp.390–3.

Yuan, Y., Cai, C., Wang, T., Xiang, L., Jia, L., and Chen, Y. (2014) Redox condition during Ediacaran-Cambrian transition in the Lower Yangtze deep water basin, South China: constraints from iron speciation and $\delta^{13}C_{org}$ in the Diben section, Zhejiang. *Chinese Science Bulletin*, Vol. 59, Issue 28, pp. 3638-3649.

Zakrevskaya, M.A. and Ivantsov, A.Y. (2017) *Dickinsonia costata*: the first evidence of neoteny in Ediacaran organisms. *Invertebrate Zoology*, Vol. 14, pp. 92-98.

Zegeye, A., Bonneville, S., Benning, L.G., Sturm, A., Fowle, D.A., Jones, C., Canfield, D.E., Ruby, C., MacLean, L.C., Nomosatryo, S. and Crowe, S.A. (2012) Green rust formation controls nutrient availability in a ferruginous water column. *Geology*, Vol. 40, No. 7, pp. 599-602.

Zhai, L., Wu, C., Ye, Y., Zhang, S. and Wang, Y. (2017) Fluctuations in chemical weathering on the Yangtze Block during the Ediacaran–Cambrian transition: Implications for paleoclimatic conditions and the marine carbon cycle. *Palaeogeography, Palaeoclimatology, Palaeoecology*. Vol. 490, pp. 280-292.

Zhang, J., Fan, T., Zhang, Y., Lash, G.G., Li, Y. and Wu, Y. (2017) Heterogeneous oceanic redox conditions through the Ediacaran-Cambrian boundary limited the metazoan zonation. *Scientific Reports*, Vol. 7, pp. 8550.

Zhang, L.Y. (1986) A discovery and preliminary study of the late stage of late Gaojiashan biota from Sinian in Ningqiang County, Shaanxi. *Bulletin of the Xi'a Institute of Geology and Mineral Resources, Chinese Academy of Geological Sciences*, Vol. 13, pp. 67–88.

Zhang, P., Hua, H. and Liu, W. (2014) Isotopic and REE evidence for the paleoenvironmental evolution of the late Ediacaran Dengying Section, Ningqiang of Shaanxi Province, China. *Precambrian Research*, Vol. 242, pp. 96-111.

Zhang, S., Li, H., Jiang, G., Evans, D.A.D., Dong, J., Wu, H., Yang, T., Liu, P., and Xiao, Q. (2015) New paleomagnetic results from the Ediacaran Doushantuo Formation in South China and their paleogeographic implications. *Precambrian Research*, Vol. 259, pp. 130-142.

Zhang, S., Wang, X., Wang, H., Bjerrum, C.J., Hammarlund, E.U., Costa, M.M., Connelly, J.N., Zhang, B., Su, J. and Canfield, D.E. (2016) Sufficient oxygen for animal respiration 1,400 million years ago. *Proceedings of the National Academy of Sciences*, p.6pp.

Zhou, C., and Xiao S. (2007) Ediacaran δ13C chemostratigraphy of South China. *Chemical Geology*, Vol. 237, pp. 89–108.

Zhao, X., Wang, X., Shi, X., Tang, D. and Shi, Q. (in press) Stepwise oxygenation of early Cambrian ocean controls early metazoan diversification. *Palaeogeography, Palaeoclimatology, Palaeoecology*. doi:10.1016/j.palaeo.2018.05.009. (in press)

Zhao, Z., Xing, Y., Ding, Q., Liu, G., Zhao, Y., Zhang, S., Meng, X., Yin, C., Ning, B., Han, P., (1988) *The Sinian System of Hubei*. China University of Geosciences Press, Wuhan, pp. 205.

Zhou, C., Jiang S., Xiao S., Chen Z., and Yuan X. (2012) Rare earth elements and carbon isotope geochemistry of the Doushantuo Formation in South China: Implication for middle Ediacaran shallow marine redox conditions. *Chinese Science Bulletin*, Vol. 57, pp. 1998–2006.

Zhou, L., Algeo, T.J., Shen, J., Hu, Z., Gong, H., Xie, S., Huang, J. and Gao, S. (2015) Changes in marine productivity and redox conditions during the Late Ordovician Hirnantian glaciation. *Palaeogeography, Palaeoclimatology, Palaeoecology*, Vol. 420, pp. 223-234.

Zhou, X., Jenkyns, H.C., Lu, W., Hardisty, D.S., Owens, J.D., Lyons, T.W., Lu, Z. (2017) Organically bound iodine as a bottom-water redox proxy: Preliminary validation and application. *Chemical Geology*, Vol. 457, pp.95-106.

Zhu, M. and Li, X.H. (2017) Introduction: from snowball Earth to the Cambrian explosion–evidence from China. *Geological Magazine*, Vol. 154, No. 6, pp. 1187-1192.

Zhu, M., Li, G.-X., Zhang, J.-M., Steiner, M., Qian, Y., and Jiang, Z.-W. (2001) Early Cambrian stratigraphy of east Yunnan, southwestern China: A synthesis. *Acta Palaeontologica Sinica*, Vol. 40 (Supplement), pp. 4 - 39.

Zhu, M., Zhang, J., Yang, A., Li, G., Steiner, M., and Erdtmann, B.D. (2003) Sinian-Cambrian stratigraphic framework for shallow- to deep-water environments of the Yangtze Platform: an integrated approach. *Progress in Natural Science*, Vol. 13, Issue 12, pp. 951-960.

Zhu, M.Y., Zhang, J.M., Li, G.X. and Yang, A.H. (2004) Evolution of C isotopes in the Cambrian of China: implications for Cambrian subdivision and trilobite mass extinctions. *Geobios*, Vol. 37, no. 2, pp. 287-301.

Zhu, M.Y., Babcock, L.E. and Peng, S.C. (2006) Advances in Cambrian stratigraphy and paleontology: integrating correlation techniques, paleobiology, taphonomy and paleoenvironmental reconstruction. *Palaeoworld*, Vol. 15, Issues 3-4, pp. 217-222.

Zhu, M., Zhang, J. and Yang, A. (2007) Integrated Ediacaran (Sinian) chronostratigraphy of South China. *Palaeogeography, Palaeoclimatology, Palaeoecology*, Vol. 254, Issues 1-2, pp.7–61.

Zhu, M., Gehling, J.G., Xiao, S., Zhao, Y., and Droser, M.L. (2008) Eight-armed Ediacara fossil preserved in contrasting tahonomic windows from China and Australia. *Geology*, Vol. 36, No. 11, pp. 867-870.

Zhu, M., Lu, M., Zhang, J., Zhao, F., Li, G., Yand, A., Zhao, X., Zhao, M. (2013) Carbon isotope chemostratigraphy and sedimentary facies evolution of the Ediacaran Doushantuo Formation in western Hubei, South China. *Precambrian Research*, Vol. 225, pp.7–28.

Zhu, M., Zhuravlev, A.Y., Wood, R.A., Zhao, F., and Sukhov, S.S. (2017) A deep root for the Cambrian explosion: Implications of new bio- and chemostratigraphy from the Siberian Platform. *Geology*, Vol. 45, No. 5, pp. 459 – 462.

Zhuravlev, A.Yu., Vintaned, J.A.G., and Ivantsov, A.Y. (2009) First finds of problematic Ediacaran fossil *Gaojiashania* in Siberia and its origin. *Geological Magazine*, Vol. 146, No. 5, pp. 775-780.

Zhuravlev, A.Y., Linan, E., Vintaned, J.A.G., Debrenne, F. and Fedorov, A.B. (2012) New Finds of Skeletal Fossils in the Terminal Neoproterozoic of the Siberian Platform and Spain. *Acta Palaeontologica Polonica*, Vol. 57, pp.205–224.

Zhuravlev, A.Y., Wood, R.A. and Penny, A.M. (2015) Ediacaran skeletal metazoan interpreted as a lophophorate. *Proceedings of the Royal Societs B*, Vol. 282, Issue 1818, pp.1–10.

Ziebis, W., Forster, S., Huettel, M. and Jørgensen, B.B. (1996) Complex burrows of the mud shrimp *Callianassa truncata* and their geochemical impact in the sea bed. *Nature*, Vol. 382, No. 6592, pp. 619.

Appendix A

Figure 1.1 details

a) Redox schematic

Schematic redox representation based on compiled iron speciation data in Canfield et al. (2008), Sperling et al. (2015a) and Bowyer et al. (2017) and inspired by Poulton (2017) in addition to Cryogenian redox data from primary dolomite cements of the Umberatana Group (Australia) in Hood and Wallace (2015) and evidence for localised euxinia during the SPICE event from Gill et al. (2011) Alum shale, Sweden.

Blue: Oxic, Black: Anoxic ferruginous, Orange: Anoxic euxinic. Diagonal striping indicates regional differences in redox state, not uncertainty. Paucity of truly basinal shale makes redox state of the global oceanic deep basin unknown (indicated by white erotemes).

b) $\delta^{13}C_{carb}$ data

C isotope profile largely adapted after Macdonald et al. (2010, 2013) and Bowyer et al. (2017) with Cambrian C isotope curve conforming to curve of Zhu et al. (2006) using available published raw data.

-Late Cambrian C isotopes of the Kyrshabakty River, Kazakhstan from Saltzman et al. (2000).

-Late Cambrian C isotope profile of Green Point Formation (Cambrian-Ordovician GSSP, Cow Head Group, Western Newfoundland) from unpublished data of Ripperdan presented in Azmy et al. (2014).

-C isotope profile compiled from Ravensthroat-Sheepbed-Sheepbed carbonate-June Beds-Gametrail-Blueflower-Risky Formations from Macdonald et al. (2013).

-C isotope profile of upper Cambrian SPICE event at Shingle Pass (Nevada) across Emigrant Springs-Johns Wash-Corset Spring-Whipple Cave Formations from Saltzman et al. (1998).

-Composite C isotope profile of Doushantuo-Qinshudong Formations after data in Zhou et al. (2012) (Doushantuo Fm., Jiulongwan section), Wang et al. (2016) (Doushantuo-Liuchapo Fms., Siduping section), Tahata et al. (2013) (Nantuo-Dengying Fms.Wuhe-Aijiahe drill sites), Ishikawa et al. (2008) (Dengying-Yanjiahe-Shuijingtuo-Shipai Fms., Three Gorges, Wuhe-Aijiahe section drill core), Ishikawa et al. (2014) (Shipai Fm., Three Gorges, Drill core 6, Wuhe-Aijiahe section), Chang et al. (2017) (Dengying-Mufushan-Paotaishan Fms., K2 well nea Kunshan city; Hetang-Dachenling-Yangliugang Fms., WN2 well, SE of Xuancheng city), Zhu et al. (2004) (Huaqiao-Aoxi-Qingshudong Fms., Wangcun section).

-C isotope profile for Rasthof-Gruis-Ombaatjie-Karibib Formations of the Abenab Subgroup, Otavi Group, Namibia from Halverson et al. (2005). The underlying Chuos Formation is a diamictite thought to be of Sturtian age and the base of the Chuos Formation is defined by an erosional unconformity (Hoffmann et al., 2004; Halverson et al., 2005). The C isotope profile for the Abenab Subgroup has been condensed relative to that represented in Macdonald et al. (2010) in order to conform to the potential extent of the Sturtian glacial represented by the upper age of the Wilverpa Formation diamictite (Fanning and Link, 2008).

-C isotope profile for Kuibis and Schwarzrand subgroups of the Nama Group, Namibia is from Kaufman et al. (1991) (Buschmannsklippe-Schwarzrand Subgroups), Smith (1998, unpublished Masters thesis) (Driedoornvlakte reef, Upper Omkyk Member, Zaris Formation, Kuibis Subgroup) and Wood et al. (2015) (Kuibis and Schwarzrand Subgroups).

-C isotope profile of Hadash, Masirah Bay, Kufai, Shuram, and Buah Formations from Fike et al. (2006). C isotope profile for Ara Group from Amthor et al. (2003).

-C isotope profile for Nuccaleena, Bunyeroo, and Wonoka Formations from Calver et al. (2000). Additional C isotope data for Wonoka Formation from Husson et al. (2015). Composite C isotope profile for middle Cambrian including Parachilna-Woodendina-Wilkawillina-Andamooka-Ouldburra-Kulpara Formations across 4 sections from Hall (2012, unpublished PhD thesis).

-C isotope profile of Aim and Ust' Yudoma Formations, Kyra-Ytyga section, Yudoma River from Zhu et al. (2017).

-Composite C isotope profile from Anti-Atlas Mountains, Morocco (Maloof et al., 2005). Adoudou and Lie de Vin Formations of the Taroudant Group and Igoudine, Amouslek and Issafene Formations of the Tata Group. Composite measured sections MS3-12 of Maloof et al. (2005): 3 (Talat N'Yisi), 4 (Tagrara), 6 (Tiout, data from Tucker, 1986 and Magaritz et al., 1991), 7 (Oued Sdas), 8 (Oued N'Oulili), 10 (Adrar Minount), 11 (North Bougzoul) and 12 (South Bougzoul).

-Composite C isotope profile from the Zavkhan terrane, SW Mongolia. Carbon isotopes from the Cryogenian to Ediacaran Tsagaan Oloom Formation from Macdonald et al. (2009). Carbon isotope data from Bayan Gorge and Orolgo Gorge sections (Zuun-Arts to Salaany Gol (/Salaagol) Formations) from Smith et al., 2016.

Cambrian C isotope peaks 1p-7p and II-IV follow Kouchinsky et al. (2007) and Maloof et al. (2010)

c) Major evolutionary milestones

[1]Origin of metazoans from molecular clock dating 850–650 Ma (dos Reis et al., 2015); [2]713 Ma, Maximum age of demosponge biomarkers (24-isopropylcholestane), Huqf Supergoup, Oman (line structure of C skeleton for 24-ipc; Love et al., 2009); [3]Minimum age for marine planktonic algae (Archaeplastida) 659 – 645 Ma inferred from abundant erogstane and stigmastane biomarkers (Brocks et al., 2017); [4]635–590 Ma, Possible stem-group Cnidaria *Lantianella laevis,* preserved in black shale of Lantian member II, Anhui Province, South China, scale bar=3mm (Yuan et al., 2011); [5]Phosphatised proposed animal embryos of the Doushantuo members II and III at Weng'an section, Guizhou province, scale bar 200µm (Xiao et al., 1998), [6]>570.95 Ma Juvenile *Charnia masoni* (Ford, 1958), specimen from the Drook Formation (Liu et al., 2012; chronological constraint after Pu et al., 2016), [7]~558–555 Ma, Earliest motile bilaterian body fossil, *Kimberella* (PIN 3993-5604 of Fedonkin et al., 2007), [8]~550 Ma, Earliest skeletal animals *Cloudina* (Germs, 1972b) and earliest evidence for predation in *Cloudina* from the Gaojiashan Member, Shaanxi, South China (image Hua et al., 2003) scale bar 200µm, [9]< 550 Ma, *Anabarites valkovi* from the Ust'-Yudoma Formation after Zhu et al. (2017), scale bar is 100µm for *Anabarites*, [10]First appearance datum of *Treptichnus pedum* trace fossil in the Chapel Island Formation of Fortune Head (Narbonne et al., 1987; image credit Herringshaw et al., 2017) scale bar 1 cm, [11]Example of earliest trilobite (Richter, 1932): *Profallotaspis jakutensis* cephalon in lower Atdabanian strata, Pestrotsvet Formation, Lena River, Siberian platform (image credit: Pegel, 2000), scale bar approximately 1cm.

d) Subgroup/Formation/Member abbreviations

Colour coding dominant stratigraphy: Black: Glacial diamictite, Blue carbonates (dark – light: deep to shallow), Red siliciclastics (dark – light: deep to shallow). Darkest: lower slope, mid: mid – shelf, lightest: shallow shelf. It should be recognised that this lithological key oversimplifies individual areas which represent the full shelf – basin transect (e.g. Yangtze Block where deep water equivalents to the Doushantuo – Dengying Formations include the Lantian and Liuchapo/Piyuancun Formations).

Dark Brown:

East European Platform (Baltica)

Correlation of Vychegda – Kotlin Formations is based on conservative estimates of Johnston et al. (2012) after consideration of Ediacaran Complex Acanthomorph – dominated Palynoflora distribution

elsewhere.

Kyrsh.: Kyrshabakty River Section (Kazakhstan)

Pink:

Corumbá Group (Brazil)

Boc: Bocaina Formation, Guai: Guaicurus Formation (lithological and facies information from Spangenberg et al., 2014 and Parry et al.., 2017)

Purple:

West Avalonia (eastern Newfoundland)

MB: Mall Bay Formation, G: Gaskiers Formation, Br: Briscal Formation, MP: Mistaken Point Formation, T: Trepassey Formation, Ferm: Fermeuse Formation, R: Renews Head Formation, SHG: Signal Hill Group, Green P: Green Point Formation.

Navy Blue:

Eastern Avalonia, Charnian Supergroup (England)

Ives H. = Ives Head Formation (Blackbrook Group), Bl. = Blackbrook Reservoir Formation (Blackbrook Group), BH = Beacon Hill Formation (Maplewell Group), Brad = Bradgate Formation (Maplewell Group), Hang = Hanging Rocks Formation (Maplewell Group), Brand Group.

Black:

Laurentia (NW Canada)

IB: Ice Brook Formation, R: Ravensthroat Formation, SB: Sheepbed Formation, Sheepbed C: Sheepbed Carbonate unit, GT: Gametrail Formation, BF: Blueflower Formation, Ri: Risky Formation, Em – WC: Emigrant Springs-Whipple Cave Formations

Light Blue:

Yangtze Block (South China)

ND: Nantuo Diamictite, I: Doushantuo Formation, Member 1, DST II: Doushantuo Formation, Member 2, DST III: Doushantuo Formation, Member 3, IV: Doushantuo Formation, Member 4, Mfs – Qn: Mufushan to Qingshudong Formations (Note that this correlation does not reflect Formation subdivision within a single section but rather relative ages of Formations across different sections.)

Red:

Combined Congo and Kalahari Cratons (Namibia)

Ras.: Rasthof Formation, G.: Gruis Formation, O.: Ombaatjie Formation (Ras. – O. together with underlying Chuos Sturtian glacial diamictite comprise the Abenab Subgroup), Gh: Ghaub Marinoan

glacial diamictite, B: Buschmannsklippe Formation, Kuib: Kuibis Subgroup, Sch: Schwarzrand Subgroup

Green:

Arabian-Nubian Shield (Oman)

GM: Ghadir Manqil Marinoan glacial diamictite, H: Hadash cap carbonate, Buah Formation, Ara: Ara Group

Yellow:

South Australia

E: Elatina Formation, N: Nuccaleena Formation, ABC: ABC Range Formation, B: Bonney Sandstone, R: Rawnsley Quartzite, P: Parachilna Formation, W: Woodendinna Dolomite, Wl: Wilkawillina Formation, A: Andamooka Limestone Formation, K: Kulpara Formation, O: Ouldburra Formation

Dark Blue:

White Sea, Winter Coast (Baltica)

ZA – ZC: Zimnie Gory section Units A – C. (Martin et al., 2000)

Grey:

Yudoma-Maya depression (southeast Siberian Platform)

A: Aim Formation, U'Yud.: Ust' Yudoma Formation

Light Brown:

Olenek Uplift (northeast Siberian Platform)

Zher.: Zherba Formation, M. – Turk.: Maastakh – Khatyspyt – Turkut Formations (Knoll et al., 1995; Pelechaty et al., 1998; Rogov et al., 2012)

Gold:

Composite C isotope profile from Anti-Atlas Mountains, Morocco (Maloof et al., 2005). Adoudou and Lie de Vin Formations of the Taroudant Group and Igoudine, Amouslek and Issafene Formations of the Tata Group.

Bright Green:

Composite C isotope profile from the Zavkhan terrane, SW Mongolia (Macdonald et al., 2009; Smith et al., 2016). Tsagaan Oloom Formation, MU: Malkhan Ul Member, K: Khongoryn Member diamictite, Ol: Ol Member. Zn: Zuun-Arts Formation, Bayan: Bayangol Formation, SG: Salaany Gol (/Salaangol) Formation.

e) U-Pb ages

659 ± 6 Ma: zircon U-Pb SHRIMP age for tuffaceous horizon within uppermost Sturtian diamictites (Wilyerpa Formation) of the Umberatana Group (stratigraphically above the Burra Group and below the Wilpena Group) in the northern Adelaide Geosyncline (Fanning and Link, 2008). Cryogenian reef complexes of the Balcanoona Formation in Wallace et al. (2015) and Hood and Wallace (2015) occur within the Umberatana Group.

635.47 ± 1.05 Ma: U-Pb age from six concordant single grain analyses. Ash bed within glacial deposits of the Ghaub Formation. (Hoffmann et al., 2004; Schmitz, 2012)

635.26 ± 1.07 Ma: zircon U-Pb CA-ID-TIMS age from 3 concordant (of 18) single grain analyses. Top of Nantuo diamictite (min. age). (Condon et al., 2005)

632.48 ± 1.02 Ma: zircon U-Pb CA-ID-TIMS age from 3 concordant (of 9) single grain analyses. Top of Nantuo diamictite (min. age). (Condon et al., 2005)

614 ± 9 Ma: zircon U-Pb SHRIMP age. Weighted mean of 18 single grains. Middle Doushantuo Formation. Wanjiagou Section, Zhangcunping area. (Liu et al., 2009)

580.9 ± 0.4 Ma: zircon U-Pb CA-ID-TIMS age of Upper Mall Bay Formation. Nine single grain analyses. (Pu et al., 2016)

579.88 ± 0.4 Ma: zircon U-Pb CA-ID-TIMS age of lower Drook Formation. Five single grain analyses. (Pu et al., 2016)

570.94 ± 0.38 Ma: zircon U-Pb CA-ID-TIMS age of upper Drook Formation. Five single grain analyses. (Pu et al., 2016)

569.09 ± 0.45 Ma: zircon U-Pb CA-ID-TIMS age from 2 concordant (of 12) single grain analyses. Bennscliffe Breccia between Blackbrook Reservoir Fm and Beacon Hill Formation (Charnian Supergroup). (Noble et al., 2015)

566.25 ± 0.35 Ma: zircon U-Pb CA-ID-TIMS age. 33.65m above base of Mistaken Point Formation (sample MPMP33.56). Five single grain analyses. (Pu et al., 2016)

565.22 ± 0.33 Ma: zircon U-Pb CA-ID-TIMS age from 2 concordant (of 5) single grain analyses. Beacon Hill Formation (Maplewell Group, Charnian Supergroup). (Noble et al., 2015).

561.85 ± 0.34 Ma: zircon U-Pb CA-ID-TIMS age from 7 concordant (of 12) single grain analyses. Bradgate Formation (Maplewell Group, Charnian Supergroup). (Noble et al., 2015).

556.6 ± 6.4 Ma (not noted due to space): zircon U-Pb CA-ID-TIMS age from 4 single grain analyses. Hanging Rocks Formation (Maplewell Group, Charnian Supergroup). (Noble et al., 2015).

555.18 ± 0.3 Ma: zircon U-Pb CA-ID-TIMS age from 8 (of 8) concordant single grain analyses. Ash bed in upper Bocaina Formation. (Parry et al., 2017)

552.85 ± 2.62 Ma: Weighted mean zircon $^{207}Pb/^{206}Pb$ age for Zimnie Gory section. Uppermost Ust Pinega Formation, near base of sequence B. Nineteen single grain and small multigrain fractions (Martin et al., 2000; recalculated in Schmitz, 2012)

551.09 ± 1.02 Ma: Weighted mean zircon $^{206}Pb/^{238}U$ CA-ID-TIMS age from 2 concordant (of 10) single grain analyses. Ash bed in upper Doushantuo Formation, Member IV at Jiuqunao. (Condon et al., 2005).

547.32 ± 0.65 Ma: zircon U-Pb CA-ID-TIMS age from 8 single grain analyses. Lower Hoogland member, Zaris Formation, Kuibis Subgroup, Nama Group, Namibia. (Bowring et al., 2007; recalculated in Schmitz, 2012).

546.72 ± 0.66 Ma: zircon U-Pb CA-ID-TIMS age from 8 single grain analyses. Ara Group, middle of A0 carbonate unit. (Bowring et al., 2007)

545.76 ± 0.66 Ma: zircon U-Pb CA-ID-TIMS age from 5 single grain analyses. Lower Liuchapo Formation, deep slope Longbizui section, Hunan, South China. Not included due to space (Yang et al., 2017).

542.9 ± 0.63 Ma: zircon U-Pb CA-ID-TIMS age from 8 single grain analyses. Ara Group, 3m above base of A3 carbonate unit. Originally in (Bowring et al., 2007)

541.85 ± 0.75 Ma: zircon U-Pb CA-ID-TIMS age from 5 concordant single grain analyses. Volcanic tuff from Upper Tamengo Formation. (Parry et al., 2017)

540.61 ± 0.88 Ma: zircon U-Pb air abrasion ID-TIMS age from ten multigrain zircon fractions. Silicified volcanic tuff deposit in upper Spitskop Member, Urusis Formation, Schwarzrand Subgroup, Nama Group, Namibia. (Grotzinger et al., 1995; recalculated in Schmitz, 2012).

539.4 ± 2.9 Ma: U-Pb SHRIMP age of bentonites. Meishucun section, bed 5 (Zhongyicun Member, Zhujiaqing Formation). (Compston et al., 2008).

529.56 ± 0.24 Ma: zircon U-Pb (TIMS) age from volcanic tuff of the Mattaia Formation (Kessyusa Group). (Kaufman et al., unpublished 2012)

526.5 ± 1.1 Ma: U-Pb SHRIMP age of bentonites. Meishucun section, bed 9 (base of Shiyantou Formation). (Compston et al., 2008).

525.23±0.61Ma. zircon U-Pb CA-ID-TIMS age from eight single grain analyses. Ash bed at level of major positive C isotope excursion at Nemakit-Daldynian/Tommotian boundary. (Maloof et al., 2005; Schmitz, 2012)

518.03 ± 0.71 Ma: Youngest zircon U-Pb CA-ID-TIMS age (incorporating U-Pb tracer calibration uncertainty) from five single grain analyses of detrital zircons from the Maotianshan shale immediately underlying Chengjiang biota. Taken as maximum depositional age for the Chengjiang biota. (Yang et al., 2018)

Figure 2.2 details

References:

0) Baiguoyuan (Hubei)- Shallow platform (Fan et al., 2014)

1) Miaohe (Hubei)- SCALE- Shallow platform, shelf-lagoon (Li et al., 2015b)

2) Liuhuiwan (Hubei)- Shallow Platform (Fan et al., 2014)

3) Jiuqunao (Hubei)- Shallow Platform (Och et al., 2015; Li et al., 2015b, 2017: composite Jiuqunao-Wangjiaping)

4) Jiulongwan (Hubei)-Intra-shelf basin (Li et al., 2010; Och et al., 2015)

5) Zhongling (Hunan)- Elevated shelf margin (Li et al., 2010)

6) Maoshi (Guizhou)- Protected basin/ lagoon (Och et al., 2015)

7) Minle (Hunan)-Slope condensed (Li et al., 2010)

8) Wuhe (Guizhou)- Lower slope (Sahoo et al., 2012, 2016; Han and Fan, 2015; Li et al., 2017: composite Wuhe-Geyi)

9) Jinjiadong (Hunan)- Basin (Huang et al., 2017)

10) Yuanjia (Hunan)- Basin (Sahoo et al., 2012)

11) Longe (Guizhou)- Basin (Li et al., 2010; Huang et al., 2017)

12) Xiangtan (Hunan)- Basin (Han and Fan, 2015)

13) Lantian (Anhui)- Deep basin (Shen et al., 2008); b) Cheng et al. (2017)

13.5) Chunye-1 drill core (Zhejiang)- Deep basin (Xiang et al., 2017)

14) Xiaotan (NE Yunnan)- Platform (Och et al., 2013)

15) Meishucun (Yunnan)- condensed platform margin (Och et al., 2013)

16) Jijiapo (Hubei)-Platform (Och et al., 2015)

17) Jinsha (Guizhou)- SCALE- Outer shelf (Jin et al., 2016)

18) Zhongnan (Guizhou) SCALE- Platform margin/protected basin (Och et al., 2013)

19) Yangjiaping (Hunan)- Shelf margin-Outer Shelf (Feng et al., 2014)

20) Weng'an (Guizhou)- Outer shelf (Jin et al., 2016)

21) Songtao (Guizhou)- Protected basin (Canfield et al., 2008; Feng et al., 2014)

22) Huanglian (Guizhou)-Protected basin (Och et al., 2015)

23) Longbizui (Hunan)- Protected basin (Wang et al., 2012; Och et al., 2015)

24) Diben (Zhejiang)- Protected Basin (Yuan et al., 2014)

25) Zhalagou (Guizhou)- Basin (Li et al., 2017)

26) CJ1 (a) and CJ2 (b) drill cores (Yunnan)- offshore slope and shelf (Hammarlund et al., 2017)

“ Wuhe (Hubei)- Protected intra-shelf basin (this study)

‘ Yinchangpo (Yunnan)- Platform (this study)

Detailed biostratigraphy: Xiao et al. (2014), Jin et al. (2016) and references therein, Broce et al. (2014)

● Fe_{HR}/Fe_T ● Fe_{py}/Fe_{HR}

0) Baiguoyuan, Fan et al. (2014)

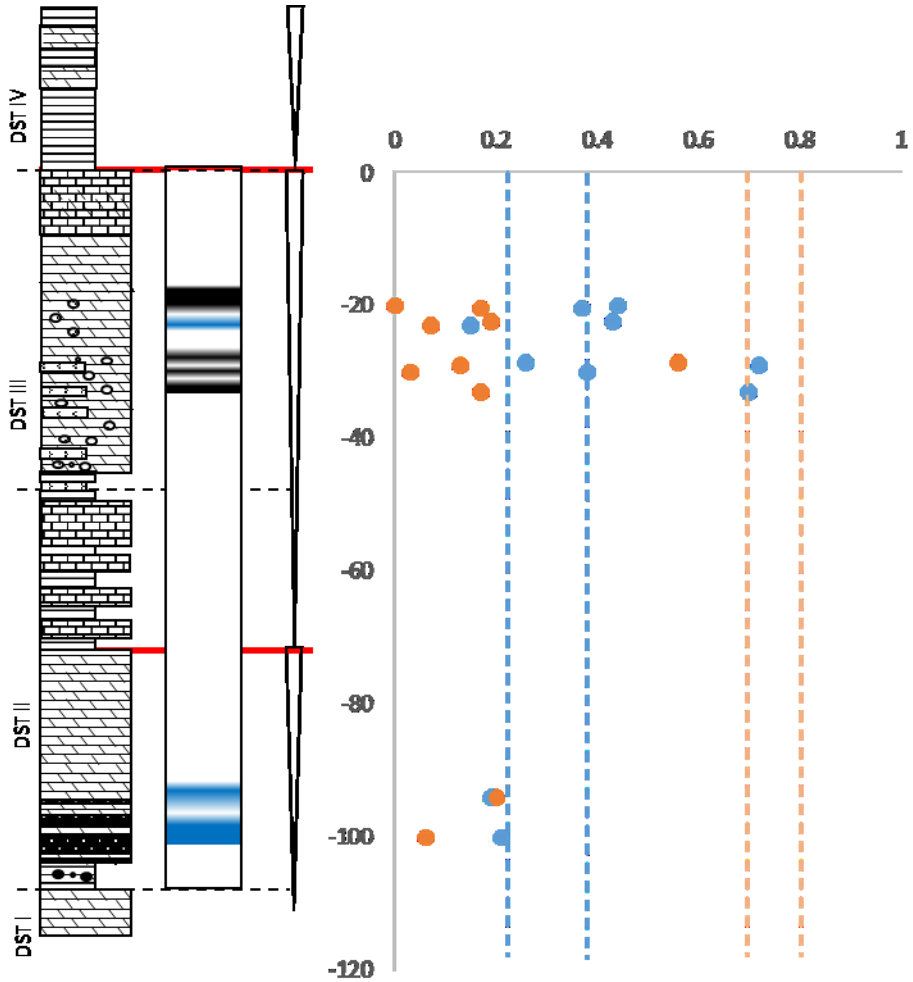

1) Miaohe, Li et al. (2015)

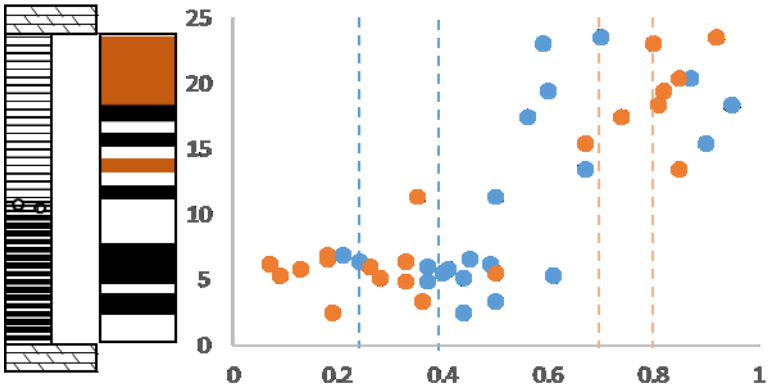

2) Liuhuiwan, Fan et al. (2014)

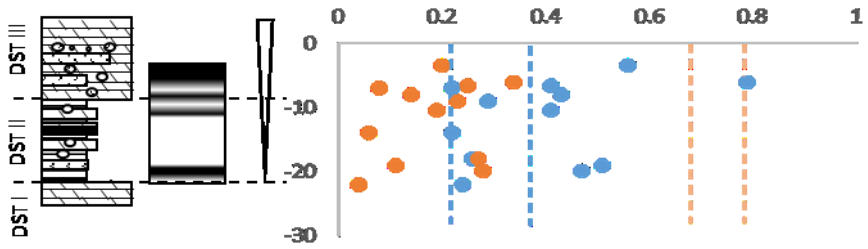

3) Jiuqunao

Och et al. (2015)

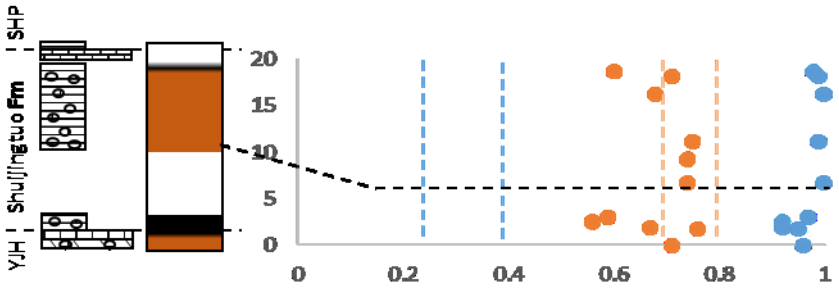

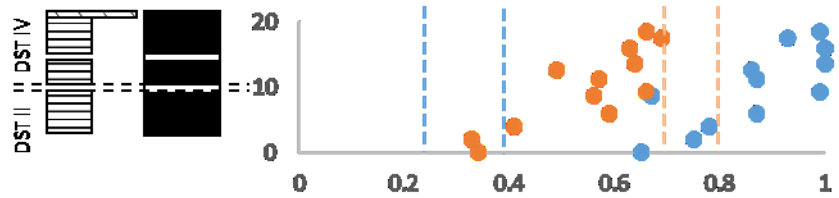

Li et al. (2017)

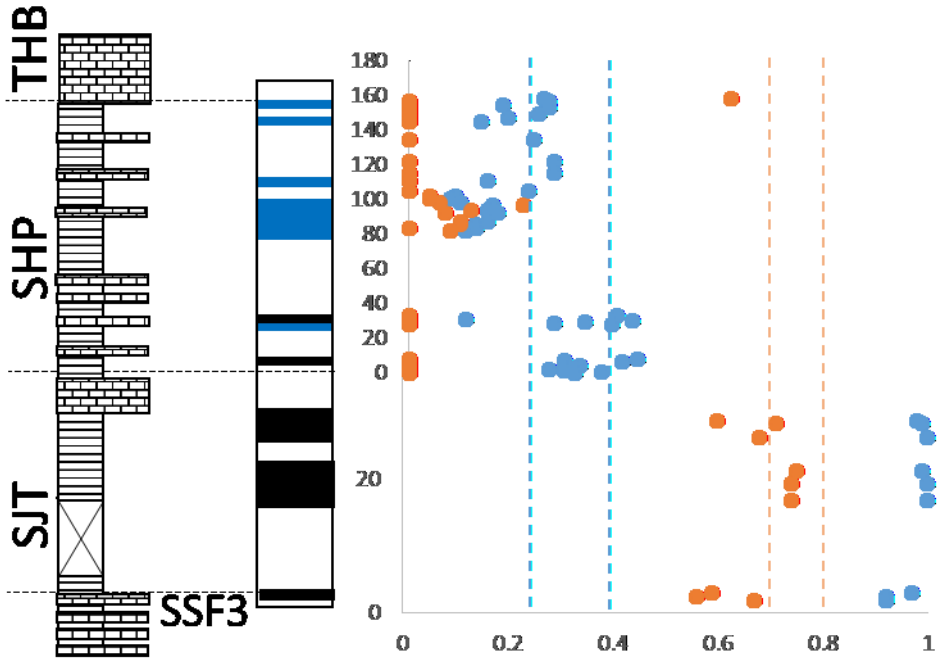

Li et al. (2015)

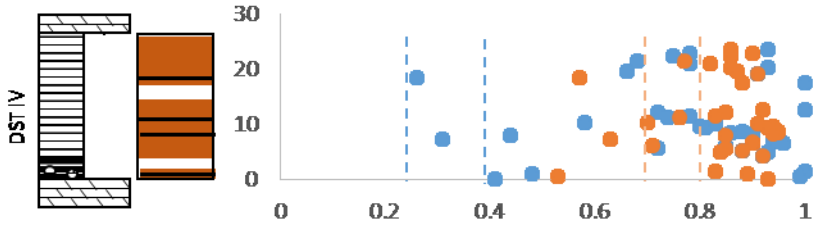

4) Jiulongwan

Li et al. (2010)

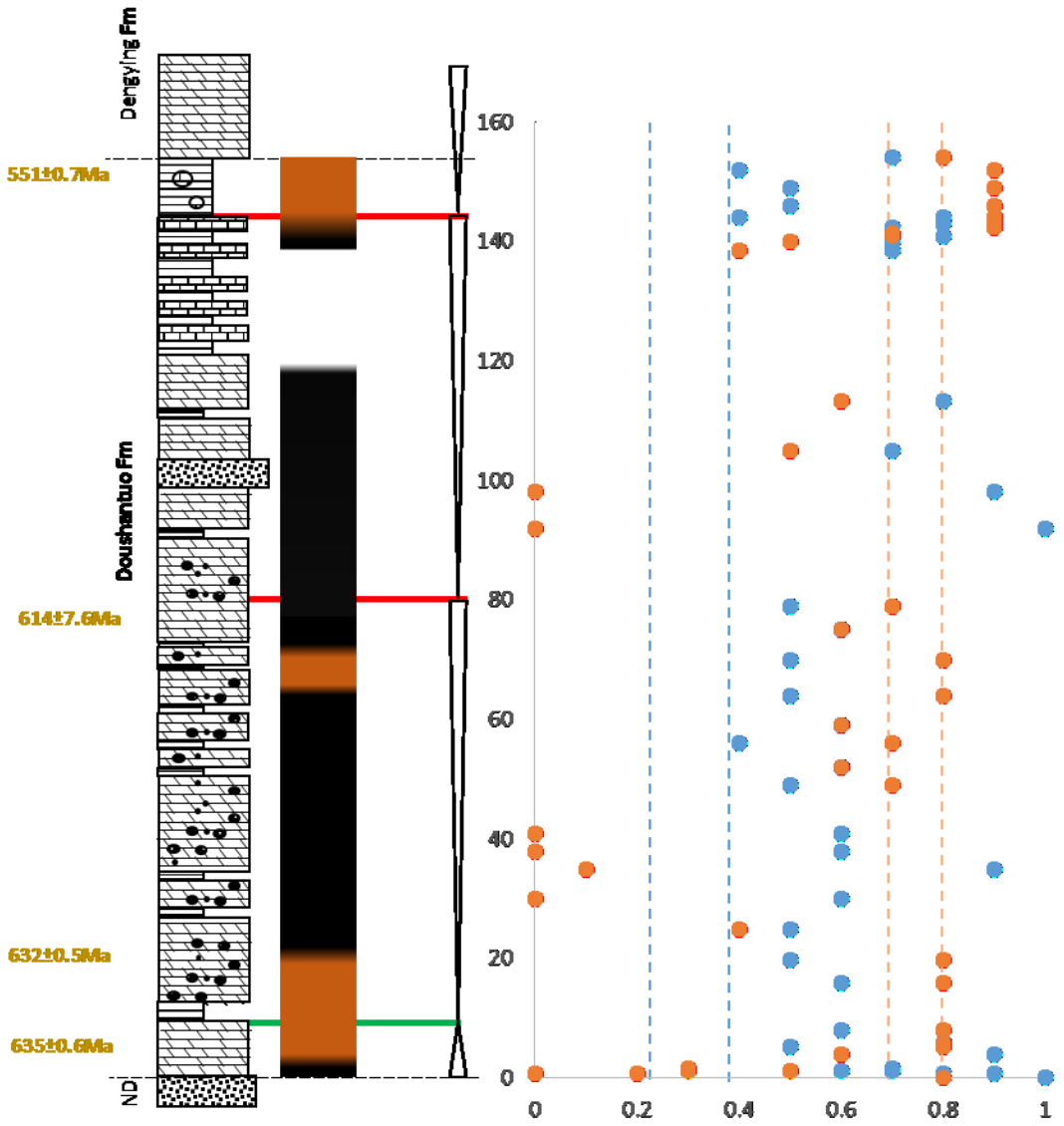

Jiulongwan-
Intra-shelf

Och et al. (2015)

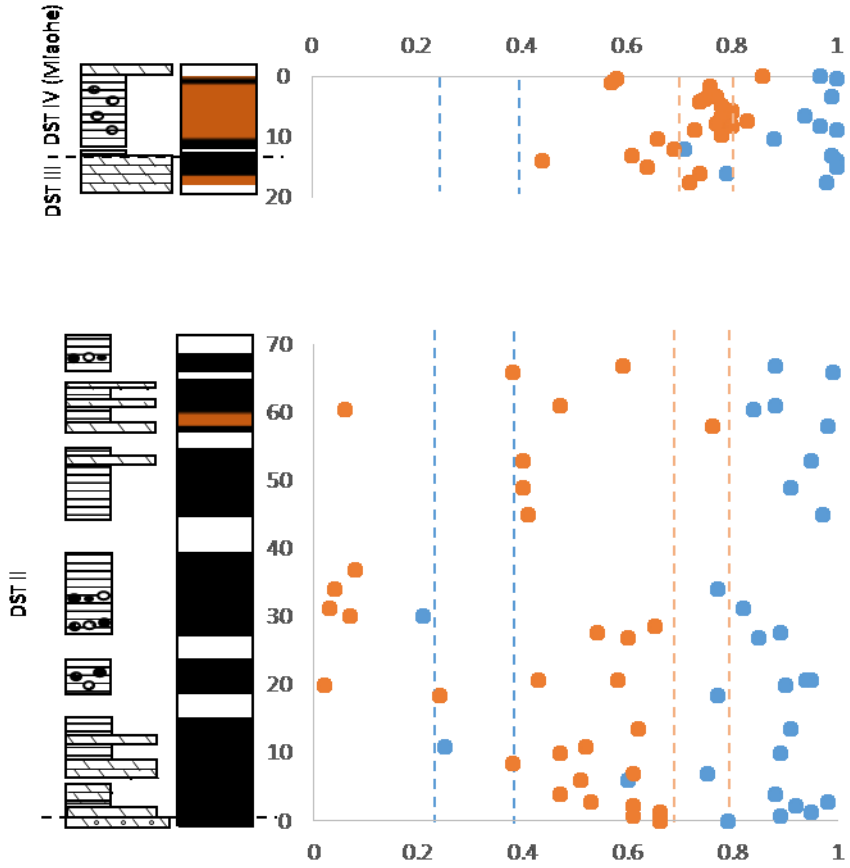

5) Zhongling: Li et al. (2010)

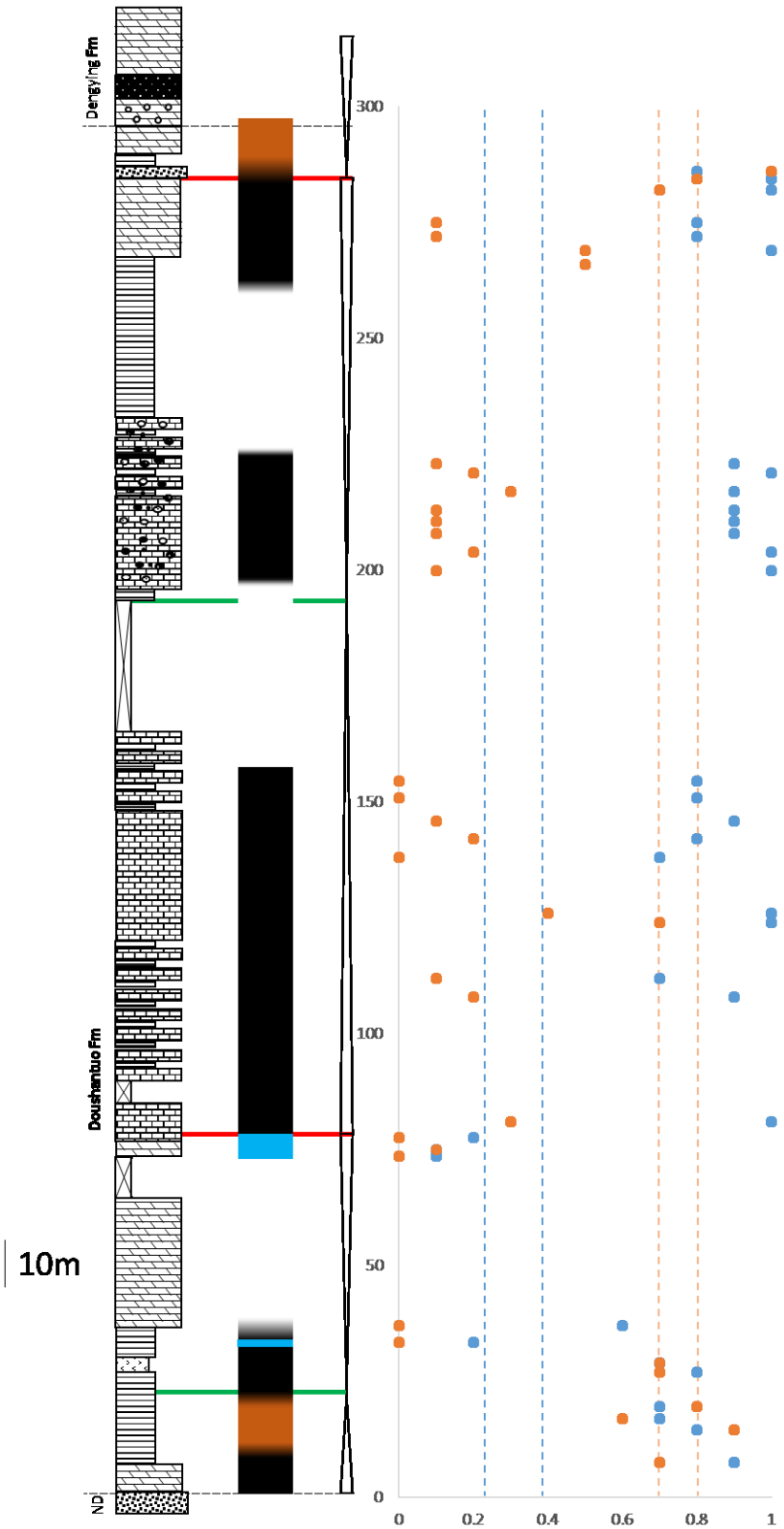

6) Maoshi: Och et al. (2015)

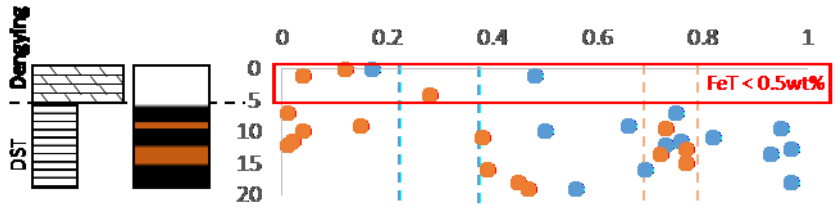

7) Minle: Li et al. (2010)

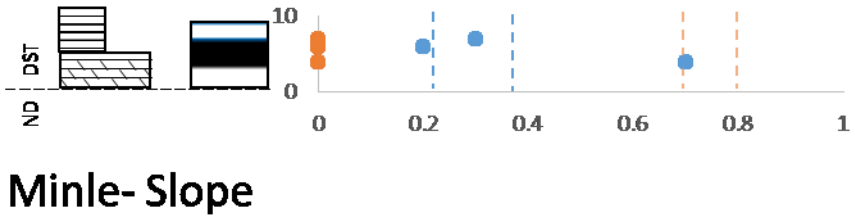

Minle- Slope

8) Wuhe

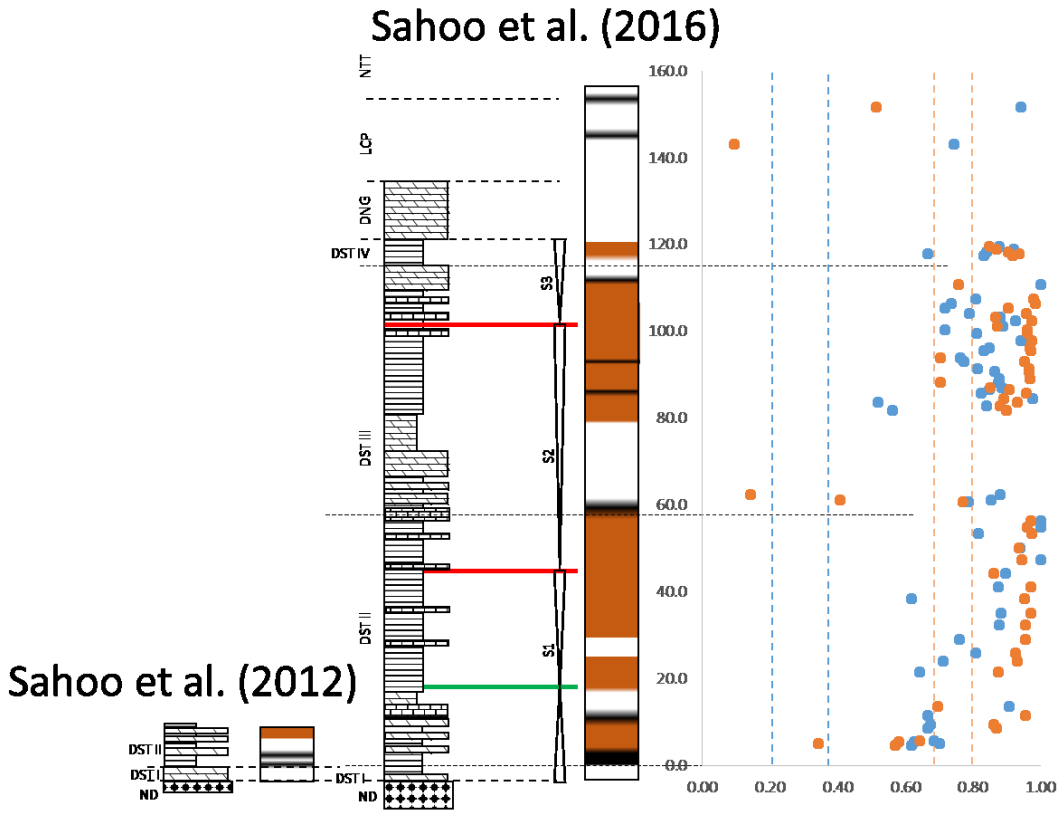

Han and Fan (2016)

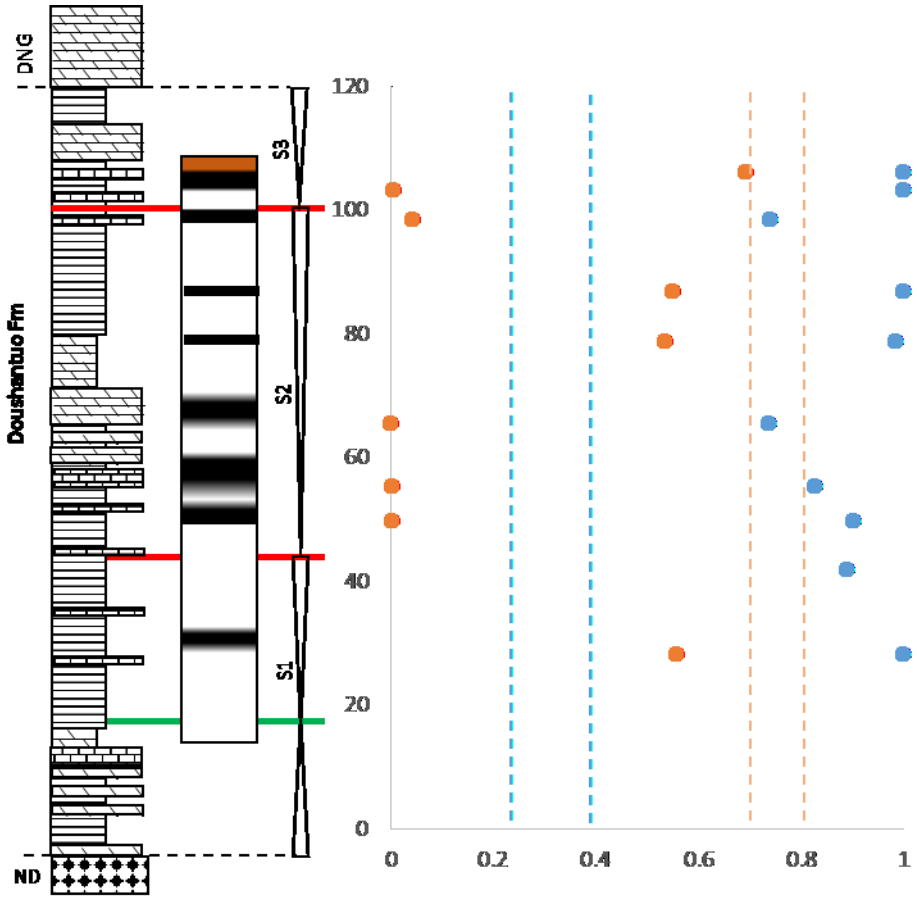

8) Wuhe, (Liuchapo to Balang Formations)

Li et al. (2017)

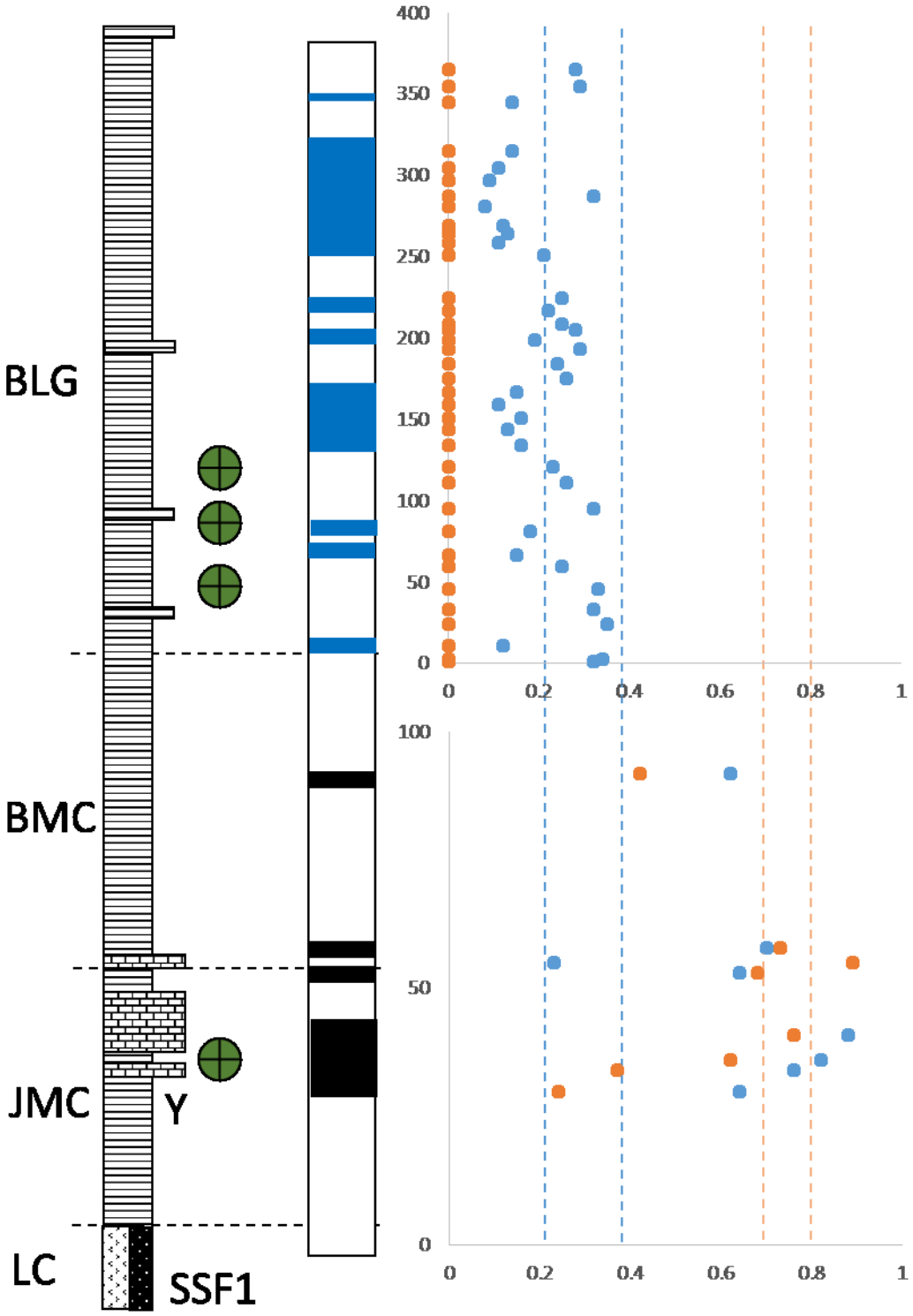

9) Jinjiadong: Huang et al. (2017)

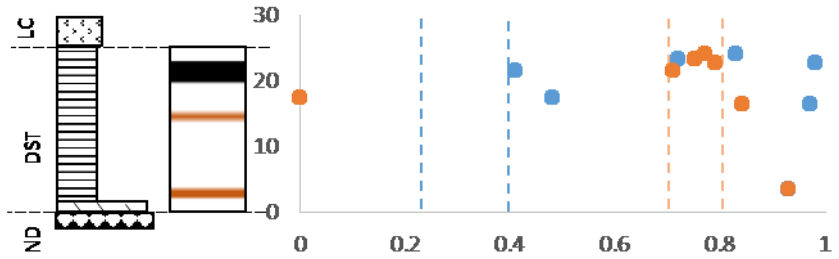

10) Yuanjia: Sahoo et al. (2012)

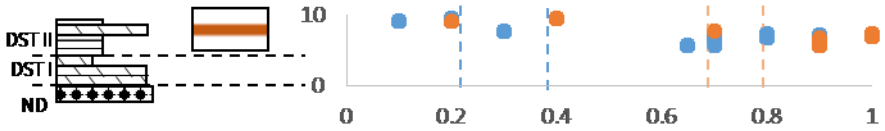

11) Longe

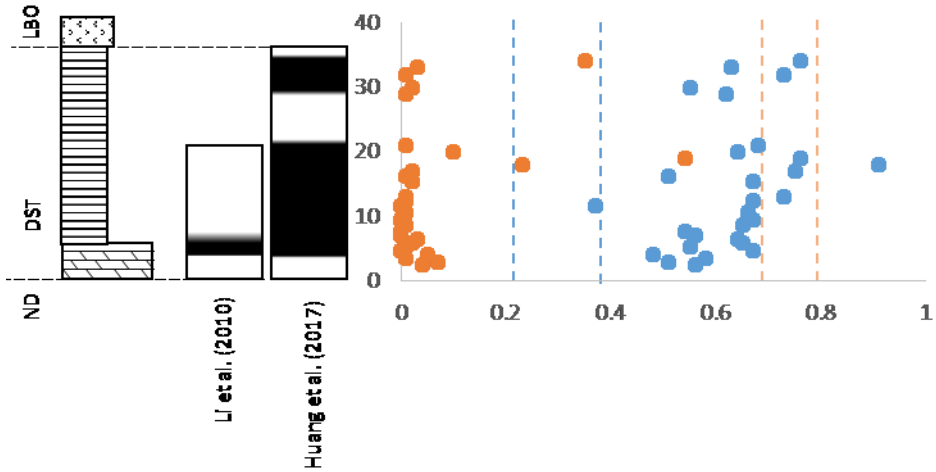

12) Xiangtan: Han and Fan (2016)

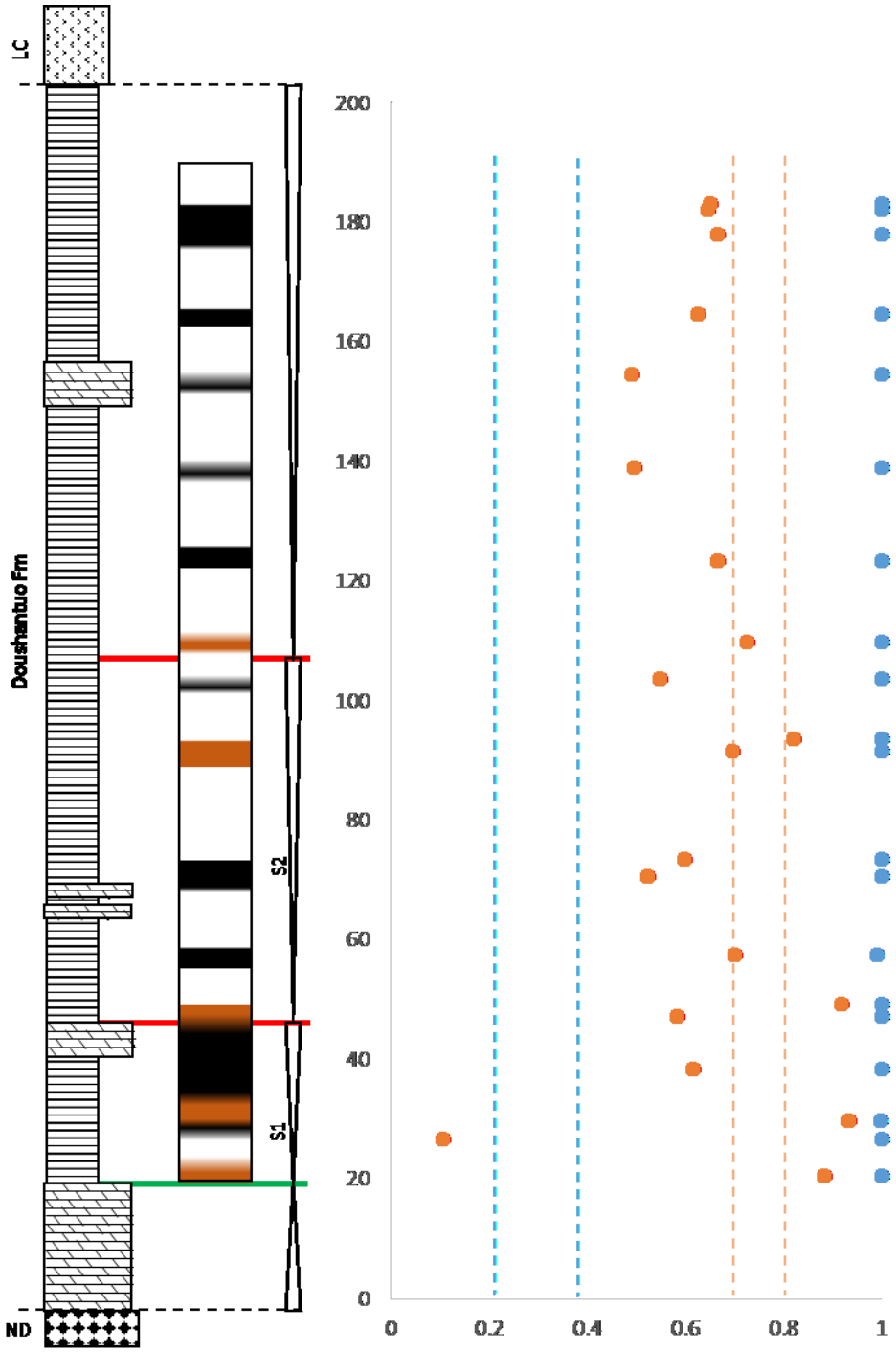

13) Lantian

Cheng et al. (2017)

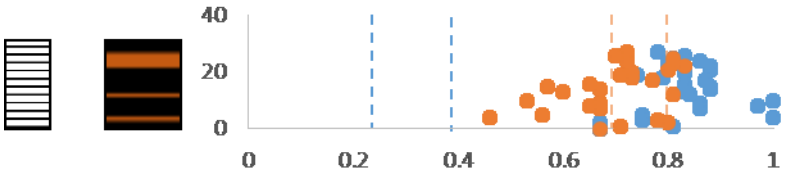

Shen et al. (2008)

-Different Fe speciation method used dithionite-only for Fe_{HR}/Fe_T

-No Fe_{py}/Fe_{HR} data provided. Ferruginous vs euxinic environment indistinguishable.

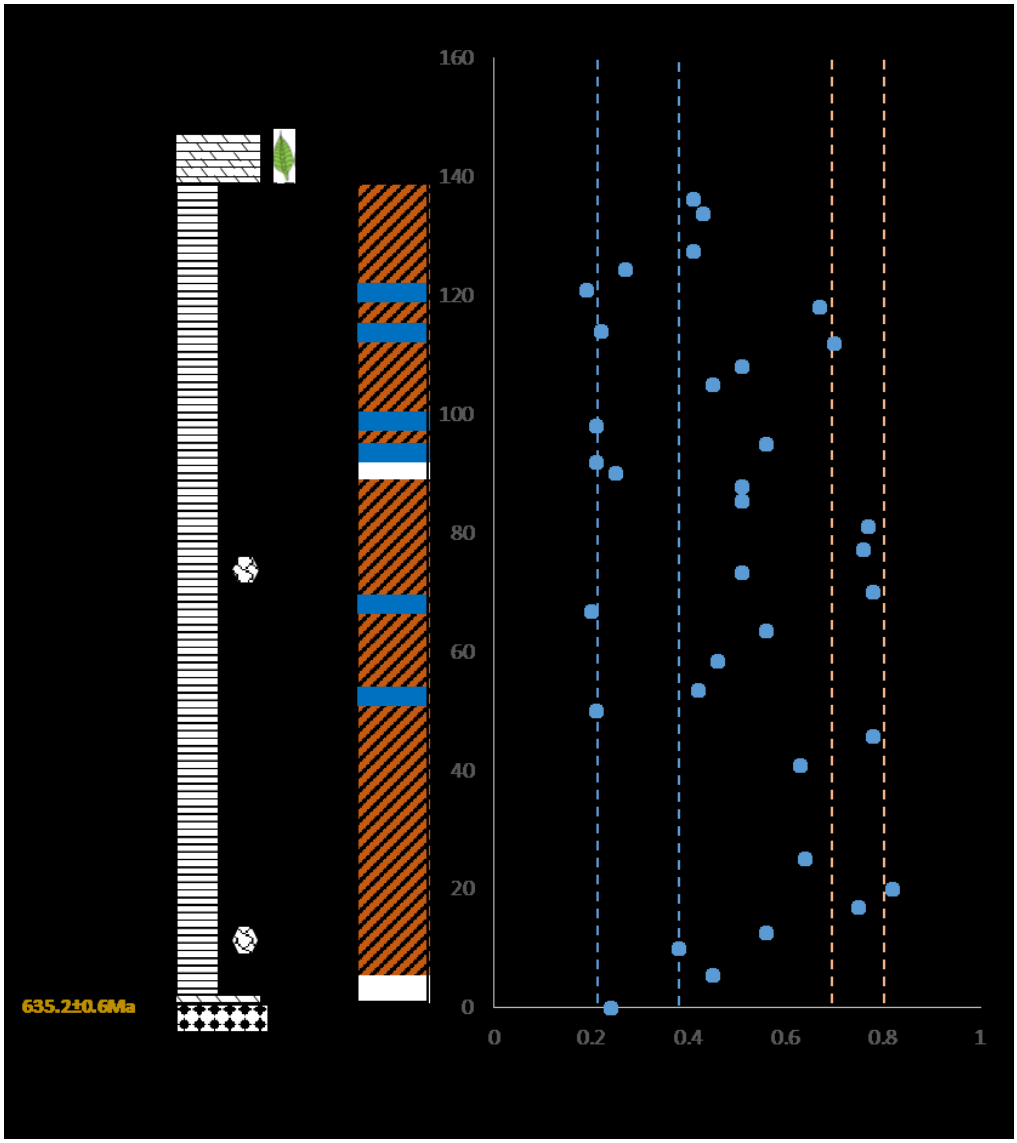

13.5) Chunye-1 drill core, Zhejiang province

Xiang et al. (2017)

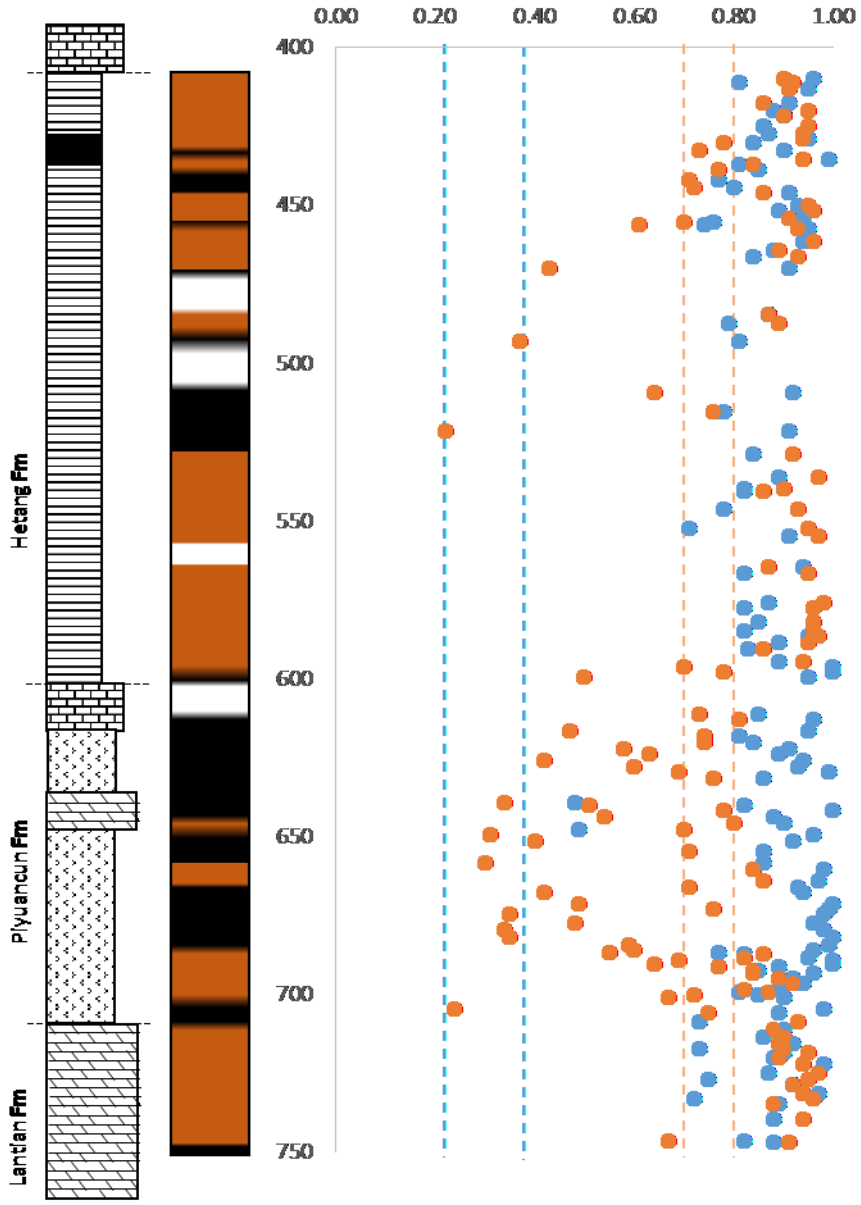

14) Xiaotan, Och et al. (2013)

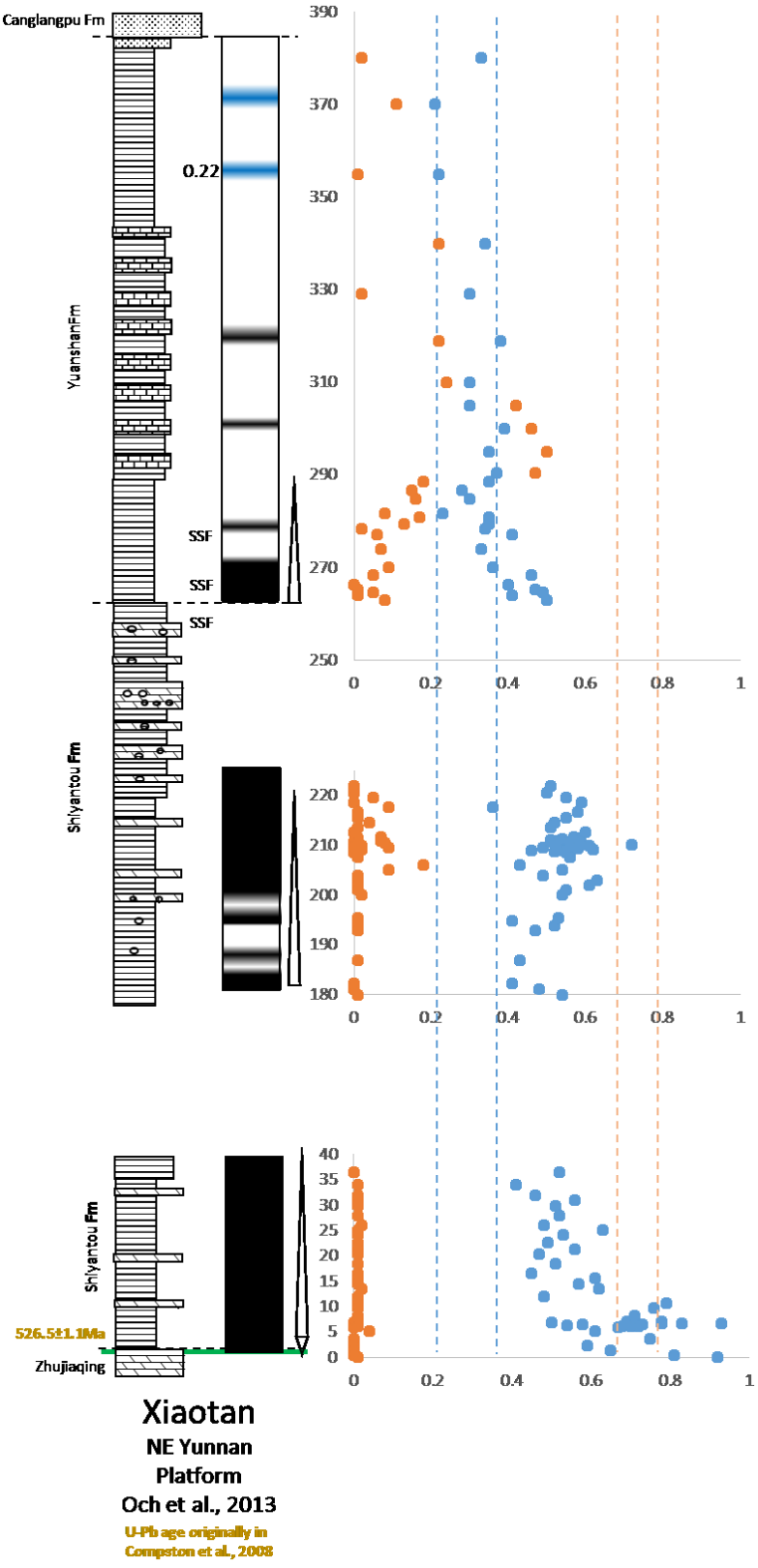

15) Meishucun, Och et al. (2013)

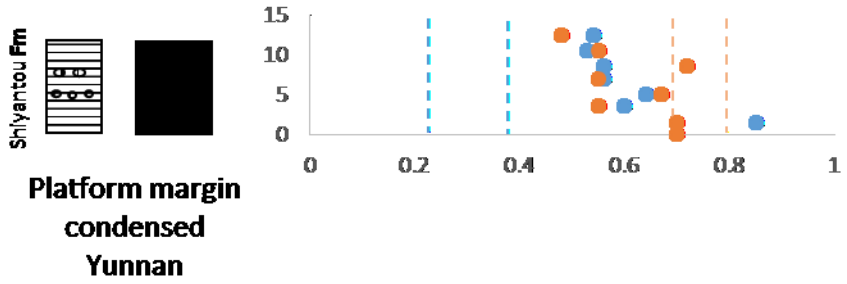

16) Jijiapo, Och et al. (2015)

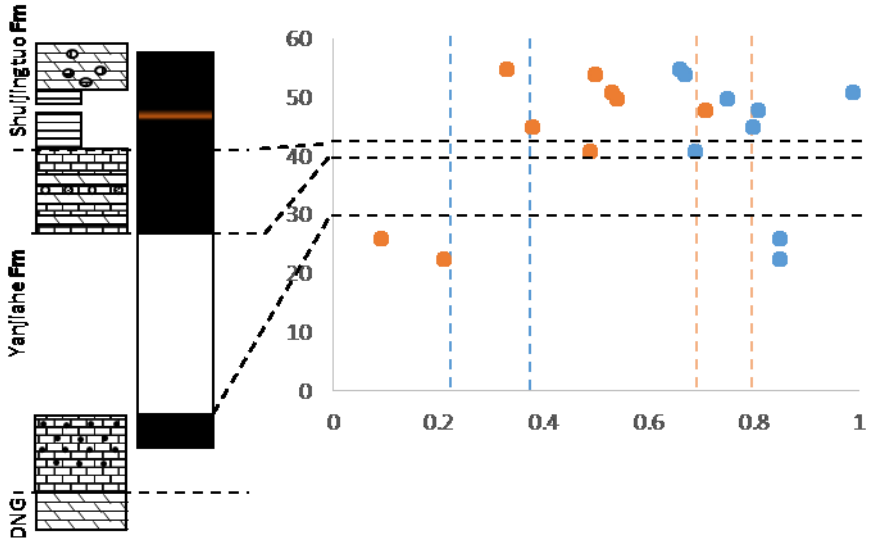

17) Jinsha, Jin et al. (2016)

Many Fe/Al <0.40 (these data are omitted from the schematic representation)

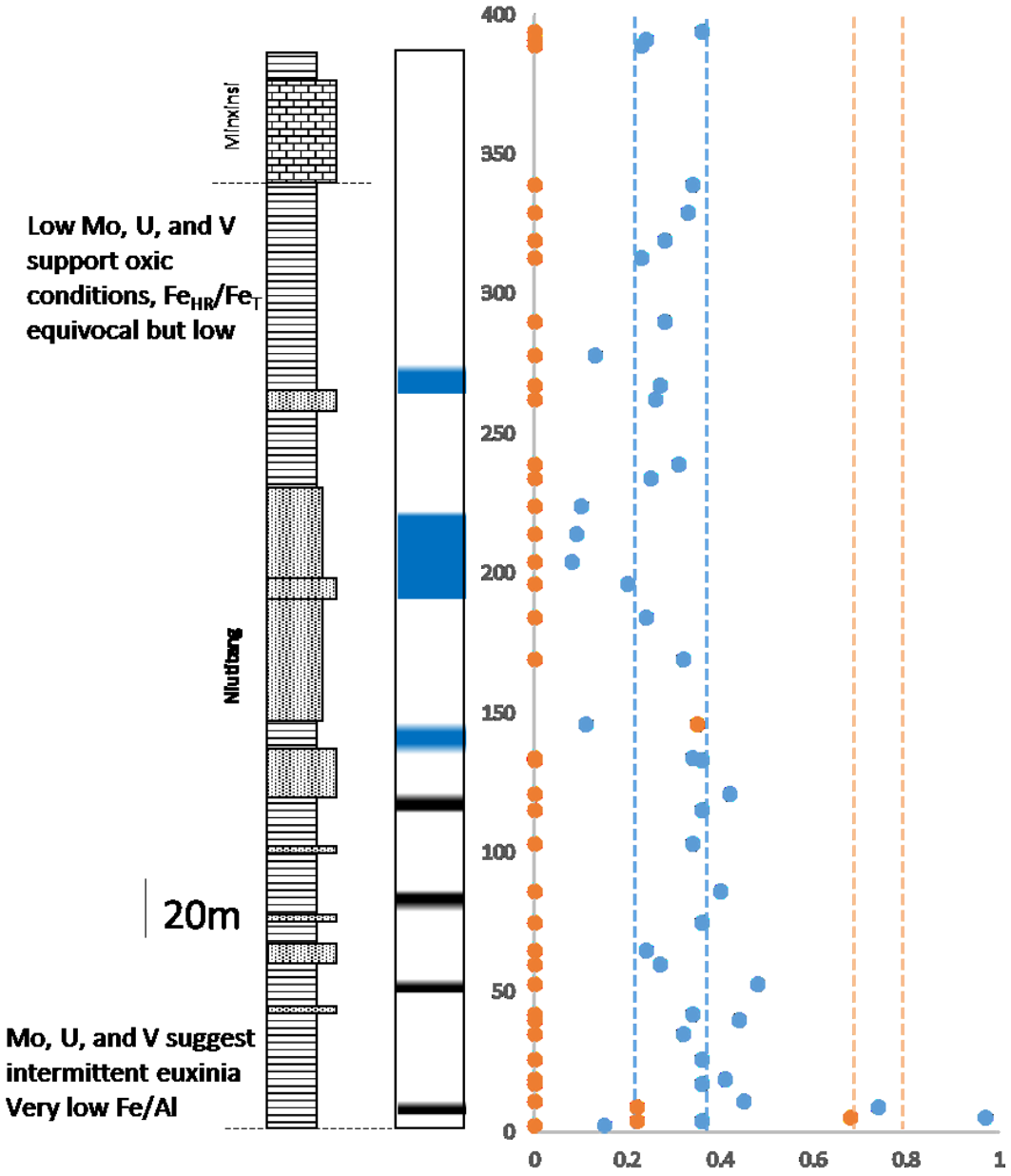

18) Zhongnan, Och et al. (2013)

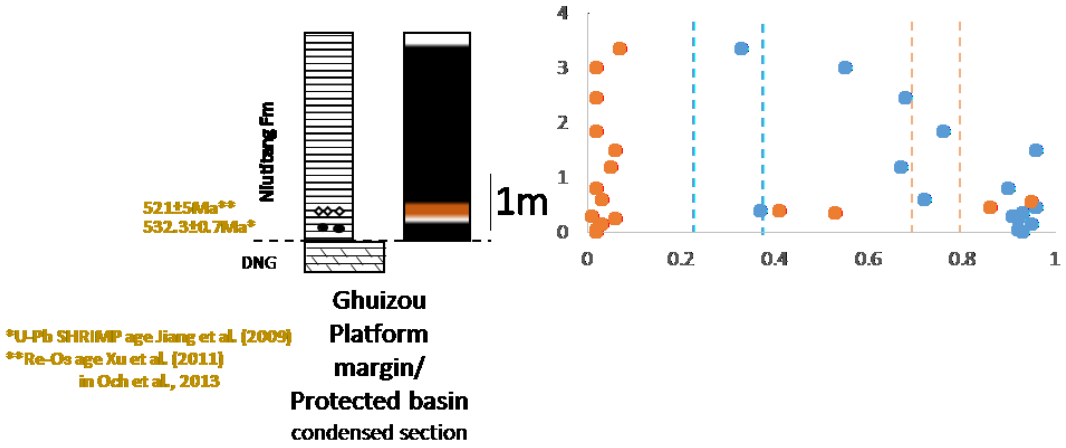

19) Yangjiaping, Feng et al. (2014)

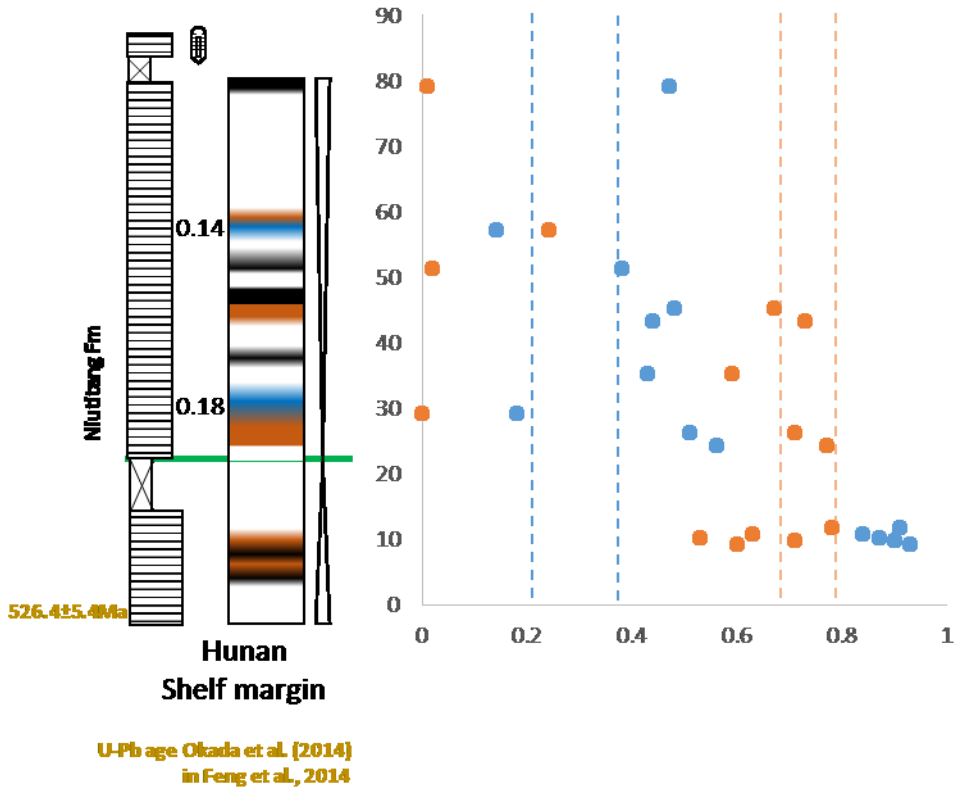

20) Weng'an, Jin et al. (2016)

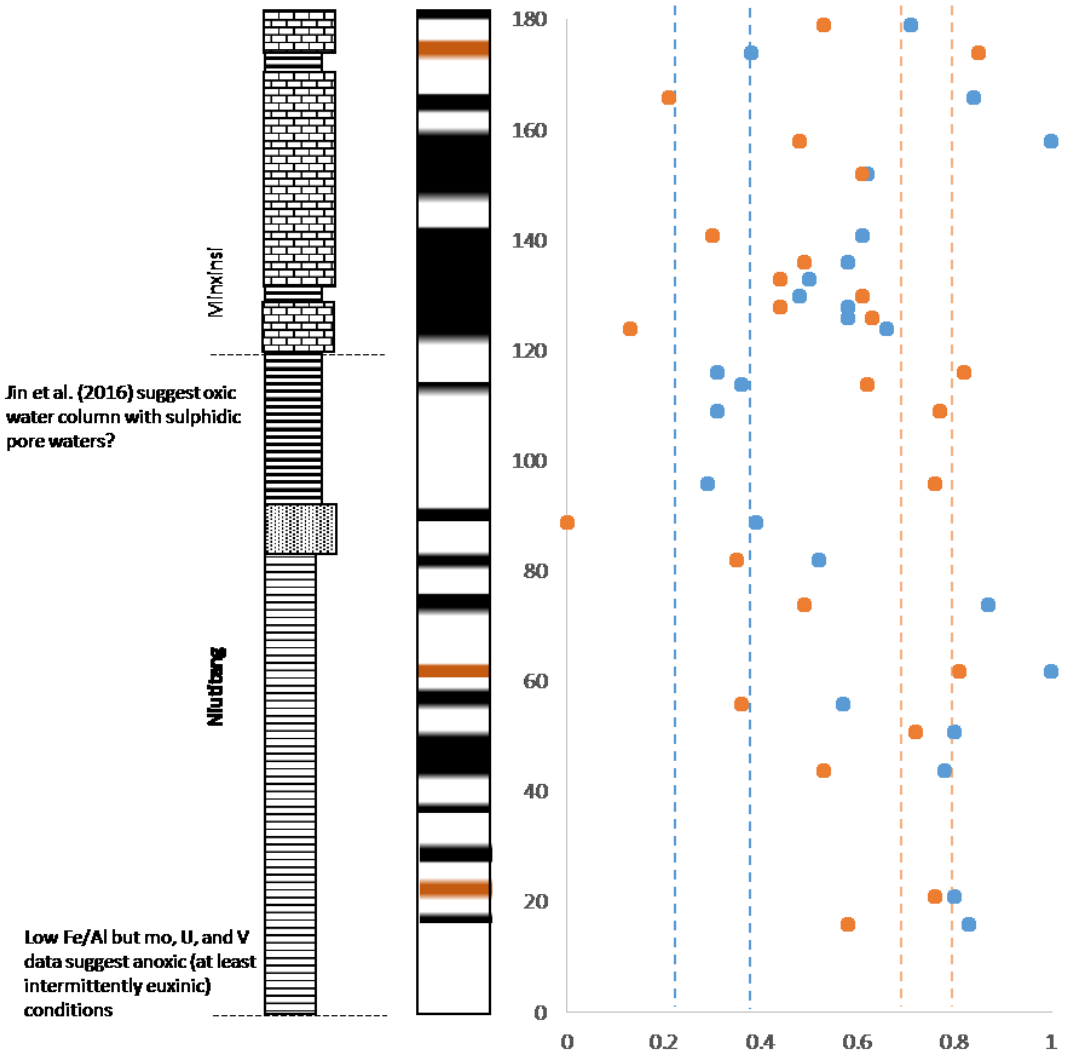

21) Songtao, Canfield et al. (2008), Feng et al. (2014)

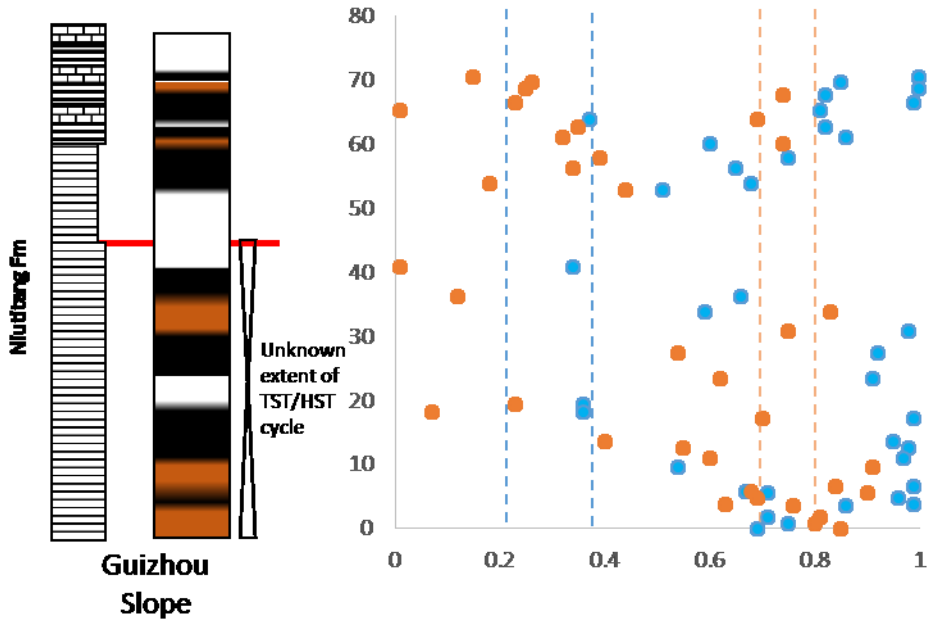

22) Huanglian, Och et al. (2015)

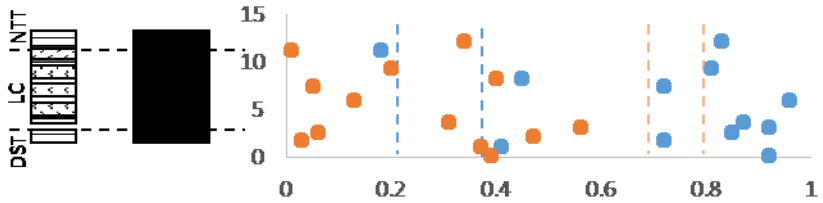

23) Longbizui

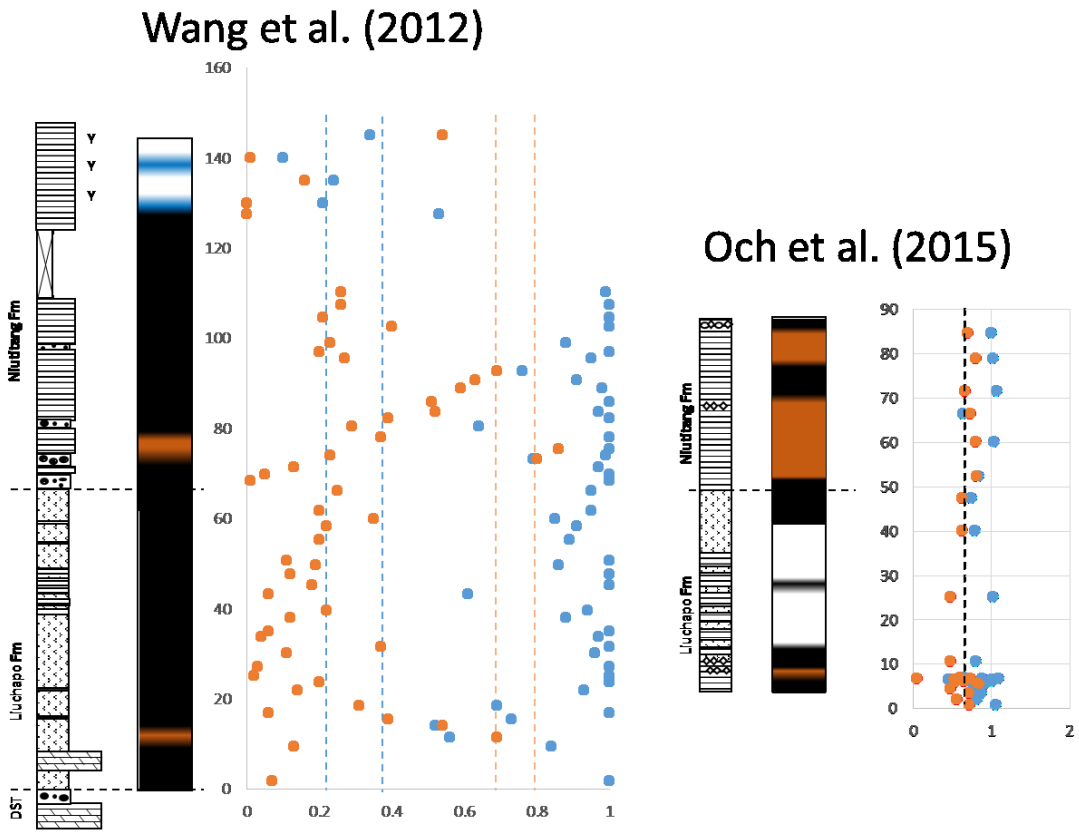

24) Diben, Yuan et al. (2014), note scale

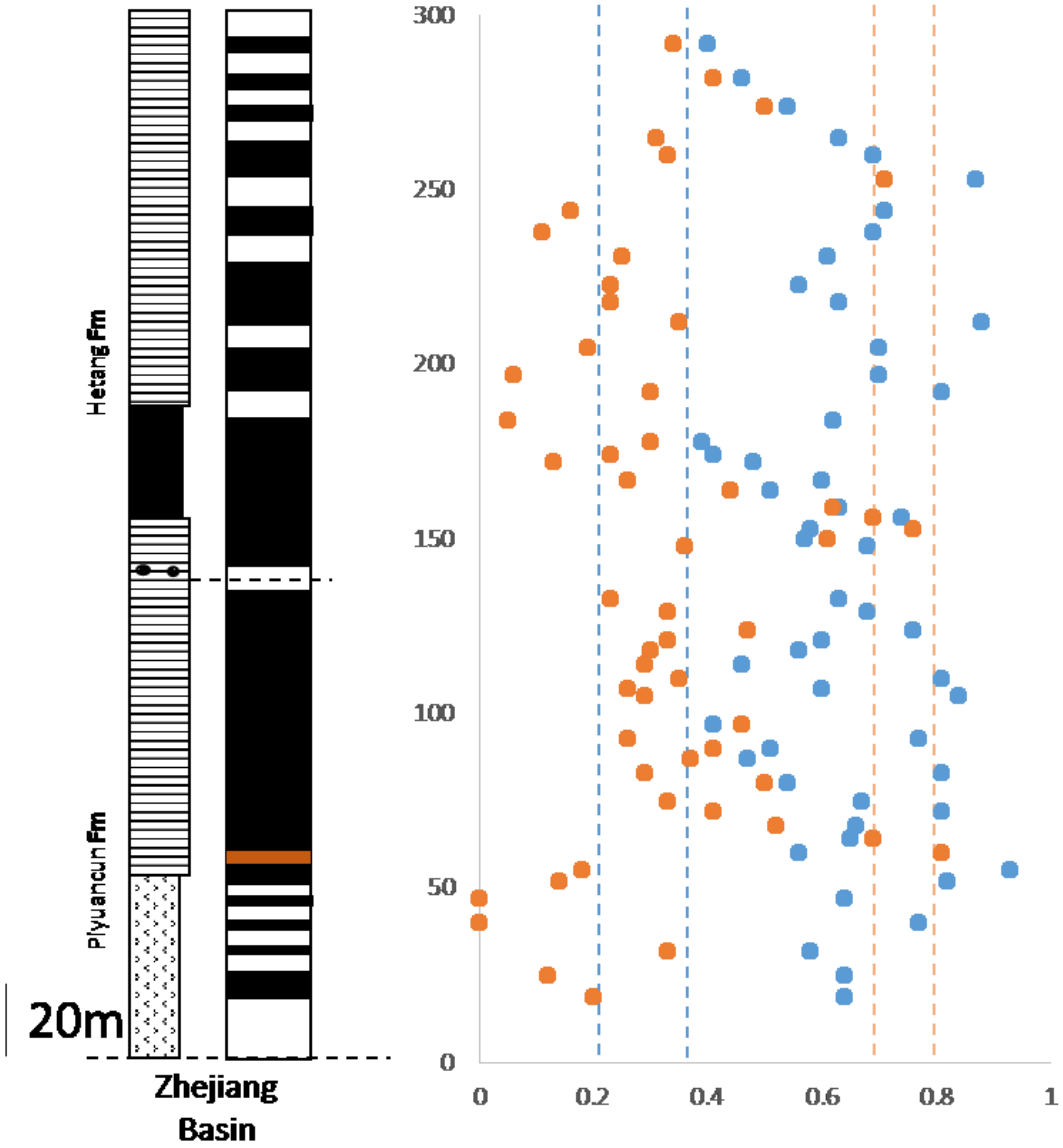

25) Zhalagou, Li et al. (2017)

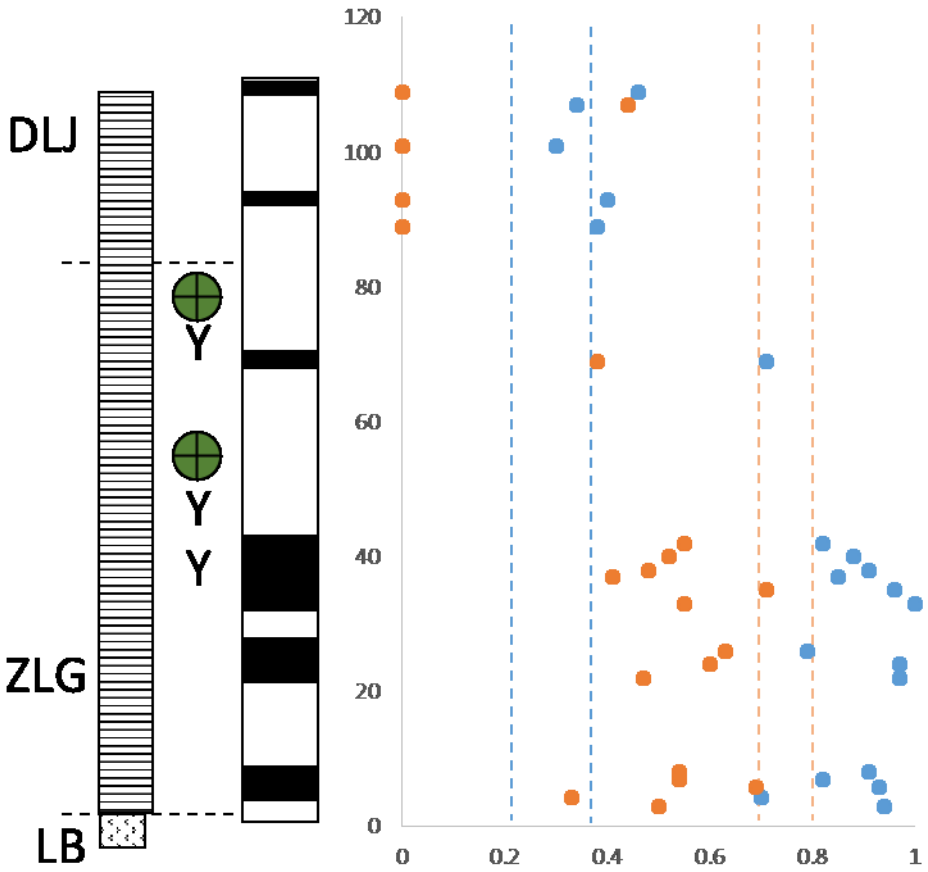

26) CJ1 and CJ2 drill cores, Hammarlund et al. (2017)

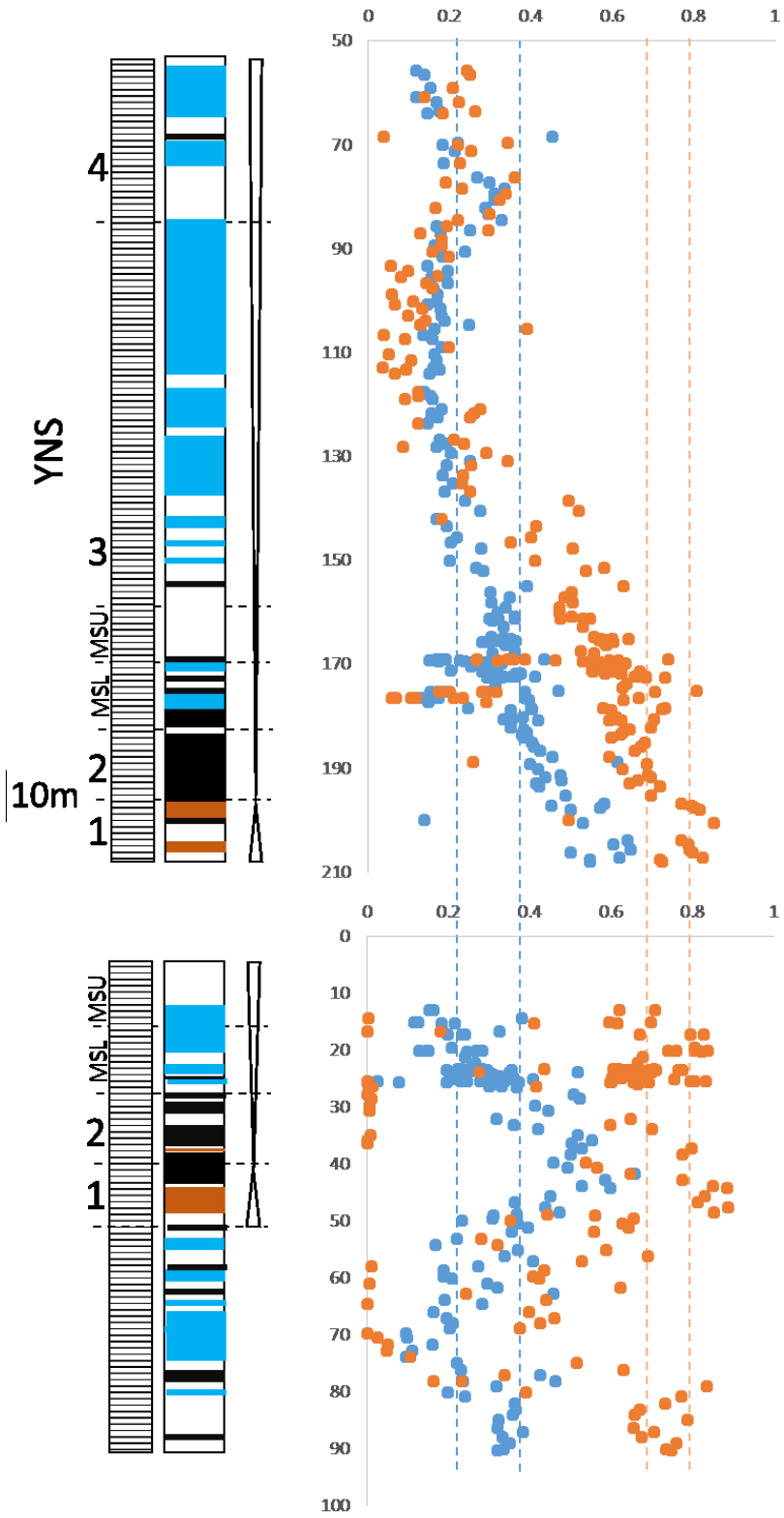

Figure 2.3 details (including additional details)

a) Goz Creek, Wernecke Mountains, Johnston et al. (2013)

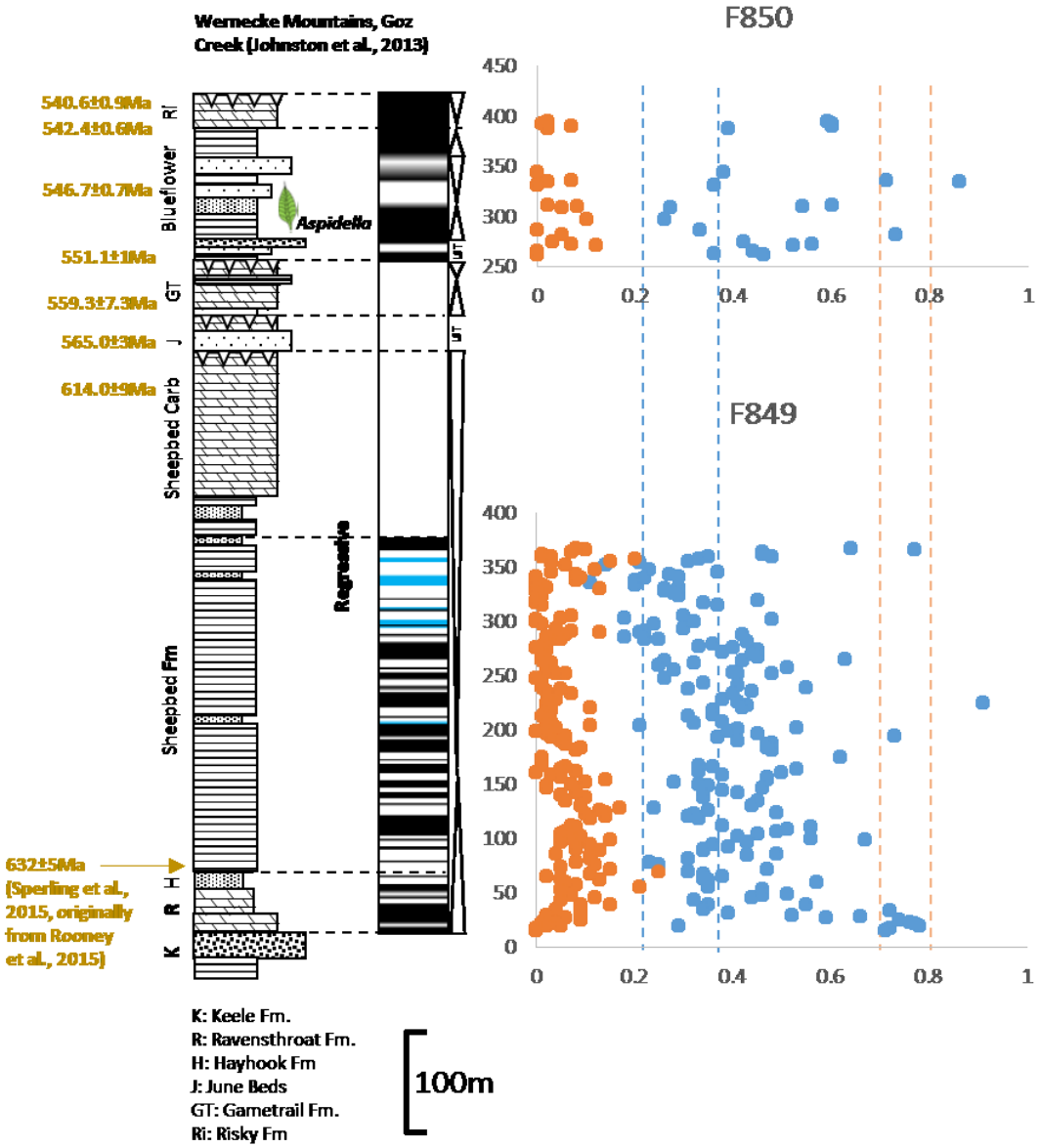

b) Sekwi Brook, Mackenzie Mountains, Sperling et al. (2015b)

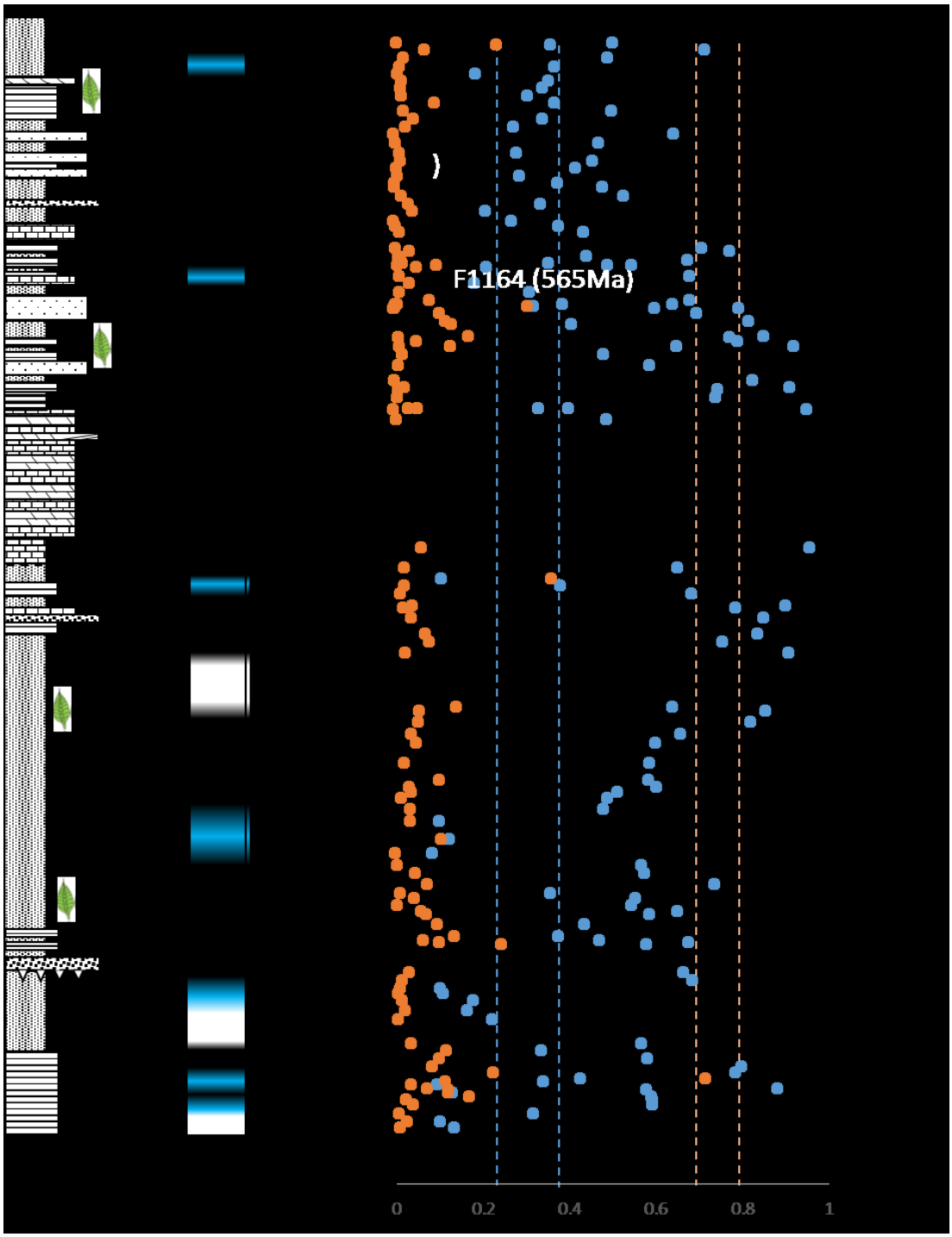

c) Cariboo Mountains, Canfield et al. (2008)

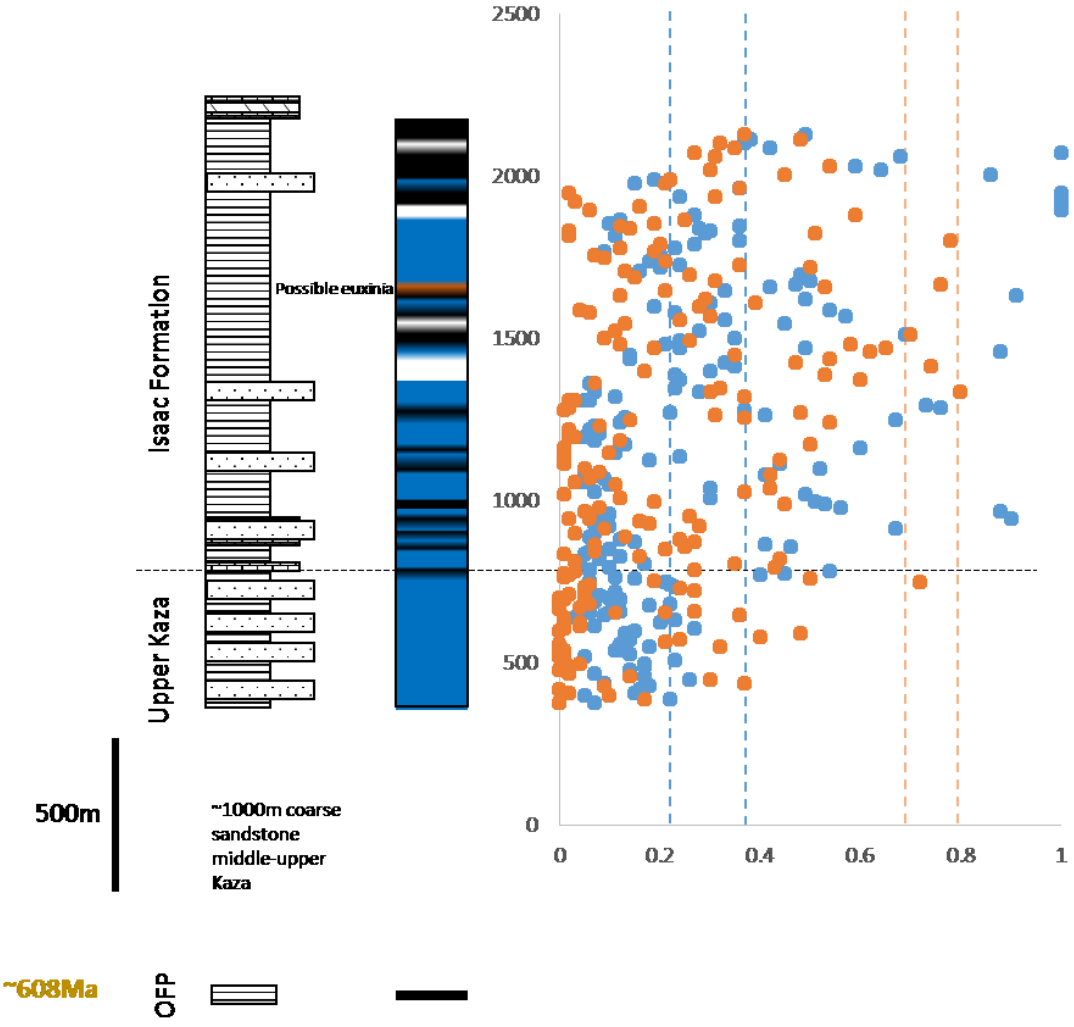

Re-Os age Kendall et al. (2004)

Note:
Only 1 sample with Fepy/FeHR >0.7 distinguished by FeHR/FeT > 0.38

d1) Stoneknife Creek, Northwest Territories, Miller et al. (2017), Shelf (Note: Almost all data collected indicate Fe/Al <0.44)

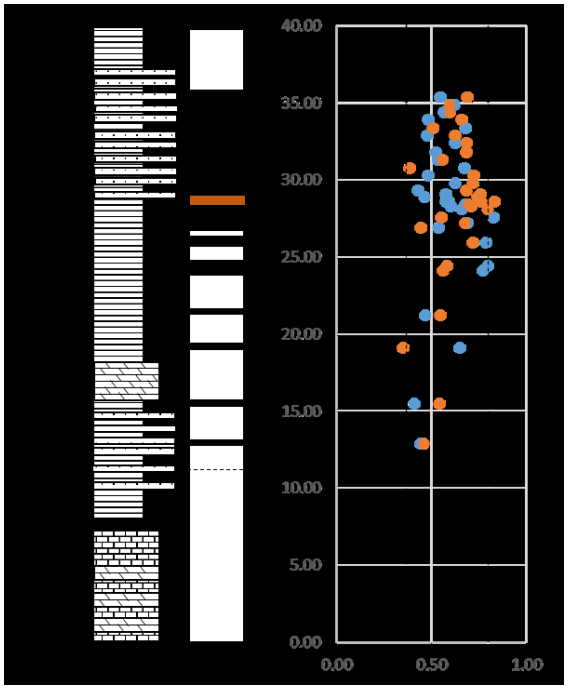

d2) Sheepbed Creek, Mackenzie Mountains, Northwest Territories, Miller et al. (2017), Shelf (Note: Almost all data collected indicate Fe/Al <0.44)

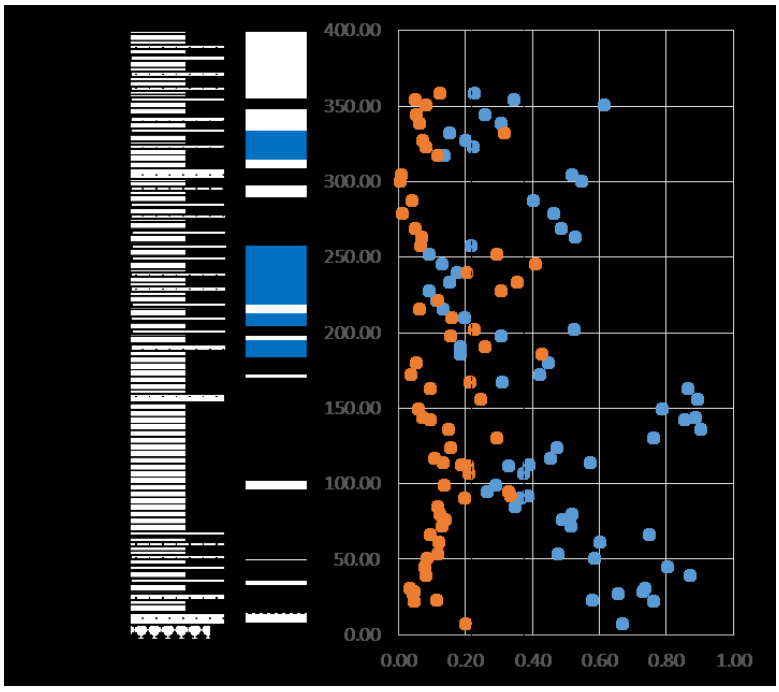

d3) Rackla, Yukon, Miller et al. (2017), Distal Slope, (Note: Almost all data collected indicate Fe/Al <0.44)

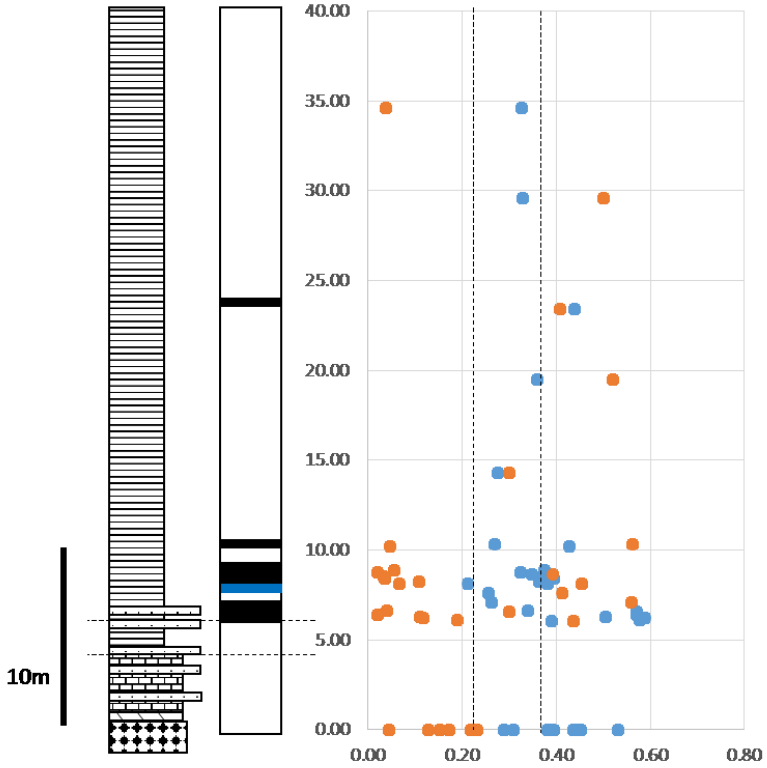

Figure 2.4 details

Newfoundland, Canfield et al. (2007)

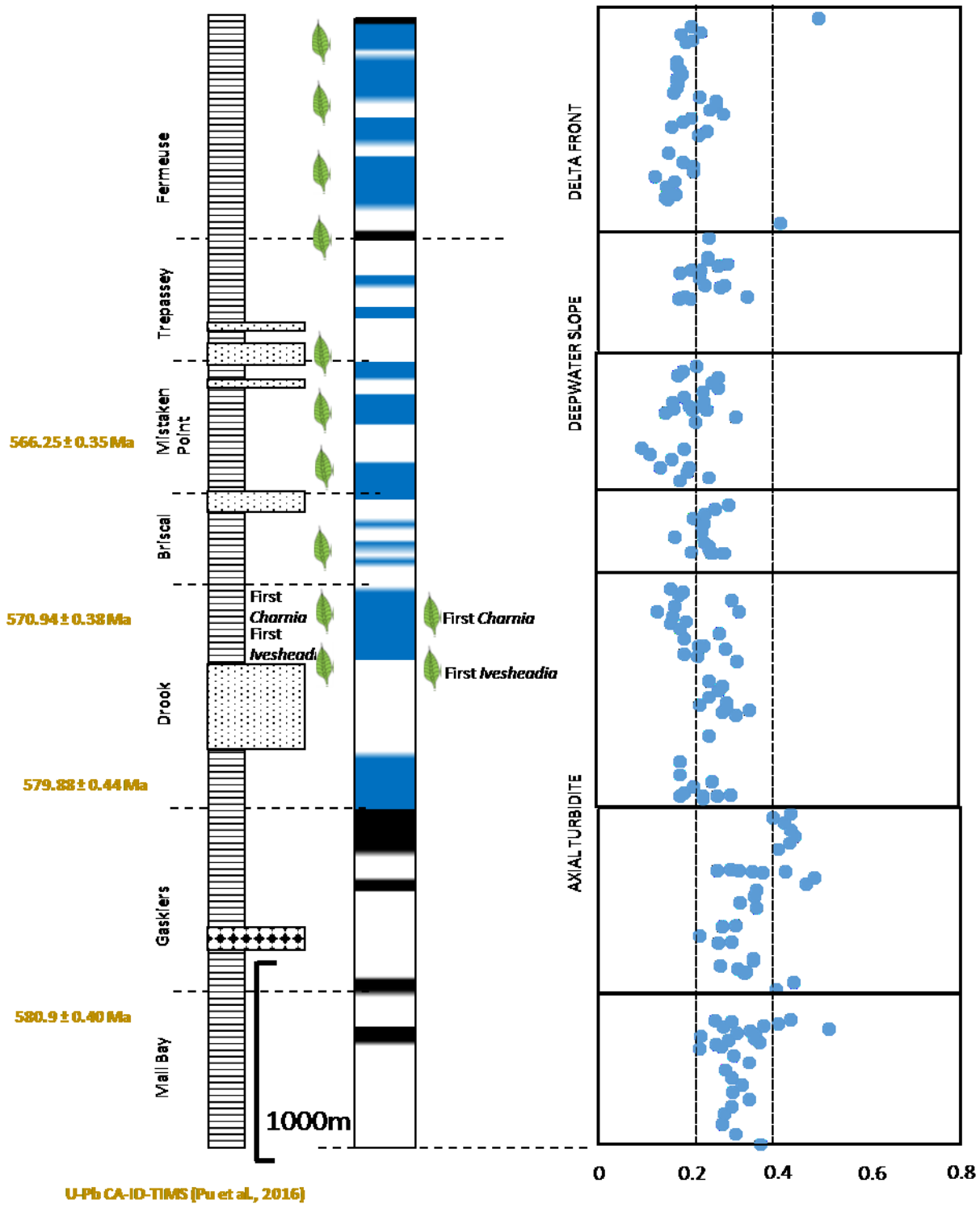

West Russia, Johnston et al. (2012)

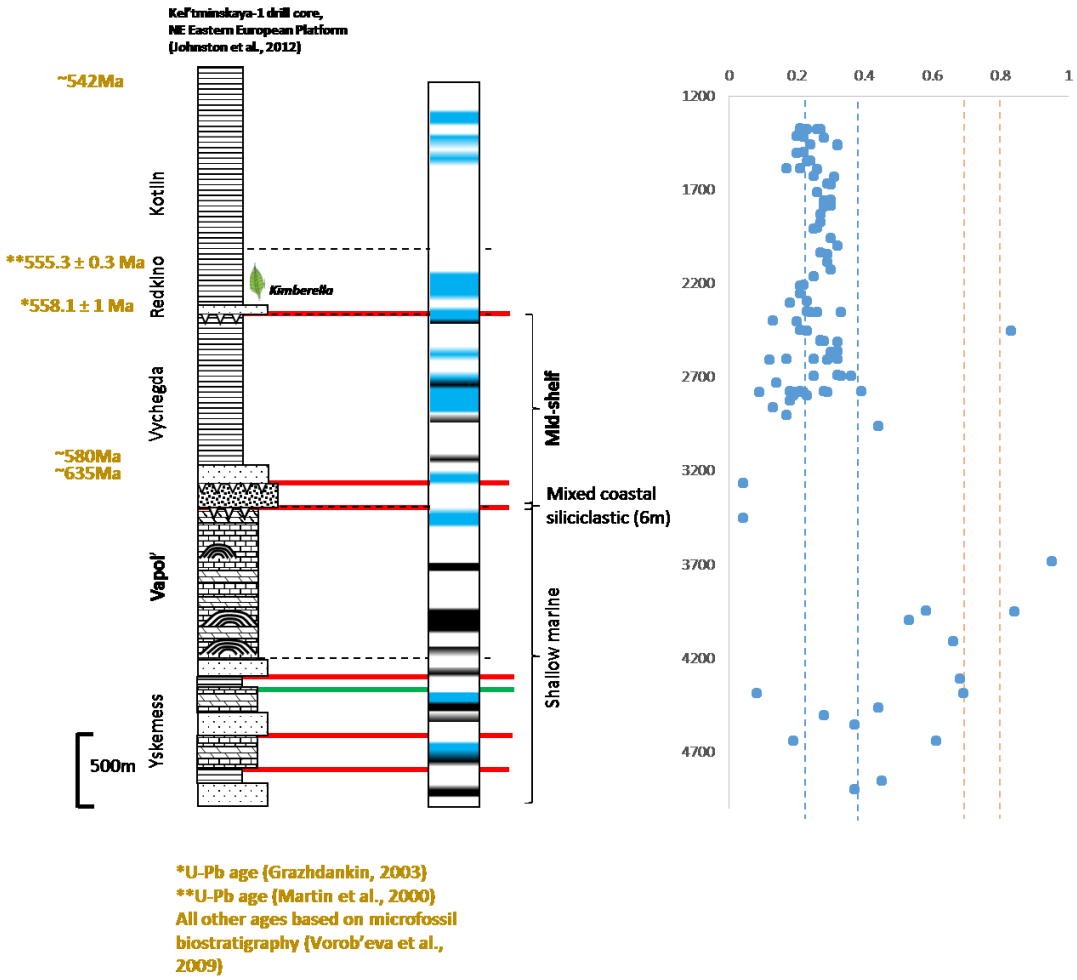

*U-Pb age (Grazhdankin, 2003)
**U-Pb age (Martin et al., 2000)
All other ages based on microfossil biostratigraphy (Vorob'eva et al., 2009)

Uruguay, Frei et al. (2013)

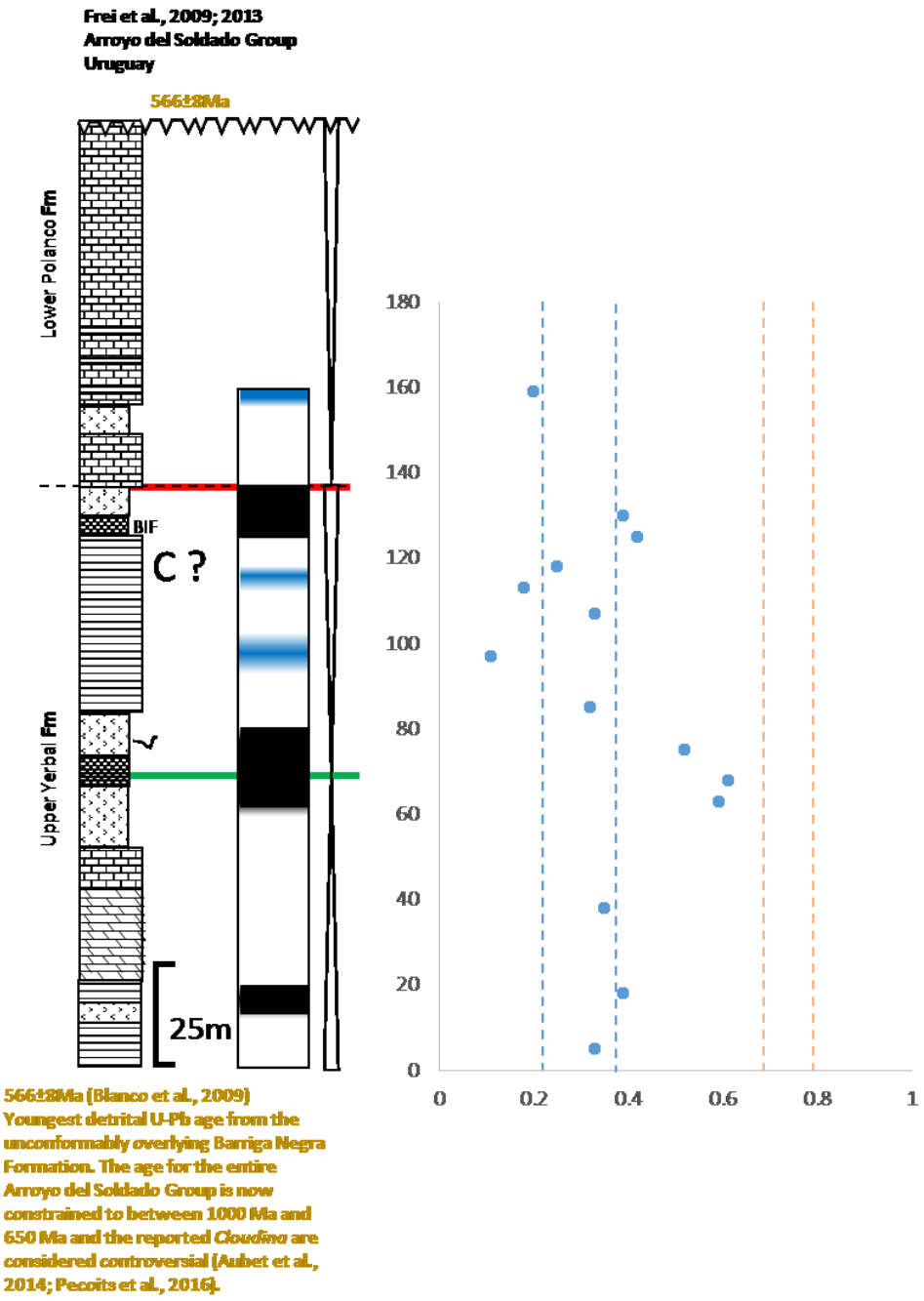

566±8Ma (Blanco et al., 2009) Youngest detrital U-Pb age from the unconformably overlying Barriga Negra Formation. The age for the entire Arroyo del Soldado Group is now constrained to between 1000 Ma and 650 Ma and the reported *Cloudina* are considered controversial (Aubet et al., 2014; Pecoits et al., 2016).

Figure 2.5 details (including additional details)

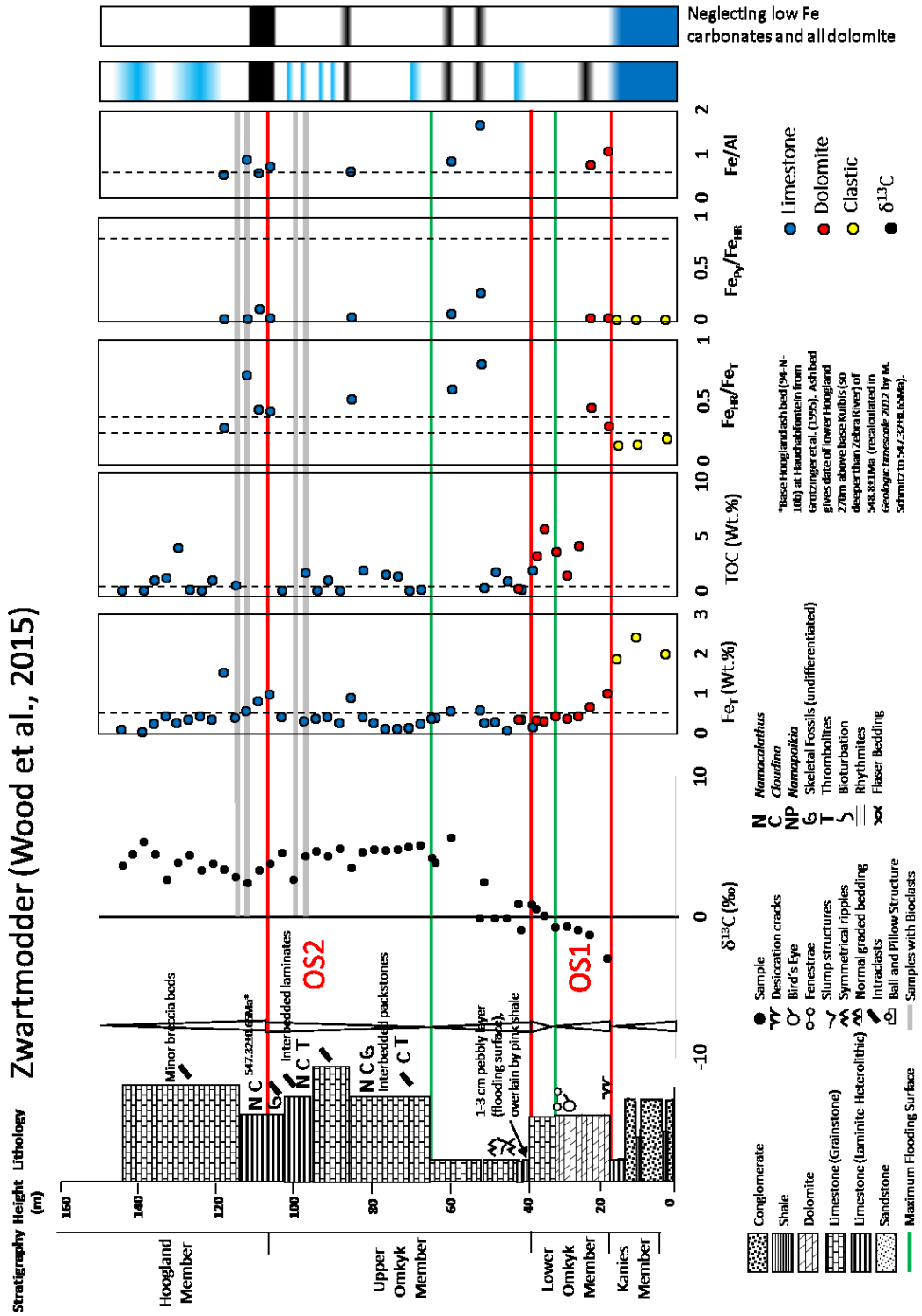

Wood et al. (2015); Tostevin et al. (2016b); this study

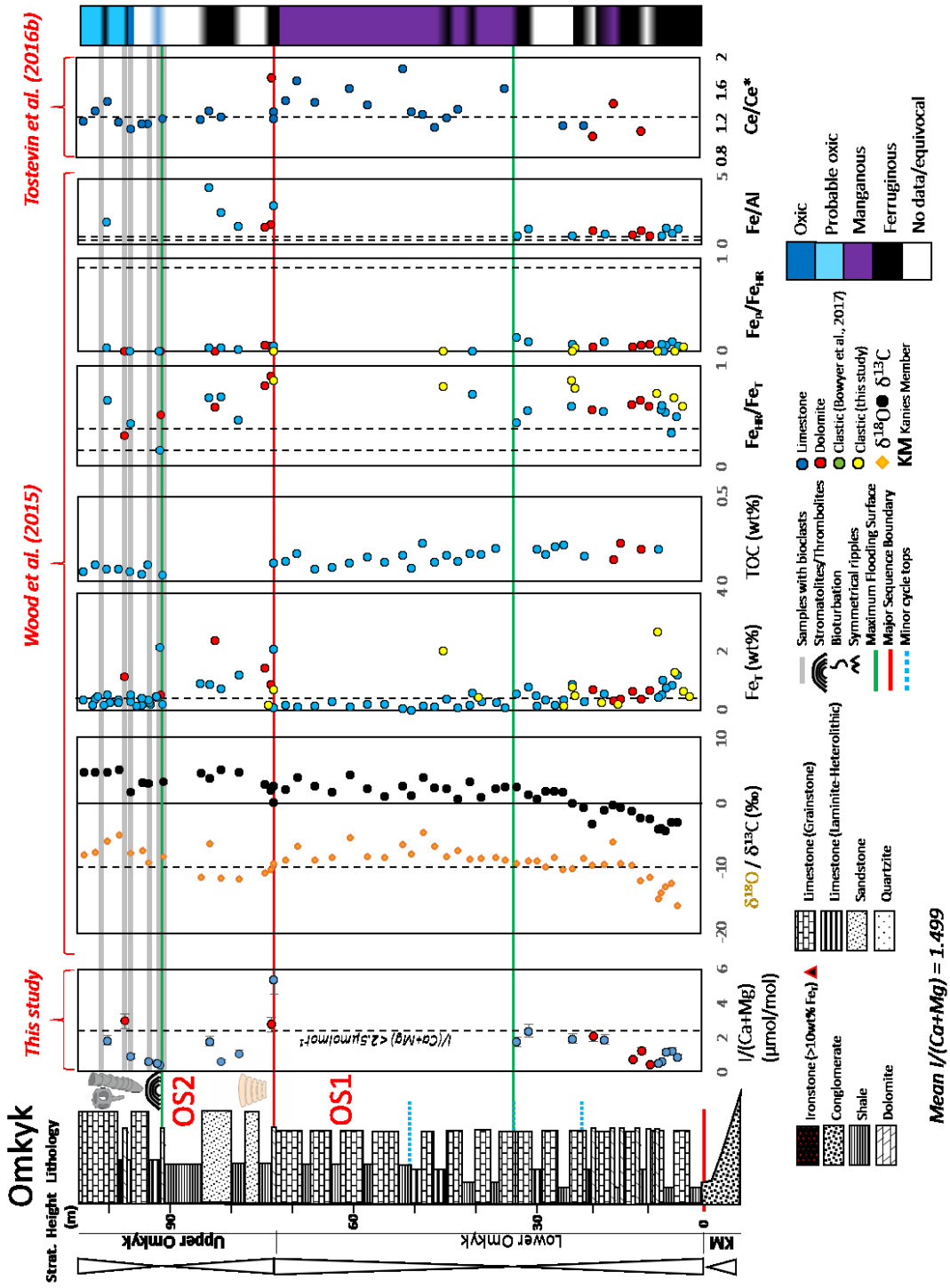

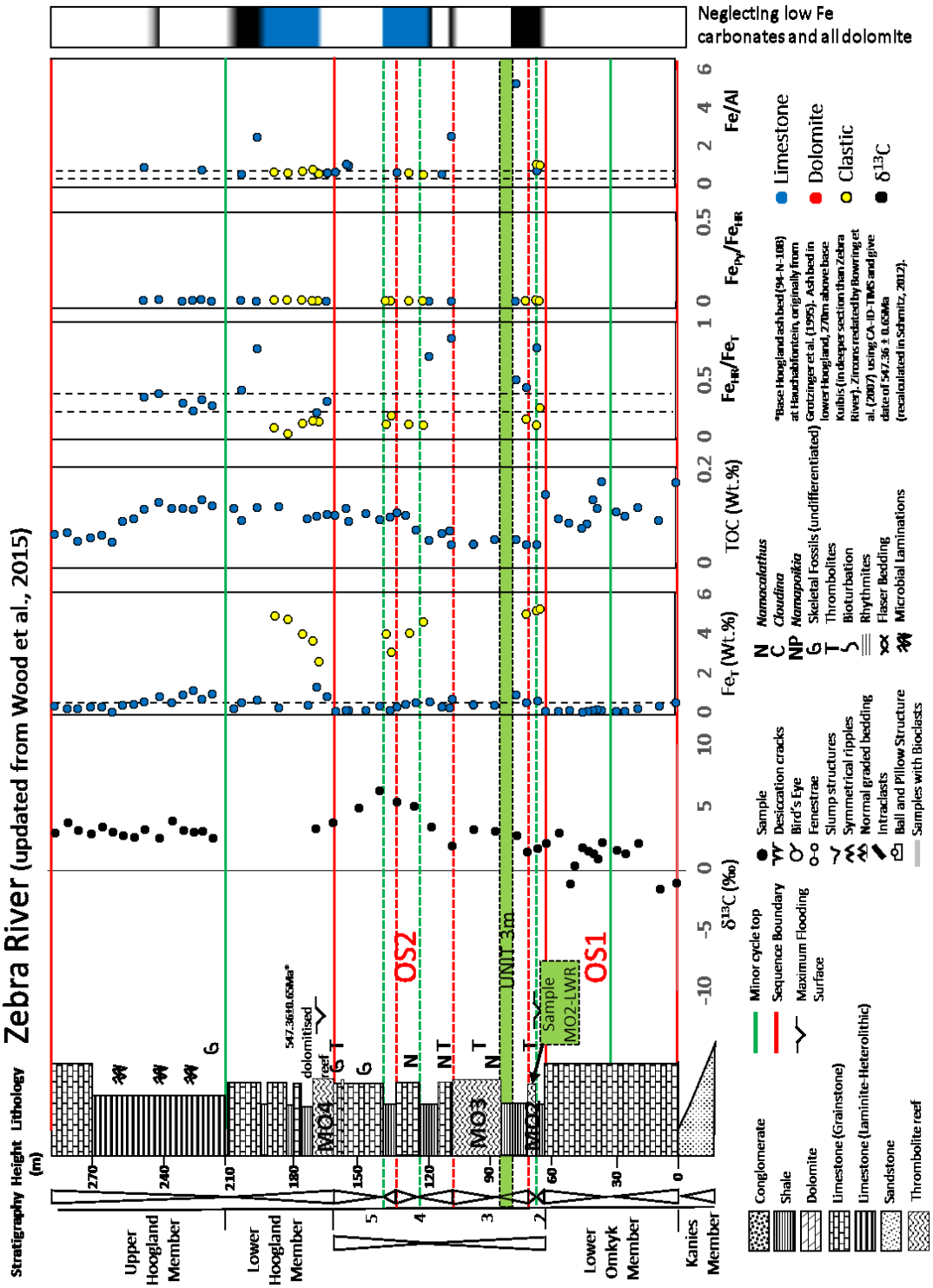
Zebra River (updated from Wood et al., 2015)
Stratigraphy
Height (m)
Lithology
Upper Hoogland Member
Lower Hoogland Member
Lower Omkyk Member
Kanies Member
547.36±0.65Ma*
dolomitised reef
MO4
MO3
MO2
OS2
OS1
UNIT 3m
Sample MO2-LWR
Neglecting low Fe carbonates and all dolomite
δ13C (‰)
FeT (Wt.%)
TOC (Wt.%)
FeHR/FeT
FePy/FeHR
Fe/Al
Limestone
Dolomite
Clastic
δ13C
Conglomerate
Shale
Dolomite
Limestone (Grainstone)
Limestone (Laminite-Heterolithic)
Sandstone
Thrombolite reef
Minor cycle top
Sequence Boundary
Maximum Flooding Surface
Sample
Desiccation cracks
Bird's Eye
Fenestrae
Slump structures
Symmetrical ripples
Normal graded bedding
Intraclasts
Ball and Pillow Structure
Samples with Bioclasts
Namacalathus
Cloudina
Namapoikia
Skeletal Fossils (undifferentiated)
Thrombolites
Bioturbation
Rhythmites
Flaser Bedding
Microbial Laminations
*Base Hoogland ash bed (94-N-108) at Haushabfontein, originally from Grotzinger et al. (1995). Ash bed in lower Hoogland, 278m above base Kuibis (in deeper section than Zebra River). Zircons redated by Bowring et al. (2007) using CA-ID-TIMS and give date of 547.36 ± 0.65Ma (recalculated in Schmitz, 2012).

Driedoornvlakte, Wood et al. (2015); Bowyer et al. (2017); this study

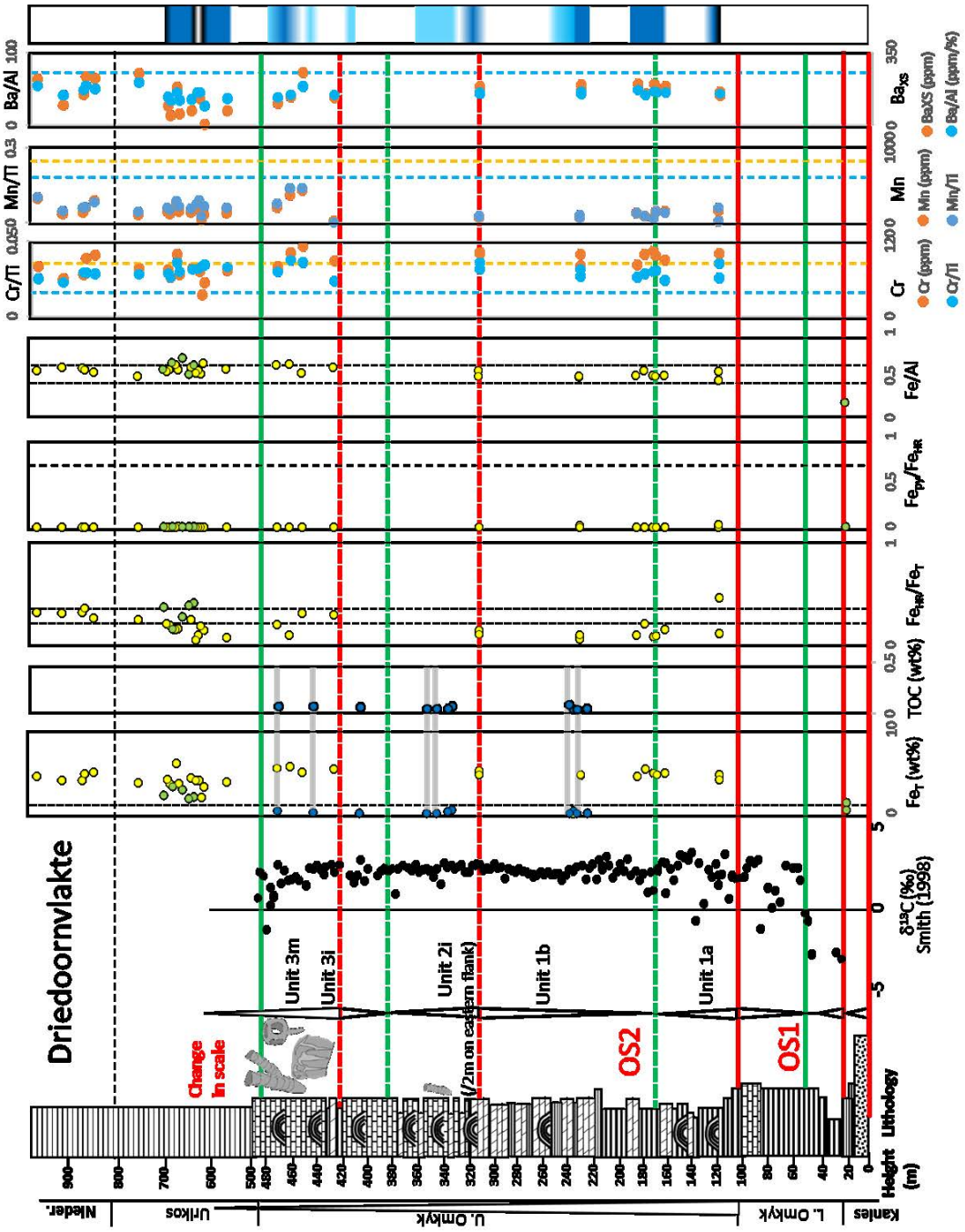

Brak, Wood et al. (2015)

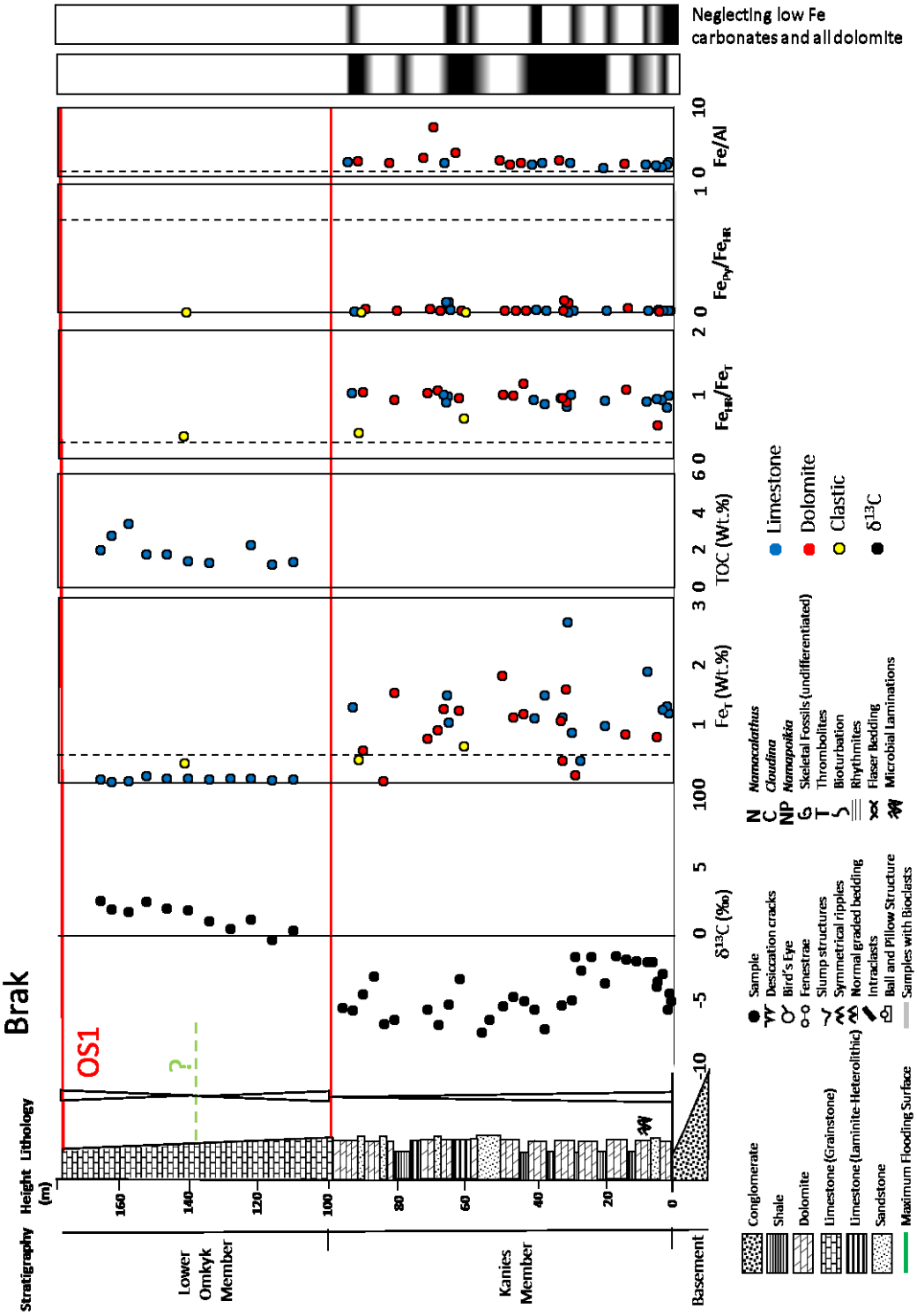

D850, Bowyer et al. (2017); this study

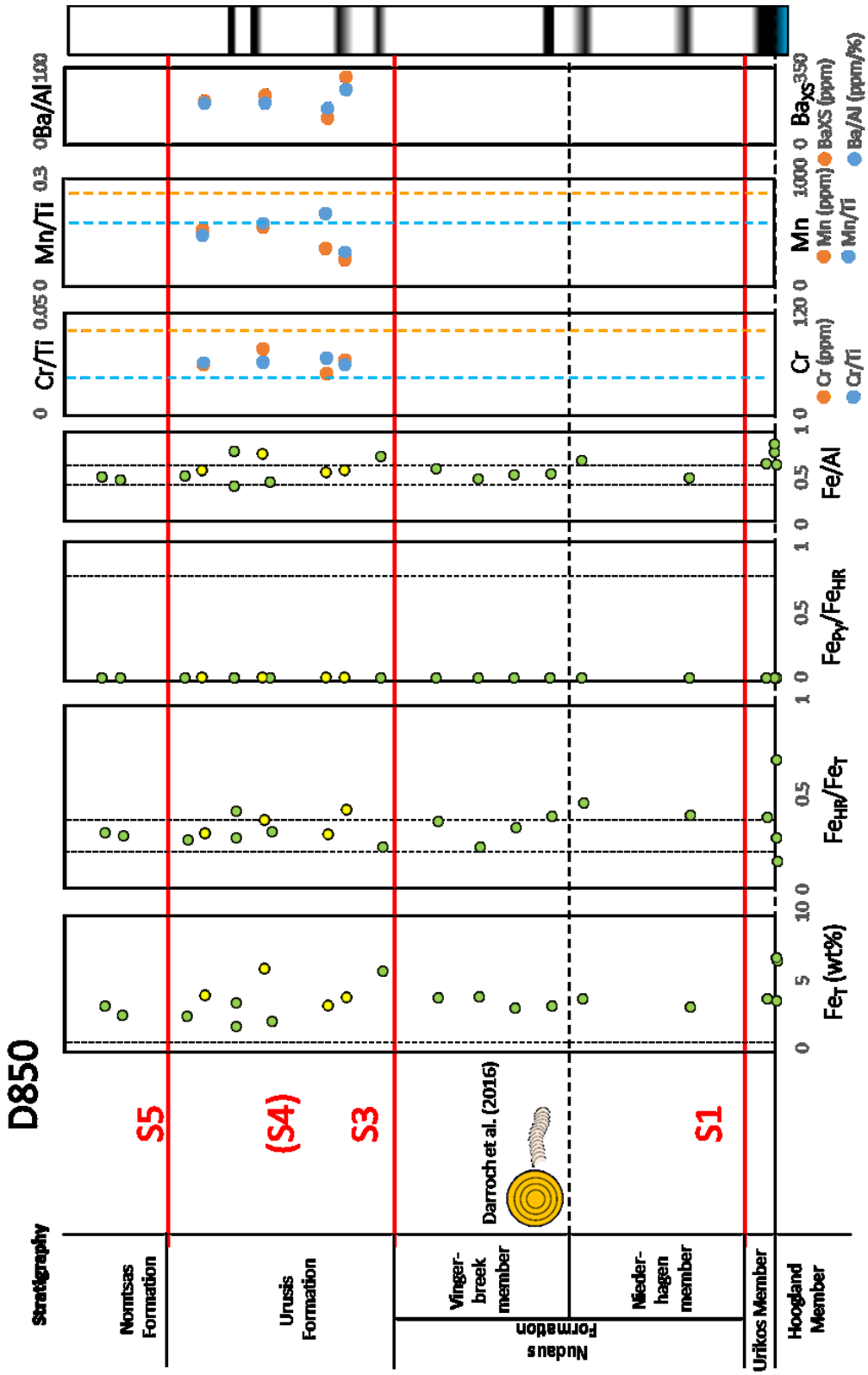

D860/C14, this study

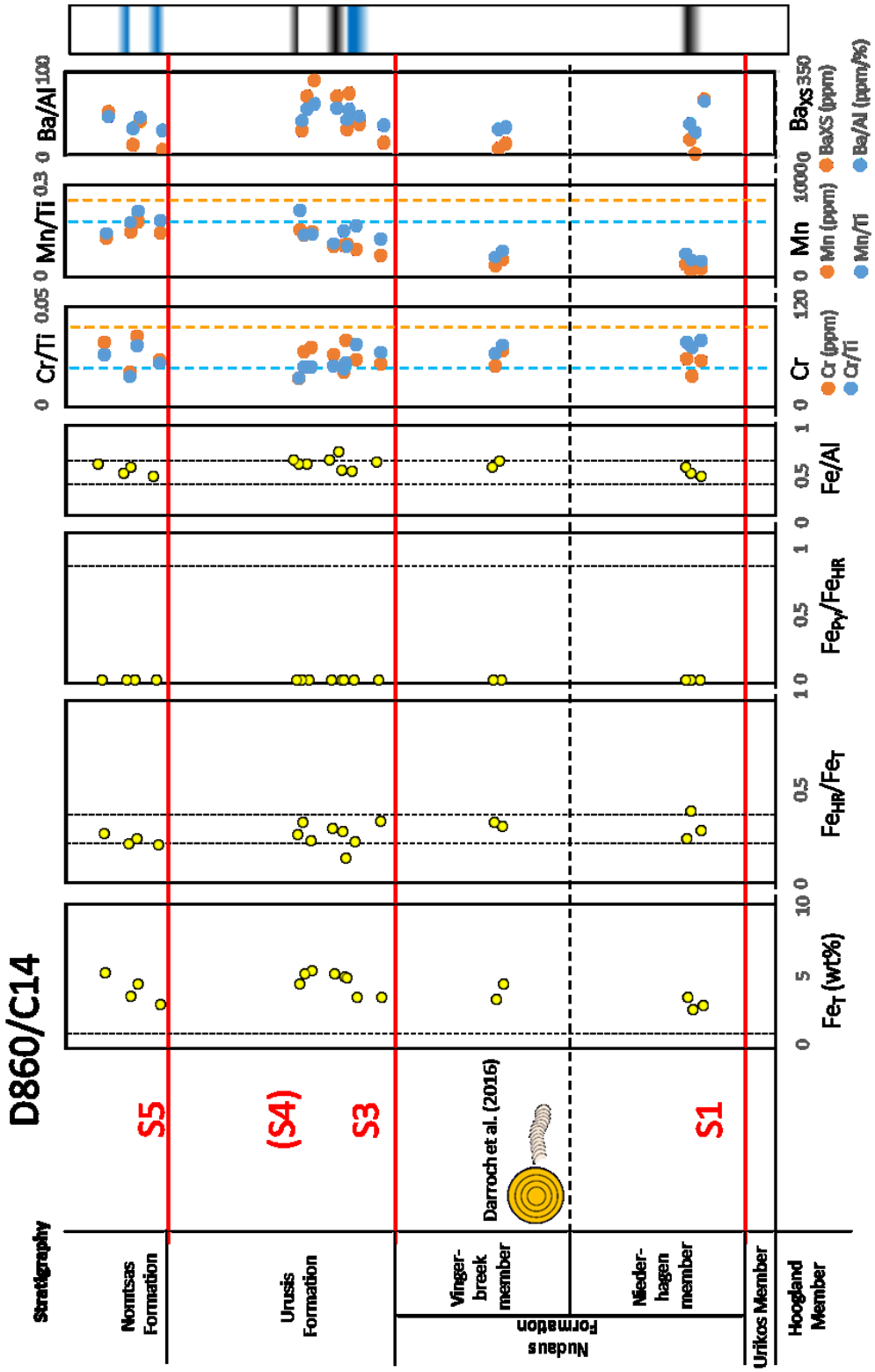

Arasab, Wood et al. (2015)

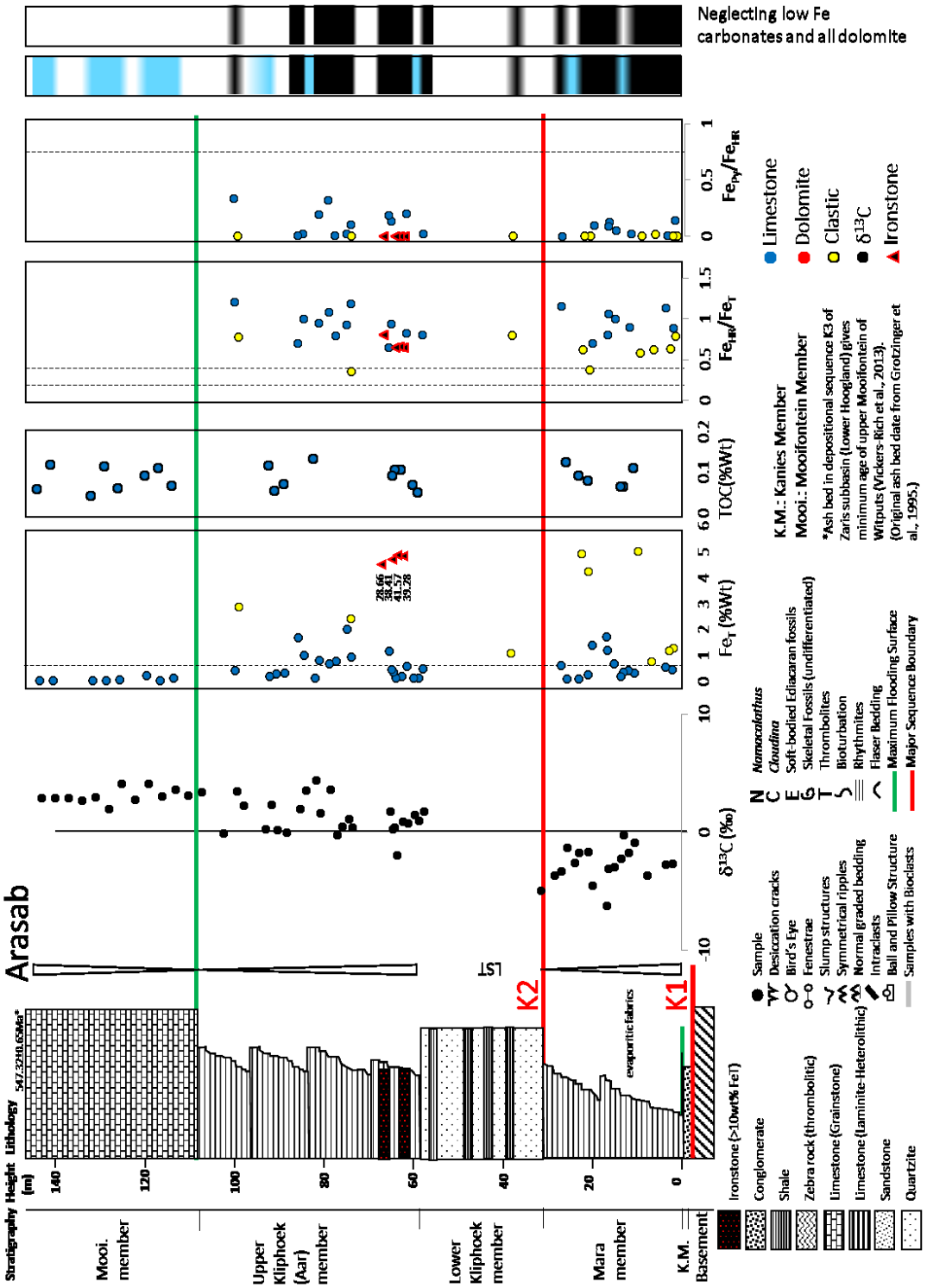

Grens, Wood et al. (2015)

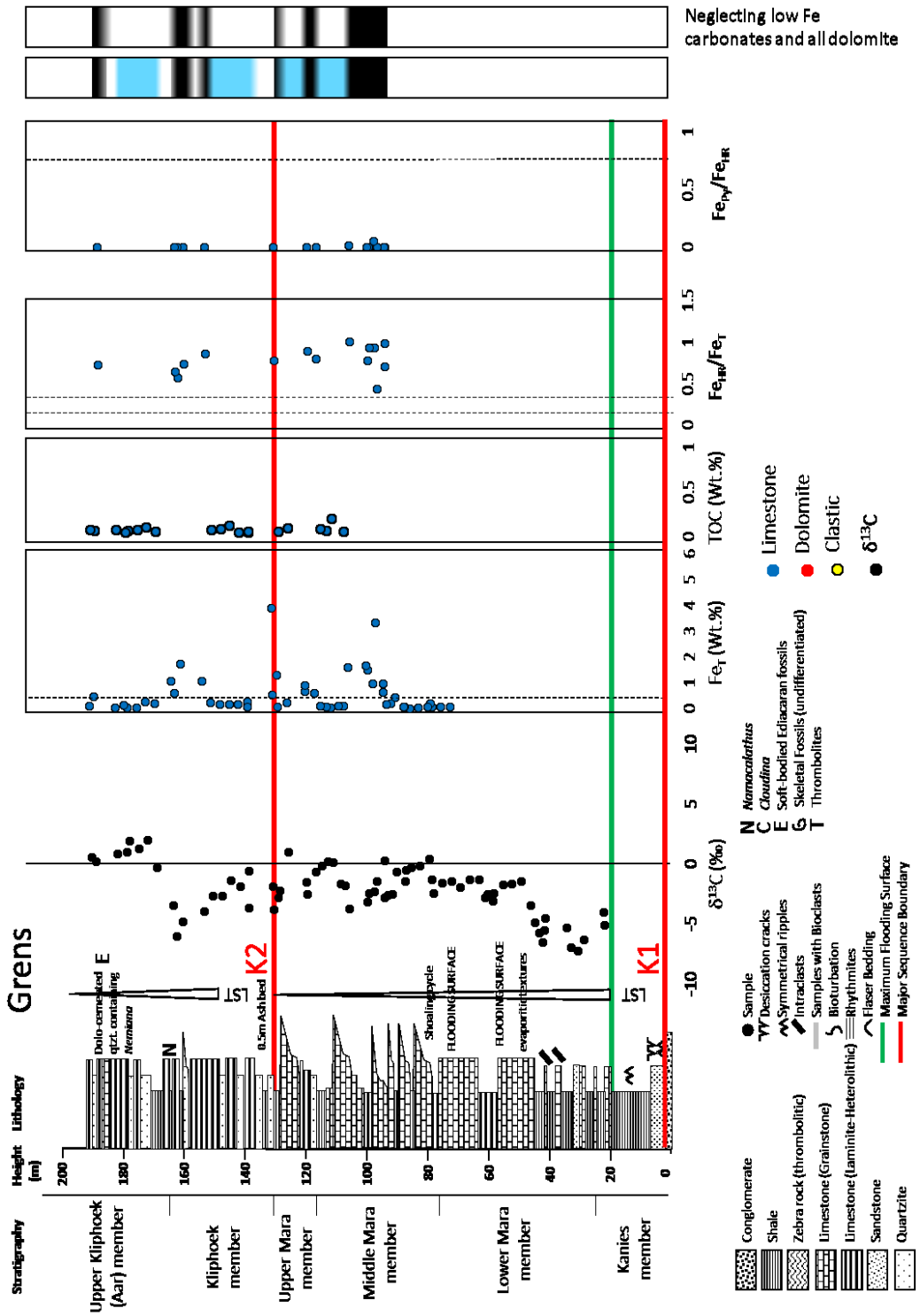

Farm Kliphoek, this study

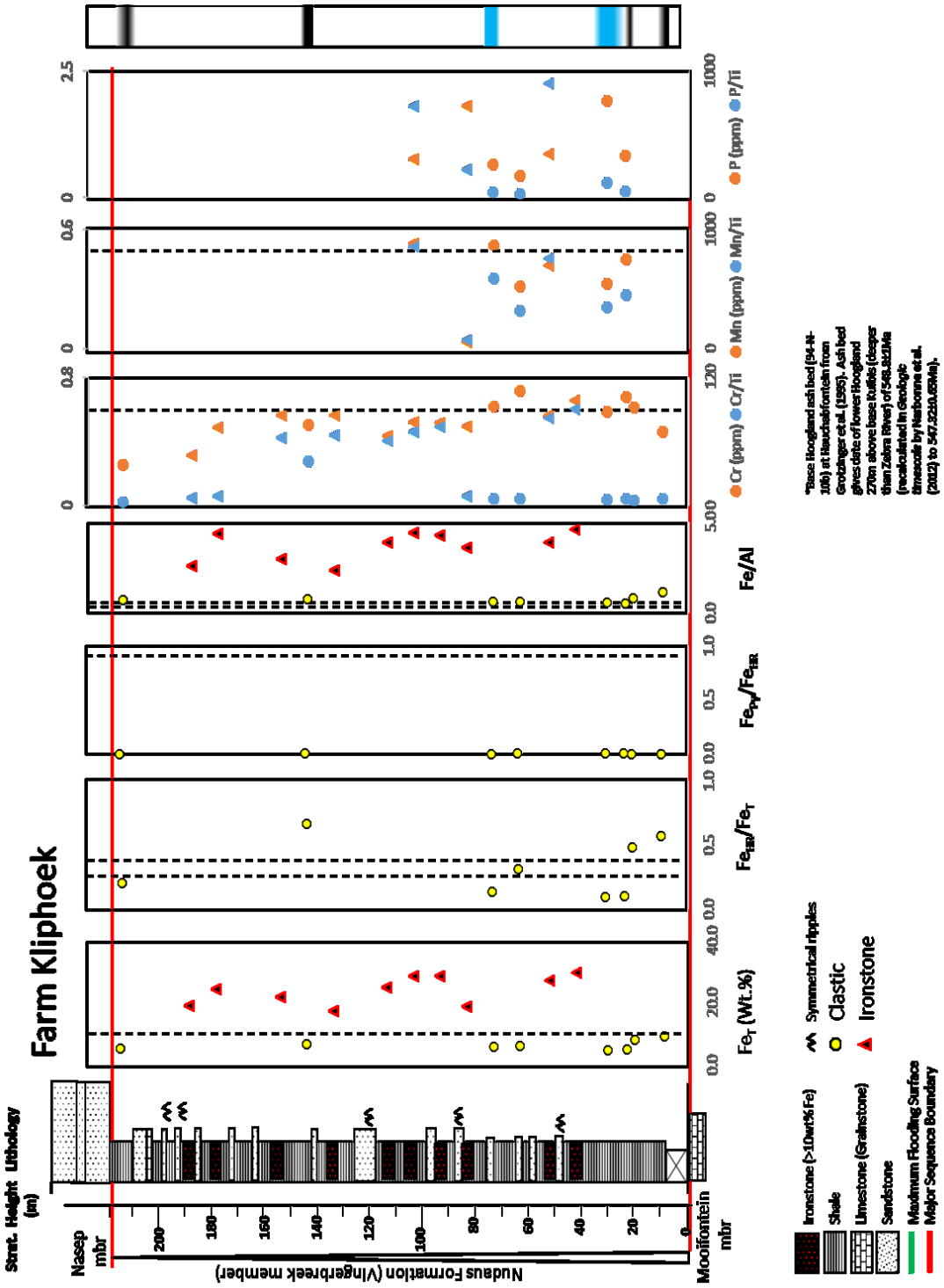

Pinnacle Reefs, Wood et al. (2015)

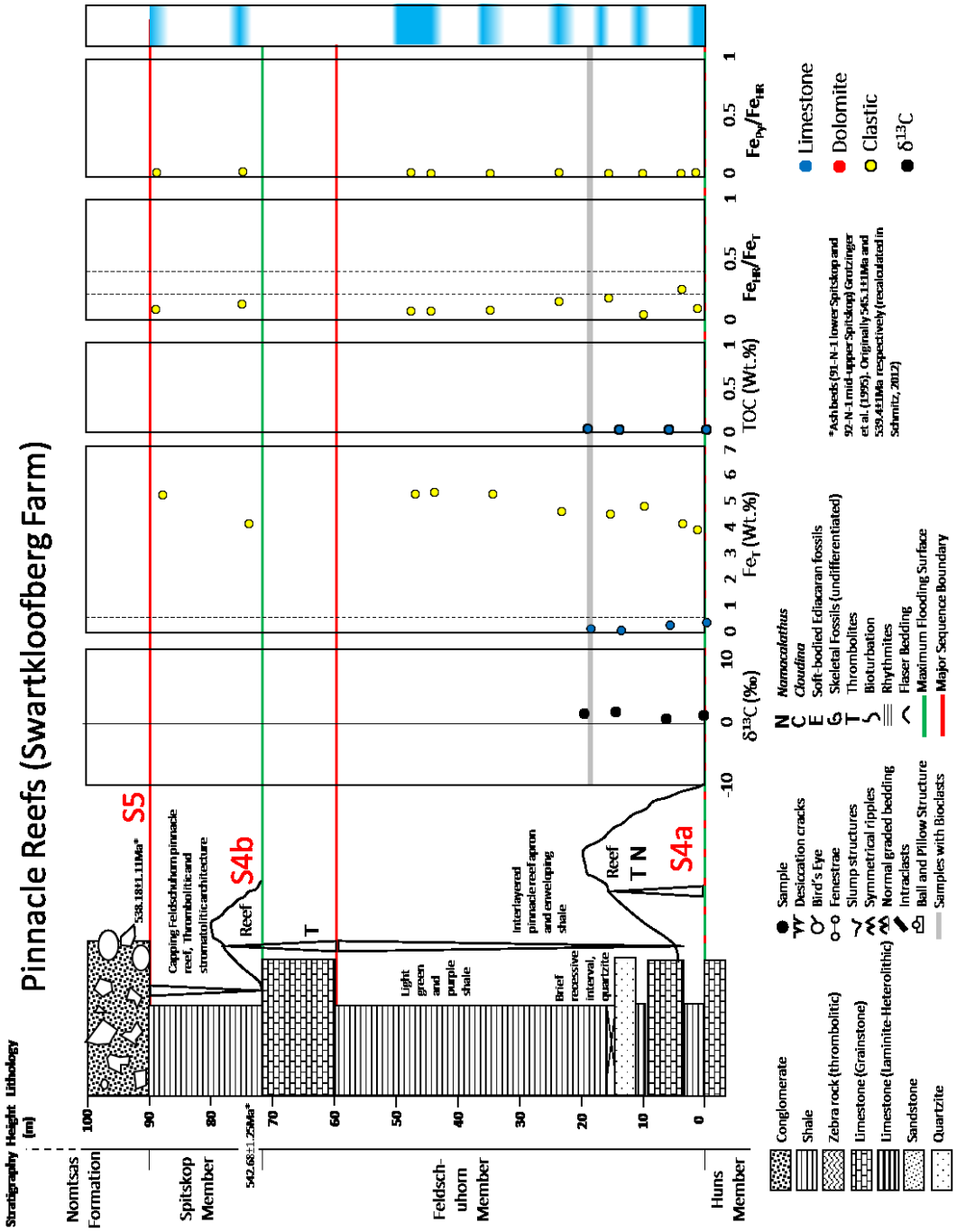

Swartpunt: Wood et al. (2015); updated with new CA-ID-TIMS ages

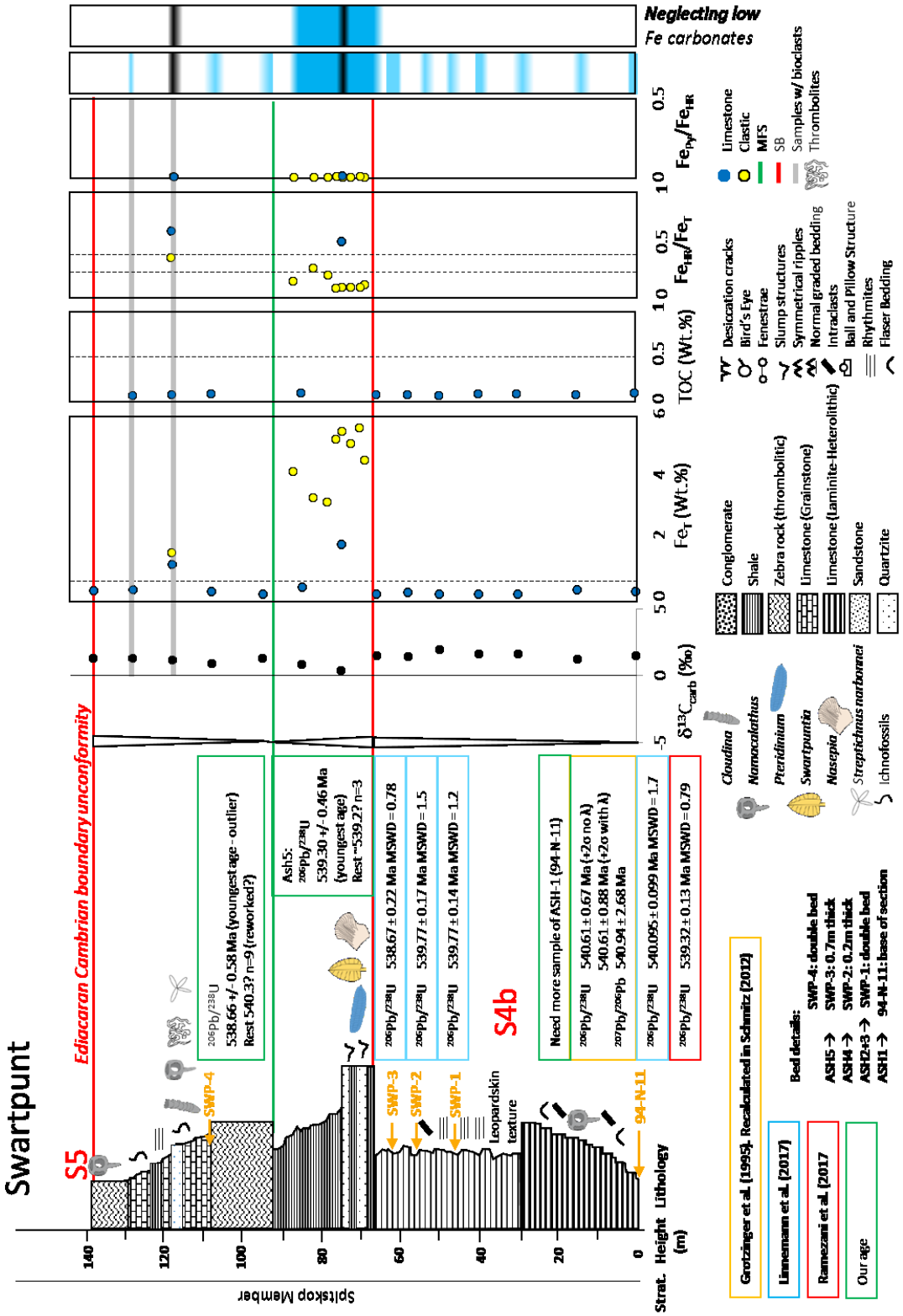

Swartpunt, Sperling et al. (2015a)

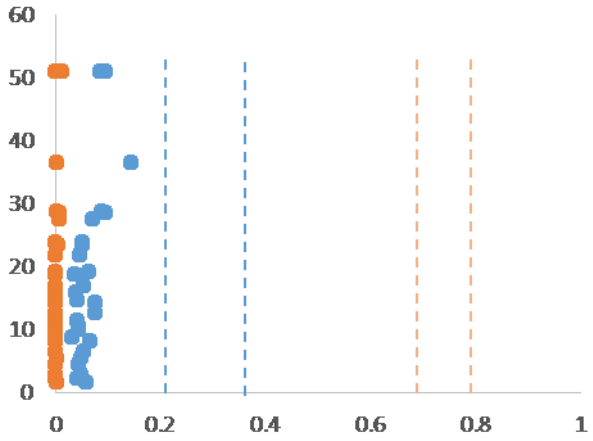

Zuurburg, Sperling et al. (2015a)

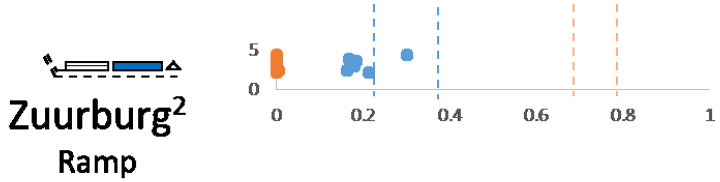

FSH, Sperling et al. (2015a)

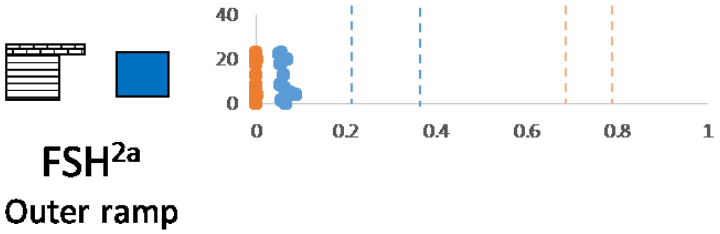

VF1, Sperling et al. (2015a)

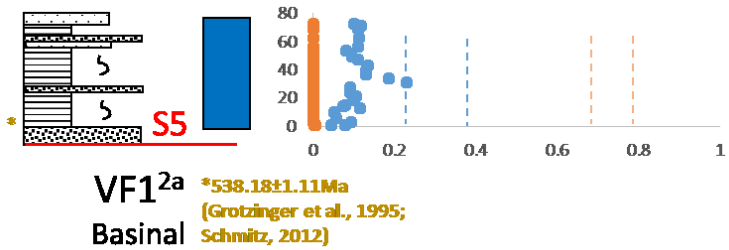

Figure 3.10a details

Previous attempts at integrated regional section correlation, employing carbon isotope chemostratigraphy and detailed sequence stratigraphic mapping have proved highly successful in the Nama and Witvlei Groups (Kaufman et al., 1991; Saylor et al., 1998). The resulting composite carbon isotope curve is characterised by four intervals of discrete and correlatable trends (Saylor et al., 1998) outlined below. The first (N_{pg}) interval is defined by negative $\delta^{13}C_{carb}$ values as low as -6 to -7‰ which gradually recover to 0‰ in the lower Kuibis Subgroup. The N_{pg} interval was recognised from postglacial stratigraphy of the Buschmannsklippe Formation in the Gobabis and Witvlei area to the east of Windhoek and the rising limb characterises sedimentary units in the overlying Dabis Formation (Kuibis Subgroup) in both Zaris and Witputs subbasin deposits. However, it is now considered likely that the unconformity at the base of the Nama Group in the Gobabis – Witvlei area represents a major hiatus (of up to 70 Myrs, K.-H. Hoffmann pers. comm.) and that the negative excursion recorded in the Buschmansklippe Formation may instead correlate with strata immediately post-dating Marinoan-age glacial diamictites, such as the Maieberg Formation deposited atop the Marinoan Ghaub diamictite on the Congo Craton which today outcrops in northwest Namibia (Halverson et al., 2005).

In the Witputs subbasin, the N_{pg} interval continues through sequence K1 and lower sequence K2 (Mara to Lower Kliphoek Members) of Saylor et al. (1995). The second (P_r) interval is defined by a rising limb from ~0‰ to maximum values in the range 4 to 5‰. The apex of this trend is recorded in the Omkyk Member of the Zaris Formation (Kuibis Subgroup) and is followed by a gradual decline in $\delta^{13}C_{carb}$ (P_f interval), culminating in a brief return to mildly negative values in the Upper Zaris Formation. The P_f interval (which largely corresponds to sequence K3) is notably absent from stratigraphy of the Witputs subbasin and K2 is capped by an erosive unconformity, infilled by Nudaus Formation sediments (Saylor et al., 1998). Stratigraphy of the overlying Schwarzrand Subgroup is largely siliciclastic, however where carbonate horizons are present (predominantly Huns and Spitskop Members of the Urusis Formation), $\delta^{13}C_{carb}$ values remain positive and relatively invariant, conforming to the globally-recognisable late Ediacaran positive carbon isotope plateau (EPIP, Zhu et al., 2006).

Recently, carbon isotopic data published by Wood et al. (2015), in addition to data of Smith (1998) from the Driedoornvlakte carbonate platform have greatly increased the chemostratigraphic resolution of the Nama Group. Furthermore, iron speciation and $\delta^{13}C_{carb}$ data reported by Wood et al. (2015) were collected in tandem from sampled sections, thus allowing relative sample position to be approximated between sections across the subbasin divide.

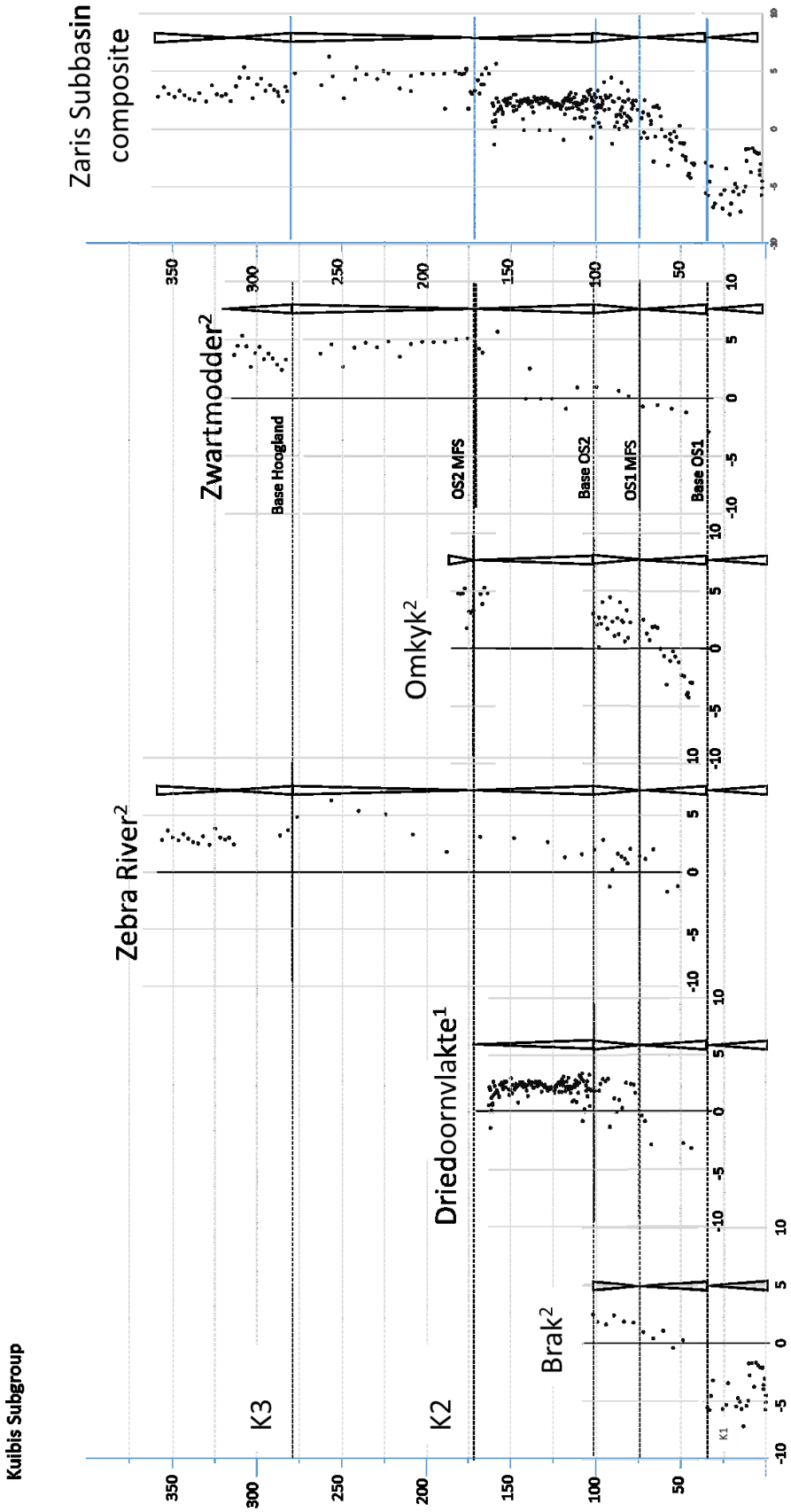
Kuibis Subgroup
Zaris Subbasin composite
Zwartmodder2
Omkyk2
Zebra River2
Driedoornvlakte1
Brak2
Base Hoogland
OS2 MFS
Base OS2
OS1 MFS
Base OS1
K3
K2
K1

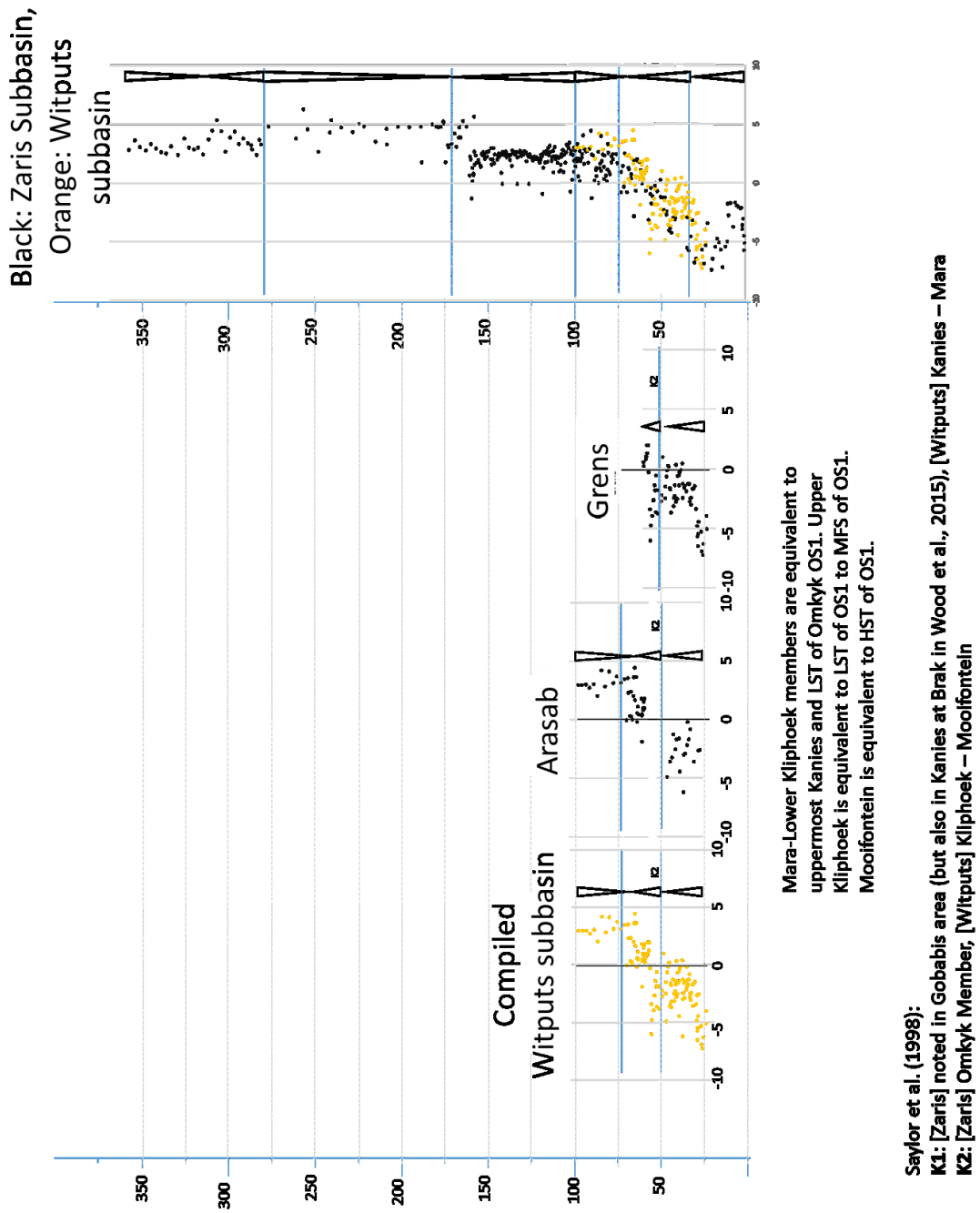

Figure AA1. Carbon isotopic data of carbonates from sections of the Kuibis Subgroup in the Zaris subbasin plotted against relative height and tied to sequence stratigraphy (data from [1]Smith, 1998 and [2]Wood et al., 2015).

Figure AA2 (this page). Carbon isotopic data of carbonates from sections of the Kuibis Subgroup in the Witputs subbasin plotted against relative height and tied to sequence stratigraphy (data from Wood et al., 2015).

Figures AA1 and AA2 illustrate section correlation in the Kuibis Subgroup of the Zaris and Witputs subbasins respectively. The most negative $\delta^{13}C_{carb}$ reported from Brak (-7.4‰) and Grens (-7.25‰) are lower than values reported from the N_{pg} interval of Saylor et al. (1998). Particularly, the record at Brak appears to show a 'double-dip' whereby an initial increase in $\delta^{13}C_{carb}$ from -5.73‰ to -1.68‰ in the lower Kanies Member is followed by a falling trend to the most negative values. As such, the lower Kanies Member at Brak is considered to represent the oldest transgressive unit of the classic Nama Group sampled to date and the $\delta^{13}C_{carb}$ nadir preserves the expression of the Shuram – Wonoka excursion on the Kalahari Craton as previously proposed (Saylor et al., 1998; Wood et al., 2015).

Another prominent feature of the composite carbon isotope curve is the abrupt decrease from positive to negative $\delta^{13}C_{carb}$, followed by an apparent jump back to positive values (at ~120m relative height). This is suggested to represent an artefact of the high resolution $\delta^{13}C_{carb}$ record of Smith (1998) whereby an rate of tectonic subsidence during transgression following Omkyk OS2, Unit 3m resulted in a rapid deepening in the vicinity of Driedoornvlakte. The brief shift to negative $\delta^{13}C_{carb}$ may therefore relate to a localised deepening at the maximum flooding surface coupled to organic carbon remineralisation at depth. In contrast, carbon isotop values in correlative shallower sections (e.g. Zebra River) remain positive until the upper Hoogland Member (K3) where a short-lived negative excursion has been previously reported by Saylor et al. (1998).

Nama Group Geochronology

Approximately twenty silicified volcanic tuff deposits are distributed throughout the Nama Group and have provided the basis for attempts at chemically constraining sequence stratigraphic architecture in addition to yielding zircons for radiometric dating (Grotzinger et al., 1995; Saylor, 2003; Saylor et al., 2005; Bowring et al., 2007). Only one ash bed (94-N-10B) is well documented from the Kuibis Subgroup and lies at the base of the Hoogland Member in the Zaris subbasin (Grotzinger et al., 1995). However, a second possible ash layer has been reported within the lower Kliphoek Member at Farm Grens (Wood et al., 2015) and, if confirmed as volcanic in origin, this bed would (according to carbon isotope chemostratigraphy) be the oldest ash deposit in the Nama Group. The overlying Schwarzrand Subgroup is host to the remaining nineteen ash beds, the majority of which are concentrated in the upper Urusis Formation and the stratigraphically highest of which (92-N-1) lies in the Nomtsas Formation immediately above the Ediacaran-Cambrian boundary unconformity (Grotzinger et al., 1995; Saylor, 2003; Saylor et al., 2005). Figure AA3 shows the distribution of volcanic tuff deposits pinned to

individual host sequences in the Nama Group after Saylor (2003) and Saylor et al. (1998; 2005) and tied to relative position in a composite carbon isotope profile (Saylor et al., 1998; Wood et al., 2015).

Zircon U-Pb ID-TIMS data are published for four of these ash layers: 94-N-10B, 91-N-1, 94-N-11 and 92-N-1, marked as black pins on Figure AA3 (Grotzinger et al., 1995; Bowring et al., 2007). More recently however, re-dating of two ash beds (94-N-11 and 92-N-1) alongside data from three additional beds were presented at the International Symposium on the Ediacaran-Cambrian transition in St. John's, Newfoundland (June, 2017) (Linnemann et al., 2017; Ramezani et al., 2017) and, whilst these data remain unpublished, they are presented in Figure AA3 with accompanying 2σ uncertainties (where available).

It is important to note that the resulting compilation of radiometric ages represents a mixture of legacy data (Grotzinger et al., 1995) and data for which the justifications for age interpretations remain unpublished to date (Linnemann et al., 2017; Ramezani et al., 2017). The past twenty years have seen rapid advancements in isotope dilution methods, isotopic tracers, instrumentation and knowledge of the uranium decay constant which together raise a number of uncertainties that must be acknowledged when integrating new and legacy data.

Firstly, the U-Pb zircon data of Grotzinger et al. (1995) are the product of an older pre-treatment method which utilised air abrasion to remove portions of the zircon crystals which had undergone open system behaviour and Pb-loss. An updated chemical abrasion method (CA-ID-TIMS, Mattinson, 2005) has since become standard practice for isotope dilution geochronology and has been employed in all subsequent zircon dating analyses of Nama Group tuff deposits (Bowring et al., 2007; Linnemann et al., 2017; Ramezani et al., 2017). This is most significant when attempting to integrate data from 91-N-1 (lower Spitskop Member), where the only available age constraint is provided by an air abrasion ID-TIMS $^{207}Pb/^{206}Pb$ age of 542.68 ± 2.80 Ma (Grotzinger et al., 1995; recalculated with updated U decay constant of Mattinson, 2010 by Schmitz, 2012) and 92-N-1 (lower Nomtsas), where 2σ uncertainties and redated CA-ID-TIMS ages remain unpublished (Ramezani et al., 2017).

Differences in the ionisation potentials of U and Pb and complications associated with correcting for element/mass bias mean that it is not possible to directly measure the relative concentrations of U and Pb via isotope ratio mass spectrometry (Condon et al., 2015). Mixed tracer solutions for U-Pb geochronology (^{235}U - ^{233}U - ^{205}Pb (- ^{202}Pb)) are calibrated such that their isotopic ratios are known to a very high precision (Condon et al., 2015). Zircon crystals which have undergone chemical abrasion and total dissolution are spiked using mixed tracer solutions prior to column chemistry and ratios of $^{206}Pb/^{207}Pb$ and $^{238}U/^{235}U$ are subsequently measured via thermal ionisation mass spectrometry

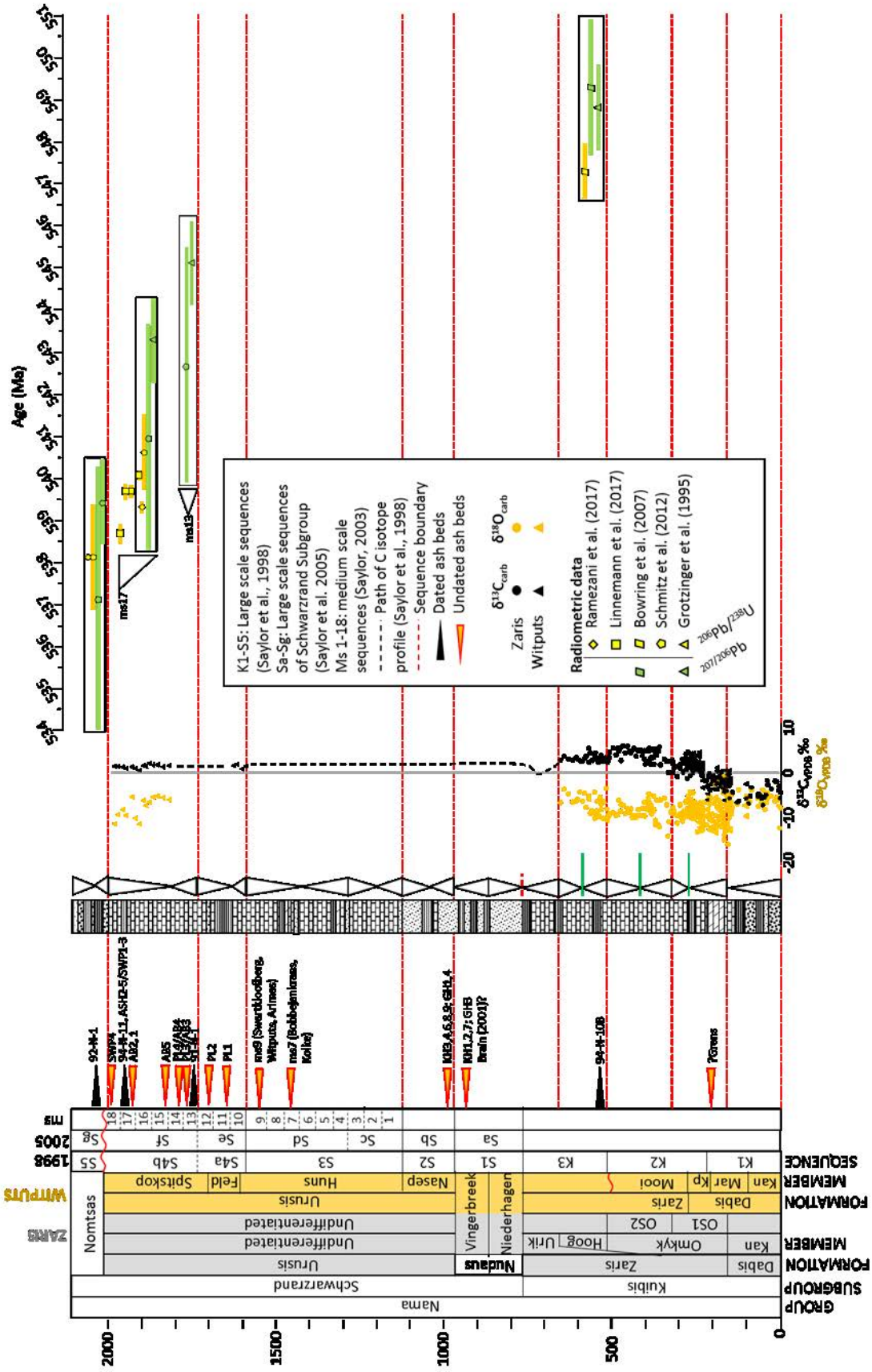

Figure AA3. Positions and radiometric data for ash beds of the Nama Group.

(TIMS). In this way, the U/Pb ratio of the sample is determined relative to that of the well-characterised tracer solution, allowing for the accuracy of the tracer to directly control that of the sample U/Pb ratio (Condon et al., 2015). In the past ten years, concentrated efforts have resulted in the successful calibration of inter-laboratory U-Pb tracers (e.g. EARTHTIME ET535 and double-spike ET2535) (Condon et al., 2015; McLean et al., 2015). Mass-dependent fractionation during TIMS analysis also contributes a significant proportion of the analytical uncertainty for low-blank measurements and are corrected for through use of a double-spike tracer (e.g. ET2535, ^{235}U - ^{233}U - ^{205}Pb - ^{202}Pb). Double-spike tracers incorporate a precisely calibrated ratio of synthetic or artificially enriched isotopes (e.g. ^{202}Pb and ^{205}Pb) from which the measured deviation is indicative of the mass fractionation during TIMS analyses (Rudge et al., 2009).

The isotopic data presented in Grotzinger et al. (1995) represent a mixture of multigrain and single grain analyses and interpreted ages are presented for both the ^{206}Pb/^{238}U and ^{207}Pb/^{206}Pb chronometers. All other ages presented in Figure AA3 are the products of ^{206}Pb/^{238}U data derived from the weighted means of numerous single grain CA-ID-TIMS analyses (Bowring et al., 2007; Linnemann et al., 2017; Ramezani et al., 2017). In contrast to all other ash bed ages in the Nama Group, the accuracy of 206Pb/238U data presented in Grotzinger et al. (1995) was not constrained by measurements of the isotopic ratio of EARTHTIME tracers and therefore, the comparison between the ash bed dates of Grotzinger et al. (1995) and subsequent dates (Bowring et al., 2007; Linnemann et al., 2017; Ramezani et al., 2017) requires the integration of systematic errors relating to the calibration of the tracer used by Grotzinger et al. (1995). Unfortunately, details of the tracer employed are not reported by Grotzinger et al. (1995). Whilst ^{207}Pb/^{206}Pb ages do not suffer the uncertainties associated with tracer calibration, they remain limited by uncertainties in the U decay constant ratio (Mattinson, 2010). The ^{207}Pb/^{206}Pb ages of Grotzinger et al. (1995) shown in Figure AA3 are supplemented by recalculated values based upon the updated high precision U decay constant ratio of Mattinson (2010) (Schmitz, 2012).

Numerous additional advancements have been made in mass spectrometry since the isotopic measurements of Grotzinger et al. (1995) including the use of high purity zone-refined rhenium ribbon as filament material for TIMS analyses which replaces older, lower purity Re filaments. It is difficult to quantify the effect this has had on the precision of ^{205}Pb measurements, however older Re filaments commonly incorporated trace thallium resulting in interference on the 205Pb peak. Other improvements include higher sensitivity ion-counters and low-noise signal amplifiers for analysis of very low U and Pb concentrations alongside ionisation of U and Pb as UO_2^+ through filament loading in a matrix of phosphoric acid and silica gel (Gerstenberger and Haase, 1997). The benefits of ionisation as UO_2^+

(after correction for isobaric interference by variable $^{18}O/^{16}O$) include lower filament temperature for ionisation and reduced filament blank contribution (Gerstenberger and Haase, 1997; Condon et al., 2010; Condon et al., 2015). In sum, significant improvements in isotope dilution geochronology have been made in the twenty three years since the first Nama ash bed ages were published (Grotzinger et al., 1995) and many of these changes remain underestimated uncertainties when integrating legacy ages with those provided by updated methods.

Of the ash bed ages presented in Figure AA3, only 91-N-1 remains undated via CA-ID-TIMS and age data (including 2σ uncertainty) remain unpublished for 92-N-1 (Ramezani et al., 2017). In theory then, it should be possible to directly integrate all ash bed 206Pb/238U ages with the exception of 91-N-1 and 92-N-1. However, whilst the standardised CA-ID-TIMS technique and inter-lab use of the calibrated EARTHTIME mixed tracer solutions should result in negligible inter-laboratory differences in interpreted U-Pb dates for a homogeneous zircon population, procedural modifications in some geochronology laboratories (e.g. 12 hour HF pre-leach at 210°C versus 180°C) introduce new uncertainties. The justification for these minor inter-laboratory differences remain unpublished and their influence upon the resulting U-Pb age determinations are unknown.

Figure 5.1 details

U-Pb ages

518.03 ± 0.71 Ma: CA-ID-TIMS U-Pb age (incorporating U-Pb tracer calibration uncertainty) of detrital zircons from the Maotianshan shale immediately underlying Chengjiang biota. Taken as maximum depositional age for the Chengjiang biota. (Yang et al., 2018)

526.5 ± 1.10 Ma: SHRIMP U-Pb age for the base of the Shiyantou Formation, bed 9 of the Meishucun section, Yunnan Province, South China (Compston et al., 2008)

530.02 ± 1.20 Ma: zircon U-Pb air abrasion ID-TIMS age. Approximate age of the Chapel Island Formation lithofacies association (Member) 5 (Mystery Lake Member) after regional litho- and biostratigraphic correlation (Landing, 1991, 1994) with sections in Saint John, New Brunswick (Middle part of trace fossil zone *Rusophycus avalonensis*, Plancentian Series) (Isachsen et al., 1994; recalculated in Schmitz, 2012).

538.18 ± 1.24 Ma: zircon U-Pb air abrasion ID-TIMS age of an ash bed (92-N-1) in the lower Nomtsas Formation exposed on Swartkloofberg Farm, west of Swartpunt (Grotzinger et al., 1995, recalculated in Schmitz, 2012)

539.4 ± 2.90 Ma: SHRIMP U-Pb age of bentonites, Zhongyicun Member of the Zhujiaqing Formation, bed 5 at Meishucun section, Yunnan Province, South China (Compston et al., 2008). This date constrains the upper limit for the BACE at no later than 536.5 Ma.

538.67 ± 0.22 Ma: zircon U-Pb CA-ID-TIMS age of the second highest ash bed exposed in the upper Spitskop Member of the section on Farm Swartpunt (unpublished data presented at ISECT 2017, Linnemann et al., 2017)

540.61 ± 0.88 Ma: zircon U-Pb air abrasion ID-TIMS age of an ash bed (94-N-11) in the upper Spitskop Member at the base of the section on Farm Swartpunt (Grotzinger et al., 1995, recalculated in Schmitz, 2012)

542.68 ± 2.80 Ma: zircon $^{207}Pb/^{206}Pb$ air abrasion ID-TIMS age of an ash bed (91-N-1 or BZS-7) in the lower Spitskop Member on Farm Witputs (Grotzinger et al., 1995, recalculated in Schmitz, 2012)

545.67 ± 0.66 Ma: zircon U-Pb CA-ID-TIMS age of an ash bed in the lower Liuchapo Formation, deep slope Longbizui section, Hunan Province, South China (Yang et al., 2017)

551.09 ± 1.02 Ma: zircon U-Pb CA-ID-TIMS age of an ash in Doushantuo Member IV (Miaohe Member) at Jiuqunao section, Hubei Province (Yangtze Gorges area), South China (Condon et al., 2005, recalculation within error of original value and 2σ from Schmitz, 2012)

Last Appearance:

Cloudina

Kalahari Craton: The last appearance datum of *Cloudina* in the Nama Group is tightly constrained between the upper Spitskop age of 538.67 ± 0.22 Ma and the lower Nomtsas age of 538.18 ± 1.24 Ma, however this constraint is weakened by the lack of suitable lithologies for *Cloudina* preservation in the Nama Group after deposition of the upper Spitskop limestone. Nomtsas and overlying Formations all represent siliciclastic deposition.

Southeast Siberian Platform: The last appearance datum of *Cloudina* in the southeastern Siberian Platform is constrained by carbon isotope chemostratigraphy to below the BACE and specimens co-occur

with the most basal SSFs of the *Anabarites trisulcatus* assemblage in the Ust'-Yudoma Formation below the regionally extensive sub-Tommotian unconformity (Zhu et al., 2017).

South China: Extinction of *Cloudina* in South China is in the Gaojiashan Member, Shaanxi Province, constrained below the BACE but above the ~551 Ma ash bed for the Upper Doushantuo Member IV (Miaohe) at Jiuqunao section, Hubei Province (Condon et al., 2005).

First Appearances:

Treptichnus isp.

Kalahari Craton: FAD of *Treptichnus isp.* in Nama Group deposits of lower Huns Member (Jensen and Runnegar, 2005). This outcrop is bounded above and below by dated ash beds (540.61 ± 0.67 and 538.18 ± 1.11 Ma) (Grotzinger et al., 1995, recalculated in Schmitz, 2012)

Parasammichnites pretzeliformis

Kalahari Craton: FAD of *P. pretzeliformis* in the shallow (wave dominated) coarse clastic deposits of the lower Spitskop Member near Koelkrans (southeast Witputs subbasin) (Buatois et al., 2018). This outcrop is conformable with deposits to the west which have been dated with a lower and upper age of 542.69 ± 1.25 and an upper age of 538.18 ± 1.11 Ma (Grotzinger et al., 1995; recalculated in Schmitz, 2012).

Lamonte trevallis

Yangtze Block: *L. trevallis* is restricted to laminated bituminous limestone deposits of the Shibantan Member (Dengying Formation) which are loosely constrained based upon regional correlation to dated ash beds of eastern Yunnan (Jiucheng Member: 553.6 ± 2.7 Ma and 546.3 ± 2.7 Ma, Yang et al., 2016) which are recorded in deposits which show stable positive C isotope values characteristic of the EPIP.

Treptichnus pedum

Western Avalonia: Chapel Island Formation, lithofacies association /'member' 2 marks the FAD of *Treptichnus pedum*, with outcropping strata at Fortune Head (Newfoundland) consequently marking the Ediacaran-Cambrian GSSP. The exact age of CIF LA 2 is unknown but is certainly > 530.02 ± 1.20 Ma (Landing, 1994; Isachsen et al., 1994).

Kalahari Craton: The FAD of *T. pedum* is best constrained in the lower Nomtsas Formation of the Nama Group at Farms Swartkloofberg (Germs, 1972a) and Sonntagsbrunn (Grotzinger et al., 1995 and Valley Fill 2 of Wilson et al., 2012). These fossiliferous beds are constrained by a CA-ID-TIMS age of an

ash bed in the upper Spitskop Member of the Urusis Formation (538.67 ± 0.22 Ma at Swartpunt, Linnemann et al., 2017) and an air abrasion ID-TIMS age from an ash bed in the lower Nomtsas Formation (538.18 ± 1.24 Ma at Swartkloofberg) (Grotzinger et al., 1995, recalculated in Schmitz, 2012).

South China: The FAD of *T. pedum* in early Cambrian sections of the Yangtze Block is constrained to shallow phosphorites of the lower Zhongyicun Member of the Zhujiaqing Formation (Yin et al., 1993). The BACE is recorded to occur in carbonates of the underlying Daibu Member (Brasier et al., 1990; Li et al., 2009; Zhu and Li, 2017) and, with a U-Pb SHRIMP age of 539.4 ± 2.9 Ma for bentonites of the Zhongyicun Member, an uppermost age constraint of 536.5 Ma is placed on the rising limb of the BACE.

***Anabarites* (and SSFs of the *Anabarites trisulcatus – Prothertzina anabarica* zone)**

Western Avalonia: Carbonate outcrops of the Chapel Island Formation are limited and their sparsity and degree of burial alteration leaves them relatively unfit for use in chemostratigraphic correlation (Brasier et al., 1992), however these carbonate beds have proven useful in identification of a rich SSF assemblage which constrains deposition to the Nemakit-Daldynian (Landing et al., 1989). The FAD of *Anabarites* sits in the Chapel Island Formation lithofacies association /'member' 4 at Little Dantzic Cove, however many other SSFs occur in these strata below *Anabarites* including *Ladatheca cylindrica* (the lowest occurring skeletal fossil, which outcrops first in Member 2) (Landing et al., 1989). This is constrained by regional litho- and biostratigraphy to below correlative deposits in New Brunswick dated at 530.02 ± 1.20 Ma (Landing, 1991, 1994; Isachsen et al., 1994, recalculated in Schmitz, 2012).

Southeast Siberian Platform: In outcrops of the Ust'-Yudoma Formation along the Yudoma River of southeast Siberia, *Anabarites* co-occurs with *Cloudina* and the relative age is weakly constrained but definitively upper Ediacaran based on a chemostratigraphic position in the EPIP and below the BACE (Zhu et al., 2017).

South China: In the classic Meishucun section of south China, SSFs of the *Anabarites-Protohertzina* assemblage zone first outcrop in the lower Zhongyicun Member. This is contrary to previous ascription of the FAD to the upper Baiyanshao ('Xiaowatoushan') Member which has since yielded no SSFs (Li et al., 2009). The middle Zhongyicun Member bentonite above the FAD of SSFs yields an age of 539.4 ± 2.9 Ma (Compston et al., 2008). The youngest age of Zhongyicun Member bentonites (according to 2σ error) is 536.5 Ma.

Additional C isotope data

South China: Drill core samples of the Three Gorges area Dengying-Yanjiahe-Shuijingtuo Formations (Ishikawa et al., 2008).

Southeast Siberia: Dvortsy section of the Aldan River (Magaritz et al., 1986). If C isotope profile fits global DIC, rising limb of Ust'-Yudoma Fm must be rising limb of BACE. If rising limb in this Formation is equivalent to recovery from the Shuram, the erosional gap below the Pestrotsvet would be inconceivably long (over 20 Myrs). A position of the outcrop above the erosional unconformity at the summit of the Yudoma River sections and a correspondingly shorter duration for the unconformity in sections of the Aldan River (~3-4 Myrs) is proposed herein (see Figure 5.3).

The negative excursion at the top of the Ust'-Yudoma Formation at Kyra-Ytyga (Zhu et al., 2017) must postdate 538 Ma if it reflects global DIC (based on stable positive C isotopes and radiometric dates at Swartpunt). Furthermore, the upper limit for the nadir of the BACE in South China is constrained by 536.5 Ma based on the 'youngest age' for SHRIMP U-Pb dating of bentonites in overlying deposits of the Zhongyicun Member of the Zhujiaqing Formation (Compston et al., 2008; Zhu and Li, 2017). Carbon isotope values of samples from the Zhongyicun and much of the Dahai Members are omitted due to $\delta^{18}O < -10‰$ and suspected isotopic values unrepresentative of changes in global DIC.

Sampling site coordinates

Nama Group, Namibia (Chapters 2-4)

Sampling Site	Formation/Members	GPS Coordinates
VF1-S [3]	Nomtsas Formation	17°38.216'E, 27°16.635'S
Swartpunt 74 [1, 2, 3, 4]	Spitskop Member	16°41.692'E, 27°28.566'S
Pinnacle Reefs [1, 2] (Swartkloofberg 95)	Feldschuhhorn – Spitskop Members	16°33.727'E, 27°26.804'S
FSH[3]	Feldschuhhorn Member	17°37.991'E, 27°16.461'S
Farm Kliphoek 72 [4]	Vingerbreek Member	16°46.793'E, 27°17.088'S
Farm Quagga-spoort 79 [4]	Vingerbreek Member	17°9.574'E, 27°25.817'S
Zebra River 122 [1,2,3]	Omkyk – Urikos Members	16°13.031'E, 24°31.012'S
Zwartmodder 101 [1,2]	Kanies – Hoogland Members	16°19.517'E, 24°53.683'S
Omkyk 149 [1,2]	Omkyk Member	16°13.750'E, 24°48.317'S
Driedoornvlakte [1,2,4]	Omkyk – Niederhagen Members	16°39.202'E, 23°52.038'S
Arasab 43 [1,2]	Kanies – Mooifontein Members	16°27.433'E, 26°57.809'S
Grens 92 [1,2]	Kanies – Aar Members	16°21.973'E, 27°10.624'S
Zuurberg 46 [3]	Mara Member	16°59.287'E, 26°15.677'S
Brak [1,2]	Kanies – Lower Omkyk Members	16°8.108'E, 23°58.283'S

[1] Wood et al. (2015), [2] Tostevin et al. (2016), [3]Sperling et al. (2015) (Section details in Wilson et al., 2012 and Darroch et al., 2015), [4]Bowyer et al. (2017, and in progress)

Yudoma Group, Eastern Siberia (Chapter 5)

Sampling Site	Formation/Members	Sampling GPS Coordinates
Yudoma-Maya Confluence	Aim – Ust-Yudoma Forrmations	135°13.625'E, 59°9.270'N
Nuuchchalakh	Aim – Pestrotsvet Formations	136°15.163'E, 59°25.149'N
Kyra-Ytyga	Ust'-Kerbi – Ust-Yudoma Formations	136°54.353'E, 59°24.069'N

Yangtze Block, South China (Chapter 5)

Sampling Site	Formation/Members	Sampling GPS Coordinates
Yinchangpo	Denlongtan – Dahai Members	103°12.600'E, 26°29.399'N
Wuhe (/Gaojiaxi)	Hamajing – Yanjiahe Members	111°1.295'E, 30°48.136'N

Appendix B

Compiled elemental data

1) Nama Group: Full manipulated data spreadsheet available upon request.

2) Yudoma Group: Sections of the Yudoma River, Republic of Sakha, Yakutia.

3) Yangtze Block: Sections of NE Yunnan and SW Hubei Provinces.

Farm Omkyk: Iodine/(Calcium +Magnesium)

Sample ID	Height (m)	Lithology	Fe speciation interpretation	Bioclasts	I/(Ca+Mg) (µmol/mol)	Repeat 1	Repeat 2
OMK1/13	101.5	Limestone	anoxic	Absent	1.85063	-	-
OMK4/15	98.5	Dolomite	equivocal	PRESENT	2.96809	-	-
OMK4/14	97.5	Limestone	anoxic	PRESENT	0.93588	-	-
OMK4/10	94.4	Limestone	low FeT	PRESENT	0.64412	-	-
OMK4/6	92.9	Limestone	low FeT	PRESENT	0.52025	-	-
OMK4/5	92.5	Limestone	oxic	PRESENT	0.41958	-	-
OMK1/6	84	Limestone	anoxic	Absent	1.79921	-	-
OMK1/5	82	Limestone	anoxic	Absent	0.61222	-	-
OMK1/4	79	Limestone	anoxic	Absent	1.09852	-	-
OMK1/2	73.5	Dolomite	anoxic	Absent	2.77675	-	-
OMK1/1	73	Limestone	anoxic	Absent	5.38411	-	-
OMK2/20	31.5	Limestone	anoxic	Absent	1.76340	-	-
OMK2/19	29	Limestone	anoxic	Absent	2.41025	-	-
OMK2/14	22	Limestone	anoxic	Absent	1.95483	-	-
OMK2/12	18.5	Dolomite	anoxic	Absent	2.08347	-	-
OMK2/11	16.5	Limestone	anoxic	Absent	1.89950	-	-
OMK2/8	11.75	Dolomite	anoxic	Absent	0.72192	-	-
OMK2/7	10.25	Dolomite	low FeT	Absent	1.23494	-	-
OMK2/6	8.75	Dolomite	anoxic	Absent	0.44367	-	-
OMK2/5	7.25	Limestone	low FeT	Absent	0.53661	0.72425	0.67108
OMK2/4	6.75	Limestone	anoxic	Absent	0.63735	0.54202	0.70452
OMK2/3	6	Limestone	anoxic	Absent	1.16126	1.35639	1.49819
OMK2/2	5	Limestone	equivocal	Absent	1.23421	1.22391	1.53450
OMK2/1	4	Limestone	anoxic	Absent	0.88741	0.72841	0.76083

Iodine Duplicate Analyses and reproducibility. Data analysed by Dalton Hardisty and Charles Diamond at Wood's Hole Oceanographic Institute and the University of California, Riverside respectively. Iodine detection limit varied between 40ppt and 50ppt (minimum sample I concentration = 75ppt).

Sample ID	I (µmol)	Ca (mol)	Mg (mol)	I/(Ca+Mg) (µmolmol^{-1}) JCP corrected
OMK2/1	0.0013	0.0015	0.00004	0.89
OMK2/1duplicate	0.0010	0.0015	0.00003	0.73
OMK2/1duplicate2	0.0010	0.0015	0.00003	0.76
RSD (%)				**10.61**
OMK2/2	0.0018	0.0015	0.00019	1.23
OMK2/2duplicate	0.0021	0.0017	0.00019	1.22
OMK2/2duplicate2	0.0025	0.0016	0.00018	1.53
RSD (%)				**13.26**
OMK2/3	0.0019	0.0017	0.00012	1.16
OMK2/3duplicate	0.0022	0.0017	0.00012	1.36
OMK2/3duplicate2	0.0030	0.0021	0.00015	1.50
RSD (%)				**12.64**
OMK2/4	0.0009	0.0015	0.00003	0.64
OMK2/4duplicate	0.0008	0.0016	0.00003	0.54
OMK2/4duplicate2	0.0012	0.0018	0.00003	0.70
RSD (%)				**13.00**
OMK2/5	0.0010	0.0020	0.00005	0.54
OMK2/5duplicate	0.0013	0.0020	0.00005	0.72
OMK2/5duplicate2	0.0012	0.0019	0.00004	0.67
RSD (%)				**14.44**

Farm Driedoornvlakte sample details

Sample ID	Lithology	GPS	Subgroup	Formation	Member	Unit	Systems Tract
			Farm Driedoornvlakte 490				
DV2-23	Shale/mudstone	S23°53.028' E016°39.607'	Kuibis	Zaris	Niederhagen	undefined	HST
DV2-24	Shale/mudstone	S23°52.763' E016°39.983'	Kuibis	Zaris	Niederhagen	undefined	HST
DV2-25	Shale/mudstone	S23°52.665' E016°39.928'	Kuibis	Zaris	Niederhagen	undefined	HST
DV2-26	Shale/mudstone	S23°52.663' E016°39.924'	Kuibis	Zaris	Niederhagen	undefined	HST
DV2-27	Shale/mudstone	S23°52.641' E016°39.893'	Kuibis	Zaris	Niederhagen	undefined	HST
DV2-28	Shale/mudstone	S23°52.490' E016°39.813'	Kuibis	Zaris	Urikos	undefined	TST
U6	Shale/mudstone	-	Kuibis	Zaris	Urikos	undefined	TST
DV2-30	Shale/mudstone	S23°52.338' E016°39.800'	Kuibis	Zaris	Urikos	undefined	TST
DV2-29	Shale/mudstone	S23°52.338' E016°39.800'	Kuibis	Zaris	Urikos	undefined	TST
DV2-22	Shale/mudstone	S23°52.624' E016°39.182'	Kuibis	Zaris	Urikos	undefined	TST
DV2-21	Shale/mudstone	S23°52.624' E016°39.182'	Kuibis	Zaris	Urikos	undefined	TST
U5.5	Shale/mudstone	-	Kuibis	Zaris	Urikos	undefined	TST
DV5	Shale/mudstone	S23°52.590' E016°39.207'	Kuibis	Zaris	Urikos	undefined	TST
DV4	Shale/mudstone	S23°52.583' E016°39.210'	Kuibis	Zaris	Urikos	undefined	TST

Sample ID	Lithology	GPS	Subgroup	Formation	Member	Unit	Systems Tract
U4	Shale/mudstone	-	Kuibis	Zaris	Urikos	undefined	TST
U3	Shale/mudstone	-	Kuibis	Zaris	Urikos	undefined	TST
DV3	Shale/mudstone	S23°52.574' E016°39.208'	Kuibis	Zaris	Urikos	undefined	TST
U1	Shale/mudstone	-	Kuibis	Zaris	Urikos	undefined	TST
DV2	Shale/mudstone	S23°52.542' E016°39.175'	Kuibis	Zaris	Urikos	undefined	TST
DV1	Shale/mudstone	S23°52.530' E016°39.176'	Kuibis	Zaris	Urikos	undefined	TST
DV2-31	Shale/mudstone	S23°52.369' E016°39.368'	Kuibis	Zaris	Urikos	undefined	TST
DV2-20	Shale/mudstone	S23°52.113' E016°39.331'	Kuibis	Zaris	Omkyk	OS2 Unit 3m	TST
DV2-19	Shale/mudstone	S23°52.045' E016°39.400'	Kuibis	Zaris	Omkyk	OS2 Unit 3m	TST
DV2-18	Shale/mudstone	S23°51.969' E016°39.491'	Kuibis	Zaris	Omkyk	OS2 Unit 3i	TST
DV2-17	Shale/mudstone	S23°51.665' E016°40.027'	Kuibis	Zaris	Omkyk	OS2 Unit 3i	TST
DV2-15	Shale/mudstone	S23°51.513' E016°39.825'	Kuibis	Zaris	Omkyk	Stratigraphically above DV2-14, OS2 Unit 2m	SB
DV2-16	Shale/mudstone	S23°51.549' E016°39.932'	Kuibis	Zaris	Omkyk	Down-dip equivalent to DV2-15, OS2 Unit 2m	SB
DV2-8	Shale/mudstone	S23°51.499' E016°39.712'	Kuibis	Zaris	Omkyk	Stratigraphically above DV2-13, OS2 Unit 1b	HST
DV2-14	Shale/mudstone	S23°51.495' E016°39.762'	Kuibis	Zaris	Omkyk	Stratigraphically equivalent to DV2-8, OS2 Unit 1b	HST
DV2-13	Shale/mudstone	S23°51.488' E016°39.736'	Kuibis	Zaris	Omkyk	Stratigraphically below DV2-8 and above DV2-7, OS2 Unit 1b	HST

Sample ID	Lithology	GPS	Subgroup	Formation	Member	Unit	Systems Tract
DV2-7	Shale/mudstone	S23°51.475' E016°39.685'	Kuibis	Zaris	Omkyk	OS2 Unit 1b, 3m stratigraphically above DV2-6	HST
DV2-6	Shale/mudstone	S23°51.474' E016°39.684'	Kuibis	Zaris	Omkyk	OS2 Unit 1b	MFS
DV2-12	Shale/mudstone	S23°51.440' E016°39.673'	Kuibis	Zaris	Omkyk	MFS stratigraphically above DV2-11, below DV2-6, OS2 Unit 1b	MFS
DV2-11	Shale/mudstone	S23°51.439' E016°39.662'	Kuibis	Zaris	Omkyk	Stratigraphically above DV2-10 but down-dip, OS2 Unit 1a	TST
DV2-9	Shale/mudstone	S23°51.416' E016°39.624'	Kuibis	Zaris	Omkyk	OS2 Unit 1a	TST
DV2-10	Shale/mudstone	S23°51.429' E016°39.637'	Kuibis	Zaris	Omkyk	Up-dip equivalent to DV2-9, OS2 Unit 1a	TST
N1	Shale/mudstone	-	Kuibis	Zaris	Omkyk	OS1	SB
N1a	Shale/mudstone	-	Kuibis	Zaris	Omkyk	OS1	SB

Iron speciation replicate analyses. Sequential extractions measured by AAS at the University of Leeds, Cohen Laboratories. Pyrite data acquired through hot chromous chloride distillation at the University of Edinburgh. Samples in bold red denote in-house reference materials C165 (used routinely in Leeds University Cohen Laboratories) and PY (crushed pure Peruvian FeS_2 used as standard at the University of Edinburgh, Grant Institute).

Sample ID	Fecarb (%)	Feox (%)	Femag (%)
DV2-24a	0.048	1.110	0.139
DV2-24b	0.053	1.068	0.130
DV2-24c	0.054	1.045	0.130
DV2-24d	0.053	1.061	0.139
DV2-24e	0.051	1.034	0.138
RSD (%)	**4.72**	**2.72**	**3.66**
C165a	0.847	0.324	0.858
C165b	0.868	0.331	0.887
RSD (%)	**1.70**	**1.54**	**2.33**

Sample ID	Fepy (%)
PY3	41.49
PY4	41.054
PY5	42.675
PY6	43.034
PY7	42.365
PY8	43.137
RSD (%)	**2.00**

In-house replicate concentrations for C165: $Fe_{carb} = 0.84 \pm 0.16$ wt%, $Fe_{ox} = 0.33 \pm 0.04$ wt%, $Fe_{mag} = 0.80 \pm 0.11$ wt%.
In-house pyrite standard. Improved yields were associated with reduced sample masses. 99% yield at sample mass 0.03g.

Total digestion replicate analyses. Measured by either AAS (Fe only) or ICP-OES at the University of Edinburgh, Grant Institute.

Certified Reference Material official concentrations.

Sample ID	Al (%)	Ba (ppm)	Ca (%)	Cr (ppm)	Fe (%)	K (%)	Mn (ppm)	Mo (ppm)	Na (%)	Ni (ppm)	P (ppm)	Sr (ppm)	Ti (%)
PACS2	6.62 ± 0.21		1.96 ± 0.18	90.7 ± 4.6	4.09 ± 0.06	1.24 ± 0.05	440 ± 19	5.43 ± 0.28	3.45 ± 0.17	39.5 ± 2.3	960 ± 40	276 ± 30	0.443 ± 0.032
SCO-1					3.63 ± 0.254								
JB-1					6.27								

Elemental limits of detection (LOD). Measured via ICP-OES.

Al (%)	Ba (ppm)	Ca (%)	Cr (ppm)	Fe (%)	K (%)	Mn (ppm)	Mo (ppm)	Na (%)	Ni (ppm)	P (ppm)	Sr (ppm)	Ti (%)
0.03	10	0.01	4	0.03	0.03	5	4	0.05	10	10	2	0.01

Reproducibility. Samples in bold red denote certified reference materials (certified values given below).

Sample ID	Al (%)	Ba (ppm)	Ca (%)	Cr (ppm)	Fe (%)	K (%)	Mn (ppm)	Mo (ppm)	Na (%)	Ni (ppm)	P (ppm)	Sr (ppm)	Ti (%)
DV2-22a	7.466	313.80	-	74.00	4.120	2.118	145.10	-	0.452	35.90	543.60	42.60	0.257
DV2-22b	7.370	281.50	0.260	76.40	4.424	2.065	135.70	-	0.425	39.60	565.80	43.30	0.256
DV2-22c	7.314	298.20	0.256	75.70	4.241	2.103	146.60	-	0.440	38.70	555.50	42.80	0.255
DV2-22d	7.285	297.20	0.255	74.50	4.213	2.096	145.80	-	0.438	38.80	546.10	42.70	0.252
DV2-22e	7.342	288.90	0.257	76.40	4.266	2.096	140.20	-	0.443	39.00	562.60	43.30	0.229
RSD (%)	**0.95**	**4.08**	**0.72**	**1.43**	**2.60**	**0.92**	**3.24**	**-**	**2.26**	**3.75**	**1.76**	**0.82**	**4.67**
PACS2a	6.522	878.60	1.886	87.80	4.053	1.27	429.90	-	3.389	-	990.20	261.30	0.411
PACS2b	6.500	874.90	1.894	86.80	4.070	1.27	432.70	-	3.329	-	986.70	264.00	0.417
RSD (%)	**0.25**	**0.30**	**0.30**	**0.84**	**0.30**	**0.38**	**0.45**	**-**	**1.27**	**-**	**0.25**	**0.72**	**1.10**
PACS2c					4.054								
PACS2d					4.054								
RSD (%)					**0.00**								
SCO-1a					3.527								
SCO-1b					3.543								
SCO-1c					3.517								
SCO-1d					3.632								
RSD (%)					**1.48**								
JB1a					6.224								
JB1b					6.248								
RSD (%)					**0.27**								

Farm Driedoornvlakte raw elemental data. Units in ppm unless noted. Bold red denote concetrations near LOD

Sample ID	Height (m)	Al (%)	Ba	Ca (%)	Cr	Fe (%)	K (%)	Mn	Mo	Na (%)	Ni	P	Sr	Ti (%)	K-corr CIA (%)
DV2-23	910	7.95	430	-	79	4.45	2.50	320	-	0.50	37	512	33	0.32	-
DV2-24	880	6.55	270	-	60	3.98	1.80	115	-	0.65	30	702	36	0.26	-
DV2-25	835	6.75	320	-	66	3.97	2.00	134	-	0.55	33	878	39	0.23	-
DV2-26	830	8.30	450	-	92	4.74	2.80	191	-	0.35	42	646	35	0.32	-
DV2-27	820	9.20	460	-	97	4.95	3.10	289	-	0.30	40	247	39	0.35	-
DV2-28	750	7.50	440	-	76	3.67	2.70	111	-	0.80	36	541	37	0.27	-
U6	685	-	-	-	-	2.12	-	-	-	-	-	-	-	-	-
DV2-30	685	7.60	330	-	77	4.03	2.40	186	-	0.70	34	614	41	0.25	-
DV2-29	680	7.20	320	-	71	4.01	2.20	195	-	0.90	35	532	41	0.23	-
DV2-22	676	7.45	290	-	74	4.12	2.10	145	-	0.45	37	554	43	0.26	-
DV2-21	670.00	6.25	210	-	62	3.59	1.60	121	-	0.90	30	451	47	0.24	-
U5.5	665.00	-	-	-	-	3.18	-	-	-	-	-	-	-	-	-
DV5	660	9.55	430	-	99	6.03	3.00	230	-	0.40	52	598	40	0.28	-
DV4	650	6.45	220	-	66	3.66	1.70	147	-	1.00	30	479	46	0.23	-
U4	647.5	-	-	-	-	2.81	-	-	-	-	-	-	-	-	-
U3	645	-	-	-	-	1.77	-	-	-	-	-	-	-	-	-
DV3	640	7.10	260	-	77	4.26	1.80	135	-	0.85	36	437	48	0.24	-
U1	630	-	-	-	-	2.00	-	-	-	-	-	-	-	-	-
DV2	610	3.75	-	-	34	1.99	0.60	27	-	0.80	16	131	30	0.10	-
DV1	600	4.95	130	-	54	3.21	1.00	101	-	0.85	25	252	36	0.16	-
DV2-31	550	6.60	240	0.17	73	3.83	1.80	127	4	0.70	34	422	42	0.23	82.14
DV2-20	470	8.65	330	0.26	79	5.46	2.70	201	-	0.80	-	487	-	0.27	82.56
DV2-19	460	8.90	370	0.30	101	5.70	2.90	369	-	0.05	48	695	32	0.27	89.04

Sample ID	Height (m)	Al (%)	Ba	Ca (%)	Cr	Fe (%)	K (%)	Mn	Mo	Na (%)	Ni	P	Sr	Ti (%)	K-corr CIA (%)
DV2-18	450	9.20	490	0.22	111	4.96	3.10	428	-	0.75	49	194	13	0.31	83.14
DV2-17	425	8.85	360	-	88	5.34	3.70	15	-	-	38	228	36	0.38	-
DV2-15	310	9.15	400	-	99	5.12	3.40	77	-	0.45	45	367	42	0.32	-
DV2-16	310	9.40	430	0.17	101	4.70	3.60	66	4	0.25	46	289	38	0.29	86.95
DV2-8	230	9.45	440	-	98	4.59	3.50	61	-	0.50	44	918	39	0.31	-
DV2-14	230	9.40	410	0.40	80	4.67	3.50	83	-	1.20	-	396	-	0.30	79.40
DV2-13	185	8.85	430	1.38	81	4.49	3.10	124	-	1.05	-	338	-	0.31	81.32
DV2-7	179	9.45	400	-	97	5.34	3.60	88	-	-	39	329	21	0.35	-
DV2-6	172	9.65	450	-	104	4.91	3.50	60	-	0.25	44	316	38	0.35	-
DV2-12	170	9.50	430	0.48	95	4.73	3.60	146	-	0.75	-	324	-	0.31	81.53
DV2-11	163	9.65	440	1.07	89	4.87	3.60	155	-	1.10	-	292	-	0.38	81.85
DV2-9	120	8.50	360	-	100	4.65	3.10	17	-	**0.00**	32	219	23	0.39	-
DV2-10	120	9.20	400	-	100	4.15	3.50	162	-	0.40	40	247	48	0.29	-
N1	20	-	-	-	-	1.25	-	-	-	-	-	-	-	-	-
N1a	20	-	-	-	-	0.44	-	-	-	-	-	-	-	-	-

Farm Driedoornvlakte iron speciation data

Sample ID	Height (m)	Fecarb (%)	Feox (%)	Femag (%)	Fepy (%)	FeHR (%)	FeHR/FeT	Fepy/FeHR	Fe/Al
DV2-23	910	0.11	1.09	0.28	0.001	1.48	0.33	0.000	0.56
DV2-24	880	0.05	1.11	0.14	0.001	1.28	0.32	0.000	0.61
1DV2-25	835	0.05	1.11	0.16	0.000	1.32	0.33	0.000	0.59
9DV2-26	830	0.12	1.98	0.26	0.001	1.77	0.37	0.000	0.57
DV2-27	820	0.05	1.15	0.15	0.001	1.35	0.27	0.000	0.54
DV2-28	750	0.05	0.77	0.11	0.000	0.93	0.25	0.000	0.49
U6	685	0.10	0.62	0.07	0.000	0.80	0.38	0.000	0.57
DV2-30	685	0.08	0.08	0.08	0.000	0.24	0.06	0.000	0.53
DV2-29	680	0.10	0.24	0.09	0.000	0.43	0.11	0.001	0.56
DV2-22	676	0.14	0.59	0.17	0.000	0.89	0.22	0.000	0.55
DV2-21	670.00	0.17	0.37	0.17	0.003	0.72	0.20	0.004	0.58
U5.5	665.00	0.09	0.35	0.07	0.000	0.52	0.16	0.001	0.65
DV5	660	0.18	0.62	0.20	0.001	0.99	0.17	0.001	0.63
DV4	650	0.14	0.36	0.12	0.003	0.62	0.17	0.005	0.57
U4	647.5	0.26	0.34	0.20	0.001	0.79	0.28	0.001	0.71
U3	645	0.08	0.55	0.07	0.000	0.70	0.39	0.001	0.51
DV3	640	0.25	0.59	0.24	0.001	1.08	0.25	0.001	0.60
U1	630	0.21	0.47	0.16	0.001	0.84	0.42	0.002	0.62
DV2	610	0.13	0.19	0.08	0.000	0.39	0.20	0.000	0.53
DV1	600	0.16	0.23	0.10	0.000	0.49	0.15	0.000	0.65
DV2-31	550	0.07	0.20	0.05	0.000	0.32	0.08	0.000	0.58
DV2-20	470	0.16	0.80	0.20	0.000	1.16	0.21	0.000	0.63
DV2-19	460	0.17	0.24	0.19	0.000	0.59	0.10	0.001	0.64
DV2-18	450	0.09	1.47	0.14	0.000	1.69	0.33	0.000	0.54
DV2-17	425	0.03	1.43	0.19	0.000	1.65	0.31	0.000	0.61

Sample ID	Height (m)	Fecarb (%)	Feox (%)	Femag (%)	Fepy (%)	FeHR (%)	FeHR/FeT	Fepy/FeHR	Fe/Al
DV2-15	310	0.09	0.63	0.08	0.002	0.80	0.16	0.002	0.56
DV2-16	310	0.14	0.32	0.09	0.001	0.55	0.12	0.001	0.50
DV2-8	230	0.10	0.10	0.09	0.004	0.29	0.06	0.015	0.49
DV2-14	230	0.17	0.20	0.10	0.001	0.48	0.10	0.001	0.50
DV2-13	185	0.16	0.21	0.10	0.000	0.47	0.10	0.001	0.51
DV2-7	179	0.09	1.00	0.08	0.001	1.17	0.22	0.001	0.56
DV2-6	172	0.10	0.26	0.07	0.001	0.43	0.09	0.002	0.51
DV2-12	170	0.18	0.15	0.12	0.001	0.45	0.10	0.002	0.50
DV2-11	163	0.26	0.32	0.20	0.001	0.78	0.16	0.001	0.51
DV2-9	120	0.04	2.09	0.05	0.004	2.19	0.47	0.002	0.550
DV2-10	120	0.12	0.29	0.07	0.014	0.49	0.12	0.029	0.45
N1	20	0.08	0.07	0.10	0.000	No S data	-	-	0.46
N1a	20	0.27	0.08	0.15	0.001	0.50	1.13	0.003	0.18

D850 sample details

Sample ID	Lithology	GPS	Subgroup	Formation	Member	Systems Tract
			D850			
S15	Shale/mudstone	S24° 42.937' E16° 54.809'	Schwarzrand	Nomtsas	Niep	TST
S14	Shale/mudstone	S24° 41.278' E16° 52.752'	Schwarzrand	Nomtsas	Niep	TST
S13	Shale/mudstone	S24° 40.818' E16° 47.066'	Schwarzrand	Urusis	unconstrained	HST
D850-1	Shale/mudstone	S24°40.892' E016°46.263'	Schwarzrand	Urusis	unconstrained	HST
S12b	Shale/mudstone	S24° 40.820' E16° 44.285'	Schwarzrand	Urusis	unconstrained	HST
S12a	Shale/mudstone	S24° 40.820' E16° 44.285'	Schwarzrand	Urusis	unconstrained	HST
D850-2	Shale/mudstone	S24°39.677' E016°42.374'	Schwarzrand	Urusis	unconstrained	HST
S11	Shale/mudstone	S24° 39.592' E16° 42.209'	Schwarzrand	Urusis	unconstrained	HST
D850-3	Shale/mudstone	S24°38.561' E016°40.770'	Schwarzrand	Urusis	unconstrained	HST
D850-4	Shale/mudstone	S24°37.992' E016°40.187'	Schwarzrand	Urusis	unconstrained	HST
D850-5	Shale/mudstone	S24°37.906' E016°39.064'	Schwarzrand	Urusis	unconstrained	HST
D850-6	Shale/mudstone	S24°37.866' E016°38.041'	Schwarzrand	Urusis	unconstrained	HST
S10	Shale/mudstone	S24° 37.909' E16° 36.382'	Schwarzrand	Urusis	unconstrained	HST
S9	Shale/mudstone	S24° 37.859'	Schwarzrand	Nudaus	Vingerbreek	TST

Sample ID	Lithology	GPS	Subgroup	Formation	Member	Systems Tract
		E16° 33.386'				
S8	Shale/mudstone	S24° 36.646' E16° 30.396'	Schwarzrand	Nudaus	Vingerbreek	TST
S7	Shale/mudstone	S24° 34.112' E16° 28.681'	Schwarzrand	Nudaus	Vingerbreek	TST
S6	Shale/mudstone	S24° 32.317' E16° 26.355'	Schwarzrand	Nudaus	Vingerbreek	TST
S5	Shale/mudstone	S24° 29.846' E16° 25.556'	Schwarzrand	Nudaus	Niederhagen	HST
S4	Shale/mudstone	S24° 28.919' E16° 23.199'	Schwarzrand	Nudaus	Niederhagen	HST
S3	Shale/mudstone	S24° 29.316' E16° 20.502'	Kuibis	Zaris	Urikos	TST
S2b	Shale/mudstone	S24° 29.162' E16° 19.232'	Kuibis	Zaris	Urikos	TST
S2a	Shale/mudstone	S24° 29.162' E16° 19.232'	Kuibis	Zaris	Urikos	TST
S1	Shale/mudstone	S24° 29.162' E16° 19.232'	Kuibis	Zaris	Urikos	TST

D850 raw elemental data. Units in ppm unless noted.

Sample ID	Relative height	Al (%)	Ba	Ca (%)	Cr	Fe (%)	K (%)	Mn	Mo	Na (%)	Ni	P	Sr	Ti (%)	K-corr CIA (%)
S15	23	-	-	-	-	3.20	-	-	-	-	-	-	-	-	-
S14	22	-	-	-	-	2.50	-	-	-	-	-	-	-	-	-
S13	21	-	-	-	-	2.41	-	-	-	-	-	-	-	-	-
D850-1	20	6.80	370	0.39	58	3.89	2.20	526	3	1.00	32	605	67	0.23	78.48
S12b	19	-	-	-	-	3.37	-	-	-	-	-	-	-	-	-
S12a	18	-	-	-	-	1.64	-	-	-	-	-	-	-	-	-
D850-2	17	7.85	430	0.42	77	5.87	2.60	549	3	0.60	42	676	40	0.30	82.29
S11	16	-	-	-	-	2.06	-	-	-	-	-	-	-	-	-
D850-3	15	-	-	-	-	-	-	-	-	-	-	-	-	-	-
D850-4	14	5.80	270	0.29	48	3.16	1.60	352	-	1.20	25	763	58	0.17	76.03
D850-5	13	-	-	-	-	-	-	-	-	-	-	-	-	-	-
D850-6	12	6.70	490	0.36	64	3.81	2.30	243	-	1.00	32	578	75	0.26	78.21
S10	11	-	-	-	-	5.69	-	-	-	-	-	-	-	-	-
S9	10	-	-	-	-	3.77	-	-	-	-	-	-	-	-	-
S8	9	-	-	-	-	3.82	-	-	-	-	-	-	-	-	-
S7	8	-	-	-	-	2.98	-	-	-	-	-	-	-	-	-
S6	7	-	-	-	-	3.13	-	-	-	-	-	-	-	-	-
S5	6	-	-	-	-	3.68	-	-	-	-	-	-	-	-	-
S4	5	-	-	-	-	3.11	-	-	-	-	-	-	-	-	-
S3	4	-	-	-	-	3.73	-	-	-	-	-	-	-	-	-
S2b	3	-	-	-	-	6.68	-	-	-	-	-	-	-	-	-
S2a	2	-	-	-	-	3.56	-	-	-	-	-	-	-	-	-
S1	1	-	-	-	-	6.49	-	-	-	-	-	-	-	-	-

D850 iron speciation data

Sample ID	Relative height	Fecarb (%)	Feox (%)	Femag (%)	Fepy (%)	FeHR (%)	FeHR/FeT	Fepy/FeHR	Fe/Al
S15	23	0.10	0.71	0.15	0.001	0.96	0.30	0.001	0.51
S14	22	0.08	0.52	0.12	0.000	0.71	0.28	0.000	0.48
S13	21	0.07	0.48	0.08	0.001	0.63	0.26	0.001	0.52
D850-1	20	0.09	0.91	0.15	0.001	1.15	0.30	0.001	0.57
S12b	19	0.11	1.06	0.22	0.001	1.40	0.42	0.001	0.78
S12a	18	0.09	0.29	0.08	0.000	0.45	0.27	0.001	0.41
D850-2	17	0.27	1.38	0.49	0.000	2.13	0.36	0.000	0.75
S11	16	0.06	0.49	0.07	0.000	0.62	0.30	0.000	0.45
D850-3	15	-	-	-	-	-	-	-	-
D850-4	14	0.09	0.71	0.11	0.001	0.91	0.29	0.001	0.55
D850-5	13	-	-	-	-	-	-	-	-
D850-6	12	0.20	1.05	0.34	0.001	1.59	0.42	0.001	0.57
S10	11	0.15	0.84	0.27	0.001	1.27	0.22	0.001	0.73
S9	10	0.17	0.94	0.25	0.001	1.36	0.36	0.001	0.60
S8	9	0.11	0.60	0.13	0.001	0.85	0.22	0.001	0.48
S7	8	0.23	0.56	0.19	0.001	0.98	0.33	0.001	0.53
S6	7	0.30	0.64	0.27	0.000	1.21	0.39	0.000	0.54
S5	6	0.20	1.20	0.24	0.000	1.65	0.45	0.000	0.68
S4	5	0.29	0.68	0.25	0.002	1.22	0.39	0.001	0.50
S3	4	0.26	0.88	0.28	0.000	1.41	0.38	0.000	0.65
S2b	3	0.65	0.73	0.43	0.000	1.81	0.27	0.000	0.86
S2a	2	1.02	0.97	0.45	0.000	2.44	0.69	0.000	0.76
S1	1	0.20	0.56	0.19	0.001	0.95	0.15	0.001	0.64

D860/C14 sample details

Sample ID	Lithology	GPS	Subgroup	Formation	Member	Systems Tract
			D860/C14			
D860-21	Shale/mudstone	S24°34.983' E016°55.819'	Schwarzrand	Nomtsas	Niep member	TST
D860-20	Shale/mudstone	S24°28.784' E016°52.943'	Schwarzrand	Nomtsas	Niep member	TST
D860-19	Shale/mudstone	S24°26.828' E016°52.114'	Schwarzrand	Nomtsas	Niep member	TST
D860-18	Shale/mudstone	S24°25.410' E016°50.713'	Schwarzrand	Nomtsas	Kreyrivier member	TST
D860-17	Shale/mudstone	S24°23.006' E016°47.155'	Schwarzrand	Urusis Formation	unconstrained	HST
D860-16	Shale/mudstone	S24°21.100' E016°46.178'	Schwarzrand	Urusis Formation	unconstrained	HST
D860-15	Shale/mudstone	S24°19.322' E016°47.682'	Schwarzrand	Urusis Formation	unconstrained	HST
D860-14	Shale/mudstone	S24°14.908' E016°51.355'	Schwarzrand	Urusis Formation	unconstrained	HST
D860-13	Shale/mudstone	S24°13.092' E016°51.262'	Schwarzrand	Urusis Formation	unconstrained	HST
D860-12	Shale/mudstone	S24°12.243' E016°50.770'	Schwarzrand	Urusis Formation	unconstrained	HST
D860-11	Shale/mudstone	S24°11.675' E016°50.537'	Schwarzrand	Urusis Formation	unconstrained	HST
D860-10	Shale/mudstone	S24°10.589' E016°51.228'	Schwarzrand	Urusis Formation	unconstrained	HST
D860-9	Shale/mudstone	S24°10.687' E016°51.939'	Schwarzrand	Urusis Formation	unconstrained	HST

Sample ID	Lithology	GPS	Subgroup	Formation	Member	Systems Tract
D860-8	Shale/mudstone	S24°10.490' E016°52.701'	Schwarzrand	Urusis Formation	unconstrained	HST
D860-7	Shale/mudstone	S24°10.165' E016°53.322'	Schwarzrand	Urusis Formation	unconstrained	HST
D860-6	Shale/mudstone	S24°09.118' E016°55.417'	Schwarzrand	Urusis Formation	unconstrained	HST
D860-5	Shale/mudstone	S24°06.957' E016°58.359'	Schwarzrand	Nudaus	Vingerbreek member	TST
D860-4	Shale/mudstone	S24°06.900' E016°58.436'	Schwarzrand	Nudaus	Vingerbreek member	TST
D860-3	Shale/mudstone	S24°05.915' E016°59.696'	Schwarzrand	Nudaus	Niederhagen member	HST
D860-2	Shale/mudstone	S24°05.856' E016°59.743'	Schwarzrand	Nudaus	Niederhagen member	HST
D860-1	Shale/mudstone	S24°05.592' E016°59.801'	Schwarzrand	Nudaus	Niederhagen member	HST

D860/C14 raw elemental data. Units in ppm unless noted.

Sample ID	Relative height	Al (%)	Ba	Ca (%)	Cr	Fe (%)	K (%)	Mn	Mo	Na (%)	Ni	P	Sr	Ti (%)	K-corr CIA (%)
D860-21	21	8.35	400	0.25	76	5.23	3.00	418	-	1.10	-	691	-	0.30	80.62
D860-20	20	6.85	230	0.35	40	3.58	2.05	483	-	2.00	-	946	-	0.28	71.85
D860-19	19	7.55	340	0.25	83	4.46	2.70	590	4	1.00	45	543	43	0.28	80.32
D860-18	18	6.00	180	0.38	55	2.94	1.60	469	0	1.50	33	1030	60	0.26	73.76
D860-17	17	-	-	-	-	-	-	-	-	-	-	-	-	-	-
D860-16	16	6.65	280	0.33	33	4.45	1.85	510	-	1.85	-	832	-	0.24	72.37
D860-15	15	8.30	460	0.39	64	5.16	2.55	451	-	1.35	-	723	-	0.34	77.83
D860-14	14	8.60	540	0.33	69	5.38	2.85	488	-	1.35	-	768	-	0.35	78.75
D860-13	13	-	-	-	-	-	-	-	-	-	-	-	-	-	-
D860-12	12	-	-	-	-	-	-	-	-	-	-	-	-	-	-
D860-11	11	-	-	-	-	-	-	-	-	-	-	-	-	-	-
D860-10	10	6.30	290	0.19	54	3.47	1.75	292	3	1.00	29	463	40	0.18	78.72
D860-9	9	8.85	490	0.25	78	4.90	2.90	354	-	1.25	-	808	-	0.36	80.29
D860-8	8	6.60	290	0.21	40	4.97	1.60	336	-	1.55	-	501	-	0.22	74.92
D860-7	7	7.80	450	0.31	61	5.20	2.35	333	-	1.55	-	704	-	0.31	76.48
D860-6	6	5.35	200	0.18	50	3.47	1.15	232	3	1.10	26	294	47	0.19	76.21
D860-5	5	5.65	180	0.18	48	3.31	1.30	117	3	0.95	27	223	47	0.18	77.71
D860-4	4	6.75	230	0.12	66	4.42	1.75	185	2	0.80	34	96	50	0.22	81.07
D860-3	3	5.85	220	0.10	56	3.48	1.50	128	2	0.90	34	60	42	0.18	79.36
D860-2	2	4.90	140	0.10	35	2.58	1.10	62	3	0.95	28	97	36	0.12	76.80
D860-1	1	5.85	380	0.16	53	2.91	1.80	82	3	1.15	35	179	44	0.16	76.53

D860/C14 iron speciation data

Sample ID	Relative height	Fecarb (%)	Feox (%)	Femag (%)	Fepy (%)	FeHR (%)	FeHR/FeT	Fepy/FeHR	Fe/Al
D860-21	21	0.07	1.20	0.15	0.001	1.42	0.27	0.001	0.62
D860-20	20	0.08	0.56	0.14	0.000	0.78	0.22	0.000	0.52
D860-19	19	0.08	0.74	0.25	0.001	1.07	0.24	0.001	0.59
D860-18	18	0.15	0.31	0.17	0.001	0.62	0.21	0.001	0.49
D860-17	17	-	-	-	-	-	-	-	-
D860-16	16	0.07	0.95	0.15	0.001	1.18	0.27	0.001	0.67
D860-15	15	0.10	1.32	0.28	0.000	1.70	0.33	0.000	0.62
D860-14	14	0.03	1.10	0.12	0.001	1.26	0.23	0.001	0.63
D860-13	13	-	-	-	-	-	-	-	-
D860-12	12	-	-	-	-	-	-	-	-
D860-11	11	-	-	-	-	-	-	-	-
D860-10	10	0.08	0.57	0.13	0.000	0.78	0.22	0.000	0.55
D860-9	9	0.08	0.48	0.13	0.000	0.68	0.14	0.000	0.55
D860-8	8	0.10	1.13	0.16	0.001	1.39	0.28	0.001	0.75
D860-7	7	0.14	1.09	0.32	0.000	1.55	0.30	0.000	0.67
D860-6	6	0.13	0.90	0.14	0.001	1.17	0.34	0.001	0.65
D860-5	5	0.09	0.86	0.13	0.000	1.08	0.33	0.000	0.59
D860-4	4	0.12	1.06	0.18	0.000	1.36	0.31	0.000	0.66
D860-3	3	0.06	0.72	0.06	0.000	0.84	0.24	0.000	0.59
D860-2	2	0.08	0.84	0.09	0.001	1.01	0.39	0.001	0.53
D860-1	1	0.07	0.67	0.10	0.000	0.84	0.29	0.000	0.50

Farm Kliphoek 72 sample details

Sample ID	Lithology	GPS	Subgroup	Formation	Member	Systems Tract
			Farm Kliphoek 72			
NUD-20	Shale/mudstone	S27°16.798' E016°46.575'	Schwarzrand	Nudaus	Vingerbreek	TST
NUD-19	Ironstone	-	Schwarzrand	Nudaus	Vingerbreek	TST
NUD-18	Ironstone	-	Schwarzrand	Nudaus	Vingerbreek	TST
NUD-17	Shale/mudstone	-	Schwarzrand	Nudaus	Vingerbreek	TST
NUD-16	Ironstone	-	Schwarzrand	Nudaus	Vingerbreek	TST
NUD-15	Shale/mudstone	-	Schwarzrand	Nudaus	Vingerbreek	TST
NUD-14	Ironstone	-	Schwarzrand	Nudaus	Vingerbreek	TST
NUD-13	Shale/mudstone	-	Schwarzrand	Nudaus	Vingerbreek	TST
NUD-12	Ironstone	-	Schwarzrand	Nudaus	Vingerbreek	TST
NUD-11	Ironstone	-	Schwarzrand	Nudaus	Vingerbreek	TST
NUD-10	Ironstone	-	Schwarzrand	Nudaus	Vingerbreek	TST
NUD-9	Ironstone	-	Schwarzrand	Nudaus	Vingerbreek	TST
NUD-8	Shale/mudstone	-	Schwarzrand	Nudaus	Vingerbreek	TST
NUD-7	Shale/mudstone	-	Schwarzrand	Nudaus	Vingerbreek	TST
NUD-6	Ironstone	-	Schwarzrand	Nudaus	Vingerbreek	TST
NUD-5	Ironstone	-	Schwarzrand	Nudaus	Vingerbreek	TST
NUD-4	Shale/mudstone	-	Schwarzrand	Nudaus	Vingerbreek	TST
NUD-3	Shale/mudstone	-	Schwarzrand	Nudaus	Vingerbreek	TST
NUD-2	Shale/mudstone	S27°17.037' E016°46.726'	Schwarzrand	Nudaus	Vingerbreek	TST
NUD-1	Shale/mudstone	S27°17.088' E016°46.793'	Schwarzrand	Nudaus	Vingerbreek	TST

Farm Kliphoek 72 raw elemental data. Units in ppm unless noted.

Sample ID	Height (m)	Al (%)	Ba	Ca (%)	Cr	Fe (%)	K (%)	Mn	Mo	Na (%)	Ni	P	Sr	Ti (%)	K-corr CIA (%)
NUD-20	214	7.55	410	0.21	38	5.54	2.30	477	-	1.50	-	792	-	0.21	77.318
NUD-19	188.00	3.70	390	0.14	47	19.27	2.80	-	-	1.50	-	207	-	0.10	-
NUD-18	178.00	5.65	320	0.20	73	24.59	2.10	-	-	1.15	-	595	-	0.12	-
NUD-17	168	-	-	-	-	-	-	-	-	-	-	-	-	-	-
NUD-16	154	7.45	-	0.29	85	22.08	1.90	-	-	-	-	-	83	0.20	-
NUD-15	144	8.70	-	0.30	75	6.99	1.90	-	-	-	-	-	174	0.28	-
NUD-14	134	7.40	-	0.22	85	17.55	1.80	-	-	-	-	-	83	0.19	-
NUD-13	124	-	-	-	-	-	-	-	-	-	-	-	-	-	-
NUD-12	114	6.45	-	0.22	65	25.05	1.60	-	-	-	-	-	64	0.16	-
NUD-11	104	6.50	290	0.11	78	28.69	2.00	883	**4**	**0.05**	48	308	70	0.17	-
NUD-10	94	6.70	-	0.20	77	28.78	1.80	-	-	-	-	-	53	0.16	-
NUD-9	84	5.25	180	0.16	74	18.87	1.40	56	**7**	0.35	33	730	89	0.13	-
NUD-8	74	9.20	380	0.13	93	5.96	2.70	869	**4**	0.85	53	259	73	0.24	83.16
NUD-7	64	9.80	420	0.15	107	6.34	3.00	524	**6**	0.15	95	169	99	0.27	87.57
NUD-6	53	7.05	290	0.16	84	27.35	2.00	698	**5**	0.15	54	349	87	0.15	-
NUD-5	43	6.50	-	0.27	98	29.77	1.80	-	-	-	-	-	80	0.16	-
NUD-4	31	8.60	350	0.23	88	4.94	2.30	547	**3**	0.80	45	765	63	0.26	83.12
NUD-3	24.00	9.50	400	0.16	101	5.07	2.90	748	**5**	0.70	53	334	62	0.28	84.30
NUD-2	21.00	9.70	420	0.11	92	8.17	3.10	764	-	1.05	-	254	-	0.31	82.38
NUD-1	10	8.00	290	0.14	69	9.41	2.10	568	-	1.50	-	499	-	0.18	78.03

Farm Kliphoek 72 raw elemental data. Units in ppm unless noted. Samples in bold red are designated **ironstones**

Sample ID	Height (m)	Fecarb (%)	Feox (%)	Femag (%)	Fepy (%)	FeHR (%)	FeHR/FeT	Fepy/FeHR	Fe/Al
NUD-20	214	0.15	0.78	0.22	0.001	1.14	0.21	0.001	0.73
NUD-19	188.00	0.02	17.33	0.25	0.003	17.60	0.92	0.000	2.60
NUD-18	178.00	0.02	21.42	0.47	0.000	21.90	0.89	0.000	4.35
NUD-17	168	-	-	-	-	-	-	-	-
NUD-16	154	0.01	16.18	0.71	0.001	16.90	0.77	0.000	2.96
NUD-15	144	0.03	4.40	0.24	0.002	4.67	0.67	0.000	0.80
NUD-14	134	0.02	14.68	0.30	0.002	15.00	0.86	0.000	2.37
NUD-13	124	-	-	-	-	-	-	-	-
NUD-12	114	0.01	17.94	0.76	0.000	18.72	0.75	0.000	3.89
NUD-11	104	-	-	-	0.000	-	-	-	4.41
NUD-10	94	0.02	22.40	0.88	0.001	23.29	0.81	0.000	4.29
NUD-9	84	-	-	-	-	-	-	-	3.59
NUD-8	74	0.15	0.56	0.10	0.001	0.81	0.14	0.001	0.65
NUD-7	64	0.09	1.84	0.09	0.001	2.02	0.32	0.000	0.65
NUD-6	53	-	-	-	0.001	-	-	-	3.89
NUD-5	43	0.01	15.75	0.74	0.002	16.51	0.55	0.000	4.59
NUD-4	31	0.19	0.16	0.13	0.001	0.48	0.10	0.002	0.58
NUD-3	24.00	0.11	0.34	0.07	0.000	0.52	0.10	0.001	0.54
NUD-2	21.00	0.16	3.61	0.18	0.002	3.96	0.48	0.000	0.83
NUD-1	10	0.14	5.09	0.18	0.001	5.41	0.58	0.000	1.16

Yudoma-Maya Confluence sample details

Sample ID	Lithology	GPS	Formation	Sequence Stratigraphy
YMC 11	Glauconitic siltstone	N59° 9.270' E135° 13.625'	Aim	TST
YMC 10	Micrite	N59° 9.270' E135° 13.625'	Aim	TST

Yudoma-Maya Confluence raw elemental data. Units in ppm unless noted.

Sample ID	Height (m)	Al (%)	Ba	Ca (%)	Cr	Fe (%)	K (%)	Mn	Na (%)	P	Sr	Ti (%)
YMC 11	13.2	0.10	-	9.20	115	0.13	**0.03**	-	**0.05**	92	-	**0.01**
YMC 10	12.3	**0.05**	-	-	-	**0.05**	**0.01**	-	0.10	78	-	**0.00**

Nuuchchalakh sample details

Sample ID	Lithology	GPS	Formation	Sequence Stratigraphy
PET2	Dolomite	N59° 25.149' E136° 15.163'	Pestrotsvet	HST?
N18/2m	Limestone	N59° 25.149' E136° 15.163'	Ust-Yudoma	HST?
N14/2m	Limestone	N59° 25.149' E136° 15.163'	Ust-Yudoma	HST?
N10/2m	Limestone	N59° 25.149' E136° 15.163'	Ust-Yudoma	HST?
N192	Dolomite	N59° 25.149' E136° 15.163'	Ust-Yudoma	HST?
N165	Dolomite	N59° 25.149' E136° 15.163'	Ust-Yudoma	HST?
N115	Dolomite	N59° 25.149' E136° 15.163'	Ust-Yudoma	HST?
N104	Dolomite	N59° 25.149' E136° 15.163'	Ust-Yudoma	HST?
N91	Dolomite	N59° 25.149' E136° 15.163'	Ust-Yudoma	HST?
N84	Dolomite	N59° 25.149' E136° 15.163'	Ust-Yudoma	HST?
N55a	Dolomite	N59° 25.149' E136° 15.163'	Ust-Yudoma	TST
N54	Dolomite	N59° 25.149' E136° 15.163'	Ust-Yudoma	TST
N52	Limestone	N59° 25.149' E136° 15.163'	Aim	HST
N51.5a	Black limestone	N59° 25.149' E136° 15.163'	Aim	HST
N51	Siltstone	N59° 25.149' E136° 15.163'	Aim	HST
N50	Stromatolitic carbonate	N59° 25.149' E136° 15.163'	Aim	HST
N56	Thrombolitic carbonate	N59° 25.149' E136° 15.163'	Aim	TST
N41	Siltstone	N59° 25.149' E136° 15.163'	Aim	MFS
N37	Siltstone	N59° 25.149' E136° 15.163'	Aim	TST
N35	Siltstone	N59° 25.149' E136° 15.163'	Aim	TST
N33	Siltstone	N59° 25.149' E136° 15.163'	Aim	TST
N31	Siltstone	N59° 25.149' E136° 15.163'	Aim	TST
N29	Siltstone	N59° 25.149' E136° 15.163'	Aim	TST
N27	Siltstone	N59° 25.149' E136° 15.163'	Aim	TST
N25	Siltstone	N59° 25.149' E136° 15.163'	Aim	TST

Sample ID	Lithology	GPS	Formation	Sequence Stratigraphy
N22	Dolostone	N59° 25.149' E136° 15.163'	Aim	HST
N18	Dolostone	N59° 25.149' E136° 15.163'	Aim	HST
N13	Dolostone	N59° 25.149' E136° 15.163'	Aim	HST
N9	Dolostone	N59° 25.149' E136° 15.163'	Aim	HST
N6	Silty dolostone	N59° 25.149' E136° 15.163'	Aim	HST

Nuuchchalakh raw elemental data. Units in ppm unless noted

Sample ID	Height (m)	Al (%)	Ba	Ca (%)	Cr	Fe (%)	K (%)	Mn	Na (%)	P	Sr	Ti (%)	K-corr CIA (%)	$\delta^{44/40}$Ca (‰)	Ca isotope 2 sd (%)	I/(Ca+Mg) (µmol/mol)
PET2	315	0.75	BD	35.83	10	0.42	0.50	75	0.65	247	190	0.04	-	0.165 0.080	0.030 0.031	1.243
N18/2m	311	0.15	BD	28.48	**4**	0.18	0.10	773	0.55	130	102	BD	-	0.031	0.021	1.906
N14/2m	307	**0.05**	BD	28.29	BD	**0.01**	**0.05**	133	0.50	204	88	BD	-	0.336	0.027	0.193
N10/2m	303	**0.05**	BD	21.70	BD	**0.02**	**0.05**	67	0.50	159	50	BD	-	0.024	0.024	0.289
N192	293.5	**0.05**	BD	21.64	BD	**0.02**	**0.05**	74	0.45	114	44	BD	-	-0.219	0.039	0.078
N165	261	0.10	BD	21.82	BD	BD	**0.05**	20	0.50	147	40	BD	-	-0.103	0.027	0.052
N115	205	**0.00**	BD	22.19	BD	BD	0.10	BD	1.10	425	20	BD	-	-0.067 -0.188	0.026 0.023	0.047
N104	177	**0.05**	BD	21.77	BD	**0.03**	**0.05**	84	0.50	141	44	BD	-	-0.122 0.002 -0.113	0.030 0.020 0.036	0.058
N91	141	0.10	BD	21.68	BD	0.06	0.10	51	0.55	216	47	BD	-	-0.161	0.045	-
N84	129	0.20	BD	21.31	BD	0.07	0.15	43	0.50	652	76	BD	-	-0.166	0.026	0.217
N55a	105.4	0.10	BD	21.34	BD	0.07	0.10	35	0.49	268	44	BD	-	-0.094	0.024	0.125

Sample ID	Height (m)	Al (%)	Ba	Ca (%)	Cr	Fe (%)	K (%)	Mn	Na (%)	P	Sr	Ti (%)	K-corr CIA (%)	$\delta^{44/40}$Ca (‰)	Ca isotope 2 sd (%)	I/(Ca+Mg) (µmol/mol)
N54	102.9	0.05	BD	21.51	BD	**0.02**	0.10	38	0.60	246	38	BD	-	-0.088	0.026	0.389
N52	100.9	0.30	BD	36.54	BD	0.17	0.30	BD	0.70	595	overcal	BD	-	-0.196	0.027	0.843
N51.5a	100	3.10	170	17.30	25	2.17	2.70	138	0.50	316	134	0.17	-	-0.312	0.039	0.505
N51	99.9	0.35	BD	38.12	BD	0.19	0.30	BD	0.70	409	overcal	**0.00**	-	-	-	0.825
N50	99	1.35	60	27.29	BD	0.95	1.20	183	0.70	417	183	0.06	-	-0.036	0.028	0.580
N56	99	0.30	**2**	33.41	BD	0.80	0.30	161	0.60	303	overcal	BD	-	-0.117	0.025	0.345
N41	95.4	3.25	250	-	42	1.84	3.00	216	0.10	191	-	0.16	78.53	-	-	-
N37	89.2	0.70	BD	-	11	2.14	0.60	423	**0.05**	99	-	0.03	72.54	-	-	-
N35	85.2	4.95	170	7.26	76	2.96	3.60	237	**0.05**	487	-	0.23	80.26	-	-	-
N33	81.9	1.10	BD	-	19	1.59	0.90	470	0.10	266	-	0.05	72.54	-	-	-
N31	77.4	1.50	**2**	-	24	1.89	1.20	630	0.10	599	-	0.06	75.34	-	-	-
N29	74.1	1.55	40	-	23	1.45	1.30	398	0.10	98	-	0.07	75.37	-	-	-
N27	70.6	0.70	BD	-	**8**	1.31	0.60	297	**0.05**	67	-	0.03	69.76	-	-	-
N25	67.1	1.45	20	-	22	1.26	1.20	151	**0.05**	351	-	0.07	76.01	-	-	-
N22	64.6	0.30	BD	20.07	BD	1.12	0.30	108	0.60	1416	55	BD	-	0.046 0.077 0.060	0.023 0.026 0.070	0.568
N18	55.6	0.15	BD	20.60	BD	0.37	0.20	179	0.55	241	42	BD	-	0.082 0.182	0.026 0.027	1.696
N13	45.6	0.56	25.891	19.50	BD	0.28	0.70	36	0.60	242	57	**0.01**	-	0.012 0.008 0.004	0.030 0.023 0.024	0.178
N9	37.6	0.45	BD	20.44	BD	0.31	0.50	60	0.60	334	63	**0.01**	-	-	-	-
N6	29.6	0.10	BD	21.69	BD	0.11	0.10	168	0.60	231	76	BD	-	-	-	0.131

Nuuchchalakh iron speciation data

Sample ID	Height (m)	Fecarb (%)	Feox (%)	Femag (%)	Fepy (%)	FeHR (%)	FeHR/FeT	Fepy/FeHR	Fe/Al
PET2	315	-	-	-	-	-	-	-	0.57
N18/2m	311	-	-	-	-	-	-	-	1.19
N14/2m	307	-	-	-	-	-	-	-	0.14
N10/2m	303	-	-	-	-	-	-	-	0.31
N192	293.5	-	-	-	-	-	-	-	0.24
N165	261	-	-	-	-	-	-	-	-
N115	205	-	-	-	-	-	-	-	-
N104	177	-	-	-	-	-	-	-	0.44
N91	141	-	-	-	-	-	-	-	0.76
N84	129	-	-	-	-	-	-	-	0.33
N55a	105.4	-	-	-	-	-	-	-	0.58
N54	102.9	-	-	-	-	-	-	-	0.27
N52	100.9	-	-	-	-	-	-	-	0.52
N51.5a	100	0.77	0.04	0.01	0.912	1.74	0.80	0.526	0.69
N51	99.9	-	-	-	-	-	-	-	0.53
N50	99	0.68	0.02	0.01	0.010	0.71	0.75	0.014	0.69
N56	99	0.36	0.21	0.01	0.227	0.80	1.00	0.285	2.49
N41	95.4	0.93	0.23	0.01	0.325	1.50	0.82	0.217	0.56
N37	89.2	1.72	0.38	0.00	0.002	2.10	0.98	0.001	3.01
N35	85.2	0.84	0.82	0.03	0.002	1.70	0.57	0.001	0.60
N33	81.9	1.26	0.10	0.01	0.003	1.37	0.86	0.002	1.45
N31	77.4	0.78	0.49	0.02	0.001	1.29	0.68	0.001	1.23
N29	74.1	0.79	0.32	0.00	0.001	1.11	0.77	0.001	0.92
N27	70.6	1.04	0.13	0.00	0.000	1.17	0.90	0.000	1.93
N25	67.1	0.88	0.10	0.00	0.104	1.09	0.86	0.095	0.86

Sample ID	Height (m)	Fecarb (%)	Feox (%)	Femag (%)	Fepy (%)	FeHR (%)	FeHR/FeT	Fepy/FeHR	Fe/Al
N22	64.6	0.63	0.41	0.00	0.006	1.05	0.94	0.005	3.70
N18	55.6	-	-	-	-	-	-	-	2.43
N13	45.6	-	-	-	-	-	-	-	0.50
N9	37.6	-	-	-	-	-	-	-	0.71
N6	29.6	-	-	-	-	-	-	-	0.88

Kyra-Ytyga sample details

Sample ID	Lithology	GPS	Formation	Sequence Stratigraphy
KY7	Siltstone	N59° 24.069' E136° 54.353'	Aim	TST
KY6	Siltstone	N59° 24.069' E136° 54.353'	Aim	TST
KY5	Siltstone	N59° 24.069' E136° 54.353'	Aim	TST
KY4	Siltstone	N59° 24.069' E136° 54.353'	Aim	TST
KY2A	Siltstone	N59° 24.069' E136° 54.353'	Aim	TST
KY3A	Siltstone	N59° 24.069' E136° 54.353'	Aim	TST

Kyra-Ytyga raw elemental data. Units in ppm unless noted.

Sample ID	Height (m)	Al (%)	Ba	Ca (%)	Cr	Fe (%)	K (%)	Mn	Na (%)	P	Ti (%)	K-corr CIA (%)
KY7	29	3.60	**10**	1.16	31	2.29	3.00	44	0.10	122	0.17	77.35
KY6	28	2.10	**0**	9.11	34	2.65	1.50	793	**0.05**	285	0.09	78.29
KY5	27	1.60	**0**	9.34	26	2.28	1.00	588	0.30	130	0.07	62.55
KY4	26	2.30	**10**	-	38	2.54	1.90	875	0.10	151	0.10	75.26

KY2A	7	2.90	20	0.05	14	0.56	1.80	**0**	**0.05**	26	0.06	79.76
KY3A	5	3.50	150	0.08	15	1.11	1.60	**7**	0.30	169	0.09	75.79

Kyra-Ytyga iron speciation data.

Sample ID	Height (m)	Fecarb (%)	Feox (%)	Femag (%)	Fepy (%)	FeHR (%)	FeHR/FeT	Fepy/FeHR	Fe/Al
KY7	29	0.17	0.55	0.06	0.001	0.78	0.34	0.001	0.64
KY6	28	1.46	0.13	0.04	0.001	1.63	0.62	0.001	1.25
KY5	27	1.54	0.02	0.00	0.454	2.01	0.88	0.226	1.41
KY4	26	1.39	0.20	0.03	0.000	1.62	0.64	0.000	1.12
KY2A	7	0.03	0.03	0.00	0.002	0.06	0.11	0.033	0.19
KY3A	5	0.07	0.03	0.05	0.000	0.14	0.12	0.000	0.32

Yinchangpo sample details. Yinchangpo section. 3km NE of Wanzicun, Huize County, Yunnan.

Sample ID	Lithology	GPS	Formation	Member	Sequence Stratigraphy
Daibu 10	phosphatic dolostone	N26° 29.593' E103° 13.604'	Zhujiaqing	Dahai	TST
Daibu 9	phosphatic dolostone	N26° 29.593' E103° 13.604'	Zhujiaqing	Dahai	TST
Daibu 9b	phosphatic dolostone	N26° 29.593' E103° 13.604'	Zhujiaqing	Dahai	TST
Daibu 8	phosphatic dolostone	N26° 29.593' E103° 13.604'	Zhujiaqing	Dahai	TST
Daibu 7	phosphatic dolostone	N26° 29.593' E103° 13.604'	Zhujiaqing	Dahai	TST
Daibu 6	phosphorite	N26° 29.593' E103° 13.604'	Zhujiaqing	Zhongyicun	HST
Daibu 5	phosphorite	N26° 29.593' E103° 13.604'	Zhujiaqing	Zhongyicun	HST
Daibu 4a	phosphorite	N26° 29.593' E103° 13.604'	Zhujiaqing	Zhongyicun	HST
Daibu 4b	phosphorite	N26° 29.593' E103° 13.604'	Zhujiaqing	Zhongyicun	HST
Daibu 3a	phosphorite	N26° 29.593' E103° 13.604'	Zhujiaqing	Zhongyicun	HST
Daibu 3b	phosphorite	N26° 29.593' E103° 13.604'	Zhujiaqing	Zhongyicun	HST
Daibu 1	siltstone	N26° 29.593' E103° 13.604'	Zhujiaqing	Daibu	TST
Daibu 0	white limestone	N26° 29.593' E103° 13.604'	Zhujiaqing	Daibu	TST
BYS 10	white marl	N26° 29.593' E103° 13.604'	Dengying	Baiyanshao	HST

Sample ID	Lithology	GPS	Formation	Member	Sequence Stratigraphy
BYS 9	white dolostone	N26° 29.593' E103° 13.604'	Dengying	Baiyanshao	HST
BYS 8	white dolostone	N26° 29.593' E103° 13.604'	Dengying	Baiyanshao	HST
BYS 7	white dolostone	N26° 29.593' E103° 13.604'	Dengying	Baiyanshao	HST
BYS 6	white dolostone	N26° 29.593' E103° 13.604'	Dengying	Baiyanshao	HST
BYS 5	white dolostone	N26° 29.593' E103° 13.604'	Dengying	Baiyanshao	HST
BYS 4	white dolostone	N26° 29.593' E103° 13.604'	Dengying	Baiyanshao	HST
BYS 3	white dolostone	N26° 29.593' E103° 13.604'	Dengying	Baiyanshao	HST
BYS 2	white dolostone	N26° 29.593' E103° 13.604'	Dengying	Baiyanshao	HST
BYS 1	grey dolostone	N26° 29.593' E103° 13.604'	Dengying	Baiyanshao	HST
Jiucheng 11	limestone laminite	N26° 29.593' E103° 13.604'	Dengying	Jiucheng	TST
Jiucheng 10	limestone	N26° 29.593' E103° 13.604'	Dengying	Jiucheng	TST
Jiucheng 8	dark grey limestone	N26° 29.593' E103° 13.604'	Dengying	Jiucheng	TST
Jiucheng 7	white limestone	N26° 29.593' E103° 13.604'	Dengying	Jiucheng	TST
Jiucheng 3	dolostone	N26° 29.593' E103° 13.604'	Dengying	Jiucheng	TST
Jiucheng 2	dolostone	N26° 29.593' E103° 13.604'	Dengying	Jiucheng	TST

Sample ID	Lithology	GPS	Formation	Member	Sequence Stratigraphy
DLT 17	micritic dolomite	N26° 29.593' E103° 13.604'	Dengying	Donglongtan	HST
DLT 16	micritic dolomite	N26° 29.593' E103° 13.604'	Dengying	Donglongtan	HST
DLT 15a	stromatolitic limestone	N26° 29.593' E103° 13.604'	Dengying	Donglongtan	HST
DLT 15b	stromatolitic limestone	N26° 29.593' E103° 13.604'	Dengying	Donglongtan	HST
DLT 14	micritic dolomite	N26° 29.593' E103° 13.604'	Dengying	Donglongtan	HST
DLT 13	micritic dolomite	N26° 29.593' E103° 13.604'	Dengying	Donglongtan	HST

Yinchangpo raw elemental data. Units in ppm unless noted.

Sample ID	Height (m)	$\delta^{13}C_{carb}$ (‰)	$\delta^{18}O_{carb}$ (‰)	Al (%)	Ba	Cr	Fe (%)	K (%)	Mn	Na (%)	P	Sr	Ti (%)
Daibu 10	782	-0.321	-12.387	2.50	220	10.480	4.437	1.375	3609.510	0.113	3003.361	69.490	0.093
Daibu 9	777	1.466	-9.931	0.85	150	4.685	0.568	0.594	740.247	0.106	558.100	91.447	0.033
Daibu 9b	777	-1.175	-11.052	1.90	300	13.940	0.947	1.061	815.845	0.102	overcal	112.304	0.064
Daibu 8	772	3.017	-14.016	0.40	50	4.295	0.229	0.307	207.930	0.174	1009.207	overcal	0.013
Daibu 7	768	3.686	-14.005	0.50	50	4.561	0.277	0.369	235.061	0.187	1154.253	overcal	0.017
Daibu 6	765	-8.042	-13.773	6.05	630	44.293	4.477	2.398	258.422	0.089	647.809	21.297	0.185
Daibu 5	763	-4.610	-11.673	4.90	350	32.167	2.981	2.053	311.249	0.101	508.725	22.430	0.155
Daibu 4a	761	-7.390	-11.441	7.10	660	83.848	2.673	3.458	141.371	0.232	1119.485	36.722	0.027
Daibu 4b	761	-7.505	-11.663	7.20	710	85.517	2.827	3.534	498.095	0.214	1149.703	36.025	0.259
Daibu 3a	757	-6.486	-12.127	6.80	590	69.989	3.576	2.786	194.306	1.092	1055.730	75.419	0.241

Sample ID	Height (m)	$\delta^{13}C_{carb}$ (‰)	$\delta^{18}O_{carb}$ (‰)	Al (%)	Ba	Cr	Fe (%)	K (%)	Mn	Na (%)	P	Sr	Ti (%)
Daibu 3b	757	-7.640	-11.431	7.25	640	87	3.93	3.10	198	0.95	1044	63	0.28
Daibu 1	751	-	-	1.15	120	17	-	0.50	365	**0.05**	1662	30	0.04
Daibu 0	750	-1.497	-9.294	0.10	**10**	13	0.19	0.10	431	0.10	713	32	**0.00**
BYS 10	715	1.214	-8.864	0.10	**10**	**1**	0.25	0.10	247	**0.05**	309	31	**0.00**
BYS 9	675	1.036	-8.722	**0.05**	20	**2**	0.36	0.10	375	0.10	288	36	**0.00**
BYS 8	650	1.683	-8.284	**0.00**	**10**	**1**	0.14	0.10	148	0.15	212	25	**0.00**
BYS 7	635	0.728	-8.079	**0.00**	**0**	**1**	0.09	0.10	106	0.10	189	29	**0.00**
BYS 6	629	1.174	-8.276	**0.00**	**0**	**1**	0.13	0.10	116	0.10	143	27	**0.00**
BYS 5	625	1.350	-8.471	**0.00**	**0**	**1**	0.17	0.10	154	0.10	407	25	**0.00**
BYS 4	620	1.395	-8.541	**0.00**	**0**	**1**	0.19	0.10	137	0.10	345	20	**0.00**
BYS 3	585	1.322	-8.050	**0.00**	**10**	**3**	0.36	0.10	200	0.10	1991	37	**0.00**
BYS 2	515	1.667	-6.047	**0.05**	**10**	6	0.12	0.10	94	0.10	1168	39	**0.00**
BYS 1	485	1.385	-7.286	0.45	**10**	7	0.23	0.30	125	0.10	1776	57	**0.01**
Jiucheng 11	472	1.214	-8.440	0.20	**10**	**3**	0.23	0.20	106	0.15	530	50	**0.01**
Jiucheng 10	470	0.738	-6.984	0.90	20	6	1.16	0.70	911	0.15	355	41	0.03
Jiucheng 8	467	3.255	-8.329	0.25	**10**	5	0.18	0.20	89	0.15	1025	44	**0.01**
Jiucheng 7	466	2.008	-8.897	0.45	**10**	**4**	0.39	0.30	404	0.15	172	33	**0.02**
Jiucheng 3	462	1.741	-5.842	1.00	30	12	0.36	0.60	143	0.15	155	42	0.04
Jiucheng 2	460	1.787	-5.094	0.55	20	7	0.30	0.40	92	0.15	94	60	0.03
DLT 17	440	1.100	-6.556	-	-	-	0.16	-	-	-	-	-	-
DLT 16	370	1.199	-5.841	-	-	-	0.03	-	-	-	-	-	-
DLT 15a	350	2.041	-4.215	-	-	-	0.12	-	-	-	-	-	-
DLT 15b	350	2.041	-3.579	-	-	-	0.10	-	-	-	-	-	-
DLT 14	250	2.391	-5.296	-	-	-	0.17	-	-	-	-	-	-
DLT 13	205	2.239	-2.626	-	-	-	0.14	-	-	-	-	-	-

Yinchangpo iron speciation data.

Sample ID	Height (m)	Fecarb (%)	Feox (%)	Femag (%)	Fepy (%)	FeHR (%)	FeHR/FeT	Fepy/FeHR	Fe/Al
Daibu 10	782	3.37	0.06	0.05	0.619	4.11	0.93	0.151	1.76
Daibu 9	777	0.27	0.01	0.01	0.002	0.29	0.50	0.008	0.66
Daibu 9b	777	0.17	0.58	0.01	0.001	0.76	0.80	0.001	0.50
Daibu 6	765	0.12	2.43	0.43	0.007	2.98	0.67	0.002	0.74
Daibu 5	763	0.07	1.97	0.06	0.002	2.12	0.71	0.001	0.61
Daibu 4a	761	0.05	1.64	0.06	0.005	1.75	0.66	0.003	0.38
Daibu 4b	761	0.05	1.71	0.07	0.004	1.82	0.64	0.002	0.39
Daibu 3a	757	0.11	1.63	0.19	0.002	1.93	0.54	0.001	0.53
Daibu 3b	757	0.17	1.75	0.27	0.004	2.19	0.56	0.002	0.54
Jiucheng 10	470	0.71	0.27	0.00	0.001	0.99	0.85	0.002	1.27

Wuhe sample details. Wuhe section. South of Sandoupiing, Yangtze Gorges, Hubei.

Sample ID	Lithology	GPS	Formation	Member	Sequence Stratigraphy
Yanjiahe 6	grey dolostone	N30° 48.136' E111° 1.295'	Yanjiahe	undefined	TST
Yanjiahe 5	grey dolostone	N30° 48.136' E111° 1.295'	Yanjiahe	undefined	TST
Yanjiahe 4	grey dolostone	N30° 48.136' E111° 1.295'	Yanjiahe	undefined	TST
Yanjiahe 3	grey dolostone	N30° 48.136' E111° 1.295'	Yanjiahe	undefined	TST
Yanjiahe 2	grey dolostone	N30° 48.136' E111° 1.295'	Yanjiahe	undefined	TST
Yanjiahe 1	grey dolostone	N30° 48.136' E111° 1.295'	Yanjiahe	undefined	TST
Baimatuo 13	dolomite	N30° 48.136' E111° 1.295'	Dengying	Baimatuo	HST
Baimatuo 12	dolomite	N30° 48.136' E111° 1.295'	Dengying	Baimatuo	HST
Baimatuo 11	dolomite	N30° 48.136' E111° 1.295'	Dengying	Baimatuo	HST
Baimatuo 10	dolomite	N30° 48.136' E111° 1.295'	Dengying	Baimatuo	HST
Baimatuo 9	dolomite	N30° 48.136' E111° 1.295'	Dengying	Baimatuo	HST
Baimatuo 8	dolomite	N30° 48.136' E111° 1.295'	Dengying	Baimatuo	HST
Baimatuo 7	dolomite	N30° 48.136' E111° 1.295'	Dengying	Baimatuo	HST
Baimatuo 4	dolomite	N30° 48.136' E111° 1.295'	Dengying	Baimatuo	HST

Sample ID	Lithology	GPS	Formation	Member	Sequence Stratigraphy
Baimatuo 3	dolomite	N30° 48.136' E111° 1.295'	Dengying	Baimatuo	HST
Baimatuo 2	dolomite	N30° 48.136' E111° 1.295'	Dengying	Baimatuo	HST
Baimatuo 1	dolomite	N30° 48.136' E111° 1.295'	Dengying	Baimatuo	HST
Shibantan 13	bituminous limestone	N30° 48.136' E111° 1.295'	Dengying	Shibantan	TST
Shibantan 12	bituminous limestone	N30° 48.136' E111° 1.295'	Dengying	Shibantan	TST
Shibantan 11	bituminous limestone	N30° 48.136' E111° 1.295'	Dengying	Shibantan	TST
Shibantan 10	bituminous limestone	N30° 48.136' E111° 1.295'	Dengying	Shibantan	TST
Shibantan 9	bituminous limestone with burrows	N30° 48.136' E111° 1.295'	Dengying	Shibantan	TST
Shibantan 6	bituminous limestone	N30° 48.136' E111° 1.295'	Dengying	Shibantan	TST
Shibantan 5	bituminous limestone	N30° 48.136' E111° 1.295'	Dengying	Shibantan	TST
Shibantan 4	bituminous limestone	N30° 48.136' E111° 1.295'	Dengying	Shibantan	TST
Shibantan 3	bituminous limestone	N30° 48.136' E111° 1.295'	Dengying	Shibantan	TST
Shibantan 2	bituminous limestone	N30° 48.136' E111° 1.295'	Dengying	Shibantan	TST
Shibantan 1	bituminous limestone	N30° 48.136' E111° 1.295'	Dengying	Shibantan	TST
Hamajing 6	dolostone	N30° 48.136' E111° 1.295'	Dengying	Hamajing	HST

Sample ID	Lithology	GPS	Formation	Member	Sequence Stratigraphy
Hamajing 5	wavy laminated dolostone (stromatolitic)	N30° 48.136' E111° 1.295'	Dengying	Hamajing	HST
Hamajing 4	dolostone breccia (teepee structure)	N30° 48.136' E111° 1.295'	Dengying	Hamajing	HST
Hamajing 3	dolostone	N30° 48.136' E111° 1.295'	Dengying	Hamajing	HST
Hamajing 2	dolostone	N30° 48.136' E111° 1.295'	Dengying	Hamajing	HST
Hamajing 1	dolostone	N30° 48.136' E111° 1.295'	Dengying	Hamajing	HST

Wuhe raw elemental data. Units in ppm unless noted.

Sample ID	Height (m)	$\delta^{13}C_{carb}$ (‰)	$\delta^{18}O_{carb}$ (‰)	Al (%)	Ba	Cr	Fe (%)	K (%)	Mn	Na (%)	P	Sr	Ti (%)
Yanjiahe 6	268.5	-1.543	-7.095	2.15	110	100	1.14	1.90	361	0.15	267	38	1.14
Yanjiahe 5	264.5	-0.732	-7.809	2.80	210	116	1.03	2.50	88	0.10	566	33	1.43
Yanjiahe 4	263.5	-0.018	-6.177	2.25	120	107	1.03	2.20	99	0.15	456	56	1.29
Yanjiahe 3	262.5	0.298	-5.413	1.45	60	52	0.87	1.30	106	0.15	1724	71	0.71
Yanjiahe 2	261.5	0.826	-5.401	1.60	60	62	0.85	1.40	107	0.15	841	78	0.78
Yanjiahe 1	260.5	0.732	-5.686	1.85	100	77	0.87	1.60	128	0.15	1058	68	0.94
Baimatuo 13	250.8	-0.015	-6.918	0.05	BD	**2**	0.09	0.10	195	0.10	287	47	**0.01**
Baimatuo 12	250	0.180	-5.792	0.05	BD	**3**	0.09	0.10	69	0.10	793	52	0.02
Baimatuo 11	249	0.050	-5.989	0.05	BD	**1**	**0.04**	0.10	65	0.10	259	37	0.02
Baimatuo 10	248	-0.060	-6.075	0.05	BD	**2**	0.05	0.10	90	0.10	490	38	0.02
Baimatuo 9	228	0.736	-5.994	**0.00**	BD	**2**	0.06	**0.05**	93	0.10	633	44	**0.01**
Baimatuo 8	208	0.703	-5.722	**0.00**	BD	**1**	**0.04**	0.10	80	0.10	688	42	**0.01**

Sample ID	Height (m)	$\delta^{13}C_{carb}$ (‰)	$\delta^{18}O_{carb}$ (‰)	Al (%)	Ba	Cr	Fe (%)	K (%)	Mn	Na (%)	P	Sr	Ti (%)
Baimatuo 7	198	0.079	-6.042	**0.00**	BD	**1**	0.05	**0.05**	80	0.10	947	35	**0.00**
Baimatuo 4	191	2.949	-5.614	**0.00**	BD	**3**	BD	**0.05**	27	0.10	305	35	**0.01**
Baimatuo 3	176	2.121	-5.688	**0.00**	BD	**1**	**0.03**	**0.05**	36	0.10	320	35	**0.01**
Baimatuo 2	175	2.044	-5.556	**0.00**	BD	**1**	BD	0.10	41	0.10	411	38	**0.01**
Baimatuo 1	172.5	2.027	-6.943	**0.00**	BD	**1**	0.06	**0.05**	191	0.10	671	50	**0.01**
Shibantan 13	167	2.580	-6.686	**0.00**	BD	**1**	**0.04**	0.10	245	0.10	510	62	**0.01**
Shibantan 12	162	1.522	-7.913	0.05	BD	**2**	0.13	0.10	350	0.10	1125	48	0.03
Shibantan 11	157	1.493	-7.265	**0.00**	BD	**2**	0.07	**0.05**	333	0.10	1015	45	**0.01**
Shibantan 10	154	1.061	-7.343	**0.00**	BD	**1**	**0.04**	**0.05**	233	0.10	341	50	**0.01**
Shibantan 9	151	0.380	-7.065	**0.00**	10	**1**	**0.03**	**0.05**	154	0.10	549	48	**0.01**
Shibantan 6	101	4.050	-5.266	0.05	BD	9	**0.04**	0.10	BD	0.20	916	overcal	0.02
Shibantan 5	94	3.479	-4.467	0.05	BD	**4**	BD	0.10	BD	0.20	803	overcal	**0.01**
Shibantan 4	88	3.523	-5.708	0.05	30	8	BD	0.10	BD	0.25	1297	overcal	0.02
Shibantan 3	36	4.137	-5.790	0.05	20	**3**	BD	**0.05**	BD	0.20	418	overcal	**0.00**
Shibantan 2	32	4.381	-6.416	0.10	20	11	**0.04**	0.10	BD	0.25	839	overcal	0.03
Shibantan 1	21.1	5.512	-6.325	**0.00**	10	5	0.06	0.10	BD	0.15	641	overcal	0.02
Hamajing 6	14	0.917	-4.769	0.30	10	**4**	0.10	0.15	145	0.15	27	71	0.11
Hamajing 5	11.2	1.012	-3.538	0.05	10	**2**	**0.04**	**0.00**	78	0.10	77	82	0.02
Hamajing 4	11	2.665	-3.403	0.05	BD	**2**	0.05	**0.00**	109	0.15	125	57	**0.01**
Hamajing 3	8	2.773	-1.714	0.05	BD	**2**	0.08	**0.05**	49	0.15	143	93	0.02
Hamajing 2	4	2.741	-2.130	0.10	BD	**3**	0.19	0.10	58	0.20	107	91	0.02
Hamajing 1	1	-1.287	-3.286	0.45	10	8	0.20	0.35	1063	0.15	681	59	0.15

Wuhe iron speciation data.

Sample ID	Height (m)	Fecarb (%)	Feox (%)	Femag (%)	Fepy (%)	FeHR (%)	FeHR/FeT	Fepy/FeHR	Fe/Al
Yanjiahe 6	268.5	0.33	0.51	0.01	0.003	0.85	0.74	0.003	0.53
Yanjiahe 5	264.5	0.10	0.49	0.01	0.148	0.75	0.73	0.196	0.37
Yanjiahe 4	263.5	0.19	0.60	0.01	0.004	0.80	0.78	0.006	0.45
Yanjiahe 3	262.5	0.12	0.61	0.01	0.002	0.74	0.84	0.002	0.61
Yanjiahe 2	261.5	0.04	0.63	0.01	0.002	0.68	0.80	0.003	0.54
Yanjiahe 1	260.5	0.04	0.63	0.01	0.002	0.68	0.78	0.003	0.47

Supplementary Figures

Figures AB1-AB11 = Nama Group. AB1 Iron partitioning of samples from the inner ramp. Combined data of Wood et al., (2015) Sperling et al. (2015a) and this study.

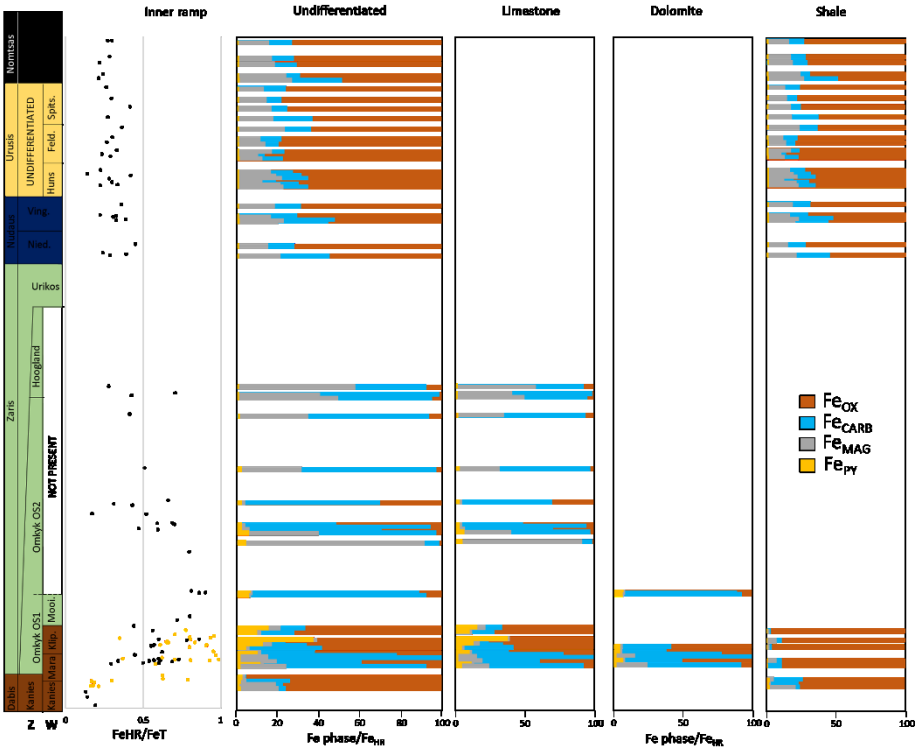

Figure AB2 Iron partitioning of samples from the mid ramp.

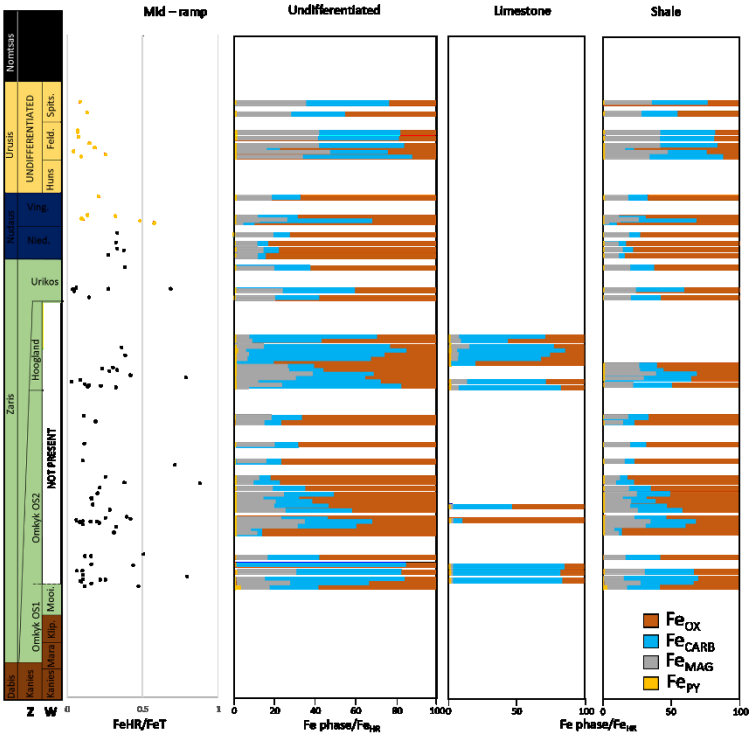

Figure AB3 Iron partitioning of samples from the outer ramp

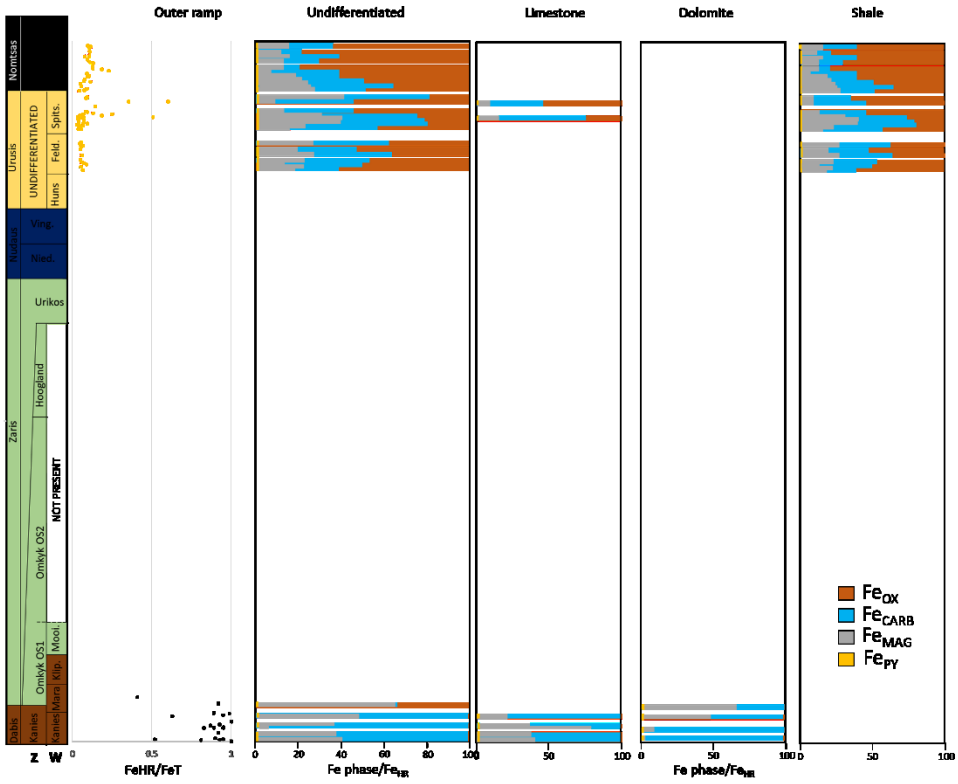

Figures AB4 to AB6: Data points coloured according to interpreted palaeoredox.

Figure AB4 Selected elemental concentrations and ratios of the July 2016 sample dataset.

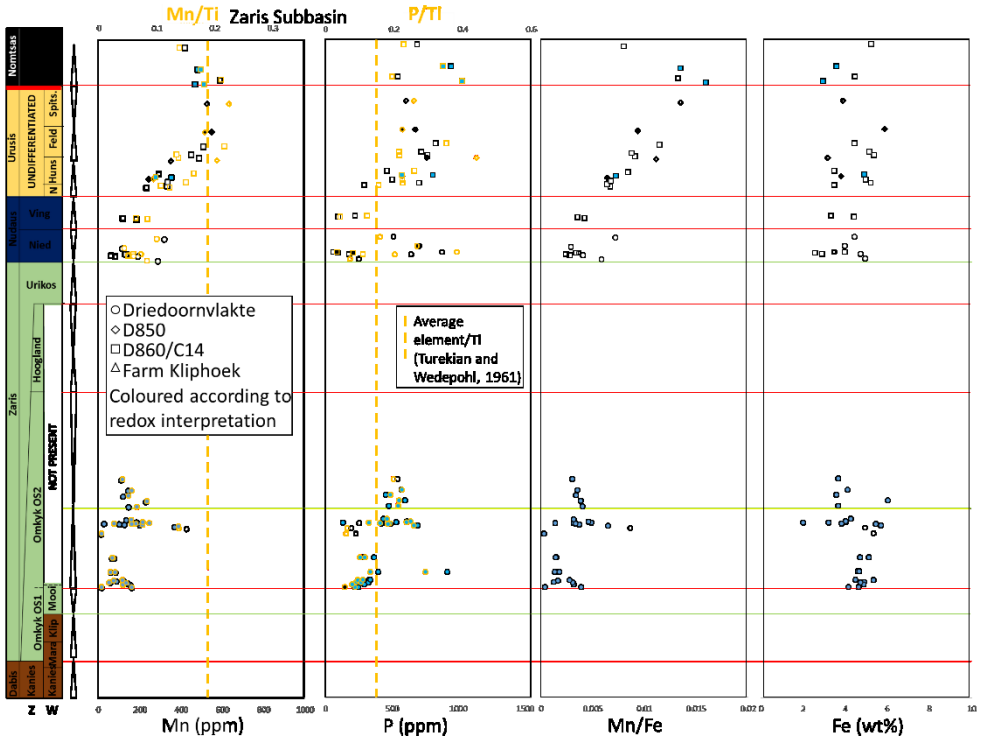

Figure AB5 Selected elemental concentrations and ratios of the July 2016 sample dataset.

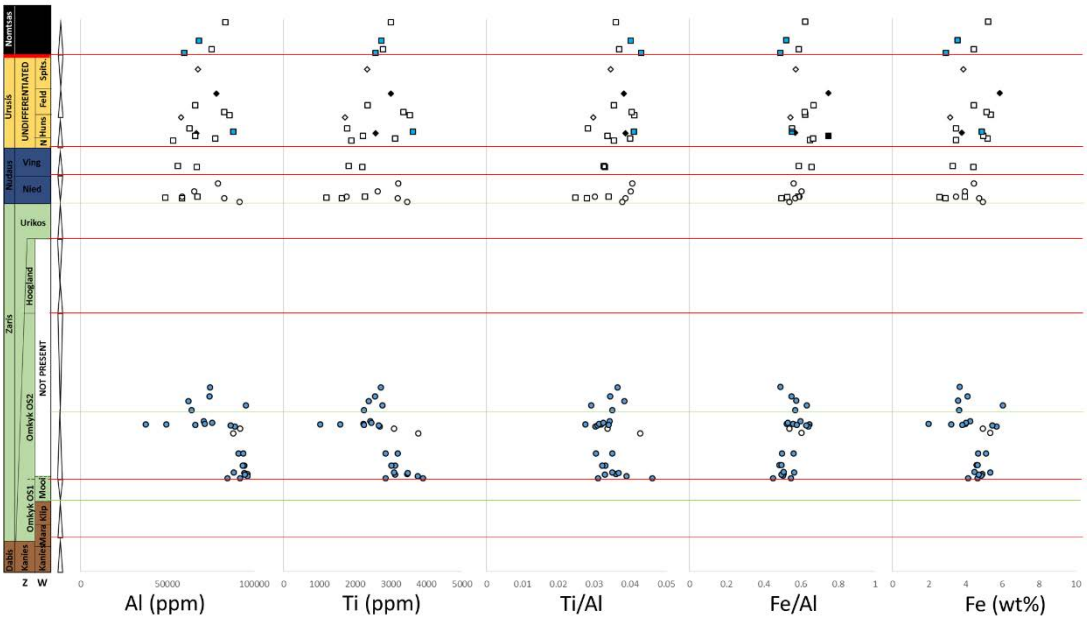

Figure AB6 Selected elemental concentrations and ratios plotted against the chemical index of alteration (CIA) for samples of the July 2016 dataset.

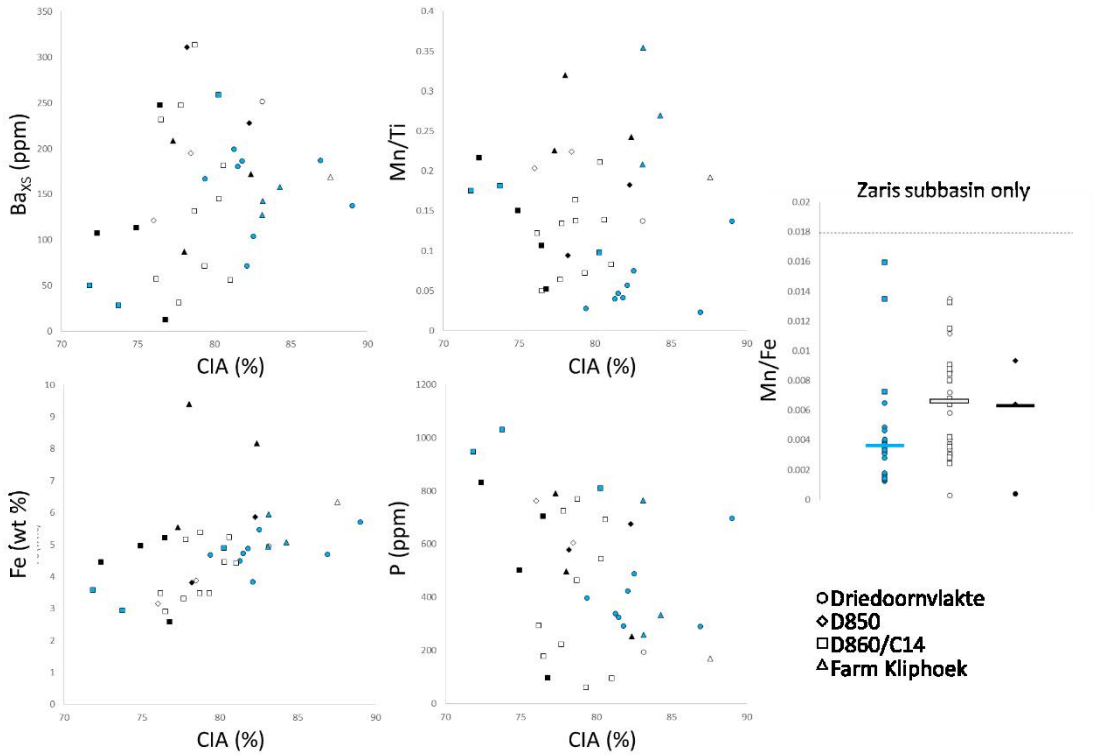

Figure AB7 Binned iron speciation data, ranges and normalised frequency.

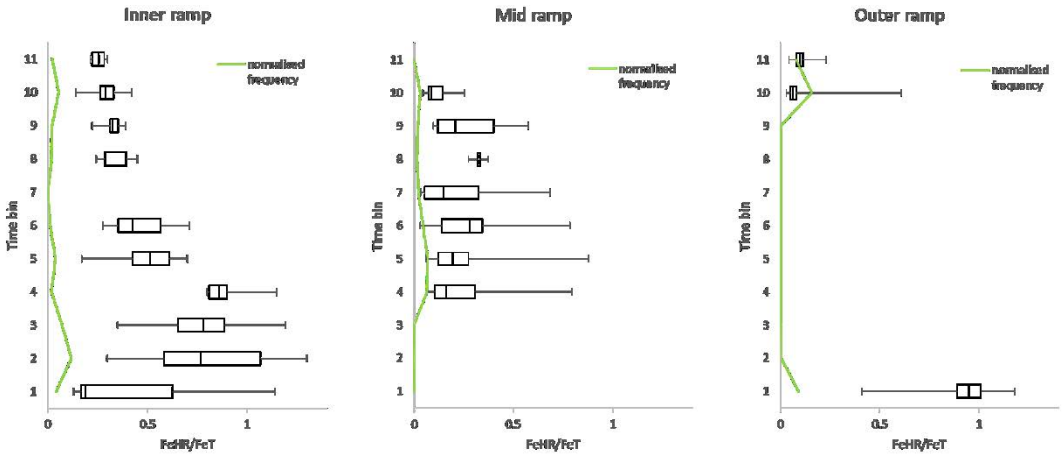

Figures AB8 – AB11 key:

D860/C14 ● Driedoornvlakte ◆ D850 ▲ Farm Kliphoek

Figure AB8 The relationship between P/Ti and Fe_{HR}/Fe_T

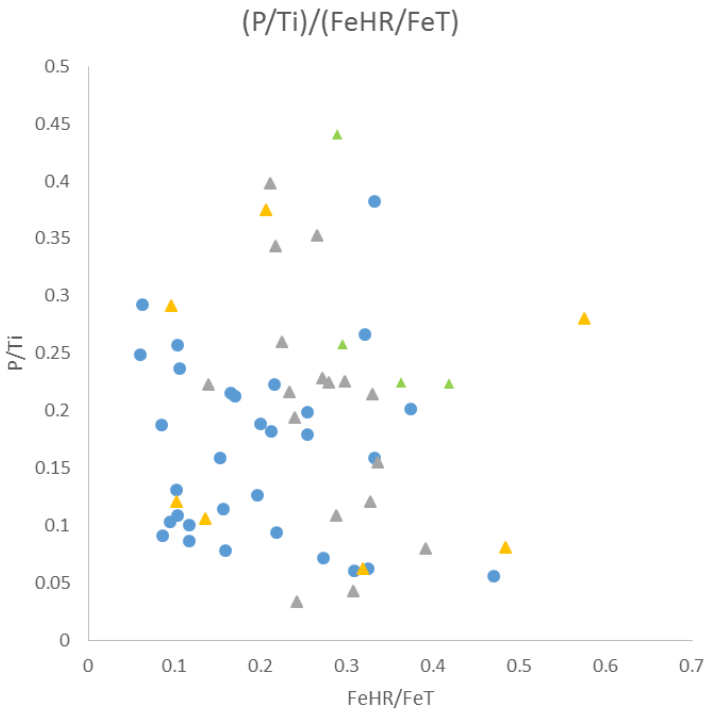

Figure AB9 The relationship between Ba (ppm) and Al (wt%) in the Nama Group

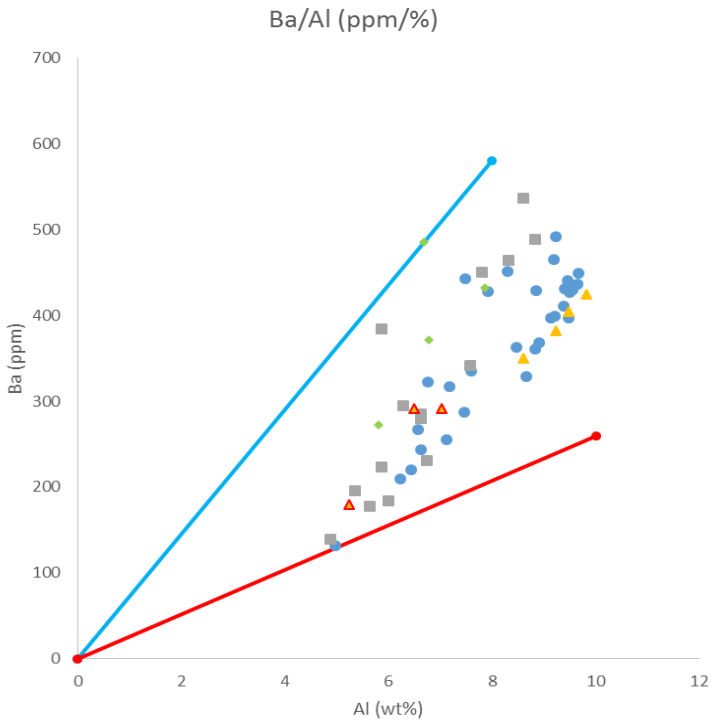

Figure AB10 The lack of covariation between Ba_{XS} (ppm) and Fe_{ox} (wt%) in the Nama Group

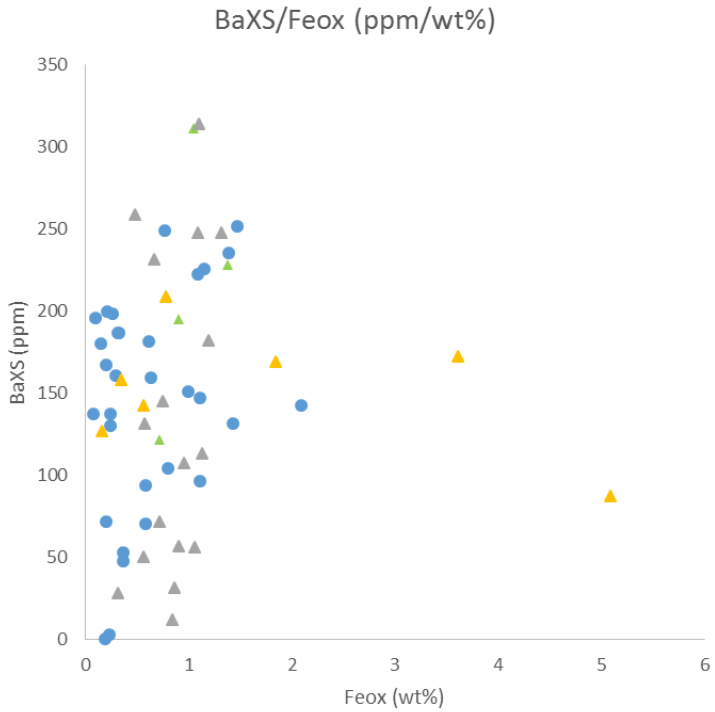

Figure AB11 The lack of covariation between Ba_{XS} (ppm) and Mn (ppm) in the Nama Group

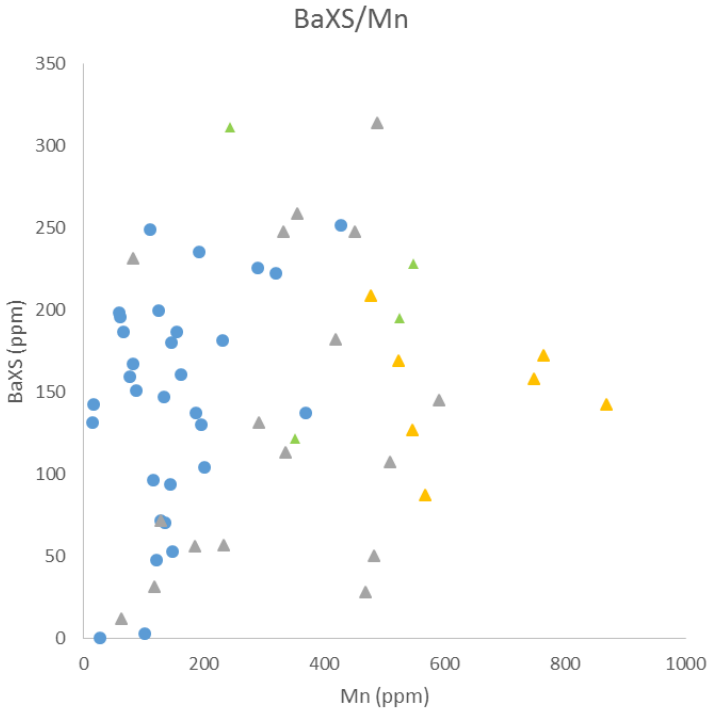

Figures AB12 to AB15. 3D dioramas representing the evolution of redox throughout the final ~10 Myrs of the Nama Group with associated fossil distribution. See Appendix D for key to fossil symbols.

Figure AB12. Kanies Member to Omkyk OS1/OS2 sequence boundary

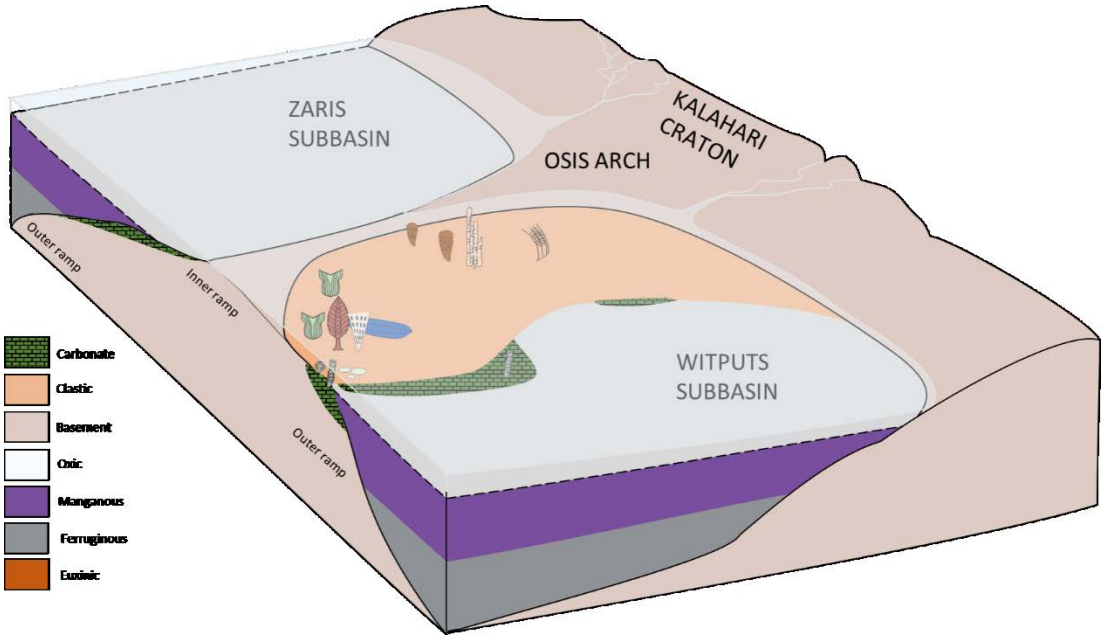

Figure AB13. Omkyk OS2 Unit 3m to Urikos/Niederhagen sequence boundary

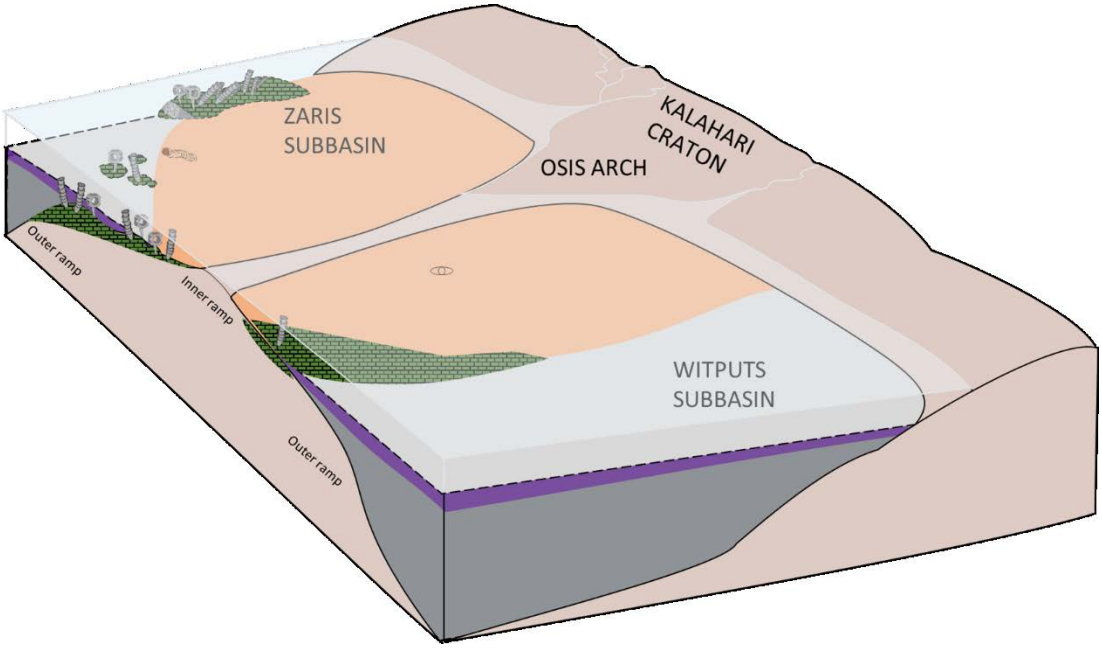

Figure AB14. Vingerbreek Member

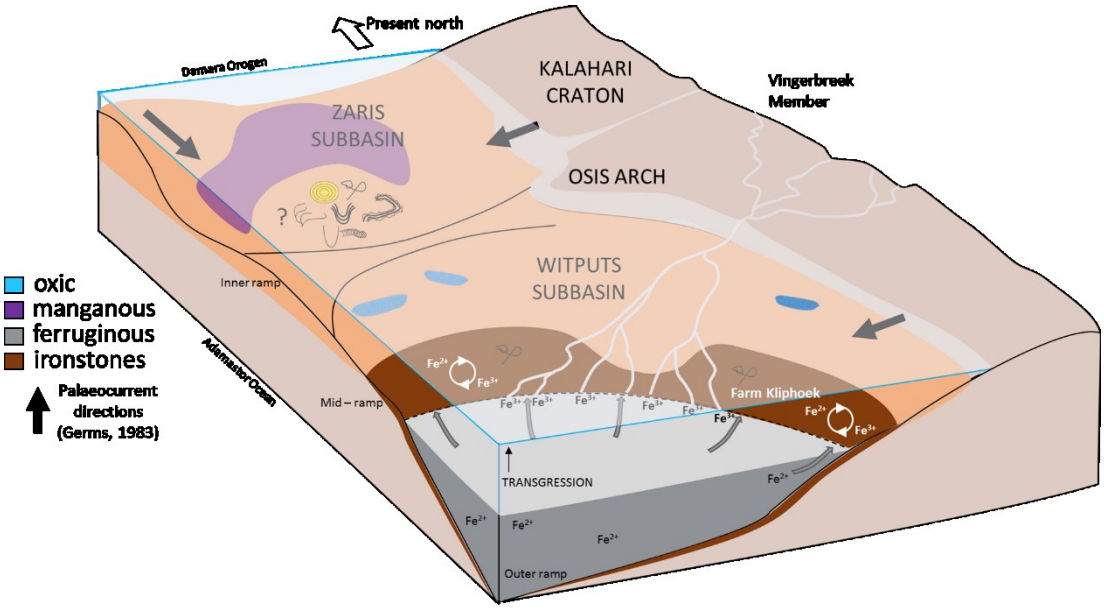

Figure AB15. Spitskop Member

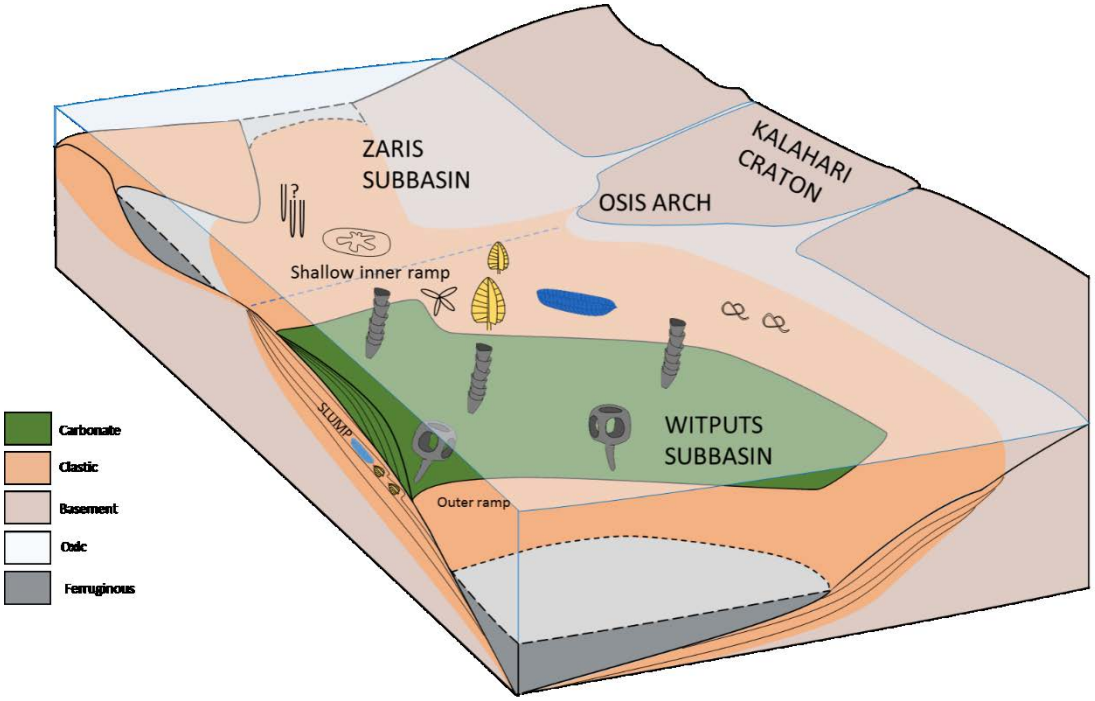

Figure AB16 = Yudoma Group (overleaf).

a) – c) Calcium oxide contributed in silicates (CaO*) in sections of the Yudoma River. Calculated via correcting for calcium contributed in carbonates and apatite. **d)** The relationship between Fe_{HR}/Fe_T and the chemical index of alteration (CIA) for siliciclastic samples of Nuuchchalakh and Kyra-Ytyga sections.

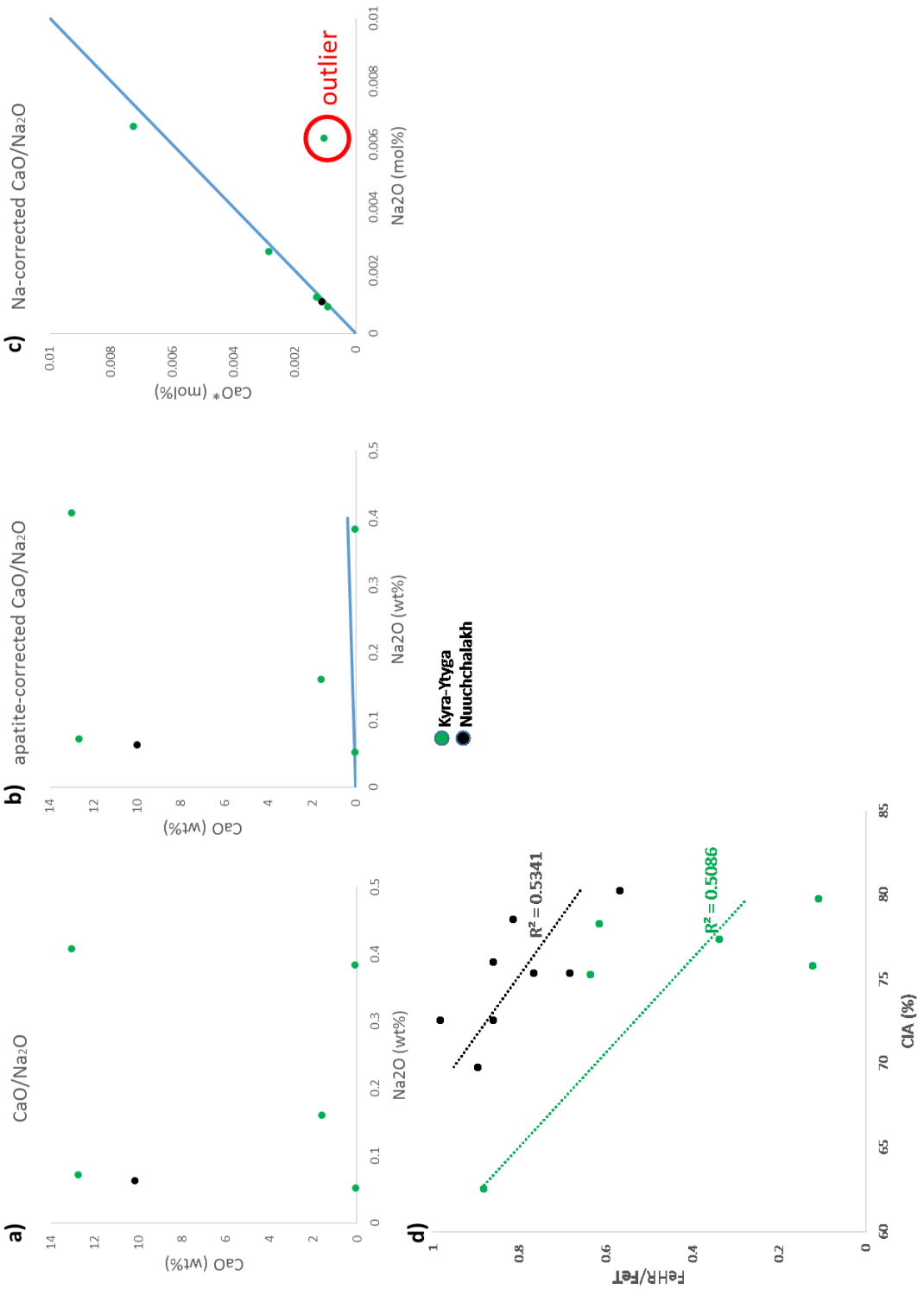
a)
CaO/Na2O
CaO (wt%)
Na2O (wt%)
b)
apatite-corrected CaO/Na2O
CaO (wt%)
Na2O (wt%)
c)
Na-corrected CaO/Na2O
CaO* (mol%)
Na2O (mol%)
outlier
d)
Kyra-Ytyga
Nuuchchalakh
FeHR/FeT
CIA (%)
R² = 0.5341
R² = 0.5086

Appendix C

EPMA cement stratigraphy raw data

This appendix includes raw elemental data interpreted in Chapter 4.

ID	Component	Ca (%)	Ca (mol)	Mg (%)	Mg (mol)	Mn (ppm)	Fe (ppm)	Sr (ppm)	Mg/Ca	mMg/Ca	Mn/Sr	Mn LOD (ppm)	Fe LOD (ppm)	Sr LOD (ppm)
D2_5_1	DS	22.23	5.55	12.65	5.21	368	1553	59	0.569	-	6.237	99	131	121
D2_5_2	DS	22.46	5.60	12.53	5.15	342	1331	98	0.558	-	3.490	99	130	122
D2_5_3	DS	22.52	5.62	13.53	5.57	387	1745	57	0.601	-	6.789	102	135	123
D2_5_4	DS	22.54	5.62	12.95	5.33	248	1755	133	0.574	-	1.865	102	131	122
D2_5_5	DS	22.63	5.65	12.62	5.19	351	1304	151	0.558	-	2.325	99	127	116
D2_10_2	DS	22.26	5.55	12.59	5.18	551	2037	95	0.565	-	5.800	99	131	122
D2_10_3	DS	22.94	5.72	12.63	5.20	99	330	80	0.551	-	1.238	100	129	121
D2_10_4	DS	22.41	5.59	12.64	5.20	164	604	47	0.564	-	3.489	99	126	121
D2_10_5	DS	23.50	5.86	12.48	5.14	224	785	24	0.531	-	9.333	98	131	122
D2_12_4	DS	22.85	5.70	11.92	4.90	290	1471	27	0.521	-	10.741	98	133	125
D2_12_5	DS	20.83	5.20	11.30	4.65	205	3455	94	0.542	-	2.181	101	136	128
D2_12_6	DS	22.38	5.58	12.43	5.11	257	2944	83	0.555	-	3.096	99	135	123
D2_12_7	DS	21.99	5.49	12.47	5.13	280	4291	116	0.567	-	2.414	99	133	120
D2_12_8	DS	22.51	5.62	12.80	5.26	169	2191	96	0.568	-	1.760	99	130	120
D2_12_9	DS	22.14	5.52	13.31	5.48	341	1988	100	0.601	-	3.410	101	131	121
D2_12_10	DS	22.30	5.56	12.85	5.29	259	2677	137	0.576	-	1.891	100	131	116
D2_12_11	DS	22.26	5.55	12.96	5.33	403	1264	115	0.582	-	3.504	98	131	122
D2_2_1	DS	21.34	5.32	12.35	5.08	182	2412	159	0.579	-	1.145	98	132	122
D2_2_2	DS	22.01	5.49	12.52	5.15	122	1329	164	0.569	-	0.744	99	129	118
D2_2_3	DS	21.99	5.49	10.76	4.43	150	3311	161	0.489	-	0.932	97	130	120
D2_2_4	DS	22.27	5.56	12.71	5.23	173	1925	80	0.571	-	2.163	99	129	124
D2_2_5	DS	21.83	5.45	12.73	5.24	73	2044	119	0.583	-	0.613	100	131	122
D2_2_6	DS	22.01	5.49	12.74	5.24	144	1731	130	0.579	-	1.108	99	130	120
DR1_1_1	DS	23.02	5.74	13.16	5.41	185	1512	288	0.572	-	0.642	98	128	118
DR1_2_1	DS	22.67	5.66	13.28	5.46	51	959	183	0.586	-	0.279	99	132	118

ID	Component	Ca (%)	Ca (mol)	Mg (%)	Mg (mol)	Mn (ppm)	Fe (ppm)	Sr (ppm)	Mg/Ca	mMg/Ca	Mn/Sr	Mn LOD (ppm)	Fe LOD (ppm)	Sr LOD (ppm)
DR1_2_2	DS	22.32	5.57	13.57	5.58	68	1788	174	0.608	-	0.391	100	131	117
DR1_2_3	DS	24.00	5.99	12.77	5.26	72	847	129	0.532	-	0.558	97	125	117
DR1_2_4	DS	22.50	5.61	13.29	5.47	83	849	97	0.591	-	0.856	99	128	120
DR1_2_5	DS	22.63	5.65	13.17	5.42	90	463	102	0.582	-	0.882	100	128	120
DR1_3_1	DS	22.16	5.53	13.81	5.68	20	388	119	0.623	-	0.168	100	129	122
DR1_3_2	DS	22.45	5.60	13.18	5.42	219	623	120	0.587	-	1.825	98	129	115
DR1_3_9	DS	22.86	5.70	13.05	5.37	254	1329	171	0.571	-	1.485	97	129	118
DR1_3_12	DS	22.02	5.49	14.42	5.93	144	1368	114	0.655	-	1.263	100	131	121
DR1_3_15	DS	22.52	5.62	13.30	5.47	220	2156	171	0.591	-	1.287	100	132	123
DR1_3_18	DS	22.41	5.59	13.24	5.45	25	791	50	0.591	-	0.500	100	128	122
DR1_4_1	DS	25.05	6.25	10.61	4.37	193	386	276	0.424	-	0.699	99	130	118
DR1_4_4	DS	24.22	6.04	12.64	5.20	71	446	86	0.522	-	0.826	99	126	121
DR1_4_6	DS	22.48	5.61	13.33	5.48	364	2226	92	0.593	-	3.957	96	129	119
DR1_4_9	DS	23.24	5.80	12.61	5.19	197	1744	171	0.543	-	1.152	100	130	121
DR1_4_12	DS	22.40	5.59	13.32	5.48	240	1122	129	0.594	-	1.860	97	129	120
DRY_B_9_1	DS	22.16	5.53	13.64	5.61	77	1225	213	0.616	-	0.362	97	127	115
DRY_B_9_2	DS	22.24	5.55	13.18	5.42	78	1608	154	0.592	-	0.506	100	131	120
DRY_B_9_4	DS	21.75	5.43	14.08	5.79	123	2801	136	0.648	-	0.904	99	132	122
DRY_B_9_8	DS	22.38	5.58	13.24	5.45	86	1456	158	0.592	-	0.544	97	128	116
DOL_2_3/1	DS	22.40	5.59	13.73	5.65	263	6848	470	0.613	-	0.560	103	140	117
DOL_2_3/2	DS	27.29	6.81	14.07	5.79	259	4256	229	0.516	-	1.131	102	138	122
DOL_2_4/1	DS	21.37	5.33	12.68	5.22	135	5435	109	0.593	-	1.239	101	139	125
DOL_2_4/2	DS	22.80	5.69	15.06	6.20	200	2681	151	0.661	-	1.325	102	135	124
DR3_1ca_6	DS	23.24	5.80	11.92	4.91	140	1621	151	0.513	-	0.927	101	130	122
DR3_1ca_7	DS	22.97	5.73	11.90	4.90	286	2308	220	0.518	-	1.300	99	130	119

ID	Component	Ca (%)	Ca (mol)	Mg (%)	Mg (mol)	Mn (ppm)	Fe (ppm)	Sr (ppm)	Mg/Ca	mMg/Ca	Mn/Sr	Mn LOD (ppm)	Fe LOD (ppm)	Sr LOD (ppm)
DR3_1ca_8	DS	30.19	7.53	7.56	3.11	443	2888	511	0.250	-	0.867	106	138	122
DR3_A1_0	DS	21.98	5.48	12.71	5.23	999	6490	377	0.578	-	2.650	102	134	122
DRY_B_1_1	AC	40.05	9.99	0.20	0.08	19	314	471	0.005	-	0.040	110	131	119
DRY_B_1_3	AC	39.80	9.93	0.32	0.13	21	225	1195	0.008	-	0.018	108	132	114
DRY_B_1_6	AC	40.63	10.14	0.16	0.07	130	60	460	0.004	-	0.283	105	131	112
DRY_B_1_7	AC	40.06	10.00	0.20	0.08	24	266	416	0.005	-	0.058	109	130	120
DRY_B_1_8	AC	40.03	9.99	0.20	0.08	17	98	584	0.005	-	0.029	109	132	119
DRY_B_1_9	AC	39.54	9.86	0.30	0.12	50	171	446	0.008	-	0.112	107	129	117
DRY_B_6_1	AC	40.27	10.05	0.18	0.08	121	5	342	0.005	-	0.354	106	134	119
DRY_B_6_2	AC	39.62	9.89	0.20	0.08	33	311	511	0.005	-	0.065	106	132	118
DRY_B_6_3	AC	38.86	9.70	0.21	0.09	48	319	429	0.005	-	0.112	109	140	123
DRY_B_6_4	AC	40.59	10.13	0.08	0.03	27	190	119	0.002	-	0.227	109	129	116
DRY_B_6_5	AC	40.31	10.06	0.31	0.13	83	188	662	0.008	-	0.125	106	133	117
DRY_B_8_2	AC	39.95	9.97	0.25	0.10	51	399	551	0.006	-	0.093	108	134	118
DRY_B_8_3	AC	40.21	10.03	0.28	0.12	84	182	719	0.007	-	0.117	106	127	117
DR3_1ca_1	AC	39.92	9.96	0.36	0.15	128	25	1150	0.009	-	0.111	100	138	118
DR3_1ca_3	AC	40.13	10.01	0.02	0.01	96	15	4637	0.000	-	0.021	102	138	121
DR3_1ca_9	AC	39.52	9.86	0.32	0.13	116	129	3549	0.008	-	0.033	100	136	122
DR3_1ca_10	AC	39.78	9.92	0.19	0.08	18	0	3187	0.005	-	0.006	103	139	121
DR3_1ca_15	AC	39.56	9.87	0.04	0.02	100	174	4918	0.001	-	0.020	102	138	122
DR3_1cb_1	AC	39.99	9.98	0.16	0.06	94	46	3324	0.004	-	0.028	102	141	122
DR3_1cb_10	AC	39.66	9.90	0.02	0.01	116	0	6889	0.001	-	0.017	102	138	119
DR3_1cb_15	AC	39.69	9.90	0.08	0.03	36	0	5133	0.002	-	0.007	101	136	123
D2_7_4	D1	22.81	5.69	12.50	5.14	307	1052	90	0.548	47.47	3.411	99	129	117
D2_7_5	D1	22.48	5.61	12.54	5.16	249	2393	152	0.558	47.92	1.638	101	133	120

ID	Component	Ca (%)	Ca (mol)	Mg (%)	Mg (mol)	Mn (ppm)	Fe (ppm)	Sr (ppm)	Mg/Ca	mMg/Ca	Mn/Sr	Mn LOD (ppm)	Fe LOD (ppm)	Sr LOD (ppm)
D2_7_6	D1	23.61	5.89	12.87	5.29	143	441	129	0.545	47.34	1.109	101	133	121
D2_7_7	D1	22.96	5.73	13.36	5.50	174	457	95	0.582	48.96	1.832	99	133	121
D2_7_8	D1	22.96	5.73	12.73	5.24	182	502	80	0.554	47.76	2.275	100	131	123
D2_7_9	D1	22.07	5.51	13.77	5.66	228	629	70	0.624	50.70	3.257	99	130	124
D2_9_5	D1	22.35	5.58	12.35	5.08	302	1241	85	0.553	47.67	3.553	100	130	122
D2_9_6	D1	22.85	5.70	12.59	5.18	485	1607	155	0.551	47.62	3.129	100	129	118
D2_9_7	D1	22.29	5.56	12.72	5.23	556	3481	138	0.571	48.48	4.029	101	133	119
DRY_B_5_2	D1	22.18	5.53	13.25	5.45	101	1074	166	0.597	49.63	0.608	98	131	117
DRY_B_7_2	D1	0.00	0.00	0.00	0.00	114	881	202	-	-	0.564	105	137	125
DRY_B_8_1	D1	22.75	5.68	13.39	5.51	111	561	115	0.589	49.25	0.965	98	127	120
DRY_B_10_1	D1	0.00	0.00	0.00	0.00	47	1232	182	-	-	0.258	102	133	121
DRY_B_10_2	D1	22.63	5.65	12.82	5.28	144	1588	141	0.567	48.31	1.021	98	129	117
DRY_B_10_3	D1	22.18	5.53	14.53	5.98	46	1247	171	0.655	50.00	0.269	99	130	118
DRY_B_11_1	D1	24.07	6.01	12.14	5.00	81	1119	194	0.505	45.42	0.418	100	131	118
DRY_B_11_2	D1	22.39	5.59	13.17	5.42	32	1209	204	0.588	49.24	0.157	100	127	117
DOL_1	D1	24.90	6.21	11.68	4.81	14	464	134	0.469	43.62	0.104	102	135	122
DOL_1	D1	23.90	5.96	13.62	5.60	79	77	129	0.570	48.44	0.612	100	128	110
DOL_1	D1	22.48	5.61	13.70	5.64	160	2226	260	0.609	50.00	0.615	103	137	120
DOL_1	D1	22.77	5.68	15.04	6.19	43	292	136	0.661	50.00	0.316	104	134	117
DOL_1	D1	23.68	5.91	12.98	5.34	31	533	68	0.548	47.48	0.456	100	132	122
DOL_1	D1	22.06	5.50	14.03	5.77	2	460	159	0.636	50.00	0.013	102	134	119
DOL_1	D1	23.23	5.80	13.22	5.44	29	245	148	0.569	48.41	0.196	102	135	117
DOL_1	D1	23.92	5.97	12.34	5.08	86	16	114	0.516	45.96	0.754	102	134	121
DOL_1	D1	23.67	5.91	14.35	5.90	8	455	122	0.606	49.99	0.066	101	129	117
DOL_1	D1	22.33	5.57	13.96	5.74	41	491	126	0.625	50.00	0.325	102	131	120

ID	Component	Ca (%)	Ca (mol)	Mg (%)	Mg (mol)	Mn (ppm)	Fe (ppm)	Sr (ppm)	Mg/Ca	mMg/Ca	Mn/Sr	Mn LOD (ppm)	Fe LOD (ppm)	Sr LOD (ppm)
DOL_1	D1	23.20	5.79	13.70	5.64	38	46	140	0.591	49.34	0.271	100	134	114
DOL_1	D1	23.27	5.81	13.03	5.36	11	438	156	0.560	48.01	0.071	102	133	118
DOL_1	D1	22.49	5.61	13.78	5.67	95	593	83	0.613	50.00	1.145	102	130	119
DOL_1	D1	23.15	5.78	12.29	5.06	20	69	120	0.531	46.69	0.167	102	135	116
DOL_1	D1	22.80	5.69	12.97	5.33	14	39	139	0.569	48.40	0.101	101	133	119
DOL_1	D1	22.80	5.69	13.17	5.42	125	955	256	0.578	48.79	0.488	101	133	106
DOL_1	D1	22.73	5.67	14.03	5.77	15	934	286	0.617	50.00	0.052	103	133	114
DOL_1	D1	22.60	5.64	13.48	5.55	84	1711	211	0.597	49.59	0.398	101	134	118
DR3_1ca_4	D1	23.33	5.82	12.30	5.06	58	738	91	0.527	46.50	0.637	100	128	126
DR3_A1_1	D1	21.91	5.47	12.38	5.09	724	6790	550	0.565	48.23	1.316	102	135	123
DR3_A1_2	D1	22.90	5.71	12.23	5.03	607	6966	160	0.534	46.82	3.794	102	135	126
DR3_A1_2.5	D1	21.97	5.48	12.19	5.01	818	9749	724	0.555	47.77	1.130	99	140	121
D2_5_6	D2	22.38	5.58	12.86	5.29	73	826	134	0.575	48.66	0.545	101	129	119
D2_5_7	D2	23.91	5.97	12.12	4.99	170	868	7	0.507	45.53	24.286	100	131	125
D2_5_8	D2	23.26	5.80	12.60	5.18	122	140	61	0.542	47.17	2.000	99	130	121
D2_5_9	D2	22.89	5.71	12.51	5.15	70	210	89	0.547	47.41	0.787	99	126	117
D2_5_10	D2	22.79	5.69	12.53	5.16	167	1124	81	0.550	47.56	2.062	100	131	122
D2_5_12	D2	22.74	5.67	12.61	5.19	224	1098	154	0.554	47.76	1.455	100	128	116
D2_5_13	D2	23.02	5.74	11.94	4.91	216	947	99	0.519	46.11	2.182	98	130	122
D2_5_14	D2	24.24	6.05	11.72	4.82	210	911	83	0.483	44.35	2.530	100	130	118
D2_5_15	D2	23.75	5.93	11.99	4.93	366	43	125	0.505	45.42	2.928	102	130	117
D2_5_16	D2	23.56	5.88	11.67	4.80	276	192	75	0.495	44.96	3.680	101	130	122
D2_8_1	D2	22.35	5.58	12.69	5.22	301	1235	97	0.568	48.37	3.103	100	133	120
D2_8_2	D2	22.53	5.62	13.10	5.39	365	5230	91	0.581	48.94	4.011	100	134	123
D2_8_3	D2	22.11	5.52	12.94	5.32	367	5738	100	0.585	49.11	3.670	101	139	124

ID	Component	Ca (%)	Ca (mol)	Mg (%)	Mg (mol)	Mn (ppm)	Fe (ppm)	Sr (ppm)	Mg/Ca	mMg/Ca	Mn/Sr	Mn LOD (ppm)	Fe LOD (ppm)	Sr LOD (ppm)
D2_8_4	D2	22.69	5.66	12.62	5.19	439	6158	114	0.556	47.84	3.851	101	140	121
D2_8_5	D2	27.02	6.74	10.69	4.40	292	2831	417	0.395	39.47	0.700	102	131	117
D2_8_6	D2	22.57	5.63	13.48	5.55	381	1922	132	0.597	49.63	2.886	101	131	120
D2_8_7	D2	22.00	5.49	13.58	5.59	409	778	116	0.617	50.00	3.526	103	131	121
D2_8_8	D2	22.48	5.61	13.41	5.52	390	1141	151	0.596	49.58	2.583	101	125	119
D2_8_11	D2	22.67	5.66	12.57	5.17	285	2052	132	0.554	47.76	2.159	100	132	122
D2_8_12	D2	22.72	5.67	12.42	5.11	296	2120	102	0.546	47.40	2.902	101	131	120
D2_8_13	D2	21.78	5.43	12.60	5.18	286	2190	16	0.579	48.82	17.875	100	133	124
D2_8_14	D2	22.20	5.54	13.32	5.48	485	7024	192	0.600	49.73	2.526	101	139	119
D2_8_15	D2	22.12	5.52	13.42	5.52	394	1071	101	0.607	50.00	3.901	102	125	121
D2_8_16	D2	23.00	5.74	13.15	5.41	112	123	67	0.572	48.53	1.672	98	125	121
D2_8_17	D2	24.03	5.99	12.43	5.11	82	361	99	0.517	46.03	0.828	100	131	122
D2_8_22	D2	22.62	5.64	12.66	5.21	307	2707	60	0.560	48.01	5.117	101	135	122
D2_8_23	D2	22.38	5.58	12.65	5.21	296	2182	96	0.565	48.25	3.083	99	133	120
D2_8_24	D2	22.35	5.58	12.45	5.12	526	2580	131	0.557	47.88	4.015	101	131	120
D2_8_25	D2	22.68	5.66	12.58	5.18	602	1524	149	0.555	47.78	4.040	100	130	115
D2_8_26	D2	22.71	5.67	12.55	5.16	410	874	178	0.553	47.68	2.303	100	129	115
D2_8_27	D2	22.59	5.64	12.66	5.21	294	3394	159	0.561	48.04	1.849	99	133	117
D2_8_28	D2	22.12	5.52	12.92	5.32	296	1122	77	0.584	49.06	3.844	99	130	119
D2_8_29	D2	0.00	0.00	0.00	0.00	185	715	86	-	-	2.151	103	136	122
D2_9_8	D2	24.09	6.01	12.81	5.27	447	1514	129	0.532	46.72	3.465	101	125	116
D2_9_9	D2	22.66	5.65	12.55	5.16	366	994	84	0.554	47.74	4.357	100	129	121
D2_9_10	D2	22.27	5.56	12.61	5.19	343	1093	78	0.566	48.29	4.397	99	131	118
D2_9_11	D2	22.77	5.68	12.68	5.22	227	749	81	0.557	47.87	2.802	99	126	120
D2_9_12	D2	23.62	5.89	11.51	4.74	50	279	118	0.487	44.56	0.424	101	129	119

ID	Component	Ca (%)	Ca (mol)	Mg (%)	Mg (mol)	Mn (ppm)	Fe (ppm)	Sr (ppm)	Mg/Ca	mMg/Ca	Mn/Sr	Mn LOD (ppm)	Fe LOD (ppm)	Sr LOD (ppm)
D2_9_13	D2	23.21	5.79	12.31	5.07	146	1214	81	0.530	46.66	1.802	99	132	119
D2_9_14	D2	22.30	5.56	12.76	5.25	371	805	22	0.573	48.56	16.864	100	130	121
D2_9_15	D2	22.65	5.65	12.69	5.22	421	5849	62	0.561	48.04	6.790	102	140	122
D2_9_16	D2	22.53	5.62	12.60	5.19	351	5929	113	0.559	47.98	3.106	101	136	119
D2_9_17	D2	22.67	5.66	12.60	5.18	281	4759	88	0.556	47.81	3.193	99	135	119
D2_11_4	D2	23.42	5.84	11.98	4.93	805	1126	168	0.512	45.76	4.792	100	131	122
D2_11_5	D2	22.15	5.53	12.90	5.31	372	2344	83	0.582	48.99	4.482	101	129	122
D2_11_6	D2	22.21	5.54	13.33	5.48	280	3254	125	0.600	49.74	2.240	99	132	117
D2_11_7	D2	22.62	5.64	12.85	5.29	293	1430	77	0.568	48.36	3.805	99	129	120
D2_11_8	D2	22.21	5.54	12.99	5.34	379	1399	49	0.585	49.09	7.735	100	132	124
D2_11_9	D2	23.44	5.85	12.35	5.08	154	499	45	0.527	46.49	3.422	100	131	124
D2_11_10	D2	22.66	5.65	12.70	5.22	290	751	19	0.560	48.02	15.263	100	128	122
D2_11_11	D2	23.16	5.78	12.45	5.12	270	308	82	0.538	46.99	3.293	99	128	120
D2_11_12	D2	24.65	6.15	12.21	5.02	454	155	152	0.495	44.95	2.987	100	128	115
D2_11_13	D2	22.64	5.65	12.40	5.10	366	5739	40	0.548	47.47	9.150	101	135	122
D2_12_12	D2	0.00	0.00	0.00	0.00	149	739	541	-	-	0.275	104	137	119
D2_12_13	D2	24.50	6.11	12.35	5.08	206	718	147	0.504	45.39	1.401	101	128	122
D2_12_14	D2	22.05	5.50	14.08	5.79	222	509	134	0.638	50.00	1.657	99	130	119
D2_12_15	D2	22.72	5.67	13.63	5.61	643	139	131	0.600	49.73	4.908	100	131	117
D2_12_16	D2	22.28	5.56	13.49	5.55	327	386	56	0.606	49.97	5.839	100	128	121
D2_12_17	D2	22.36	5.58	13.55	5.57	166	761	19	0.606	49.98	8.737	99	125	121
D2_13_1	D2	22.40	5.59	13.47	5.54	169	649	81	0.602	49.80	2.086	100	132	121
D2_13_2	D2	22.50	5.61	13.32	5.48	192	435	56	0.592	49.39	3.429	102	135	125
D2_13_3	D2	22.06	5.50	13.84	5.70	240	1423	29	0.628	50.00	8.276	99	129	123
D2_13_4	D2	23.17	5.78	13.18	5.42	584	126	42	0.569	48.40	13.905	102	127	123

ID	Component	Ca (%)	Ca (mol)	Mg (%)	Mg (mol)	Mn (ppm)	Fe (ppm)	Sr (ppm)	Mg/Ca	mMg/Ca	Mn/Sr	Mn LOD (ppm)	Fe LOD (ppm)	Sr LOD (ppm)
D2_13_5	D2	21.36	5.33	13.62	5.60	378	6269	18	0.638	50.00	21.000	101	139	124
D2_13_6	D2	22.39	5.59	13.55	5.58	250	2641	135	0.605	49.95	1.852	99	121	118
D2_13_7	D2	22.30	5.56	13.65	5.62	425	6766	15	0.612	50.00	28.333	100	139	125
D2_13_8	D2	22.37	5.58	13.76	5.66	315	6069	103	0.615	50.00	3.058	102	141	124
D2_13_9	D2	22.38	5.58	13.77	5.67	390	3198	121	0.615	50.00	3.223	101	124	122
D2_13_10	D2	22.47	5.61	13.89	5.72	241	2001	100	0.618	50.00	2.410	100	122	120
D2_13_11	D2	22.14	5.53	13.65	5.61	341	1153	34	0.616	50.00	10.029	100	131	123
DRY_B_3_1	D2	21.66	5.40	13.67	5.62	128	2319	142	0.631	50.00	0.901	100	133	126
DRY_B_3_2	D2	22.12	5.52	13.04	5.37	174	1223	192	0.590	49.30	0.906	99	129	120
DRY_B_3_3	D2	22.21	5.54	13.12	5.40	129	2350	131	0.591	49.35	0.985	99	132	119
DRY_B_3_4	D2	22.07	5.51	12.79	5.26	155	1837	220	0.579	48.86	0.705	99	131	118
DRY_B_3_5	D2	21.87	5.46	13.11	5.39	143	1627	211	0.599	49.71	0.678	99	130	120
DRY_B_3_6	D2	22.54	5.62	13.07	5.38	143	1153	151	0.580	48.88	0.947	98	129	121
DRY_B_3_7	D2	22.32	5.57	12.72	5.23	126	1184	67	0.570	48.44	1.881	99	127	126
DRY_B_3_8	D2	22.45	5.60	12.79	5.26	135	1265	145	0.570	48.45	0.931	98	129	120
DRY_B_3_9	D2	22.16	5.53	13.01	5.35	156	2151	194	0.587	49.19	0.804	99	131	118
DRY_B_3_10	D2	22.60	5.64	12.71	5.23	150	1742	156	0.562	48.10	0.962	99	130	120
DRY_B_3_11	D2	21.95	5.48	12.95	5.33	151	1868	120	0.590	49.33	1.258	97	127	120
DRY_B_3_12	D2	22.25	5.55	12.84	5.28	115	708	107	0.577	48.77	1.075	96	125	118
DRY_B_4_5	D2	21.60	5.39	14.00	5.76	71	1560	128	0.648	50.00	0.555	98	125	120
DRY_B_4_6	D2	22.06	5.50	14.08	5.79	32	618	162	0.638	50.00	0.198	98	129	117
DRY_B_4_7	D2	25.75	6.43	10.84	4.46	11	216	194	0.421	40.97	0.057	99	130	118
DRY_B_4_8	D2	21.95	5.48	13.46	5.54	66	1369	150	0.613	50.00	0.440	99	129	117
DRY_B_4_9	D2	22.01	5.49	14.03	5.77	109	1624	150	0.637	50.00	0.727	98	128	117
DRY_B_4_10	D2	24.00	5.99	13.37	5.50	57	843	106	0.557	47.88	0.538	100	132	123

ID	Component	Ca (%)	Ca (mol)	Mg (%)	Mg (mol)	Mn (ppm)	Fe (ppm)	Sr (ppm)	Mg/Ca	mMg/Ca	Mn/Sr	Mn LOD (ppm)	Fe LOD (ppm)	Sr LOD (ppm)
DRY_B_4_11	D2	22.57	5.63	14.24	5.86	106	2260	135	0.631	50.00	0.785	102	134	125
DRY_B_4_12	D2	22.22	5.54	13.91	5.72	59	1414	216	0.626	50.00	0.273	98	130	116
DR1_1_10	D2	22.34	5.57	13.41	5.52	115	1101	198	0.600	49.75	0.581	97	128	117
DR1_1_11	D2	22.54	5.62	13.40	5.52	196	86	95	0.595	49.52	2.063	99	126	119
DR1_1_12	D2	23.52	5.87	12.71	5.23	172	189	154	0.541	47.13	1.117	100	131	123
DR1_1_13	D2	22.76	5.68	13.63	5.61	156	1365	206	0.599	49.69	0.757	97	128	116
DR1_1_14	D2	22.61	5.64	13.32	5.48	11	86	117	0.589	49.29	0.094	97	123	112
DR1_1_15	D2	22.60	5.64	13.53	5.57	99	797	89	0.599	49.69	1.112	100	129	120
DR1_1_16	D2	22.45	5.60	13.52	5.56	48	350	40	0.603	49.84	1.200	101	127	124
DR1_2_11	D2	22.60	5.64	12.78	5.26	406	140	171	0.566	48.26	2.374	99	128	120
DR1_2_12	D2	23.18	5.78	13.25	5.45	247	554	172	0.572	48.52	1.436	96	124	116
DR1_2_14	D2	25.10	6.26	12.62	5.19	318	167	152	0.503	45.34	2.092	99	126	117
DR1_2_15	D2	22.73	5.67	13.15	5.41	200	22	94	0.579	48.83	2.128	99	127	118
DR1_2_16	D2	24.35	6.08	11.56	4.76	172	94	142	0.475	43.92	1.211	96	124	117
DR1_2_17	D2	22.35	5.58	13.40	5.51	116	12	51	0.600	49.72	2.275	95	125	117
DRY_B_5_8	D2	22.93	5.72	13.07	5.38	125	786	171	0.570	48.45	0.731	99	126	119
DRY_B_5_9	D2	22.71	5.67	13.11	5.39	167	838	114	0.577	48.77	1.465	98	129	122
DRY_B_5_10	D2	22.84	5.70	12.72	5.23	154	845	165	0.557	47.88	0.933	99	128	117
DRY_B_5_11	D2	22.76	5.68	13.19	5.43	193	762	159	0.579	48.86	1.214	98	130	118
DRY_B_7_3	D2	24.53	6.12	11.76	4.84	101	609	188	0.479	44.15	0.537	101	131	121
DRY_B_7_4	D2	22.55	5.63	13.23	5.44	178	209	144	0.587	49.17	1.236	99	131	121
DRY_B_8_4	D2	22.64	5.65	13.46	5.54	103	1117	130	0.595	49.51	0.792	100	131	121
DRY_B_8_5	D2	22.38	5.58	13.95	5.74	88	779	171	0.623	50.00	0.515	100	134	118
DRY_B_8_6	D2	22.24	5.55	13.52	5.56	156	824	96	0.608	50.00	1.625	99	131	121
DRY_B_8_7	D2	22.31	5.57	13.18	5.42	154	593	168	0.591	49.35	0.917	98	127	116

ID	Component	Ca (%)	Ca (mol)	Mg (%)	Mg (mol)	Mn (ppm)	Fe (ppm)	Sr (ppm)	Mg/Ca	mMg/Ca	Mn/Sr	Mn LOD (ppm)	Fe LOD (ppm)	Sr LOD (ppm)
DRY_B_8_8	D2	22.21	5.54	13.35	5.49	109	1744	159	0.601	49.77	0.686	98	132	117
DRY_B_10_4	D2	22.17	5.53	13.52	5.56	57	1428	126	0.610	50.00	0.452	97	130	118
DRY_B_10_5	D2	22.00	5.49	13.79	5.67	95	1324	82	0.627	50.00	1.159	99	132	125
DRY_B_10_6	D2	22.24	5.55	13.07	5.38	139	457	177	0.588	49.21	0.785	98	129	121
DOL_2_1/1	D2	22.60	5.64	13.47	5.54	212	104	87	0.596	49.56	2.437	101	131	123
DOL_2_1/2	D2	23.07	5.76	13.61	5.60	129	33	89	0.590	49.32	1.449	101	132	121
DOL_2_1/3	D2	23.51	5.87	12.99	5.35	5	5	120	0.553	47.68	0.042	102	134	124
DOL_2_1/4	D2	23.43	5.85	11.93	4.91	92	132	194	0.509	45.63	0.474	103	132	115
DOL_2_2/3	D2	23.20	5.79	13.78	5.67	103	99	98	0.594	49.48	1.051	103	132	121
DOL_2_2/4	D2	22.77	5.68	14.76	6.07	137	988	152	0.648	50.00	0.901	103	133	116
DOL_2_2/5	D2	22.66	5.65	13.66	5.62	10	0	64	0.603	49.85	0.156	101	134	119
DOL_2_2/6	D2	23.05	5.75	13.68	5.63	175	219	245	0.593	49.46	0.714	104	136	121
DOL_2_3/3	D2	23.65	5.90	12.95	5.33	15	86	32	0.548	47.45	0.469	100	131	127
DOL_2_3/4	D2	22.81	5.69	12.56	5.17	25	56	121	0.550	47.58	0.207	101	132	119
DOL_2_3/5	D2	23.14	5.77	13.21	5.43	206	195	109	0.571	48.48	1.890	100	131	122
DOL_2_3/6	D2	23.14	5.77	13.48	5.55	55	238	131	0.582	48.99	0.420	101	130	120
DOL_2_4/3	D2	27.94	6.97	12.40	5.10	125	700	153	0.444	42.27	0.817	103	132	119
DOL_2_4/4	D2	22.86	5.70	13.97	5.75	47	146	104	0.611	50.00	0.452	101	135	118
DOL_2_4/5	D2	24.30	6.06	12.66	5.21	38	82	198	0.521	46.21	0.192	103	135	118
DOL_2_4/6	D2	0.00	0.00	0.00	0.00	13	104	293	-	-	0.044	104	137	115
DR3_1ca_11	D2	0.00	0.00	0.00	0.00	192	865	327	-	-	0.587	102	130	125
DR3_1ca_12	D2	23.77	5.93	12.43	5.12	78	425	196	0.523	46.31	0.398	101	128	123
DR3_1ca_13	D2	22.85	5.70	12.63	5.19	18	48	94	0.553	47.68	0.191	101	126	123
DR3_1ca_16	D2	23.03	5.75	12.03	4.95	35	127	136	0.522	46.28	0.257	99	126	122
DR3_1ca_17	D2	23.74	5.92	11.74	4.83	60	311	136	0.495	44.93	0.441	101	128	121

ID	Component	Ca (%)	Ca (mol)	Mg (%)	Mg (mol)	Mn (ppm)	Fe (ppm)	Sr (ppm)	Mg/Ca	mMg/Ca	Mn/Sr	Mn LOD (ppm)	Fe LOD (ppm)	Sr LOD (ppm)
DR3_1cb_7	D2	22.99	5.74	12.24	5.04	171	1068	115	0.532	46.75	1.487	100	130	122
DR3_1cb_12	D2	22.87	5.71	12.14	5.00	140	1865	277	0.531	46.68	0.505	100	129	124
DR3_A1_5	D2	21.97	5.48	12.52	5.15	757	4196	670	0.570	48.43	1.130	101	133	120
DR3_A1_6	D2	21.93	5.47	12.23	5.03	845	4636	427	0.557	47.89	1.979	100	129	123
DR3_1cb_19	D2	22.36	5.58	11.92	4.90	820	5519	248	0.533	46.77	3.306	100	130	122
DR3_1cb_20	D2	21.97	5.48	12.03	4.95	574	3484	228	0.547	47.44	2.518	100	129	124
D2_7_1	CS	40.32	10.06	0.18	0.07	388	68	248	0.005	-	1.565	105	128	115
D2_7_2	CS	40.43	10.09	0.18	0.07	140	109	359	0.004	-	0.390	108	127	116
D2_7_3	CS	39.92	9.96	0.22	0.09	1134	141	789	0.005	-	1.437	107	127	114
D2_8_9	CS	40.83	10.19	0.15	0.06	70	41	541	0.004	-	0.129	110	131	119
D2_8_10	CS	40.10	10.01	0.63	0.26	66	286	498	0.016	-	0.133	108	141	117
D2_9_1	CS	39.89	9.95	0.41	0.17	168	63	572	0.010	-	0.294	106	129	116
D2_9_2	CS	40.62	10.13	0.17	0.07	378	91	371	0.004	-	1.019	102	127	113
D2_9_3	CS	39.72	9.91	0.19	0.08	339	110	367	0.005	-	0.924	103	127	116
D2_9_4	CS	40.67	10.15	0.18	0.08	532	224	735	0.004	-	0.724	103	128	115
D2_11_1	CS	40.02	9.99	0.25	0.10	314	31	427	0.006	-	0.735	100	129	112
D2_11_2	CS	40.21	10.03	0.17	0.07	299	96	270	0.004	-	1.107	102	127	111
D2_11_3	CS	39.92	9.96	0.22	0.09	203	9	289	0.005	-	0.702	102	129	115
D2_12_1	CS	40.11	10.01	0.19	0.08	214	111	642	0.005	-	0.333	107	126	113
D2_12_2	CS	40.63	10.14	0.21	0.09	101	64	269	0.005	-	0.375	110	133	119
D2_12_3	CS	40.24	10.04	0.30	0.13	871	345	403	0.008	-	2.161	109	130	122
DRY_B_4_1	CS	40.29	10.05	0.14	0.06	156	20	378	0.004	-	0.413	99	133	114
DRY_B_4_2	CS	40.08	10.00	0.21	0.09	179	57	675	0.005	-	0.265	101	135	116
DRY_B_4_3	CS	40.26	10.05	0.24	0.10	185	37	407	0.006	-	0.455	103	137	116
DRY_B_4_4	CS	40.34	10.07	0.25	0.10	129	46	399	0.006	-	0.323	100	131	117

ID	Component	Ca (%)	Ca (mol)	Mg (%)	Mg (mol)	Mn (ppm)	Fe (ppm)	Sr (ppm)	Mg/Ca	mMg/Ca	Mn/Sr	Mn LOD (ppm)	Fe LOD (ppm)	Sr LOD (ppm)
DR1_1_2	CS	40.00	9.98	0.20	0.08	38	87	255	0.005	-	0.149	108	136	119
DR1_1_3	CS	40.23	10.04	0.14	0.06	5	164	202	0.003	-	0.025	108	131	121
DR1_1_4	CS	40.36	10.07	0.20	0.08	79	20	419	0.005	-	0.189	107	129	116
DR1_1_5	CS	40.06	10.00	0.12	0.05	73	169	216	0.003	-	0.338	106	133	118
DR1_1_6	CS	40.54	10.11	0.16	0.07	48	52	346	0.004	-	0.139	106	133	117
DR1_1_7	CS	40.42	10.08	0.13	0.05	120	39	244	0.003	-	0.492	105	128	113
DR1_1_8	CS	40.26	10.05	0.24	0.10	22	34	502	0.006	-	0.044	106	127	117
DR1_1_9	CS	40.13	10.01	0.20	0.08	76	127	340	0.005	-	0.224	105	124	115
DR1_2_6	CS	40.07	10.00	0.15	0.06	24	77	260	0.004	-	0.092	107	128	114
DR1_2_7	CS	40.03	9.99	0.28	0.12	2	108	933	0.007	-	0.002	108	131	117
DR1_2_8	CS	39.72	9.91	0.13	0.05	27	107	182	0.003	-	0.148	108	136	122
DR1_2_9	CS	40.22	10.04	0.19	0.08	55	109	449	0.005	-	0.122	106	127	114
DR1_2_13	CS	39.21	9.78	3.05	1.25	162	108	702	0.078	-	0.231	106	132	115
DR1_2_10	CS	39.87	9.95	0.20	0.08	73	113	315	0.005	-	0.232	104	135	114
DRY_B_5_1	CS	39.96	9.97	2.28	0.94	11	321	403	0.057	-	0.027	106	139	117
DRY_B_5_3	CS	40.28	10.05	0.27	0.11	52	244	580	0.007	-	0.090	109	139	119
DRY_B_5_4	CS	39.84	9.94	0.21	0.09	29	126	616	0.005	-	0.047	108	130	118
DRY_B_5_5	CS	40.17	10.02	0.15	0.06	19	93	462	0.004	-	0.041	109	132	118
DRY_B_5_6	CS	39.50	9.86	0.43	0.17	57	39	461	0.011	-	0.124	107	135	118
DRY_B_5_7	CS	40.12	10.01	0.41	0.17	136	32	444	0.010	-	0.306	105	130	116
DRY_B_7_1	CS	39.89	9.95	0.24	0.10	43	145	1117	0.006	-	0.038	108	131	118
DRY_B_9_3	CS	39.30	9.80	1.65	0.68	156	452	866	0.042	-	0.180	105	130	119
DRY_B_9_5	CS	40.10	10.01	0.31	0.13	46	626	527	0.008	-	0.087	105	129	116
DRY_B_9_7	CS	39.67	9.90	0.22	0.09	26	157	327	0.006	-	0.080	108	130	118
DRY_B_11_3	CS	39.57	9.87	0.81	0.33	136	226	500	0.020	-	0.272	102	127	116

ID	Component	Ca (%)	Ca (mol)	Mg (%)	Mg (mol)	Mn (ppm)	Fe (ppm)	Sr (ppm)	Mg/Ca	mMg/Ca	Mn/Sr	Mn LOD (ppm)	Fe LOD (ppm)	Sr LOD (ppm)
DOL_2_2/1	CS	39.95	9.97	0.56	0.23	104	140	1607	0.014	-	0.065	109	143	111
DOL_2_2/2	CS	33.31	8.31	8.10	3.33	49	11	273	0.243	-	0.179	104	136	118
DR3_1cb_16	CS	40.05	9.99	0.10	0.04	100	192	389	0.002	-	0.257	100	139	118
DR3_A1_13	CS	40.01	9.98	0.25	0.10	15	123	220	0.006	-	0.068	99	136	120
DR3_A1_14	CS	40.02	9.99	0.22	0.09	278	622	484	0.006	-	0.574	100	141	117
D2_6_2	C1a	40.27	10.05	0.28	0.12	373	10	98	0.007	-	3.806	105	137	119
D2_6_3	C1a	39.94	9.96	0.23	0.10	142	22	222	0.006	-	0.640	109	133	118
D2_6_4	C1a	39.95	9.97	0.21	0.08	221	12	184	0.005	-	1.201	108	136	121
D2_6_5	C1a	40.26	10.05	0.24	0.10	289	32	126	0.006	-	2.294	109	135	117
D2_6_6	C1b	39.31	9.81	0.18	0.08	3514	302	332	0.005	-	10.584	117	146	125
D2_6_7	C1b	40.62	10.14	0.15	0.06	1184	139	248	0.004	-	4.774	103	128	115
D2_7_10	C1a	39.93	9.96	0.32	0.13	94	61	245	0.008	-	0.384	107	136	114
D2_7_11	C1a	39.84	9.94	0.33	0.13	99	97	103	0.008	-	0.961	103	131	117
D2_7_12	C1b	39.60	9.88	0.21	0.09	2452	170	150	0.005	-	16.347	113	132	122
D2_7_13	C1b	39.79	9.93	0.20	0.08	2807	210	245	0.005	-	11.457	112	132	122
D2_7_14	C1b	39.85	9.94	0.20	0.08	947	150	418	0.005	-	2.266	106	131	116
D2_8_18	C1a	39.95	9.97	0.21	0.09	194	98	597	0.005	-	0.325	103	127	113
D2_8_19	C1b	39.77	9.92	0.28	0.12	1591	162	358	0.007	-	4.444	106	131	117
D2_8_20	C1b	39.94	9.97	0.18	0.07	1320	10	324	0.005	-	4.074	105	128	112
D2_8_21	C1b	39.99	9.98	0.29	0.12	1931	201	326	0.007	-	5.923	106	131	115
D2_11_14	C1a	38.50	9.60	4.72	1.94	202	4763	269	0.122	-	0.751	103	126	110
D2_11_15	C1a	39.76	9.92	0.38	0.16	228	577	655	0.010	-	0.348	104	127	114
D2_11_16	C1a	39.74	9.91	0.35	0.14	294	585	511	0.009	-	0.575	101	127	119
D2_11_17	C1a	39.81	9.93	0.32	0.13	187	514	501	0.008	-	0.373	105	128	115
D2_12_18	C1a	40.39	10.08	0.31	0.13	926	394	215	0.008	-	4.307	107	132	116

ID	Component	Ca (%)	Ca (mol)	Mg (%)	Mg (mol)	Mn (ppm)	Fe (ppm)	Sr (ppm)	Mg/Ca	mMg/Ca	Mn/Sr	Mn LOD (ppm)	Fe LOD (ppm)	Sr LOD (ppm)
D2_12_19	C1a	39.74	9.92	0.17	0.07	511	0	139	0.004	-	3.676	102	128	115
D2_12_20	C1b	39.88	9.95	0.08	0.03	3703	92	334	0.002	-	11.087	110	127	118
D2_12_21	C1a	39.96	9.97	0.26	0.11	114	15	55	0.007	-	2.073	103	127	117
D2_12_22	C1a	39.40	9.83	0.33	0.14	627	68	231	0.008	-	2.714	106	127	117
D2_12_23	C1a	39.97	9.97	0.28	0.11	375	100	205	0.007	-	1.829	101	127	113
D2_12_24	C1a	40.33	10.06	0.31	0.13	99	11	15	0.008	-	6.600	102	129	120
D2_12_25	C1a	40.32	10.06	0.25	0.10	97	8	132	0.006	-	0.735	107	129	117
D2_12_26	C1b	39.82	9.93	0.30	0.12	1790	145	666	0.008	-	2.688	100	133	111
D2_12_27	C1b	39.88	9.95	0.15	0.06	976	190	323	0.004	-	3.022	106	134	116
DR3_1cb_3	C1a	39.80	9.93	0.32	0.13	52	96	355	0.008	-	0.146	102	137	121
DR3_1cb_4	C1b	38.70	9.66	0.67	0.28	1126	15	515	0.017	-	2.186	104	140	123
DR3_1cb_13	C1b	39.48	9.85	0.36	0.15	695	23	508	0.009	-	1.368	100	135	120
DR3_1cb_17	C1b	39.75	9.92	0.42	0.17	502	7	800	0.011	-	0.628	101	137	118
DR3_A1_7	C1a	39.83	9.94	0.32	0.13	27	101	1093	0.008	-	0.025	100	137	118
DR3_A1_8	C1c	40.20	10.03	0.19	0.08	396	0	406	0.005	-	0.975	99	139	120
DR3_A1_10	C1a	39.93	9.96	0.15	0.06	70	242	680	0.004	-	0.103	99	135	117
DR3_A1_11	C1a	40.39	10.08	0.17	0.07	61	651	837	0.004	-	0.073	101	132	118
DR3_A1_12	C1c	40.22	10.04	0.19	0.08	405	94	556	0.005	-	0.728	100	133	117
D2_6_8	C2	40.79	10.18	0.04	0.02	117	20	114	0.001	-	1.026	105	129	112
D2_6_9	C2	40.34	10.06	0.03	0.01	96	19	99	0.001	-	0.970	107	130	113
DR1_1_17	C2	40.12	10.01	0.10	0.04	39	157	139	0.003	-	0.281	108	132	121
DR1_1_18	C2	40.02	9.99	0.08	0.03	31	132	123	0.002	-	0.252	108	135	120
DR1_2_18	C2	40.00	9.98	0.19	0.08	117	111	195	0.005	-	0.600	109	139	121
DR1_2_19	C2	39.79	9.93	0.31	0.13	58	38	367	0.008	-	0.158	105	126	115
DR1_2_20	C2	39.97	9.97	0.15	0.06	24	25	292	0.004	-	0.082	106	126	111

ID	Component	Ca (%)	Ca (mol)	Mg (%)	Mg (mol)	Mn (ppm)	Fe (ppm)	Sr (ppm)	Mg/Ca	mMg/Ca	Mn/Sr	Mn LOD (ppm)	Fe LOD (ppm)	Sr LOD (ppm)
DR3_1ca_5	C2	39.48	9.85	0.43	0.18	37	-50	4068	0.011	-	0.009	101	139	120
DR3_1ca_14	C2	39.87	9.95	0.20	0.08	55	142	520	0.005	-	0.106	101	134	117
DR3_1cb_5	C2	39.15	9.77	0.54	0.22	9	97	1725	0.014	-	0.005	103	134	121
DR3_1cb_14	C2	39.91	9.96	0.38	0.16	127	29	1738	0.010	-	0.073	99	138	119
DR3_1cb_18	C2	39.74	9.91	0.24	0.10	15	-16	724	0.006	-	0.021	100	137	117
DR3_A1_3	C2	40.03	9.99	0.16	0.07	199	329	589	0.004	-	0.338	97	135	117
DR3_A1_4	C2	39.88	9.95	0.29	0.12	113	125	550	0.007	-	0.205	99	137	118
DR3_A1_9	C2	40.21	10.03	0.18	0.07	104	378	638	0.004	-	0.163	99	138	116
D2_5_11	C2	38.20	9.53	0.92	0.38	137	126	292	0.024	-	0.469	109	133	120

Carbon isotope data

Sample ID	δ^{18}Ocarb	δ^{12}Ccarb	Component
DRY-A	-8.31	1.67	Thrombolite
PR-3	-4.09	2.15	C2
DRY-A	-7.28	2.12	C2
DR1/3	-9.94	2.06	C2
DR2/1	-10.79	1.79	C2
DR1/3b	-8.22	2.34	C2
DR2/1	-10.53	1.15	AC
DR2/1	-9.24	2.49	AC
DR2/1	-10.99	1.45	AC
DR1/3	-7.88	2.72	AC
DR1/13b	-8.08	2.85	AC
DR-7	-8.33	2.85	AC
DR-7	-7.24	2.99	AC
DR3/2A	-6.73	3.02	AC
DR3/2A	-6.63	2.90	AC
DR3/2A	-7.89	2.23	CS
DR3/2A	-6.73	2.36	CS
DR2/1	-7.13	2.20	Dolomite
DR2/1	-6.58	1.48	Dolomite
DR2/1	-8.43	2.09	Dolomite
DR3/1B	-9.52	0.06	Dolomite
DRY	-7.09	2.31	Dolomite
DR2/10	-4.15	2.62	Dolomite
DR3	-11.60	-0.29	Dolomite
DR3/1A	-9.17	0.49	Dolomite
DR3/1ca	-10.05	0.05	Dolomite

Characterising dolomite via XRD analyses

The following preliminary data were collected on two samples for approximation of dolomite characteristics in samples from the terminal Ediacaran Nama and Yudoma Groups. Due to the microcrystalline nature of dolomite cements in samples of the Nama Group, it was not possible to separate cements from dolomitised sediment when preparing samples for XRD analysis. As such, the XRD profile and values of stoichiometry, ordering and percent dolomite below reflect the combination of dolomitised sediment and cement in Nama Group samples. Conversely, the sample analysed from the Yudoma Group may be approximated as pure dolomite (see Wood et al., 2017a).

Samples of the Driedoornvlakte *Cloudina* pinnacle reef (Nama Group) and the *Suvorovella* shell hash of the Upper Aim Formation (Yudoma Group) were crushed and homogenised in an agate pestle and mortar using acetone to avoid sample loss, resultant powders were spiked with a pre-prepared quartz-bearing solution and immediately loaded onto glass slides using a pipette. Care was taken to ensure that sample slurries dried completely level and homogeneous.

Dolomite stoichiometry

The stoichiometry of dolomite was calculated using the following equation (after Lumsden and Chimahusky, 1980):

$$\textbf{Mol\% } CaCO_3 \textbf{ in the dolomite lattice} = (333.33 * d) - 911.99$$

In this equation, '**d**' is the inter-planar lattice spacing within the crystal structure in Angstroms (Å) which is calculated using the Bragg equation:

$$d = \lambda_0/(2(\sin\theta))$$

Where 'θ' is the X-ray incidence angle (in radians) calculated relative to the quartz internal standard and 'λ_0' is the wavelength of the incident X-rays (in Å). For copper radiation, λ_0 is: Kα weighted-mean 1.541838Å, Kα 1 = 1.540562Å, and Kα 2 = 1.544390 Å.

The conversion factor for degrees to radians is $\alpha_{rad} = \alpha_{deg}(\pi/180)$, where α_{rad} and α_{deg} represent the angle in radians and degrees respectively .

Cation ordering

The degree of cation ordering is numerically defined by the ratio of the $^{d}015$ to $^{d}110$ peaks (Goldsmith and Graf, 1958). Poorly ordered dolomite, where Mg and Ca cations are distributed unevenly, show correspondingly low values of $^{d}015/^{d}110$. Conversely, where lattice planes in the crystal structure are characterised by alternating and evenly distributed Ca and Mg cations, dolomite is considered to be well ordered and $^{d}015/^{d}110$ approach 1 (Goldsmith and Graf, 1958; Reeder, 1981; Kaczmarek and Sibley, 2007, 2011).

Percent dolomite

An approximation of the percent dolomite in each sample was determined using the ratio of intensities of the principle dolomite and calcite peaks (Royse et al., 1971). This follows the equation:

$$\%\text{Dolomite} = I_{dolo} / (I_{dolo} + I_{calc})$$

Where I_{dolo} and I_{calc} are the intensities of the principle dolomite and calcite (104) peaks respectively.

<u>Nama Dolomite</u>

Stoichiometry of Nama dolomite:

Using a 2θ angle of 30.9° for the $^{d}104$ peak in the Driedoornvlakte sample (Figure AC1a) and a weighted-mean incident wavelength for CuKα radiation of 1.541838 Å yields a 'd' spacing of:

$$\mathbf{d} = 1.541838 / 2\sin[0.5*30.9*(\pi/180)] = \mathbf{2.894\ Å}.$$

Therefore,

$$\text{Mol\% } CaCO_3 = (333.33 * 2.894) - 911.99 = 52.667$$

Consequently, Mol% $MgCO_3$ = 100 - 52.667 = **47.33**

With Kα 1, Mol% $CaCO_3$ = 51.83, Mol% $MgCO_3$ = 48.17

With Kα 2, Mol% $CaCO_3$ = 54.22, Mol% $MgCO_3$ = 45.78

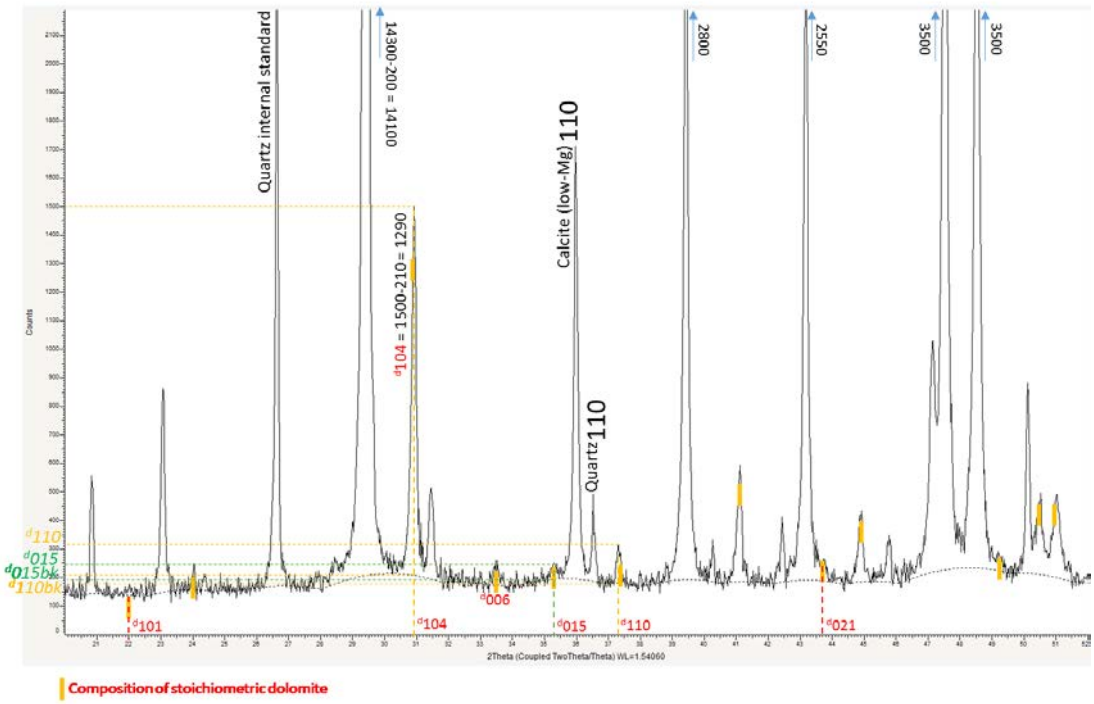

Figure AC1a: XRD spectrum for Driedoornvlakte Unit 3m dolomite sample with relevant peaks labelled

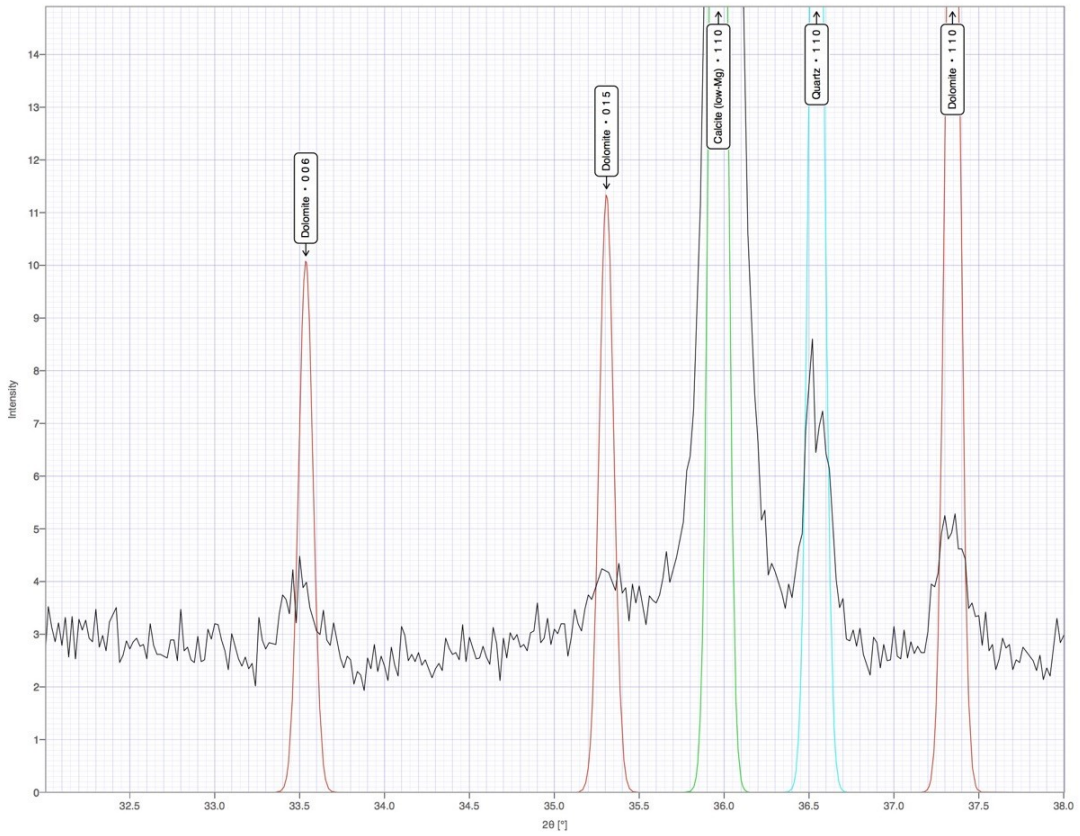

Figure AC1b: XRD spectrum of Driedoornvlakte dolomite relative to standards (image courtesy of Nick Tosca)

Cation ordering in Nama dolomite:

When subtracting the maximum background intensity, the ratio of the $^{d}015$ to $^{d}110$ peak heights in the Driedoornvlakte sample are:

$^{d}015/^{d}110$ = (250 – 195) / (320 – 180) = 0.39

This equates to the minimum possible value for this sample due to the full removal of the background for each peak intensity. However, a more robust interpretation of dolomite ordering incorporates the relative intensity of the 015 to 006 peak (N. Tosca pers. com.). In the case of the Driedoornvlakte dolomite sample, both the 006 and 015 peaks are attenuated relative to 110 (which is not uncommon in well-ordered dolomite, N. Tosca pers. com.) and additionally, there is no significant difference between the intensities of the 006 and 015 peaks. Furthermore, each of the characteristic dolomite peaks remain within the range of peak positions for the stoichiometric dolomite standard (Figure AC1b). Together, these data imply that the Driedoornvlakte sample can be described as relatively well-ordered.

Percent dolomite in Nama sample:

Using the relative peak intensities of principle dolomite and calcite peaks (following removal of the background intensity for each), the percent dolomite in the carbonate sample from Driedoornvlakte is:

% Dolomite = 1290 / (1290 + 14100) = 0.0838 = ~ 8.4%

<u>Yudoma Dolomite</u>

Stoichiometry of Yudoma dolomite:

Using a 2θ angle of 30.99° for the $^{d}104$ peak in the *Suvorovella* sample (Figure AC2) and a weighted-mean incident wavelength for CuKα radiation of 1.541838 Å yields a 'd' spacing of:

$$\mathbf{d} = 1.541838 / 2\sin[0.5*30.99* (\pi/180)] = \mathbf{2.886\ Å}.$$

Therefore,

$$\text{Mol\% } CaCO_3 = (333.33 * 2.894) – 911.99 = 50$$

Consequently, Mol% $MgCO_3$ = 100 - 50 = **50**

As such, dolomite of the Aim Formation is effectively stoichiometric in composition.

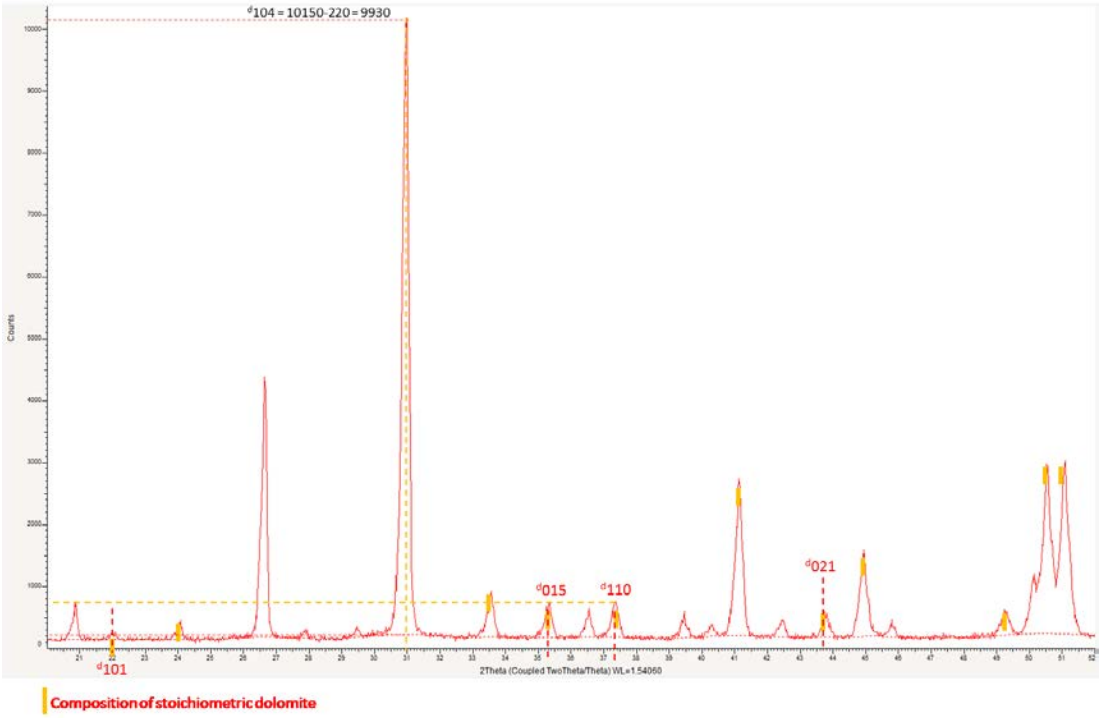

Figure AC2: XRD spectrum of *Suvorovella* dolomite from the Aim Formation of the Yudoma Group, (Yudoma-Maya confluence section, southeast Siberia**)**

Cation ordering in Yudoma dolomite:

When subtracting the maximum background intensity, the ratio of the $^{d}015$ to $^{d}110$ peak heights in the Aim Formation sample are:

$^{d}015/^{d}110$ = (750 – 200) / (750 – 200) = 1

The two ordering peaks have almost identical intensities, which is suggestive of a well-ordered structure.

Percent dolomite in the Yudoma sample:

The calcite 104 peak in the dolomite sample is negligible when compared to the magnitude of the dolomite 104 peak and consequently, this sample can be approximated as pure dolomite.

% Dolomite = 9930 / (9930 + 100) = 0.99 = ~ 99%

Figure AC3. Selected additional CL photomicrographs of Driedoornvlakte Unit 3m

AC3a) Twinning in late stage C2 cement infilling porosity within a *Cloudina* individual. **AC3b)** Longitudinal section of a *Cloudina* individual, showing patchy bright luminescence comparable to C1b. **AC3c** and **AC3d)** Transmitted light and cathodoluminescence photomicrographs of shelter porosity created by *Cloudina* individual, with localisation of elevated iron concentration in dolomite (e.g. dull luminescent rim of crystal in upper central quadrant) with proximity to breach in *Cloudina* skeleton (left). **AB3e)** Opaque, euhedral crystals within dolomitised micritic sediment. Probable iron oxide after pyrite.

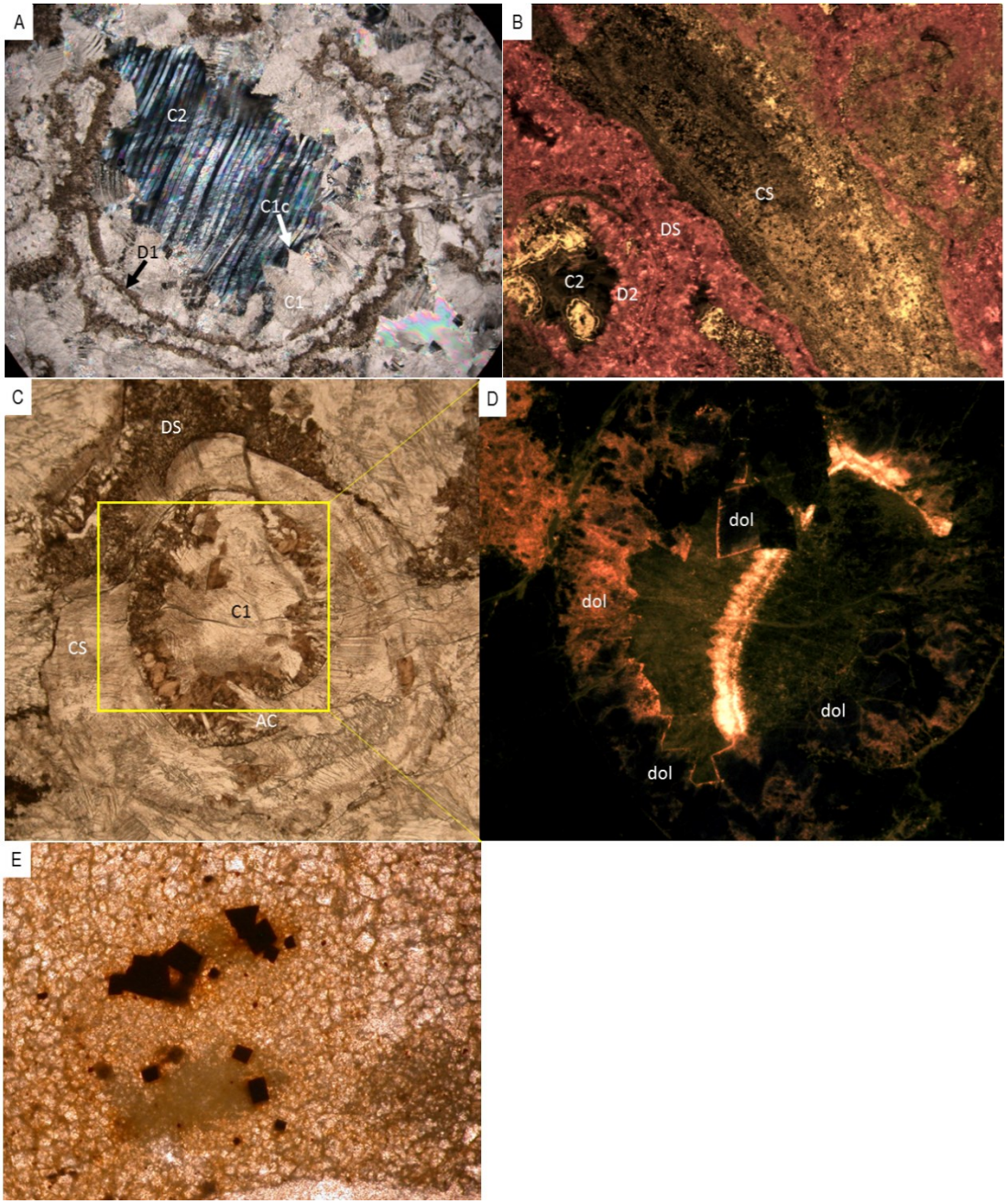

Selected electron microprobe transect maps

DR3

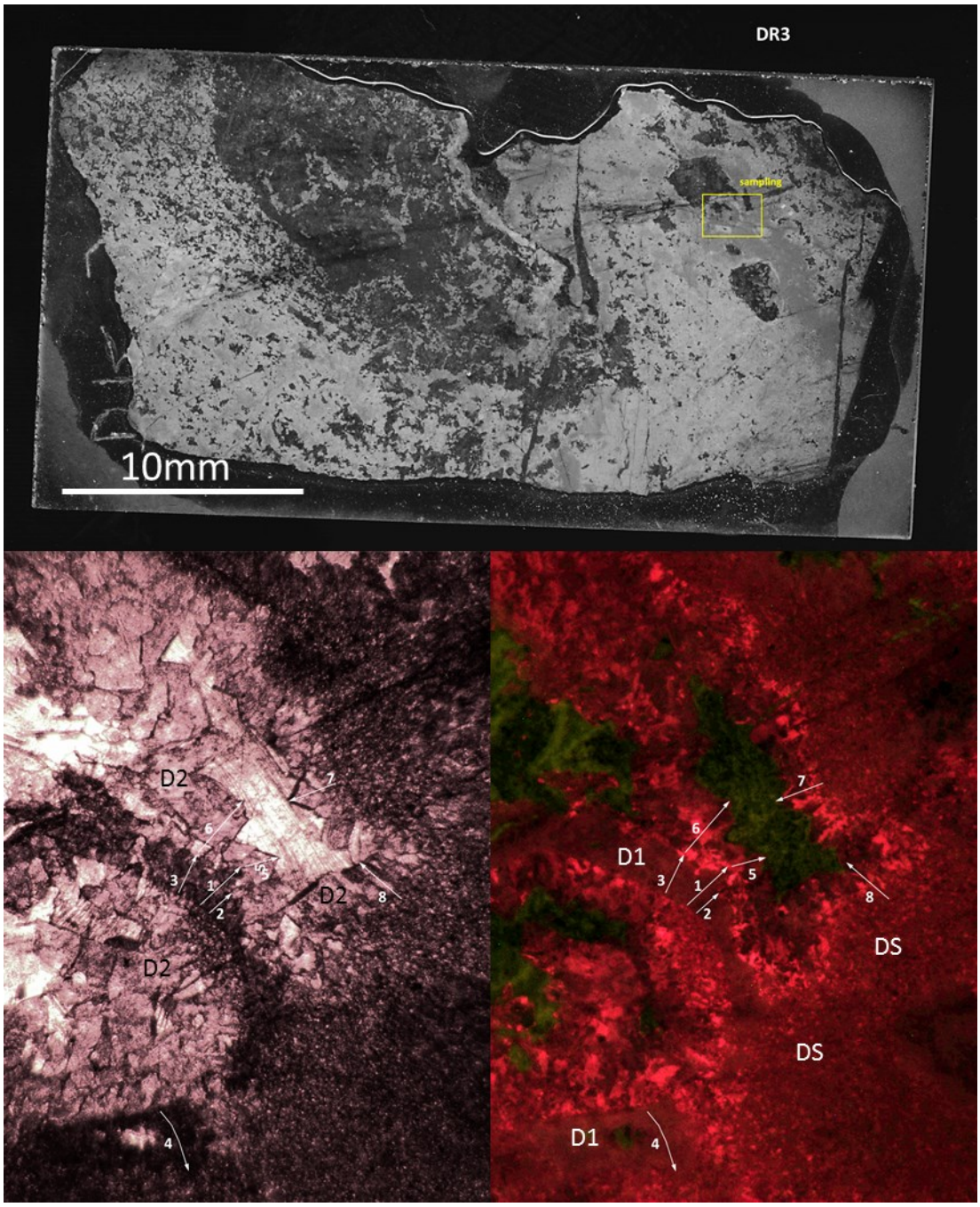

DRY_B

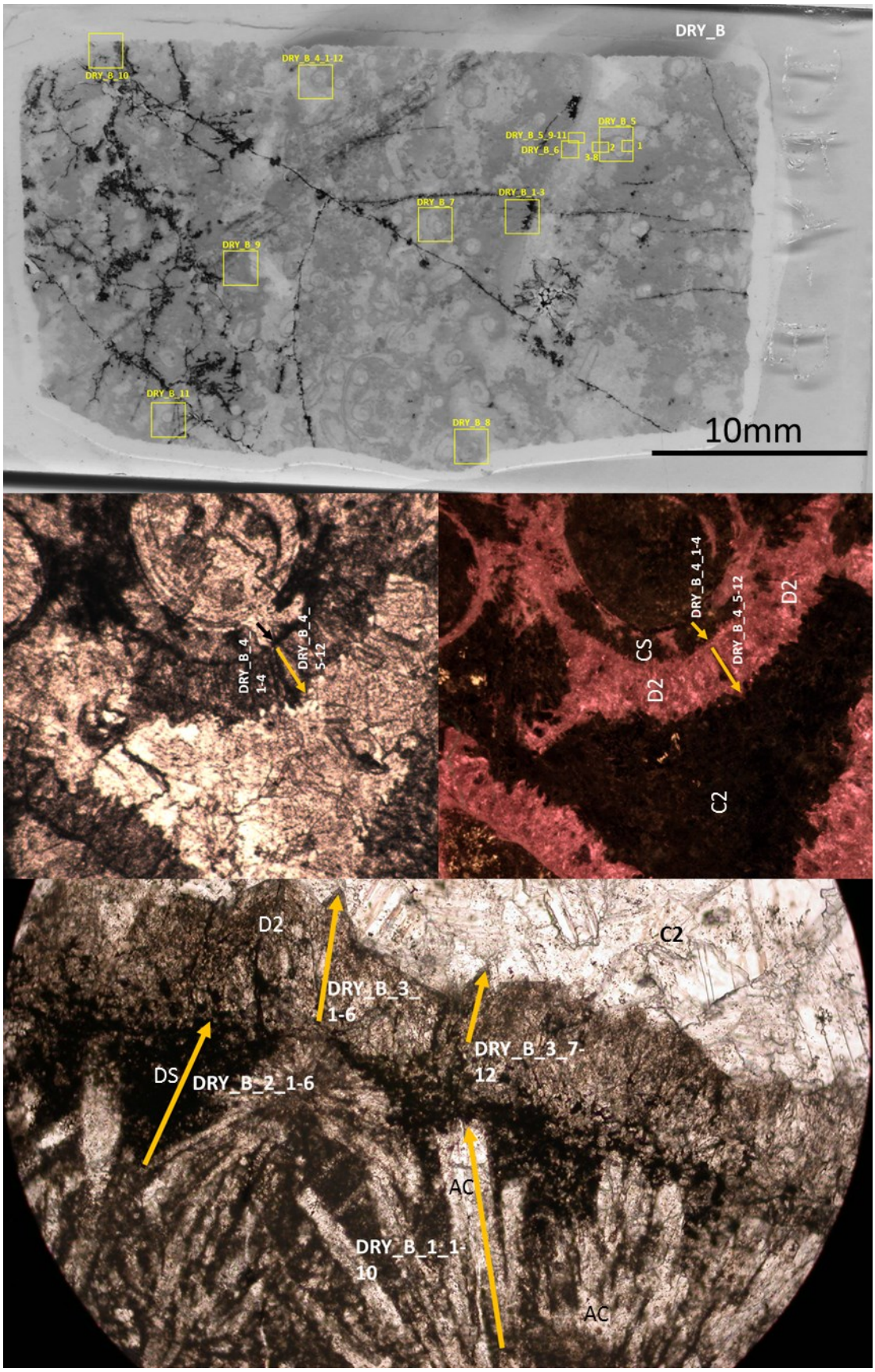
DRY_B
DRY_B_10
DRY_B_4_1-12
DRY_B_5
DRY_B_5_9-11
DRY_B_6
DRY_B_7
DRY_B_1-3
DRY_B_9
DRY_B_11
DRY_B_8
10mm
DRY_B_4_1-4
DRY_B_4_5-12
CS
D2
C2
DRY_B_3_1-6
DRY_B_3_7-12
DS
DRY_B_2_1-6
AC
DRY_B_1_1-10

D2

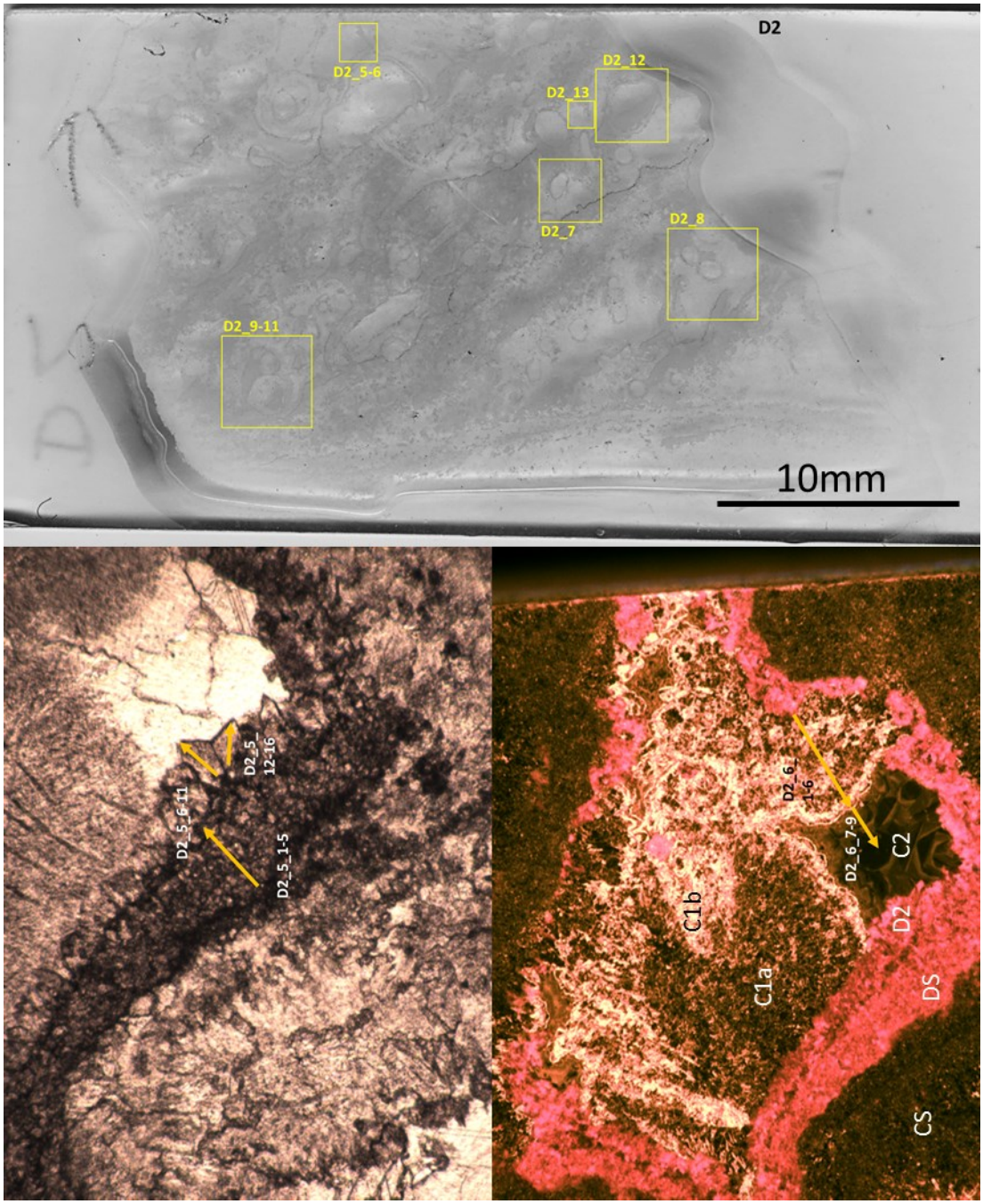
D2
D2_5-6
D2_12
D2_13
D2_7
D2_8
D2_9-11
10mm
D2_5_12-16
D2_5_6-11
D2_5_1-5
D2_6_1-6
D2_6_7-9
C2
C1b
C1a
D2
DS
CS

D2

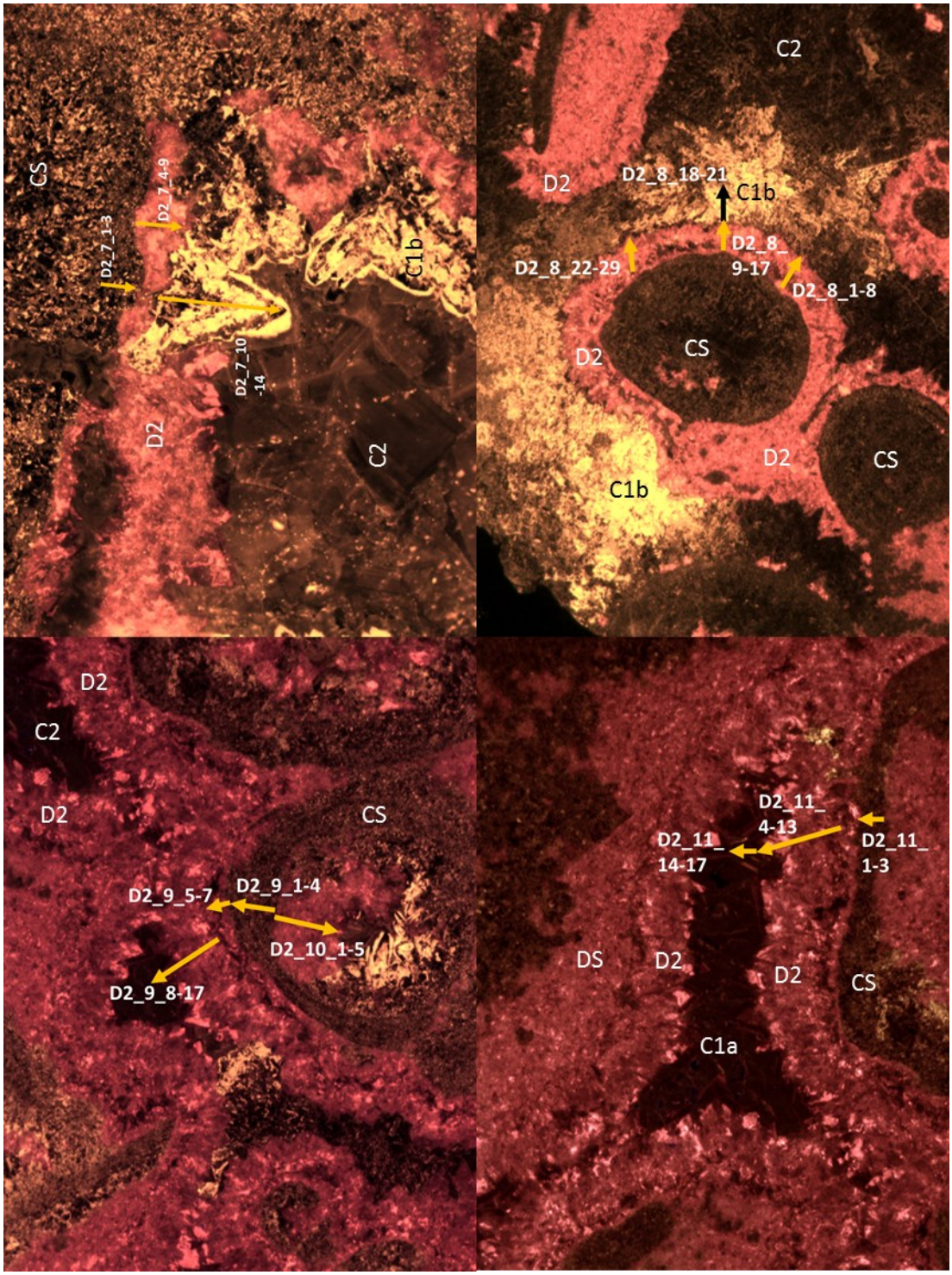
CS
D2_7_4-9
D2_7_1-3
C1b
D2_7_10
-14
D2
C2
C2
D2
D2_8_18-21
C1b
D2_8_
9-17
D2_8_22-29
D2_8_1-8
D2
CS
D2
CS
C1b
D2
C2
D2
CS
D2_9_5-7
D2_9_1-4
D2_10_1-5
D2_9_8-17
D2_11_
4-13
D2_11_
14-17
D2_11_
1-3
DS
D2
D2
CS
C1a

D2

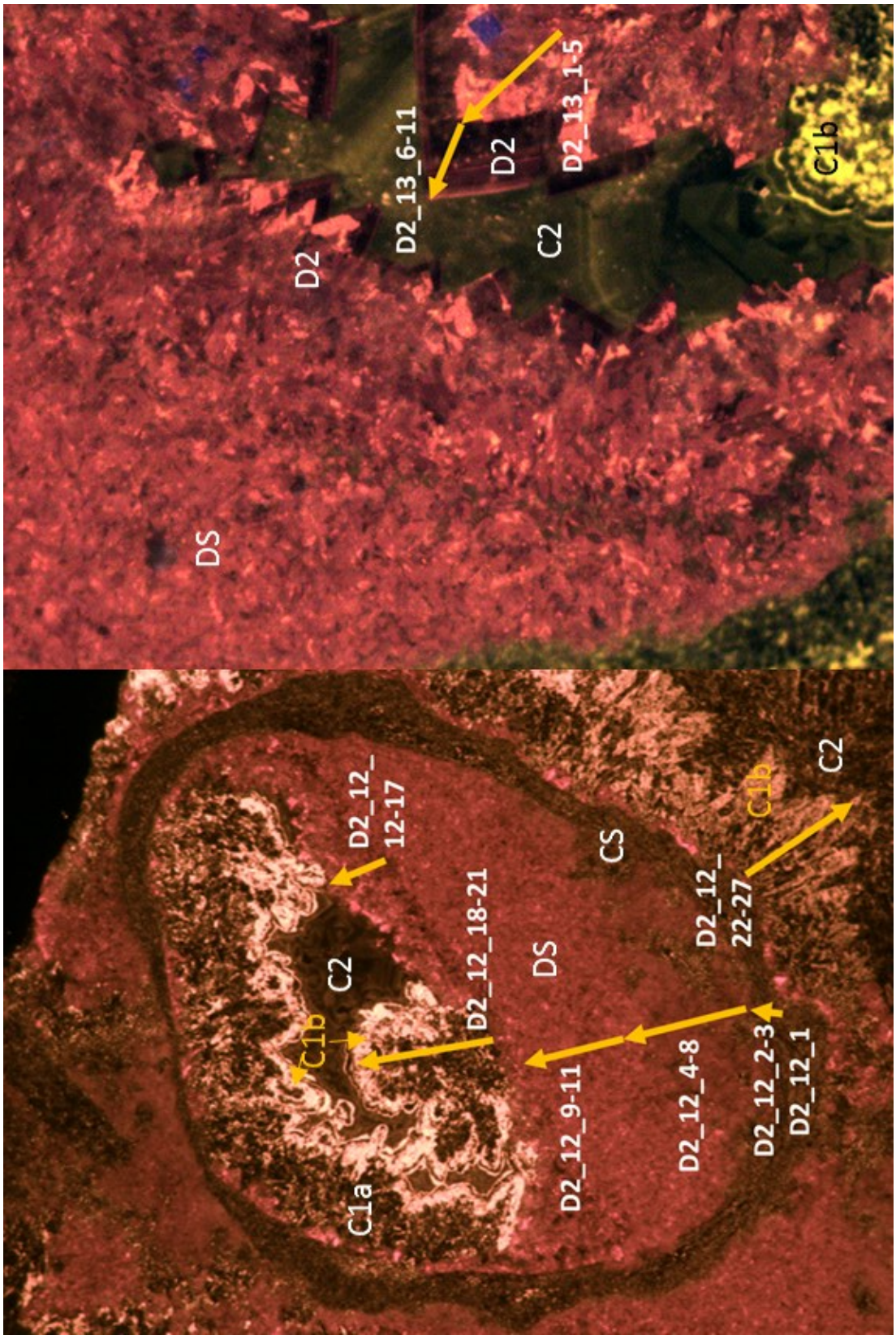
DS
D2
D2_13_6-11
D2
D2_13_1-5
C2
C1b
C1a
C1b
C2
D2_12_
12-17
D2_12_18-21
DS
CS
D2_12_9-11
D2_12_4-8
D2_12_2-3
D2_12_1
D2_12_
22-27
C1b
C2

DR1

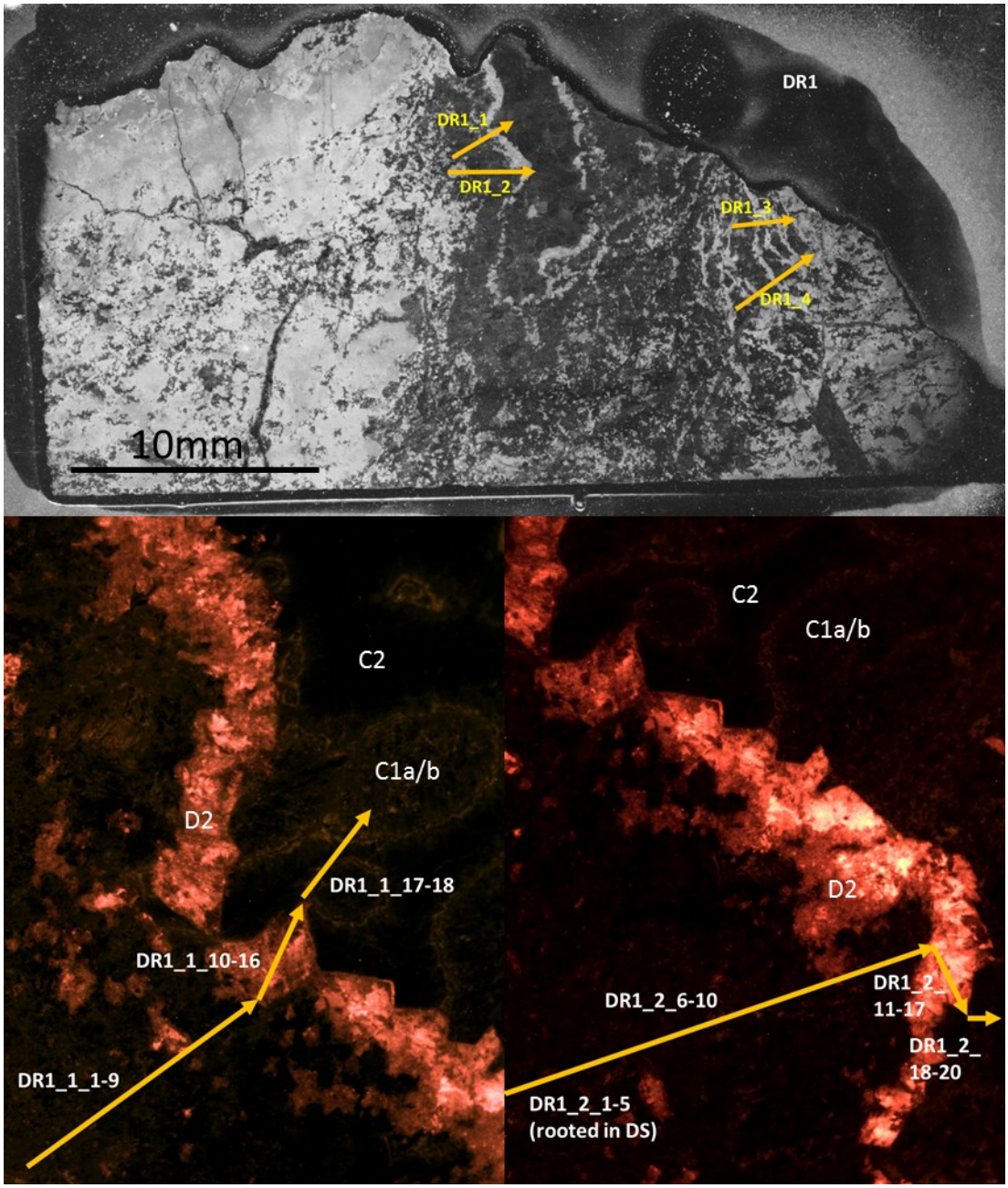
DR1
DR1_1
DR1_2
DR1_3
DR1_4
10mm
C2
C1a/b
D2
DR1_1_17-18
DR1_1_10-16
DR1_1_1-9
C2
C1a/b
D2
DR1_2_6-10
DR1_2_
11-17
DR1_2_
18-20
DR1_2_1-5
(rooted in DS)

DR3_1ca

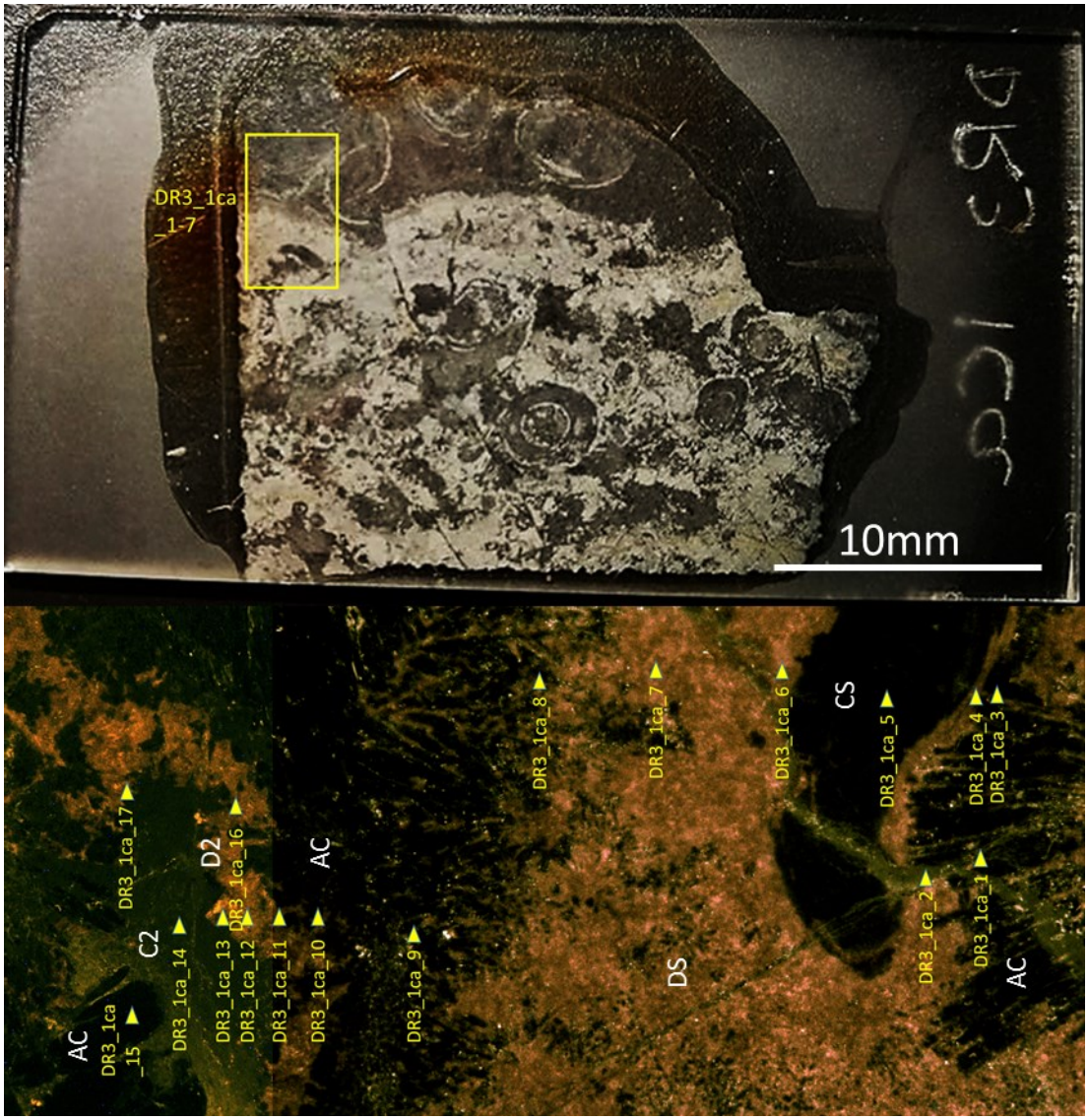
DR3_1ca
_1-7
10mm
AC
DR3_1ca
_15
C2
DR3_1ca_14
DR3_1ca_17
D2
DR3_1ca_13
DR3_1ca_12
DR3_1ca_16
DR3_1ca_11
AC
DR3_1ca_10
DR3_1ca_9
DR3_1ca_8
DR3_1ca_7
DS
DR3_1ca_6
CS
DR3_1ca_5
DR3_1ca_4
DR3_1ca_3
DR3_1ca_2
DR3_1ca_1
AC

DR3_1cb

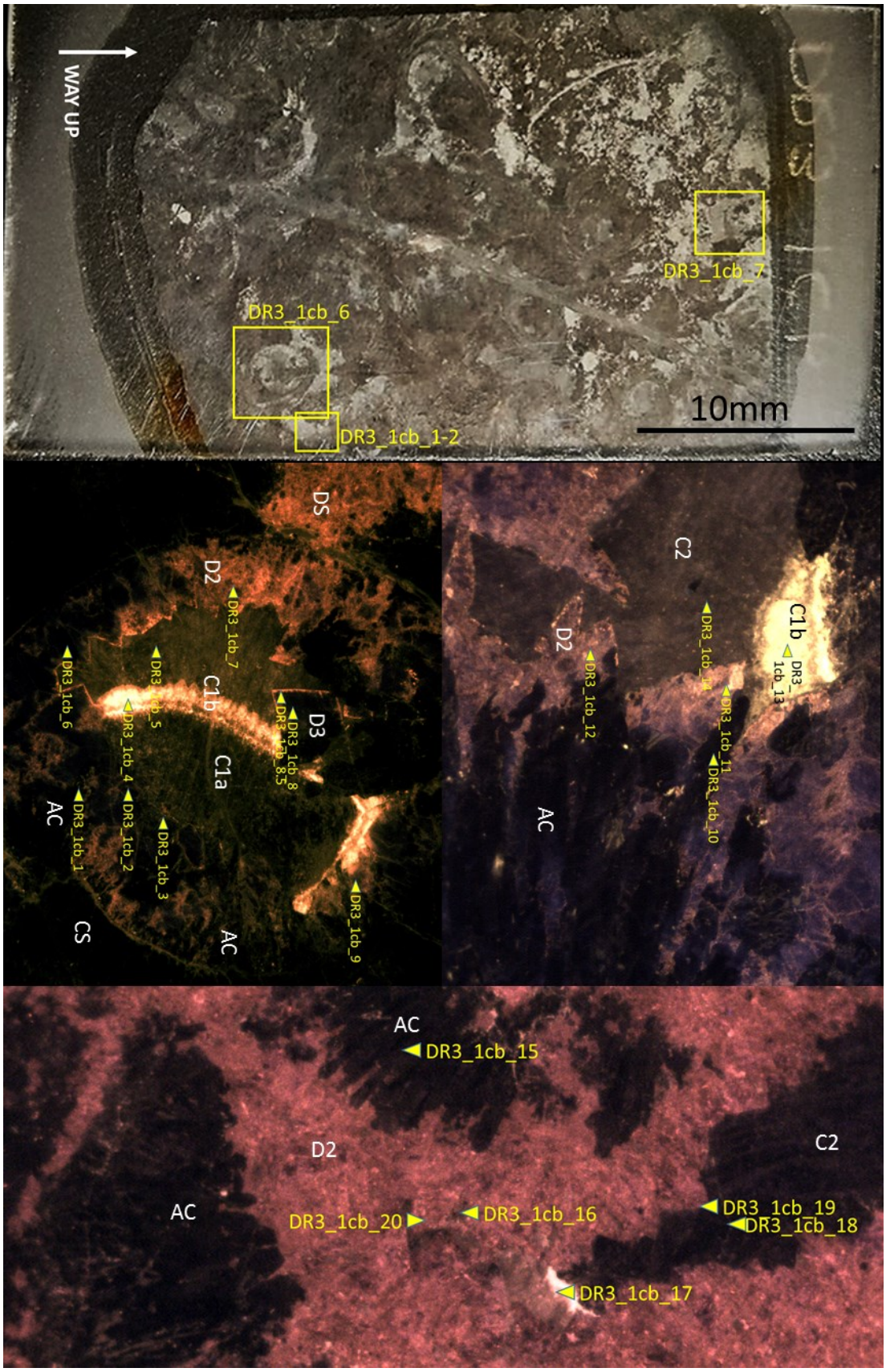
WAY UP
DR3_1cb_7
DR3_1cb_6
DR3_1cb_1-2
10mm
DS
D2
DR3_1cb_7
DR3_1cb_6
DR3_1cb_5
C1b
DR3_1cb_8
DR3_1cb_8.5
D3
C1a
DR3_1cb_4
DR3_1cb_2
DR3_1cb_3
AC
DR3_1cb_1
CS
AC
DR3_1cb_9
C2
D2
DR3_1cb_12
DR3_1cb_14
C1b
DR3_1cb_13
DR3_1cb_11
DR3_1cb_10
AC
AC
DR3_1cb_15
D2
C2
AC
DR3_1cb_20
DR3_1cb_16
DR3_1cb_19
DR3_1cb_18
DR3_1cb_17

DR3_A1

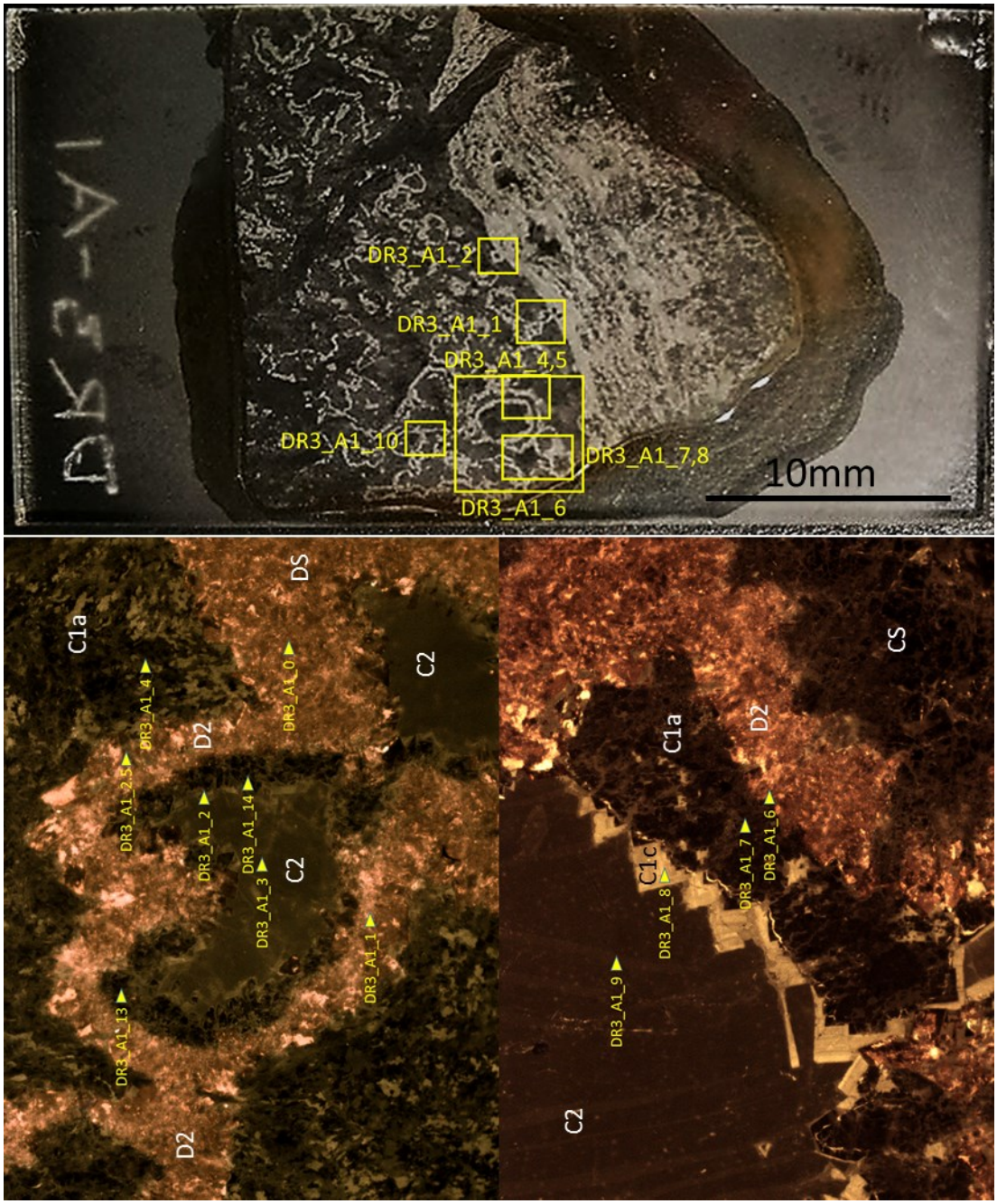
DR3-A1
DR3_A1_2
DR3_A1_1
DR3_A1_4,5
DR3_A1_10
DR3_A1_7,8
DR3_A1_6
10mm
C1a
DS
C2
D2
DR3_A1_4
DR3_A1_0
DR3_A1_2.5
DR3_A1_2
DR3_A1_14
DR3_A1_3
DR3_A1_1
DR3_A1_13
CS
C1c
DR3_A1_7
DR3_A1_6
DR3_A1_8
DR3_A1_9

Appendix D

Fossil key and occurrence catalogue

Ichnofossils					
Symbol	**ID**	**Notable occurrences**	**Stratigraphic Position**	**References**	**Notes**
	*Archaeichnium*	Namibia: Witputs subbasin, Farms Arimas and Groendorn. Zaris subbasin, Farm Harughas. Australia.	Lower Huns Member. Nasep Member. Rawnsley Quartzite.	Glaessner (1963, 1978); Germs (1972a); Jensen et al. (2000); Noffke et al. (2002); Gehling and Droser (2013)	Possible body fossil (Acenolaza et al., 2009)
	*Bergaueria*	Witputs subbasin, Farm Kuibis	Urikos Member	Crimes and Germs (1982)	May be *Intrites* in the Nama Group (Crimes, 1989). May represent MISS (Menon et al., 2016)
	*Brooksella*	Witputs subbasin, Farm Huns. Zaris subbasin.	Nasep Member. Urusis Formation.	Crimes and Germs (1982)	Possible body fossil after Xiao and Kaufman (2006). Possible sponge (Ciampaglio et al., 2006)
	*Buchholzbrunnichnus kroeneri*	Witputs subbasin, Farm Buchholzbrunn	Kliphoek Member	Germs (1973b)	Reinterpreted as body fossil of unknown affinity (Jensen and Runnegar, 2005)
	Possible *Chondrites*	Zaris subbasin, Farm Kuderup	Vingerbreek Member	Crimes and Germs (1982)	Uncertain affinity. Possibly *Archaeonassa* (Jensen and Runnegar, 2005)
	Cochlichnus	Witputs subbasin, Farm Arimas	Lower Huns Member	Jensen and Runnegar (2005)	
	Complex backfilled burrows	Zaris subbasin, Hauchabfontein Farm	Upper Omkyk Member	Macdonald et al. (2014)	Similar to *Zoophycos* (but see Buatois and Mangano, 2016). Possible Palaeopasichnid (Zhuravlev, pers. com.)
	*Conichnus*	Zaris subbasin, Road transect (D850 and D855), Witputs subbasin, Farm Arimas	Vingerbreek Member, Huns Member	Darroch et al. (2016); Jensen and Runnegar (2005)	
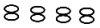	*Diplichnites*	Witputs subbasin, Farm Vergelee	Nomtsas Formation	Crimes and Germs (1982)	
	*Diplocraterion*	Zaris subbasin, Farm Haruchas, Farm Berghoek, Farm Kuderup	Niederhagen and Vingerbreek Members	Crimes and Germs (1982); Germs (1995)	Possibly more simple than *Diplocraterion* (Grant, 1990; Jensen and Runnegar, 2005)
	*Helminthoidichnites*	South Australia. South China	Rawnsley Quartzite, Dengying Formation, Gaojiashan and Shibantan Members.	Gehling and Droser (2013). Weber et al. (2007)	
	*Helminthopsis*	Witputs subbasin, Farm Arimas	Lower Huns Member	Jensen and Runnegar (2005)	

	*Lamonte trevallis*	South China, Hubei, Yangtze Gorges, Wuhe section	Dengying Formation, Shibantan Member	Meyer et al. (2014)	
	*Multina minima*	Brazil, Corumba Group.	Tamengo and Guaicurus Formations	Parry et al. (2017)	
	*Neonereites*	Witputs subbasin, Farm Vergelee	Nomtsas Formation	Crimes and Germs (1982)	Two proposed ichnospecies: *uniserialis* and *biseriali*. However, reinterpreted as either *Archaeonassa* (Jensen, 2003; Jensen and Runnegar, 2005) possible body fossil of unknown affinity (Xiao and Kaufman, 2006).
	*Nereites*	Zaris subbasin, Farm Haruchas	Vingerbreek Member	Crimes and Germs (1982)	Reinterpreted as possible body fossil of unknown affinity (Xiao and Kaufman, 2006).
	*Olenichnus*	Witputs subbasin, Farm Holoog	Huns Member	Jensen and Runnegar (2005)	
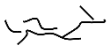	*Palaeophycus*	South China, Hubei, Sandouping Quarry	Dengying Formation, Shibantan Member	Weber et al. (2007)	
	*Parasammichnites pretzeliformis*	Nama Group, Witputs subbasin, 1.2 km ESE of Koelkrans camp, Fish River Canyon	Lower Spitskop Member	Buatois et al. (2018)	
	*Planolites*	Nama Group: Zaris subbasin. South China: Hubei, Sandouping Quarry.	Niederhagen Member. Dengying Formation, Shibantan Member	Germs (1995); Weber et al. (2007)	
	Possible *Skolithos*	Zaris subbasin, Farm Grootplaas. Witputs subbasin, Farm Geinochas	Kliphoek Member. Urusis Formation	Crimes and Germs (1982); Pickford (1995)	Uncertain affinity in Kliphoek Member. Nama Group examples reinterpreted as probable body fossil (Crimes and Fedonkin, 1996)
	*Streptichnus narbonnei*	Witputs subbasin, Farm Swartpunt	Spitskop Member (medium scale seq 18 of Saylor, 2003)	Jensen and Runnegar (2005)	

	*Taenidium*	Witputs subbasin, Farm Arimas, Farm Sonntagsbrunn	Nasep Member, Feldschuh-horn Member	Germs (1972a)	
	*Treptichnus isp.*	Witputs subbasin, Farm Arimas	Huns Member	Jensen et al. (2000)	
	*Treptichnus pedum*	Witputs subbasin, Farm Sonntagsbrunn	Nomtsas Formation (VF2 of Wilson et al., 2012)	Germs (1972a); Grotzinger et al. (1995); Geyer and Uchman (1995); Wilson et al. (2012)	
	Unnamed trace fossil	Newfoundland, Mistaken Point.	Mistaken Point Formation	Liu et al. (2010)	
	*Beltanelliformis*	Witputs subbasin, Farm Grens, Farm Aar	Kliphoek Member	Jensen et al. (2000); Vickers-Rich et al. (2013); Wood et al., (2015)	*Nemiana* and *Hagenetta* synonymised with *Beltanelli-formis (Grant, 1990;* Ivantsov et al., 2014)
	Stromatolites and thrombolites	Zaris subbasin, Farms Zebra River, Donkergange, and Driedoornvlakte Witputs subbasin, Farm Swartkloofberg	Lower Spitskop Member, Huns Member, Omkyk Member, Mooifontein Member	Germs (1972a; 1995); Grotzinger et al. (2000)	
	Microbially induced sedimentary structures (MISS)	Nambia: Zaris subbasin, (D850), Farm Haruchas, Farm Bullsport. Witputs subbasin, Farm Aar. South China: Hubei, Wuhe section.	Niederhagen Member, Vingerbreek Member, Kliphoek Member. Dengying Formation, Shibantan Member.	Noffke et al. (2002); Bouougri and Porada (2007); Darroch et al. (2016); Vickers-Rich et al. (2013). Meyer et al. (2014)	e.g. Biolaminites in siliciclastic deposits, inferred microbial textures in shallow water limestones
	*Torrowangea*	Purported occurrence in Nama Group. South China, Hubei, Yangtze Gorges	Nasep Member, Urusis Formation, Schwarzrand Subgroup. Dengying Formation, Shibantan Member	Geyer and Uchman (1995); Weber et al. (2007)	
	*Vendotaenia antiqua*	Nama Group. Farm Nutupsdrift, borehole. Witputs subbasin, Tses Borehole and Farms Kliphoek and Sonntagsbrunn. South China, Hubei, Shaanxi.	Vingerbreek and Feldschuhhorn Members. Dengying Formation.	Germs et al. (1986); Cohen et al. (2009); Wilson et al., 2012. Sun (1986); Zhao et al. (1988); Weber et al. (2007)	Below FWWB in the Nama.
	Possible cyanobacterial representatives including *Bavlinella faveolata*	Zaris subbasin, Nutupsdrift borehole. Witputs subbasin, Tses borehole	Urusis Formation (Witputs). Vingerbreek Member (both subbasins). Kuibis Subgroup (Witputs)	Germs et al. (1986)	Possible cyanobacterial sheaths, *Chuaria circularis* and *Bavlinella faveolata* (Mansuy and Vidal, 1983)

APPENDIX D: FOSSIL KEY AND OCCURRENCE CATALOGUE

Body Fossils					
Soft-bodied					
Symbol	**ID**	**Notable occurrences**	**Stratigraphic Position**	**References**	**Notes**
	*Aspidella*, *Paramedusium*, *Cyclomedusium*	Nama Group, Zaris subbasin, Road transect (D850 and D855). Witputs subbasin, Farm Groendorn (Grondorner). Yudoma Group, Yudoma-Maya confluence.	Vingerbreek Member. Huns Member. Nasep Member. Kliphoek Member. Aim Formation.	Darroch et al. (2016); Germs (1972a); Jensen et al. (2000); Pickford (1995). Zhu et al. (2017)	Junior synonyms of *Aspidella* after Gehling et al. (2000)
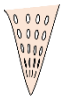	*Ausia fenestrata*	Namibia, Witputs subbasin, Farm Plateau. Russia, White Sea Area.	Kliphoek Member, Verkhovka and Lower Yorga Formations	Hahn and Pflug (1985); Pickford (1995); Grazhdankin (2004)	Possible tunicate?
	*Avalofractus abaculus*	Newfoundland, Avalon Peninsula, Spaniard's Bay	Trepassey Formation	Narbonne et al. (2009)	
	*Beothukis*	Newfoundland, Avalon Peninsula, Mistaken Point. Bonavista Peninsula, Burnt Point.	Mistaken Point 'E' surface, MUN surface	Brasier and Antcliffe (2009); Laflamme et al. (2012); Liu et al. (2016)	*Culmofrons plumosa* synonymised with species *Beothukis plumosa* in Liu et al. (2016)
	*Bradgatia*	Newfoundland, Avalon Peninsula. England, Charnwood Forest.	Mistaken Point. Mercian assemblage, Bed B, North Quarry.	Boynton and Ford (1996); Flude and Narbonne (2008); Wilby et al. (2011)	
	*Charnia*	Newfoundland, Bonavista Peninsula, Avalon Peninsula. England, Charnwood Forest.	Mistaken Point, Drook – Fermeuse Formations. Charnwood Forest, Mercian assemblage.	Ford (1958); Wilby et al. (2011); Liu et al. (2015)	
	*Charniodiscus*	Newfoundland and Charnwood Forest, Australia. South China, 3 Gorges area	Drook – Fermeuse Formations. Rawnsley Quartzite. Shibantan Member	Ford (1958); Glaessner and Daily (1959); Glaessner and Wade (1966); Laflamme et al. (2004); Chen et al. (2014)	
	*Conotubus*	South China (Southern Shaanxi)	Gaojiashan Lagerstatte	Zhang (1986); Lin et al. (1986); Cai et al. (2011)	

	*Coronacollina*	Australia	Ediacara Member, Rawnsley Quartzite	Clites et al. (2012); Droser and Gehling (2013)	Multi-element, partially skeletonised?
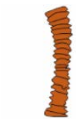	*Corumbella*	Brazil, Corumbá Group. California, Wood Canyon. Paraguay.	Tamengo Formation. Wood Canyon Formation. Itapucumi Group.	Hahn (1982); Hagadorn and Waggoner (2000); Warren et al. (2012)	
	*Curviacus* (palaeo-pasichnid)	South China, Hubei, Muzhuxia section	Dengying Formation, Shibantan Member	Shen et al. (2017)	
	Dickinsoniomorph	Australia. White Sea	Ediacara Member, Rawnsley Quartzite. White Sea (Vendian Group),	Sprigg (1947); Grazhdankin (2004)	
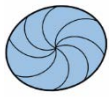	*Eoandromeda*	South China, Wenghui (Guizhou). Australia.	Doushantuo Member IV (Miaohe Member). Rawnsley Quartzite.	Tang et al. (2008); Zhu et al. (2008)	
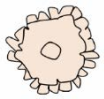	*Eoporpita*	Flinders Ranges, Ediacara Range and Brachina Gorge	Rawnsley Quartzite, Ediacara Member	Wade (1972); Seilacher (2003)	Proposed hydrozoan, xeno-phyophoran or holdfast
	*Ernietta*	Witputs subbasin, Farm Plateau, Farm Aar, Farm Wegkruip, Farm Hansburg	Upper Kliphoek (Aar) Member, Kanies Member	Pflug (1966); Dzik (1999); Bouougri et al. (2011); Elliott et al. (2016)	
	*Fractofusus*	Newfoundland.	Briscal – Fermeuse Formations	Gehling and Narbonne (2007)	
	*Gaojiashania*	Namibia, Zaris subbasin, Farm Donkergange. South China, Shaanxi, Gaojiashan Section. Eastern Siberia, Yudoma – Maya depression.	Hoogland Member. Gaojiashan Member. Aim Formation.	Smith et al. (2017). Hong et al. (2007); Cai et al. (2014); Zhuravlev et al. (2009)	Note possible reinterpreta-tion as *Shaanxilithes* for specimens of Eastern Siberia after Zhu et al. (2017)

	*Haootia*	Newfoundland, Bonavista Peninsula	Fermeuse Formation	Liu et al. (2014)	
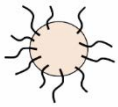	*Hiemalora*	Russian Platform, Siberia, Podolia and White Sea Region, Khorbusuonka River, Olenek Uplift. Mackenzie Mountains, Sekwi Brook. Avalon and Bonavista Peninsulas. South China, 3 Gorges.	Khatyspyt Formation. Sheepbed Formation. Mistaken Point – Fermeuse Formations. Shibantan Member.	Fedonkin (1981); Narbonne (1994); Gehling et al. (2000); Hofmann et al. (2005); Fedonkin et al. (2007a); Chen et al. (2014)	
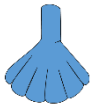	*Inaria*	Russia, White Sea region	Vendian Group	Grazhdankin (2004)	
	*Inkrylovia*	Mackenzie Mountains, Sekwi Brook	Lower Blueflower Formation	Sperling et al. (2015b)	Reconstructed after Fig 253 in Fedonkin et al. (2007a)
	*Ives-headiomorph*	Newfoundland	Drook – Fermeuse Formations	Boynton and Ford (1996); Liu et al. (2011)	Post-mortem decay (Liu et al., 2011)
	*Kimberella*	Australia. Russia, Winter Coast, White Sea region.	Rawnsley Quartzite. Vendian Group	Glaessner and Daily (1959); Fedonkin and Waggoner (1997)	
	*Kuibisia glabra*	Witputs subbasin, Farm Plateau	Dabis Formation (Kliphoek Member?)	Hahn and Pflug (1985)	Uncertain affinity. Possibly *Ernietta* (Runnegar, 1992) or external surface of *Ausia* (Fedonkin et al., 2007a)
	*Namalia*	Witputs subbasin, multiple localities. Aus-Buchholzbrunn to Helmeringhausen	Kliphoek Member	Germs (1968)	
	*Nasepia altae*	Witputs subbasin, Farm Swartpunt, Farm Arimas. Australia, Rawnsley Quartzite.	Spitskop Member, Nasep Member. Ediacara Member.	Germs (1973a); Darroch et al. (2015); Gehling and Droser (2013)	

	*Nilpenia*	Nilpena, Flinders Ranges	Rawnsley Quartzite, Ediacara Member	Droser et al. (2015)	
	*Onegia*	Russia, White Sea region.	Vendian Group	Grazhdankin (2004)	Considered synonymous with *Pteridinium* (Fedonkin et al., 2007a)
	*Orthogonium parallelum*	Nama Group, Witputs subbasin, Farm Kuibis	Kliphoek Member	Gurich (1930, 1933); Germs (1995); Pickford (1995)	Only specimen lost in WW2
	*Palaeopasichnus*	Nama Group, Witputs subbasin. Yudoma Group, Yudoma-Maya confluence	Kliphoek Member. Aim Formation	Jensen et al. (2000); Zhu et al. (2017)	Personal observation: *Palaeopasichnus gracilis* at base of Upper Omkyk Member, Farm Omkyk
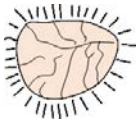	*Palaeophragmodictya*	South Australia. White Sea Region	Ediacara Member	Gehling and Rigby (1996); Serezhnikova (2007)	Probable sponge (Gehling and Rigby, 1996). Problematica with both sponge and coelenterate morphology (Serezhnikova, 2007)
	*Paracharnia*	South China, Hubei, Wuhe section.	Dengying Formation, Shibantan Member	Sun (1986)	
	*Parvancorina*	Australia. Russia, White Sea region	Rawnsley Quartzite. Vendian Group.	Glaessner (1958); Grazdankin (2004); Ivantsov et al. (2004); Naimark and Ivantsov (2009)	
	*Primocandelabrum*	Newfoundland. Bonavista Peninsula. England, Charnwood Forest.	Mistaken Point – Fermeuse Formations. Mercian assemblage.	Hofmann et al. (2008); Wilby et al. (2011)	
	*Protechiurus edmondsi*	Witputs subbasin, Farm Plateau	Dabis Formation, Kliphoek Member?	Glaessner (1979)	Dubiofossil? (Runnegar, 1992) or proto-chordate? Pickford (1995); Fedonkin et al. (2007a)

	*Pteridinium*	Witputs subbasin, Farm Swartpunt, 25km north of Farm Helmeringhausen (Kosos?), Farm Aar. South China, 3 Gorges, Hubei. Australia. North Carolina, Stanley County, Carolina Slate Belt.	Spitskop Member, Vingerbreek Member, Niederhagen Member, Upper Kliphoek (Aar) Member. Shibantan Member. Rawnsley Quartzite.	Gurich (1930, 1933); Glaessner (1963); Pflug (1970); Grant (1990); Germs (1995); Narbonne et al. (1997); Elliott et al. (2011); Chen et al. (2014); Gehling and Droser (2013). Gibson et al. (1984)	
	*Rangea*	Witputs subbasin, Farms Kuibis, Vrede, Aar and Chamis. South China, 3 Gorges, Hubei. Austrlia.	Niederhagen Member, Kliphoek Member. Shibantan Member. Rawnsley Quartzite.	Gurich (1930a, b); Germs (1973a); Jenkins (1985); Grant (1990); Vickers-Rich et al. (2013); Chen et al. (2014); Gehling and Droser (2013)	
	*Shaanxilithes*	Nama Group: Zaris subbasin, Road transect (D850). South China: Shaanxi, Lijiagou, Kuanchuanpu and Gaojiashan sections. Eastern Siberia, Nuuchchalakh valley	Vingerbreek Member. Gaojiashan Member. Aim Formation.	Darroch et al. (2016). Xing et al. (1984); Bengtson and Zhao (1992); Weber et al. (2007); Zhu et al. (2017)	*Shaanxilithes* in Vingerbreek Member be misidentified *Palaeopasichnus delicatus/linearis* (Zhuravlev, A.Y. pers. com.)
	*Spriggina*	Australia	Rawnsley Quartzite	Glaessner (1958); Gehling and Droser (2013)	
	*Stromatoveris*	South China, Yunnan, Meishucun, Jianshan	Chengjiang Formation	Shu et al. (2006)	
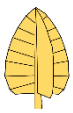	*Swartpuntia*	Witputs subbasin, Farm Swartpunt. Nevada.	Spitskop Member, Feldschuhhorn Member. Wood Canyon Formation.	Narbonne et al. (1997); Jensen et al. (2000); Hagadorn and Waggoner (2000)	
	*Thaumaptilon*	British Columbia, Walcott Quarry	Stephen Formation	Conway Morris (1993)	

	*Trepassia wardae*	Newfoundland, Avalon Peninsula, Spaniard's Bay	Drook-Trepassey Formations	Narbonne and Gehling (2003); Narbonne et al. (2009)	Originally attributed to *Charnia wardi*
	*Tribrachidium*	Australia. Ukraine, Podolia. Russia, White Sea region.	Rawnsley Quartzite. Vendian Group.	Glaessner (1959); Fedonkin (1983); Fedonkin et al. (2007a)	
	Vase-shaped microfossils (VSM)	South China, Shaanxi, Gaojiashan section.	Dengying Formation, Gaojiashan Member	Hong et al. (2007)	
	*Velancorina martina*	Witputs subbasin, Farms Aar and Schakalskuppe	Kuibis Formation (Kliphoek Member)	Pflug (1966)	Phylum Petalonamae
	*Ventogyrus*	Russia, White Sea region, Onega River.	Vendian Group	Ivantsov and Grazhdankin(1997); Fedonkin and Ivantsov (2007)	
	*Windermeria*	Mackenzie Mountains, Sekwi Brook	Upper Blueflower Formation	Narbonne (1994)	
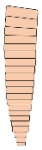	*Wutubus*	South China, 3 Gorges, Hubei	Shibantan Member	Chen et al. (2014)	
	*Yangtziramulus*	South China, Hubei, Muzhuxia and Miaohe sections.	Dengying Formation, Shibantan Member	Xiao et al. (2005); Shen et al. (2009)	
	*Yorgia*	Russia, Winter Coast, White Sea Region.	Vendian Group	Ivantsov (1999)	

Skeletal					
	*Cloudina*	Zaris subbasin, Farms Zwartmodder, Omkyk, Zebra River, Donkergange, Driedoornvlakte. Witputs subbasin, Farm Swartpunt, Farm Mooifontein, Farm Uitsig, Vioolsdrif region (South Africa)	Spitskop Member, Huns Member, Hoogland Member, Upper Omkyk Member, Mooifontein Member, Mara Member	Germs (1972b, 1995); Grant (1990); Penny et al. (2014); Wood and Curtis (2015); Wood et al. (2017b)	Two possible species in Namibia: *hartmannae* and *riemkeae* but based on growth mode not size distribution (Germs, 1972a; Wood et al., 2017). Probable total group cnidarian. Additional two species noted in South China: *C. ningqiang-ensis* and *C. xuanjiangping-ensis* (Cai et al. (2017)
	*Hyolithellus*	North Greenland, Lower Cambrian	Buen and Aftenstjerneso Formations	Skovsted and Peel (2010)	
	*Multiconotubus chinensis*	South China, Shaanxi, Lijiagou section	Dengying Formation, Beiwan Member	Cai et al. (2017)	
	*Namacalathus*	Zaris subbasin, Farms Zwartmodder, Omkyk, Zebra River, Driedoornvlakte. Witputs subbasin, Farms Swartpunt, Swartkloofberg and Grens	Spitskop Member, Feldschuhhorn Member, Upper Omkyk Member and Kliphoek Member	Grotzinger et al. (1995); Watters (MSci thesis, MIT, 2000); Wood et al. (2015); Penny et al. (2016)	Putative lophophorate (Zhuravlev et al., 2015)
	*Namapoikia*	Zaris subbasin, Farm Driedoornvlakte	Omkyk Member	Wood et al. (2002); Wood and Penny (2018)	Probable poriferan
	*Sinotubulites*	Siberia. Spain. Mexico. South China.		Zhao et al. (1988); Chen et al. (2008); Zhuravlev et al. (2012); Cai et al. (2015)	
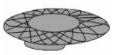	*Suvorovella*	Eastern Siberia, Yudoma – Maya depression	Aim Formation	Vologdin and Maslov (1960); Wood et al. (2017a)	

	*Anabarites*				
	*Cambrotubulus*			Rozanov et al. (1969); Zhuravlev et al. (2012)	
	*Chancelloriid*	South China, Chengjiang. Utah, Wheeler Shale. Canada. Siberia. Mongolia. Australia.	Early-Middle Cambrian. Yuanshan Formation. Wheeler Shale. Burgess Shale.	Walcott (1920); Bengtson et al. (1990); Bengtson and Hou (2001); Janussen et al. (2002); Porter (2011)	
	*Fomitchella*			Clarkson, E.N.K. (1979)	
	*Halkieriid*			Conway Morris and Peel (1990); Porter (2004)	
	*Orthothecimorph*			e.g. Novozhilova (2013)	
	*Protoherzina*			Clarkson, E.N.K. (1979)	

Please note, this catalogue is <u>not</u> exhaustive.

Table AD2: Farms which host outcrop of the classic Nama Group. Note that given codes do not correspond to official Farm numbers but are instead a key to Figures AD1 to AD7.

Number	Farms (South of Osis)	Number	Farms (North of Osis)
1	Binz	1	Namakorabis
2	Blutputz	2	Guisis
3	Maguams	3	Abbabis
4	Chamchawib	4	Wagner
5	Blenheim	5	Steizenfels
6	Saraus	6	Nauzerus
7	Kosos	7	Nuwedam
8	Wittmanshaar	8	Diamant
9	Dabis	9	Klein Aub
10	Volkerust	10	Abendruhe
11	Auas	11	Die Vake
12	Helmeringhausen	12	Arbeid Adek
13	Auas sud	13	Aais
14	Kunjas	14	Gneisab
15	Goais	15	Remhoogte
16	Corunna	16	Noab
17	Rotterdam	17	Ebenhout
18	Frisgewaagd	18	Oos
19	Gamochas	19	Tsabisis 340
20	Karadaus	20	Blasskranz
21	Mooifontein	21	Driedoornvlakte
22	Stockdale	22	Cambells Aub
23	Nabibis	23	Dikdoorn
24	Hoamoed	24	Diep Rivier
25	Nuweplaas	25	Weltevrede 402
26	Ausis	26	Tsams West
27	Chamis sud	27	Tsams Ost
28	Soetdoring	28	Naukluft
29	Tiras	29	Bullsport
30	Neisip	30	Kambes
31	Twyfel	31	Rietoog
32	Wegkruip	32	Rooidrai
33	Zuurberg	33	Gannavlak
34	Dreylingen	34	Kobas
35	Bossie	35	Klein Angous
36	Untersee	36	Khos
37	Tokio	37	Ghaap
38	Pronksberg	38	Gavind
39	Duinsig	39	Safneck

Number	Farms (South of Osis)	Number	Farms (North of Osis)
40	Aris	40	Sand Rivier
41	Hansburg	41	Schlip
42	Umub	42	Slangkolk
43	Oberndorf	43	Blauputz
44	Olams	44	Rondebos
45	Ganikeis	45	Chauchab
46	Radfordsputs and Bree-rivier	46	Auchabmund
47	Carolinahof	47	Gaibes
48	Dorpsgrood (Townlands) and Bethanie	48	Zaugab
49	Wasserfall	49	Aries
50	Dorpsig	50	Draaihoek
51	Augustfelde	51	Vingerbreek
52	Kwessieputs	52	Kanaams
53	Sonderwater	53	Arurueis
54	Vrede	54	Kreyrivier
55	Kloofland	55	Fahlhuk
56	Klipdrif	56	Niep
57	Florsheim	57	Schlip Mundung
58	Hunsruck	58	De Hoop
59	Schakalskuppe	59	Kamaseb
60	Weltevrede	60	Herma
61	Kuibis nord	61	Nooitverwag
62	Nord Klein	62	Gamis Nord
63	Riverside	63	Gamis Ost
64	Schwarzkuppe	64	Gamis
65	Soromaas	65	Corabasin
66	Gangeis	66	Verlos
67	Plateau	67	Namtsis
68	Geelschaap	68	Swartkobus
69	Doorns	69	Goabosoah
70	Kalkfontein	70	Van Wyk
71	Kuibis sud	71	Wes Heitzwasies
72	Macduffs Castle	72	Arusis
73	Buchholz west	73	Varkboseh
74	Buchholzbrunn	74	Dirichas
75	Isaaksbrunn	75	Schadeck
76	Kosis	76	Lomoenputs
77	Schnepfenrivier	77	Ubusis
78	Aar	78	Neu Onis
79	Tsachanabis	79	Felseneck
80	Shanghai	80	Goede Hoop

Number	Farms (South of Osis)	Number	Farms (North of Osis)
81	Akam	81	Urikos
82	Uitviug	82	Neuras
83	Brackwasser	83	Onis
84	Simplon	84	Kyffhauser
85	Kesslersbrunn	85	Haruchas
86	Kanas	86	Kuderup
87	Kaalvlakte	87	Nudaus
88	Arasab	88	Lahnstein
89	Hoogland	89	Urusis
90	Kalkrand	90	Nomtsas
91	Nastom	91	Narobmund
92	Harris	92	Auros West
93	Aukum	93	Hauchabfontein
94	Heigums	94	Donker Gange
95	Koppie	95	Zebra River
96	Rietputs	96	Friedland
97	Hudab West	97	Kamkas
98	Irene	98	Kameelberg
99	West Feldschuhhorn	99	Gorges
100	Sandverhaar	100	Karab
101	Feldschuhhorn Ost	101	Marlon Reitz
102	Vogelstrausskluft	102	Kabib
103	Arulot	103	Sandhof
104	Kokerboomkloof	104	Wildpark
105	Sabidas (west side of farm used to be Raraugabib)	105	Ober Packriem
106	Diamantpoort	106	Gluckauf
107	Haaswater	107	Odette
108	Waldsee	108	Poburke
109	Tweespruit	109	Mooirivier
110	Grens	110	Hoogland
111	Pockenbank	111	Theronsterg
112	Ruspunt	112	Hoheacht
113	Rooiberg	113	Niederhagen
114	Rooipunt	114	Nutupsdrift
115	Geigoab	115	Namseb
116	Totem	116	Townlands - Maltahohe
117	Inachab	117	Sandpforte
118	Anib	118	Kampe
119	Anusi	119	Omkyk
120	Kliphoek	120	Zwartmodder
121	Kanies	121	Uitkoms

Number	Farms (South of Osis)	Number	Farms (North of Osis)
122	Blauputs	122	Kalkhugel
123	Nuichas	123	Halifax
124	Kaalberg	124	Grootplaats
125	Sandykop	125	Dawet
126	Swartkloofberg	126	Kachauchab
127	Swartpunt	127	Karichab
128	Tierkloof	128	Breckhorn
129	Geelperdshoek	129	Zaris
130	Piet-se Puts	130	Steinfeld
131	Nuwerus	131	Bergplaas
132	Abos	132	Noib
133	Quaggaspoort	133	Plattfontein
134	Huns	134	Christiania
135	Hope	135	Burgsdorf
136	Zaracheibis	136	Garub
137	Churutabis - Sonntagsbrunn	137	Hohenfelde
138	Nord Witputs	138	Nam
139	Sud Witputs	139	Gorab
140	Aub	140	Keerom
141	Kolke	141	Aukens
142	Zebrafontein	142	Portjes
143	Arimas	143	Tourlosie
144	Uitsig	144	Grootfontein 91
145	Augurabis	145	Moreson
146	Leyerbreek	146	Haseweb
147	Einaug	147	Shakalslust
148	Gabasis Ost	148	Nord Schwarzrand
149	Louisenhohe	149	Nooitgedag
150	Steinfeld	150	Rooiberg
151	Narnbaes	151	Nord Kleinfontein
152	Aikanes	152	Kleinfontein
153	Altdorn 32	153	Eisenach
154	Arep	154	Aandrus
155	Nordeck	155	Sandrucken
156	Autsas	156	Ellsenhof
157	Zukous	157	Naudaus
158	Hoas Nord	158	Rooiberg Sud
159	Hoas	159	Schwarzkuppe
160	Wolfsschlucht	160	Zugspitze
161	Karenhork	161	Wartburg
162	Schwarzkupper	162	Amhub

Number	Farms (South of Osis)	Number	Farms (North of Osis)
163	Stamprivier	163	Stubbenkammer
164	Holoog		
165	Tsawisis		
166	Grundorn		
167	Holoogberg		
168	Karios		
169	Geiaus		
170	Altdorn 3		
171	Kanebis		
172	Frankfurt		
173	Rotegab		
174	Mooiplaats		
175	Weltevrede 302		
176	Bergzicht		
177	Goedgevonder		
178	Geis		
179	Kanus		
180	Spes Bona		
181	Nanzes		
182	Bismarckaue		
183	Liebenrust		
184	Genadenda		
185	Us		
186	Realkoppe		
187	Maradas		
188	Groenrivier		
189	Hauchanas		
190	Vredenhof		
191	Uitkomst		
192	Duurdrift Nord		
193	Ariams		
194	Stinkdorn		
195	Garub		
196	Nukois		
197	Kralkuft		
198	Garis		
199	Sandmund		
200	Kachena		
201	Krantzberg		
202	Geltsanes		
203	Sandmodder		

Number	Farms (South of Osis)	Number	Farms (North of Osis)
204	Naauwpoort		
205	Goa-ab		
206	Khorrobees		
207	Amas		
208	Kubub West		
209	Kubub Ost		
210	Nieuwefontein		
211	Oab		
212	Karob		
213	Uheib		
214	Tzamab Groendorn		
215	Vlissingen		
216	Austerlitz		
217	Kentucky		
218	Bockiesbank Ost		
219	Elansdraai		
220	Heiragabis		
221	Blyderverwacht		
222	Jericho		
223	Platrand		
224	Border		
225	Witkop		
226	Nababis		
227	Nabas		
228	Ukamas		
229	Nakop		

Additional note:
Germs (1983): '*The trace fossils generally occur within the transgressive and regressive intertidal to very shallow subtidal clastic sediments. The Ediacaran fauna occurs in intertidal but mainly shallow subtidal clastic sediments, which were laid down landwards from carbonates, in which Cloudina and stromatolites occur. Neither trace nor body fossils have been found in the few offshore sediments of the Nama Group.*'

Figures AD1 to AD7

Nama Group Farm Map

The following maps were redrawn using a combination of GoogleEarth, Microsoft Powerpoint and numerous Namibian geological maps (1:1000000, 1963, 1978, and revised 1980 editions, 1:250000 Mariental 2416, and Rehoboth 2316, Geological Survey of Namibia, Ministry of Mines and Energy)

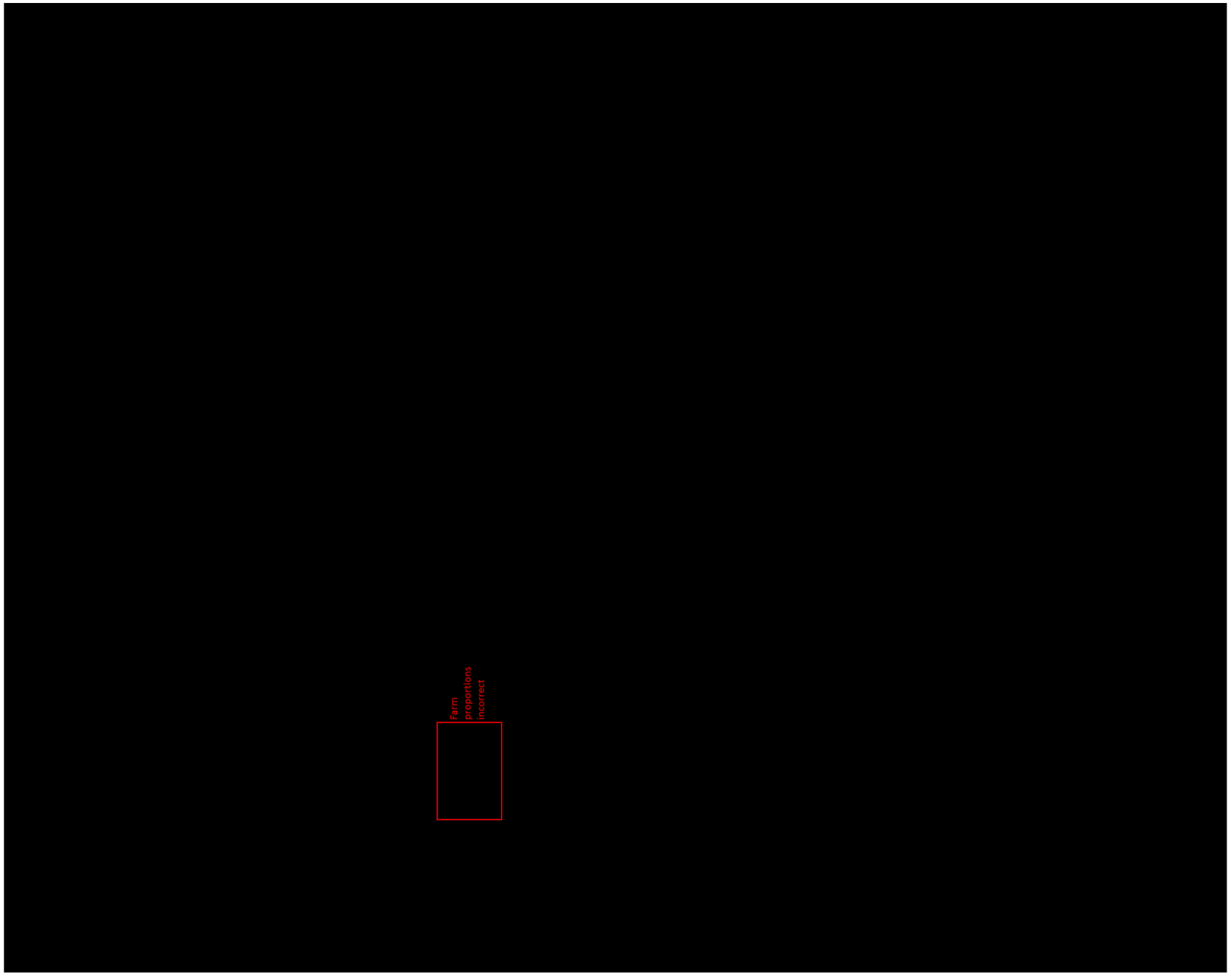
Farm
proportions
incorrect

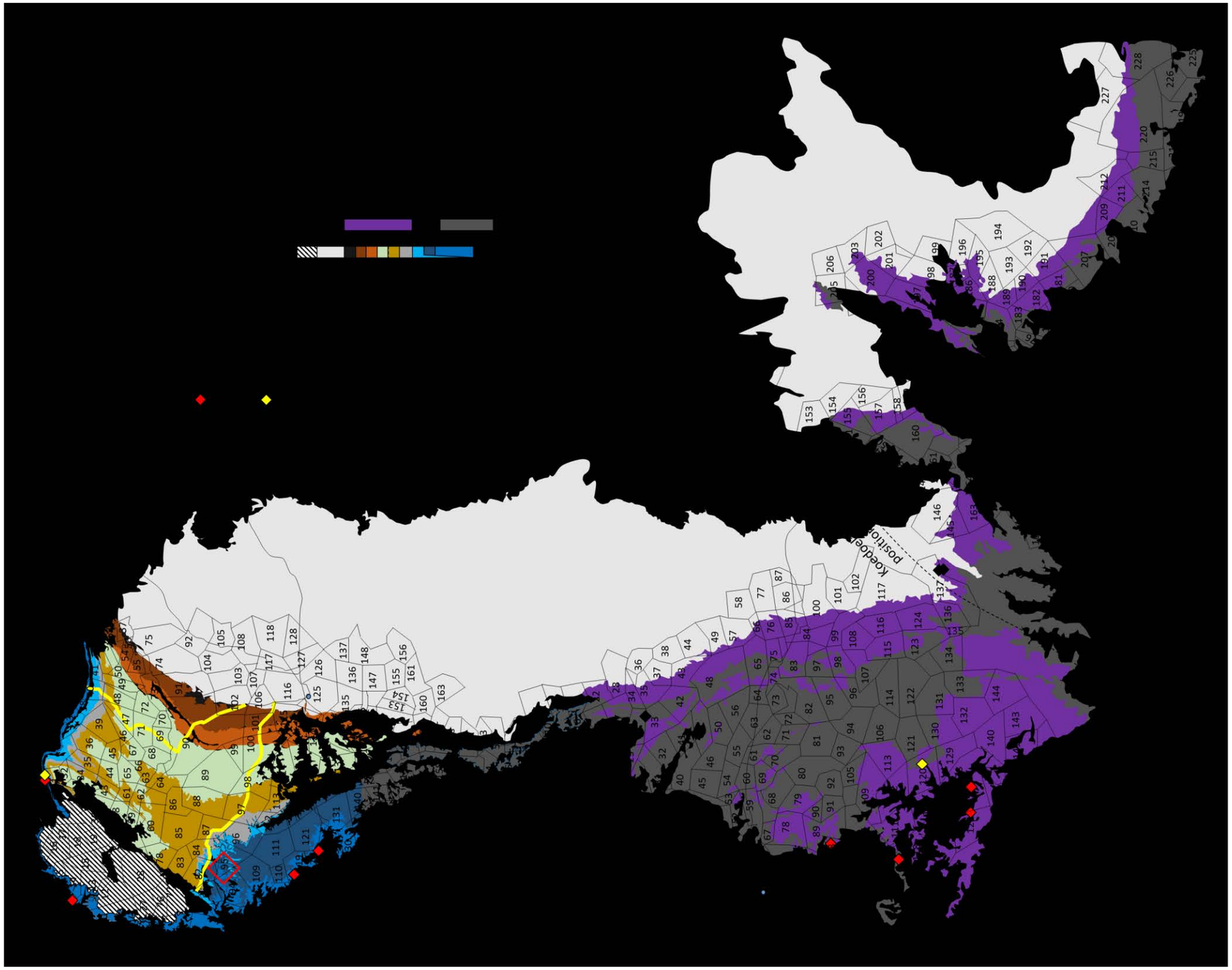

APPENDIX D: FOSSIL KEY AND OCCURRENCE CATALOGUE

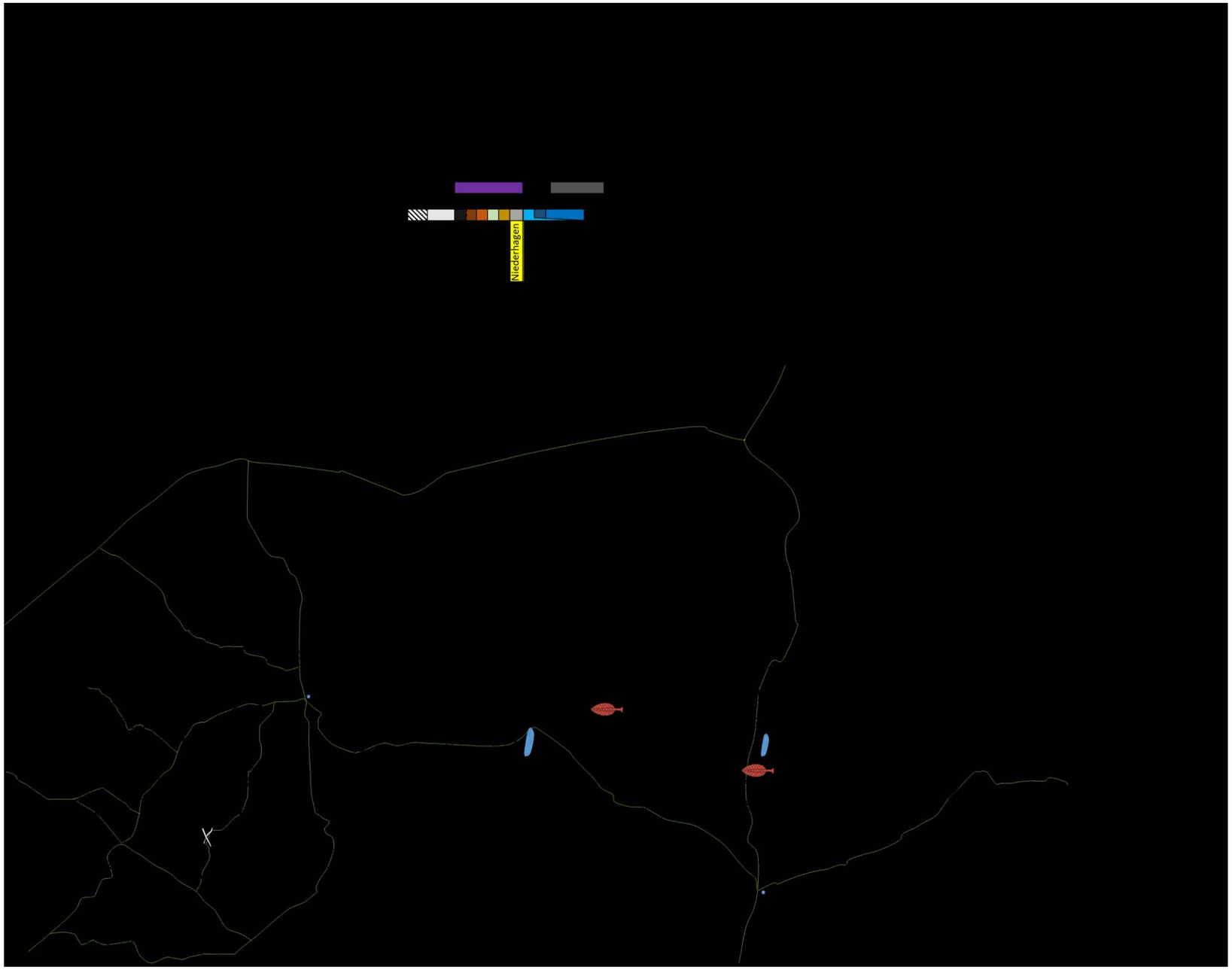
Niederhagen

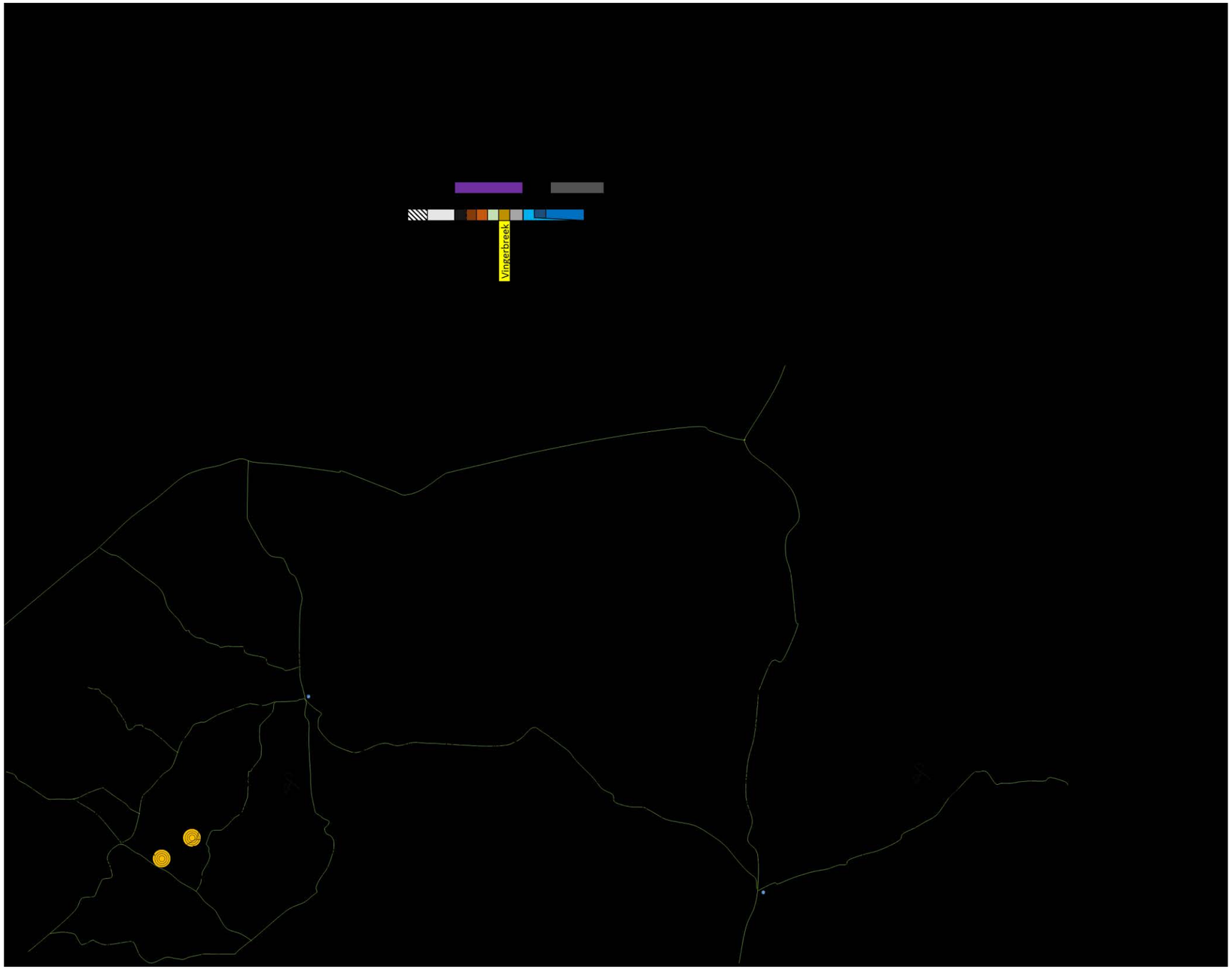
Vingerbreek

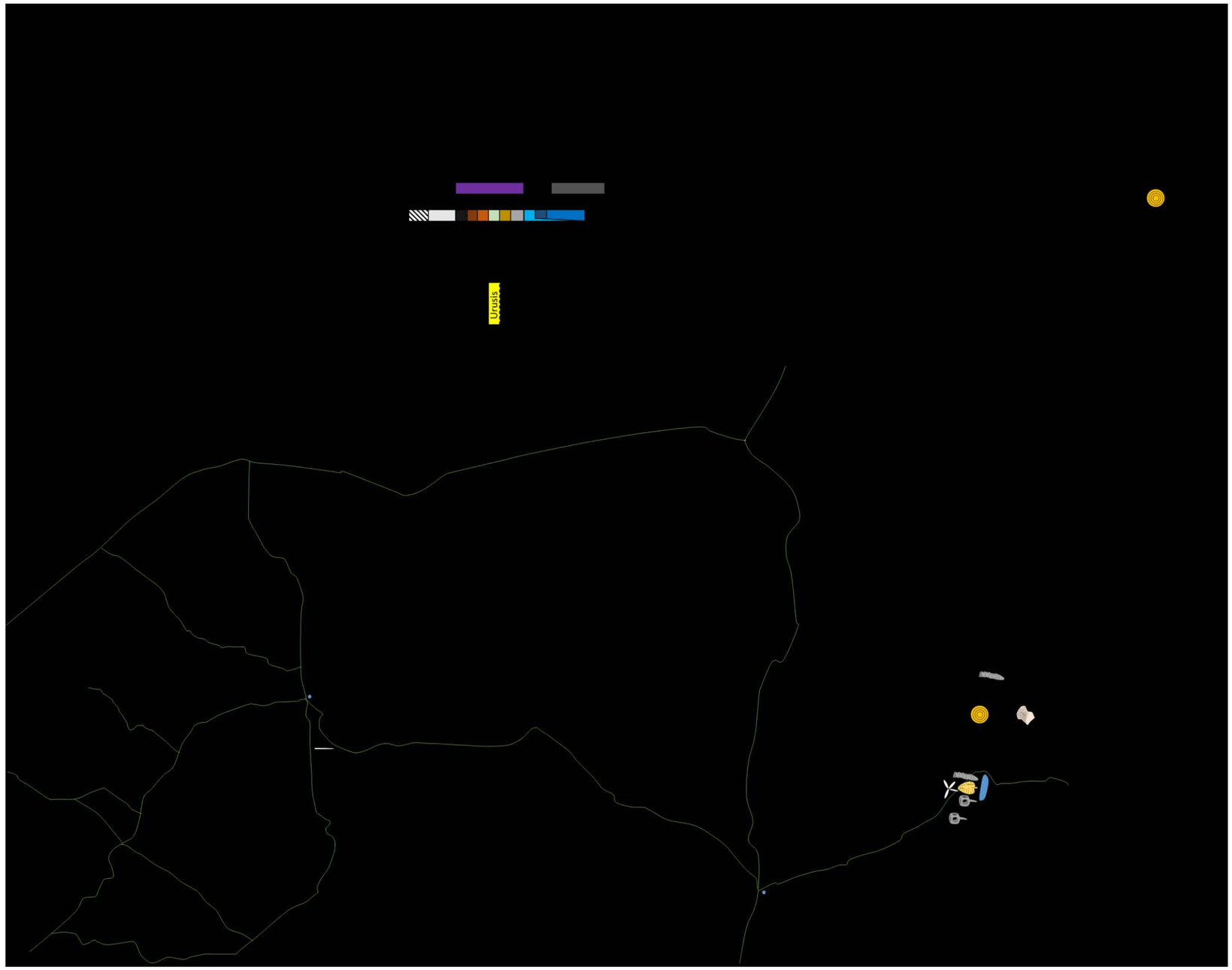
Urusis


Formation
Member
WITPUTS SUBBASIN
ZARIS SUBBASIN
Member
Formation
Naukluft Nappe Complex
Fish River Subgroup
Schwarz -rand Subgroup
Kulbis Subgroup
Vergesig
Nomtsas
Urusis
Nudaus
Niep
Krevrivier
Vingerbrook
Niederhagen
Zaris
Dabis
Urikos
Hoogland
Omkyk
Kanies
Nomtsas
Spitskop
Feldschuhorn
Huns
Naseep
Urusis
Nudaus
Zaris
Dabis
Urikos
ABSENT
Mooifontein
Aar
Kliphoek
Mara
Kanies
N
Auas
Osis

APPENDIX D: FOSSIL KEY AND OCCURRENCE CATALOGUE

Appendix E

Contribution to scientific publications

The following list documents my contributions to peer-reviewed scientific publications to date. A short description is included detailing how the information in these publications relate to the work presented in this thesis. These are ordered by publication date beginning with most recent.

Wood R., Liu A.G., **Bowyer F.**, Wilby P.R., Dunn F.S., Kenchington C.G., Hoyal Cuthill J.F., Mitchell E.G., and Penny A. (*in prep*) The rise of early metazoan ecosystems: challenging the 'Cambrian Explosion'.

> **Contribution**: I compiled carbon isotope data and section information for construction of the composite figure presented in Figure 1.1 of this thesis. I constructed fossil symbols and dioramas to represent various palaeoenvironments (Appendix D and Figure 6.1). Three of the dioramas depicted in Figure 6.1 (a, d and e) show a schematic representation of both palaeoecological and palaeoredox association garnered from compiled redox data presented in Chapter 2 and Bowyer et al. (2017). Figure 6.2 was jointly constructed with other co-authors. I have also written the geochemical discussion section of this paper and helped edit the manuscript.

Wood R., **Bowyer F.**, Penny A.M. and Poulton S.W. (2018) Did anoxia terminate Ediacaran benthic communities? Evidence from early diagenesis. ***Precambrian Research***, Vol. 313, pp. 134-147.

https://doi.org/10.1016/j.precamres.2018.05.011

> **Contribution**: I performed the Alizarin red thin section staining, transmitted light and cathodoluminescence microscope analyses and electronprobe microanalyses for which data are provided in this paper. I also constructed the figures, discussed the data and helped devise the paragenetic cement sequence and model for dolomite genesis and helped write and edit the manuscript. The findings of this paper are presented in Chapter 4.

Bowyer F., Wood R.A., and Poulton S.W. (2017) Controls on the evolution of Ediacaran metazoan ecosystems: A redox perspective, ***Geobiology***, Vol. 15, Issue 4, pp. 516-551.

https://doi.org/10.1111/gbi.12232

> **Contribution**: I performed the iron speciation analyses for which some of the Nama Group data are presented and I compiled the remaining published iron speciation data. I also compiled the sequence stratigraphic information and constructed the figures for each palaeoenvironment. The findings of this paper constitute the majority of Chapters 1 and 2, however some sections have been altered for this thesis after new data and information. Particularly, Figure 2.2 now incorporates numerous additional sections for which data have become available post-publication (e.g. Hammarlund et al., 2017). The chronostratigraphic position of the Arroyo del Soldado Group is also reconsidered in this thesis after findings presented in Aubet et al. (2014) and Pecoits et al. (2016) (see Section 2.2.5 and updated Figure 2.4c).

Tostevin, R., He, T., Turchyn, A.V., Wood, R.A., Penny, A.M., **Bowyer, F.**, Antler, G., Shields, G.A. (2017) Constraints on the late Ediacaran sulfur cycle from carbonate associated sulfate, ***Precambrian Research***, Vol. 290, pp. 113-125.

https://doi.org/10.1016/j.precamres.2017.01.004

Contribution: I helped collect samples for $\delta^{34}S_{CAS}$ analysis at the Zebra River Farm sections on a field excursion to the Nama Group in December 2013. I also helped edit the manuscript and construct figures. The corresponding data are not presented in this thesis but the findings are discussed briefly in Chapter 2 with respect to superheavy pyrite in the Nama Group.

Wood, R.A., Curtis, A., Penny, A., Zhuravlev, A.Y., Curtis-Walcott, S., Iipinge, S., and **Bowyer, F.** (2017) Flexible and responsive growth strategy of the Ediacaran skeletal *Cloudina* from the Nama Group, Namibia, ***Geology***, Vol. 45, Issue 3, pp. 259-262.

https://doi.org/10.1130/G38807.1

Contribution: I helped collect the palaeoecological data presented in this study during a field excursion to the Nama Group in 2016. The findings of this paper have contributed significantly to the integrated ecological and palaeoredox model of the Nama Group outlined in Chapter 3.

Tostevin R., Wood R.A., Shields G.A., Poulton S.W., Guilbaud R., **Bowyer F.**, Penny A.M., He, T., Curtis A., Hoffman K.-H., and Clarkson M.O. (2016) Low oxygen waters limited habitable space for early animals, ***Nature Communications***, Vol. 7, No. 12818

https://doi.org/10.1038/ncomms12818

Contribution: I helped collect samples for Ce/Ce* analyses during a field excursion to the Nama Group in December 2013. I also helped edit the manuscript. The findings of this study are an integral component of the palaeoredox model proposed for the Nama Group outlined in Chapter 3.

Penny A.M., Wood R.A., Zhuravlev A.Y., Curtis A., **Bowyer F.**, and Tostevin R. (2017) Intraspecific variation in an Ediacaran skeletal metazoan: *Namacalathus* from the Nama Group, Namibia, ***Geobiology***, Vol. 15, Issue 1, pp. 81-93.

https://doi.org/10.1111/gbi.12205

Contribution: I helped collect palaeoecological data of *Namacalathus* distribution during field excursions to the Nama Group in 2013 and 2016. I aided in the geochemical discussion section of this paper. The ecological distribution of *Namacalathus* was likely partly restricted by local palaeoredox stability and the fossil distribution is another integral aspect of the palaeoenvironmental reconstruction of the Nama Group outlined in Chapter 3.

Clarkson M.O., Wood R.A., Poulton S.W., Richoz S., Newton R.J., Kasemann S.A., **Bowyer F.**, and Krystyn, L. (2016) Dynamic anoxic ferruginous conditions during the end-Permian mass extinction and recovery, ***Nature Communications***, Vol. 7, No. 12236.

https://doi.org/10.1038/ncomms12236

Contribution: I analysed archived total digestion solutions to provide major element data via ICP-OES and provided feedback during manuscript preparation.

Wood R.A., Poulton S.W., Prave A.R., Hoffmann K.-H., Clarkson M.O., Guilbaud R., Lyne J.W., Tostevin R., **Bowyer F.**, Penny A.M., Curtis A., and Kasemann S.A. (2015) Dynamic redox conditions control late Ediacaran metazoan ecosystems in the Nama Group, Namibia, ***Precambrian Research***, Vol. 261, pp. 252-271.

https://doi.org/10.1016/j.precamres.2015.02.004

Contribution: I collected samples during a field excursion to the Nama Group in 2013 and performed all aspects of the iron speciation procedure for Arasab, Grens, Pinnacle Reefs and Swartpunt Farm sections. I also helped interpret the regional palaeoredox record and write the manuscript. This study has formed the backbone to all subsequent Nama Group palaeoredox investigations outlined in Chapter 2 (Section 2.2.6) and Chapters 3 and 4.

Penny A.M., Wood R., Curtis A., **Bowyer F.**, Tostevin R. and Hoffman K.-H. (2014) Ediacaran metazoan reefs from the Nama Group, Namibia, ***Science***, Vol. 344, Issue 6191, pp. 1504-1506.

https://doi.org/10.1126/science.1253393

Contribution: I aided in-field interpretation of the Driedoornvlakte *Cloudina* reef outcrop during a field excursion to the Nama Group in 2013 and provided feedback during manuscript preparation.